



VYSOKÉ UČENÍ TECHNICKÉ V BRNĚ

Fakulta chemická

Habilitační práce v oboru

Chemie a technologie ochrany životního prostředí

MOŽNOSTI LASEROVÉ ABLACE S HMOTNOSTNÍ SPEKTROMETRIÍ INDUKČNĚ VÁZANÉHO PLAZMATU V PRVKOVÉ ANALÝZE A ZOBRAZOVÁNÍ POVRCHU PEVNÝCH LÁTEK

Mgr. Michaela Vašinová Galiová, Ph.D.

Brno 2019

Ráda bych na tomto místě poděkovala všem kolegům a studentům, se kterými jsem měla možnost spolupracovat.

OBSAH

ÚVOD	4
CÍLE HABILITAČNÍ PRÁCE	6
SEZNAM KOMENTOVANÝCH PRACÍ	7
LASEROVÁ ABLACE S HMOTNOSTNÍ SPEKTROMETRIÍ INDUKČNĚ VÁZANÉHO PLAZMATU	10
VÝZNAM LASEROVÉ ABLACE ICP HMOTNOSTNÍ SPEKTROMETRIE	12
2D ZOBRAZOVÁNÍ POVRCHU POMOCÍ LA-ICP-MS	15
Laserová ablace ICP hmotnostní spektrometrie v analýze biominerálů	17
a) Jednofázová analýza – apatitová fáze zubů a kostí	17
b) Jednofázová analýza – karbonátová fáze otolitů	23
c) Vícefázová analýza biominerálů	25
Laserová ablace ICP hmotnostní spektrometrie v analýze měkkých tkání	30
Laserová ablace ICP hmotnostní spektrometrie a její uplatnění v geologii	45
ZÁVĚR	54
REFERENCE	55
PŘÍLOHY	60

ÚVOD

Předložená habilitační práce je věnována metodě laserové ablaci ve spojení s hmotnostní spektrometrií indukčně vázaného plazmatu známou pod zkratkou LA-ICP-MS a ukazuje její možnosti a využití a také limitace v analýze pevných materiálů. Za posledních více než 10 let jsem odkryla širokou působnost této metody, kterou rozhodně není možné považovat za rutinní. V zásadě se tato analytická metoda dá použít pro analýzu téměř jakéhokoli materiálu v základním i aplikačním výzkumu. Nicméně její využití je především v multidisciplinárním výzkumu a klade velký důraz na pochopení mechanismů v nejrůznějších oborech a osvojení si pojmu typické pro danou oblast výzkumu.

Základem této metody je ICP hmotnostní spektrometrie, která slouží k analýze kapalných vzorků a je hojně využívána ke stanovení průměrného složení. Indukčně vázané plazma, vedle dalších dějů, zajišťuje ionizaci aerosolu. Následně jsou ionty děleny na základě jejich poměru hmotnost / náboj. Hmotnostní spektrometr tedy rozlišuje izotopy téhož prvku, a tak vedle analýzy průměrného složení umožňuje stanovení izotopových poměrů. Ionizační účinnost ICP je natolik vysoká, že dokáže ionizovat téměř všechny prvky periodického systému a vyznačuje se širokým lineálním dynamickým rozsahem. Je vhodná ke stanovení kovů i nekovů a je využívána především v ultrastopové analýze díky vysoké citlivosti a nízkým LOD. Všechny tyto výhody předurčují metodu pro její využití téměř ve všech přírodních vědách.

Její spojení s laserovou ablaci jako vzorkovacího systému, které nastalo o dva roky později, kdy byl uveden první komerčně dostupný ICP hmotnostní spektrometr, otevřelo novou éru výzkumu. Aplikace metody jsou silně spjaty s vhodnou volbou ICP-MS hmotnostních spektrometrů, přesněji analyzátorů, které se odlišují konstrukcí a tím rychlosí analýzy, citlivostí, LOD, rozlišením, precizností a pořizovacími náklady. Podobně by bylo možné definovat rozdíly při aplikaci různých ablačních systémů z hlediska délky pulzu, vlnové délky, hustoty zářivé energie, frekvence a velikosti laserového svazku.

Ač má LA-ICP-MS nesporné výhody ve srovnání s jinými analytickými technikami, její využití s sebou nese celou řadu negativních efektů, které musejí být řešeny. Mezi nejvíce diskutované patří matriční efekty, frakcionace aerosolu při samotné laserové abaci, transportu nebo v ICP, výskyt polyatomických interferencí a hmotnostní diskriminace.

Přes uvedené nevýhody našla LA-ICP-MS metoda široké uplatnění ve vědních oborech jako jsou environmetální chemie, medicína, biologie, geochemie, forenzní chemie, aj. a to nejen pro stanovení obsahů specifických oblastí vzorku, ale také sledování prvkové distribuce v μm měřítka a stanovení izotopových poměrů.

CÍLE HABILITAČNÍ PRÁCE

Cílem je prezentovat **možnosti** a zároveň **limity** a **překážky** při využití laserové ablaci hmotnostní spektrometrie indukčně vázaného plazmatu v analýze různorodých materiálů. Metoda byla aplikována ve studiu složení individuálních bodů a stejně tak i při sledování prvkové distribuce v jednofázových i vícefázových. Materiály pro studium byly vybírány s ohledem na možný přínos do specifických vědních oborů – archeologie, paleontologie, medicína, biologie, životní prostředí, geologie a geochemie.

Habilitační práce je rozdělena do tří hlavních částí podle typu studovaného materiálu. První část práce je věnována využití **LA-ICP-MS v analýze biominerálů**, následuje **výzkum v oblasti měkkých tkání**, a nakonec je práce zakončena **aplikacemi v geologii**.

Na první pohled by se mohlo zdát, že se jedná pouze o aplikaci metody samotné, ale každá problematika s sebou nese specifické problémy ohledně 1) přípravy vzorku, 2) řešení interferencí, 3) kvantifikace, 4) studia interakce laserového svazku se vzorkem – souvislost mezi matricí a mírou absorpce, souvislosti mezi jednotlivými ablačními parametry a spolehlivostí výsledků a 5) výběru vhodného ablačního módu vs. rozlišení.

Během své více jak desetileté práce s metodou LA-ICP-MS jsem měla možnost prostudovat výhody a nevýhody všech typů hmotnostních spektrometrů – kvadrupolového vybaveného kolizní reakční celou, kvadrupolového vybaveného dynamickou reakční celou i trojitého kvadrupolu, ICP-MS s analyzátorem doby letu, ICP-MS s dvojí fokusací i s multikolektorovou detekcí, a účelově je použít pro přesně dané cíle výzkumu. Stejně tak jsem pracovala i s různými nanosekundovými ablačními systémy.

Navíc díky multidisciplináritě této habilitační práce bylo nutné si osvojit problematiku jiného oboru a metod, které byly využívány pro ověřování výsledků výzkumu s využitím LA-ICP-MS.

Ke splnění cíle bylo vybráno 19 prací, z nichž jedna představuje recenzovanou kapitolu v knize. Pro úplnost jsou uváděny i bakalářské a diplomové práce studentů, které byly vypracovány pod mým vedením, protože dokreslují řešenou problematiku, a také část nepublikovaných výsledků, které ukazují směr mého výzkumu před nástupem na mateřskou dovolenou. Práce vznikaly v souladu s probíhajícím výzkumem na Ústavu chemie PřF MU, aby bylo možné vysvětlit pozorované diskrepance. Vzhledem k jejich potenciálu jsou stejně jako část nepublikovaných výsledků stále ještě předmětem výzkumu a jsou z nich připravovány publikace.

SEZNAM KOMENTOVANÝCH PRACÍ

- I. **M. Galiova**, J. Kaiser, F. J. Fortes, K. Novotny, R. Malina, L. Prokes, A. Hrdlicka, T. Vaculovic, M. Nyvltova Fisakova, J. Svoboda, V. Kanicky, J. J. Laserna: Multielemental analysis of prehistoric animal teeth by Laser-Induced Breakdown Spectroscopy and Laser Ablation Inductively Coupled Plasma Mass Spectrometry, APPL OPTICS 49 (2010) 191-199.
- II. **M. Vasinova Galiova**, M. Nyvltova Fisaková, J. Kynicky, L. Prokes, H. Neff, A.Z. Mason, P. Gadas, J. Kosler, V. Kanicky: Elemental mapping in fossil tooth root section of Ursus arctos by laser ablation inductively coupled plasma mass spectrometry (LA-ICP-MS), TALANTA 105 (2013) 235-243.
- III. **M. Vasinova Galiova**, R. Copjakova, R. Skoda, K. Stepankova, M. Vankova, J. Kuta, L. Prokes, J. Kynicky, V. Kanicky: 2D elemental mapping of sections of human kidney stones using laser ablation-inductively coupled plasma-mass spectrometry: Possibilities and limitations, SPECTROCHIM ACTA B 100 (2014) 105115.
- IV. **M. Vasinova Galiova**, K. Stepankova, R. Copjakova, J. Kuta, L. Prokes, J. Kynicky and V. Kanicky: Preparation and testing of phosphate, oxalate and uric acid matrix-matched standards for accurate quantification of 2D elemental distribution in kidney stones sections using 213 nm nanosecond laser ablation inductively coupled plasma mass spectrometry, J ANAL ATOM SPECTROM, 30 (2015) 1356-1368.
- V. K. Stepankova, K. Novotný, **M. Vasinova Galiova**, V. Kanicky, J. Kaiser, D. W. Hann: Laser ablation methods for analysis of urinary calculi: Comparison study based on calibration pellets, SPECTROCHIM ACTA B 81 (2013) 43-49.
- VI. K. Proksova, K. Novotny, **M. Galiova**, T. Vaculovic, J. Kuta, M. Novackova, V. Kanicky: Study of Elemental Distribution in Urinary Stones by Laser Ablation Inductively Coupled Plasma Mass Spectrometry, CHEM LISTY 106 (2012) 229-235.
- VII. K. Proksova, K. K. Novotny, **M. Galiova**, T. Vaculovic, V. Kanicky: Study of distribution of elements in urinary stones using laser ablation ICP-MS spectrometry. CHEM LISTY 105 (2011) S58-S61.
- VIII. S. Turkova, **M. Vasinova Galiova**, K. Stulova, Z. Cadkova, J. Szakova, V. Otruba, V. Kanicky: Study of metal accumulation in tapeworm section using laser ablation-inductively coupled plasma-mass spectrometry (LA-ICP-MS), MICROCHEM J 133 (2017) 380-390.

- IX. **M. Galiova**, J. Kaiser, K. Novotny, M. Hartl, R. Kizek, P. Babula: Utilization of Laser-Assisted Analytical Methods for Monitoring of Lead and Nutrition Elements Distribution in Fresh and Dried Capsicum annuum L. Leaves, MICROSC RES TECHNIQ 74 (2011) 845-852.
- X. **M. Vasinova Galiova**, J. Szakova, L. Prokes, Z. Cadkova, P. Coufalik, V. Kanicky, V. Otruba, P. Tlustos: Variability of trace element distribution in *Noccaea* spp., *Arabidopsis* spp., and *Thlaspi arvense* leaves: the role of plant species and element accumulation ability, ENVIRONMENTAL MONITORING AND ASSESSMENT 191 (2019).
- XI. **M. Vasinova Galiova**, J. Havlis, V. Kanicky: Laser Ablation Inductively Coupled Plasma Mass Spectrometry as a Tool in Biological Sciences, in Natural Products Analysis: Instrumentation, Methods, and Applications, eds. Vladimír Havlíček and Jaroslav Spížek USA: Wiley, 2014, 313-348, ISBN 978-1-118-46661-2.
- XII. K. Breiter, M. Hlozkova, Z. Korbelova, **M. Vasinova Galiova**: Diversity of lithium mica compositions in mineralized granite–greisen system: Cinovec Li-Sn-W deposit, Erzgebirge, Ore Geology Reviews 106 (2019) 12-27.
- XIII. K. Breiter, J. Durisova, T. Hrstka, Z. Korbelova, **M. Vasinova Galiova**, A. Mueller, B. Simons, R. K. Shail, B. J. Williamson, J.A. Davies: The transition from granite to banded aplite-pegmatite sheet complexes: An example from Megiliggar Rocks, Tregonning topaz granite, Cornwall, LITHOS 302 (2018) 370-388.
- XIV. M. Novak, J. Cicha, R. Copjakova, R. Skoda, **M. Vasinova Galiova**: Milarite-group minerals from the NYF pegmatite Velka skala, Pisek district, Czech Republic: sole carriers of Be from the magmatic to hydrothermal stage, EUR J MINER 29 (2017) 755-766.
- XV. R. Copjakova, R. Skoda, **M. Vasinova Galiova**, M. Novak, J. Cempirek: Sc- and REE-rich tourmaline replaced by Sc-rich REE-bearing epidote-group mineral from the mixed (NYF + LCT) Kracovice pegmatite (Moldanubian Zone, Czech Republic), AM MINERAL 100 (2015) 1434-1451.
- XVI. R. Skoda, J. Plasil, R. Copjakova, M. Novak, E. Jonsson, **M. Vasinova Galiova**, D. Holtstam: Gadolinite-(Nd), a new member of the gadolinite supergroup from Fe-REE deposits of Bastnas-type, Sweden, MINERAL MAG 82 (2018) S133-S145.
- XVII. J. Cempirek, E.S. Grew, A.R. Kampf, C. Ma, M. Novak, P. Gadas, R. Skoda, **M. Vasinova Galiova**, F. Pezzotta, L.A. Groat, S.V. Krivovichev: Vranaite, ideally

- $\text{Al}_{16}\text{B}_4\text{Si}_4\text{O}_{38}$, a new mineral related to boralsilite, $\text{Al}_{16}\text{B}_6\text{Si}_2\text{O}_{37}$, from the Manjaka pegmatite, Sahatany Valley, Madagascar, AM MINERAL 101 (2016) 2108-2117.
- XVIII. J. Loun, M. Novak, J. Cempirek, R. Skoda, **M. Vasinova Galiova**, L. Prokes, M. Dosbaba, R. Copjakova: Geochemistry and secondary alterations of microlite from eluvial deposits in the Numbi mining area, South Kivu, Democratic Republic of the Congo, Can Mineral 56 (2018) 203-220.
- XIX. L. Prokes, **M. Vasinova Galiova**, S. Huskova, T. Vaculovic, A. Hrdlicka, A.Z. Mason, H. Neff, A. Prichystal, V. Kanicky: Laser microsampling and multivariate methods in provenance studies of obsidian artefacts, CHEM PAP 69 (2015) 761-778.

LASEROVÁ ABLACE S HMOTNOSTNÍ SPEKTROMETRIÍ INDUKČNĚ VÁZANÉHO PLAZMATU

Samotná hmotnostní spektrometrie je známa více jak 100 let. Historicky je její vývoj propojen s rozvojem atomové fyziky, která přispěla k potvrzení hypotézy o atomové struktuře hmoty. Je spojena se jmény J. J. Thomson (fyzika, 1906), W. Wien (fyzika, 1911), F. W. Aston (chemie, 1922), L. Paul (chemie, 1954), J. B. Fenn a K. Tanaka (chemie, 2002), R. F. Curl, H. W. Kroto a R. E. Smalley (chemie, 1996), kteří byli oceněni Nobelovou cenou a ve svém výzkumu využívali metodu hmotnostní spektrometrie nebo přispěli k jejímu rozvoji. Přes objevení elektronu a vytvoření modelu atomu, studium ionizovaného plynu a následně konstrukce prvního hmotnostního spektrografova a prokázání existenci izotopů není tedy pochyb, že vývoj MS prošel velmi dlouhou cestou, než instrumentace a s ní spojené možnosti aplikace dostaly nynější podobu.

Za otce hmotnostní spektrometrie je považován Thomson, který prokázal, že izotopy mají sice stejně chemické chování, ale liší se svou hmotností a také zavedl pojem „hmotnostní spektrum“ (1920). Od konstrukce prvního parabolického hmotnostního spektrografova následoval vývoj prvního hmotnostního spektrometru s 180° magnetickým sektorovým hmotnostním analyzátem (**Dempster**, 1918). Následovala konstrukce MS s dělením iontů v elektrickém a následně v magnetickém poli (**Thomson a Aston**, 1919). Aston zkonztruoval hmotnostní spektrometr umožňující elektromagnetické zaostření iontového toku a díky tomu se podařilo identifikovat 212 izotopů a byl oceněn Nobelovou cenou v roce 1922.

Další progres v instrumentaci obecně spočíval v teoretických i praktických studiích geometrie elektrického a magnetického analyzátoru, jejich vzájemného upořádání, a tedy konstrukce hmotnostního spektrometru s dvojí fokusací. Jméno **Nier** je spojováno s prvním komerčně dostupným (1942) MS s magnetickým analyzátem, který byl limitovaný požadavkem minimální energetické divergence původního iontového toku. Tento komerčně dostupný MS sehrál svou roli v projektu „Manhattan“ ve 40. letech 20. století. Díky tomu nezahálel vývoj **MS s dvojí fokusací (SF)**, který dokáže separovat i vysoce energetické iontové svazky. **Ewald** (1946) vycházel z Mattauch-Herzog geometrie ($31,8^\circ$ B a 90° E) a jeho úpravou dosáhl zvýšení rozlišení. Dodnes je tato konfigurace společně s Nier-Johnson (1952, 90° B a 90° E) využívána v moderních hmotnostních spektrometrech. Poslední geometrie je v provedení jak E-B, tak i B-E. Moderní hmotnostní spektrometry s dvojím zaostřením dosahují rozlišení až 20 000.

Mezi analyzátorysty dostupné pro anorganickou MS analýzu vedle MS s dvojí fokusací patří také kvadrupolový analyzátor (Q) a analyzátor doby letu (TOF).

Kvadrupolový analyzátor (Paul a Stein, 1953) je univerzálním hmotnostním filtrem, vyznačuje se vysokou stabilitou, vysokou rychlostí analýzy a širokým dynamickém rozsahem. Také díky nízkým pořizovacím nákladům je nejčastějším vybavením anorganických hmotnostních laboratoří. Jeho nevýhodou je dosažení maximálně nízkého rozlišení ($m/\Delta m < 400$), které v případě některých aplikací či analýz složitých matric nemusí být dostačující a výsledky jsou pak zatíženy spektrálními interferencemi. **Analyzátor doby letu** (Cameron a Eggers, 1948) nabízí velmi rychlou analýzu. Díky principu dělení jsou záznamy spekter simultánním pro celý hmotnostní rozsah a dosahují rozlišení až 10 000.

V oblasti vývoje anorganické hmotnostní spektrometrie je kladen důraz na spojení s vhodnou ionizační technikou zajišťující produkci dostatečně intenzivního konstantního toku iontů. Takovýto iontový zdroj musí zajistit v nejjednodušším případě atomizaci a ionizaci u plynných látek a u kapalných vzorků navíc desolvataci. Velký progres zaznamenala anorganická hmotnostní spektrometrie v době, kdy bylo popsáno indukčně vázané plazma (Fassel a Greenfield, 1964). První komerčně dostupné ICP-MS s kvadrupolovým analyzátem je datováno roku 1983. Následně byl uveden SF-ICP-MS (1989). SF-ICP-MS umožňuje dělení iontů s rozlišením $m/\Delta m = 300\text{--}20\,000$, rychlé stanovení prvků v ultrastopovém množství a měření izotopových poměrů. Jeho nevýhodou jsou však vyšší pořizovací náklady a také pokles citlivosti a tím dosažení nižší preciznosti izotopových poměrů při práci ve vyšším rozlišení. Za účelem minimalizace interferencí prošel dalším vývojem i Q-ICP-MS, a to zařazením kolizní-reakční cely a dynamické reakční cely. Zvýšení preciznosti stanovení izotopových poměrů díky simultánnímu statickému měření umožňuje **ICP-MS s dvojí fokusací a multikolektorovou detekcí** (MC-ICP-MS). Má však velmi vysoké pořizovací náklady.

Vzorkování pevných materiálů vyžaduje ještě předřazení **laserového ablačního systému** k ICP-MS. První spojení proběhlo již v roce 1985 a od roku 1990 byly komerčně dostupné první ablační systémy. Vývoj ablačních systémů je spojen s délkou pulzu laserového záření, jeho vlnovou délkou, ale také s možnostmi volby průměru laserového svazku, maximální hodnoty hustoty zářivé energie a frekvence. Kladen je důraz také na design a objem ablačních cel a na další přídavná zařízení, která umožňují dosáhnout stabilního signálu při velmi malém množství uvolněného materiálu.

VÝZNAM LASEROVÉ ABLACE ICP HMOTNOSTNÍ SPEKTROMETRIE

Analytická chemie čítá velký počet metod, které lze využít ke kvalitativní i kvantitativní analýze. Liší se základními principy, instrumentací, cenou a také použitelností v různých vědních oborech. Obecně lze říci, že předmětem studia bývá stanovení průměrného složení vzorku, ovšem výběr vhodné metody závisí na skupenství zkoumaného materiálu. Většina metod pracuje standardně v režimu analýzy kapalných roztoků, a tak analýza prvkového složení pevných látek vyžaduje jejich rozklad. Tento krok zvyšuje náklady na samotnou analýzu prostřednictvím chemikálií a je samozřejmě časově náročný. Jako další negativní efekt je zvýšení rizika kontaminace, které je zvláště kritické u ultrastopové analýzy, a také možnost neúplného rozložení chemicky odolného materiálu. Při splnění všech potřebných podmínek v kroku přípravy vzorku je výběr metody dán i obsahem prvků. Není třeba volit vysoce citlivou techniku, jestliže předmětem studia jsou procentuální obsahy. Problémem spíše bývá opak, kdy obsahy prvků dosahují hodnot $\mu\text{g kg}^{-1}$ a níže. V takovém případě je nutné přihlédnout k limitům detekce metody.

Standardním vybavení analytických laboratoří zabývajících se analýzou anorganických látek bývá nejčastěji kombinace atomové absorpční spektrometrie (AAS), optické emisní spektrometrie indukčně vázaného plazmatu (ICP-OES) a ICP-MS metoda, tak aby byl pokryt celý koncentrační rozsah. Výhodou je i jejich využití v analýze pevných látek. V případě AAS ve spojení s grafitovou kyvetou a v případě ICP-OES nebo ICP-MS ve spojení s laserovou ablací. Metody anorganické analýzy pevných látek můžeme porovnat stejným způsobem jako metody roztokové, a to z hlediska jejich citlivosti, nároků na přípravu vzorku, rozsahu měřených prvků a v neposlední řadě i z hlediska pořizovacích a provozních nákladů nebo jejich aplikovatelnosti.

Obecně jde vývoj analytických metod kupředu a postupně jsou jednotlivé parametry metod zlepšovány, což vede ke zvyšování citlivosti a použitelnosti. Tento aspekt je z pohledu analytického chemika velmi pozitivní, na druhou stranu s sebou nese vyšší požadavky na dokonalou znalost příslušné analytické techniky a také samotné instrumentace, která díky vývoji vyžaduje opatrný přístup k aplikacím a často omezení v rutinní analýze a otevírá široké pole působnosti ve výzkumu.

Hmotnostní spektrometrie indukčně vázaného plazmatu patří mezi velmi citlivé analytické metody. První výhody této metody plynou právě z ICP ionizačního zdroje,

který umožňuje stanovení téměř všech prvků (kovů i celou řadu nekovů) periodické soustavy s výjimkou prvků, které mají ionizační energii vyšší, než má samotný plazmový plyn. Nejčastějším ionizačním plynem bývá argon, a tak znemožňuje stanovení samotného argonu a také He a F. Citlivost plyne z účinnosti ionizace vzorku, která dosahuje téměř 100 %, ale tento fakt závisí na dané matrici. Díky tomu je metoda často aplikována ve stopové a ultrastopové analýze s LOD v řádech ppt. Na druhou stranu má i velmi široký dynamický rozsah 0,0005–100 µg l⁻¹.

Doposud byla tato metoda zmiňována pouze v souvislosti se stanovením průměrného složení vzorku, ale právě díky jejímu principu, tzn. analýze na základě měření intenzity iontového toku se specifickým poměrem hmota / náboj (m / z), je využívána také ke stanovení izotopových poměrů. Navíc i aplikace izotopového zřed'ování, jako kvantitativní metody, předurčuje tuto metodu k certifikaci standardních referenčních materiálů.

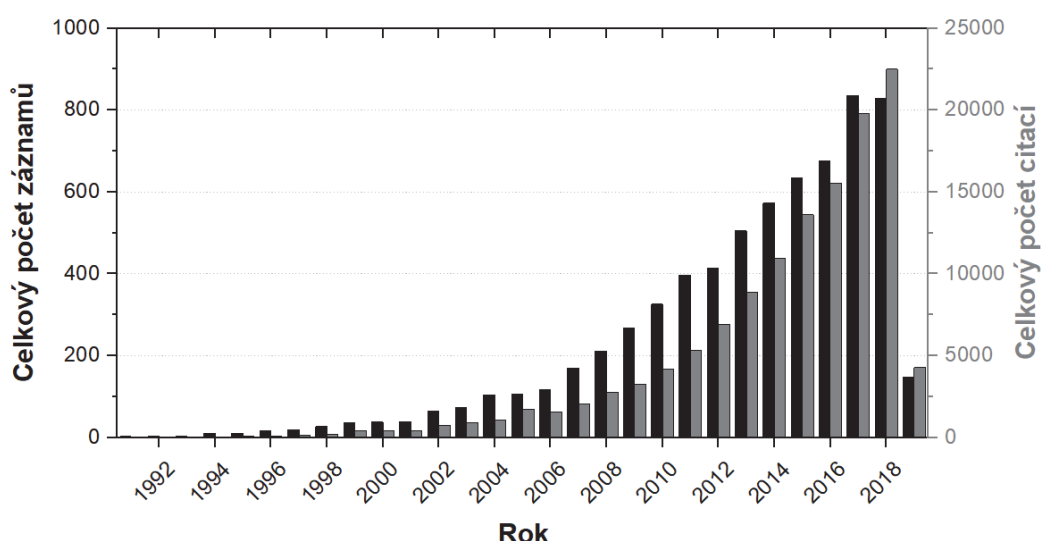
Samotná ICP-MS technika je využívána v analýze kapalných vzorků, ale jejím spojením s vhodným vzorkovacím systémem, kterým je právě laserové záření, umožňuje také analýzu pevných materiálů. Přímá analýza pevného materiálu eliminuje již zmíněná negativa chemického rozkladu, ale navíc poskytuje možnosti analýzy nejen průměrného složení, ale také specifických oblastí vzorku. Nabízí stanovení asociace prvků a využití metody také jako zobrazovací techniky, studium struktury nebo studium vrstevnatých materiálů a izotopovou analýzu. Ve srovnání s jinými metodami nevyžaduje, aby materiál podrobený studiu disponoval specifickými vlastnostmi, jako např. vodivost povrchu jako je tomu v případě elektronové mikroskopie. Díky zaostření laserového svazku na velmi malou plochu vzorku (řádově několik µm) dosahuje metoda i vysokého laterálního rozlišení s minimálním množstvím vzorku potřebného k analýze. Po interakci zanechává laserový paprsek na povrchu ablační stopu, která je však velmi malá, a díky tomu je metoda považována za prakticky nedestruktivní.

Samotná ICP-MS technika s sebou nese svoji aplikovatelnost v celé řadě analýz a ve spojení s in-situ analýzou, možností izotopové analýzy s vysokou citlivostí a stanovení většiny prvků PSP se dostává na přední místo mezi analytickými metodami. Stejně tak její využití v nejrůznějších vědních disciplínách se značně rozšiřuje.

Využití metody roste úměrně s vývojem instrumentace přes kvadrupólové analyzátoru kombinované s dynamickou reakční celou nebo kolizní reakční celou, ICP hmotnostní spektrometry s dvojí fokusací, analyzátoru doby letu nebo multikolektorové ICP-MS vyznačující se vyšším počtem detektorů nebo specifických detektorů umožňující

plně simultánní stanovení nejen obsahu, ale také izotopového poměru skrze celé hmotnostní spektrum.

LA-ICP-MS je jednou z moderních analytických metod, která za posledních 30 let prošla velkým vývojem a expandovala do značného počtu vědních oborů. Stoupající popularitu dokazuje i Obr. 1 sestavený z dat dostupných na portálu „Web of Science“ při jednoduchém vyhledávání s klíčovým slovem „LA-ICP-MS“. Data byla získána v rozmezí let 1991-2019 a čítá celkově 6 662 publikací. Celkový počet citací je 127 984, respektive 89 815 bez autocitací. Za posledních deset let počet výstupů, jejichž výsledky a závěry jsou získány právě použitím LA-ICP-MS analytické techniky, stouplo o 25 %.



Obr. 1: Celkový počet záznamů a citací na portálu „Web of Science“ s klíčovým slovem „LA-ICP-MS“.

Tyto záznamy jsou dedikovány celkově 125 rozdílným oblastem výzkumu. Samozřejmě, že každá publikace je přiřazena k více než jednomu vědnímu oboru, ovšem nejpočetnější skupinu tvoří geologie, mineralogie, geochemie, geofyzika a jim další přidružené disciplíny. Celkově se jedná o 6 000 záznamů z celkového počtu 9 831. V první desítce se nachází právě analytická chemie s 893 záznamy, spektroskopie 633, archeologie 231, environmentální vědy 136 a antropologie 112. Druhá desítka záznamů již zasahuje do oblasti s bioaplikacemi a obecně materiálových věd a tvoří 7,8 % z celkového počtu záznamů, což je v porovnání s první desítkou (81,4 %) minoritní část.

2D ZOBRAZOVÁNÍ POVRCHU POMOCÍ LA-ICP-MS

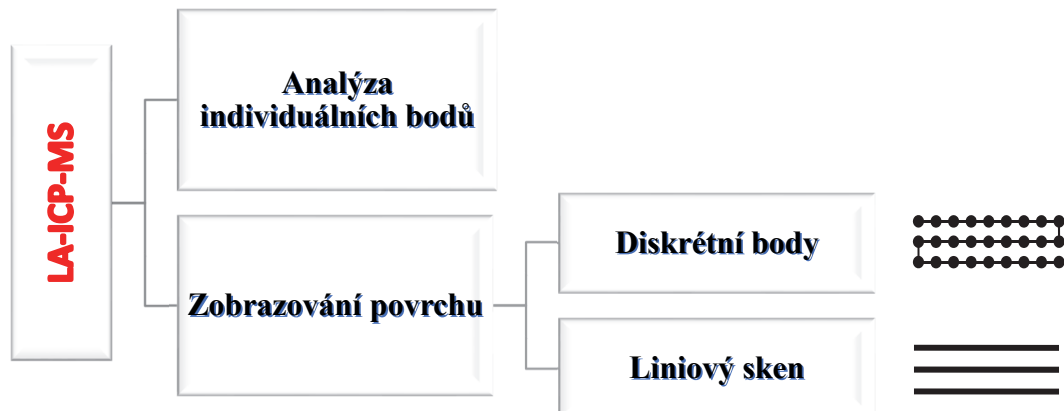
LA-ICP-MS metoda umožňuje analyzovat individuální plochy ve specifických oblastech vzorku. U většině aplikací je však využívána k zobrazení prvkové distribuce povrchů od měkkých tkání (buňky, orgány, nádorové tkáně, vlasy) přes kalcifikované tkáně (zuby, kosti, otolity, rybí šupiny, ulity) nebo různé organické matrice s obsahem anorganických prvků (dřevo, jehličí). Nabízí mapování povrchu prostřednictvím diskrétních bodů nebo liniového skenu. Tyto módy ablaci ovlivňují zejména hloubku ablační stopy a tím i distribuci velikosti uvolněných částic a laterální rozlišení. Zobrazení povrchu pomocí ablaci diskrétních bodů je ovlivněno průměrem laserového svazku a umístěním bodů v osách x a y. Výhodou tohoto módu je analýza aerosolu z přesně definovaného místa na rozdíl od liniového skenu, kdy dochází k posunu vzorku současně se vzorkováním povrchu. Při liniové ablaci je tak dosaženo menších hloubek ablační stopy, uvolnění větších částic a také horšího laterálního rozlišení. Tím může docházet k mixování signálu z různých matric heterogenního vzorku nebo smývání rozdílu v distribuci sledovaného prvku matričně homogenního povrchu. To však také závisí na dalších parametrech laserové ablaci a ICP hmotnostního spektrometru (Obr. 2).

Ze základních aspektů mapování jsou v publikacích řešena následující téma:

- Možnosti využití femtosekundové ablaci vs. nanosekundové.
- Vliv vlnové délky laserového svazku na distribuci velikosti částic a tím na kvalitu ICP-MS signálu.
- Vliv designu a velikosti ablační cely na rychlosť vymývání aerosolu a tím i vliv na laterální rozlišení.
- Vliv rychlosti analyzátoru ICP hmotnostního spektrometru na kvalitu ICP-MS signálu a preciznost výsledků.
- Kvantifikační postupy a příprava standardních materiálů.
- Vliv matice a struktury vzorku, obsahu vody aj. při interakci s laserovým svazkem.
- Citlivost metody vůči změnám chemického složení různých matric.
- Využití porovnávacích prvků pro normalizaci signálu.
- A v neposlední řadě vyhodnocení dat a vývoj softwarů pro 2D zobrazování.

Vedle těchto základních aspektů musí být řešeno také praktické využití metody LA-ICP-MS, a tedy její aplikace v různých odvětvích vědy a výzkumu. Stejně je tomu i v této

habilitační práci, kde jsou diskutovány vybrané základní aspekty společně s možností praktického uplatnění metody a získání informací důležitých pro dané odvětví výzkumu. Z tohoto důvodu jsou v každé z kapitol úvody do problematiky daného oboru.



Diskrétní body	Liniový sken	Vliv parametrů LA
Průměr laserového svazku	Průměr laserového svazku	
Vzdálenost bodů v osách x, y	Délka linie	
Doba ablace	Rychlosť posunu	Hloubka ablační stopy
Časová prodleva mezi body vs. rychlosť vymývání	Časová prodleva mezi liniemi vs. rychlosť vymývání	→ Distribuce velikosti častic Laterální rozlišení
Energie	Energie	
Frekvence	Frekvence	

Obr. 2: Schéma využití LA-ICP-MS a parametry bodové ablaci a liniového skenu a jejich vliv na ICP-MS signál.



Laserová ablace ICP hmotnostní spektrometrie v analýze biominerálů

Do poměrně početné skupiny *biominerálů* jsou obecně řazeny anorganické minerální látky produkované živými organismy. Mají různorodé chemické složení přes karbonáty, fosfáty, silikáty, oxalaláty, citráty, sulfidy, halidy, oxidy železa i mangantu a jsou spojovány také s působením bakterií a hub. I přes stejné chemické složení mohou mít biominerály rozličné fyzikálně-chemické vlastnosti a tím i rozdílnou roli v organismu.

Obsahem této části habilitační práce je aplikace LA-ICP-MS v analýze zobrazování povrchu 1) **jednofázových systémů** (fosfátová fáze zubů a kostí a karbonátová fáze otolitů) a 2) **vícefázových systémů** – urolitů.

Vždy se jedná o komplexní přístup zohledňující matrici vzorku, použití vhodných laserových ablačních systémů i různých typů ICP hmotnostních spektrometrů, vliv různých experimentálních parametrů tak, aby výsledky výzkumu byly v souladu s cíli studií v daných oborech, ve kterých jsou předmětem bádání. Jako červená nit se touto částí táhne mapování povrchu vzorků přes jednofázový systém apatitu s jeho rozdílnými vlastnostmi v různých částech vzorku a pokračuje přes mapování vícefázového systému se zcela odlišnou matricí. Výsledky jsou součástí 7 prací (I-VII), jejichž popis je obohacen o výčet mnou vedených bakalářských a diplomových prací, které se dané tématice také věnují a jejich experimentálně ověřené výsledky jsou spojeny přímo s některými publikacemi nebo nepřímo prostřednictvím nabytých zkušeností aplikovaných v dalším výzkumu. Část nepublikovaných výsledků diplomových prací je stále ještě předmětem výzkumu a je připravována publikace.

a) Jednofázová analýza – apatitová fáze zubů a kostí

Tato část habilitační práce ukazuje možnost aplikace LA-ICP-MS v analýze kosterních pozůstatků, poukazuje na možné komplikace způsobené rozdílnou stavbou zubů a alterací bioapatitu, kvantifikaci a navrhuje možná řešení nebo naopak pozitivního využití alterace v zobrazování struktury.

Neznámějšími biominerály jsou fosfáty a karbonáty vápníku. Fosfát vápníku, přesněji řečeno hydroxyapatit, je hlavní složkou kostí a zubů, a právě jeho proměnlivé chemické

složení a stavba předurčují kalcifikované tkáně jako potenciální zdroj různorodých informací využitelných v medicíně, materiálových vědách, biologii, ale i geologii, archeologii či paleontologii. Zjednodušeně slouží jako archiv chronologického záznamu výživy, migrace, zdravotního stavu, ale také důležitých environmentálních či vývojových událostí.¹⁻⁶ Jistě by bylo možné definovat další vědní obory, které se zabývají výzkumem apatitové fáze, nicméně výzkum prezentovaný touto habilitační prací je zaměřený na využití LA-ICP-MS v určení migrace, výživy, stanovení vhodných ukazatelů alterace bioapatitu a také přispění k objasnění procesu diageneze kosterních pozůstatků.

Jak je velmi dobře známo, zuby patří mezi nejvíce mineralizovanou tkánь lidského těla a jsou považovány za nejtvrdší část lidského organismu. Hlavní složkou je *bioapatit* ($\text{Ca}_{10}(\text{PO}_4)_6\text{OH}_2$) lišící se však podílem anorganické fáze (95-98 % ve sklovině, 70 % dentinu a 50 % cementu), organické fáze a vody, strukturou, způsobem růstu v jednotlivých svých částech a jeho resistance vůči chemickým změnám.⁷ Změna chemického složení biogenního apatitu nastává u recentních vzorků prostřednictvím inkorporace prvků, které jsou součástí například přijímané stravy a odráží také na základě izotopového poměru $^{87}\text{Sr}/^{86}\text{Sr}$ geografický původ. Tohoto faktu se využívá právě při určování výživy starověké populace, což může sloužit k určení sociálního postavení skupiny, rodiny, jednice nebo samotné oblasti.⁹⁻¹¹ Vše je také spojeno s migrací/mobilitou tehdejší lidské populace nebo zvířat.¹²⁻¹⁵ Běžně jsou pro určení stravy používány izotopy dusíku ($\delta^{15}\text{N}$) a uhlíku ($\delta^{13}\text{C}$). V případě poměru izotopů uhlíku je hodnota dána rozdílným metabolismem rostlin (C3, C4 a CAM cyklus). Naproti tomu dusík ukazuje na trofickou úroveň, dokáže rozlišit rostlinnou, masitou a také mořskou stravu. Dále jsou k tomuto účelu využívány Sr, Ba, Zn. Součástí bioapatitu jsou také prvky v minoritním, stopovém či nižším množství – Na, Mg, Fe, Al, Pb, Sn, Cu, Hg, Mn.^{3,7,8}

Možnost využití LA-ICP-MS metody pro mapování zubní tkáně je popsána v publikaci I Multielemental analysis of prehistoric animal teeth by Laser-Induced Breakdown Spectroscopy and Laser Ablation Inductively Coupled Plasma Mass Spectrometry“, která kombinuje nejen cílovou metodu LA-ICP-MS, ale také spektrometrii laserem indukovaného mikroplazmatu (LIBS). Při výběru prvků byl brán ohled na limity detekce především metody LIBS a na možnost prostudovat využití těchto metod v archeologii. Byly detekovány prvky Sr, Ba, Zn společně s Na, Mg a také Ca a P. Byla prokázána nehomogenní distribuce většiny sledovaných prvků. Výrazný byl pokles

v obsahu Na nebo naopak nárůst Fe v oblasti kořenového kanálku. Zobrazení celé plochy dentinu prostřednictvím prvků a jejich poměrů pak vykazovalo poměrně nízkou fluktuaci v obsazích, především v obsahu stroncia. Při detailním pohledu bylo patrné, že tato fluktuace koresponduje se strukturou dentinu, který vykazuje střídání tmavých a světlých koncentrických kruhů odpovídajících zimnímu a letnímu období.

V publikaci **I** bylo prokázáno, že LA-ICP-MS může být aplikována ke sledování distribuce prvků v kosterních pozůstatcích. Byly nastíněny prvotní překážky a zároveň bylo demonstrováno, že má metoda dostatečnou citlivost vůči změně chemického složení s následným použitím v archeologii. Publikace „*Elemental mapping in fossil tooth root section of Ursus arctos by laser ablation inductively coupled plasma mass spectrometry (LA-ICP-MS)*“ (**II**) je navazující studií a zabývá se detailně využitím metody v analýze apatitu stejného vzorku. Věnuje se kvantifikaci pomocí kostní moučky (NIST SRM 1486), kdy pro normalizaci bylo nutné využít vápník nejen jako normalizačního prvku, ale také jako prvku porovnávacího pro korekci rozdílné ablační rychlosti mezi vzorkem a práškovým standardem, který byl analyzován ve formě slisované tablety. Díky tomu mohla být provedena kvantifikace map měřených izotopů prvků a vypočten průměrný obsah. V této publikaci byly jednoznačně prokázány sezonné fluktuace Zn a také Sr/Zn, čehož by mohlo být použito pro určení migrace a výživy. Nižší hodnoty byly detekovány v zimním období, kdy dochází k poklesu příjmu potravy. Podle průměrných hodnot obsahů Sr, Zn a Ba získaných pomocí LA-ICP-MS pouze pro dentin je možné získat také složení stravy a v případě toho vzorku byly výsledky z laserové ablaci v souladu s výsledky geochemické analýzy N a C. Aby analýza byla kompletní, pro určení migrace medvěda hnědého byla studie doplněna o výsledky izotopového poměru Sr ($\delta^{87}\text{Sr}$), který byl stanoven pomocí metody TIMS (Thermal Ionisation MS) na University of Bergen (Norsko).

U archeologických nálezů je nutné diskutovat substituci, a tedy iontovou výměnu mezi kosterními pozůstatky s okolním prostředím. Nejčastěji dochází k nahrazení hydroxylové skupiny za fluoridové nebo uhličitanové ionty. Uhličitanová skupina však také substituuje fosfátovou skupinu, a to zejména v procesu fosilizace. V této pozici je možné detektovat také přítomnost chloridových iontů nebo molekuly vody. Velmi známé jsou i substituce Sr^{2+} , Mg^{2+} nebo Na^+ iontů místo Ca^{2+} aj. Alterace apatitu vede ke změnám jeho vlastností, jako je například rozpustnost nebo parametry krystalové mřížky,

a mění se tak jeho citlivost vůči dalším chemickým změnám. Ta roste v řadě sklovina – dentin – cement.¹⁶⁻¹⁹ Diageneze (změna chemického složení) může být mikrobiálního původu, projevuje se ztrátou organické hmoty, rozkladem DNA či minerálními změnami. Proces diageneze ovlivňují redoxní podmínky prostředí a pH, teplota a okolní voda. Vedle alterace samotného apatitu se mohou na jeho povrchu sorbovat další látky nebo může dojít k vytvoření sekundárních minerálů (např. kalcit, sulfidické minerály).⁷

Objasnění procesu diageneze a nalezení ukazatele alterace je věnována celá řada publikací, stejně jako publikace **I** a **II**.

Z hlediska chemického složení a alterace bioapatitu byla v publikaci **I** korelována tvrdost materiálu s hloubkou ablační stopy zanechané na povrchu laserovým svazkem. Korelace mezi hloubkou kráteru a chemickým složením tedy ukázala, že apatit v okolí kořenového kanálku, který není chráněný žádnou další vrstvou, je alterovaný více, nabohacený o Fe, a naopak zde dochází i vymývání prvků, např. Na. Z toho důvodu je sledování signálu prvků, jejichž distribuce by měla být v dané ploše „homogenní“ bez signifikantních odchylek, nutností. V případě této studie byla úspěšně aplikována normalizace na signál Ca. Náhlý pokles signálu Ca a P poukazuje na přítomnost praskliny či fáze se zcela odlišným chemickým složením. Závěr, zda obsah minoritních a stopových prvků je v dané oblasti vyšší či nižší, musí být korigován minimálně pomocí poměrů.

Podobně i publikace **II** obsahuje část věnovanou studiu diageneze. Tento krok je nutné považovat za nevyhnutelný, pokud mají být LA-ICP-MS data dále správně interpretována a používána pro zmíněné účely. Bioapatit ve své nepříliš diageneticky pozměněné podobě přirozeně obsahuje určité množství Na, Mg, Sr, Ba, Zn atd. U fosilního medvědího špičáku však byl pozorován pokles v obsahu Na ve specifických oblastech dentinu (viz **I**). Že se jedná o vliv diageneze, ukazuje i opačné chování uranu, který se běžně v apatitu nevyskytuje. Pokud mají být výsledky interpretovány správně, pak je třeba určit míru alterace apatitu, kdy právě sodík a uran mohou sloužit jako indikátory. V cementu byly také při detailní analýze identifikovány částice o velikosti 1 µm odpovídající oxidům-hydroxidům Fe a Mn. V publikaci **II** je také pojednáno o vhodnosti využití kvadrupólového ICP hmotnostního spektrometru, který může být v jistých ohledech „pomalý“, jelikož se jedná o sekvenční záznam. Z toho důvodu byla provedena srovnávací měření s analyzátorem doby letu (TOF-ICP-MS) na California State University Long Beach v rámci projektu „Laser ablation inductively coupled plasma mass spectrometry and laser induced breakdown spectroscopy in archaeology and

anthropology“ v programu KONTAKT. Je diskutována také korekce driftu ICP hmotnostního spektrometru při dlouhotrvající analýze

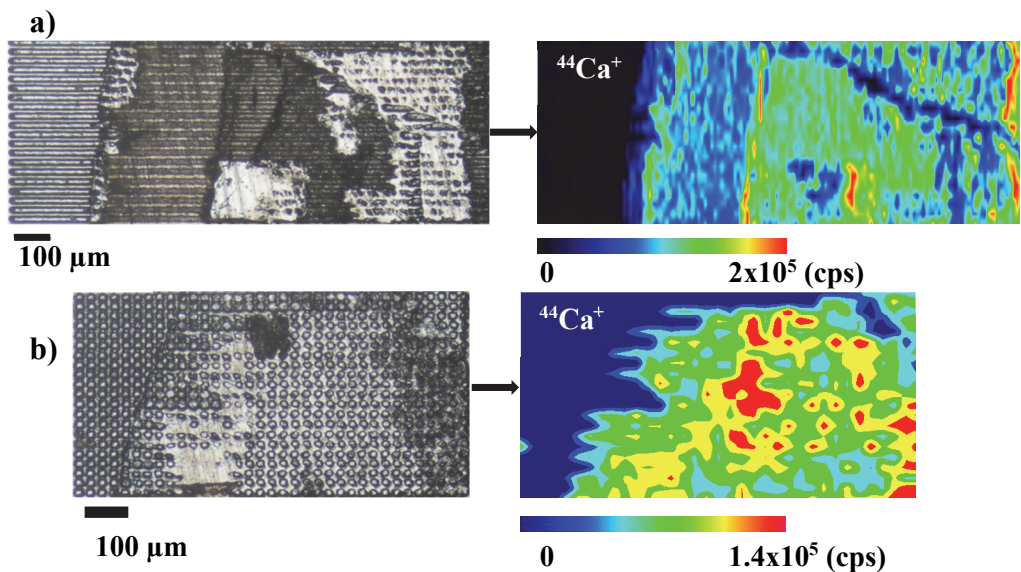
Tomuto tématu byly věnovány úspěšně obhájené 2 bakalářské práce a 2 diplomové práce vypracované na Ústavu chemie Masarykovy univerzity pod mým vedením. Jejich náplň je uvedena z důvodu objasnění vývoje a směru výzkumu, který stále pokračuje.

Bakalářská práce Mgr. Simony Kaupové s názvem „**Studium diageneze kostí pomocí LA-ICP-MS**“ (2011) byla věnována studiu míry a mechanismu alterace bioapatitu dlouhé kosti. Samotný experiment spočíval v charakterizaci bioapatitu před a po deproteinaci a v obou případech popisu změn chemického složení vlivem působení Sr^{2+} , Zn^{2+} a Ba^{2+} solí o různých koncentracích.

Další úspěšně obhájená **bakalářská práce** nese název „**Studium distribuce prvků ve vzorcích zubů pomocí LA-ICP-MS**“ (2011). Práce vypracovaná Mgr. Lenkou Tenorovou byla zaměřena na analýzu zvířecích zubů. I přes vysoký stupeň diageneze byly diskutovány možnosti využití metody v archeologii pro stanovení původu vzorku. Pozitivně byla také využita alterace bioapatitu při vykreslení jemné struktury dentinu některých vzorků související s uspořádáním dentinových pórů a chemickým složením v jejich okolí.

Na předchozí práci navazovala **diplomová práce** vypracovaná stejnou autorkou Mgr. Lenkou Tenorovou s názvem „**Analýza kosterních pozůstatků pomocí laserové ablaci**“ (2013). Jejím cílem byla specifikace jednotlivých kroků a jejich zhodnocení vedoucí k úspěšné analýze kosterních pozůstatků s ohledem na řešený analytický i archeologický problém. Tato velmi rozsáhlá práce zahrnuje studium vlivu *i)* přípravy vzorku, *ii)* volby ablačního módu (Obr. 3), *iii)* výběru plochy k analýze, *iv)* prostorového rozlišení na signály archeologicky významných izotopů a *v)* celkové zhodnocení Ba/Ca vs. Sr/Ca za účelem sledování složení stravy a porovnání s výsledky izotopové analýzy uhlíku ($\delta^{13}\text{C}$) a dusíku ($\delta^{14}\text{N}$).

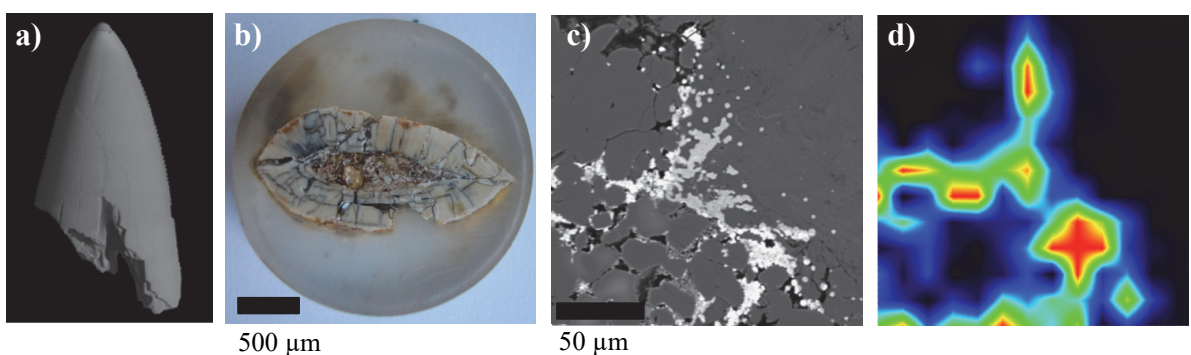
Výsledky této diplomové práce jsou dále rozšírovány o analýzu izotopového poměru $\delta^{87}\text{Sr}$ pomocí multikolektorového ICP-MS a jsou předmětem dalšího výzkumu.



Obr. 3: Srovnání povrchu vzorku po interakci s laserovým svazkem u a) liniového skenu i b) bodové analýzy a jejich vliv na výslednou distribuci matričního prvku vápníku.

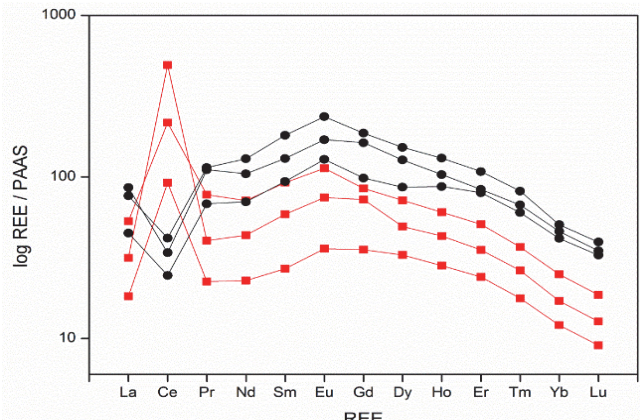
Jelikož hydroxyapatit jako biominerál představuje archív celé řady procesů týkajících se živého organismu, ale také životního prostředí, byla jeho studiu věnována ještě další *diplomová práce „Laserová ablace v analýze petrifikovaných tkání“* (2013) vypracovaná Mgr. Michaelou Hložkovou (roz. Vaňkovou).

Prvním řešeným úkolem byla kvantifikace REE v apatitové fázi, protože běžné využití kostní moučky nebo kostního popela (NIST SRM 1400) bylo komplikováno nepřítomností stanovených REE a velmi nízkými obsahy dalších prvků jako Ti, V atd. Díky kombinaci s NIST 610 bylo možné spolehlivě kvantifikovat obsahy REE (suma REE+Y až 1,9-2,8 hm.%) a stanovit míru alterace.



Obr. 4: a) Tomografické zobrazení analyzovaného vzorku zuba, b) řez vzorku zality v epoxidové pryskyřici, c) BSE obrázek povrchu, který byl analyzován 8 μm laserovým svazkem a d) výsledná distribuce ¹⁴⁰Ce.

Distribuce však poukazovaly na přítomnost několika fází odpovídající složení sedimentu nebo přítomnost fáze s vysokým obsahem Ce (až 50 hm.%), ale i Fe a Mn. REE paterny normalizované na PAAS také poukázaly na negativní cerovou anomálii fosfátové fáze, a naopak pozitivní v případě Ce fáze (Obr. 5). Chování potvrzuje změnu oxidačního stavu Ce a tedy i změnu okolních podmínek v průběhu fosilizace. Obě fáze se také vyznačovaly malou pozitivní Eu anomálií. V jednom případě bylo provedeno také mapování povrchu s Ce fází s průměrem laserového svazku 8 μm (Obr. 4).



Obr. 5: REE patern fosfátové (černá) a cerové fáze (červená) získaný LA-ICP-MS analýzou zubu.

Jedná se tedy o rozsáhlou studii, která zachycuje velké množství dat, jejich statistické zpracování a interpretaci a je přínosem na poli studia fosfátové fáze a jejího využití k rekonstrukci environmetálních změn a popisu mechanismu diagenetických procesů. Práce je v rámci disertační práce studentky ještě prohloubena a nyní je zpracovávána publikace popisující diagenezi apatitu.

Studu fosfátové fáze zubů i kostí se věnuje stále velký počet publikací a jsou v dnešní době zaměřeny na mapování složení povrchu s vysokým prostorovým rozlišením, studium procesu diageneze a také míry alterace a nalezení vhodných indikátorů. Uvedené práce tedy mají přínos ke studované problematice.

b) Jednofázová analýza – karbonátová fáze otolitů

Vedle apatitové fáze bylo studováno složení otolitů v rámci *diplomové práce* Mgr. Barbory Svatošové s názvem „*Hmotnostní spektrometrie indukčně vázaného plazmatu v analýze antarktických otolitů*“ (2016). Jedná se o komplexní studii unikátních vzorků otolitů (28) odebraných z 5 druhů ryb chycených při pobřeží ostrova **Jamese Rosse** poblíž nejsevernějšího výběžku antarktického poloostrova. Práce byla zaměřena na sledování distribuce vybraných prvků a detekci možných kontaminantů životního prostředí a odkrytí chování různých druhů ryb na základě $\delta^{87}\text{Sr}$. **Každá**

informace získaná pro tyto druhy je jedinečná, jelikož jejich život není zmapován v celosvětovém měřítku. Imaging povrchu otolitu s matricí uhličitanu vápenatého klade větší nároky na nastavení experimentálních parametrů z hlediska LOD a jejich velikosti.²⁰⁻²⁵

Analýza pevných vzorků byla realizována pomocí hmotnostní spektrometrie sekundárních iontů (SIMS)²⁶, částicemi indukovaná rentgenová spektrometrie (PIXE)²⁷, rentgenová fluorescence (XRF)²⁸, neutronová aktivační analýza (NAA)²⁹ a elektronová mikrosonda (EMPA)³⁰ aj. Využití LA-ICP-MS v analýze otolitů bylo publikováno již v roce 2002³¹, nicméně počet publikací ve srovnání s předchozími lety stoupal právě od roku 2016 na téměř dvojnásobek a stále se tento trend udržuje.

Práce je unikátní také díky porovnání **nanosekundové** (ns) ablaci s **femtosekundovou** (fs) ablaci za použití téměř shodných hmotnostních spektrometrů (Element 2 a Element XR). Práce vznikla na základě spolupráce Masarykovy univerzity s Université de Pau et des Pays de l'Adour (Francie) v rámci pobytu studentky v programu Erasmus. Dle očekávání fs ablaci poskytla i o dva řády vyšší citlivost a lepší LOD. Byly detekovány prvky Sr, Ba, Mg, Ca, Fe a Cu. Spojení s fs systémem umožnilo detektovat navíc Zn a Mn. Z těžkých kovů byly měřeny Cr, Ag, Cd, Hg a Pb, ale žádným systémem nebyly detekovány. V obou případech byly úspěšně zaznamenány fluktuace jednotlivých přírůstků na poměrech Ba/Ca, Sr/Ca a Mn/Ca a identifikována poloha jádra indikující biologické a environmentální změny.

Byly úspěšně zobrazeny přírůstkové linie pomocí Sr. U stroncia byla část studia zaměřena na izotopový poměr $\delta^{87}\text{Sr}$ měřený u vzorků vod a také části otolitů v pevném stavu. K tomuto účelu byl použitý multikolektorový systém ve Francii (LA-ICP-MS) a v případě roztokové analýzy ICP-MS byly vzorky vod analyzovány Mgr. Jitkou Míkovou, Ph.D. z České geologické služby.

V rámci jednotlivých přírůstků byly zaznamenány jen velmi malé změny v poměrech, které poukazují na pohyb v relativně stabilním prostředí bez výrazných environmentálních změn. V neposlední řadě byla vyhodnocena variabilita v prvkových obsazích mezi jednotlivými zkoumanými druhy ryb. O atraktivitě tématu a kvalitě zpracování vypovídá i umístění studentky na **1. místě v Soutěži mladých spektroskopiků** v roce 2016 a získání **2. místa** v posterové sekci **21. Slovensko-české spektroskopické konference** (Liptovský Ján, 2016) prezentované předkladatelkou habilitační práce. Práce je dále rozšiřována a výsledky jsou podrobovány statistické analýze dat.

c) Vícefázová analýza biominerálů

Pro studium kosterních pozůstatků a otolitů je charakteristická analýza především jedné fáze. Ve specifických případech byla detekována přítomnost další jiné fáze nebo se jednalo o stejnou fázi, avšak rozdílného chemického složení nejen na úrovni minoritních a stopových složek, ale také s rozdílnými fyzikálními vlastnostmi.

Studium močových konkrementů, také patřící mezi biominerály, ukázalo další možné využití laserové ablaci ICP-MS spojené s řešením problémů 2D mapování vícefázového systému. Ke vzniku kamenů dochází díky vzniku malých krystalků, přítomnosti pevných částic či bakterií. Jednotlivé fyzikálně-chemické procesy vzniku močových kamenů, a tedy onemocnění nazývané „urolitiaza“, jsou podmíněny různými faktory³² – pH moči, metabolické faktory, sociologické faktory, věk, pohlaví, klima nebo i roční období. Chemické složení těchto biominerálů, které se mohou vyskytovat v parenchymu a dutinách ledvin, ledvinovém kalichu či pánvičce, močovém měchýři a trubici, je poměrně rozmanité – přes fosfáty, oxaláty, močany, uhličitanové, sírany, cystinové nebo xantinové kameny, aj. Ve většině případů je složení jednoho konkrementu právě kombinací dvou (50 %) či více fází (35 %), kdy nejčastěji vyskytující se kombinací je oxalát / apatit.

Studie, které se dotýkají tématu močových konkrementů, se zabývají mineralizačními či inhibičními mechanismy vzniku močových kamenů³³⁻³⁵, vlivem různých faktorů na jejich vznik³⁶⁻³⁸, fragmentací při interakci s vysoce energetickým laserovým svazkem^{39,40} a různými léčebnými procesy^{38,41}. Podobně je velké množství publikací v medicínských nebo chemických žurnálech věnováno studiu chemického složení, krystalografickým studiím těchto biominerálů a jejich klasifikaci.⁴²⁻⁴⁵ Právě pochopení mechanismu vzniku močových kamenů, jejich chemického složení a nalezení maximálního počtu faktorů ovlivňujících jejich nukleaci a růst představuje důležitý krok v prevenci a léčebných procesech. Za tímto účelem byla aplikována celá řada metod: infračervená spektroskopie s Fourierovou transformací (FTIR)⁴⁶, blízká IČ reflektanční spektroskopie, XRF, rentgenová difrakce (XRD), X-ray fotoelektronová spektroskopie (XPS), skenovací elektronová mikroskopie (SEM), EMPA, polarizační optická mikroskopie, LIBS⁴⁷, SIMS, Ramanova spektroskopie (RS)^{46,47}, tomografie (CT)^{37,42,48}.

Aplikace metody LA-ICP-MS v analýze močových konkrementů není častá, což dokazuje minimální počet publikací (žlučové⁴⁹, prostatické, ledvinové³², močové^{32,50}, lékové, atd.). Analýza přímo pevného vzorku pomocí LA-ICP-MS je ojedinělou

záležitostí a spíše jsou aplikovány metody analýzy průměrného složení – ICP-MS, ICP-OES a AAS.⁵⁰

Obecně platí, že analýza vícefázového systému je nejen při vzorkování laserovým svazkem, ale také samotné ICP-MS analýze komplikovanější než v případě analýzy jednoho druhu minerálu. Nastavení experimentálních parametrů laserové ablaci a stejně tak vytvoření ICP-MS metodiky nemusí být pro různé fáze shodné a odvíjí se jak od chemického složení, tak i jejich fyzikálních vlastností. A právě možnosti 2D mapování povrchu vzorku jsou diskutovány v publikaci III s názvem „2D elemental mapping of sections of human kidney stones using laser ablation-inductively coupled plasma-mass spectrometry: Possibilities and limitations“. Práce vznikla ve spolupráci s prof. Frankem Vanhaeckem, mezinárodně uznávaným odborníkem v oblasti ICP-MS, působícím na Ústavu analytické chemie, Ghent University (Belgie) v rámci mého 3měsíčního vedecko-výzkumného pobytu. Předmětem studia bylo 8 vzorků s rozdílným poměrem oxalát / fosfát a jeden konkrement jako zástupce urátových kamenů (90 % kyseliny močové). Ablaci byla provedena pomocí dvou instrumentací: *i)* 213nm laserový ablační systém spojený s kvadrupólovým ICP hmotnostním spektrometrem (Ústav chemie, Masarykovy univerzity) a *ii)* 193nm laserový ablační systém spojený s ICP hmotnostním spektrometrem s dvojí fokusací (Ústavu analytické chemie, Ghent University). Publikace ukazuje souhrn výsledků týkající se propojení mezi tvrdostí, hustotou, krystalografickou strukturou materiálu, chemickým složením se stabilitou / intenzitou zaznamenaného ICP-MS signálu. Diskutuje možnosti prvkové asociace, které jsou také předmětem studia výše citovaných publikací. Rozdílem je však určení akumulace vybraných prvků přímo ve specifické fázi na rozdíl od přístupu, kdy je konkrement brán jako celek. Publikace navíc ukazuje možnost využití LA-ICP-MS jako metody pro klasifikaci kamenů podle jejich mineralogického složení. Stanovení průměrného obsahu vybraných prvků v rámci jednotlivých fází bylo řešeno pomocí komerčně dostupného standardu kostní moučky NIST SRM 1486. Výsledky získané výzkumem za použití LA-ICP-MS jsou doplněny, podpořeny a ověřeny pomocí dalších metod (FTIR, SEM, EMPA, roztoková ICP-MS, Vickers test tvrdosti). Součástí publikace je poměrně detailně rozebírána terminologie laterálního / prostorového rozlišení v souvislosti s módem ablaci a rychlostí načítání dat hmotnostním spektrometrem.

Achillovou patou LA-ICP-MS metody je kvantifikace, což právě v případě zejména směsných kamenů může vést ke zkreslení získaných výsledků. Podobná situace je i v případě „čistých“ kamenů, protože dostupnost standardů pro jednotlivé složky konkrementů je dosti omezená z hlediska makroprvků i stopových prvků. Obecně možnosti, které jsou využívány ke kvantifikaci LA-ICP-MS dat, je hned několik. Univerzální metodou kvantifikace při využití ICP hmotnostní spektrometrie se nabízí izotopové zřeďování. Tato absolutní metoda kvantifikace je využívána i při stanovení obsahů prvků v certifikovaných / standardních referenčních materiálech.⁵¹ Nicméně její využití právě při spojení ICP-MS se vzorkováním s laserovým svazkem je dosti problematické.⁵²⁻⁵⁴ Jako další možnost se nabízí použití standardů v kapalném stavu, třeba i v kombinaci s izotopovým zřeďováním, které jsou zmlžovány simultánně se vzorkováním povrchu.⁵⁵ Vzhledem k tomu, že suchý aerosol vzorku a vlhký aerosol dávají rozdílnou odezvu při samotném měření, jsou před vstupem do ICP mixovány. Standardní roztok může být zmlžován přímo do ablační cely⁵⁶ a vlhký aerosol před smícháním vysušen.^{57,58} Je možné využít želatiny⁵⁹⁻⁶¹, agarosy⁶² či vysoce viskózního media určeného pro krytomickou přípravu vzorků⁶³, polymethylmetakrylátu⁶⁴, které jsou spikované zájmovými prvky. Tohoto přístupu se nejčastěji využívá pro bioaplikace při analýze měkkých tkání či analýze nanočástic. Je možné setkat se i se standardy vytvořenými zaschnutím kapalného standardu – tzv. Dried Droplet Calibration Approach (DDCA) na nosiči⁶⁵⁻⁶⁷ nebo přímo na povrchu vzorku⁶⁸.

Další možnosti je využití komerčně dostupného standardu, který však nemusí obsahovat všechny stanovované prvky nebo nemusejí být ve vhodném obsahu. V takovém případě lze využít spikování pomocí standardních roztoků.^{69,70} Ovšem variabilita z hlediska matric analyzovaných pomocí LA-ICP-MS je velmi vysoká a možnost kvantifikace s využitím dostupných standardů naopak nízká. Je tedy možné přistoupit k přípravě standardů z *matričních materiálů*⁷¹⁻⁷³, jako jsou různé práškové materiály, které svým chemickým složením odpovídají vzorku, nebo využití přímo *reálných vzorků*⁷⁴. Ve většině případů se jedná o práškové materiály, které jsou lisovány do tablet atď už s pojivem, nebo bez něj. Další možnost představuje využití sol-gel techniky.⁷⁴⁻⁷⁶

Obecně lze tvrdit, že oblast týkající se kvantifikačních postupů při aplikaci LA-ICP-MS metody v analýze nejrůznějších vzorků, je stále ještě ne zcela probádaná a středem zájmu celé řady výzkumných projektů. Výhodám a nevýhodám různých kalibračních přístupů z hlediska metrologie je věnována publikace Sargent et al.⁷⁷

Dalším krokem bylo připravit a otestovat standardy vhodné pro analýzu močových kamenů a výsledky byly zveřejněny v Journal of Analytical Atomic Spectrometry v publikaci pod názvem „**Preparation and testing of phosphate, oxalate and uric acid matrix-matched standards for accurate quantification of 2D elemental distribution in kidney stones sections using 213 nm nanosecond laser ablation inductively coupled plasma mass spectrometry**“ (IV).

Vzhledem k rozmanitosti chemického složení, využití dostupných standardních materiálů v práškové podobě nebylo dostačující. Byla připravena sada kalibračních tablet – *matrix matched* – z reálných konkrementů mající rozdílný podíl oxalátu (whewelitu i wedellitu), fosfátu (amorfni apatit, struvit) a také kyseliny močové. Publikace dává přínos v oblasti samotné přípravy, testování laboratorně připravených tablet z hlediska homogeneity, hustoty, tvrdosti i soudržnosti pelety, jejich chování při interakci s laserovým svazkem. Ukazuje dosaženou linearitu (s koeficientem determinace $>0,9955$), LOD pro stanovení P, Na, Sr, Zn, Ba a Pb ($>2 \text{ mg kg}^{-1}$) a koncentrační rozsahy, pro které jsou kalibrační standardy vhodné. Hodnoty charakterizující jednotlivé kalibrační závislosti vycházejí ze statistického zpracování dat beroucí v úvahu chyby stanovení všech vstupních hodnot, testování odlehlych hodnot a výpočet konfidenčních a predikčních pasů a LOD pro každou závislost. Je také diskutována problematika vnitřního standardu a srovnání čtyřbodové kalibrace vs. jednobodový kalibrační přístup, který je hojně využíván při aplikaci LA-ICP-MS. Porovnání je provedeno i prostřednictvím komerčně dostupného standardu kostní moučky.

V závěru publikace je ukázána aplikace matrix-matched standardů přímo při ablaci povrchu urolitu, který obsahoval jak část fosfátovou, tak i oxalátovou a jsou diskutovány jednotlivé kroky vedoucí ke kvantifikaci naměřené prostorové distribuce.

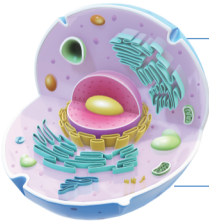
Díky komplexnímu přístupu k jednotlivým krokům přípravy matrix-matched tablet, zpracování dat, a i využití standardů k zobrazení prvkové distribuce prostřednictvím interakce s laserovým svazkem a detekcí ICP-MS technikou, představuje publikace velký přínos v oblasti aplikace LA-ICP-MS.

Na podobné téma byla publikována práce s názvem „**Laser ablation methods for analysis of urinary calculi: Comparison study based on calibration pellets**“ (V). Práce vznikla na základě disertační práce Mgr. Kateřiny Štěpánkové, Ph.D. (roz. Proksové). Cílem práce bylo porovnání laserově ablačních technik (LIBS, LA-LIBS, LA-ICP-OES a LA-ICP-MS) na tabletách připravených z urolitů podobně jako v předchozím případě.

Nejedená se však o stejné tablety, protože v tomto případě byly připraveny pouze rozdrcením a rozetřením konkrementů v achátové třecí misce. Homogenita připravených tablet byla nízká, ale na druhou stranu lépe odrážela různorodost mineralogického složení skrze analyzovaný povrch vzorků. Podíl na této práci nedosahuje takové hodnoty jako u ostatních publikací právě díky použití dalších laserově ablačních technik a odpovídá pouze části práce věnující se LA-ICP-MS metodě.

Na základě dlouhodobé spolupráce s Mgr. Kateřinou Štěpánkovou, Ph.D. (roz. Proksovou), která se analýze močových kamenů věnovala v rámci své bakalářské práce, u které jsem byla oficiálně jmenována „konzultantem“, diplomové i disertační práce vznikly ještě 2 další publikace „**Laser ablation methods for analysis of urinary calculi: Comparison study based on calibration pellets**“ (VI) a „**Study of distribution of elements in urinary stones using laser ablation ICP-MS spectrometry**“ (VII) vydané v Chemických listech. Podobně jako v předchozích publikacích je zde zaměření na mapování povrchu vzorků urolitů, avšak bez jakékoli kvantifikace. Navíc je uveden rozdíl mezi bodovou ablaci a liniovým skenem a jedná se spíše o pilotní studie a prvotní výsledky získané na těchto vzorcích.

Publikace uváděné v sekci „Biominerály“ se zabývají využitím laserové ablaci ICP hmotnostní spektrometrie v oblasti zobrazení povrchu a sledování distribuce prvků. Vždy bylo nutné řešit potenciální interference, vhodné nastavení experimentálních parametrů laserové ablaci i ICP hmotnostního spektrometru tak, aby byly naplněny cíle jednotlivých prací. Práce byly hojně prezentovány na národních i mezinárodních konferencích formou posteru i přednášek. Zkušenosti s mapováním byly také shrnuty v textu s názvem „**LA-ICP-MS a laterální mapování**“, který je součástí sborníku k 8. kurzu ICP-MS/OES 2015 (ISBN 978-80-905704-3-6) v rozsahu 21 stran.



Laserová ablace ICP hmotnostní spektrometrie v analýze měkkých tkání

Další část výzkumu probíhala v oblasti využití laserové ablaci ICP-MS v analýze měkkých tkání. Z anatomického hlediska měkká tkáň představuje *nekalcifikované* a *nemineralizované* části lidského těla. Je definována jako tkáň, která *spojuje, podporuje* nebo *obklopuje* další struktury a *orgány*.

Samozřejmě, že aplikace metody se nevztahuje pouze na studium vzorků odpovídající definici podle lékařského slovníku, ale zahrnuje také soubory tkání vykonávající stejnou funkci – **orgány**, nebo naopak základní stavební jednotky tkání – **buňky**. Zároveň je třeba uvažovat také **tkáň rostlinnou**. Uplatnění metody LA-ICP-MS v analýze biologických tkání pro zodpovězení různých biomedicinských otázek je nesporné. Hojně je využívána k zobrazení prvkové distribuce, tzv. 2D imagingu, který je také označován zkratkou MSI (Mass Spectrometry Imaging) a je spojena s patologickou fyziologií, imunohistochemií, farmakologií, toxikologií, proteomikou, metabolomikou, forenzní environmentalistikou.

Začátky bioimagingu jsou spojeny s jednoduchým mapováním povrchu zvířecích i lidských tkání (jater^{78,79}, ledvin^{80,81}, plic^{81,82}, sleziny⁸¹, lymfatických uzlin⁸¹, mozkové tkáně^{79,83}), přes lidské tkáně s nádorovými objekty^{56,84,85}, tkáně po aplikaci léčiv^{61,86-88}, tkáně dopované nanočásticemi^{81,89-91}, izotopově / prvkově značenými látkami⁹²⁻⁹⁴ nebo kvantovými tečkami^{82,90} sloužícími ke sledování rakovinových markerů a diagnostiku, post-mortem analýzou lidských tkání ve forenzní patologii a toxikologii⁹⁵, až k analýze jedné buňky^{60,67,90,96-98}. V neposlední řadě jsou měkké tkáně testovány také v návaznosti na znečištění životního prostředí nebo sledování proteinů prostřednictvím vazby kov-protein.⁹⁹ Je spojována s neurodegenerativními nemocemi – Parkinson^{100,101} a Alzheimer^{53,59}, nebo také s poměrně vzácným Wilsonovým onemocněním^{79,102}. Nejčastěji jsou vzorky analyzovány ve formě tenkých plátků tkáně (~10-20 µm) uchycené na vhodném nosiči (např. skle). Ve výjimečných případech jsou analyzovány i řezy tenčí ~2-3 µm, což však klade důraz na jemné odprašování povrchu, rychlé vyplachování z ablační cely a dostatečnou citlivost ICP hmotnostního spektrometru.^{80,96}

Od samotného počátku však byla snaha získat informace také o kvantitativním zastoupení prvků a byly využívány komerčně dostupné standardy⁷⁸ nebo se jednalo o vzájemné porovnání tkání se spikem a bez něj po pečlivé homogenizaci, vymrazení a nanesení tenkého plátku na vhodný nosič^{56,83,84,103}. Postupně přibývají také publikace o využití laboratorně připravených standardů na bázi spikované želatiny⁶¹, agarósy, celulosové membrány⁹⁴, vymrazovacího média⁶³, polymethylmetakrylátu⁶⁴, souběžné zmlžování standardních roztoků s ablaci⁵⁶, izotopové zřeďování⁹³ atd., jak je uvedeno v sekci „Vícefázová analýza biominerálů“. Díky rostoucímu počtu projektů na téma bioimagingu se objevují i články, které se zabývají spíše zpracováním a vizualizací dat, a tedy prezentací softwaru nebo makra vytvořeného kolektivem autorů.¹⁰⁴⁻¹⁰⁶

Vedle LA-ICP-MS jsou využívány i další techniky jako např. FTIR^{85,107}, XFR^{99,108}, SIMS/nanoSIMS^{88,97}, MALDI-MSI^{88,109}, fluorescenční mikroskopie⁸², konfokální mikroskopie⁹⁰.

S touto problematikou souvisí publikace s názvem „**Study of metal accumulation in tapeworm section using laser ablation-inductively coupled plasma-mass spectrometry (LA-ICP-MS)**“ (VIII), jejímž cílem bylo prozkoumat akumulaci olova v těle tasemnice. Vedle olova byla sledována distribuce Zn a Fe jako prvků přirozeně se vyskytujících v biologické tkáni. Oovo bylo do těla tasemnice přenášeno prostřednictvím krysy jako nosiče tasemnice, které bylo po dobu 6 týdnů perorálně podáváno Pb ($Pb(NO_3)_2$) s celkovou dávkou 36 mg Pb. Vzorky byly analyzovány ve formě tenkých řezů zálitých do parafínu s tloušťkou 40 µm. Za účelem kvantifikace byly laboratorně připraveny standardy spikováním agarósového gelu. Diskutována je problematika přípravy, vlivu pH a ověření skutečné koncentrace prvků. Detailně je studována homogenita standardů, vliv různých parametrů laserového systému (průměr laserového svazku, hustota zářivé energie) a módy ablaci (bodová analýza vs. líniový sken). Důležitou součástí publikace je charakterizace interferencí a jejich korekce v závislosti na hloubce propálení laserového svazku skrze připravené standardy. Pro testování byly navíc použity 2 laserové systémy s rozdílnými vlnovými délками (213 nm vs. 193 nm) a je tedy porovnávána linearita kalibračních závislostí spolu s LOD a rozdíl v absorpci laserového záření samotným vzorkem i standardy. V závěru publikace je ukázána využitelnost standardů při imagingu povrchu reálného vzorku a distribuce Zn a Fe a také lokalizace míst skrze řez s vyšší akumulací Pb.

Při podrobném studiu publikací věnujícím se přípravě standardů je jen velmi malá část věnována přípravě agarosových standardů. Celkově žádná z publikací se nevěnuje porovnání různých ablačních systémů, vlivu rozdílné absorpce mezi vzorkem a standardem. Opět díky komplexnímu přístupu a zaměření na samotnou laserovou ablaci je publikace v této oblasti jedinečná.

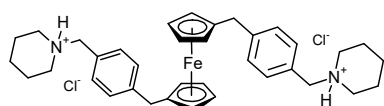
Příkladem pilotní studie analýzy rostlinného materiálu laserovým svazkem je publikace „Utilization of Laser-Assisted Analytical Methods for Monitoring of Lead and Nutrition Elements Distribution in Fresh and Dried Capsicum annuum L. Leaves“ (IX). Porovnává výsledky metody LIBS a LA-ICP-MS stejně jako v případě publikace I. Sledovaným prvkem bylo olovo, s cílem najít, kde dochází k jeho akumulaci v listech papriky. Olovo bylo zvoleno v návaznosti na fytoremediaci. Distribuce olova byla korelována s distribucí mangany a draslíku. Navíc však byly porovnávány signály získané ablaci čerstvých i sušených vzorků. Obě metody poskytovaly stejné výsledky s akumulací převážně v žilnatém systému a také ukázaly, že lepších výsledků je dosaženo na sušených vzorcích, pravděpodobně díky dosažení nižších limitů detekce. Distribuce draslíku nebyla nijak ovlivněna akumulací olova. **Přínos publikace spočívá v prezentaci možnosti obou metod a také jejich omezení v případě zpracování vzorku a nízkých koncentrací sledovaných prvků.**

S publikací VIII vznikla v rámci projektu „Elemental mapping of plant and animal accumulators of heavy metals; where are they accumulated?“ také publikace „Variability of trace element distribution in Noccaea spp., Arabidopsis spp., and Thlaspi arvense leaves: the role of plant species and element accumulation ability“ (X). V tomto případě byla metoda použita pro sledování distribuce Cd a Zn u rostlin, které jsou považovány za hyperakumulátory – *Noccaea caerulescens*, *N. praecox* a *Arabidopsis halleri* těchto prvků. Aby bylo možné provést srovnání a potvrdit schopnost akumulace vybraných rostlin, byly analýze podrobeny také *Thlaspi arvense* a *A. thaliana* jako zástupci neakumulujících rostlin. Srovnávána byla akumulace v parenchynu a žilnatém systému. Vedle již míněných prvků byla sledována odezva izotopů prvků C, Mg, P, Si, Ca, Mn, Fe, Cu a Pb. V publikaci je také diskutováno použití izotopu C pro normalizaci dat. Data byla podrobena statistickému zpracování a byly řešeny vzájemné asociace prvků a množství akumulovaných prvků rostlinami. **Tato téma bývají často diskutována v publikacích věnujících se analýze rostlinného materiálů. Předností publikace je**

využití statistických metod v imagingu a také stanovení míry akumulace prvků v rostlinách rostoucích na dlouhodobě kontaminované půdě.

Ať už se jedná o biominerály nebo analýzu měkké tkáně metodou LA-ICP-MS, jejich společná tématika je shrnuta v recenzované kapitole „Laser Ablation Inductively Coupled Plasma Mass Spectrometry as a Tool in Biological Science“ (XI), která je součástí knihy Natural Products Analysis: Instrumentation, Methods, and Applications vydaná v roce 2014 John Wiley & Sons. Tato kapitola s rozsahem 36 stran popisuje různé ablační systémy, vliv vlnové délky na distribuci velikosti částic aerosolu, ICP hmotnostní spektrometry – druhy analyzátorů, jejich přesnost, rychlosť aj., a také přídavná zařízení pro minimalizaci interferencí a jejich uplatnění, výhody i nevýhody. Diskutován je také aspekt ablačního módu, kvantifikace LA-ICP-MS dat, normalizace signálu a použití porovnávacího prvku. Poměrně rozsáhle je zpracována rešerše zobrazování povrchů tvrdých i měkkých tkání. Zahrnuta je i část popisující spojení separační techniky na polyakrylamidovém gelu (PAGE), která je hojně využívána ve studiu proteinů, a porovnání LA-ICP-MS s ostatními metodami určených ke studiu pevných materiálů.

Vedle publikací VIII-XI byl prováděn výzkum v oblasti **single cell analýzy** pomocí **LA-ICP-MS**. Práce spočívala v testování buněčné linie SK-OV-3 dopované potenciálním léčivem na bázi organokovových láték. V případě této studie se jednalo o látku na bázi ferrocenu (Obr. 6).



Obr. 6: Látka č. 10 testována jako potenciální léčivo.

Buněčná linie byla vystavená působení látky č. 10 na pracovišti RECAMO (Masarykův onkologický ústav, skupina doc. Mgr. Romana Hrstky, Ph.D.). Následně byly buňky naneseny na sklíčko a dále byly analyzovány pomocí LA-ICP-MS metody s cílem vystopovat, zda se nějaké potenciální léčivo v buňkách najde a s jakou distribucí Fe.

Single cell analýza jednoznačně nepatří mezi rutinní aplikace LA-ICP-MS metody. Obecně lze říci, že vždy při použití techniky LA-ICP-MS je nutné řešit *i*) výběr

instrumentace – ať už ablačního systému nebo ICP hmotnostního spektrometru s ohledem na analyzovaný materiál a cíl analýzy, *ii)* správně zvolený mód ablace a její podmínky, *iii)* vhodné nastavení ICP hmotnostního spektrometru, což velmi závisí na použité instrumentaci, *iv)* interference, *v)* samotná příprava vzorku, *vi)* použití dalšího zařízení pro zvýšení signálu měřených izotopů a v neposlední řadě i *vii)* samotná příprava vzorku či *viii)* příprava standardů s následnou kvantifikací. V případě analýzy jedné buňky bývá vyřešení většiny zmíněných bodů stěžechní.

Práce představuje pilotní studii, která by měla odhalit možnosti LA-ICP-MS metody v analýze jedné buňky. Vzhledem k předpokladu velmi nízkého obsahu Fe a navíc v kombinaci s velikostí buněk (jednotky-desítka μm) a tedy odprášením velmi malého množství materiálu, bylo nutné *minimalizovat počet měřených izotopů*. Z tohoto důvodu bylo měření realizováno pouze na jednom prvku – Fe a nebyly sledovány distribuce matričních (např. C) nebo potenciálních interferujících izotopů. Při výběru vhodného izotopu je nutné tedy vzít v úvahu zastoupení izotopu v přírodě. Z toho hlediska nejvíce vyhovuje ^{56}Fe . Nevýhodou toho izotopu je však možná interference s $^{40}\text{Ar}^{16}\text{O}$ nebo $^{28}\text{Si}^{28}\text{Si}$. Výběr jiného izotopu však není řešením díky kombinaci jak nízkého zastoupení, tak i výskytu interferencí. V tab. 1 je uveden pouze malý výčet základních interferencí, které je možné očekávat ať už z matrice vzorku, tak i podkladového materiálu. Nicméně, například interference pocházející z křemíku je patrná v případě tvrdších ablačních podmínek, kdy laserový svazek odpráší vzorek i s částí podkladového materiálu.

Izotop Fe	Zastoupení (%)	Příklad potenciálních interferencí
^{54}Fe	5,85	$^{54}\text{Cr}, ^{26}\text{Mg}(^{13}\text{C}^{13}\text{C})^{28}\text{Si}, ^{25}\text{Mg}(^{12}\text{C}^{13}\text{C})^{29}\text{Si}, ^{24}\text{Mg}^{28}\text{Si}^1\text{H}$
^{56}Fe	91,8	$^{40}\text{Ar}^{16}\text{O}, ^{28}\text{Si}^{28}\text{Si}, ^{12}\text{C}^{44}\text{Ca}, ^{13}\text{C}^{43}\text{Ca}$
^{57}Fe	2,12	$^{40}\text{Ar}^{17}\text{O}, ^{28}\text{Si}^{29}\text{Si}, ^{13}\text{C}^{44}\text{Ca}$
^{58}Fe	0,28	$^{40}\text{Ar}^{17}\text{O}, ^{29}\text{Si}^{29}\text{Si}, ^{58}\text{Ni}$

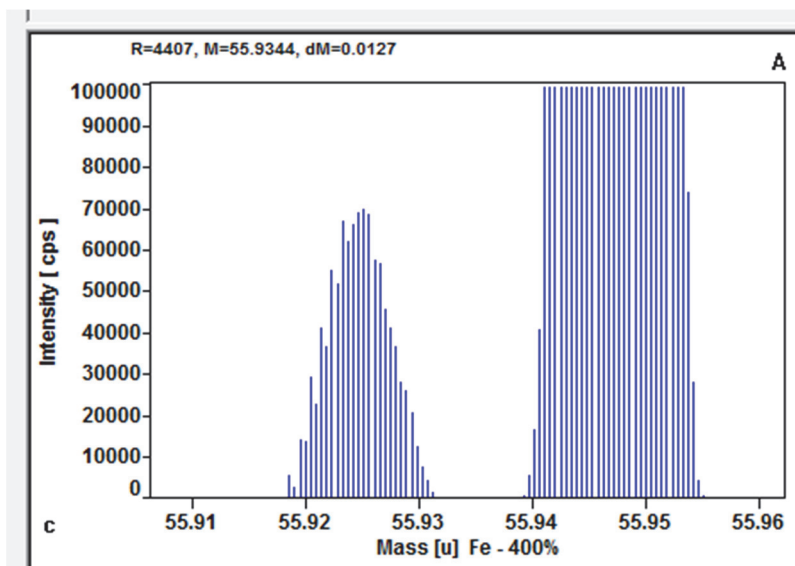
Tab. 1: Seznam izotopů železa s jejich zastoupením a možnými interferencemi.

Navíc minimalizace interferencí může být provedena i prostřednictvím samotného ICP-hmotnostního spektrometru.



Obr. 7: Fotografie ICP hmotnostního spektrometru s dvojí fokusací a díl sloužící pro výběr rozlišení. (www.thermofisher.com)

Spektrometr ICP-MS s dvojí fokusací (SF-ICP-MS) s názvem ELEMENT2 (Thermo Scientific) umožnuje minimalizovat vliv interferencí prostřednictvím výběru štěrbiny s rozdílnou tloušťkou, a tedy měření v nízkém (LR), středním (MR) a vysokém rozlišení (HR) (Obr. 7). Použití SF-ICP-MS v nízkém rozlišení odpovídá měření na samotném kvadrupólovém ICP-MS, a navíc bez kolizní cely. Nicméně ELEMENT2 dosahuje v tomto módu vyšší citlivosti. Práce ve středním rozlišení představuje značnou redukci toku iontů a výběr pouze úzké části píku. Tím je dosaženo až eliminace interferencí, ale na druhou stranu snížení intenzity signálu a zhoršení LOD. Z těchto důvodů byl hmotnostní spektrometr laděný s ohledem na maximální citlivost a také, aby došlo k rozdělení píku ^{56}Fe a $^{40}\text{Ar}^{16}\text{O}$ při měření ve středním rozlišení (Obr. 8).

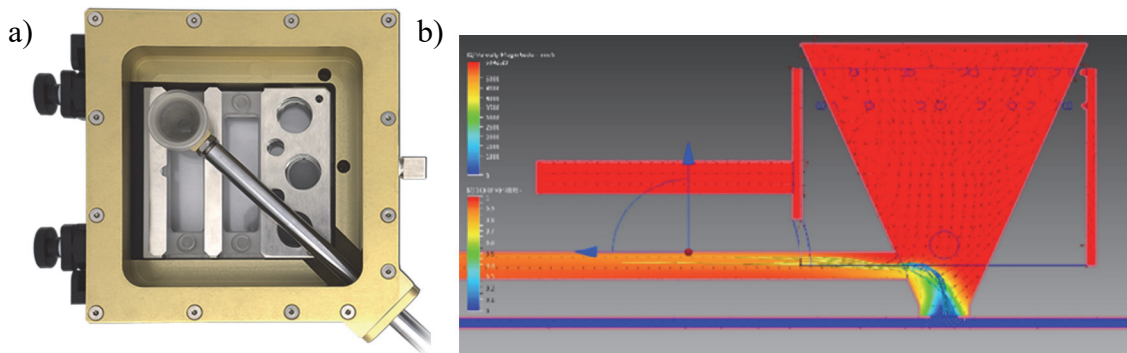


Obr. 8: Separace piků ^{56}Fe a $^{40}\text{Ar}^{16}\text{O}$ při měření ve středním rozlišení.

Stejně byly optimalizovány hodnoty šířky hmotnostního spektra, počet bodů, kterými je pík vykreslen, šířka integračního okna a integrační čas izotopu, aby celkový čas potřebný k záznamu jednoho bodu časově rozlišeného signálu byl co nejnižší, a také zaznamenávaná intenzita byla maximální. Nutno podoktnout, že optimalizace probíhala přímo na reálném vzorku a bylo nutné naměřené fluktuace korelovat s velikostí shluků ablatovaných buněk, a tím by i variabilita souvisela s rozdílnou tloušťkou vzorku, rozdílným množstvím odpařeného materiálu a rozdílnou akumulací Fe v rámci buněk. Prvotní nastavení metody bylo provedeno spíše orientačně s tím, že po optimalizaci vhodných ablačních parametrů může být metoda dodatečně upravena. K účelům studia interakce laserového svazku s buňkami byla však vhodná a dávala dostatečnou odezvu.

Ve spojení s SF-ICP-MS byl k analýze buněk zvolen ablační systém Analyte G2. Výhodou ablačního zařízení je konstrukce ablační cely. Jedná se o systém 2 cel, z nichž větší cela slouží jako prostor pro umístění držáku vzorků (Obr. 9a) a druhá cela malého objemu zajišťující odnos uvolněného aerosolu (Obr. 9b). Obě cely jsou proplachovány nosným plynem o rozdílné rychlosti průtoku. Výhodou uspořádání je možnost vložení několika vzorků v podobě tenkých plátků měkké tkáně / kvantifikačních standardů umístěných na nosiči a zároveň vložení tablet o průměru 2,5 a 1 cm. Vzorkovací cela, která je umístěna nad samotným vzorkem, je napojena na pohyblivé rameno, které společně s pohybem celé cely umožňuje vzorkování v kterémkoli místě ablační komory s konstantní vzdáleností od vzorku. Konstantní vzdálenost může být narušena navrstvením buněk v jednom místě, nicméně rozdíly ve výšce však dosahují velmi

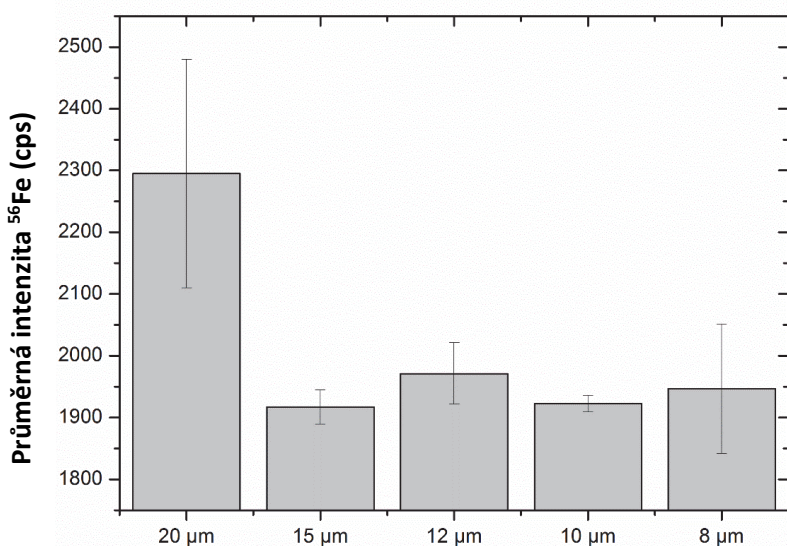
malých hodnot. Druhou velmi důležitou výhodou je objem vzorkovací cely, který ovlivňuje rychlosť vyplachování a tím i kvalitu signálu. Čím rychlejší je vymytí cely po ablaci, tím je dosaženo lepšího prostorového rozlišení a nedochází k mixování signálů z různých fází.



Obr. 9: a) Design ablační cely laserového ablačního systému Analyte G2 (Teledyne Cetac) a b) zobrazení toku ablačního plynu s aerosolem vzorku v malé sběrné cele. (<http://www.teledynecetac.com/products/laser-ablation/helexii>)

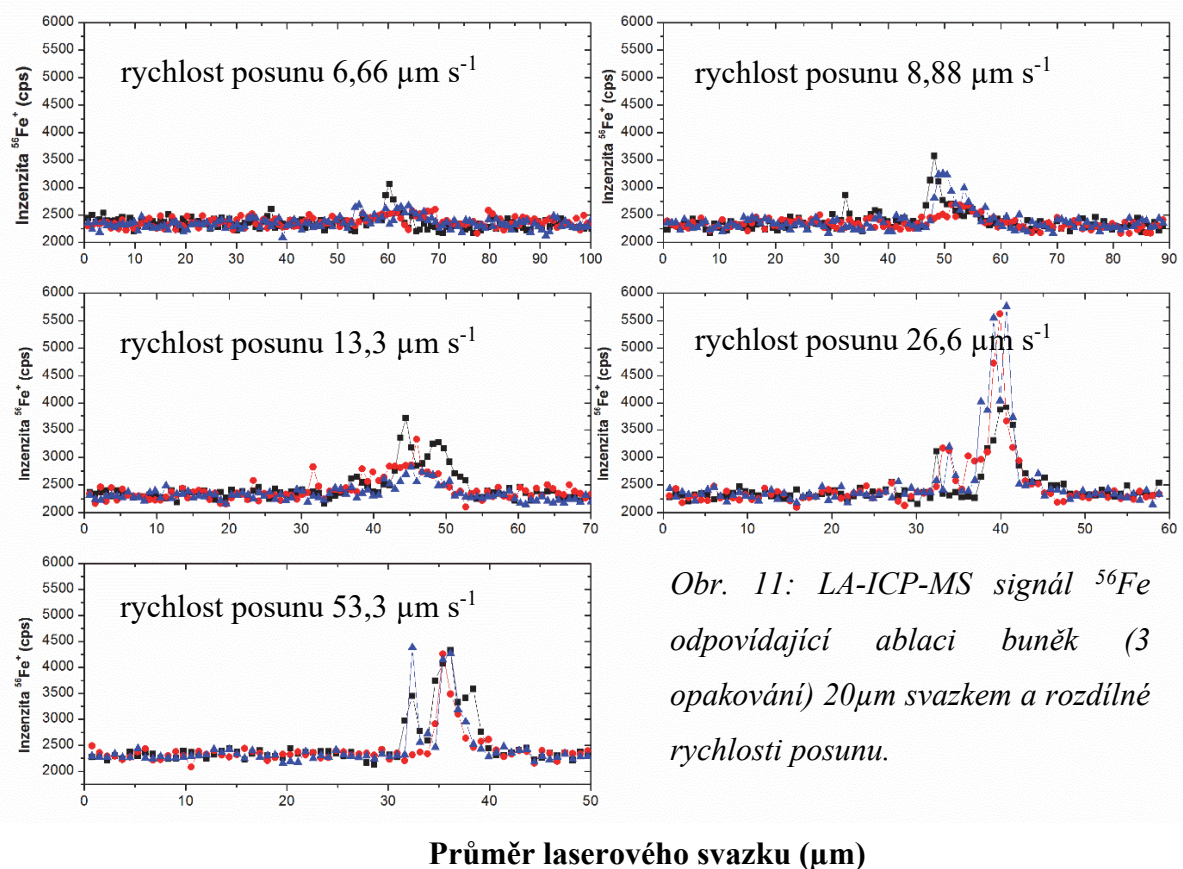
Pro studium interakce 193nm laserového svazku s buňkami byl zvolen liniový sken, který je vůči povrchu vzorku šetrnější než bodová analýza. Vzniklá ablační stopa nedosahuje takové hloubky, a navíc není časově a ani finančně náročná. Pozornost byla věnována rychlosti posunu vzorku při ablaci a také průměru laserového svazku dopadajícího na vzorek. V případě velikosti svazku byl požadavek jednoznačný – čím menší, tím větší pravděpodobnost vykreslení distribuce v rámci jedné buňky, ale tím dochází k ablaci menšího množství materiálu a ztrátě citlivosti. U rychlosti posunu je požadavek velmi podobný, čím menší překryv, tím je možné rozeznat i jádro buňky, ale opět tento přístup klade nároky na dostatečnou citlivost.

Velikost svazku byla testována v rozsahu 8-20 μm za konstantních parametrů – hustota zářivé energie, frekvence a nastavením rychlosti posunu tak, aby každý bod načítaného časově rozlišeného signálu odpovídal při frekvenci 10 Hz danému průměru. Navíc je zajištěno stejné procento překryvu kráterů v závislosti na jejich průměru (87 %). Vzhledem k tomu, že studie byla provedena na reálném vzorku, bylo každé měření opakováno 3x. Nicméně z výsledků nebyl jednoznačně prokázaný vliv průměru laserového svazku (Obr. 10) pravděpodobně díky variabilitě signálu izotopu železa závislého na počtu ablatovaných buněk.



Obr. 10: Průměrná hodnota signálu ^{56}Fe po ablaci buněk laserovým svazkem rozdílného průměru.

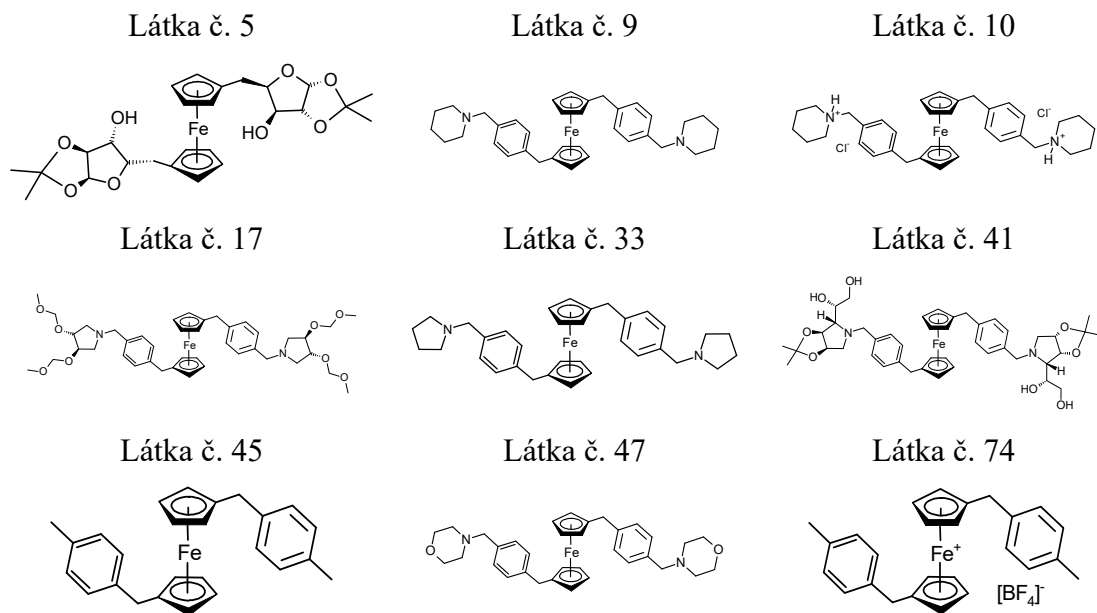
Naopak sledování změny signálu při konstantním průměru, ale rozdílné rychlosti posunu a klesajícím překryvem (A – 97 %, B – 96 %, C – 96 %, D – 87 % a E – 73 %) ukazuje, že snížení překryvu vede postupně ke zvýšení signálu pravděpodobně díky odprášení tenké povrchové vrstvy s větším podílem čerstvého povrchu (Obr. 11).



Obr. 11: LA-ICP-MS signál ^{56}Fe odpovídající ablaci buněk (3 opakování) 20 μm svazkem a rozdílné rychlosťi posunu.

Tento projekt navazoval na studii, kdy souběžně s testováním možností v laboratoři dostupné instrumentace byly opakovaně analyzovány buněčné linie SK-OV-3 a A2780 dopované i dalšími látkami na bázi ferrocenu (Tab. 3) o různých koncentracích s cílem zjistit průměrnou koncentraci Fe v buňkách a ověřit tak výsledky získané diferenční pulsní voltametrií provedené na MOÚ. Látky byly připraveny na Ústavu chemických procesů AV ČR a Ústavu fyzikální chemie J. Heyrovského AV ČR.

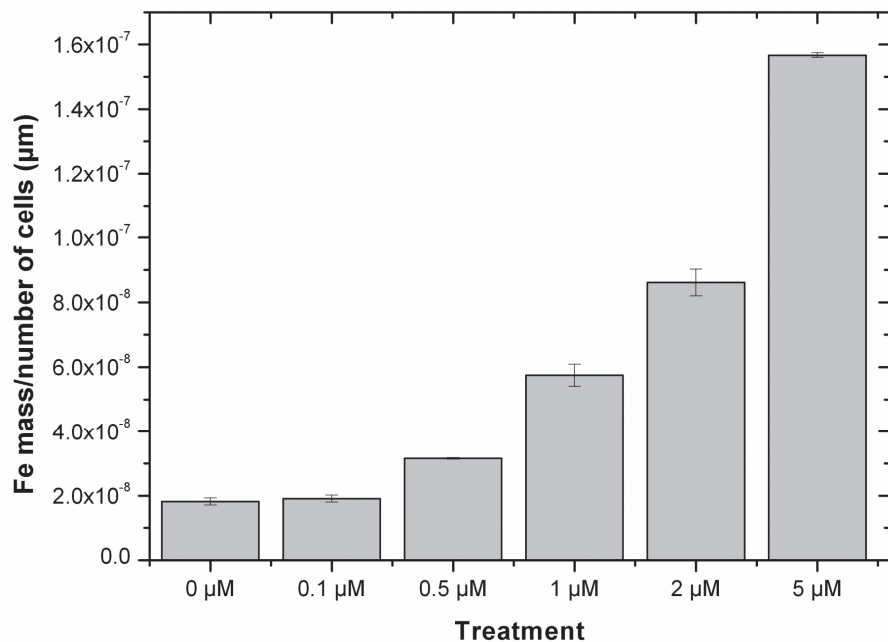
Roztoková analýza (SN-ICP-MS) nebyla rozhodně rutinní záležitostí. Musela být vypracována studie, která ukázala, jaké množství buněk je potřebných k detekci Fe po aplikaci látek a jejich proniknutí do samotných buněk. Ve většině případů byly experimenty založené na měření železa, které může být velmi snadno zatíženo kontaminací. Provádění v několika replikátech bylo z hlediska vysokého počtu buněk nereálné (1×10^7) a bylo opakováno pouze při sporných výsledcích. Rozklady byly prováděny v PFA kádinkách, do kterých byly buňky na MOU stáčeny, za přídavku HNO_3 a H_2O_2 . Aby byla zajištěna stejná matrice při měření, byly vždy rozložené vzorky odpařeny do sucha a zpětně rozpuštěny v ředěné HNO_3 . Díky předpokladu nízké koncentrace Fe, které je schopno do buňky proniknout, bylo nutné minimalizovat i celkový objem po rozkladu vzorku, který činil 2 ml.



Tab. 3: Seznam látek, které byly předmětem studia SN-ICP-MS a některé také LA-ICP-MS

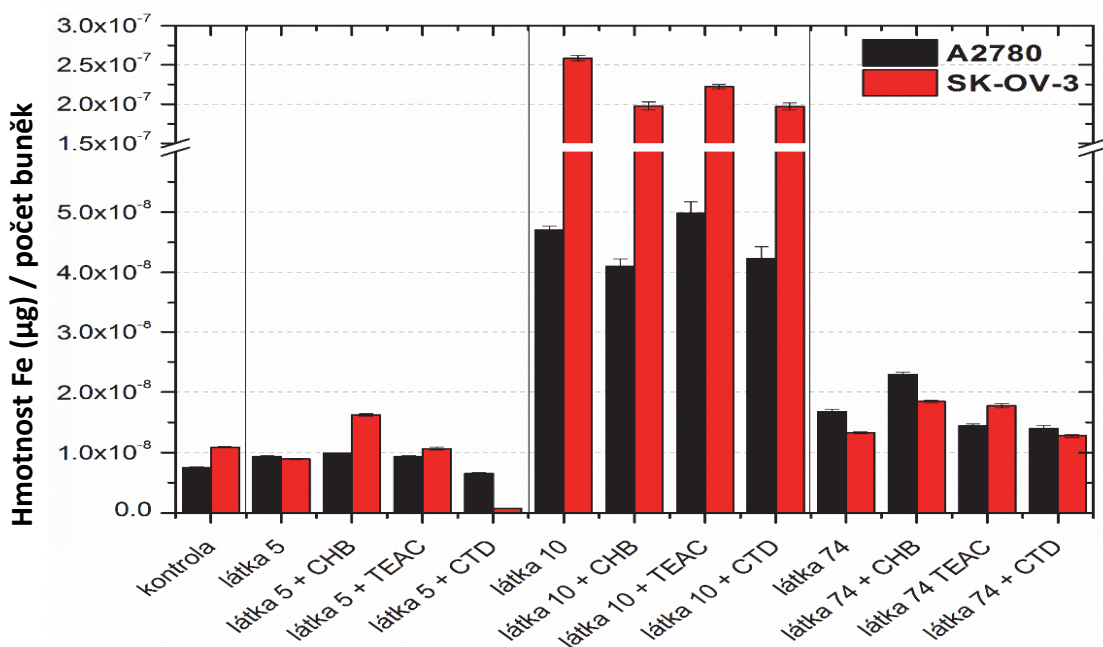
Souhrnně lze říci, že získání výsledku při analýze buněk v souvislosti s výzkumem organokovových sloučenin jako potenciálních chemoterapeutických léčiv zahrnuje několik kroků: *i)* syntéza látek, *ii)* jejich interakce s buňkou a *iii)* testování různými analytickými technikami. Je obecně známo, že pronikání organokovových látek probíhá pouze ve velmi malém procentu, a tudíž chyba každého mezikroku může vést ke zkresleným či mylným výsledkům. Z tohoto důvodu byl také ověřen krok rozkladu za pomocí látky č. 33 (Tab. 3), která byla inkubována s $6,15 \times 10^6$ buněk. Ty byly následně rozděleny na 4 díly s rostoucím počtem buněk. Odezva obsahu v závislosti na počtu buněk byla lineální s koeficientem determinace $R^2 = 0,9914$.

Příklad výsledku odezvy ICP hmotnostního spektrometru s rostoucí koncentrací po aplikaci uvedené látky do celkového množství buněk 2×10^6 je uveden na Obr. 12. Tato látka byla nejčastějším předmětem výzkumu právě díky jejímu „relativně snadnému“ proniknutí do zkoumané buněčné linie. Aplikace sloučeniny byla provedena ve dvou replikátech a vždy bylo provedeno 5 měření.



Obr. 12: Skutečný obsah Fe zjištěný pomocí SN-ICP-MS přeypočtený na celkový počet buněk v závislosti na koncentraci látky č. 10, kterou byly buňky dopované.

U vybraných látek byly koncentrace Fe testovány také po přídavku různých látek, které by mohly působit jako inhibitory – chlorazol black, cimetidin a tetraethyl ammonium chlorid (Obr. 13).



Obr. 13: Srovnání množství Fe, které proniklo do buněk při aplikaci látek 5, 10 a 74 společně s aplikací inhibitorů chlorazol black (CHB), tetraethyl ammonium chlorid (TEAC) a cimetidin (CTD). Test proveden na dvou buněčných liniích A2780 a SK-OV-3.

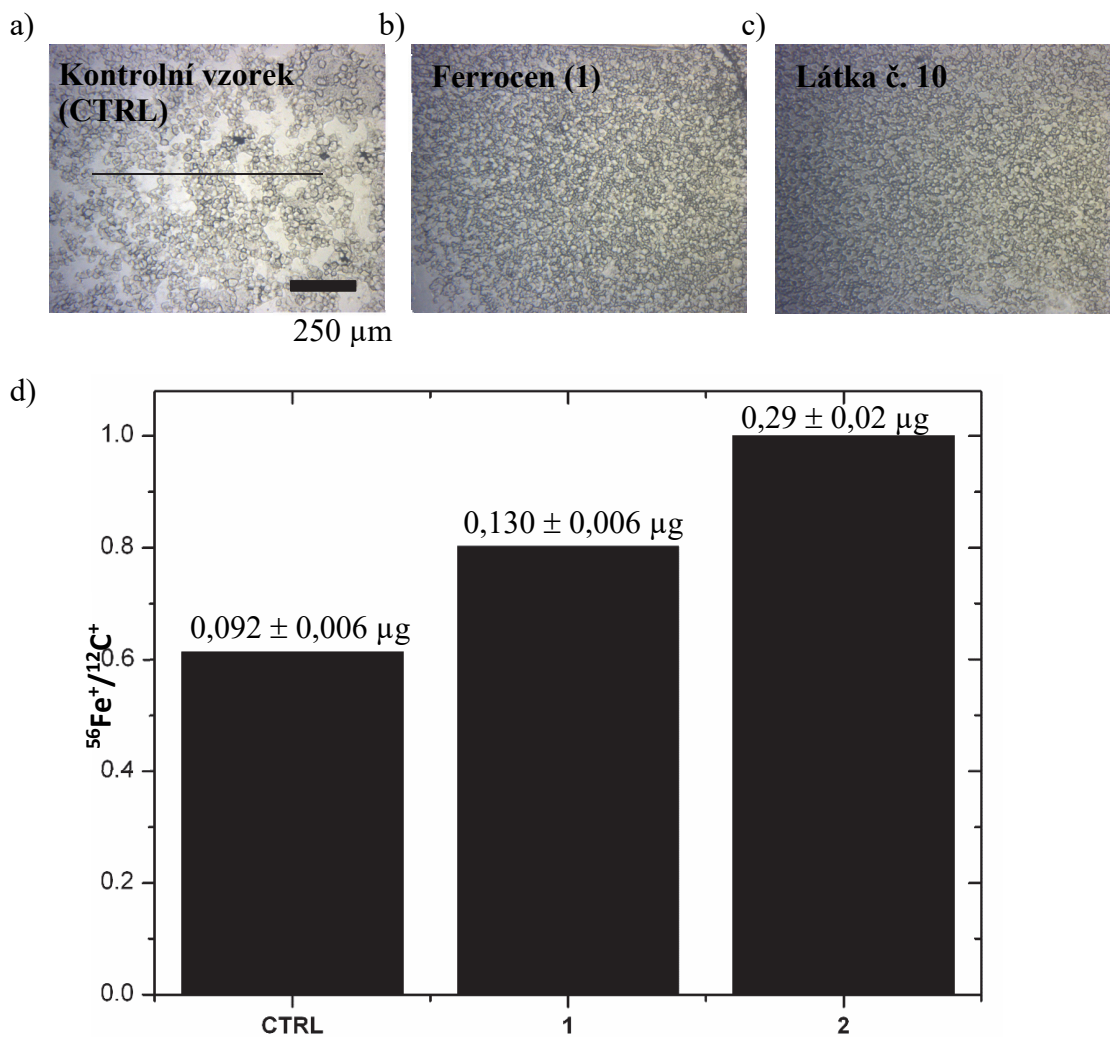
Porovnání odezvy ICP hmotnostního spektrometru po ablaci liniovým skenem s průměrem laserového svazku 15 µm byl také proveden na buňkách (A2780) bez přídavku jakékoli látky, dále za přídavku ferrocenu a látky č. 10. Ferrocen se vyznačuje velmi nízkou aktivitou, což potvrdila i laserová ablace. Skenování povrchu s buňkami dopovanými látkou č. 10 (Tab. 3) vykazuje vyšší odezvu izotopu železa děleného signálem uhlíku, který by měl charakterizovat přítomnost buňky. Porovnáním s roztokovou metodou bylo zjištěno obohacení Fe o 0,02 % u ferrocenu a 6 % u látky č. 10 (Obr. 14).

Práce byla přerušena z důvodu těhotenství a mateřské dovolené. Byla však prezentována na konferencích:

- 1) H. Skoupilová, J. Karban, J. Pinkas, M. Bartošík, **M. Vašinová Galiová**, R. Hrstka: Application of new organometallic compounds on ovarian cancer cell lines, Chemistry and biology of phytohormones and related substances, 2017.
- 2) **M. Vašinová Galiová**, R. Hrstka, K. Štúlová, K. Koubková, J. Karban, J. Pinkas a V.: Tracing of Cancer Cell-Specific Cytotoxic Drugs by Laser

Ablation ICP-MS, Winter Conference on Plasma Spectrochemistry, 2016., Tucson, USA.

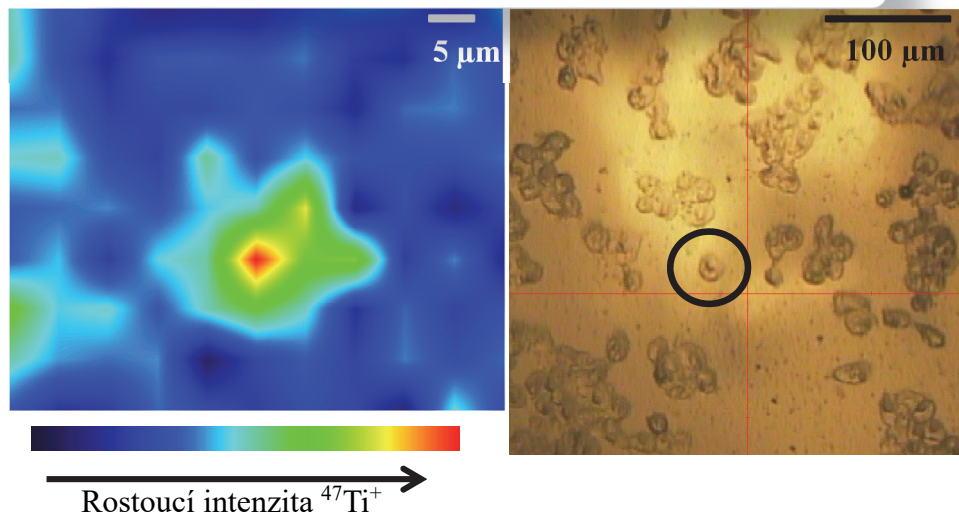
- 3) H. Skoupilová, B. Vojtěšek, R. Hrstka, M. Bartošík, **M. Vašinová Galiová**, L. Kafková, J. Karban aj. Pinkas: Feroceny a jejich potencionální protinádorový účinek, XL. Brněnské onkologické dny, 2016. ISSN 0862-495X.



Obr. 14: Fotografie povrchů vzorků buněk a) bez přídavku potenciálního léčiva, b) za přídavku ferrocenu a c) látky č. 10, které byly vzorkovány a analyzovány pomocí LA-ICP-MS, a. d) ukazuje LA-ICP-MS odezvu jednotlivých vzorků. Hodnoty představují obsah Fe zjištěný pomocí SN-ICP-MS.

Spolupráce se skupinou doc. Romana Hrstky, Ph.D. z MOU byla dlouhodobou spoluprací, v rámci které jsme se zabývali i organokovovými látkami na bázi Ru, Ti i Pt (Obr. 15).

LA-ICP-MS imaging – single cell analýza – distribuce Ti



Obr. 15. Distribuci Ti v rámci jedné buňky získaná ablaci 4 μm laserovým svazkem.

Mapování pomocí LA-ICP-MS bylo také testováno na řezu nádorové tkáně, kde předmětem studia byla distribuce Pt po neúspěšné aplikaci léčiva. Z obrázku je patrné, že Pt byla detekována převážně v oblasti atrofické tkáně vejcovodu, ale nebyl zaznamenán průnik do samotného nádoru (Obr. 16).

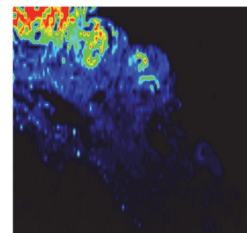
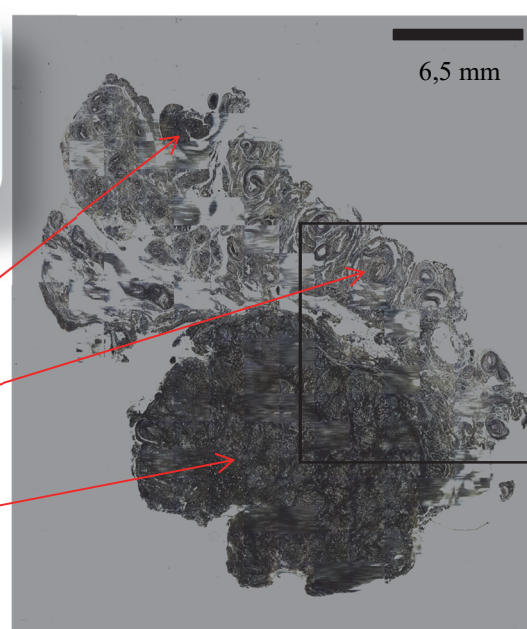
LA-ICP-MS imaging – analýza nádorové tkáně – distribuce Pt

Proliferující mezotel
nebo nádor

Zřejmě atrofická tuba
(vejcovod)

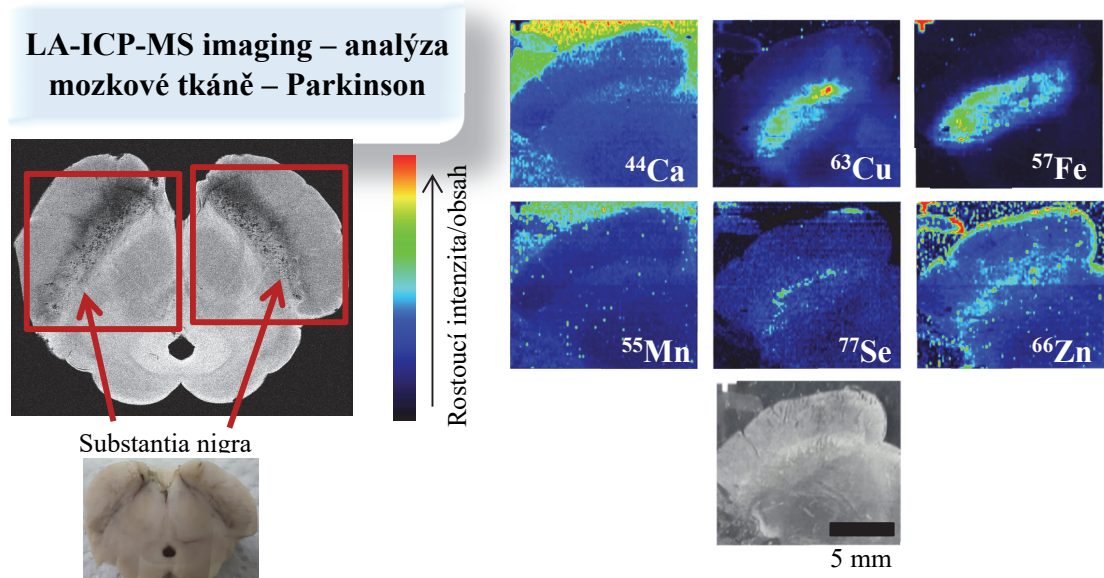
tumor

6,5 mm



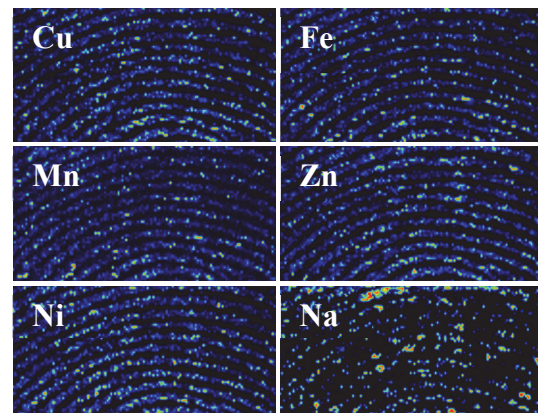
Obr. 16: Distribuce Pt v nádorové tkáně po aplikaci a neúspěšné léčbě pomocí cis-Pt.

Velmi zajímavou aplikaci představuje analýza mozkové tkáně pacientů postižených Parkinsonovou chorobou. Konkrétně se jednalo o část středního mozku – Substantia Nigra (SN) a dále také Locus coeruleus. LA-ICP-MS by v tomto případě byla využívána ke stopování Fe uloženého v dopaminergních neuronech s vazbou na neuromelanin. Znát původ železa je důležité především z hlediska sledování léčby a chelatace Fe. Jedním z projevů Parkinsonovy choroby je právě ztráta buněk v SN (poškození funkce neuronů SN) a pokles vazby nigrálního železa na neuromelanin (Obr. 17).

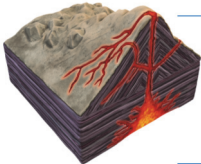


Obr 17: LA-ICP-MS v analýze mozkové tkáně.

V neposlední řadě je třeba poukázat na citlivost LA-ICP-MS metody, a tudíž vysoké požadavky na čistotu při manipulaci se vzorkem. Ta by měla vždy probíhat v rukavicích nejen z důvodu bezpečnostních, ale také z důvodu zamezení kontaminace následně analyzovaného povrchu. Obr. 18 demonstriruje použití metody pro zobrazení papilárních linií prostřednictvím nečistot, které na povrchu prstu mohou být zachyceny.



Obr 18: Otisk prstu vykreslený pomocí LA-ICP-MS.



Laserová ablace ICP hmotnostní spektrometrie a její uplatnění v geologii

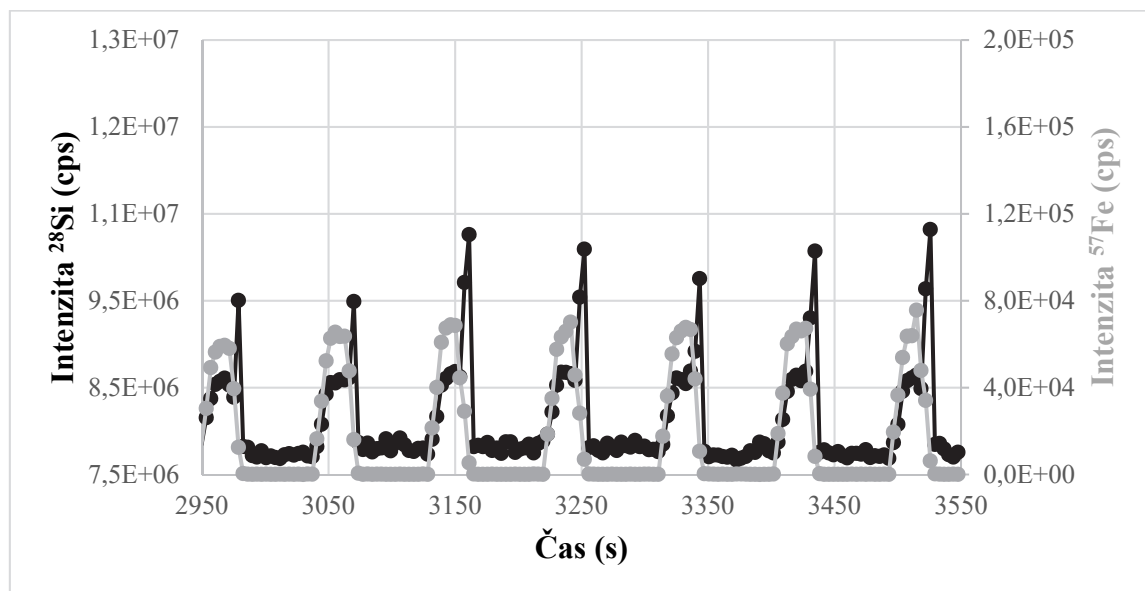
Jak bylo zmíněno na samotném začátku habilitační práce, největší počet publikací (~ 60 %) využívajících LA-ICP-MS metodu k potvrzení, ověření nebo objevení různých hypotéz tvoří právě geologie, mineralogie, geochemie a další jim přidružené obory. A využití vzrůstá právě s vývojem samotné instrumentace.

V nejjednodušším pojetí je metoda využívána k *in situ* analýze obsahu vybraných prvků v minerálech již od roku 2001, a díky zaostření laserového svazku na velmi malou plochu, také prvkové analýze v rámci zonality vybraných zrn. Není výjimkou ani aplikace metody pro 2D nebo 3D mapování povrchu v celé řadě minerálů.¹¹⁰⁻¹¹⁴ Další možnosti aplikace LA-ICP-MS je v oblasti stanovení izotopových poměrů, kdy jsou obsahem publikací nejen samotné stanovené hodnoty, jejich interpretace a vzájemné srovnání, ale jsou také zmiňovány i návaznosti na konstrukci různých typů hmotnostních spektrometrů a ablačních systémů a možnosti jejich využití z hlediska preciznosti a pravdivosti. Studovány jsou izotopové poměry $\delta^7\text{Li}$, $\delta^{11}\text{B}$, $\delta^{26}\text{Mg}$, $\delta^{32}\text{S}$, $\delta^{37}\text{Cl}$, $\delta^{44}\text{Ca}$, $\delta^{53}\text{Cr}$, $\delta^{56}\text{Fe}$, $\delta^{65}\text{Cu}$, $\delta^{66}\text{Zn}$, $\delta^{80}\text{Se}$, $\delta^{87}\text{Sr}$, $\delta^{97}\text{Mo}$, $\delta^{143}\text{Nd}$, $\delta^{176}\text{Hf}$, $\delta^{187}\text{Os}$, $\delta^{205}\text{Tl}$, nebo systémy Pb, U-Th-Pb.

S cílem popsat průběh geochemických procesů a chemismus minerálů slouží metoda LA-ICP-MS především jako nástroj ke stanovení izotopových poměrů a obsahů prvků, zejména stopových, které není možné detektovat jinými metodami, ať už z hlediska LOD nebo zcela nemožnosti daný prvek stanovit. Roli hráje i cena analýzy a nedostupnost přístrojů. Kdybychom měli porovnat aplikaci LA-ICP-MS v geologii ve srovnání s analýzou biominerálů nebo měkkých tkání, je složitost dána především vysokou variabilitou chemického složení a tím i různých fyzikálních vlastností, které se odrážejí na interakci laserového paprsku se vzorkem, frakcionaci, matričních efektech, preciznosti měření a v nejhorším případě i na vyvození chybných závěrů. Je tedy nutné přistupovat k analýze komplexně.

Cesta k preciznímu a přesnému výsledku začíná již samotnou přípravou vzorku. V geologických studiích jsou hojně využívány vzorky zpracované do formy výbrusů (tenké plátky materiálu přilepené na vhodném pokladu – nejčastěji sklo) s tloušťkou

v desítkách μm . Důvodem je jejich využití u mikroskopických metod v petrografii nebo petrologii. Nicméně pro popis geochemických procesů je často studováno chování většího množství prvků, což klade nároky na celkový čas vzorkování. Je pak velmi časté propálení laserového svazku skrze vzorek i během 30 s, což má za následek nadhodnocení nebo naopak podhodnocení signálu (Obr. 19) Řešením je příprava výbrusu s větší tloušťkou ($300 \mu\text{m}$) nebo alternativou k výbrusu je příprava vzorku ve formě pelet, kdy je možné propálení zabránit.



Obr. 19 Průběh signálu ^{28}Si a ^{57}Fe během bodové ablaci (30 s) tenkého výbrusu cordieritu. Navýšení signálu ^{28}Si ke konci ablaci naznačuje vzorkování skleněného podkladového materiálu.

Pokud je to možné, je vhodné zvážit i použitý ablační systém a ICP hmotnostní spektrometr. Pro většinu aplikací je z hlediska absorpce laserového záření materiélem, distribuce velikosti částic a frakcionace vhodné využití kratších vlnových délek, opomeneme-li délku pulzu.¹¹⁵⁻¹¹⁸ V rámci vlastních experimentů bylo zjištěno, že využití excimerového systému Analyte G2 vs. NWR UP213 vede k lepší stabilitě zaznamenávaného signálu ablatovaných minerálů. Vedle vlnové délky však hráje roli i fakt, že systémy mají rozdílný design a objem ablačních cel, které se promítají do kontaminačních efektů a nadhodnocují zaznamenávané signály a také zvyšují hodnoty LOD. Nejčastěji jsou pozorovány na Sn, Si, Ti a Fe. Důležitým aspektem je také kvalita optického systému umožňující přesnou lokalizaci analyzované oblasti. Srovnání ICP hmotnostních spektrometrů SF-ICP-MS vs. Q-ICP-MS ukázalo lepší citlivost při využití vysoko rozlišovacího systému s dvojí fokusací. Vytváření ICP-MS metod v analýze

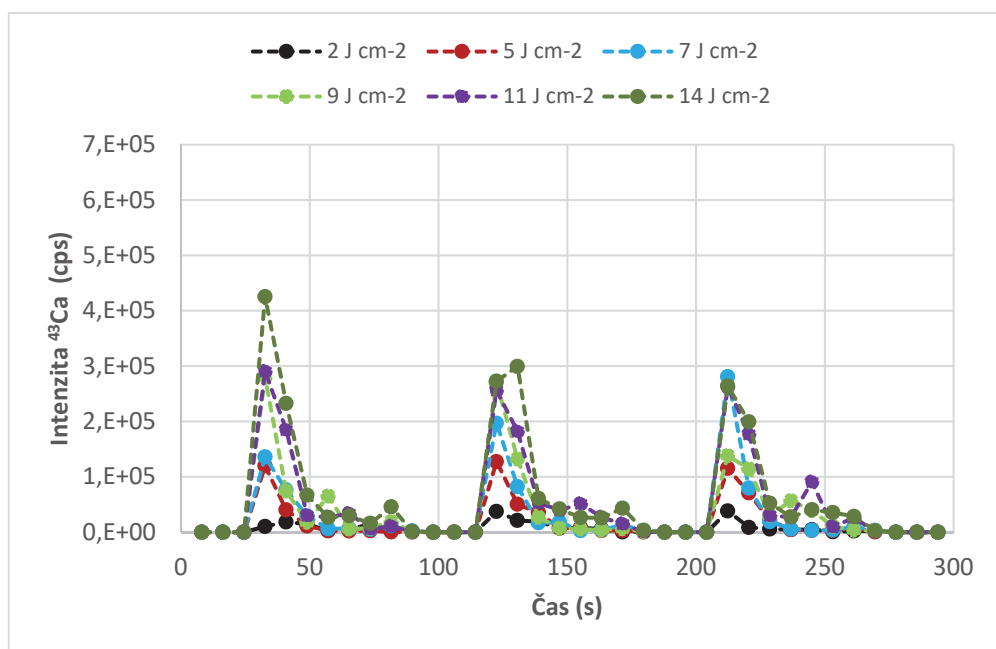
geologických materiálů je však komplikované z hlediska výskytu interferencí. U většiny studií byly zkoumány asociace i 30 prvků. Mezi nejčastěji měřené patřily prvky vzácných zemin, které po normalizaci na chondrit a zobrazení celkových REE paternů poukazují na anomálie zkoumaných systémů. Interferenční signály jsou u těchto prvků velmi časté a vyžadují sledování signálu většího počtu izotopů daného prvku. Prvky, jako např. Be, Na, Al, P, Sc, Mn, Co, As, Y, Nb, Cs, Pr, Tb, Ho, Tm, Bi, Th, jsou však monoizotopické a sledování interferencí je obtížné. V takovém případě vyžaduje jejich stanovení měření ve vyšším rozlišení. SF-ICP-MS umožňuje záznam signálu při různých rozlišeních, ale je nutné volbu zvážit, protože zvýšení rozlišení s sebou nese i pokles citlivosti díky redukcii iontového svažku, který dopadá na detektor. Kombinace rozlišení v rámci měření jednoho bodu je možná. První z možností je měření vybraných iontů nejprve v nízkém rozlišení a následně zbytek ve vyšším rozlišení. Druhou možností je měření podle stoupajícího m/z se střídavými pohyby štěrbiny (neustálé přepínání mezi rozlišeními), což klade nároky na instrumentaci a také na čas potřebný pro posun štěrbiny a celkový čas záznamu ablaci. Je však nutné vzít v úvahu, že měření bez ohledu na rozlišení probíhá sekvenčně a body časově rozlišeného signálu odpovídají materiálu z rozdílné hloubky ablačního kráteru. Když k tomu přidáme skutečnost, že jsou ionty analyzovány separátně v různých modech rozlišení, pak při dynamickém vzorkování laserovým svažkem a stálým prohlubováním ablační stopy, a tedy většími rozdíly mezi aerosolem, není kombinace rozlišení příliš vhodná. Z těchto důvodů je žádoucí provádět měření v jednom rozlišení v rámci jednoho ablatovaného místa. Zvážíme-li interference, LOD, obsahy analyzovaných prvků, konečné nastavení metody je tedy otázkou komplexního přístupu s ohledem na cíl stanovení. Z tohoto pohledu je velmi výhodné využití ICP hmotnostního spektrometru s analyzátem dobýváním, protože se jedná o simultánní záznam odpařeného materiálu od Li po U, jehož rychlosť záznamu je při porovnání všech analyzátorů nejvyšší. Rychlé vymývání částic z ablační cely pak není limitováno pomalou a sekvenční separací a detekcí.

Před analýzou jsou nastavovány stejné experimentální parametry jako v případě jakýchkoli jiných vzorků. Bohužel díky různorodosti fyzikálně-chemických vlastností minerálů, a to i v případě stejných minerálů ovšem odebraných z jiného systému, klade náročnost na frakcionaci a matriční efekty. Například zdánlivě velmi podobné minerály jako sodné hlinitokřemičitany (plagioklasy) a draselné hlinitokřemičitany (K-živce) se při ablaci chovají rozdílně a nemohou být analyzovány za stejných podmínek. V případě některých minerálů může být optimalizace ablačních parametrů značně komplikovaná a

nemusí být vždy dosaženo stabilního signálu. Typickými zástupci jsou fluorit a křemen (Obr. 20).

Předposledním krokem k získání výsledku je ablaci kvantifikačních standardů. Jak již bylo několikrát zmíněno, Achillovou patou metody je nedostatek standardů, a to právě na poli geologických materiálů. Komerčně dostupné jsou tablety basaltového skla nebo NIST SRM. Ty však matričně nemohou pokrýt analyzované vzorky. Také je možné využít reálné vzorky po předchozí verifikaci, nicméně jejich použití je značně omezené. Komerčně dostupné jsou i práškové standardy, ale jejich chování při interakci je zcela odlišné. Z tohoto důvodu jsou připravovány standardy tavením v laboratořích a následně sdíleny v komunitě analytických chemiků / geochemiků.

Posledním krokem je samotné vyhodnocení signálu. Často jsou využívány pouze průměrné hodnoty intenzit a je možné je získat téměř automaticky prostřednictvím vhodného softwaru (Iolite). Nevýhodou je nedokonalá filtrace tzv. spiků, které signál uměle nadhodnocují. Z tohoto hlediska je užitečná integrace plochy píku a zároveň identifikace bodů, které by mohly být zatíženy ablací inkluzí. Tento přístup však vyžaduje již určitou praktickou zkušenosť. V závislosti na cílech analýzy jsou aplikovány i různé statistické metody k jejich dosažení.



Obr. 20: Průběh signálu ^{43}Ca při ablaci fluoritu 213 nm laserovým svazkem a frekvenci 5 Hz.

Aplikacím LA-ICP-MS v geologii jsem se začala věnovat před více než 10 lety v rámci spolupráce s Ústavem geologických věd Masarykovy univerzity. Početná skupina geologických výzkumníků zahrnovala prof. RNDr. *Milana Nováka*, CSc., doc. Mgr. *Radka Škodu*, Ph.D., doc. Mgr. *Jana Cempírka*, Ph.D., Mgr. *Renatu Čopjakovou*, Ph.D., Mgr. *Petra Gadase*, Ph.D., doc. RNDr. *Janu Kotkovou*, CSc. a početnou skupinu jejich bakalářských, diplomových a doktorských studentů. Vedle brněnské skupiny probíhala spolupráce s RNDr. *Karlem Breiterem*, DSc. (Geologický ústav AV ČR, v. v. i.), doc. Mgr. *Jindřichem Kynickým*, Ph.D. (CEITEC, VUT), Mgr. *Jiřím Sejkorou*, Ph.D., doc. RNDr. Mgr. *Lukášem Krmíčkem*, Ph.D. a Dr. *Adamem Szuszkieviczem* (University of Wroclaw).

Z dlouholeté spolupráce vznikla celá řada publikací a konferenčních příspěvků, které využívají LA-ICP-MS většinou ke stopové analýze individuálních bodů. V menší míře byla metoda využita pro 2D mapování. V rámci této dlouhotrvající spolupráce byly podrobeny analýze nejrůznější typy minerálů, ovšem nejpočetnější skupinu tvořily silikáty turmalín, granát, beryl, cordierit, sekaninait, darrellhenryit, zirkon, plagioklas, K-živec, biotit, spodumen, thalenit, cookeit, gadolinit, milarit, fluorit, borosilikáty s mullitovým typem struktury (vránait, boralsilit, werdingit a grandidierit), slídy s rozdílným obsahem Li (jednotky mg kg^{-1} až 3,5 wt.%) aj. Byly také analyzovány minerály s matricí karbonátovou, fosfátovou nebo některé skupiny Nb-Ta minerálů (columbit-tantalit, pyrochlor-mikrolit). Vzhledem k rozmanitosti byly vytvářeny studie ohledně interakce s laserovým svazkem a její vliv na stabilitu ICP-MS signálu a věrohodnost výsledků. Byly použity 2 laserové ablační systémy (excimerová Analyte G2 a New Wave Research UP 213) a také dva hmotnostní spektrometry (kvadrupolový Agilent 7500ce a s dvojí fokusací Element 2, Thermo). Metodiky byly vytvářeny postupně podle výše popsaného schématu. Pro účely habilitační práce byly vybrány pouze některé publikace **XII** a **XVIII**. Podíl spočívá v příspěvku experimentálních dat získaných pomocí LA-ICP-MS podle výše uvedeného postupu.

V případě publikací „*Diversity of lithium mica compositions in mineralized granite-greisen system: Cinovec Li-Sn-W deposit, Erzgebirge*“ (**XII**) a „*The transition from granite to banded aplite-pegmatite sheet complexes: An example from Megiliggar Rocks, Tregonning topaz granite, Cornwall*“ (**XIII**) byla studie zaměřena na analýzu trioktaedrických Li-slíd s relativně vysokým obsahem Li (1,5 – 2,5 hm.%). Úkolem bylo sledování obsahu vybraných prvků Li, Al, Si, Sc, Ga, Ge, Nb, In, Sn, Cs, Ta W a Tl v Li-

slídách, dále draselých živcích a turmalínech pomocí LA-ICP-MS. Důraz byl kladen na průměr laserového svazku a také vhodné hustoty zářivé energie. Výsledky bylo třeba korelovat s požadavky na dosažené LOD a velikosti zrn reálných vzorků. V případě In, Ge, W a Tl byly však obsahy velmi nízké. U In dosahovaly hodnoty i nižších než 1 mg kg^{-1} . Kvadrupolové ICP-MS, které bylo k této účelům spojeno s laserovým ablačním systémem New Wave UP213, dovoluje vhodné nastavení času záznamu, nicméně signál byl rušen interferencí Sn. Ačkoli In může být měřeno na 2 izotopech, tak právě více zastoupený izotop ^{115}In je rušen signálem ^{115}Sn . Využití méně zastoupeného izotopu však nebylo v případě některých vzorků přijatelné a musely být provedeny početní korekce. Byl také řešen kontaminační efekt, který měl negativní dopad na obsahy Sn v důsledku vysokého pozadí Si. Dalším problémem při stanovení byla samotná kvantifikace. Dostupnost standardů pro stanovení prvků v Li slídách je nulová. Použití komerčně dostupných silikátových skel NIST 610, 612 a 614 nemuselo být v případě Li dostačující, protože maximální obsah Li je $\sim 350 \text{ mg kg}^{-1}$. Z toho důvodu byl testován reálný vzorek spodumenu obsahující $\sim 3,5 \text{ hm.\%}$ Li jako potenciálního standardu nejen pro stanovení, ale také minerál pro ověření obsahu vypočteného pomocí NIST SRM. V souvislosti s dlouhou dobou trvání projektu, musela být kontrolována reprodukovatelnost měření. Za tímto účelem bylo vždy při každém měření provedeno kontrolní měření vzorku testovací slidy, které poukázalo na nutnou změnu experimentálních parametrů související nejčastěji s technických stavem přístrojů. Vzhledem k známé štěpnosti slíd, byl také testován vliv orientace krystalu na intenzitu a stabilitu zaznamenávaného signálu a následně na kvantifikaci. Tato rozsáhlá studie umožnila produkci dat na téměř 40 vzorcích umožňující interpretaci vývoje granitoidů a prokázání možnosti Li-slíd akumulovat stopové prvky v procesu magmatické frakcionace a metasomatické greisenizace na základě vzájemného srovnání obsahů prvků. Studie byla provedena ve spolupráci se studentkou doktorského studijního programu, které jsem školitelkou.

Publikace „Milarite-group minerals from the NYF pegmatite Velká skala, Písek district, Czech Republic: sole carriers of Be from the magmatic to hydrothermal stage“ (XIV) je věnována studiu milaritů z oblasti NYF pegmatitů Velká skála. Na základě minerální asociace, texturních znaků a chemického složení byly rozlišeny milarity magmatického a hydrotermálního původu a nastíněn jejich vývoj. Role LA-ICP-MS metody byla ve stanovení Be a REE v případě bodových analýz. Také byla sledována distribuce Be, Sc, Si a Al pomocí $4\mu\text{m}$ laserového svazku. Distribuce Be prokázala

významný obsah Be v REE bohaté generaci milaritu IV. Chemický vývoj milaritu lze zjednodušeně vyjádřit: Al + Ca → Be + Sc → Be + Y, HREE → Be + LREE směrem k rostoucím obsahům Be a REE.

Publikace „Sc- and REE-rich tourmaline replaced by Sc-rich REE-bearing epidote-group mineral from the mixed (NYF + LCT) Kracovice pegmatite“ (XV) se věnuje analýze turmalínů z NYF i NYF+LCT pegmatitů třebíčského plutonu. Obecně je chemické složení turmalínů hojně využíváno k interpretacím geochemických procesů, podmínek a prostředí jejich vzniku. Turmalíny jsou složité borosilikáty a vzhledem k velkému množství různých strukturních pozic jsou schopny inkorporovat do své struktury celou řadu prvků. Tato studie je typickým příkladem aplikace LA-ICP-MS v analýze REE. Její význam spočívá v doposud nedostatečném prozkoumání vstupu stopových prvků do turmalínů. Nejdůležitějšími ukazateli v této publikaci byly právě obsahy REE + Y, Sc, a Li. Byla studována distribuce vybraných prvků v turmalínu a v produktech jeho rekrytalizace při přechodu z magmatického stádia krystalizace do hydrotermálního stádia krystalizace.

Další vybranou publikací je „Vránaite, ideally $Al_{16}B_4Si_4O_{38}$, a new mineral related to boralsilite, $Al_{16}B_6Si_2O_{37}$, from the Manjaka pegmatite, Sahatany Valley, Madagascar“ (XVI), kde LA-ICP-MS byla použita pro analýzu lehkých prvků (Li, Be a B), které není možné stanovit pomocí EMP. Metody EMPA a Ramanova spektroskopie a LA-ICP-MS byly využity ke stanovení složení, struktury a určení přesného vzorce nového minerálu vránaitu, který je rozpadovým produktem Li-alumosilikátu spodumenu.

Podobnou publikací jako v předchozím případě je „Gadolinite-(Nd), a new member of the gadolinite supergroup from Fe-REE deposits of Bastnas-type, Sweden“ (XVII), kdy LA-ICP-MS společně s EMP, Ramanovou spektroskopí a RTG difrakcí byla využita ke kompletnímu popisu nového minerálu gadolinitu-(Nd) $Nd_2FeBe_2Si_2O_{10}$. Obsahy Be a B získané pomocí LA-ICP-MS významně přispěly k potvrzení správnosti uvažovaného empirického i ideálního vzorce. Jako doplňující informace byly diskutovány obsahy stopových prvků, jako jsou U, Th a Eu a HREE. Tyto informace přispěly k vykreslení kompletního REE patternu gadolinitu-(Nd) z typové lokality.

Rozsáhlá práce v oblasti aplikace LA-ICP-MS vznikla v rámci komerčních analýz strategické suroviny – tantalu, týkající se studia původu Ta-Nb rud pro výrobce elektronických součástek prostřednictvím stanovení stopových prvků v „coltanu“ (kolumbit-tantalitu a mikrolitu). Díky původu těchto rud (střední Afrika) patří minerály právě mezi ty konfliktní a jsou označovány také jako „krvavý coltan“ díky ozbrojeným konfliktům, násilí a potírání lidských práv v dané oblasti. Konfliktní minerály jsou také uváděny pod zkratkou 3TG – rudy, které obsahují cín, tantal, wolfram a zlato. Vedle LA-ICP-MS analýz byl fingerprinting založen také na využití EMP a TIMA (systém pro automatickou kvantitativní mineralogii) a aplikaci pokročilých statistických metod. Cílem analýz bylo identifikovat minerály pocházející z konfliktních oblastí a tím se vyhnout nepřímé podpoře ozbrojeným konfliktům. Společně s kolegy z Ústavu geologických věd (doc. Mgr. Radek Škoda, Ph.D., Mgr. Renata Čopjaková, Ph.D. a Mgr. Jan Loun, Ph.D.) bylo analyzováno 100 vzorků. Předmětem studia byly následující prvky: Li, Na, Mg, Al, Si, Al, Sc, Ti, V, Cr, Mn, Fe, Ni, Cu, Zn, Sr, Y, Zr, Nb, Mo, Sn, Sb, Ba, REE, Hf, Ta, W, Pb, Th a U. Vzhledem k počtu prvků, musela být matrice pečlivě vyšetřena na potenciální interference a v případě jejich výskytu, musela být stanovena míra jejich vlivu na fingerprinting. K ověření správnosti výsledků byl použit laboratorně připravený standard kolumbitu. Výsledky získané na Ústavu chemie byly porovnávány s databází vytvořenou v BGR (Bundesanstalt für Geowissenschaften und Rohstoffe, Hannover), čímž byla ověřena spolehlivost výsledků. Vedle firmou požadovaných cílů vznikla i publikace „**Geochemistry and secondary alterations of microlite from eluvial deposits in the Numbi mining area, South Kivu, Democratic Republic of the Congo**“ (XVIII) věnující se studiu alteračních pochodů v U-bohatém a U-chudém mikrolitu, které prodělaly sekundární nízkoteplotní alteraci během zvětrávání pegmatitu, při které U zůstal ve struktuře mikrolitu. Vzhledem k podobným podmínkám s úložištěm jaderných odpadů, by mohl být mikrolit potenciálně použitelný pro imobilizaci U. Zjištěné zastoupení stopových prvků ve struktuře mikrolitu a jeho neobvyklé alterace jsou charakteristické pro studované lokality a mohly by tak být užitečné při zjišťování provenience tantalových rud.

Problematice provenience je věnována i publikace „**Laser microsampling and multivariate methods in provenance studies of obsidian artefacts**“ (XIX), která vznikla v rámci programu KONTAKT a projektu s názvem „Laser ablation inductively coupled plasma mass spectrometry and laser induced breakdown spectroscopy in archaeology and

anthropology“, kdy analýza obsidiánů byla provedena jak na Masarykově univerzitě a také na California State University, Long Beach v rámci několikatýdenních pobytů. Práce je složena z výsledků získaných na kvadrupólovém ICP-MS a hmotnostním spektrometru s analyzátem doby letu. Cílem projektu bylo na základě složení zdrojových obsidiánů určit původ artefaktů. Početná skupina vzorků byla podrobena LA-ICP-MS analýze a kvantifikovaná data následně zpracována pokročilými statistickými metodami, které jednoznačně prokázaly odlišení různých zdrojů na základě chemického složení stopových prvků.

Studu geologických vzorků byla věnována úspěšně obhájená (2016) *diplomová práce „Hmotnostní spektrometrie indukčně vázaného plazmatu v analýze geologických materiálů“* vypracovaná studentem Mgr. Petrem Chrástem pod mým vedením. Práce byla věnována frakcionaci, matričním efektům a volbě experimentálních parametrů LA i ICP-MS za použití 213 i 193nm ablačních systémů studovaných na komerčně dostupných NIST SRM a bazaltovém skle BCR-2G, a také sadě laboratorně připravených standardů MPI DING získaných z Max Planc Institute a kolumbitu C139 pocházející z BGR.

„*Využití excimerového laseru ve spojení s ICP-MS s dvojí fokusací*“ je název *bakalářské práce* úspěšně obhájené v roce 2014 Mgr. Jiřím Palátem opět pod mým vedením. Jedná se o rešerší zaměřenou na LA-SF-ICP-MS v analýze izotopových poměrů B, Li, Sr a také datování zirkonů.

Využití metody LA-ICP-MS geologických materiálů bylo předmětem několika přednášek v rámci 1) Summer course Geology of Lithium (2018, *Laser Ablation Inductively Coupled Plasma Mass Spectrometry: principles and applications in geology*), 2) workshopu Zobrazovací a analytické metody pro (nejen) geology v Brně (2016, *Využití laserové ablaci ve spojení s hmotnostní spektrometrií indukčně vázaného plazmatu v geologii*) a 3) workshopu Využití katodové luminiscence a LA-ICP MS při studiu vnitřní stavby minerálů (2012, *Jak dosáhnout správného výsledku metodou LA-ICP-MS?*).

ZÁVĚR

Tato habilitační práce je věnována moderní analytické metodě laserové ablaci ve spojení s hmotnostní spektrometrií indukčně vázaného plazmatu a její aplikaci v prvkové analýze a zobrazování povrchu prostřednictvím mapování distribuce prvků. Celkově ve třech kapitolách jsou na praktických příkladech prezentovány možnosti uplatnění této metody v analýze poměrně široké škály pevných materiálů.

Cílem však není ukázat pouze aplikaci samotnou, ale rozkrýt i negativní vliv různých doprovodných jevů souvisejících s instrumentací a také fyzikálně-chemickými vlastnostmi analyzovaného vzorku a ukázat jejich možná řešení. Detailní studie souvislostí při interakci laserového paprsku s povrchem materiálu a odezvou ICP hmotnostního spektrometru jsou základem úspěšné aplikace metody a správné interpretace dat. Habilitační práce poukazuje na nutnost komplexního přístupu v řešení různých analytických problémů s přesahem do dalších vědních oborů.

Souhrnný přehled aplikací publikovaných, ale i nepublikovaných výsledků ukazuje na velký potenciál LA-ICP-MS metody a směr jejího budoucího vývoje at' už instrumentálního nebo aplikačního. Díky její široké aplikovatelnosti je patrné i její uplatnění napříč všemi ústavy FCH VUT v rámci výzkumu nově podávaných projektů.

REFERENCE

- (1) Arora, M.; Hare, D.; Austin, C.; Smith, D. R.; Doble, P. *Science of the Total Environment* **2011**, *409*, 1315-1319.
- (2) Dolphin, A. E.; Goodman, A. H. *American Journal of Physical Anthropology* **2009**, *140*, 399-409.
- (3) Hare, D.; Austin, C.; Doble, P.; Arora, M. *Journal of Dentistry* **2011**, *39*, 397-403.
- (4) Humphrey, L. T.; Dean, M. C.; Jeffries, T. E. In *Dental Perspectives on Human Evolution*, Bailey, S. E.; Hublin, J. J., Eds.; Springer: New York, 2007.
- (5) Horton, M. K.; Hsu, L.; Henn, B. C.; Margolis, A.; Austin, C.; Svensson, K.; Schnaas, L.; Gennings, C.; Hu, H.; Wright, R.; Rojo, M. M. T.; Arora, M. *Environment International* **2018**, *121*, 148-158.
- (6) Liao, J. L.; Sun, X. M.; Li, D. F.; Sa, R. N.; Lu, Y.; Lin, Z. Y.; Xu, L.; Zhan, R. Z.; Pan, Y. G.; Xu, H. F. *Chemical Geology* **2019**, *512*, 58-68.
- (7) Kendall, C.; Eriksen, A. M. H.; Kontopoulos, I.; Collins, M. J.; Turner-Walker, G. *Palaeogeography Palaeoclimatology Palaeoecology* **2018**, *491*, 21-37.
- (8) Fischer, A.; Wiechula, D.; Postek-Stefanska, L.; Kwapulinski, J. *Biological Trace Element Research* **2009**, *132*, 19-26.
- (9) Szostek, K.; Glab, H.; Pudlo, A. *Homo-Journal of Comparative Human Biology* **2009**, *60*, 359-372.
- (10) Burton, J. H.; Price, T. D.; Middleton, W. D. *Journal of Archaeological Science* **1999**, *26*, 609-616.
- (11) Peek, S.; Clementz, M. T. *Geochimica Et Cosmochimica Acta* **2012**, *95*, 36-52.
- (12) Bentley, R. A. *Journal of Archaeological Method and Theory* **2006**, *13*, 135-187.
- (13) Retzmann, A.; Blanz, M.; Zitek, A.; Irrgeher, J.; Feldmann, J.; Teschler-Nicola, M.; Prohaska, T. *Analytical and Bioanalytical Chemistry* **2019**, *411*, 565-580.
- (14) Lofaro, E. M.; Kurin, D. S.; Choque, D. E. G.; Krigbaum, J. *Archaeological and Anthropological Sciences* **2019**, *11*, 1089-1105.
- (15) Oelze, V. M.; Koch, J. K.; Kupke, K.; Nehlich, O.; Zauner, S.; Wahl, J.; Weise, S. M.; Rieckhoff, S.; Richards, M. P. *American Journal of Physical Anthropology* **2012**, *148*, 406-421.
- (16) Michel, V.; Ildefonse, P.; Morin, G. *Applied Geochemistry* **1995**, *10*, 145-159.
- (17) Kohn, M. J.; Schoeninger, M. J.; Barker, W. W. *Geochimica Et Cosmochimica Acta* **1999**, *63*, 2737-2747.
- (18) Labs-Hochstein, J.; MacFadden, B. J. *Geochimica Et Cosmochimica Acta* **2006**, *70*, 4921-4932.
- (19) Tutken, T.; Vennemann, T. W.; Pfretzschner, H. U. *Palaeogeography Palaeoclimatology Palaeoecology* **2008**, *266*, 254-268.
- (20) Moll, D.; Kotterba, P.; Jochum, K. P.; von Nordheim, L.; Polte, P. *Frontiers in Marine Science* **2019**, *6*, 11.
- (21) Avigliano, E.; de Carvalho, B. M.; Miller, N.; Gironde, S. C.; Tombari, A.; Limburg, K.; Volpedo, A. V. *Marine Ecology Progress Series* **2019**, *614*, 147-157.
- (22) Benson, I. M.; Kastelle, C. R.; Helser, T. E.; Short, J. A.; Anderl, D. M. *Environmental Biology of Fishes* **2019**, *102*, 629-643.
- (23) Hoover, R. R.; Jones, C. M.; Grosch, C. E. *Canadian Journal of Fisheries and Aquatic Sciences* **2012**, *69*, 1266-1277.
- (24) Ramsay, A. L.; Milner, N. J.; Hughes, R. N.; McCarthy, I. D. *Canadian Journal of Fisheries and Aquatic Sciences* **2011**, *68*, 823-833.
- (25) Webb, S. D.; Woodcock, S. H.; Gillanders, B. M. *Marine Ecology Progress Series* **2012**, *453*, 189-199.

- (26) Willmes, M.; Lewis, L. S.; Davis, B. E.; Loiselle, L.; James, H. F.; Denny, C.; Baxter, R.; Conrad, J. L.; Fangue, N. A.; Hung, T. C.; Armstrong, R. A.; Williams, I. S.; Holden, P.; Hobbs, J. A. *Rapid Communications in Mass Spectrometry* **2019**, *33*, 1207-1220.
- (27) Pourang, N.; Rachti, M. L.; Moazami, H. R.; Mostafavi, P. G. *Environmental Monitoring and Assessment* **2018**, *190*, 13.
- (28) Limburg, K. E.; Elfman, M. *Journal of Fish Biology* **2017**, *90*, 480-491.
- (29) Suzuki, S.; Okada, Y.; Hirai, S. *Bunseki Kagaku* **2005**, *54*, 605-612.
- (30) McFadden, A.; Wade, B.; Izzo, C.; Gillanders, B. M.; Lenehan, C. E.; Pring, A. *Marine and Freshwater Research* **2016**, *67*, 889-898.
- (31) Gemperline, P. J.; Rulifson, R. A.; Paramore, L. *Chemometrics and Intelligent Laboratory Systems* **2002**, *60*, 135-146.
- (32) Chaudhri, M. A.; Watling, J.; Khan, F. A. *Journal of Radioanalytical and Nuclear Chemistry* **2007**, *271*, 713-720.
- (33) Miller, A. W.; Choy, D.; Penniston, K. L.; Lange, D. *Kidney International* **2019**, *96*, 180-188.
- (34) Lovett, A. C.; Khan, S. R.; Gower, L. B. *Urolithiasis* **2019**, *47*, 321-334.
- (35) O'Kell, A. L.; Lovett, A. C.; Canales, B. K.; Gower, L. B.; Khan, S. R. *Urolithiasis* **2019**, *47*, 335-346.
- (36) Menezes, C. J.; Worcester, E. M.; Coe, F. L.; Asplin, J.; Bergsland, K. J.; Ko, B. *American Journal of Physiology-Renal Physiology* **2019**, *317*, F65-F72.
- (37) Li, Z. X.; Jiao, G. L.; Zhou, S. M.; Cheng, Z. Y.; Bashir, S.; Zhou, Y. *Bmc Nephrology* **2019**, *20*.
- (38) Al Tinawi, B.; Jessop, M.; Salkini, M. W. *Urology Annals* **2019**, *11*, 304-309.
- (39) Hardy, L. A.; Vinnichenko, V.; Fried, N. M. *Lasers in Surgery and Medicine* **2019**, *51*, 522-530.
- (40) Mekayten, M.; Lorber, A.; Katafigiotis, I.; Sfoungaristos, S.; Leotsakos, I.; Heifetz, E. M.; Yutkin, V.; Gofrit, O. N.; Duvdevani, M. *Journal of Endourology* **2019**, *33*, 585-589.
- (41) Sultan, S.; Umer, S. A.; Ahmed, B.; Naqvi, S. A. A.; Rizvi, S. A. H. *Frontiers in Pediatrics* **2019**, *7*.
- (42) Michalak, G.; Ren, L.; Ferrero, A.; Leng, S.; McCollough, C. *Medical Physics* **2019**, *46*, E409-E410.
- (43) Wang, L. Q.; Chen, M.; He, P. Z.; Yu, H. Y.; Block, K. A.; Xie, Z. Q. *Science of the Total Environment* **2019**, *650*, 835-846.
- (44) Chatterjee, P.; Chakraborty, A.; Mukherjee, A. K. *Spectrochimica Acta Part a-Molecular and Biomolecular Spectroscopy* **2018**, *200*, 33-42.
- (45) Rodriguez, M. D. R.; Cano, A. G.; Coronado, M. R.; Mendiguchia, L. J. *Acta Bioquimica Clinica Latinoamericana* **2018**, *52*, 15-21.
- (46) Castiglione, V.; Sacre, P. Y.; Cavalier, E.; Hubert, P.; Gadisseur, R.; Ziemons, E. *Plos One* **2018**, *13*.
- (47) Shameem, K. M. M.; Chawla, A.; Mallya, M.; Barik, B. K.; Unnikrishnan, V. K.; Kartha, V. B.; Santhosh, C. *Journal of Biophotonics* **2018**, *11*.
- (48) Liden, M. *Urolithiasis* **2018**, *46*, 325-332.
- (49) Parviaainen, A.; Roman-Alpiste, M. J.; Marchesi, C.; Suarez-Grau, J. M.; Perez-Lopez, R. *Journal of Trace Elements in Medicine and Biology* **2017**, *44*, 339-348.
- (50) Kuta, J.; Machat, J.; Benova, D.; Cervenka, R.; Koristkova, T. *Central European Journal of Chemistry* **2012**, *10*, 1475-1483.
- (51) Becker, J. S.; Dietze, H. J. *Spectrochimica Acta Part B-Atomic Spectroscopy* **1998**, *53*, 1475-1506.

- (52) Phukphathanachai, P.; Vogl, J.; Traub, H.; Jakubowski, N.; Panne, U. *Journal of Analytical Atomic Spectrometry* **2018**, 33, 1506-1517.
- (53) Feng, L. X.; Wang, J.; Li, H. M.; Luo, X. Z.; Li, J. *Analytica Chimica Acta* **2017**, 984, 66-75.
- (54) Compernolle, S.; Wambeke, D.; De Raedt, I.; Vanhaecke, F. *Spectrochimica Acta Part B-Atomic Spectroscopy* **2012**, 67, 50-56.
- (55) Pickhardt, C.; Izmer, A. V.; Zoriy, M. V.; Schaumloffel, D.; Becker, J. S. *International Journal of Mass Spectrometry* **2006**, 248, 136-141.
- (56) Becker, J. S.; Zoriy, M. V.; Pickhardt, C.; Palomero-Gallagher, N.; Zilles, K. *Analytical Chemistry* **2005**, 77, 3208-3216.
- (57) Zhang, G. X.; Li, Q.; Zhu, Y.; Wang, Z. *Spectrochimica Acta Part B-Atomic Spectroscopy* **2018**, 145, 51-57.
- (58) Clases, D.; de Vega, R. G.; Adlard, P. A.; Doble, P. A. *Journal of Analytical Atomic Spectrometry* **2019**, 34, 407-412.
- (59) Cruz-Alonso, M.; Fernandez, B.; Navarro, A.; Juneda, S.; Astudillo, A.; Pereiro, R. *Talanta* **2019**, 197, 413-421.
- (60) Van Acker, T.; Buckle, T.; Van Malderen, S. J. M.; van Willigen, D. M.; van Unen, V.; van Leeuwen, F. W. B.; Vanhaecke, F. *Analytica Chimica Acta* **2019**, 1074, 43-53.
- (61) Gholap, D.; Verhulst, J.; Ceelen, W.; Vanhaecke, F. *Analytical and Bioanalytical Chemistry* **2012**, 402, 2121-2129.
- (62) Li, Y. T.; Guo, W.; Hu, Z. C.; Jin, L. L.; Hui, S. H.; Guo, Q. H. *Journal of Agricultural and Food Chemistry* **2019**, 67, 935-942.
- (63) Debeljak, M.; van Elteren, J. T.; Vogel-Mikus, K. *Analytica Chimica Acta* **2013**, 787, 155-162.
- (64) Austin, C.; Hare, D.; Rawling, T.; McDonagh, A. M.; Doble, P. *Journal of Analytical Atomic Spectrometry* **2010**, 25, 722-725.
- (65) Nunes, M. A. G.; Voss, M.; Corazza, G.; Flores, E. M. M.; Dressler, V. L. *Analytica Chimica Acta* **2016**, 905, 51-57.
- (66) Rovelli, S.; Nischkauer, W.; Cavallo, D. M.; Limbeck, A. *Analytica Chimica Acta* **2018**, 1043, 11-19.
- (67) Lohr, K.; Traub, H.; Wanka, A. J.; Panne, U.; Jakubowski, N. *Journal of Analytical Atomic Spectrometry* **2018**, 33, 1579-1587.
- (68) Villasenor, A.; Boccongelli, M.; Todoli, J. L. *Journal of Analytical Atomic Spectrometry* **2018**, 33, 1173-1183.
- (69) Hanc, A.; Piechalak, A.; Tomaszewska, B.; Baralkiewicz, D. *International Journal of Mass Spectrometry* **2014**, 363, 16-22.
- (70) Papaslioti, E. M.; Parviainen, A.; Alpiste, M. J. R.; Marchesi, C.; Garrido, C. J. *Food Chemistry* **2019**, 274, 726-732.
- (71) Zhang, G. X.; Wang, Z.; Li, Q.; Zhou, H.; Zhu, Y.; Du, Y. P. *Talanta* **2016**, 154, 486-491.
- (72) Sajnog, A.; Hanc, A.; Koczorowski, R.; Makuch, K.; Baralkiewicz, D. *Journal of Trace Elements in Medicine and Biology* **2018**, 46, 46-54.
- (73) Pluhacek, T.; Rucka, M.; Maier, V. *Analytica Chimica Acta* **2019**, 1078, 1-7.
- (74) Sela, H.; Karpas, Z.; Cohen, H.; Zakon, Y.; Zeiri, Y. *International Journal of Mass Spectrometry* **2011**, 307, 142-148.
- (75) Janotkova, I.; Prokes, L.; Vaculovic, T.; Hola, M.; Pinkas, J.; Steffan, I.; Kuban, V.; Kanicky, V. *Journal of Analytical Atomic Spectrometry* **2013**, 28, 1940-1948.
- (76) Hubova, I.; Hola, M.; Pinkas, J.; Kanicky, V. *Journal of Analytical Atomic Spectrometry* **2007**, 22, 1238-1243.

- (77) Sargent, M.; Goenaga-Infante, H.; Inagaki, K.; Ma, L.; Meija, J.; Pramann, A.; Rienitz, O.; Sturgeon, R.; Vogl, J.; Wang, J.; Yang, L. *Metrologia* **2019**, *56*.
- (78) Kindness, A.; Sekaran, C. N.; Feldmann, J. *Clinical Chemistry* **2003**, *49*, 1916-1923.
- (79) Weiskirchen, S.; Kim, P.; Weiskirchen, R. *Annals of Translational Medicine* **2019**, *7*, 17.
- (80) Moreno-Gordaliza, E.; Giesen, C.; Lazaro, A.; Esteban-Fernandez, D.; Humanes, B.; Canas, B.; Panne, U.; Tejedor, A.; Jakubowski, N.; Gomez-Gomez, M. M. *Analytical Chemistry* **2011**, *83*, 7933-7940.
- (81) Wiemann, M.; Vennemann, A.; Blaske, F.; Sperling, M.; Karst, U. *Nanomaterials* **2017**, *7*, 26.
- (82) Hsieh, Y. K.; Hsieh, H. A.; Hsieh, H. F.; Wang, T. H.; Ho, C. C.; Lin, P. P.; Wang, C. F. *Journal of Analytical Atomic Spectrometry* **2013**, *28*, 1396-1401.
- (83) Becker, J. S.; Zoriy, M. V.; Pickhardt, C.; Zilles, K. *Journal of Analytical Atomic Spectrometry* **2005**, *20*, 912-917.
- (84) Zoriy, M. V.; Dehnhardt, M.; Reifenberger, G.; Zilles, K.; Becker, J. S. *International Journal of Mass Spectrometry* **2006**, *257*, 27-33.
- (85) Ali, M. H. M.; Rakib, F.; Al-Saad, K.; Al-Saady, R.; Goormaghtigh, E. *Scientific Reports* **2019**, *9*.
- (86) O'Neill, E. S.; Kaur, A.; Bishop, D. P.; Shishmarev, D.; Kuchel, P. W.; Grieve, S. M.; Figtree, G. A.; Renfrew, A. K.; Bonnitcha, P. D.; New, E. J. *Inorganic Chemistry* **2017**, *56*, 9860-9868.
- (87) Theiner, S.; Schreiber-Brynzak, E.; Jakupc, M. A.; Galanski, M.; Koellensperger, G.; Keppler, B. K. *Metallomics* **2016**, *8*, 398-402.
- (88) Lee, R. F. S.; Theiner, S.; Meibom, A.; Koellensperger, G.; Keppler, B. K.; Dyson, P. J. *Metallomics* **2017**, *9*, 365-381.
- (89) Seuma, J.; Bunch, J.; Cox, A.; McLeod, C.; Bell, J.; Murray, C. *Proteomics* **2008**, *8*, 3775-3784.
- (90) Pisonero, J.; Bouzas-Ramos, D.; Traub, H.; Cappella, B.; Alvarez-Llamas, C.; Richter, S.; Mayo, J. C.; Costa-Fernandez, J. M.; Bordel, N.; Jakubowski, N. *Journal of Analytical Atomic Spectrometry* **2019**, *34*, 655-663.
- (91) Yamashita, S.; Yoshikuni, Y.; Obayashi, H.; Suzuki, T.; Green, D.; Hirata, T. *Analytical Chemistry* **2019**, *91*, 4544-4551.
- (92) Aljakna, A.; Lauer, E.; Lenglet, S.; Grabherr, S.; Fracasso, T.; Augsburger, M.; Sabatasso, S.; Thomas, A. *International Journal of Legal Medicine* **2018**, *132*, 1675-1684.
- (93) Moraleja, I.; Mena, M. L.; Lazaro, A.; Neumann, B.; Tejedor, A.; Jakubowski, N.; Gomez-Gomez, M. M.; Esteban-Fernandez, D. *Talanta* **2018**, *178*, 166-171.
- (94) Herrmann, A. J.; Techritz, S.; Jakubowski, N.; Haase, A.; Luch, A.; Panne, U.; Mueller, L. *Analyst* **2017**, *142*, 1703-1710.
- (95) Lauer, E.; Villa, M.; Jotterand, M.; Vilarino, R.; Bollmann, M.; Michaud, K.; Grabherr, S.; Augsburger, M.; Thomas, A. *International Journal of Legal Medicine* **2017**, *131*, 497-500.
- (96) Van Malderen, S. J. M.; Van Acker, T.; Laforce, B.; De Bruyne, M.; de Rycke, R.; Asaoka, T.; Vincze, L.; Vanhaecke, F. *Analytical and Bioanalytical Chemistry* **2019**, *411*, 4849-4859.
- (97) Yin, L.; Zhang, Z.; Liu, Y. Z.; Gao, Y.; Gu, J. K. *Analyst* **2019**, *144*, 824-845.
- (98) Jimenez-Lamana, J.; Szpunar, J.; Lobinski, R. In *Metallomics: the Science of Biometals*, Arruda, M. A. Z., Ed.; Springer International Publishing Ag: Cham, 2018, pp 245-270.

- (99) Gholap, D. S.; Izmer, A.; De Samber, B.; van Elteren, J. T.; Selih, V. S.; Evens, R.; De Schampelaere, K.; Janssen, C.; Balcaen, L.; Lindemann, I.; Vincze, L.; Vanhaecke, F. *Analytica Chimica Acta* **2010**, *664*, 19-26.
- (100) Hare, D.; Reedy, B.; Grimm, R.; Wilkins, S.; Volitakis, I.; George, J. L.; Cherny, R. A.; Bush, A. I.; Finkelstein, D. I.; Doble, P. *Metalomics* **2009**, *1*, 53-58.
- (101) Matusch, A.; Depboylu, C.; Palm, C.; Wu, B.; Hoglinger, G. U.; Schafer, M. K. H.; Becker, J. S. *Journal of the American Society for Mass Spectrometry* **2010**, *21*, 161-171.
- (102) Muller, J. C.; Lichtmannegger, J.; Zischka, H.; Sperling, M.; Karst, U. *Journal of Trace Elements in Medicine and Biology* **2018**, *49*, 119-127.
- (103) Pugh, J. A. T.; Cox, A. G.; McLeod, C. W.; Bunch, J.; Whitby, B.; Gordon, B.; Kalber, T.; White, E. *Journal of Analytical Atomic Spectrometry* **2011**, *26*, 1667-1673.
- (104) Weiskirchen, R.; Weiskirchen, S.; Kim, P.; Winkler, R. *Journal of Cheminformatics* **2019**, *11*.
- (105) Managh, A. J.; Reid, P. *Journal of Analytical Atomic Spectrometry* **2019**, *34*, 1369-1373.
- (106) Uerlings, R.; Matusch, A.; Weiskirchen, R. *International Journal of Mass Spectrometry* **2016**, *395*, 27-35.
- (107) Balbekova, A.; Lohninger, H.; van Tilborg, G. A. F.; Dijkhuizen, R. M.; Bonta, M.; Limbeck, A.; Lendl, B.; Al-Saad, K. A.; Ali, M.; Celikic, M.; Ofner, J. *Applied Spectroscopy* **2018**, *72*, 241-250.
- (108) Delfino, R.; Biasotto, M.; Candido, R.; Altissimo, M.; Stebel, M.; Salome, M.; van Elteren, J. T.; Mikus, K. V.; Zennaro, C.; Sala, M.; Addobbiati, R.; Tromba, G.; Pascolo, L. *Toxicology Letters* **2019**, *301*, 157-167.
- (109) Liu, X.; Hummon, A. B. *Scientific Reports* **2016**, *6*, 10.
- (110) Petrelli, M.; Morgavi, D.; Vetere, F.; Perugini, D. *Periodico Di Mineralogia* **2016**, *85*, 25-39.
- (111) Izmer, A.; Goderis, S.; Simonson, B. M.; McDonald, I.; Hassler, S. W.; Claeys, P.; Vanhaecke, F. *Journal of Analytical Atomic Spectrometry* **2013**, *28*, 1031-1038.
- (112) Farley, K. A.; Shuster, D. L.; Ketcham, R. A. *Geochimica Et Cosmochimica Acta* **2011**, *75*, 4515-4530.
- (113) Gundlach-Graham, A.; Burger, M.; Allner, S.; Schwarz, G.; Wang, H. A. O.; Gyr, L.; Grolimund, D.; Hattendorf, B.; Gunther, D. *Analytical Chemistry* **2015**, *87*, 8250-8258.
- (114) Burger, M.; Gundlach-Graham, A.; Allner, S.; Schwarz, G.; Wang, H. A. O.; Gyr, L.; Burgener, S.; Hattendorf, B.; Grolimund, D.; Gunther, D. *Analytical Chemistry* **2015**, *87*, 8259-8267.
- (115) Guillong, M.; Gunther, D. *Journal of Analytical Atomic Spectrometry* **2002**, *17*, 831-837.
- (116) Gunther, D.; Heinrich, C. A. *Journal of Analytical Atomic Spectrometry* **1999**, *14*, 1369-1374.
- (117) Kroslakova, I.; Gunther, D. *Journal of Analytical Atomic Spectrometry* **2007**, *22*, 51-62.
- (118) Kuhn, H. R.; Koch, J.; Hargenroder, R.; Niemax, K.; Kalberer, M.; Gunther, D. *Journal of Analytical Atomic Spectrometry* **2005**, *20*, 894-900.

PŘÍLOHY

Multielemental analysis of prehistoric animal teeth by laser-induced breakdown spectroscopy and laser ablation inductively coupled plasma mass spectrometry

Michaela Galiová,¹ Jozef Kaiser,^{2,*} Francisco J. Fortes,³ Karel Novotný,¹ Radomír Malina,² Lubomír Prokeš,¹ Aleš Hrdlička,¹ Tomáš Vaculovič,¹ Miriam Nývltová Fišáková,⁴ Jiří Svoboda,⁴ Viktor Kanický,¹ and Javier J. Laserna³

¹Department of Chemistry, Faculty of Science, Masaryk University, Kotlářská 2, 611 37 Brno, Czech Republic

²Institute of Physical Engineering, Faculty of Mechanical Engineering, Brno University of Technology, Technická 2896/2, 616 69 Brno, Czech Republic

³Department of Analytical Chemistry, Faculty of Sciences, University of Málaga, Campus de Teatinos s/n, 29071 Málaga, Spain

⁴Institute of Archaeology, Academy of Science of the Czech Republic, Královopolská 147, 612 00 Brno, Czech Republic

*Corresponding author: kaiser@fme.vutbr.cz

Received 18 September 2009; revised 31 January 2010; accepted 1 February 2010;
posted 2 February 2010 (Doc. ID 117389); published 26 March 2010

Laser-induced breakdown spectroscopy (LIBS) and laser ablation (LA) inductively coupled plasma (ICP) mass spectrometry (MS) were utilized for microspatial analyses of a prehistoric bear (*Ursus arctos*) tooth dentine. The distribution of selected trace elements (Sr, Ba, Fe) was measured on a 26 mm × 15 mm large and 3 mm thick transverse cross section of a canine tooth. The Na and Mg content together with the distribution of matrix elements (Ca, P) was also monitored within this area. The depth of the LIBS craters was measured with an optical profilometer. As shown, both LIBS and LA-ICP-MS can be successfully used for the fast, spatially resolved analysis of prehistoric teeth samples. In addition to microchemical analysis, the sample hardness was calculated using LIBS plasma ionic-to-atomic line intensity ratios of Mg (or Ca). To validate the sample hardness calculations, the hardness was also measured with a Vickers microhardness tester. © 2010 Optical Society of America

OCIS codes: 140.3440, 300.6365, 330.6100.

1. Introduction

Teeth and bones consist of an inorganic calcium phosphate mineral approximated by hydroxylapatite $\text{Ca}_{10}(\text{PO}_4)_6(\text{OH})_2$ and matrix proteins. The physical and chemical properties of these bioapatite crystals

differ from those of geologic hydroxylapatite because of the way they are formed. These unique properties are required to fulfill the biological functions of bones and teeth [1]. The chemical constituents of the tooth tissue layers (enamel and dentine) are tolerant to substitution by a range of trace elements. The enamel is the hardest and most highly mineralized substance of the body [2], whereas the dentine comprises the bulk of a tooth. A high content of trace

elements, including Zn, Sr, Fe, Al, Ba, and Pb, among others, in the ≥ 1000 ppm range [3] have been found in tooth tissue.

Permanent tooth enamel and dentine begin calcification around birth and continue to calcify into adolescence. The composition of subsurface enamel is already fixed before tooth emergence and is therefore able to provide a retrospective and relatively permanent record of the trace elements absorbed during the period of enamel formation [4]. Spatially resolved analysis of trace element concentration has a broad relevance in disciplines ranging from dentistry and health care [5] to forensics [6], anthropology [7], zoology [8], and archaeology [9].

The trace element concentration of dental tissue is traditionally studied by a bulk sampling approach [10,11]. Further techniques include the mechanical (grinding, drilling) or chemical (acid dissolution) separation of successive enamel layers and their posterior analysis [12,13]. For many years, these layers have been studied by modern analytical techniques such as x-ray fluorescence (XRF) [14,15], electron microprobe x-ray microanalysis (EPXMA) [16,17], particle (proton)-induced x-ray emission spectroscopy (PIXE) [18], or secondary ion mass spectrometry (SIMS) [19,20].

The feasibility of LA-based analytical methods for quantitative and qualitative microspatial analysis of different samples has been reported by several authors [10,21–23]. In particular, LIBS and LA-ICP-MS allow fast multielemental analysis of a broad variety of matrices. Furthermore, the excellent spatial resolution of LA-based methods offers the possibility to study the chemical distribution, namely, chemical mapping, of the elements constituents [24–27]. Additionally, LA-ICP-MS provides high sensitivity and low detection limits.

We achieved a microspatial analyses of a 26 mm \times 15 mm large and 3 mm thick transverse cross section of a permanent canine tooth of a fossil brown bear (*Ursus arctos*); see Fig. 1. The investigated sample consisted of dentine covered by a thin cementum layer. The distribution of selected trace (Sr, Ba, Fe) and matrix (Ca, P) elements was monitored. The spread of further elements (Na, Mg) was also measured. The intertooth distribution of these elements derived mainly from LA-ICP-MS measurements was reported in several earlier publications [26–28]. The choice of investigated chemical elements was further motivated by their importance in paleozoology.



Fig. 1. (Color online) Photographs of the studied sample. At left, the investigated cross section of the *Ursus arctos* canine tooth (rectangle). The bars have a length of 1 cm.

It has been observed that the Sr content decreases in the dentine toward the pulp [29–31]. Some deviations in the Sr/Ca and Sr/Ba ratios indicate population mobility [32] or social status in childhood [33]. The metabolism of Sr and Ba is similar to that of Ca. The Sr/Ca and Ba/Ca ratios generally show on the character of the nutrition [34–37], especially the proportion of foodstuff of animal and vegetable origin in the diet. These ratios can differ in geographic regions with different Sr, Ba, and Ca content in the environment. The Sr/Ba ratio in calcified tissues reflect the Sr/Ba ratio in the environment and then some deviations of these ratios in increments indicate population mobility [32]. In fossil findings, the Ba and Sr content can be increased by postdeposition processes [36]. Fe contamination is important for archaeological materials [14,38–40]; it is preferentially accumulated in cavities or along the rims of fossilized calcified tissue and can also give evidence of postmortem alterations [41,42]. Both the Na and the K content decrease in the dentine [16,43,44]. Good indicators of the contamination are also Al and Mn [37,40].

Mg plays an important role in tooth mineralization, mainly in its early phase. It is progressively replaced with Ca and behaves similar to Sr, i.e., its distribution is almost analogical but the metabolism is slightly different. Its content increases slightly from the surface through the dentine. The Mg content in dentine is substantially higher than in enamel [17,45]. It was verified for macaque, mastodon, and human ([16,43,44]), respectively. An increase from the apical toward the cervical end of the dentine was also reported [46]. The differences among the outer, the inner, and the pulpal parts of the dentine were negligible. In addition to microchemical analysis, the sample hardness was calculated using LIBS plasma ionic-to-atomic line intensity ratios of Mg. To validate the sample hardness calculations, the hardness was also measured with a Vickers microhardness tester. The ablation crater depths were determined from the cross sections measured with an optical profilometer.

2. Material and Sample Preparation

Dolní Věstonice II is one of a series of large settlements of mammoth hunters on the loess elevations at an altitude of approximately 180–240 m above sea level (a.s.l.), rising above the Dyje river and sloping further to the top of Pavlovské Vrchy (550 m a.s.l.). Archaeological excavations at this site were organized by Klíma [47] and Svoboda [48] between 1985 and 1989, and additional excavations took place in 1991, 1999, and 2005. The site became world famous for human paleontological finds including the triple burial (DV 13–15) discovered at the top of the site, the DV 16 burial on the western slope, and individual human remains scattered at various places in the cultural layer. In terms of chronology, the site probably results from repeated occupations extended over the time span of 28 thousands years before the

present (ka) to 24 ka ^{14}C BP (all ^{14}C data are uncalibrated). The first series of radiocarbon dates, around 29–27 ka ^{14}C BP, were obtained from charcoal in the underlying paleosols, with little or no evidence of human occupation, where only two dates in the lower part of the site are associated with artifacts. The second series of radiocarbon dates, all from clearly anthropogenic cultural layers and from artificial structures (settlement units) cluster around 27 ka ^{14}C BP (Early Pavlovian). A third series of dates falls into the time span of 27–25 ka ^{14}C BP (Evolved Pavlovian). This time span is framed by a series of earlier and later luminescence dates from paleosols and loess below and above, which make Dolní Věstonice V II the best dated Gravettian site in the region.

The bear tooth that we analyzed (Fig. 1) originates from field II, which is a longitudinal zone on top of the site, adjacent to the triple burial, and excavated in 1986. It can be related to the third series of radiocarbon dates obtained from the same area. The analyzed tooth (*canine-C₁*) belongs to brown bear (*Ursus arctos*). Abrasion of the tooth's occlusal area and increments of cementum of the tooth's root [49] were studied to determine the age and seasonality. This bear died at the age of 14 and the term of death is possible to estimate from unfinished summer increment and absence of winter increment between the summer and the autumn season (August to October). Both LIBS and LA-ICP-MS analyses were performed on a tooth slice indicated by the rectangle in Fig. 1.

3. Instrumentation

A. Laser-Induced Breakdown Spectroscopy Device

LIBS analysis was performed in the laser laboratory at the University of Malaga (Malaga, Spain). In brief, the second harmonic (532 nm) of a pulsed *Q*-switched Nd:YAG laser with homogeneous energy along the beam cross section (Spectron Model SL 284, pulse width 5 ns, beam diameter 4 mm) was used to generate microplasma on the sample surface in air at atmospheric pressure. The beam was expanded 3× by an optical system consisting of two lenses (a diverging BK7 lens with a 25 mm focal length and a converging BK7 lens with a 75 mm focal length) and then focused onto the sample surface with a 100 mm focal length BK7 lens. Plasma emission was collected by a (5 m long fiber optic, with a 600 μm diameter and a 0.22 NA) and guided onto the entrance slit of a 0.5 m focal length Czerny–Turner imaging spectrograph (Chromex Model 500 IS, *f*-number 8, fitted with interchangeable gratings of 300, 1200, and 2400 grooves mm^{-1}). Spectral emission was detected by an intensified charge-coupled device (Stanford Computer Optics Model 4Quik 05) with 768 × 512 pixels, each 7.8 $\mu\text{m} \times 7.8 \mu\text{m}$. This configuration provides a spectral window of ~15 nm and a spectral resolution of 0.02 nm pixel⁻¹ using an entrance slit width of 50 μm and a 2400 grooves mm^{-1} grating. Operation of the detector was controlled

with 4Spec software. The sample was positioned on two crossed motorized stages (PI Physik Instrumente) for both *X* and *Y* displacement. Moreover, a viewing system to assist with the examination and sample positioning was also used.

The LIBS spectra were acquired in appropriate spectral windows from the 253–617 nm region. The following spectral lines were used for the analysis: P (I) (253.56 and 255.32 nm); Mg (II) (279.55 and 280.27 nm); Mg (I) (285.21 nm); Fe (I) (302.40 nm); Ca (II) (315.89, 317.93, 370.60, 373.69, 393.36, and 396.85 nm); Ca (I) (422.67, 518.89, and 616.22 nm); Ba (II) (455.40 nm); Sr (I) (460.73 and 407.77 nm); and Na (I) (589.00 and 589.59 nm).

Typical single-shot LIBS spectra are shown in Fig. 2. For LIBS line scanning, spectral lines routinely used in LIBS analysis [50] were chosen. To properly relate the detected emission line intensities with the species amount, i.e., to avoid self-absorption, the microplasma emission and the detection temporal interval were optimized by preliminary measurements. The diameter of LIBS ablation craters was ~200 μm , and they were placed at a distance of ~500 μm from each other. After three cleaning shots, the LIBS signal was averaged from seven shots fired to the same sample position. During data analysis, the continuum background determined for each shot from five data points on both sides of the monitored spectral line by a linear background fit method was subtracted from the intensity value of each data point that formed the spectral line.

B. Laser Ablation Inductively Coupled Plasma Mass Spectrometry Setup

Instrumentation for LA-ICP-MS consists of a LA UP 213 system (New Wave, USA) and an ICP mass spectrometer, Model 7500 CE (Agilent, Japan). A commercial *Q*-switched Nd:YAG LA device works at the fifth harmonic frequency (213 nm). The ablation device is equipped with programmable *XY* stages to move the sample along a programmed trajectory during ablation. Target visual inspection is accomplished by means of a built-in microscope/CCD camera system. A sample was enclosed in the SuperCell (New Wave, USA) and was ablated by the laser beam, which was focused onto the sample surface through a quartz window. The ablation cell was flushed with helium (carrier gas), which transported the laser-induced aerosol to the ICP. A sample gas flow of argon (0.6 l/min) was admixed to the helium carrier gas flow (1.0 l/min) behind the LA cell. Therefore, the total gas flow was 1.6 l/min. Optimization of LA-ICP-MS conditions (gas flow rates, sampling depth, electrostatic lens voltages of the MS) was performed with the glass reference material NIST SRM 612 with respect to a maximum signal-to-noise ratio (SNR) and a minimum oxide formation (ThO^+ / Th^+ count ratio 0.2%, U^+/Th^+ count ratio 1.1%).

To analyze specific locations in the sample for LA-ICP-MS line scanning and 2D mapping LA was used in a hole drilling mode (fixed sample position during

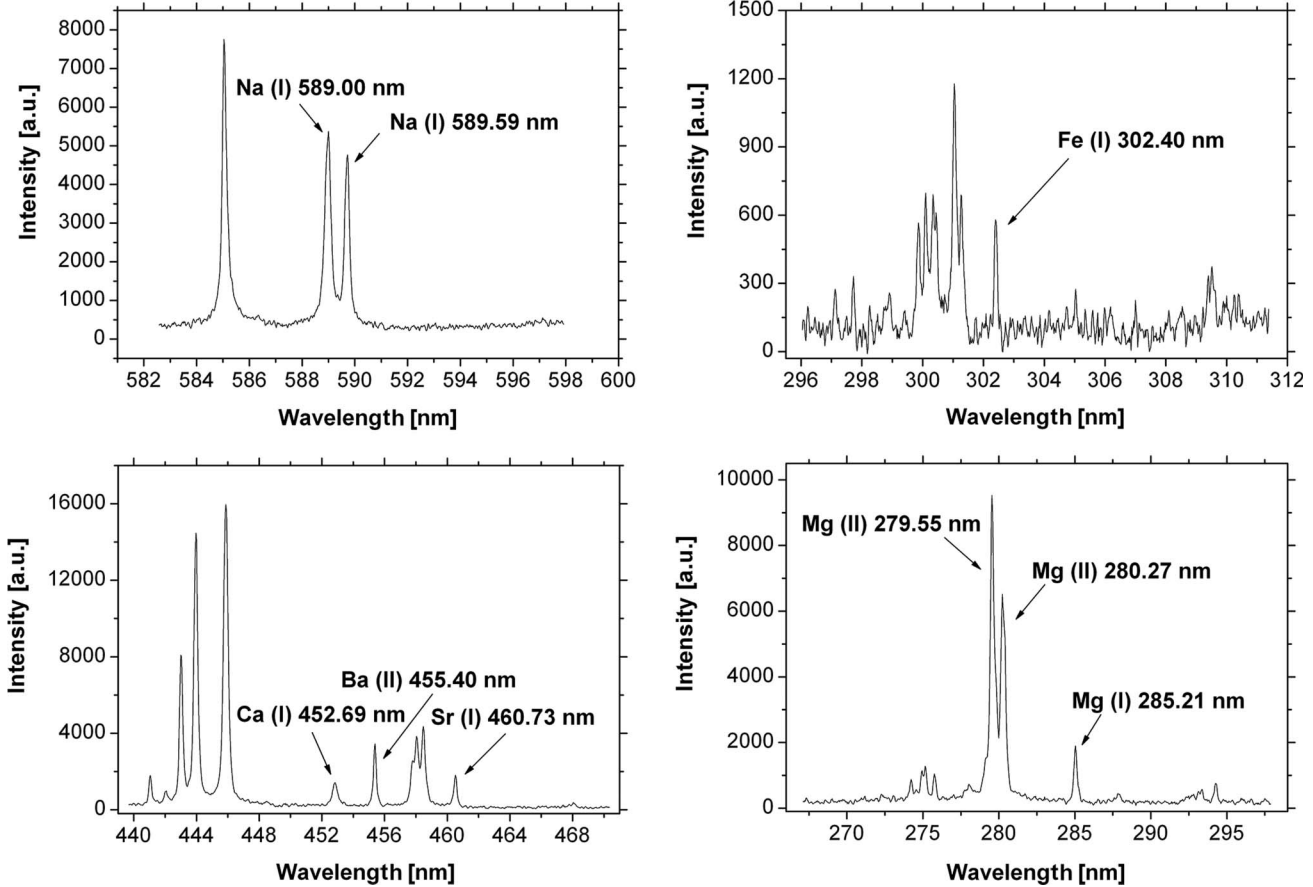


Fig. 2. Typical single-shot LIBS spectra of microplasma created by focusing the laser beam with an energy of ~ 90 mJ/pulse. The spectra were recorded with delay and integration times of 1 and $10\ \mu\text{s}$, respectively. Ba, Sr, and Ca lines were measured with a 1200 groove mm^{-1} grating; Na and Fe lines were measured with a 2400 groove mm^{-1} grating.

LA) for 6 s for each spot. The LA-ICP-MS ablation pattern consisted of ablation craters of $\sim 100\ \mu\text{m}$ diameter at a distance of $\sim 200\ \mu\text{m}$ from each other. Time delay between the end of LA of one spot and the initiation of LA of the next spot was 10 s. LA was performed with a laser spot diameter of $100\ \mu\text{m}$, a laser fluence of $12\ \text{J cm}^{-2}$, and a repetition rate of 10 Hz. The ^{23}Na , ^{24}Mg , ^{57}Fe , ^{86}Sr , ^{88}Sr , and ^{135}Ba isotopes were measured at an integration time of $0.1\ \text{s}/\text{isotope}$; ^{43}Ca , ^{44}Ca , and ^{31}P were measured at an integration time of $0.05\ \text{s}/\text{isotope}$.

The LA-ICP-MS quantitative procedure was performed by matrix-matched calibration. As a calibration standard, standard reference material (SRM) NIST 1486 (powdered bone meal) was used because its matrix is similar to that of teeth. The powdered bone meal was pressed into 10 mm diameter pellets. Pellet preparation was performed without an additional binder by use of a manual hydraulic press (Mobiko Company, Czech Republic). The influence of laser beam energy variation on the ablation rate was minimized using Ca normalization. The Ba and Sr elemental content obtained from the NIST standard were normalized to Ca content:

$$X(i)_{\text{norm}} = X(i)/X(\text{Ca}), \quad (1)$$

where $X(i)_{\text{norm}}$ is the normalized elemental content (Ba or Sr); $X(i)$ is the elemental content in the bear teeth obtained with the NIST standard; $X(\text{Ca})$ is the Ca content in bear teeth obtained using the NIST standard. The typical error of LA-ICP-MS measurements is between 7 and 10%.

C. Measurements of the Laser-Induced Breakdown Spectroscopy Ablation Crater Depths and Sample Hardness

The ablation crater depth was determined from the cross sections measured with a MicroProf optical profilometer (Fries Research and Technology, Germany). The profilometer utilizes chromatic aberration of the positive lens of the optical sensor. The white light from the halogen lamp passes through the optical fiber to the sensor CHR 150 N with high chromatic aberration so each chromatic component of the white light is focused on a different plane [51]. The sensor is set so that the surface under study would lie in the range of focal planes at a distance of approximately $300\ \mu\text{m}$. The light scattered from the surface is then collected by the same lens and transported by the same optical fiber to the spectrometer. The intensity spectral distribution processed by the spectrometer has a maximum at the wavelength focused exactly on the surface. The position of the surface is

computed using the known course of the sensor chromatic aberration with ~ 50 nm vertical resolution. A greater vertical range of the surface is measured in several slices, each less than $300 \mu\text{m}$ thick and connected automatically. The lateral resolution is given by the scanning table motion; the ablation craters were measured with $1 \mu\text{m}$ lateral resolution. The variation of the sample hardness was measured with a Leco LM247AT microhardness tester.

4. Results and Discussion

A. Line Scans and Mapping

The line scans derived from LIBS and LA-ICP-MS analysis of macroelement Na and trace element Fe are compared in Fig. 3. Both LA-based techniques revealed similar accumulation for all the tracked elements across the scanned lines. We observed similar behavior of elemental distribution inside the dentine to that reported in the literature, i.e., the differences among the Mg signal in outer, inner, and pulpal parts of the dentine were negligible. The inhomogeneity in the Na signal can indicate contamination from outside, which was further confirmed with the line and area scans of Fe. The Fe/Ca ratio also apparently increases, which indicates diagenetic changes in the root canal [Fig. 3(c)] [37,40–42]. The range of these changes was further investigated by measurements of the sample hardness (Subsection 4.B). The Na content decreases toward the root canal and corresponds to the common observations [16,43,44]. The P distribution derived from line scans was in accordance with the distribution of another studied matrix element (Ca).

The $\sim 100 \mu\text{m}$ ablation crater diameter used for the LA-ICP-MS technique allowed mapping the sample with a higher spatial resolution. The results of this elemental mapping in two different regions of the tooth cross section are shown in Fig. 4. The (normalized) variations of Sr/Ca, Ba/Ca, Na/Ca, and Fe/Ca are plotted in Fig. 4. The different chemical composition of the cementum ($\sim 1 \text{ mm}$ thick layer) can be clearly distinguished. The Mg (distribution is not shown) similar to sodium is nearly homogeneously distributed (Fig. 4). It does not show an anomaly from the theoretical expectation [16,43–46].

B. Sample Hardness and Depth of the Ablation Craters

Beyond the possibility of straightforward elemental mapping, LA-based analytical methods allow direct

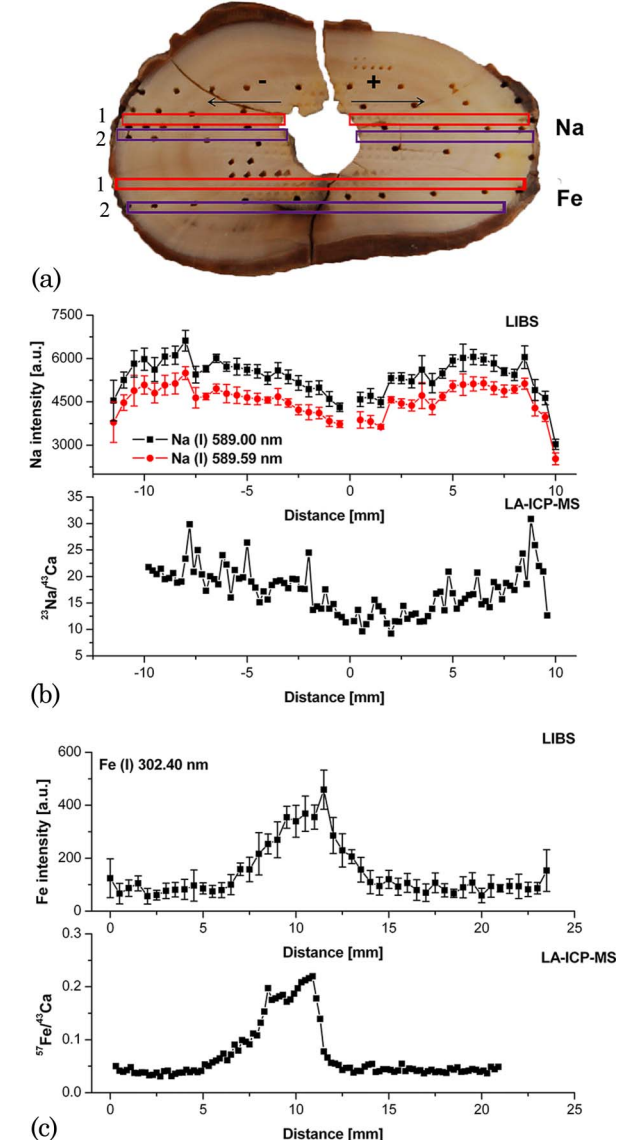


Fig. 3. (Color online) LIBS (1) and LA-ICP-MS (2) line scans positioned as shown in the photograph: (a) comparison of the elemental distribution of (b) Na and (c) Fe obtained from the cross sections of fossil brown bear (*Ursus arctos*) canine tooth dentine.

estimation of other sample properties. Estimation of the sample hardness by Mg or Ca ionic-to-atomic line intensity ratios is based on the interaction between the laser-induced shock wave and the sample surface [52]. The recoil force on a softer surface is

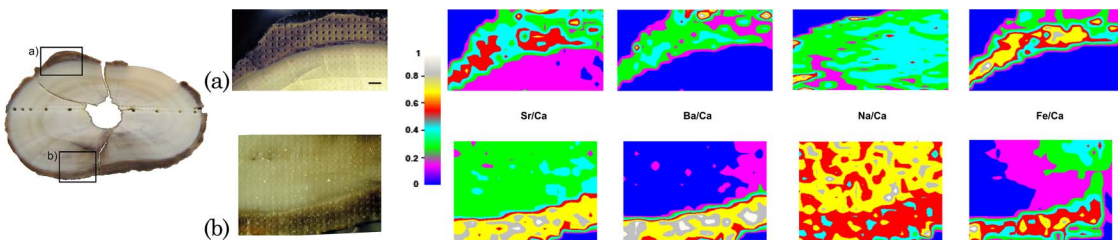


Fig. 4. (Color online) Results of LA-ICP-MS elemental mapping in two different areas of the sample. The bar has a length of $400 \mu\text{m}$.

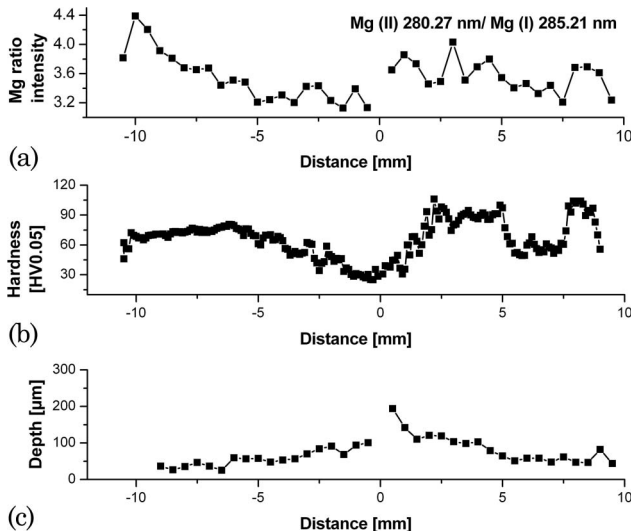


Fig. 5. (a) Sample hardness obtained with Mg ionic-to-atomic line intensity ratios along the LIBS line scan, (b) results of microhardness measurements at near proximity of the LIBS ablation craters, and (c) the ablation crater depths calculated from the cross sections as measured with an optical profilometer.

weaker and reflects the shock wave with lower velocity in comparison with that of a hard target, resulting in a reduction of the ionization effectiveness and then of the ionic-to-neutral intensity ratio.

In accordance with the expectations based on the increased Fe/Ca ratio near the root canal (Subsection 4.A), in the investigated tooth slice the dentine hardness decreases toward the root canal (Fig. 5). This is typical for archaeological teeth samples in which part of the material near the root canal is affected by diagenesis. The estimated hardness characteristic was confirmed by microhardness measurements. The sample was repolished before these measurements and the test pattern was placed near the LIBS ablation craters for Mg detection. The distance between the Vickers test dents was 100 μm. The ablation crater depths determined from the

cross sections measured with an optical profilometer are shown for comparison in Fig. 5(c).

C. Use of Sr/Ca and Sr/Ba Ratios to Determine the Bear Migration

The line and area scans of the sample were used to reconstruct the ethology of this fossil brown bear (*Ursus arctos*). The seasonal fluctuations of the Sr/Ca and Sr/Ba detected by both LA-based techniques, indicated the migration of this bear between his hibernaculum location and the place where the fossils were found. As an example, Fig. 6 shows these ratios for both LIBS line scan and LA-ICP-MS mapping. The incremental strips in the LA-ICP-MS maps are indicated by dashed curves. The dark areas are well correlated with the lower Sr/Ba ratio in the map; they are related to the narrow winter strips that can be identified in the photographs superimposed on the Sr/Ba and Sr/Ca line scans above those acquired by LIBS. The correlation of the Sr/Ca ratio with those strips is not so apparent because there are both higher and lower Sr-doped wide strips in the mapped area.

Dentine, similar to bone tissue or cementum, can be more easily affected by diagenesis in comparison with, e.g., enamel [38,54]. In the investigated sample, to minimize the effect of the diagenesis for the outcomes of the analysis, the area of the sample, where the elemental ratios were mapped (Fig. 6), was carefully selected on the basis of microscopic observation of the sample structure and sample hardness measurements reported in Subsection 4.B. For further validation of these results, the whole sample area was mapped by quantitative LA-ICP-MS procedure, as described in Subsection 3.B. On the basis of this analysis, the average amount of Ba and Sr within the investigated area of the tooth dentine was 43 and 688 mg/kg, respectively. These measurements (Fig. 7) proved the correlation between both the Sr/Ba and the Sr/Ca ratios obtained after the quantitative LA-ICP-MS procedure and narrow winter strips. The map of Ca distribution

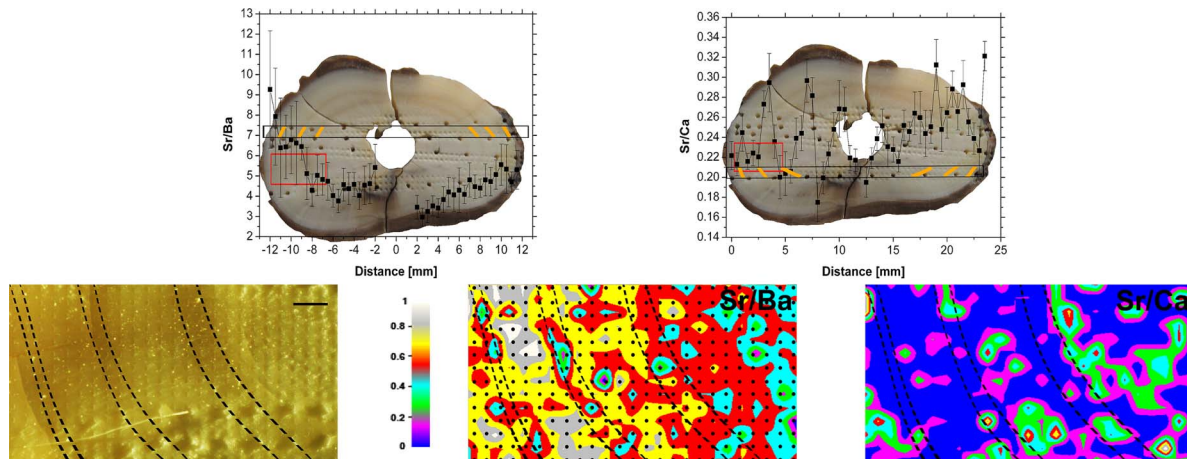


Fig. 6. (Color online) Sr/Ca and Sr/Ba ratios derived from LIBS line scan and LA-ICP-MS mapping; dotted lines represent the different regions (white, summer bands; brown, winter bands) of the tooth cross section. The bar has a length of 500 μm.

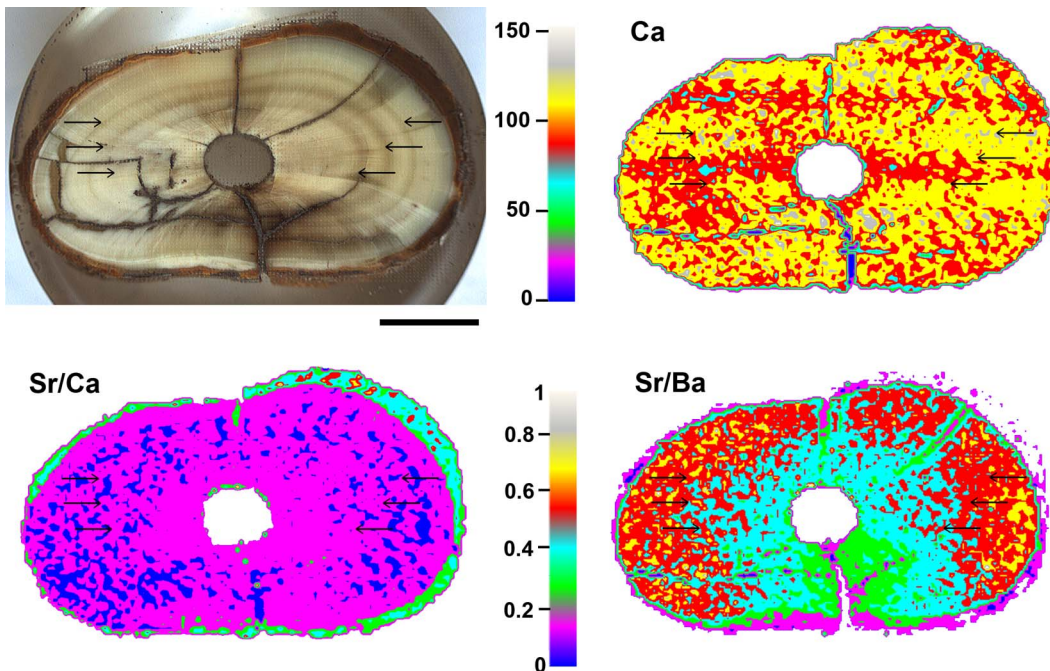


Fig. 7. (Color online) Map of Ca [mg/g] distribution and Sr/Ca, Sr/Ba ratios obtained with quantitative LA-ICP-MS mapping. The Sr/Ca and Sr/Ba ratios were normalized. The bar has a length of $500\text{ }\mu\text{m}$.

within this area, expressed in mg/g, is shown for comparison.

The somewhat homogeneous Ca distribution and the visible change in Sr/Ba and Sr/Ca values in the middle between the edge of the tooth and the root canal indicates that this part was not affected significantly by diagenesis and can be used to reconstruct the ethology of this fossil brown bear (*Ursus arctos*). The diagenesis of calcified tissue is indicated mainly by increased amounts of elements such as Fe, Mn, and Al from soil by capillary elevation of water solutions, and Ca intensity falls within these profiles.

On the basis of these measurements, it can be concluded that the bear probably consumed an animal food mainly in the hot season because of the Sr/Ca increased ratio that is visible mainly in the LIBS scans and based on parallel results of isotope geochemical ($^{86}\text{Sr}/^{87}\text{Sr}$, $^{14}\text{N}/^{15}\text{N}$, and $^{13}\text{C}/^{12}\text{C}$) analysis; Sr can be accumulated from the bodies of consumed herbivores. The bear's migration is characteristic not only for the seasons but also for different years, which is visible by comparison of the Sr/Ba ratios in the particular wide strips from the outer to the inner parts of the dentine in the LA-ICP-MS maps and by the Sr/Ba decrease observable in the LIBS scan from different soils and food chain. The bear probably changed its living territory [49,54–56].

5. Conclusion

Laser ablation-based analytical techniques were used for mapping and line-scanning a fossil animal tooth section. LIBS, similar to LA-ICP-MS, proved to be suitable for fast, spatially resolved analyses of such calcified tissues. Moreover, this technique allows straightforward estimation of the sample

hardness. From an archaeological point of view, it was possible to reconstruct the ethology of the fossil brown bear, i.e., the nutrition, health, and migration on the basis of these measurements. The measured Sr/Ca and Sr/Ba profiles across the sample showed seasonal fluctuations and proved the migration of this bear between his hibernaculum location and the place where the fossils were found. Together with the results from other techniques (i.e., study of cementum increments), we can conclude that this bear specimen most probably was hunted when it was foraging before winter dormancy and was migrating near a human settlement (where the fossils were found). We have shown that LIBS and LA-ICP-MS can be successfully applied as direct or complementary techniques in spatially resolved microchemical analysis of fossil samples.

M. Galiová, J. Kaiser, and R. Malina acknowledge the Ministry of Education, Youth, and Sports of the Czech Republic for research projects MSM 0021630508 and ME09015. K. Novotný, A. Hrdlička, T. Vaculovič, and V. Kanický acknowledge the Ministry of Education, Youth, and Sports of the Czech Republic for research projects MSM 0021622411 and ME08002. M. Nývlťová Fišáková and J. Svoboda acknowledge funding from the Grant Agency of the Academy of Sciences of the Czech Republic (GA AV CR), KJB800010701, “Hunting Strategies of Upper Palaeolithic People,” and from the Institute of the Archaeology Academy of Science of the Czech Republic, AVOZ80010507.

References

1. A. L. Boskey, “Mineralization of bones and teeth,” *Elements* **3**, 385–391 (2007).

2. M. H. Ross, G. I. Kaye, and W. Pawlina, *Histology: a Text and Atlas* (Lippincott Williams & Wilkins, 2002).
3. L. T. Runia, "Gebruik van strontium, andere sporenelementen en stabile isotopen als voedingsindicatoren in de archeologie," *Voeding* **46**, 368–375 (1985).
4. L. T. Humphrey, T. E. Jeffries, and M. Ch. Dean, "Micro spatial distributions of lead and zinc in human deciduous tooth enamel," in *Technique and Application in Dental Anthropology*, J. D. Irish and G. C. Nelson, eds. (Cambridge U. Press, 2008), 87–110.
5. F. Lochner, J. Appleton, F. Keenan, and M. Cooke, "Multi-element profiling of human deciduous teeth by laser ablation-inductively coupled plasma-mass spectrometry," *Anal. Chim. Acta* **401**, 299–306 (1999).
6. M. A. Bush, R. G. Miller, A. L. Norrlander, and P. J. Bush, "Analytical survey of restorative resins by SEM/EDS and XRF: databases for forensic purposes," *J. Forensic Sci.* **53**, 419–425 (2008).
7. A. E. Dolphin, A. H. Goodman and D. D. Amarasinghe, "Variation in elemental intensities among teeth and between pre- and postnatal regions of enamel," *Am. J. Phys. Anthropol.* **128**, 878–888 (2005).
8. L. T. Humphrey, W. Dirks, M. Ch. Dean, and T. E. Jeffries, "Tracking dietary transitions in weanling baboons (*Papio hamadryas anubis*) using strontium/calcium ratios in enamel," *Folia Primatol.* **79**, 197–212 (2008).
9. A. Cucina, J. Dudgeon, and H. Neff, "Methodological strategy for the analysis of human dental enamel by LA-ICP-MS," *J. Archaeol. Sci.* **34**, 1884–1888 (2007).
10. S. R. Copeland, M. Sponheimer, P. J. le Roux, V. Grimes, J. A. Lee-Thorp, D. J. de Ruiter, and M. P. Richards, "Strontium isotope ratios ($^{87}\text{Sr}/^{86}\text{Sr}$) of tooth enamel: a comparison of solution and laser ablation multicollector inductively coupled plasma mass spectrometry methods," *Rapid Commun. Mass Spectrom.* **22**, 3187–3194 (2008).
11. C. A. Perez, H. J. Sanchez, R. A. Barrea, M. Grenon, and J. Abraham, "Microscopic x-ray fluorescence analysis of human dental calculus using synchrotron radiation," *J. Anal. At. Spectrom.* **19**, 392–397 (2004).
12. J. E. Fergusson and N. G. Purchase, "The analysis and levels of lead in human teeth: a review," *Environ. Pollut.* **46**, 11–44 (1987).
13. J. D. Adachi, D. Arlen, C. E. Webber, D. R. Chettle, L. F. Beaumont, and C. L. Gordon, "Is there any association between the presence of bone disease and cumulative exposure to lead?," *Calcif. Tissue Int.* **63**, 429–432 (1998).
14. M. L. Carvalho, C. Casaca, T. Pinheiro, J. P. Marques, P. Chevallier, and A. S. Cunha, "Analysis of human teeth and bones from the chalcolithic period by x-ray spectrometry," *Nucl. Instrum. Methods Phys. Res. B* **168**, 559–565 (2000).
15. R. R. Martin, S. J. Naftel, A. J. Nelson, A. B. Feilen, and A. Narvaez, "Metal distributions in the cementum rings of human teeth: possible depositional chronologies and diagenesis," *J. Archaeol. Sci.* **34**, 936–945 (2007).
16. D. Grman and P. Andrik, "Local analysis of hard tooth tissues with electron microprobe," *Czech. Stomatol.* **78**, 63–68 (1978).
17. A. R. Johnson, "Strontium, calcium, magnesium, and phosphorus content of rat incisors as determined by electron microprobe analysis," *J. Dent. Res.* **51**, 115–121 (1972).
18. R. Brenn, Ch. Haug, U. Klar, S. Zander, K. W. Alt, D. N. Jamieson, K. K. Lee, and H. Schutkowski, "Post-mortem intake of lead in 11th century human bones and teeth studied by milli- and microbeam PIXE and RBS," *Nucl. Instrum. Methods Phys. Res. B* **158**, 270–274 (1999).
19. E. M. Stermer, S. Risnes, and P. M. Fischer, "Trace element analysis of blackish staining on the crowns of human archaeological teeth," *Eur. J. Oral Sci.* **104**, 253–261 (1996).
20. B. Jälevik, H. Odelius, W. Dietz, and J. G. Norén, "Secondary ion mass spectrometry and x-ray microanalysis of hypomineralized enamel in human permanent first molars," *Arch. Oral Biol.* **46**, 239–247 (2001).
21. O. Samek, D. C. S. Beddoes, H. H. Telle, G. W. Morris, M. Liška, and J. Kaiser, "Quantitative analysis of trace metal accumulation in teeth using laser-induced breakdown spectroscopy," *Appl. Phys. A* **69**, S179–S182 (1999).
22. T. Prohaska, Ch. Latkoczy, G. Schultheis, M. Teshler-Nicola, and G. Stinger, "Investigation of Sr isotope ratios in prehistoric human bones and teeth using laser ablation ICP-MS and ICP-MS after Rb/Sr separation," *J. Anal. At. Spectrom.* **17**, 887–891 (2002).
23. M. V. Zorić, D. Mayer, and J. S. Becker, "Metal imaging on surface of micro- and nanoelectronic devices by laser ablation inductively coupled plasma mass spectrometry and possibility to measure at nanometer range," *J. Am. Soc. Mass Spectrom.* **20**, 883–890 (2009).
24. K. Novotný, J. Kaiser, M. Galiová, V. Konečná, J. Novotný, R. Malina, M. Liška, V. Kanický, and V. Otruba, "Mapping of different structures on large area of granite sample using laser-ablation based analytical techniques, an exploratory study," *Spectrochim. Acta B* **63**, 1139–1144 (2008).
25. J. Kaiser, M. Galiová, K. Novotný, R. Červenka, L. Reale, J. Novotný, M. Liška, O. Samek, V. Kanický, A. Hrdlička, K. Stejskal, V. Adam, and R. Kizek, "Mapping of lead, magnesium and copper accumulation in plant tissues by laser-induced breakdown spectroscopy and laser-ablation inductively coupled plasma mass spectrometry," *Spectrochim. Acta B* **64**, 67–73 (2009).
26. K. M. Lee, J. Appleton, M. Cooke, F. Keenan, and K. Sawicka-Kapusta, "Use of laser ablation inductively coupled plasma mass spectrometry to provide element versus time profiles in teeth," *Anal. Chim. Acta* **395**, 179–185 (1999).
27. F. Lochner, J. Appleton, F. Keenan, and M. Cooke, "Multi-element profiling of human deciduous teeth by laser ablation-inductively coupled plasma-mass spectrometry," *Anal. Chim. Acta* **401**, 299–306 (1999).
28. D. Kang, D. Aamarasinghe, and A. H. Goodman, "Application of laser ablation-inductively coupled plasma-mass spectrometry (LA-ICP-MS) to investigate trace metal spatial distributions in human tooth enamel and dentine growth layers and pulp," *Anal. Bioanal. Chem.* **378**, 1608–1615 (2004).
29. R. M. Frank, M. L. Sargentini-Maier, J. C. Turlot, and M. J. F. Leroy, "Zinc and strontium analyses by energy dispersive x-ray fluorescence in human permanent teeth," *Arch. Oral Biol.* **34**, 593–597 (1989).
30. T. Molleson, "Trace elements in human teeth," in *Trace Elements in Environmental History*, G. Grupe and B. Herrmann, eds. (Springer, 1988), 67–82.
31. E. Reitznerová, D. Aamarasinghe, M. Kopčáková, and R. M. Barnes, "Determination of some trace elements in human teeth," *Fresen. J. Anal. Chem.* **367**, 748–754 (2000).
32. J. H. Burton, T. D. Price, L. Cahue, and L. E. Wright, "The use of barium and strontium abundances in human skeletal tissues to determine their geographic origins," *Int. J. Osteoarchaeol.* **13**, 88–95 (2003).
33. G. Grupe, *Dental Anthropology. Fundamentals, Limits and Prospects* (Springer, 1998).
34. J. H. Burton and T. D. Price, "The ratio of barium to strontium as a paleodietary indicator of consumption of marine resources," *J. Archaeol. Sci.* **17**, 547–557 (1990).
35. M. Sponheimer, D. de Ruiter, J. Lee-Thorp, and A. Späth, "Sr/Ca and early hominin diets revisited: new data from modern and fossil tooth enamel," *J. Hum. Evol.* **48**, 147–156 (2005).
36. J. H. Burton, "Trace elements in bone as paleodietary indicators," in *Archaeological Chemistry. Organic, Inorganic and*

- Biochemical Analysis*, V. M. Orna, ed. (American Chemical Society, 1996), pp. 327–332.
37. J. A. Ezzo, “Putting the “chemistry” back into archaeological bone chemistry analysis: modelling potential palaeodietary indicators,” *J. Anthropol. Archaeol.* **13**, 1–34 (1994).
 38. M. J. Kohn, M. J. Schoeninger, and W. W. Barker, “Altered states: effects of diagenesis on fossil tooth chemistry,” *Geochim. Cosmochim. Acta* **63**, 2737–2747 (1999).
 39. L. Rodriguez-Fernández, J. L. Ruvalcaba-Sil, M. A. Ontalba-Salamanca, J. A. Román-Berrelleza, M. L. Gallardo, D. M. Grimaldi, O. G. de Lucio, and J. Miranda, “Ion beam analysis of ancient Mexican colored teeth from archaeological sites in Mexico City,” *Nucl. Instrum. Methods Phys. Res. B* **150**, 663–666 (1999).
 40. J. Tauferová, “Can be the content of metal elements in fossil bones as indicator of the environment quality in the past?,” *Czech. Hyg.* **36**, 163–170 (1991).
 41. T. A. Elliott and G. W. Grime, “Examining the diagenetic alteration of human bone material from a range of archaeological burial sites using nuclear microscopy,” *Nucl. Instrum. Methods Phys. Res. B* **77**, 537–547 (1993).
 42. R. B. Parker and H. Toots, “Minor elements in fossil bone,” *Geol. Soc. Am. Bull.* **81**, 925–932 (1970).
 43. F. C. Besic, C. R. Knowles, M. R. Wiemann, Jr., and O. Keller, “Electron probe microanalysis of noncarious enamel and dentin and calcified tissues in mottled teeth,” *J. Dent. Res.* **48**, 131–139 (1969).
 44. J. H. Shaw, and P. K.-J. Yen, “Sodium, potassium, and magnesium concentrations in the enamel and dentin of human and Rhesus monkey teeth,” *J. Dent. Res.* **51**, 95–101 (1972).
 45. J. Steinfort, F. C. M. Driessens, H. J. M. Heijligers and W. Beertsen, “The distribution of magnesium in developing rat incisor dentin,” *J. Dent. Res.* **70**, 187–191 (1991).
 46. Sz. Arany, N. Yoshioka, D. Ishiyama, and T. Mizuta, “Investigation of trace element distribution in permanent root dentine by laser ablation inductively coupled plasma mass spectrometry,” *Akita J. Med.* **31**, 107–112 (2004).
 47. J. Svoboda, ed., “Dolni Věstonice II - western slope, ERAUL 54 (Université de Liege, 1991).
 48. B. Klíma, “Dolní Věstonice; výzkum táboryště lovčů mamutů v letech 1947–1952” (Academia Prague, 1963), in Czech.
 49. M. Nývltová Fišáková, “Seasonality of Gravettian sites by study of teeth cementum microstructures of mammals,” in *Přehledy výzkumu 48 (Research digests 48)* (Academy of Sciences of the Czech Republic, 2007) (in Czech), pp. 13–23.
 50. Applied Photonics Limited, “Analytical capabilities of LIBS,” http://www.appliedphotonics.co.uk/Libs/capabilities_libs.htm
 51. I. Ohlídal, M. Ohlídal, D. Franta, V. Čudek, V. Bursíková, P. Klapetek, and K. Páleníková, “Influence of technological conditions on mechanical stresses inside diamond-like carbon films,” *Diamond Relat. Mater.* **14**, 1835–1838 (2005).
 52. Z. A. Abdel-Salam, A. H. Galmed, E. Tognoni, and M. A. Harith, “Estimation of calcified tissues hardness via calcium and magnesium ionic to atomic line intensity ratio in laser induced breakdown spectra,” *Spectrochim. Acta B* **62**, 1343–1347 (2007).
 53. A. Zazzo, Ch. L. Ecuyer, S. M. F. Sheppard, P. Grandjean, and A. Mariotti, “Diagenesis and the reconstruction of paleoenvironments: a method to restore original $\delta^{18}\text{O}$ values of carbonate and phosphate from fossil tooth enamel,” *Geochim. Cosmochim. Acta* **68**, 2254–2258 (2004).
 54. M. Nývltová Fišáková, “Seasonality, palaeoecology and migration of fauna from the Gravettian sites,” *Abstract Books 9th Paleontological Conference* (Polish Academy of Sciences Institute of Paleobiology, 2008), 63–64.
 55. M. Nývltová Fišáková, M. Galiová, J. Kaiser, F. J. Fortes, K. Novotný, R. Malina, L. Prokeš, A. Hrdlička, T. Vaculovič, and J. J. Laserna, “Bear diet, seasonality and migration based on chemical multielemental teeth analysis,” in *Přehled výzkumu 50 (Research Digests 50)* (Academy of Sciences of the Czech Republic, 2009), pp. 27–34.
 56. M. Nývltová Fišáková, M. Galiová, J. Kaiser, F. J. Fortes, K. Novotný, R. Malina, T. Vaculovič, L. Prokeš, A. Hrdlička, J. Svoboda, J. J. Laserna, and M. Vláčík, “Bear Diet, seasonality and migration based on chemical multielemental analysis,” *Abstrakt Book, 15th Cave Bear Symposium* (Faculty of Natural Sciences, Comenius University in Bratislava, Slovak Republic, 2009), pp. 42–43.



Elemental mapping in fossil tooth root section of *Ursus arctos* by laser ablation inductively coupled plasma mass spectrometry (LA-ICP-MS)

M. Vašinová Galiová ^{a,b}, M. Nývltová Fišáková ^c, J. Kynický ^d, L. Prokeš ^a, H. Neff ^e, A.Z. Mason ^f, P. Gadas ^g, J. Košler ^h, V. Kanický ^{a,b,*}

^a Department of Chemistry, Faculty of Science, Masaryk University, Kotlářská 2, 611 37 Brno, Czech Republic

^b Central European Institute of Technology (CEITEC), Masaryk University, Kamenice 5, 625 00 Brno, Czech Republic

^c Institute of Archaeology, The Academy of Sciences of the Czech Republic, Královopolská 147, 612 00 Brno, Czech Republic

^d Department of Geology and Pedology, Faculty of Forestry and Wood Technology, Mendel University in Brno, Zemědělská 3, 613 00 Brno, Czech Republic

^e Department of Anthropology and Institute for Integrated Research in Materials, Environments, and Society (IIRMES), California State University Long Beach, Bellflower Blvd 1250, 90840 Long Beach, USA

^f Department of Biological Sciences, California State University Long Beach, Bellflower Blvd 1250, 90840 Long Beach, USA

^g Department of Geological Sciences, Faculty of Science, Masaryk University, Kotlářská 2, 611 37 Brno, Czech Republic

^h Centre for Geobiology, University of Bergen, P.O. Box 7803, N-5020 Bergen, Norway

ARTICLE INFO

Article history:

Received 30 August 2012

Received in revised form

10 December 2012

Accepted 13 December 2012

Available online 31 December 2012

Keywords:

Laser ablation ICP-MS

Geochemical analysis

Migration

Diet

Diagenesis

ABSTRACT

Laser ablation inductively coupled plasma mass spectrometry (LA-ICP-MS) was used to map the matrix (Ca, P) and trace (Ba, Sr, Zn) elements in the root section of a fossilized brown bear (*Ursus arctos*) tooth. Multielemental analysis was performed on a (2.5 × 1.5) cm² area. For elemental distribution, a UP 213 laser ablation system was coupled either with a quadrupole or a time of flight ICP-MS. The cementum and dentine on the slice of the sample surface were clearly distinguishable, especially changes in elemental distribution in the summer and winter bands in the fossil root dentine. Migration and diet of *U. arctos* were determined on the basis of fluctuations in Sr/Zn ratio and their contents. Quantification was accomplished with standard reference material of bone meal (NIST 1486) and by the use of electron microprobe analysis (EMPA). Changes in Sr/Zn and Sr/Ba ratios relating to the season, and composition of food during the lifetime of the animal are discussed on basis of analysis of light stable isotopes. It was observed that there was an increase in the Sr/Zn ratio during the winter season caused by a reduction of food intake during hibernation. Above mentioned inferences drawn from elemental data obtained by LA-ICP-MS were confirmed independently by determination of carbon, nitrogen and strontium isotopes. Moreover, diagenesis and its interfering influence on the biogenic composition of cementum and dentine were resolved. According to the distribution and/or content of the element of interest, post-mortem alterations were revealed. Namely, U, Na, Fe, Mg and F predicate about the suitability of the selected area for determination of migration and diet.

© 2013 Elsevier B.V. All rights reserved.

1. Introduction

The main components of bones and teeth are calcium and phosphorus in the form of hydroxyapatite (Ca₁₀(OH)₂(PO₄)₆) and represent 39.9%_{m/m} Ca and 18.5%_{m/m} P of the mineral-phase. Strontium, barium, zinc, copper, vanadium, manganese or magnesium and sodium occur as the trace and minor elements. Non-mineral constituents include collagen, marrow, fat, non-collagen proteins and water.

The tooth consists of a number of structurally different mineralized parts; enamel, dentine and cementum. Enamel, the hardest

skeletal tissue in the body, covers the crown and begins to form during pregnancy. Its composition reflects the diet in childhood [1]. Dentine is a metabolically active tissue and its composition is constantly renewed, thus dentine analysis provides information about dietary system 10 years prior to the death. Moreover, skeletal tissue composition can provide information on geographical origin. Strontium, calcium, zinc and barium analyses can be used to determine provenance and dietary history. Strontium has a similar ionic radius and charge to Ca and presumably enters into plants via the Ca²⁺ permeates nutrient pathway. Plants can subsequently be consumed by animals/human and become incorporated into mineralized structures [2]. The lowest strontium content is found in meat and subsequently in the skeletal remains of carnivores. In contrast, a higher content of Sr has been found in bioapatite structures of herbivores [2]. The highest Sr content in bones and teeth has been identified in animals/human with a seafood diet. The partitioning

* Corresponding author at: Department of Chemistry, Faculty of Science, Masaryk University, Kotlářská 2, 611 37 Brno, Czech Republic.

E-mail address: viktork@chemi.muni.cz (V. Kanický).

between Ca and Sr according to dietary sources enables Sr/Ca ratios to be used as a proxy for determining diet and migration [3–5]. The reconstruction of dietary history can be also performed via the Zn content and Sr/Zn ratio. The lowest amount of Zn in skeletal tissue occurs in herbivores, increasing through omnivores and is highest in carnivores. A high amount of Zn in teeth, however, might indicate inflammation in skeletal tissue or surroundings area [6]. According to the literature, barium is more sensitive than zinc as an indicator of changes in diet and Sr/Ba ratios enable terrestrial and marine dietary sources to be distinguished [7–9].

Migration of individuals is ordinarily determined by undertaking strontium isotope analysis ($^{87}\text{Sr}/^{86}\text{Sr}$) of enamel and dentine or bone tissue. The $^{87}\text{Sr}/^{86}\text{Sr}$ in this mineralized structure reflects the strontium isotopic compositions in the surrounding environment and can therefore be used to determine geographical location [10]. Isotopic ratios of Sr are well defined for geological background and sea/fresh water as well. For instance, sea water is characterized by lower $^{87}\text{Sr}/^{86}\text{Sr}$ isotopic ratios and is higher where the influence of sea water is diminished [11,12].

The conclusions drawn from elemental analyses can be confirmed by the $^{13}\text{C}/^{12}\text{C}$ ratio ($\delta^{13}\text{C}$). Differences in the ratio occur between C3 and C4 plants and their carbohydrate products [13,14]. C3 plants encompass grass, temperate trees, fruit trees, rice, and most cereals and root vegetables. C4 plants include tropical/subtropical grasses, maize, millet, sugarcane and sorghum. Nitrogen isotopes ($^{15}\text{N}/^{14}\text{N} - \delta^{15}\text{N}$) are also useful for determining trophic standing and the distinguishing between terrestrial and marine diets and those composed primarily of plants or meat [15,16].

In the case of fossil samples, trace and minor elemental content can be influenced by diagenesis. Diagenesis causes either enrichment and/or loss of elements depending on the composition of the soil, pH, and environmental conditions, e.g. [17]. The processes involved in diagenesis are poorly understood. The early phase of diagenesis of mineralized structures is probably correlated with an initial decrease in the collagen matrix [18]. Subsequently, changes in bones and teeth composition occur. It is well known that the content of fluorine ions is directly proportional to age of fossil sample. Fluorine gets incorporated into the structures of hydroxyapatite and replaces hydroxyl groups [19]. Similar behavior has been described for CO_3^{2-} , Cl^- or H_2O . Over time, the content of water and OH^- decreases as fossilization progresses [20]. The phosphate group is, in comparison with the hydroxyl component, more resistant to diagenetic change [21]. However, substitution by CO_3^{2-} has been observed [20]. Cationic changes are also evident during diagenesis. Magnesium, sodium and strontium can replace Ca in the hydroxyapatite structure and diagenesis is also typically characterized by elevated content of iron, manganese, silicon, aluminum and barium [20]. In the case of iron, manganite and smectite can be present $[(\text{Fe}^{3+}\text{Mn}^{3+})\text{O}(\text{OH})]$ [21]. Moreover, increased content of rare earth elements (REE) and U is connected with alteration of the hydroxyapatite [22].

The changes in composition of teeth have been investigated by various methods (XRD — X-ray diffraction, IR — infrared spectroscopy, PIXE — proton induced X-ray analysis, EMPA — electron microprobe analysis, SIMS — secondary ion mass spectrometry and LA-ICP-MS — laser ablation inductively coupled plasma mass spectrometry, etc.) [23–27].

Of these techniques, LA-ICP-MS is becoming increasingly popular because of its speed and ease of use. The technique provides relatively high spatial resolution on the scale of several micrometers, permits scanning of the sample surface and can be used to obtain two-dimensional maps of elemental distribution. There are other benefits such as low detection limits important in trace and ultra-trace analysis, multielemental analysis, minimization of risk of contamination and loss of volatile elements during decomposition of sample and minimal or no samples preparation

is required. The procedure has been used in archeology [28–30], biology [31] and geology, [32] for a variety of applications, from simple elemental mapping [33–36], bioimaging of soft [37–41] and hard [42,43] tissue or for determination of origin [44] and dating [45].

Quantitative LA-ICP-MS is not a routine procedure and most samples require individualized processing on a case to case basis for accurate quantitative analysis. One of the major issues is the lack of appropriate standard reference materials for the preparation of calibration standards for bias-free, matrix-matched calibration. In some cases, calibration can be achieved by generating matrix-matched laboratory standard materials pressed into the pellets. However, even in these cases, differences in the hardness, optical properties etc. of the matrix in the standard and sample may cause differences in ablation rates, aerosol particle size distributions, aerosol transport, evaporation, atomization, ionization and hence in sensitivities. These processes can lead to non-stoichiometric ablation and elemental fractionation during analysis, causing false elemental signal ratios and analytical inaccuracies [46–51]. An empirical approach to correct for differences in signal sensitivities between analyzed samples and calibration standards is to incorporate an internal standard signal. Generally, element selected as an internal standard has to be incorporated homogeneously and its concentration independently validated by means of an alternative quantitative procedure [52]. The normalization to the sum of all components to 100%_{m/m} represents another possibility [53].

Individual types of mass spectrometers differ in their advantages and limitations and therefore, the selection of an appropriate analyzer for a specific application is important. Strontium isotopic ratio measurements require precision on the level of 10⁻³% [54], which is best served using a multicollector – inductively coupled plasma mass spectrometer (MC-ICP-MS) [55]. Single collectors (e.g., quadrupole and time of flight analyzers) do not exhibit the same level of precision but have superior workflow throughput, are more versatile, are less expensive and can be used for simpler application, such as elemental distribution in simple matrices. Additionally, quadrupole instruments equipped with collision and reaction cells help to reduce polyatomic interferences, which are an important consideration when analyzing calcified tissue, which has a complex matrix characterized by many interferences that influence accuracy of determination of both major and minor elements [56].

The aim of this study is to assess the ability of LA-ICP-MS with quadrupole and time of flight analyzers to reconstruct the diet and migration pattern of a prehistoric brown bear by analyzing the distribution of minor and trace elements (zinc, barium, strontium, sodium, uranium e.g.) and matrix components (calcium and phosphorus) in the dentine of a fossilized tooth. The utility of Sr/Zn and Sr/Ba ratios to deduce changes in diet and geographical location is discussed. Calibration of the LA-ICP-MS was facilitated by results obtained with EMPA. Migration and dietary inputs were validated by using nitrogen, carbon and strontium isotopes. Diagenesis was investigated by studying content changes between cementum and dentine. Differences were observed towards the root channel of the fossilized tooth.

2. Experimental

2.1. Laser ablation inductively coupled plasma quadrupole mass spectrometry instrumentation, LA-ICP-(Q)MS

Analyses were conducted using an Agilent 7500ce (Agilent Technologies, Santa Clara, CA, USA) quadrupole ICP-MS with an attached UP 213 laser ablation system (New Wave Research, Inc., Fremont, CA, USA). The sample was placed into a SuperCell (New Wave Research, Inc., Fremont, CA, USA) having volume of 33 cm³

and ablated using a commercial Q-switched Nd:YAG laser operated at a wavelength of 213 nm (pulse duration 4.2 ns). An XY-stage was used to move the sample along a programmed trajectory and a CCD camera was used to monitor the ablation event. Ablated material was transported from the sample chamber using helium carrier gas (1 l min^{-1}) and mixed with argon (0.6 l min^{-1}) prior to the torch. Optimization of LA-ICP-MS parameters (gas flow rates, sampling depth, voltage of ion optics) was performed using glass reference material NIST SRM 612 to maximize the S/N ratio and minimum oxide formation (ThO^+/Th^+ counts ratio 0.2%) and U^+/Th^+ counts ratio 1.1%.

All laser ablation based measurements were performed with a laser fluence of 12 J cm^{-2} . Laser frequency was 20 Hz and 10 Hz for line scanning and spot analysis, respectively. ^{23}Na , ^{24}Mg , ^{57}Fe , ^{86}Sr , ^{88}Sr , ^{135}Ba and ^{238}U isotopes were measured using an integration time of 0.1 s/isotope; ^{43}Ca , ^{44}Ca and ^{31}P were recorded using an integration time of 0.05 s/isotope.

2.2. Laser ablation inductively coupled plasma time-of-flight mass spectrometry instrumentation, LA-ICP-(TOF)MS

Laser ablation experiments conducted with time-of-flight mass spectrometry were performed at the Department of Biological Sciences, California State University Long Beach, an institution collaborating via the project Laser Ablation with Inductively Coupled Plasma Spectrometry and Laser Induced Breakdown Spectroscopy in archaeology and anthropology ME10012, supported by Ministry of Education, Youth and Sports of the Czech Republic and AMVIS (American Science Information Centre, Prague, Czech Republic).

Analyses were performed using a GBC Optimass 8000 time-of-flight ICP-MS with orthogonal ion optics. Laser sampling was accomplished using a laser ablation system UP 213 using settings similar to those used for the quadrupole analyses. Signal intensities for the selected analytes were collected in five 1 s integrations, each of which recorded 30,000 spectra. A delay time of 8 s preceded collection of signal intensities. Gas flow and torch position were optimized at the beginning of each day using NIST SRM 612. Standards were run approximately every half hour during the course of the analysis. Intensities of isotopes were obtained using a laser fluence of 5 J cm^{-2} at a frequency of 20 Hz.

2.3. Electron microprobe analysis

The chemical composition of the root section was determined using a Cameca SX100 electron microprobe at Joint Laboratory of Electron Microscopy and Microanalysis, Department of Geological

Sciences, Masaryk University, Brno and The Czech Geological Survey, Brno. The instrument was operated at an accelerating voltage of 15 kV, a beam current of 10 nA and a beam size of $10\text{ }\mu\text{m}$. The following calibration standards and analytical lines were used: (K α) lines: albite (Na), almandine (Si), grossular (Al), Mg_2SiO_4 (Mg), fluorapatite (Ca, P), sanidine (K), NaCl (Cl), hematite (Fe), gahnite (Zn), topaz (F); (L α) lines: SrSO_4 (S, Sr), baryte (Ba). The peak counting times ranged from 10–30 s for all elements except for Sr (60 s). The average detection limits and standard deviations (in parentheses) under these conditions were: $\sim 1200\text{ mg kg}^{-1}$ (0.14) for Ba; $\sim 1200\text{ mg kg}^{-1}$ (0.13) for F; $\sim 1000\text{ mg kg}^{-1}$ (0.1) for Zn and Sr; $\sim 700\text{ mg kg}^{-1}$ (0.64) for Ca; $\sim 700\text{ mg kg}^{-1}$ (0.12) for Na; $\sim 500\text{--}600\text{ mg kg}^{-1}$ (0.04–0.08) for S and Fe; $\sim 400\text{ mg kg}^{-1}$ (0.4) for P and $\sim 200\text{--}300\text{ mg kg}^{-1}$ (0.02–0.04) for Si, Al, Mg, K, Cl. The analytical data were corrected using the PAP correction procedure [57].

2.4. Samples and sample preparation

The bear canine tooth analyzed in this paper (Fig. 1) was excavated in 1986 at Dolní Věstonice and originated from a brown bear (*Ursus arctos*). It was excavated from the field II, which is a longitudinal zone on top of the site, adjacent to the triple burial area. Abrasion of the tooth's occlusal area and seasonal cementum increments of tooth's root were used to determine that the animal died between August–October and was approximately 14 years old at death.

Dolní Věstonice II is one of a series of large settlements of mammoth hunters on the loess elevations at altitudes of about 180–240 m a.s.l., rising above the Dyje River and sloping further to the top of the Pavlovské vrchy in Moravia (the eastern part of the Czech Republic). Archeological excavations at this site were organized by Klíma and Svoboda between 1985 and 1989, and additional excavations took place in 1991, 1999 and 2005 [58,59]. The site is world-famous for human paleontological finds including the triple burial discovered at the top of the site, the old man burial on the western slope, and individual human remains scattered at various places in the cultural layer. The site probably had repeated occupations, extended over a timespan of 32,000 years (ka) before present (BP) to 28.5 ka BP (^{14}C). This timespan is framed by a series of earlier and later luminescence dates from paleosols and loess below and above, which make Dolní Věstonice II the best dated Gravettian site in the region.

For carbon and nitrogen isotopic analysis of collagen was performed at Czech Geological Survey. The tooth was cleaned using an ultrasonic bath, dried, gently crushed into small fragments and then treated with diluted 1 mol l^{-1} acetic acid to

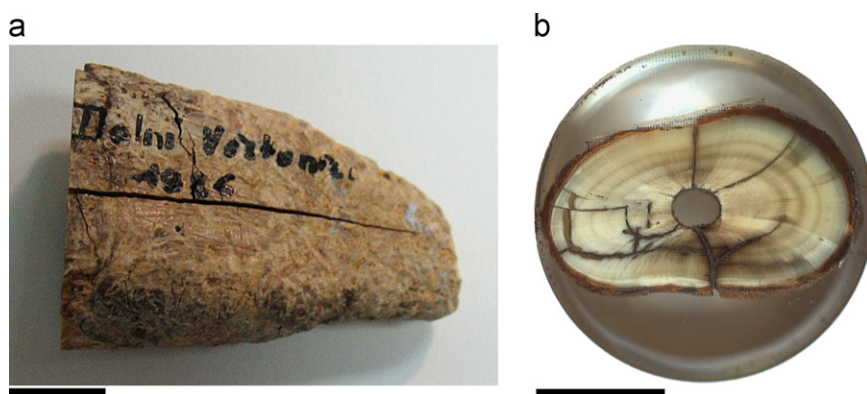


Fig. 1. Photographs: (a) of the bear canine tooth sample excavated at Dolní Věstonice and (b) of the studied sample surface, embedded in resin, with ablation pattern. The bar has a length of 1 cm.

remove surface impurities and secondary carbonates. Periodic evacuation ensured that evolved carbon dioxide was removed from the interior of the samples fragments, and that fresh acid was allowed to reach even the interior micro-surfaces. The chemically cleaned sample was then reacted under vacuum with 1 mol l⁻¹ HCl to release carbon dioxide from the bioapatite. The residue was filtered, rinsed with deionised water and, under slightly acid condition (pH=3), heated to 80 °C for 6 h to dissolve the collagen and leave humic substances in the precipitate. The collagen solution was then filtered and dried to isolate pure collagen which was then combusted at 575 °C in an evacuated/sealed Pyrex ampoule in the presence of CuO. The values δ¹³C and δ¹⁵N were measured using a MAT 251 Finnigan mass spectrometer and expressed as δ¹³C with respect to PDB (PeeDee Belemnite), with an error of less than 0.1‰, and as δ¹⁵N with respect to atmospheric nitrogen with an error of less than 0.2‰ [60].

Sr isotopic analysis conducted at University of Bergen was performed following the complete dissolution of approximately 0.1 g of powdered tooth sample in 10 ml of concentrated HNO₃ in an ETHOS One (Milestone S.r.l., Italy) microwave oven. The resulting solution was diluted with water to achieve a final HNO₃ concentration of 3 mol l⁻¹. Ion-exchange chromatography using a Sr-spec column (Eichrom Technologies, Inc., IL, USA) was employed to isolate Sr from the sample matrix. Strontium isotopes were measured with a Finnigan MAT 262 thermal ionization mass-spectrometer equipped with an array of 9 faraday detectors. Sr isotopes (masses 84, 86, 87 and 88) and interfering Rb (masses 85 and 87) were measured in a static mode from a double Re filament. The isotopic ratios were corrected for mass-dependent fractionation using ⁸⁶Sr/⁸⁸Sr=0.1194 and exponential law, and Rb interference. Repeat measurements of the NBS-987 standard over the course of the study gave a mean ⁸⁷Sr/⁸⁶Sr value of 0.710247 ± 0.000007 (2 sigma). Long term precision measurements of the Sr isotopic composition of a NBS-987 standard were 0.04‰. NIST SRM 1486 bone meal powder was also analyzed during this study and gave an ⁸⁷Sr/⁸⁶Sr value of 0.709274 ± 0.000008 (2 sigma).

3. Results and discussion

3.1. Strontium isotopic ratio

A ⁸⁷Sr/⁸⁶Sr value of 0.710029 ± 0.000007 (2 sigma) was measured from the enamel of the *U. arctos* canine excavated from Dolní Věstonice II. This value differs from the isotopic ratio characterizing geological locality of the Dolní Věstonice II, which was determined to range from 0.708914 to 0.709794 based upon the analysis of a garden snail shell (*Helix pomatia*), implying that the bear was not from this location. The observed Sr isotopic signature of the tooth more closely resembled that of the Krumlov forest and Moravian Karst, which have Sr ratios of 0.7108–0.7115 [61] and 0.710010–0.710540 (unpublished data), respectively, indicating that the animal had either migrated to the Palava region or had been captured in the Krumlov forest and Moravian Karst and subsequently transported to Dolní Věstonice. The Moravian Karst lies approx. 70 km from Dolní Věstonice. The brown bear's territory was approximately (30–40) km². However, the bear can sometimes migrate for more than 100 km [62,63].

3.2. Carbon and nitrogen isotopic ratio

Carbon and nitrogen (¹³C/¹²C a ¹⁵N/¹⁴N) isotopic ratio analyses conducted on the tooth to identify the bear's diet and palaeoenvironment provided data that was outside the variation range known for brown bears from the Pleistocene and Holocene epochs [64,65] (Table 1). The elevated content of ¹⁵N isotope in the tooth could

mean the bear either ate flesh-rich diet including freshwater fish or a diet of xeritic plants [66] originating from a rather dry environment comparable to those found in the Moravian Karst region. This latter proposition is supported by the ¹³C isotope content which indicates that the bear lived on grass steppes, open forests and tundra [66]. Such an environment was thought to exist in the Moravian Karst area during the Gravettian period (i.e. 26 ka BP).

3.3. Comparison of line scanning and spot analysis obtained by quadrupole and time-of-flight analyzers

LA-ICP-MS and EMP analyses were performed on a polished section of a tooth slice taken after embedding in resin (Fig. 1a and b). Time-resolved line scanning analyses across the middle of

Table 1
Carbon and nitrogen isotope ratio in canine tooth of the studied brown bear.

Locality	Tooth	Species	δ ¹³ C (‰)	δ ¹⁵ N (‰)	N (%)	C/N	C (%)
Dolní Věstonice II-1987	Canine	<i>Ursus arctos</i>	-20.2	13.0	15.1	2.9	43.4

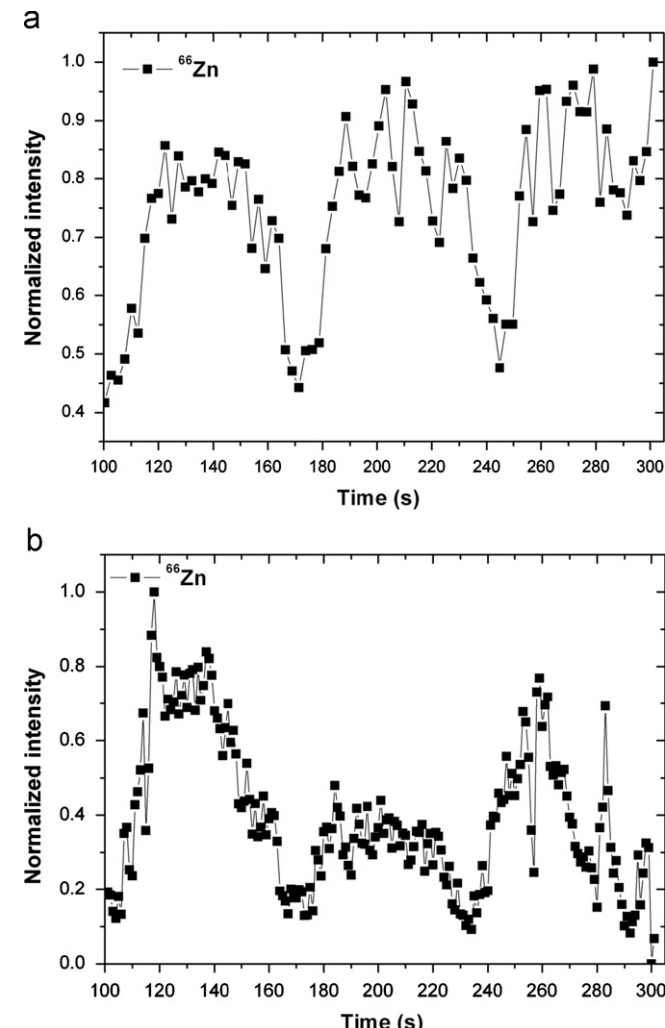


Fig. 2. LA-ICP-MS signal of ⁶⁶Zn isotope obtained by using (a) quadrupole and (b) time of flight analyzers using line scanning mode. Intensities are normalized to a maximum value.

the root section were performed by both quadrupole and time-of-flight based ICP-MS using a 50 μm diameter ablation spot scanned at a speed of 25 $\mu\text{m s}^{-1}$ at a frequency 20 Hz. Fig. 2 shows changes in the intensity of ^{66}Zn normalized to the maximum intensity value. In general, the overall spatial trends in the intensity of ^{66}Zn observed using the two types of analyzer were similar, as were the Sr/Zn ratios (Fig. 3) despite the lower mass/time resolution of the quadrupole system. The Sr/Zn ratios showed a distinct annual periodicity with spikes every ~2 mm resulting from a decrease of ratio in the winter periods (dark strips in Fig. 1) during hibernation when food intake was low. Similar trends (not shown) were obtained for other ratios (Sr/Ca and Sr/Ba) although these were not as sensitive dietary indicators as the Sr/Ba ratios [30]. This probably relates to the susceptibility of barium to undergo diagenesis relative to zinc [21].

In order to avoid the significant ablation overlap (97.5%) and memory effects that occur in line scan mode, the laser was used in a “discrete spot mode” where ablation craters of 100 μm diameter were separated by 200 μm distances. Moreover, laser sampling using line scanning mode leads to larger particle size and higher matrix effect [47]. Laser pulse-sample surface interaction took about 6 s for each spot, with a 10 s flushing time to allow for a decrease in signal concordant with a reduction in number of pulses from 20 to 10 Hz. These spatial mapping parameters were sufficient to observe spatial changes in elemental distribution

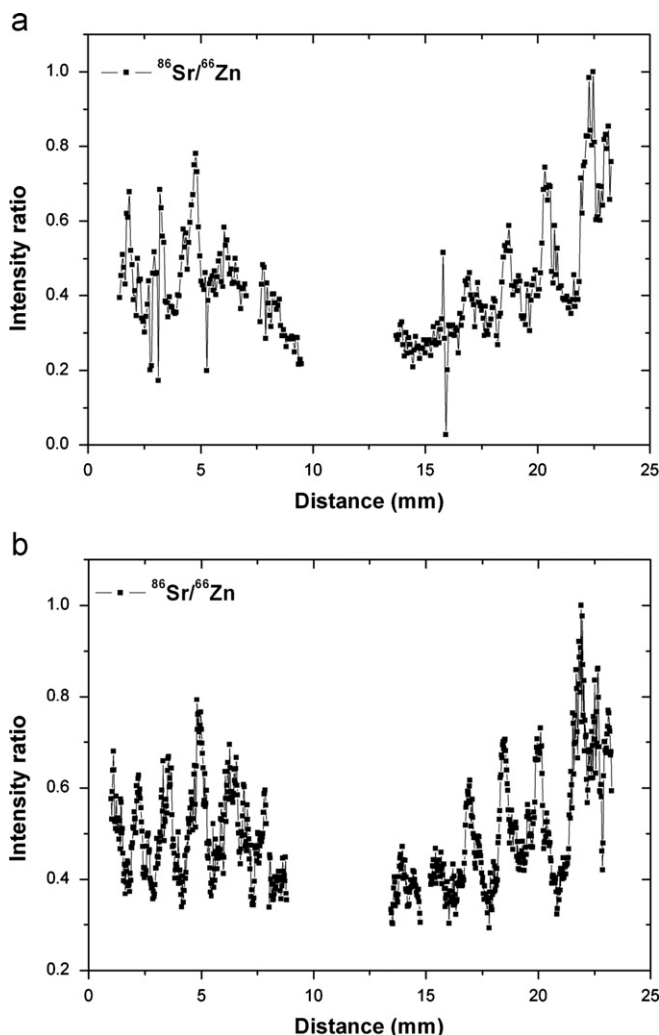


Fig. 3. Intensity ratio of $^{86}\text{Sr}/^{66}\text{Zn}$ normalized to maximum value obtained by (a) quadrupole and (b) time of flight analyzers in line scanning mode.

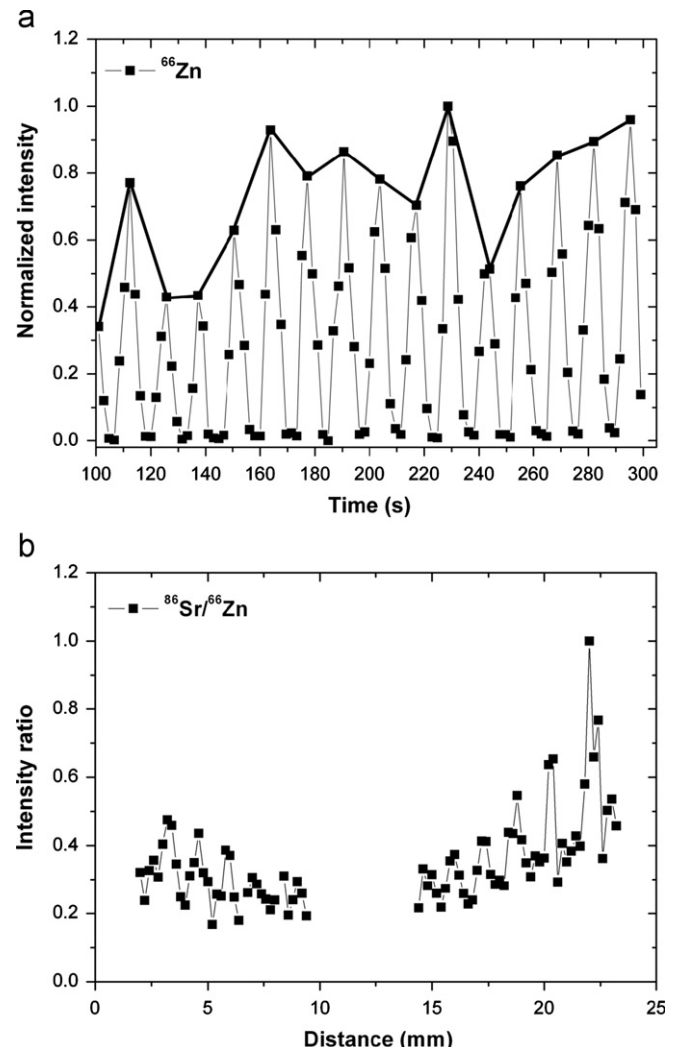


Fig. 4. Typical (Q)MS signal of (a) ^{66}Zn and (b) intensity ratio of $^{86}\text{Sr}/^{66}\text{Zn}$ recorded during ablation of individual spots. All intensities are normalized to a maximum value. The black bold line marks the distribution of ^{66}Zn in the investigated sample surface.

using quadrupole based mass spectrometry (Fig. 4a). Each ^{66}Zn intensity maximum corresponds to an individual spot analysis with the black bold line describing the distribution of zinc inside the sample surface. Periodic fluctuations of $^{86}\text{Sr}/^{66}\text{Zn}$ were clearly visible like with line scanning mode (Fig. 4b). Error in analysis was about 7–10% [30] and primarily resulted from the presence of small cavities inside the tooth sample and the inherent error of laser ablation technique itself.

3.4. Elemental mapping and quantification

Two-dimensional elemental mapping of the entire area of the bear canine root section was performed by LA-ICP-(Q)MS in the “discrete spot mode” at a spatial resolution of 200 μm . The data were visualized by GRAMS software [67] after background subtraction, matrix correction and calculation of elemental content.

The elemental composition of the root part of the fossil tooth investigated by LA-ICP-MS was quantified using compressed bone meal (SRM NIST 1486) as a calibration material. The bone meal corresponds to composition of recent bones, consisting of 26.58%_{m/m} Ca, 12.30%_{m/m} P and other elements. The fossil bones and teeth can have a higher and/or lower content of elements of interest; nevertheless, trends in elemental contents within tooth section could be distinguished using the bone meal [42,43,68].

Differences in the ablation characteristics of the tooth and the pellet were compensated for by normalizing the elemental content to the content of calcium. Content of Ca inside the root section was determined by electron microprobe (EMPA). The measurements were performed on the right part of the root section separately for dentine and cementum. Using this independent method, average values of $(35.4 \pm 2.1)\%$ _{m/m} and $(34.6 \pm 2.4)\%$ _{m/m} were obtained for Ca in the dentine and cementum, respectively. Utilization of Ca as internal reference element for correction of different ablation rate is possible due to its homogeneous distribution within the entire traced surface with exception of scratches, cracks and root channel. Homogeneous distribution has been discussed and published in our previous paper [30]. In this paper, homogeneity is obvious from EMPA measurement performed on cementum and dentine as well (Fig. 7d). The aforementioned average values corresponding to Ca content in cementum and dentine differ approximately about 2% RSD which is in the extent of calcium content variability in each tooth part (cementum and dentine). Moreover, variability and/or standard deviation of Ca content within the entire sample surface are lower than errors of LA sampling equaled to 7–10% [30]. Using NIST 1486 and calcium as internal reference element, the contents of Zn and Sr in dentine were determined as (190 ± 30) mg kg⁻¹ and (381 ± 2) mg kg⁻¹, respectively. The mean value of elemental content was calculated as the median of values obtained with 3700 spots for dentine and 250 values for cementum. LODs estimated using NIST 1486 and spot size analysis were ^{44}Ca 54 mg kg⁻¹, ^{66}Zn 1 mg kg⁻¹, ^{135}Ba 0.3 mg kg⁻¹ and ^{86}Sr 0.7 mg kg⁻¹. Limits of detection were calculated as $\text{LOD} = 3 \times s_{\text{bkg}} / [(I_{\text{isotope}} - I_{\text{bkg}})/c]$, where s_{bkg} is the standard deviation of the background, I_{isotope} and I_{bkg} are the signal intensities of the measured isotope and background respectively and c is the certified content of element in question.

The overall number of ablated spots was ~8500 due to large sample area (about 2.5 cm × 1.5 cm). The total time per one spot measurement equals to 16 s. Analysis of entire sample should

take up approximately 38 h. Fluctuation of the energy and instrumental drift are crucial points of the long-time imaging. For correction of this effect, NIST SRM 1486 was analyzed every 2 h of sample mapping. Signals of isotopes corresponding to elemental content in root section were corrected successively as the bone meal was analyzed. The correction is included into the calculation of elemental content because different parts of sample surface are quantified on temporary response from the bone meal.

Mapping showed elevated zinc content in the cementum, on the outer surface and in association with cracks in the tooth (Fig. 5a and b). These are thought to be artifacts caused by post-mortem changes in the composition of cementum and adherent contamination entering the cracks. The portion of the specimen which was less damaged and better preserved (right side in Fig. 5) showed a decrease in Zn content in four concentric rings corresponding to the visually darker bands laid down in the winter months and higher Zn content in the intervening summer months. These patterns were preserved in Zn/Ca and Sr/Zn ratio maps when the zinc was normalized to the calcium matrix and incorporated strontium (Fig. 5c and d). The areas affected by diagenesis (root channel, cracks) were also clearly visible in these maps and could be easily differentiated from the biogenic patterns that were related to the migratory and dietary changes over the life of this bear. The seasonal banding in the Sr/Zn ratio maps was significantly superior to that in Sr/Ba ratio maps, presumably because barium is more prone to diagenesis which minimizes/maximizes the elemental content inside the dentine [30].

The fluctuation in mentioned ratios reveals the changes in dietary and bear's life territory. Moreover, the content of Zn and Sr in dentine of bear tooth obtained by LA-ICP-MS falls between category of omnivore and carnivore [2]. On basis of this fact we can conclude that bear consumed meat and portion of plants in summer seasons of its life. The same results as were obtained by LA-ICP-MS were acquired by geochemical analysis according to ^{87}Sr , $\delta^{13}\text{C}$ and $\delta^{15}\text{N}$ ratio discussed in sections "Strontium isotopic ratio" and "Carbon and nitrogen isotopic ratio". Quantification

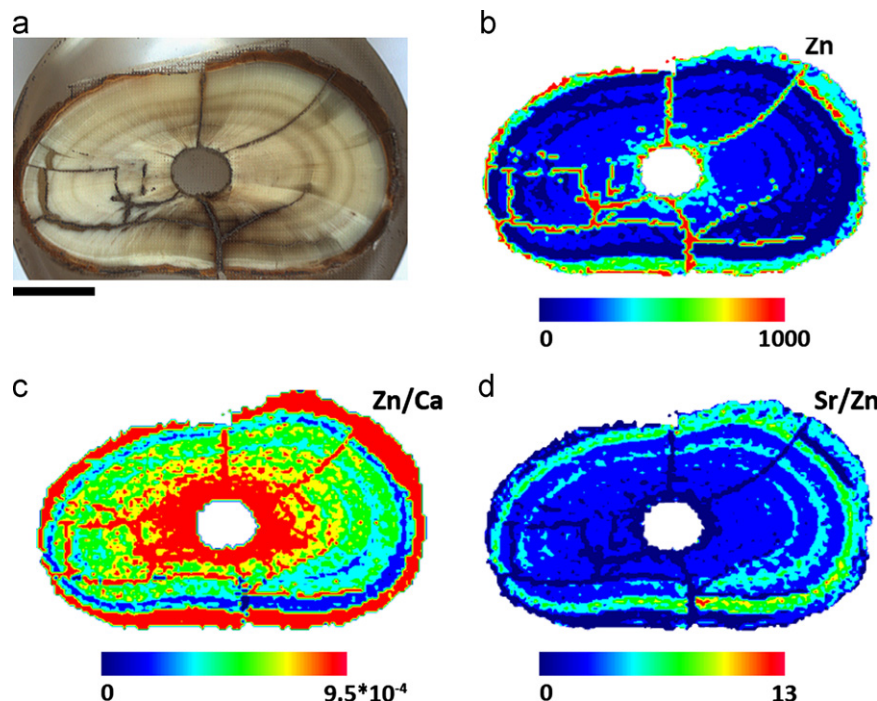


Fig. 5. Ablation pattern is visualized in (a) with a distance of ablation craters of 200 μm and 100 μm in diameter by means of LA-ICP-(Q)MS. Distribution of (b) Zn, (c) Zn/Ca and (d) Sr/Zn across the root section of brown bear's canine tooth is shown. The color scale is in unit of milligram per kilogram (mg kg⁻¹) and the bar has a length of 5 mm.

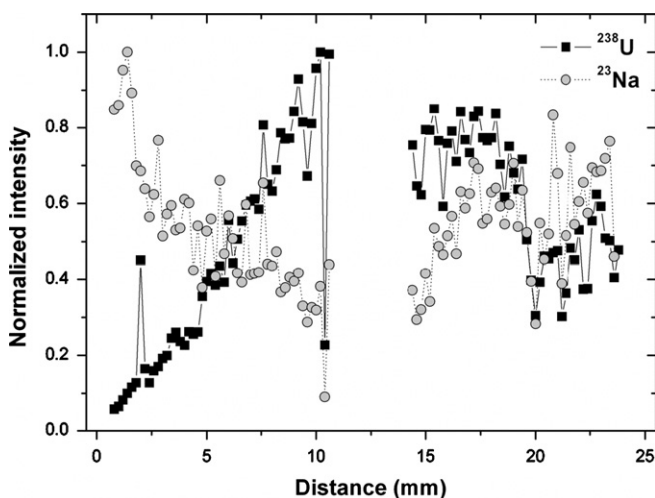


Fig. 6. Distribution of ^{23}Na and ^{238}U along the investigated sample surface obtained by LA-ICP-(Q)MS in hole drilling mode.

Table 2
Content of selected elements in cementum and dentine of canine tooth sample obtained by LA-ICP-(Q)MS.

Element	Content in cementum (mg kg ⁻¹) \pm SD	Content in dentine (mg kg ⁻¹) \pm SD
Ba	650 ± 70	56 ± 12
Zn	570 ± 200	190 ± 30
Sr	1120 ± 90	381 ± 2

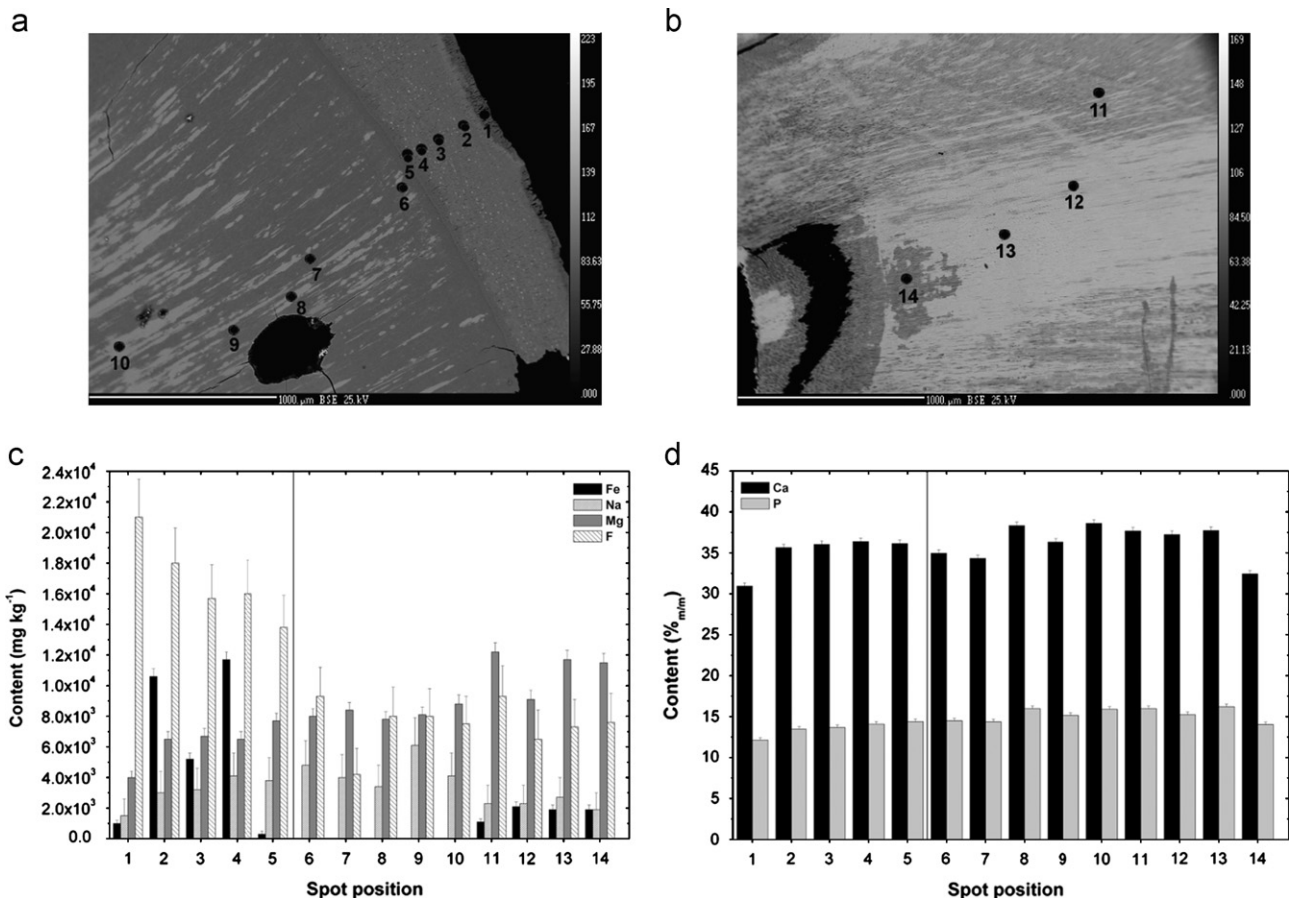


Fig. 7. Photographs: (a) of cementum and dentine and (b) of the dentine near to root channel obtained by BSE. In (a) and (b) spots where levels of elements were measured are shown. Content of (c) Fe, Na, Mg, F and (d) Ca, P obtained by EMPA.

procedure and elemental mapping could together create powerful tools, if diet and migration are investigated for a specific period of the life.

3.5. Diagenesis

The main interpretational problem in the analysis of fossilized archeological samples is identifying artefacts caused by diagenesis. In the case of the bear canine, which is about 28,500 years old, post-mortem changes have clearly occurred, especially where there are cracks and other defects. In Fig. 6, the signal of ^{23}Na isotope, measured in the middle and across the root, is attenuated towards the root channel which indicates leaching during diagenesis. Conversely, the signal of ^{238}U increases as the Na signal decreases indicating possible substitutive events. The mechanism of diagenesis is still not fully understood. However, it is known that the content of elements such as F increases with sample age. Fluorine content in recent teeth is typically in the range of (0.01–0.1)%_{m/m} [69]. EMPA analyses of the bear tooth showed a fluorine content of $(0.75 \pm 0.15)\%$ _{m/m} in the dentine and $(1.70 \pm 0.24)\%$ _{m/m} in the cementum. Additional evidence for enhanced diagenesis in the cementum is shown in LA-ICP-(Q)MS elemental analyses given in Table 2.

The fluctuations in Mg, Fe, Na and F in the cementum and dentine measured by EMPA are shown in Fig. 7. For orientation, spots "1–5" are located in the cementum with spots 1 and 2 being on the edge of cementum near to the resin and spot 5 being on the cementum dentine interface. A progressive decrease in the fluorine content is visible as one analyses spots closer to the dentine. Spots 6 to 14 are within the dentine and span from close

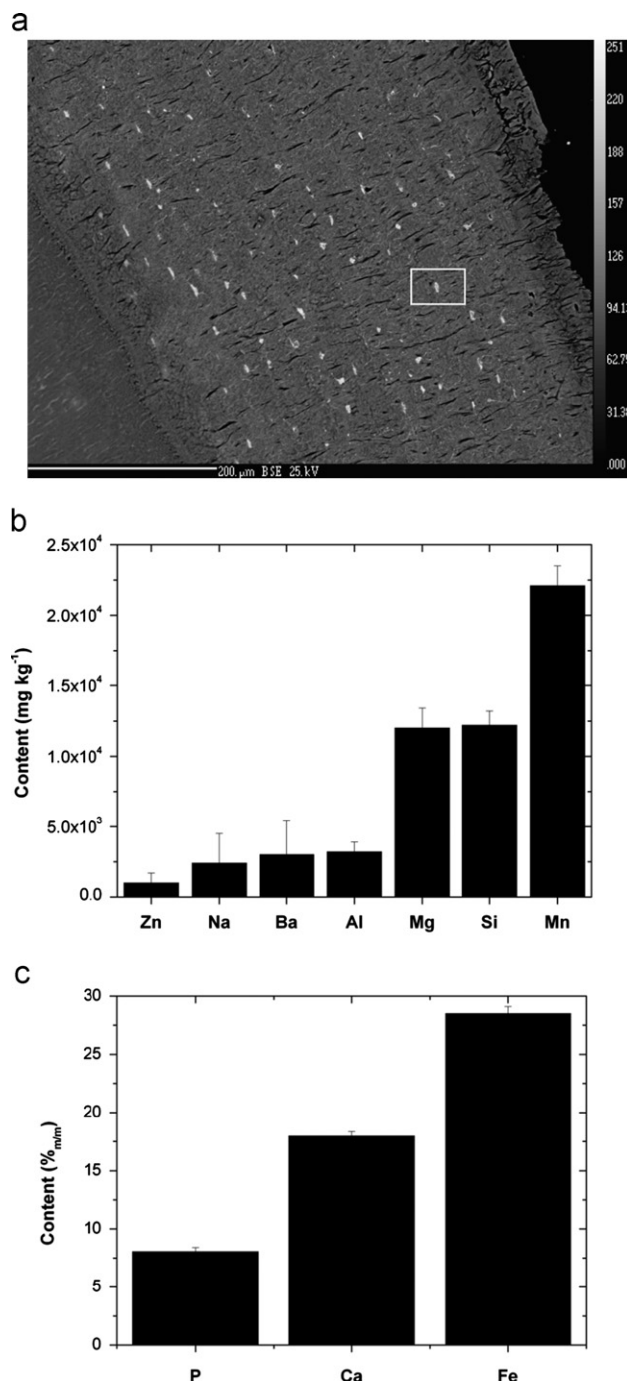


Fig. 8. (a) Detail of cementum obtained by BSE and content of (b) Zn, Na, Ba, Al, Mg, Si, Mn and (c) P, Ca, Fe in small light particles (marked by white rectangle) inside the cementum measured by EMPA.

to the cementum interface to the root channel. Analyses close to the root channel showed reduced sodium and increased Mg and Fe content —possibly due to contamination. Zinc and strontium were below the LOD in the dentine but could be readily detected in the cementum. In contrast, barium was below the LODs in both the cementum and the dentine. The cementum also had discrete particles with a diameter of about 1 μm containing 18.0%_{m/m} Ca, 8.1%_{m/m} P, 28.5%_{m/m} Fe, 2.2%_{m/m} Mn, 1.2%_{m/m} Mg, 0.2%_{m/m} Na and other trace elements indicative of oxides and hydroxides of iron (Fig. 8). Based on LA-ICP-MS and EMPA analysis, sample area which is not affected by diagenesis is clearly distinguished and can be used for reconstruction of diet/migration without any chemical

intervention enabling reduced post-mortem changes in elemental content.

4. Conclusion

In this work, laser ablation inductively coupled plasma mass spectrometry was used for elemental mapping in a fossil tooth sample having a hydroxyapatite matrix. The same shapes of isotopic intensity and/or ratio were provided using both analyzers. Generally, better precision is achieved by using TOF but precision of Q MS is sufficient for monitoring of elements in skeletal tissue. All the parts of a tooth root can be clearly distinguished together with winter and summer strips inside the dentine. It was observed that migration and diet are better reflected by the Sr/Zn ratio in comparison with Sr/Ba. It is possible to determine the content of elements by using bone meal together with an independent method for the elimination of the different ablation rates of the skeletal remains and the pellet. Quantification procedure and elemental mapping could be efficient for determination of dietary and migration in specific period of the human and animal life. Moreover, diagenesis can be revealed on the basis of the presence of elements that are not normally contained in teeth and bone. With respect to the preliminary study, all results have to be confirmed by geochemical analysis. Finally, verification requires analysis of various types of teeth and bones and an understanding of the mechanisms of diagenesis.

Acknowledgments

The authors acknowledge the AMVIS Agency and Ministry of Education, Youth and Sports of the Czech Republic for support of the Project ME10012 in program KONTAKT, the Czech Science Foundation for Grant 203/09/1394, and the European Regional Development Fund Project "CEITEC" (CZ.1.05/1.1.00/02.0068).

References

- [1] L.T. Humphrey, W. Dirks, M.Ch. Dean, T.E. Jeffries, *Folia Primatol.* 79 (2008) 197–212.
- [2] V. Smrčka, *Trace Elements in the Bone Tissue*, The Karolinum Press, Czech Republic, 2005.
- [3] M. Sponheimer, D. de Ruiter, J. Lee-Thorp, A. Späth, *J. Hum. Evol.* 48 (2005) 147–156.
- [4] A. Sillen, *J. Hum. Evol.* 23 (1992) 495–516.
- [5] A. Mays, *J. Archaeol. Sci.* 30 (2003) 731–741.
- [6] H.M. Tveiteneim, R. Eide, T. Riise, *Sci. Total. Environ.* 255 (2000) 21–27.
- [7] J.H. Burton, T.D. Price, *J. Archaeol. Sci.* 17 (1990) 547–557.
- [8] J.H. Burton, T.D. Price, W.D. Middleton, *J. Archaeol. Sci.* 36 (1999) 609–616.
- [9] K. Szostek, H. Glab, A. Pudlo, *HOMO* 60 (2009) 359–372.
- [10] R.A. Bentley, *J. Archaeol. Method Theory* 13 (2006) 135–187.
- [11] L.E. Wright, *J. Archaeol. Sci.* 32 (2005) 555–566.
- [12] S.R. Copeland, M. Sponheimer, J.A. Lee-Thorp, P.J. le Roux, D.J. de Ruiter, M.P. Richards, *J. Archaeol. Sci.* 37 (2010) 1437–1446.
- [13] A. Zazzo, M. Balasse, W.P. Patterson, *Geochim. Cosmochim. Acta* 69 (2005) 3631–3642.
- [14] T. Tütken, H. Furrer, T.W. Vennemann, *Quat. Int.* 164–165 (2007) 139–150.
- [15] M. Sponheimer, T.F. Robinson, B.L. Roeder, B.H. Passey, L.K. Ayliffe, T.E. Cerling, M.D. Dearing, J.R. Ehleringer, *J. Archaeol. Sci.* 30 (2003) 1649–1655.
- [16] M.P. Richards, S. Mays, B.T. Fuller, *Am. J. Phys. Anthropol.* 119 (2002) 205–210.
- [17] V. Balter, Ch. Lécuyer, *Geochim. Cosmochim. Acta* 74 (2010) 3449–3458.
- [18] T. Tütken, T.W. Vennemann, H.U. Pfretzschner, *Palaeogeogr. Palaeoclimatol. Palaeoecol.* 266 (2008) 254–268.
- [19] A.A.M. Gaschen, M. Doebeli, A. Markwitz, B. Barry, S. Ulrich-Bochsler, U. Krahenbuehl, *J. Archaeol. Sci.* 35 (2008) 535–552.
- [20] V. Michel, *Appl. Geochem.* 10 (1995) 146–159.
- [21] M.J. Kohn, M.J. Schoeninger, W. Barker, *Geochim. Cosmochim. Acta* 63 (1999) 2737–2747.
- [22] J. Labs-Hochstein, B.J. MacFadden, *Geochim. Cosmochim. Acta* 70 (2006) 4921–4932.

- [23] D. Negrea, C. Ducu, S. Moga, V. Malinovschi, J. Neamtu, C. Ristoscu, I.N. Mihailescu, F. Cornelia, J. Optoelectron. Adv. Mater. 12 (2010) 1194–1199.
- [24] E.T. Bergslien, M. Bush, P.J. Bush, Forensic Sci. Int. 175 (2008) 218–226.
- [25] T.R. Rautray, S. Das, A.C. Rautray, Nucl. Instrum. Methods B 14 (2010) 2371–2374.
- [26] K. Shimada, I. Sato, H. Moriyama, J. Morphol. 211 (1992) 319–329.
- [27] A.R. Lodding, P.M. Fischer, H. Odellius, J.G. Noren, L. Sennerby, C.B. Johansson, J.M. Chabal, R. Levissetti, Anal. Chim. Acta 241 (1990) 299–314.
- [28] R.J. Speakman, M.D. Glascock, R.H. Tykot, C. Descantes, J.J. Thatcher, C.E. Skinner, K.M. Lienhop, ACS Symp. Ser. 968 (2007) 275–296.
- [29] M. Resano, E. Garcia-Ruiz, F. Vanhaecke, Mass Spectrom. Rev. 29 (2010) 55–78.
- [30] M. Galiová, J. Kaiser, F.J. Fortes, K. Novotný, R. Malina, L. Prokeš, A. Hrdlička, T. Vaculovič, M. Nývltová Fišáková, J. Svoboda, V. Kanický, J.J. Laserna, Appl. Optics 49 (2010) C191–C199.
- [31] M. Galiová, J. Kaiser, K. Novotný, J. Novotny, T. Vaculovic, M. Liska, R. Malina, K. Stejskal, V. Adam, R. Kizek, Appl. Phys. A Mater. Sci. Process. 93 (2008) 917–922.
- [32] B. Stoll, K.P. Jochum, K. Herwig, M. Amini, M. Flanz, B. Kreuzburg, D. Kuzmin, M. Willbold, J. Enzweiler, Geostand. Geoanal. Res. 32 (2008) 5–26.
- [33] M.C. Santos, M. Wagner, B. Wu, J. Schneider, J. Oehlmann, S. Cadore, J.S. Becker, Talanta 80 (2009) 428–433.
- [34] J. Dobrowolska, M. Dehnhardt, A. Matusch, M. Zoriy, N. Palomero-Gallagher, P. Koscielniak, K. Zilles, J.S. Becker, Talanta 74 (2008) 717–723.
- [35] B. Wu, M. Zoriy, Y.X. Chen, J.S. Becker, Talanta 78 (2009) 132–137.
- [36] K. Novotný, J. Kaiser, M. Galiová, V. Konecna, J. Novotny, R. Malina, M. Liska, V. Kanicky, V. Otruba, Spectrochim. Acta Part B 63 (2008) 1139–1144.
- [37] D.S. Ghopal, A. Izmer, B. De Samber, J.T. van Elteren, V.S. Šelih, R. Evens, K. De Schampelaere, C. Janssen, L. Balcaen, I. Lindemann, L. Vincze, F. Vanhaecke, Anal. Chim. Acta 664 (2010) 19–26.
- [38] J. Lear, D.J. Hare, F. Fryer, P.A. Adlard, D.I. Finkelstein, P.A. Doble, Anal. Chem. 84 (2012) 6707–6714.
- [39] D.J. Hare, J.K. Lee, A.D. Beavis, A. van Gramberg, J. George, P.A. Adlard, D.I. Finkelstein, P.A. Doble, Anal. Chem. 84 (2012) 3990–3997.
- [40] B. Wu, J.S. Becker, Int. J. Mass Spectrom. 323–324 (2012) 34–40.
- [41] J.S. Becker, U. Kumtabtim, B. Wu, P. Steinacker, M. Otto, A. Matusch, Metallomics 4 (2012) 284–288.
- [42] D. Hare, C. Austin, P. Doble, M. Arora, J. Dent. 39 (2011) 397–403.
- [43] M. Arora, D. Hare, C. Austin, D.R. Smith, P. Doble, Sci. Total Environ. 409 (2011) 1315–1319.
- [44] C.E. de Barros, L.V.S. Nardi, S.R. Dillenburg, R. Ayup, K. Jarvis, R. Baitelli, J. Coastal Res. 26 (2010) 80–93.
- [45] Y.H. Lu, Y. Zhang, Y. Lai, Y.Z. Wang, Acta Petrol Sin. 25 (2009) 2902–2912.
- [46] D. Günther, B. Hattendorf, Trends Anal. Chem. 24 (2005) 255–265.
- [47] M. Guillong, D. Günther, J. Anal. At. Spectrom. 17 (2002) 831–837.
- [48] J. Kosler, M. Wiedenbeck, R. Wirth, J. Hovorka, P. Sylvester, J. Mikova, J. Anal. At. Spectrom. 20 (2005) 402–409.
- [49] J. Mikova, J. Kosler, H.P. Longerich, M. Wiedenbeck, J.M. Hanchar, J. Anal. At. Spectrom. 24 (2009) 1244–1252.
- [50] B.K. Kuhn, K. Birbaum, Y. Luo, D. Gunther, J. Anal. At. Spectrom. 25 (2010) 21–27.
- [51] J. Koch, D. Gunther, Appl. Spectrosc. 65 (2011) 155A–162A.
- [52] N.J.G. Pearce, J.A. Westgate, W.T., Quat. Int. 34–36 (1996) 213–227.
- [53] Y.S. Liu, Z.C. Hu, S. Gao, D. Günther, J. Xu, C.G. Gao, H.H. Chen, Chem. Geol. 257 (2008) 34–43.
- [54] J.S. Becker, Inorganic Mass Spectrometry: Principles and Applications, John Wiley & Sons, Chichester, 2007.
- [55] J. Košler, Proc Geol. Assoc. 118 (2007) 19–24.
- [56] D. De Muynck, F. Vanhaecke, Spectrochim. Acta Part B 64 (2009) 408–415.
- [57] L.J. Pouchou, F. Picchoir, Microb. Anal. 20 (1985) 104–105.
- [58] B. Klíma, Dolní Věstonice II, Université de Liège, Belgique, 1991.
- [59] J. Svoboda, Dolní Věstonice II — Western Slope II, Université de Liège, Belgique, 1991.
- [60] J.M. McCrea, J. Chem. Phys. 18 (1950) 849–857.
- [61] P.M. Richards, J. Montgomery, O. Nehlich, V. Grimes, Antropologie, XLVI (2008) 185–194.
- [62] R.M. Nowak, J.L. Paradiso, Walkers Mammals of the World, 4th ed., Johns Hopkins University Press, London, 1983.
- [63] J. Clutton-Brock, Mammals, Dorling Kindersley Limited, London, United Kingdom, 2002.
- [64] G.V. Hilderbrand, S.D. Farley, C.T. Robbins, T.A. Hanley, K. Titus, C. Servheen, Can. J. Zool. 74 (1996) 2080–2088.
- [65] H. Bocherens, M. Fizet, A. Mariotti, Palaeogeogr. Palaeoclimatol. Palaeoecol. 107 (1994) 213–225.
- [66] H. Bocherens, Isotopic biogeochemistry and the paleoecology of the mammoth steppe fauna, in: J.W.F. Reumer, J. De Vos, D. Mol (Eds.), Advances in Mammoth research, Proceedings of the Second International Mammoth Conference, Rotterdam, May 16–20 1999, Deinse 9, 2003 57–76.
- [67] <<http://www.thermofisher.com>>.
- [68] M. Holá, J. Kalvoda, O. Babek, R. Brzobohaty, I. Holoubek, V. Kanicky, R. Skoda, Environ. Geol. 58 (2009) 141–151.
- [69] Z. Goffer, Archaeological chemistry, Second edition, John Wiley & Sons, New Jersey, 2007.



2D elemental mapping of sections of human kidney stones using laser ablation inductively-coupled plasma-mass spectrometry: Possibilities and limitations[☆]



Michaela Vašinová Galiová ^{a,b}, Renata Čopjaková ^c, Radek Škoda ^c, Kateřina Štěpánková ^a, Michaela Vaňková ^a, Jan Kuta ^d, Lubomír Prokeš ^{a,e}, Jindřich Kynický ^f, Viktor Kanický ^{a,b,*}

^a Department of Chemistry, Faculty of Science, Masaryk University, Kotlářská 2, 611 37 Brno, Czech Republic

^b Central European Institute of Technology (CEITEC), Masaryk University, Kamenice 5, 625 00 Brno, Czech Republic

^c Department of Geological Sciences, Faculty of Science, Masaryk University, Kotlářská 2, 611 37 Brno, Czech Republic

^d Research Centre for Toxic Compounds in the Environment (RECETOX), Masaryk University, Kamenice 126/3, 625 00 Brno, Czech Republic

^e Department of Physical Electronics, Faculty of Science, Masaryk University, Kotlářská 2, 611 37 Brno, Czech Republic

^f Department of Pedology and Geology, Faculty of Forestry and Wood Technology, Mendel University in Brno, Zemědělská 3, 613 00 Brno, Czech Republic

ARTICLE INFO

Article history:

Received 13 June 2014

Accepted 27 June 2014

Keywords:

Laser ablation inductively coupled plasma mass spectrometry
Elemental mapping
Electron microprobe
Urolith
Quantification

ABSTRACT

A 213 nm Nd:YAG-based laser ablation (LA) system coupled to quadrupole-based inductively coupled plasma-mass spectrometer and an ArF* excimer-based LA-system coupled to a double-focusing sector field inductively coupled plasma-mass spectrometer were employed to study the spatial distribution of various elements in kidney stones (uroliths). Sections of the surfaces of uroliths were ablated according to line patterns to investigate the elemental profiles for the different urolith growth zones.

This exploratory study was mainly focused on the distinguishing of the main constituents of urinary calculus fragments by means of LA-ICP-mass spectrometry. Changes in the ablation rate for oxalate and phosphate phases related to matrix density and hardness are discussed. Elemental association was investigated on the basis of 2D mapping. The possibility of using NIST SRM 1486 Bone Meal as an external standard for calibration was tested. It is shown that LA-ICP-MS is helpful for determination of the mineralogical composition and size of all phases within the analyzed surface area, for tracing down elemental associations and for documenting the elemental content of urinary stones. LA-ICP-MS results (elemental contents and maps) are compared to those obtained with electron microprobe analysis and solution analysis ICP-MS.

© 2014 Elsevier B.V. All rights reserved.

1. Introduction

Kidney stones, also known as renal calculi, are crystal aggregations that originate from substances dissolved in urine. Hence, the other term used for a kidney stone, i.e. a urinary stone (or urolith), which is a concretion of mineral salts (biominerals) that develops in a hollow part of the kidneys (*nephrolithiasis*), a ureter (*ureterolithiasis*), the bladder (*cystolithiasis*), the urethra (*urethrolithiasis*), or the prostate (*prostatholithiasis*). About 15 crystalline substances have been described in uroliths [1–3]. These comprise calcium oxalate monohydrate

(whewellite), calcium oxalate dihydrate (weddellite), magnesium hydrogen phosphate trihydrate (newberryite), magnesium ammonium phosphate hexahydrate (struvite), hydroxyapatite, carbonate–apatite, calcium hydrogen phosphate dihydrate (brushite), uric acid, uric acid dihydrate, ammonium urate, sodium urate monohydrate, cystine and xanthine. Uroliths have been systematically divided into five categories, i.e.: i) calcium oxalate; ii) struvite; iii) uric acid; iv) calcium phosphate, and v) cystine [4]. Various causes of formation exist for particular urolith types and these relate to both acquired and inherited metabolic conditions.

A literature search provided 11,300 records related to the terms *urinary stones* or *kidney stones* 66% of which are dedicated to urology and nephrology, 4% to general and internal medicine, 2% to surgery, 3% to radiology, nuclear medicine and medical imaging, 2% to pediatrics, 1% to pharmacology and pharmacy, 2% to endocrinology and metabolism, 1% to nutrition and dietetics and 12% to research and experimental medicine, and finally about 5% dedicated to chemical and physical analysis

[☆] This paper is dedicated to Nicoló Omenetto, on the occasion of his 75th birthday, in recognition of his outstanding contributions to the field of laser spectrochemistry and as an editor of Spectrochimica Acta Part B.

* Corresponding author.

E-mail address: viktork@chemi.muni.cz (V. Kanický).

[5]. A similar distribution was found for the approximately 17,800 related to the term *calculi*, restricted solely to its medicinal meaning. It is obvious that significant attention is devoted to analysis of urinary stones.

A profound insight into the mechanisms of urolith formation is of significant importance for prevention and medical treatment of this disease. To study kidney stones, the following methods have been routinely used in various laboratories [6]: macroscopic and microscopic examination using light microscopy, X-ray diffraction spectroscopy (XRD), infrared spectroscopy (IR), chromatography, molecular fluorescence spectroscopy of organic compounds, polarization optical crystallography, chemical microscopy, ultraviolet-visible spectroscopy and photomicroscopy. In the domain of IR spectroscopy [7–14], especially the Fourier transform variety [9–11] and as near-infrared spectroscopy in reflectance mode [12] have been frequently employed, as well as Raman spectroscopy [14–16]. Crystallographic analysis of urinary stones by XRD [16–19] has been combined with IR spectroscopy [16] and X-ray photoelectron spectroscopy [18]. Surface analysis of uroliths is carried out by means of polarization microscopy [20] and scanning electron microscopy [21–23]. Recently, atomic force microscopy was used for the measurement of adhesion forces of the calcium oxalate monohydrate crystal surface to various functional groups that occur in urinary species. These interactions are responsible for the undesirable growth of crystals and their attachment to epithelial cells lining the renal tubules [24]. A review of classification of the methods used for calculi investigation has been presented in Ref. [25].

Determination of the bulk elemental composition of uroliths has been reported in a large number of papers. However, only a few articles (mostly reporting the use of scanning electron microscopy) are focused on the spatial distribution of the elements of interest. The spatial distribution of Ca, Mg, P, Zn, Sr, Rb and Pb has been studied in human kidney and bladder stones via laser ablation-inductively coupled plasma-mass spectrometry (LA-ICP-MS) and the information thus obtained was related to knowledge on the initiation and formation of the calculi [26]. A custom-made 266 nm frequency-quadrupled fine-focus Nd:YAG laser ablation unit, coupled to a quadrupole-based ICP-MS instrument, was used for elemental mapping. A line scan was carried out across the urolith surface at a scan speed of 1 mm min^{-1} . Elemental mapping of the urolith surface took several minutes, depending on the sample size. The lateral resolution achieved was $50 \mu\text{m}$. The study focused only on inter-elemental association patterns without aiming at any identification of the biominerals studied or any classification into mineralogical groups. No quantification approach was applied and also fundamental processes affecting the MS signal were considered to be beyond the scope of their exploratory study.

Uroliths represent a complicated matrix, not only because of the different mineral phases, but also due to the considerable carbon content, resulting both from the presence of inorganic (oxalate, carbonate-apatite) and organic (urate, uric acid) compounds. Consequently, multiplicative interferences may arise due to the enhanced ionization of some elements with ionization energies in the range 9–11 eV [27–32].

Nowadays, urolithiasis affects approximately 1% of the population of the Czech Republic. This ordinary ailment is caused by various factors [33]. The calculus specimens studied in this work originate from a population of the northern part of the Moravia region of the Czech Republic. More than 11,000 urinary stones were surgically removed in the Ostrava city hospital during a period of 30 years. Kidney stones were characterized and archived. Mineralogical analyses of the above set of urogenous concrements have been performed. However, changes in elemental composition over time and correlation to environmental factors have not been studied so far. Beside LA-ICP-MS, laser induced breakdown spectroscopy was used for study of spectrochemical analysis of kidney stones [34,35].

Highly efficient aerosol formation by pulsed laser ablation and appropriately small size of a laser beam focus together with almost complete sample ionization in inductively coupled plasma source and fast

multielemental measurement capability of mass spectrometry render LA-ICP-MS suitable for local analysis and elemental mapping of solids. Moreover, low limits of detection make it possible to record signals of trace elements. Various materials have already been subjected to visualization of the elemental distribution, including e.g. skeletal remains or plant tissues [36–38]. Recently, LA-ICP-MS method has been frequently used for investigation of soft tissues [39–42].

The aim of this study is the development of quantitative elemental mapping of uroliths using LA-ICP-MS. This method is commonly used for elemental mapping of single-phase matrices or local analysis; however, kidney stones are usually composed of several constituents (minerals), differing in physical and chemical properties. In our study, the variability in density, hardness, absorption properties and ablation rate is discussed with respect to the chemical and mineralogical composition of kidney stones. Heterogeneity and lack of suitable standard reference materials make quantification difficult.

In summary, in this study we aimed at: (1) 2D elemental mapping of urolith sections; (2) revealing the composition of particular phases; (3) studying the influence of density and hardness on the LA-ICP-MS signal; (4) investigation of inter-element associations in particular urolith constituents and (5) quantitative determination of elemental contents.

Association of elements in particular kidney stones and their constituents was expressed using correlation coefficients. LA-ICP-MS and scanning electron microscopy (SEM) elemental maps were employed to confirm these inter-element correlations. Major and minor elemental contents were determined by electron microprobe (EMP). Relations between the mineralogy of uroliths and the inter-element correlations are discussed.

2. Experimental

2.1. Mineralogical characteristics of the studied uroliths

The samples of human kidney stones (uroliths) examined exhibit a wide range of variability in size, mineralogical structure and chemical composition, due to the effect of the patient's disorder, gender and age. The uroliths selected for (LA)-ICP-MS and EMP analysis are presented in Table 1, together with their mineralogical composition as determined by infrared spectroscopy (FTIR Nicolet Avatar 2000, Thermo Scientific, USA). The samples originate from a collection of Prof. Petr Martinec, a co-author of a project, entitled "Chemical, mineralogical and statistical analysis of set of urinary stones of patients of Ostrava city agglomeration" GA 203-09-1394 supported by the Czech Science Foundation. In Table 1, it can be seen that they differ from one another in oxalate and phosphate ratio. Whewellite, weddellite, apatite, carbonate apatite and uric acid are the main mineralogical constituents of these uroliths. Uric acid is the main constituent of one urolith (no. 10806), the others exhibit a calcium oxalate (whewellite and weddellite) from ca. 50 to ca. 90%. The selection of samples was done such that a representative collection of the most common urolith species was obtained.

2.2. Sample preparation

Uroliths were cut into two parts using a diamond saw. One part was crushed, milled and homogenized. A portion of the powdered sample (25 mg) was totally decomposed by mixture of 2 ml HNO_3 and 0.2 ml H_2O_2 in a PFA beaker on a hot plate. Clear solution was transferred into the volumetric flask (25 ml) and diluted up to the mark with deionized water [43].

The other part of the urolith, intended for elemental mapping by LA-ICP-MS and SEM/EMP, was embedded into polymethylmethacrylate resin in a mold and the cut surface was polished with diamond paste.

Table 1Mineralogical composition of studied kidney stones (%_{m/m}) determined by infrared spectrometry.

Sample	No. in graphs (Fig. 9)	Oxalate	Phosphate	Uric acid
11560	1	50% WH	25% AP + 25% carbonate apatite	–
11561	2	70% WH + 10% WD	20% AP	–
11684	3	30% WH + 40% WD	20% AP	10%
11726	4	80% WH + 10% WD	10% AP	–
11847	5	50% WH + 30% WD	10% AP + 10% carbonate apatite	–
11966	6	90% WH	10% AP	–
11727	7	90% WH	10% AP	–
10806	8	10% WH	~	90%
11681	9	30% WH + 60% WD	10% AP	–

WH = whewellite ($\text{Ca}(\text{C}_2\text{O}_4 \cdot \text{H}_2\text{O})$), WD = wedellite ($\text{Ca}(\text{C}_2\text{O}_4 \cdot 2\text{H}_2\text{O})$).AP = amorphous apatite ($\text{Ca}_5(\text{PO}_4)_3(\text{F},\text{OH})$), carbonate apatite ($\text{Ca}_5(\text{PO}_4,\text{CO}_3)_3(\text{F},\text{OH})$). ¹ Discredited by International Mineralogical Association in 2008 as the mineral.Uric acid = $\text{C}_5\text{H}_4\text{N}_4\text{O}_3$.

2.3. Bulk analysis

Average content of major (Ca, P, Mg), minor, and trace elements (Na, Al, K, V, Cr, Mn, Fe, Co, Ni, Cu, Zn, As, Se, Rb, Sr, Zr, Mo, Cd, Sn, Sb, Ba, Pb) in studied uroliths was determined by ICP-MS in solutions prepared by above procedure. An Agilent 7500ce ICP-MS (Agilent Technologies, Santa Clara, CA, USA) was employed with the collision cell operated in He-mode in order to minimize polyatomic interferences. Reliability of this already published procedure [43] was verified using NIST SRM 1486 Bone Meal. The total carbon content was determined by means of a carbon analyzer LiquiTIC II (Elementar Analysensysteme GmbH, Hanau, Germany). Thus obtained average composition was used in discussion of elemental maps.

2.4. Elemental mapping by laser ablation-inductively coupled plasma-mass spectrometry

The LA-ICP-MS experiments were accomplished with two different instrumental setups. A quadrupole-based ICP-MS instrument Agilent 7500ce was connected to a pulsed Nd:YAG-based laser ablation system UP 213 (New Wave Research, Inc., Fremont, CA, USA). This system is installed at the Laboratory of Atomic Spectrochemistry (LAS) of the Department of Chemistry, Masaryk University. The other system, installed at the Atomic and Mass Spectrometry (A&MS) research unit, Department of Analytical Chemistry, Ghent University, consists of an Element XR double-focusing sector field ICP-MS instrument (Thermo Scientific) connected to a UP193HE ArF* excimer-based laser ablation device (New Wave Research, Inc., Fremont, CA, USA).

The experiments at LAS were focused on mapping of large areas of uroliths, which included almost the whole cut surfaces, while experiments at A&MS were devoted to elemental mapping of specific part of cut, and to quantitative analysis with standardization using NIST SRM 1486. The maps obtained at A&MS were used to check those obtained with LA-ICP-QMS system at LAS.

The UP 213 ablation device is equipped with a SuperCell, designed for rapid elution of the ablation-generated aerosol with a carrier gas (1.0 l min^{-1} He). The aerosol is transported through 1 m long polyurethane tubing (4 mm i.d.) into the ICP source of the quadrupole-based Agilent 7500ce ICP-MS unit (Agilent Technologies, Santa Clara, CA, USA).

The ICP-QMS unit is equipped with a collision-reaction cell for minimization of potential polyatomic interferences. The signals of the $^{43,44}\text{Ca}$ isotopes could suffer from spectral overlap as a result of the occurrence of $^{12}\text{C}^{16}\text{O}_2$, $^{14}\text{N}_2^{16}\text{O}$, $^{28}\text{Si}^{16}\text{O}$, ^{88}Sr , $^{31}\text{P}^{13}\text{C}$, $^{14}\text{N}_3^{1}\text{H}$, $^{27}\text{Al}^{16}\text{O}$, ^{86}Sr and $^{31}\text{P}^{12}\text{C}$ ion signals, while the determination of ^{31}P might be hindered as a result of the occurrence of $^{14}\text{N}^{16}\text{O}^{1}\text{H}$ and $^{15}\text{N}^{16}\text{O}$ [44]. Self-evidently, also the signals from the minor elements investigated (Zn, Mg, K, Sr, etc.) might be subject to overlap with signals of polyatomic ions (e.g., $^{40}\text{Ar}^{26}\text{Mg}$, $^{40}\text{Ar}^{28}\text{Si}$, $^{12}\text{C}_2$, $^{23}\text{Na}^{16}\text{O}$). In this context, whenever

possible, the signal of >1 isotope of each element present in kidney stone matrix was monitored. Measurement conditions were optimized in both, collision and reaction mode. Hydrogen and helium are widely used for this purpose [45,46]. Optimization of the helium gas flow rate (collision mode) was carried out in the range of $0\text{--}5.5 \text{ ml min}^{-1}$ in the absence of hydrogen. An increase in the He flow rate results in a reduction of the signal intensities of both the analyte and the interfering ion. The use of H_2 did not provide an improvement in the S/B. As a result, the instrument was operated with the collision-reaction cell in He mode (2.5 ml min^{-1}).

A UP193HE ablation device is equipped with a standard ablation cell. The ICP-SFMS instrument was operated in low mass resolution mode ($m/\Delta m = 300$).

The mapping was carried out in the line scanning mode using optimized laser ablation and ICP-MS operating conditions. The settings for both laser ablation units are summarized in Table 2. The sample cuts were ablated along a raster composed of an appropriate number of parallel lines, $100 \mu\text{m}$ and $35 \mu\text{m}$ apart from one another for LA-ICP-QMS and LA-ICP-SFMS, respectively.

LA-ICP-QMS was employed for elemental mapping of large parts of sample cut surfaces. Rasters composed of long parallel lines (5 to 9 mm) spaced apart $100 \mu\text{m}$ cover sufficiently large areas to encompass more mineral phases and a squared ($65 \mu\text{m} \times 65 \mu\text{m}$) ablation imprint yields appropriate lateral resolution for their identification and distinction. Sample displacement took place at a speed of $40 \mu\text{m s}^{-1}$, while the laser shot frequency was 5 Hz, which resulted in a laser shot event at each $8 \mu\text{m}$ of sample displacement. In other words, each surface area measuring $65 \mu\text{m} \times 65 \mu\text{m}$ was ablated by 8 laser shots with the exception of the first and last $57 \mu\text{m}$ of the line scan.

Specific part of the cut surface was studied using LA-ICP-SFMS. Small areas were rastered with 2 mm long lines spaced apart $35 \mu\text{m}$ using a laser spot diameter of $30 \mu\text{m}$ to reveal fine changes in elemental distribution. With the scan speed of $18 \mu\text{m s}^{-1}$ (calculated with respect to the mass spectrometer sweep time of 1.7 s and the laser beam diameter), and the laser shot frequency of 10 Hz a laser shot event occurs at each $1.8 \mu\text{m}$ of sample displacement.

The signals of ^{12}C , ^{23}Na , ^{24}Mg , ^{31}P , ^{39}K , $^{43,44}\text{Ca}$, ^{55}Mn , ^{57}Fe , ^{63}Cu , ^{66}Zn , ^{88}Sr , ^{109}Ag , ^{118}Sn and ^{208}Pb were recorded by LA-ICP-QMS. The signals of all of the isotopes listed above were detectable, but only the time-

Table 2

Laser ablation systems and optimized operating conditions.

Operating condition	UP 213	UP193HE
Wavelength	213 nm	193 nm
Laser ablation mode	Line scan	Line scan
Laser beam spot size	$65 \mu\text{m}$ (square)	$30 \mu\text{m}$ (circle)
Distance between lines	$100 \mu\text{m}$	$35 \mu\text{m}$
Scan speed	$40 \mu\text{m s}^{-1}$	$18 \mu\text{m s}^{-1}$
Fluence	7.5 J cm^{-2}	5 J cm^{-2}
Frequency	5 Hz	10 Hz

resolved signals of ^{23}Na , ^{24}Mg , ^{31}P , $^{42,43,44}\text{Ca}$, ^{66}Zn , $^{86,88}\text{Sr}$ and $^{135,137}\text{Ba}$ isotopes were treated in this work. The other isotopes were recorded for medical and environmental purposes, beyond the scope of this study. The integration time was set to 0.1 s for all isotopes, with the exception of $^{43,44}\text{Ca}$ (0.01 s). The time span between two consecutive measurements of the mass spectrometer (two ICP-MS data points) was 1.32 s. This means that the MS signal reading appeared whenever the sample moved over a distance of 53 μm . A simple calculation shows that new data is obtained every 7 laser shots. Consequently, final lateral resolution results from combination of the laser spot diameter, the scan speed, and data acquisition time. In this regard, one QMS data point contains information (on the signal level) on the average composition of a sample surface area of 53 $\mu\text{m} \times 65 \mu\text{m}$.

In the case of LA-ICP-SFMS, the following isotopes were recorded: ^{13}C , ^{23}Na , $^{24,26}\text{Mg}$, ^{27}Al , ^{31}P , ^{39}K , $^{43,44}\text{Ca}$, ^{55}Mn , ^{57}Fe , $^{63,65}\text{Cu}$, $^{64,66}\text{Zn}$, ^{85}Rb , $^{86,88}\text{Sr}$, ^{118}Sn , $^{135,137}\text{Ba}$, $^{206,208}\text{Pb}$ and ^{238}U . The monitoring of all selected isotopes within one cycle corresponded to laser beam diameter. The average composition of involved particles/one laser shot concerns the area of 706 μm^2 and thus one MS data point contains the information corresponding to 1624 μm^2 area.

A typical time-resolved ICP-QMS signal (Fig. 1) exhibits a sudden drop in the middle of the record as a result of a change in the elemental distribution and/or a change in surface characteristics (porosity) or the occurrence of a crack. Prior to the ablation, background signals were recorded and their average values calculated over the preablation time were subtracted from the gross signal intensities recorded within the ablation period. The net signal intensities thus obtained were used for constructing the 2D maps. Series of signals within individual line scans were arranged to form the original ablation pattern – the raster. The elemental distribution was visualized using the GRAMS software package [47]. The same procedure was applied to LA-ICP-SFMS data evaluation and image preparation. A theoretical resolution of 53 $\mu\text{m} \times 100 \mu\text{m}$ (LA-ICP-QMS) and 31 $\mu\text{m} \times 35 \mu\text{m}$ (LA-ICP-SFMS) is influenced by washout time of ablation cells. Due to a rapid elution of the SuperCell the signal reaches the background level in ~1.3 s after ablation is stopped (Fig. 1). This value is equal to sweep time and no mixing of particles from individual cycles should occur.

2.5. Scanning electron microscopy and electron microprobe analysis

Elemental imaging by a scanning electron microscope (SEM) was accomplished prior to LA-ICP-MS experiments. The MIRA II and VEGA III TS 5136XM SEM instruments equipped with a backscattered electron (BSE) detector were employed. The software modules *Image Snapper* and *Positioner* provide an easy way to locate particular zones of interest and to store/recall their positions for additional evaluation. With

common resolution of about 0.1 Z the BSE detector yields good contrast for the mean atomic number elements which enables to distinguish particular phases. Elemental X-ray maps and BSE images (1024×1024 pixels) were measured under the following analytical conditions: an accelerating voltage of 20 kV and a beam current of 20 nA. The electron beam spot size covers an area of about 1 μm in diameter, and is shifted to scan the surface at nominally 1 μm per step. The SEM measurements were performed at laboratories of TESCAN, a. s., Brno, Czech Republic.

The chemical composition of individual phases of kidney stones was determined using a Cameca SX100 electron microprobe (Department of Geological Sciences, Masaryk University, Brno). The instrument was operated at an accelerating voltage of 15 kV, a beam current of 10 nA and a beam size of 10 μm for apatite group minerals and a beam current of 4 nA and a beam size of 30 μm for calcium oxalate group. The following calibration standards and analytical lines were used: ($\text{K}\alpha$) lines: fluorapatite (Ca, P), albite (Na), sanidine (Si, Al, K), Mg_2SiO_4 (Mg), NaCl (Cl), hematite (Fe), gahnite (Zn) and topaz (F); ($\text{L}\alpha$) lines: SrSO_4 (S, Sr) and baryte (Ba). The peak counting times ranged from 10 to 30 s for all elements, except for Sr (60 s). The average detection limits for apatite group minerals/calcium oxalate group under used conditions were: $\sim 0.07/0.07\%_{\text{m/m}}$ for Ca; $\sim 0.04/0.06\%_{\text{m/m}}$ for P; $\sim 0.12/0.24\%_{\text{m/m}}$ for F; $\sim (0.04-0.06)/(0.04-0.08)\%_{\text{m/m}}$ for Si, Al, Mg, K, Cl, S and Fe; $\sim 0.07/0.04\%_{\text{m/m}}$ for Na; $\sim 0.12/0.13\%_{\text{m/m}}$ for Ba; and $\sim 0.10/0.10\%_{\text{m/m}}$ for Zn and Sr. The matrix effects were corrected using the PAP routine [48].

2.6. Ablation rate study

Depth of ablation craters (tracks) was measured with SEM MIRA II and with optical profilometer Veeco NT9080 (Somerset, NJ, USA) for ablation experiments with 213 nm and 193 nm laser, respectively. Vickers nanohardness of oxalate and phosphate phases was measured with Ultra Nanoindentation Tester (CSM Instruments, Switzerland). During this test, the loading and unloading time was kept constant at 30 s and the dwell time was set at 10 s. Peak loads were set at 10 mN for each measured point.

3. Results and discussion

3.1. Elemental maps and inter-element correlations

Elemental maps of samples 11684 and 11966 were obtained by LA-ICP-MS and a complementary study by SEM was performed to confirm the position and extent of particular mineral phases. Preferential occurrence of selected elements in phosphate phase was proved by correlation analysis. Sample nos. 11684 and 11966 represent the group of oxalate-based kidney stones (Table 1). Calcium oxalate ($\sim 70\%_{\text{m/m}}$) is the main constituent of the sample 11684 and is accompanied by phosphate ($\sim 20\%_{\text{m/m}}$) and uric acid ($\sim 10\%_{\text{m/m}}$). A urinary stone no. 11966 consists of $\sim 90\%_{\text{m/m}}$ oxalate and $\sim 10\%_{\text{m/m}}$ of apatite.

On the pebble-shaped brownish urolith no. 11684 with crystalline structure (Fig. 2a), an area of 10.1 mm \times 8.8 mm was examined with LA-ICP-QMS using a raster consisting of 89 lines. Distribution of calcium as the matrix element, which is common for whewellite, weddellite and apatite, is shown in Fig. 2b. The occurrence of phosphate phase can be identified mainly around the crystalline nucleus (Fig. 2c).

Two LA-ICP-MS scanned areas of the 11684 urolith section surface were selected for the EMP analysis. One is situated in the expected oxalate zone while the other is limited to increased signal of phosphorus. Unaffected surface between ablation lines was analyzed in several spots of both phases, allowing the combined standard uncertainty accompanying the results to be estimated. The area denoted as "1" is situated in the oxalate phase, while the area "2" lies in the apatite-rich domain (Fig. 2b). A Ca content of $(30.5 \pm 1.6)\%_{\text{m/m}}$ was determined in oxalate, while Ca contents of $(33.59 \pm 0.88)\%_{\text{m/m}}$ and $(17.37 \pm$

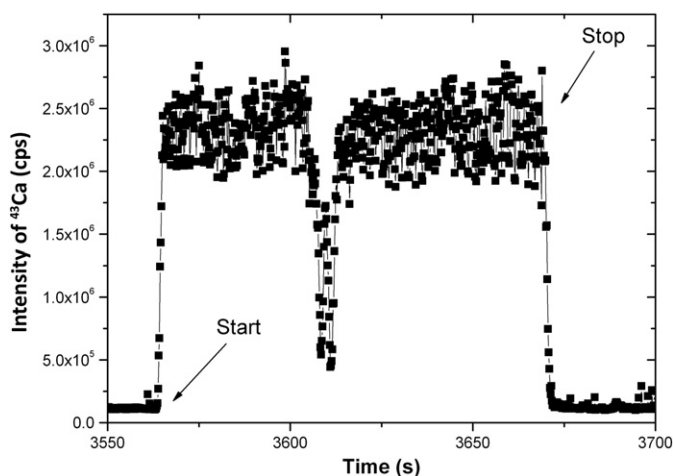


Fig. 1. Typical LA-ICP-QMS signal of ^{43}Ca recorded during ablation of sample 11727.

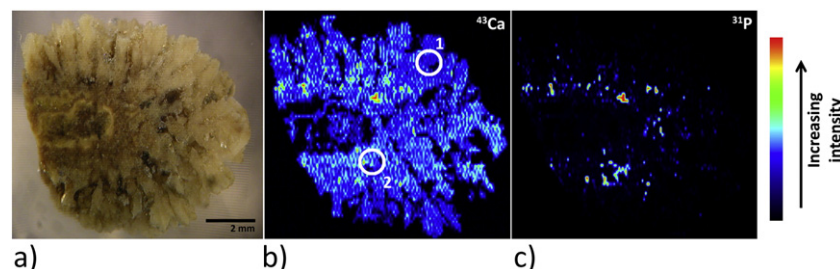


Fig. 2. a) Photograph of 11684 urinary calculus section, and distribution of b) ^{43}Ca and c) ^{31}P on the sample surface with marked rings where EMP analysis was carried out.

0.63) %_{m/m} of phosphorus were found in the phosphate phase by EMP analysis.

In the BSE image (Fig. 3a) of the 11684 sample, the prevailing oxalate phase corresponds to a medium gray zone, while the phosphate phase is characterized by a bright gray shade. The dark gray areas indicate cavities filled with resin. BSE and SEM images (Fig. 3) confirm the distribution of matrix elements found with LA-ICP-MS. While calcium is almost uniformly distributed over the section surface (Fig. 3b) with exception of cavities filled with resin (dark zones), the bright blue spots highlight the ring of phosphate grains around the urolith core (Fig. 3c), which is virtually identical with the image obtained using LA-ICP-MS (Fig. 2c).

A section of 11.5 mm × 5.4 mm on the surface of the sample no. 11966 was examined using a raster of 55 LA-ICP-MS line scans (Fig. 4a). As expected from the approximate mineralogical composition, calcium is the predominant element dispersed throughout the sample (Fig. 4b). Areas with the highest calcium signal intensity correspond to areas of maximum phosphorus signal intensity (Fig. 4b, c), thus indicating the location of the apatite grains.

The element distributions presented in Fig. 4d–g show the increase in signal intensity of ^{23}Na , ^{24}Mg , ^{88}Sr and ^{66}Zn in the same areas in which phosphorus signal reaches highest values. This indicates known positive inter-elemental association in the phosphate phase. The EMP analyses performed in oxalate zone (ring number “1” in Fig. 4b) and apatite-rich domain (ring “2” in Fig. 4b) provided the composition of both phases. The phosphate phase contains (34.7 ± 1.1) %_{m/m} Ca, (17.86 ± 0.77) %_{m/m} P, (0.96 ± 0.33) %_{m/m} Na and (0.450 ± 0.098) %_{m/m} Mg. The oxalate phase contains (30.7 ± 1.0) %_{m/m} Ca, (0.173 ± 0.088) %_{m/m} P and (0.10 ± 0.11) %_{m/m} Na. However, levels of Sr and Zn contents are below EMP detection limits (LOD) in both phases, which do not allow a comparison with the distribution obtained by LA-ICP-MS. Nevertheless, based on the EMP results for P, Na and Mg, at least the positive correlation of P signal with Na and Mg signals observed in LA-ICP-MS elemental maps was confirmed.

Relations between signals of ^{31}P and ^{43}Ca , ^{24}Mg , ^{23}Na , ^{88}Sr and ^{66}Zn were expressed via Pearson and Spearman correlation coefficients [49].

Pearson correlation coefficient is a measure of linear relationship, while Spearman rank correlation coefficient is a measure of both linear and non-linear dependence [50]. Both correlation coefficients have been calculated for the pairs consisting of the ^{31}P signal on one side and those of ^{43}Ca , ^{24}Mg , ^{23}Na , ^{88}Sr , and ^{66}Zn on the other side (Fig. 5). Higher value of Spearman coefficient in comparison with Pearson one indicates a non-linear relationship which may be due to the presence of elements in more than a single compound/mineral, i.e. more than one stoichiometry exists. For instance, calcium and/or phosphorus are associated not only with apatite, but also with other minerals (e.g., carbonate apatite, struvite) in the phosphate phase.

Elemental correlations were also confirmed using SEM mapping. Light and dark polygonal areas on the SEM image of the 11966 urolith section in Fig. 6a correspond to phosphate and oxalate, respectively. Part of the scanned section, which has been further studied in detail, is indicated in Fig. 6a with the rectangle. This selected area is shown as full-frame in Fig. 6b in rotated position, together with the corresponding elemental maps (Fig. 6d–g). The areas with higher intensities for Na (Fig. 6e), Mg (Fig. 6f) and Sr (Fig. 6g) correspond to the map of phosphorus occurrence (Fig. 6d), which illustrates the preferred presence of these elements in the phosphate phase rather than in oxalate one [51]. It follows that LA-ICP-MS offers a certain advantage over SEM in determination of elemental association, especially in case of contents of some toxic elements that are usually below detection limits of SEM and might be important in assessing exposure of human population to environment.

3.2. Ablation rate and material properties

Generally, in the absence of any matrix effect, the ratio of calcium signals in oxalate and phosphate phase should be equal to the ratio of Ca contents in both phases. However, the oxalate/phosphate calcium content ratio determined using EMP was 0.9, whereas the ^{43}Ca intensity (oxalate)/ ^{43}Ca intensity (phosphate) ratio in sample 11966 was found to be only 0.7. It is known that LA-ICP-MS signal is affected by material properties influencing ablation rate and aerosol particle size. One of

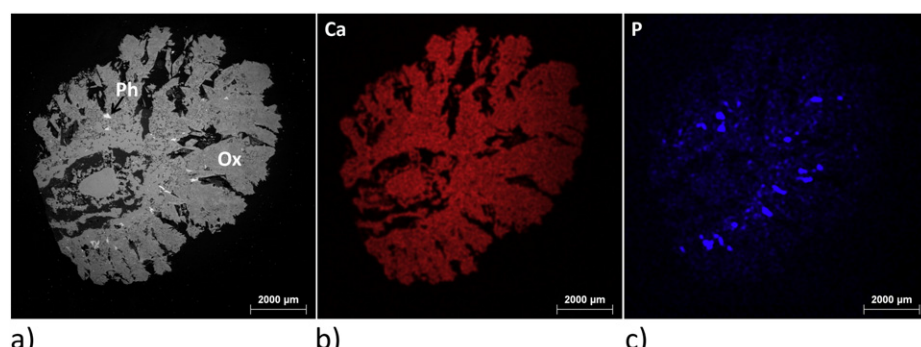


Fig. 3. a) BSE image, and b) Ca, c) P 2D maps of 11684 sample section obtained by SEM. Ph – phosphate phase, Ox – oxalate phase.

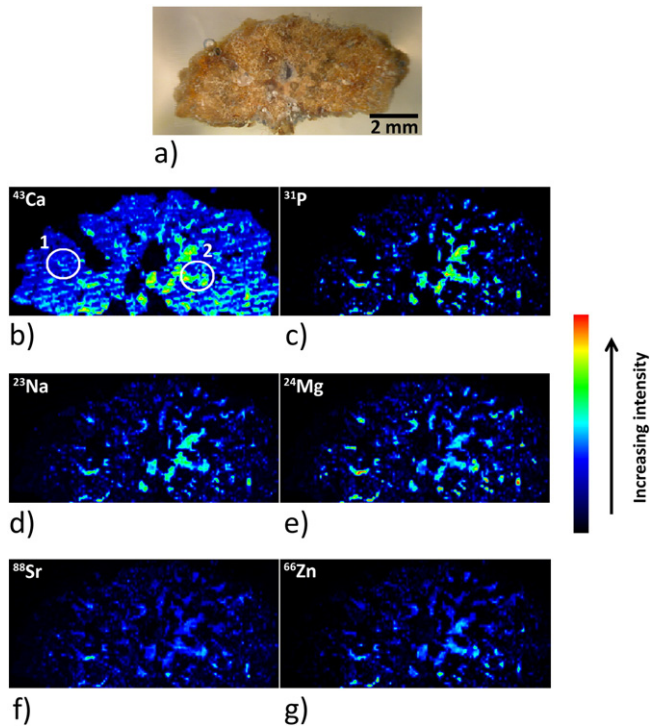


Fig. 4. a) Photograph of analyzed surface of 11966 urinary stone cut, and distribution of b) ^{43}Ca , c) ^{31}P , d) ^{23}Na , e) ^{24}Mg , f) ^{88}Sr and g) ^{66}Zn in 11966 sample section with marked rings where EMP analysis was carried out.

such properties is hardness. Mohs hardness value decreases from apatite (5), through weddellite (4) to whewellite (3) [52]. If the hardness was the only influencing parameter and the phases were of the same hardness as theoretically expected, the ratio of Ca signals should be on the contrary higher than 0.9. However, based on the detail (BSE) of the sample 11966 (Fig. 6c) with the ragged structure and lower density, it can be assumed that the hardness of oxalate and phosphate phase in kidney stone can differ from that in pure natural minerals. The apatite phase in these samples is amorphous and thus a lower hardness can be expected (Fig. 6c) which could be responsible for more efficient ablation. To prove this, hardness and ablation track depth have to be measured and discussed in connection with LA-ICP-MS data.

Sample no. 11727 (Fig. 7a) was employed for the determination of ablation rate and hardness because of larger entire area of phosphate

phase in comparison with urolith no. 11966. Phosphate area, marked in Fig. 7a by a rectangle and clearly visible in BSE image (Fig. 7b), was also identified by the LA-ICP-SFMS measurement. Thus obtained maps of ^{43}Ca (Fig. 7c) and ^{31}P (Fig. 7d) signals confine the apatite zone. Besides, ^{23}Na , ^{24}Mg , ^{88}Sr and ^{66}Zn maps (7e–7 h) demonstrate already discussed positive correlation with phosphate. Identical elemental distributions in this sample were also obtained with LA-ICP-QMS [53]. Although infrared spectrometry analysis identified ~90% oxalate and ~10% of phosphate matrix in the 11727 sample (Table 1), LA-ICP-MS elemental maps demonstrate that only 1.3% of the whole section surface area corresponds to phosphate phase.

The Ca content obtained on the section of sample 11727 by EMP is $(28.5 \pm 1.6)\text{ \%}_{\text{m/m}}$ and $(30.0 \pm 1.2)\text{ \%}_{\text{m/m}}$, in oxalate and phosphate, respectively. Similarly, as in case of the sample 11966, the ratio of ^{43}Ca signals from oxalate and phosphate matrix, respectively, does not correspond to the actual ratio of Ca contents in oxalate/phosphate. Based on ablation crater (track) depth measurement, the ablation rate for 213 nm laser wavelength was found to be in the range of $(0.42\text{--}0.55)\text{ }\mu\text{m s}^{-1}$ in oxalate while the range of ablation rate in phosphate was systematically up to 15% higher. On the other hand, the widths measured at the bottom of ablation tracks were consistently in the range from $55\text{ }\mu\text{m}$ to $61\text{ }\mu\text{m}$ both in oxalate and phosphate areas. The higher ablation rate in phosphate partially explains the lower ^{43}Ca intensity (oxalate)/ ^{43}Ca intensity (phosphate) ratio than expected. The higher ablation rate in phosphate was also observed with 193 nm laser. In this case, a depth of ablation tracks was measured by optical profilometer. The scanned surface area of $(466 \times 622)\text{ }\mu\text{m}^2$, provided with a relative scale, is presented in Fig. 8. Here, the blue, deeper part corresponds to the phosphate phase and the surrounding green, shallower area to the oxalate matrix. Thus, ablation rate both at 213 nm and 193 nm is higher in phosphate phase than in oxalate.

To prove the assumption that hardness of oxalate and phosphate phases in urolith differs from that of pure minerals the Vickers nanohardness test was performed on the sample no. 11727. The measurement demonstrated that the phosphate phase exhibited lower hardness (121 ± 18) HV than the oxalate phase (209 ± 24) HV, which is in turn compared with the hardness of pure minerals. The lower nanohardness of the phosphate phase than expected for pure mineral is probably related to the amorphous structure of apatite (Fig. 6c). Lower hardness of phosphate as compared with oxalate might be partly responsible for higher ablation rate in phosphate phase. However, ablation rate in the phosphate phase is higher not only because of the lower hardness, but also due to the smaller material density. This fact might partly account for the lower ^{43}Ca intensity (oxalate)/ ^{43}Ca intensity (phosphate) ratio in comparison with ratio of calcium content in both phases.

Moreover, other effects can apply. The lower sensitivity of LA-ICP-MS for calcium in oxalate phases can also be caused by the presence of crystal water in whewellite and weddellite. In contrast, the phosphorus signal can be enhanced due to increased light absorption of phosphate in the UV region, caused by the presence of impurities of some elements in its structure [54,55]. Recorded signals are also affected by elemental fractionation, while also particle size is having an influence on vaporization and ionization efficiencies in the ICP [56–58]. It was reported that line scanning mode provides larger particle size [59]. Chemical and physical processes taking place during the laser pulse-sample surface interaction and effects occurring in ICP and mass spectrometer as well are still not fully examined in the case of oxalate and bioapatite matrix, therefore, explanation of different behaviors of isotopic signals requires other exploratory study.

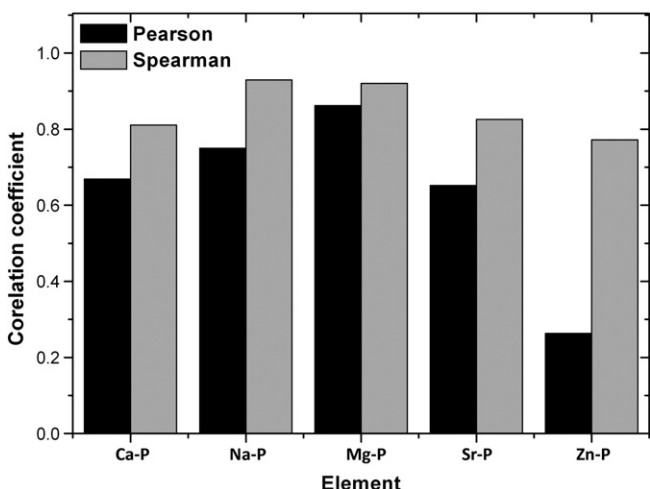


Fig. 5. Pearson and Spearman correlation coefficients for pairs Na–P, Mg–P, Sr–P and Zn–P over the sample 11966 section surface.

3.3. Elemental association

As mentioned in the section “Elemental mapping”, elemental associations were observed in the phosphate phase, as Na, Mg, Sr and Zn exhibit positive correlations with P. The LA-ICP-MS data were therefore

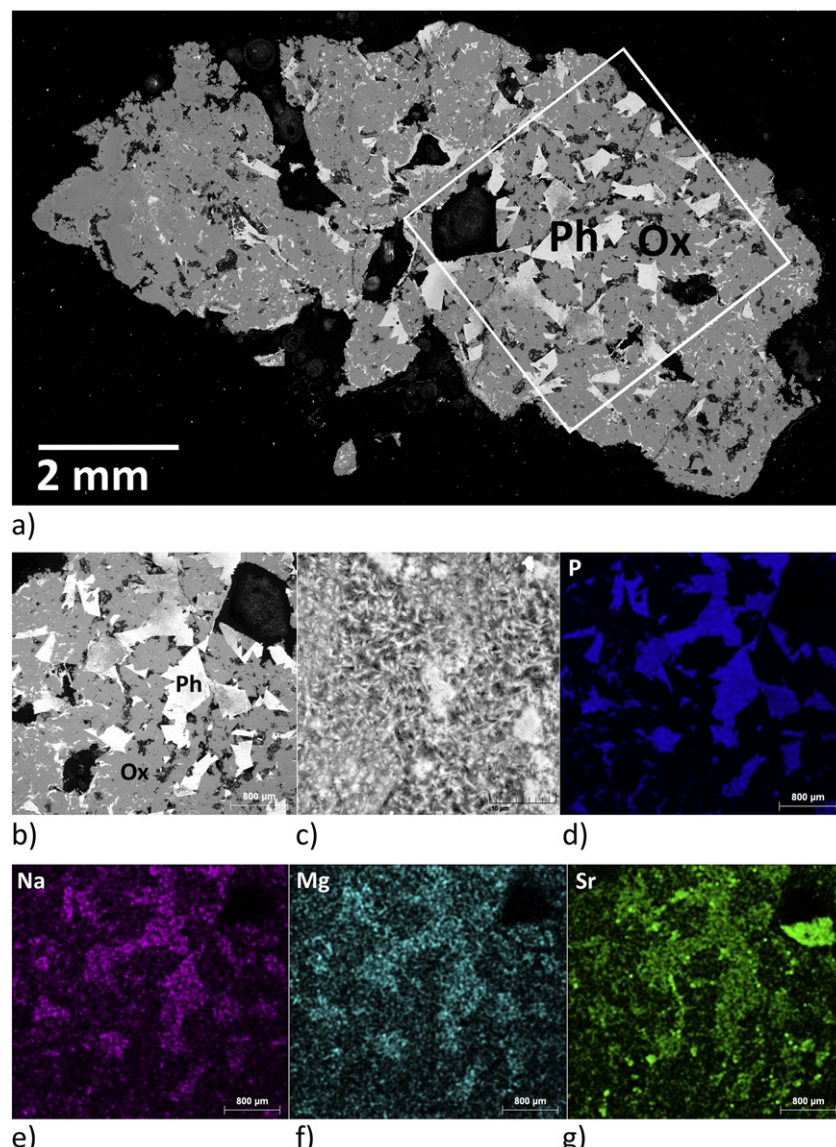


Fig. 6. a) BSE image of entire sample 11966, b) and c) details of scanned area; d) Ca, e) P, f) Na, g) Mg and h) Sr distribution in 11966 section obtained by SEM; Ph – phosphate phase, Ox – oxalate phase.

processed so that they can classify the samples according to the main constituents into groups.

Sorting of uroliths in the three groups mentioned below is based on: i) the evaluation of the $^{43}\text{Ca}/^{31}\text{P}$ signal ratios; and ii) the occurrence of Na, Mg, Sr and Zn. The Ca/P signal ratio characterizes the size of the areas with calcium and phosphorus. Ca is present in both oxalate and phosphate phases, P is only present in phosphate phase.

In the first step of the elemental association procedure, the net signal intensities of Na, Mg, Sr and Zn were calculated for the entire sample surface. The second step consisted in elimination of values corresponding to the resin area from the corrected matrix and remaining values were used for calculation of average value. The average of the signals of Na, Mg, Sr and Zn was plotted as a function of the $^{43}\text{Ca}/^{31}\text{P}$ signal ratio.

Based on the plots presented in Fig. 9, three groups of uroliths were identified with regard to the content of phosphate. The quite different composition (~90% uric acid and ~10% oxalate) of urolith 10806 (#8 in all graphs) is associated with a high Ca/P signal ratio, which separates this urolith from other samples (Fig. 9).

The second group comprises kidney stones with an oxalate matrix that are positioned in the Ca/P ratio range between 2 and 3 (Fig. 9).

The uroliths containing 90 and 70% oxalate are included in this group, i.e. samples 11684 (#3), 11727 (#7) and 11681 (#9).

The largest group of the examined urolith collection consists of mixed-matrix kidney stones, containing oxalate and phosphate, i.e. samples 11560 (#1), 11561 (#2), 11726 (#4), 11847 (#5) and 11966 (#6) (Table 1). The sequence of all samples in the direction of the x axis (Fig. 9), however, cannot unambiguously correlate with the portion of phosphate in the entire sample (3D) and the exact mineralogical composition within the group containing oxalate and phosphate matrix. The size of the phosphate area is dependent on the position of the investigated slice and its depth in kidney stone. Nevertheless, sorting into groups: i) oxalate, ii) oxalate/phosphate and iii) uric acid based kidney stones is beyond any doubt.

The sequence of samples with respect to their actual phosphate area, e.g. % of phosphate occurrence throughout the sample surface, is not possible based on the Ca/P signal ratio due to their different ionization potentials. Utilization of the one isotope for evaluation of mineral area, specifically calcium ($^{43}\text{Ca}_{\text{phosphate}}/^{43}\text{Ca}_{\text{sample}}$), leads to a correct result, but only if differences in the ablation rate and in Ca content and in

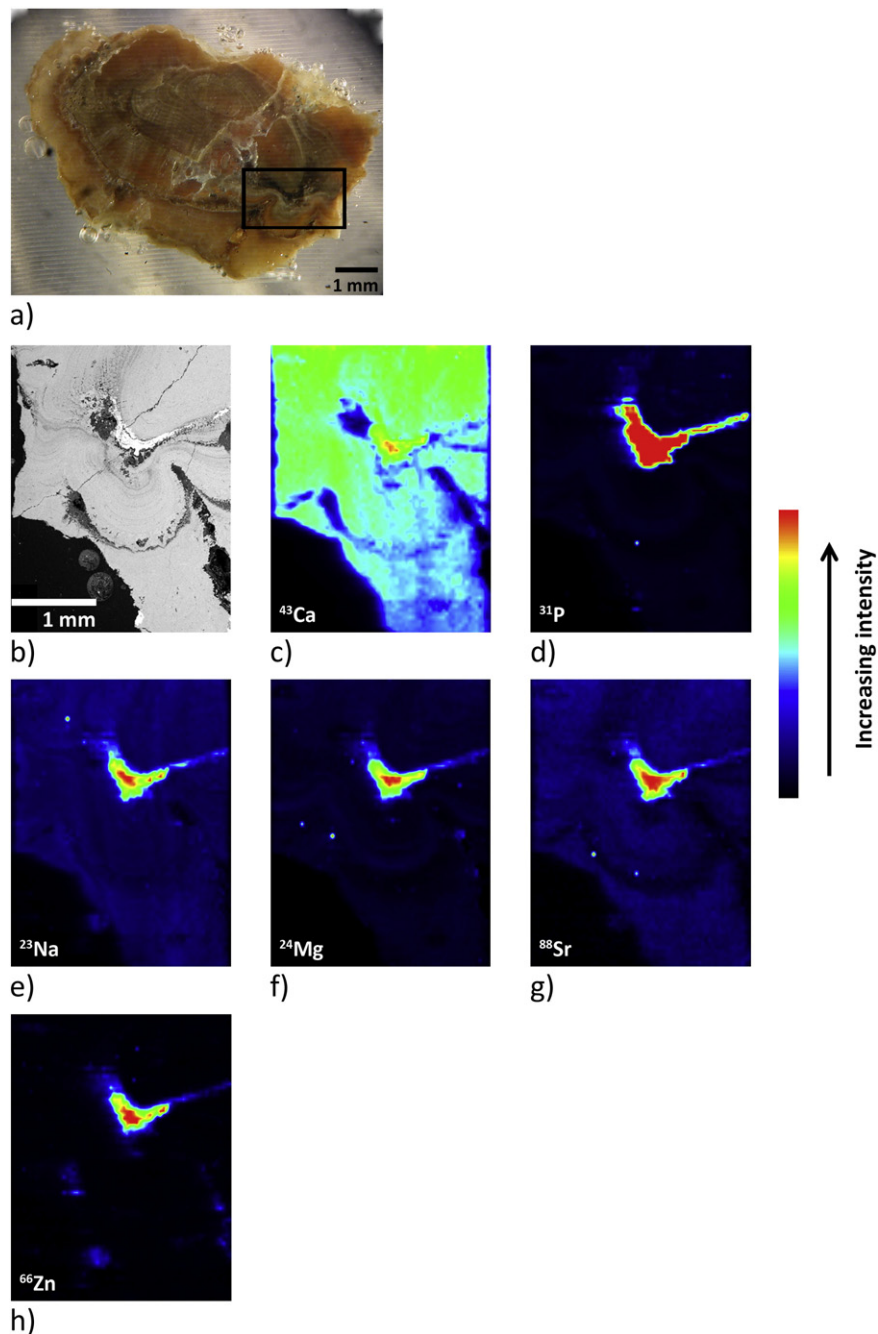


Fig. 7. a) Photograph of 11727 urinary stone, b) BSE image of area containing phosphate phase, and distribution of c) ^{43}Ca , d) ^{31}P , e) ^{23}Na , f) ^{24}Mg , g) ^{88}Sr and h) ^{66}Zn measured by LA-ICP-SFMS.

density of both phases are taken into account. After that, correct sequencing of samples within oxalate/phosphate group will be reached and the size of the phosphate area will be evident from the plot (Fig. 9). On the other hand, the size of phosphate area can be easily estimated from matrix and/or 2D maps. In the case of the human kidney stone studied, phosphate area decreases in the following sequence: 11847 (#5) (41%), 11560 (#1) (30%), 11966 (#6) (20%), 11561 (#2) (14%) and 11726 (#4) (5%).

Fig. 9, moreover, provides the information about average content of elements in studied area. It follows that the average signals of interest plotted as a function of the Ca/P ratio shows separation of samples into the groups according to their matrix and sequencing in each group is based on average content. These samples contain Na, Mg, Sr and Zn, the signals of which tightly correlate with the proportion of the oxalate and phosphate phases. The signals of these isotopes yield

not only the average elemental content throughout the investigated area, but also the average elemental content which corresponds to the oxalate and/or the phosphate surfaces as well.

3.4. Quantification

Quantification is the most challenging stage in the development of a particular analytical method based on laser ablation ICP-MS. It is necessary to solve the drawbacks associated with the lack of standard reference material having a matrix similar to that of the samples analyzed. In the case of urinary stone, quantification can be solved via SRM NIST 1486 Bone Meal, the matrix of which is close to that of the phosphate phase. Bone meal powder has been pressed into the pellet about 1 cm in diameter. An attempt for quantitative analysis was done for sample no. 11727, consisting of ~90% oxalate and ~10% phosphate. The

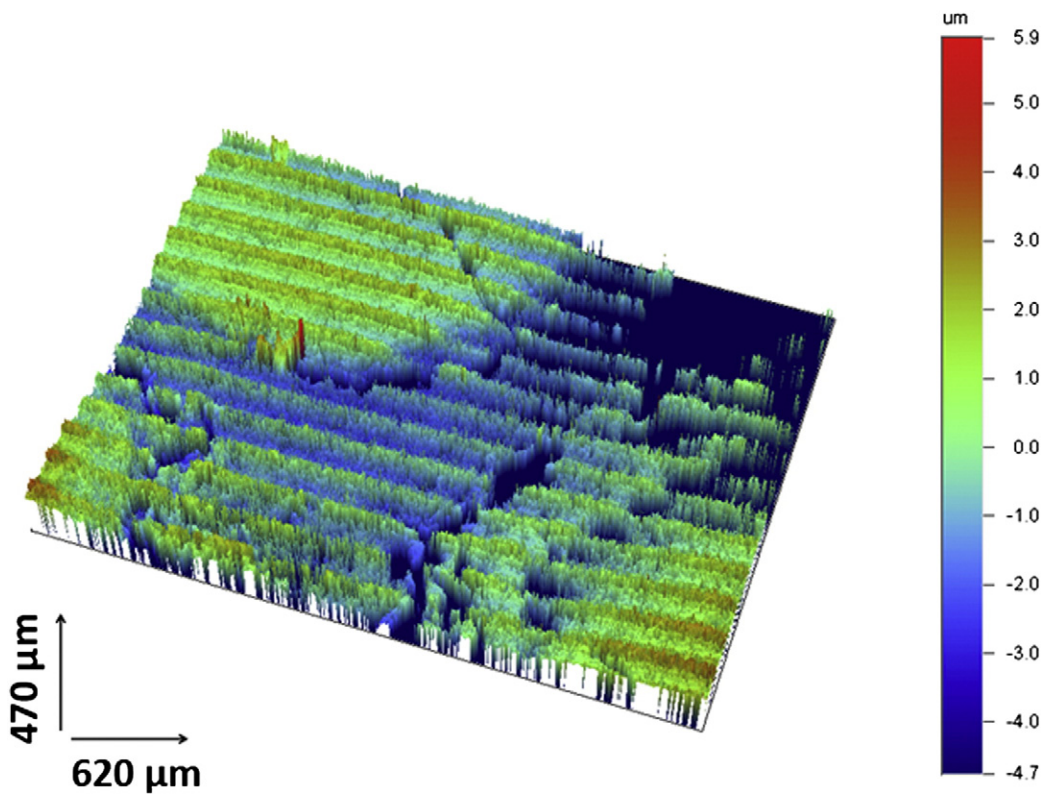


Fig. 8. The depth of ablation tracks (193 nm) on a small section of surface of sample 11727.

elemental contents, however, had to be calculated separately for the oxalate and phosphate matrix, because of the different ablation rate in both phases. The effect of the difference in ablation rates between the

bone meal pellet and the oxalate/phosphate matrix was counteracted via the use of calcium as an internal standard. The Ca content in both phases was determined by EMP analysis. Finally, the contents of P, Na,

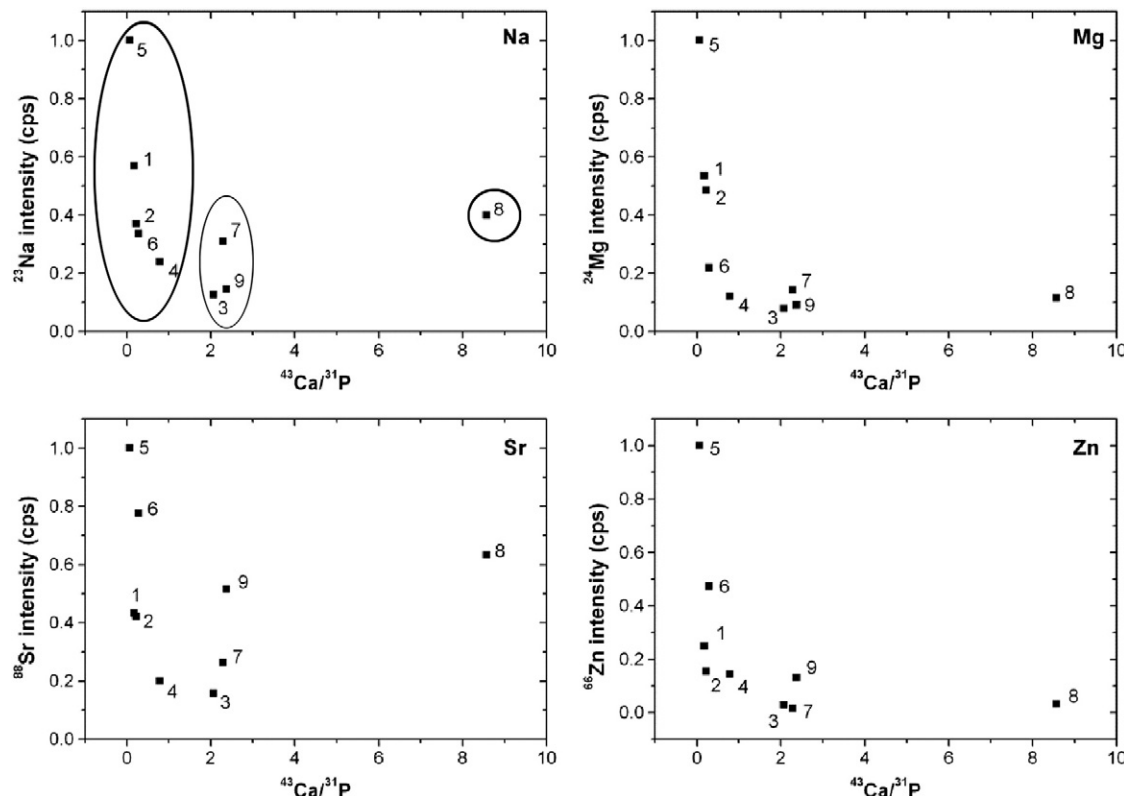


Fig. 9. Intensities of ^{23}Na , ^{24}Mg , ^{88}Sr and ^{66}Zn normalized to maximum intensity obtained on particular samples vs $^{43}\text{Ca}/^{31}\text{P}$ intensity ratio measured on 11560 (1), 11561 (2), 11684 (3), 11726 (4), 11847 (5), 11966 (6), 11727 (7), 10806 (8) and 11681 (9) kidney stones by means of LA-ICP-MS.

Table 3

Contents (C) with standard deviations (SD) and LODs of Ca, P, Na, Mg, Sr and Zn in oxalate and phosphate areas of the sample 11727 cut determined by EMP and LA-ICP-SFMS, and results of bulk analysis by solution ICP-MS analysis (SN-ICP-MS).

Matrix	Oxalate		Phosphate		LOD		Bulk analysis	
	EMP C ± SD (% _{m/m}) ^a	LA-ICP-MS C ± SD (% _{m/m}) ^b	EMP C ± SD (% _{m/m}) ^c	LA-ICP-MS C ± SD (% _{m/m}) ^d	EMP C (% _{m/m})	LA-ICP-MS C (% _{m/m})	LA-ICP-MS C ± SD (% _{m/m}) ^e	SN-ICP-MS C (% _{m/m}) ^f
Ca	28.5 ± 1.6	28.5 ± 3.4	30.0 ± 1.2	30.0 ± 5.1	7 · 10 ⁻²	7 · 10 ⁻²	26.6 ± 6.3	26.5
P	0.28 ± 0.14	0.32 ± 0.11	15.10 ± 0.70	16.6 ± 3.6	4 · 10 ⁻²	8 · 10 ⁻³	0.80 ± 2.2	1.36
Na	0.116 ± 0.094	0.127 ± 0.022	0.65 ± 0.28	0.60 ± 0.12	7 · 10 ⁻²	2 · 10 ⁻³	0.144 ± 0.080	0.160
Mg	(4.0 ± 5.2) · 10 ⁻²	(2.90 ± 0.99) · 10 ⁻²	0.307 ± 0.041	0.283 ± 0.063	3 · 10 ⁻²	8 · 10 ⁻⁴	(3.8 ± 4.6) · 10 ⁻²	4.78 · 10 ⁻²
Sr	<LOD	(3.08 ± 0.67) · 10 ⁻³	<LOD	(1.60 ± 0.31) · 10 ⁻²	6 · 10 ⁻²	7 · 10 ⁻⁵	(3.4 ± 2.2) · 10 ⁻³	5.5 · 10 ⁻³
Zn	<LOD	(1.25 ± 0.15) · 10 ⁻³	<LOD	(5.2 ± 1.3) · 10 ⁻²	9 · 10 ⁻²	3 · 10 ⁻⁴	(2.8 ± 7.6) · 10 ⁻³	4.4 · 10 ⁻³

^a Number of replicates is equal to 7.

^b Number of replicates is equal to 500.

^c Number of replicates is equal to 3.

^d Number of replicates is equal to 50.

^e Number of replicates is equal to 4355 and is obtained over the whole urolith section area, i.e. average values and standard deviations are calculated from phosphate and oxalate phases in common.

^f Relative standard deviation of SN-ICP-MS measurement is equal to 3% for Ca, P, and Na; and 5% for Mg, Sr, and Zn.

Mg, Sr and Zn were calculated as average values for the oxalate and phosphate phases separately. Approximately 500 points for oxalate and 50 points for phosphate from the total number of 4355 points were used for calculation of difference in ablation rate. The results of elemental contents and their standard deviations (SD) are summarized in Table 3. The SD of values obtained by EMP was calculated as combined standard uncertainty, while SD of LA-ICP-MS measurement equal to standard deviation of average including the variability in elemental content in dependence on position in single phase. The results obtained for P, Na and Mg by LA-ICP-MS were comparable with outcomes attained by EMP. Small differences (see Table 3) are caused by the line scanning ablation mode, the larger diameter of ablation spot and the lower spatial resolution, resulting in ablation of both phases and distortion of the analytical signal that should correspond to either oxalate or phosphate matrix. EMP analysis was performed with beam size of 7 μm, which ensures analysis of a single matrix. In spite of this fact, results obtained by LA-ICP-MS can be considered quantitative. Additionally, the average content of the entire sample area was determined by excimer-based laser ablation and calculated with respect to different ablation rates of each phase. These results are compared with solution ICP-MS analysis as the half of sample was digested and elemental content was determined. Nevertheless, the average content of calcium is in a good agreement with bulk analysis (26.6%_{m/m} vs 26.5%_{m/m}). Higher differences were observed in the contents of Sr and Zn which is due to their low content itself. Generally, the variations are given by elemental distribution that is the core of this study.

4. Conclusions

The spatial distribution of elements in uroliths was studied by means of LA-ICP-MS analysis of structured kidney stone sections. The study was mainly focused on elemental mapping by LA-ICP-MS and SEM. The main phases of the uroliths were identified. The samples were selected on basis of their mineralogical composition. Sets of uroliths included oxalate, apatite and uric acid matrices and their combination. All phases were clearly distinguished with spatial resolution of (53 × 100) μm² and (31 × 35) μm².

Moreover, elemental associations were derived from LA-ICP-MS distributions. Positive correlation of Na, Mg, Zn and Sr with the phosphate phases was indicated through the Pearson correlation coefficient. Results obtained by LA-ICP-MS were confirmed via SEM imaging.

LA-ICP-MS signals were also used for comparison of elemental associations for each kidney stone. First of all, samples were sorted to groups according to Ca/P ratio derived from isotope intensities. Ca/P ratio is given by sample surface composition, and thus main constituents of uroliths were identified. Moreover, plotting of Na, Mg, Sr, Zn vs Ca/P

showed increase in their intensities with increasing phosphate surface area in dependence on their contents.

The results of our study show that bone meal can be used for elemental content determination in oxalate and phosphate matrix, if the structure, density and thus different ablation rates are taken into account.

Finally, LA-ICP-MS method could prove helpful for the determination of mineralogical composition, the size of all phases on the traced surface area, elemental association as well as elemental content in urinary stones. Quantitative analysis of kidney stones is complicated by the presence of different constituents and their various optical properties. Our ongoing work will be focused on the preparation of the matrix-matched calibration standards. Effects occurring on the urolith surfaces during laser ablation and taking place in ICP or mass spectrometer have to be studied in more details.

Acknowledgments

The authors acknowledge the Czech Science Foundation for grant 203/09/1394 and AMVIS Agency for support of the project ME10012. This work was also supported by the European Regional Development Fund project "CEITEC" (CZ.1.05/1.1.00/02.0068). Frank Vanhaecke is acknowledged for providing access to the ArF* excimer LA — sector field ICP-MS instrumentation at Ghent University. The authors acknowledge Andrei Izmer for his help with LA-ICP-MS measurement and profilometry study at Ghent University.

References

- [1] L. Prien, C. Frondel, Studies in urolithiasis. 1. The composition of urinary calculi, *J. Urol.* 57 (1947) 949–994.
- [2] M.L. Stoller, M.V. Meng, *Urinary Stone Disease: The Practical Guide to Medical and Surgical Management*, Humana press, New Jersey, 2007.
- [3] N. Mandel, *Clinical-chemistry. 3. Urinary-tract calculi*, *Lab. Med.* 17 (1986) 449–458.
- [4] E. Königsberger, L.C. Königsberger, *Biominerization: Medical Aspects of Solubility*, Wiley, New York, 2006.
- [5] Available from <http://portal.isiknowledge.com/> (last accessed May 30, 2014).
- [6] Available from <http://www.herringlab.com/> (last accessed May 30, 2014).
- [7] Y.H. Tan, J.M. Ouyang, J. Ma, H.H. Feng, F. Huang, The application of infrared spectrophotometry on the study of calcium oxalate calculi, *Spectrosc. Spectr. Anal.* 23 (2003) 700–704.
- [8] P.G. Sofia, I. Ionescu, G. Rodica, P. Anisoara, The use of infrared spectroscopy in the investigation of urolithiasis, *Rev. Rom. Med. Lab.* 18 (2010) 67–77.
- [9] V.S. Joshi, M.J. Joshi, FTIR spectroscopic, thermal and growth morphological studies of calcium hydrogen phosphate dihydrate crystals, *Cryst. Res. Technol.* 38 (2003) 817–821.
- [10] R. Selvaraju, G. Thiruppathi, A. Raja, FT-IR spectral studies on certain human urinary stones in the patients of rural area, *Spectrochim. Acta A* 93 (2012) 260–265.
- [11] M. Volmer, J.C.M. de Vries, H.M.J. Goldschmidt, Fourier transform infrared analysis for the analysis of urinary stones, using a single reflection diamond accessory and a neural network interpretation algorithm, *Clin. Chem.* 46 (2000) A148–A148.

- [12] E. Peuchant, X. Heches, D. Sess, M. Clerc, Discriminant analysis of urinary calculi by near-infrared reflectance spectroscopy, *Clin. Chim. Acta* 205 (1992) 19–30.
- [13] L. Maurice-Estepa, P. Levillain, B. Lacour, M. Daudon, Advantage of zero-crossing-point first-derivative spectrophotometry for the quantification of calcium oxalate crystalline phases by infrared spectrophotometry, *Clin. Chim. Acta* 298 (2000) 1–11.
- [14] L.A. Pinales, R.R. Chianelli, W.G. Durrer, R. Pal, M. Narayan, F.S. Manciu, Spectroscopic study of inhibition of calcium oxalate calculi growth by *Larrea tridentata*, *J. Raman Spectrosc.* 42 (2011) 259–264.
- [15] R. Selvaraju, A. Raja, G. Thiruppathi, Chemical composition and binary mixture of human urinary stones using FT-Raman spectroscopy method, *Spectrochim. Acta A* 114 (2013) 650–657.
- [16] Y.C. Chiu, H.Y. Yang, S.H. Lu, H.K. Chiang, Micro-Raman spectroscopy identification of urinary stone composition from ureteroscopic lithotripsy urine powder, *J. Raman Spectrosc.* 41 (2010) 136–141.
- [17] M.T.D. Orlando, L. Kuplich, D.O. de Souza, H. Belich, J.B. Depianti, C.G.P. Orlando, E.F. Medeiros, P.C.M. da Cruz, L.G. Martinez, H.P.S. Correa, R. Ortiz, Study of calcium oxalate monohydrate of kidney stones by X-ray diffraction, *Powder Diffr.* 23 (2008) S59–S64.
- [18] J.M. Ouyang, Combined analyses of mixed urinary stones by XPS and XRD, *Spectrosc. Spectr. Anal.* 23 (2003) 391–395.
- [19] V. Uvarov, I. Popov, N. Shapur, T. Abdin, O.N. Gofrit, D. Pode, M. Duvdevani, X-ray diffraction and SEM study of kidney stones in Israel: quantitative analysis, crystallite size determination, and statistical characterization, *Environ. Geochem. Health* 33 (2011) 613–622.
- [20] I. Ansorge, Polarization microscopy of urinary stones, *J. Clin. Chem. Clin. Biochem.* 26 (1988) 842–843.
- [21] P. Winter, A. Hesse, K. Klocke, M. Schaefer, Scanning electron microscopy of 2,8-dihydroxyadenine crystals and stones, *Scanning Microsc.* 7 (1993) 1075–1080.
- [22] D.B. Leusmann, Scanning electron-microscopy and microanalysis of urinary stones, *J. Clin. Chem. Clin. Biochem.* 26 (1988) 843–844.
- [23] A. Hesse, G. Sanders, D.B. Leusmann, Analysis of canine urinary stones using infrared spectroscopy and scanning electron microscopy, *Scan. Electron Microsc.* 4 (1986) 1705–1712.
- [24] J.A. Wesson, M.D. Ward, Pathological biominerization of kidney stones, *Elements* 3 (2007) 415–421.
- [25] M. Daudon, C.A. Bader, P. Jungers, Urinary calculi: review of classification methods and correlations with etiology, *Scanning Microsc.* 7 (1993) 1081–1106.
- [26] M.A. Chaudhri, J. Watling, F.A. Khan, Spatial distribution of major and trace elements in bladder and kidney stones, *J. Radioanal. Nucl. Chem.* 271 (2007) 713–720.
- [27] P. Allain, L. Jaunault, Y. Maura, J.M. Mermet, T. Delaporte, Signal enhancement of elements due to the presence of carbon-containing compounds in inductively coupled plasma mass spectrometry, *Anal. Chem.* 63 (1991) 1497–1498.
- [28] M.J. Campbell, C. Demesmay, M. Ollié, Determination of total arsenic concentrations in biological matrices by inductively coupled plasma mass spectrometry, *J. Anal. At. Spectrom.* 9 (1994) 1379–1384.
- [29] F.R. Abou-Shakra, M.P. Rayman, N.L. Ward, V. Hotton, G. Bastian, Enzymatic digestion for the determination of trace elements in blood serum by inductively coupled plasma mass spectrometry, *J. Anal. At. Spectrom.* 12 (1997) 429–433.
- [30] E.H. Larsen, S. Stürup, Carbon-enhanced inductively coupled plasma mass spectrometric detection of arsenic and selenium and its application to arsenic speciation, *J. Anal. At. Spectrom.* 9 (1994) 1099–1105.
- [31] B. Gammelgaard, O. Jons, Determination of selenium in urine by inductively coupled plasma mass spectrometry: interferences and optimization, *J. Anal. At. Spectrom.* 14 (1999) 867–874.
- [32] G. Grindlay, J. Mora, M. de Loos-Vollebregt, F. Vanhaecke, A systematic study on the influence of carbon on the behavior of hard-to-ionize elements in inductively coupled plasma-mass spectrometry, *Spectrochim. Acta B* 86 (2013) 42–49.
- [33] M.S. Pearle, *Urolithiasis, an Issue of Urologic Clinics*, Elsevier-Saunders, New York, 2007.
- [34] A.K. Pathak, R. Kumar, V.K. Singh, R. Agrawal, S. Rai, A.K. Rai, Assessment of LIBS for spectrochemical analysis: a review, *Appl. Spectrosc. Rev.* 47 (2012) 14–20.
- [35] B.G. Oztoprak, J. Gonzales, J. Yoo, T. Gulecen, N. Mutlu, R.E. Russo, O. Gundogdu, A. Demir, Analysis and classification of heterogeneous kidney stones using laser-induced breakdown spectroscopy (LIBS), *Appl. Spectrosc.* 66 (2012) 1353–1361.
- [36] M. Vasinova Galiova, M. Fisakova, J. Kynicky, L. Prokes, H. Neff, A.Z. Mason, P. Gadas, J. Kosler, V. Kanicky, Elemental mapping in fossil tooth root section of *Ursus arctos* by laser ablation inductively coupled plasma mass spectrometry (LA-ICP-MS), *Talanta* 105 (2013) 235–243.
- [37] M. Siebold, P. Leidich, M. Bertini, G. Deflorio, J. Feldmann, E.M. Krupp, E. Halmschlager, S. Woodward, Application of elemental bioimaging using laser ablation ICP-MS in forest pathology: distribution of elements in the bark of *Picea sitchensis* following wounding, *Anal. Bioanal. Chem.* 402 (2012) 3323–3331.
- [38] J.O. Lill, M. Himberg, L. Harju, P. Ek, A. Lindroos, T. Wiklund, K. Gunnellius, J.H. Smartt, S.J. Heselius, H. Hagerstrand, Strontium and zinc concentrations in otoliths of common fish species in the northern Baltic Sea, *Nucl. Instr. Meth. B* 318 (2014) 109–112.
- [39] F. Blaske, O. Reifschneider, G. Gosheger, C.A. Wehe, M. Sperling, U. Karst, G. Hauschild, S. Hoell, Elemental bioimaging of nanosilver-coated prostheses using X-ray fluorescence spectroscopy and laser ablation-inductively coupled plasma-mass spectrometry, *Anal. Chem.* 86 (2014) 615–620.
- [40] M. Debeljak, J.T. van Elteren, K. Vogel-Mikus, Development of a 2D laser ablation inductively coupled plasma mass spectrometry mapping procedure for mercury in maize (*Zea mays L.*) root cross-sections, *Anal. Chim. Acta* 787 (2013) 155–162.
- [41] J.S. Becker, U. Kumtabtim, B. Wu, P. Steinacker, M. Otto, A. Matusch, Mass spectrometry imaging (MSI) of metals in mouse spinal cord by laser ablation ICP-MS, *Metalomics* 4 (2012) 284–288.
- [42] A. Izmer, D. Ghosh, K. De Houwer, F. Cuyckens, F. Vanhaecke, Frank, A pilot study on the use of laser ablation-ICP-mass spectrometry for assessing/mapping the distribution of a drug and its metabolites across the body compartments of rats, *J. Anal. At. Spectrom.* 27 (2012) 413–418.
- [43] J. Kuta, J. Machát, D. Benova, R. Červenka, T. Koříšková, Urinary calculi – atypical source of information on mercury in human biomonitoring, *Cent. Eur. J. Chem.* 10 (2012) 1475–1483.
- [44] D. De Muynck, F. Vanhaecke, Development of a method based on inductively coupled plasma-dynamic reaction cell-mass spectrometry for the simultaneous determination of phosphorus, calcium and strontium in bone and dental tissue, *Spectrochim. Acta B* 64 (2009) 408–415.
- [45] P.R.D. Mason, W.J. Kraan, Attenuation of spectral interferences during laser ablation inductively coupled plasma mass spectrometry (LA-ICP-MS) using an rf only collision and reaction, *J. Anal. At. Spectrom.* 17 (2002) 858–867.
- [46] S.D. Tanner, V.I. Baranov, D.R. Bandura, Reaction cells and collision cells for ICP-MS: a tutorial review, *Spectrochim. Acta B* 57 (2002) 1361–1452.
- [47] Available from <http://www.thermofisher.com> (last accessed May 30, 2014).
- [48] J.L. Pouchou, F. Pichoir, "PAP", procedure for improved quantitative microanalysis, in: J.T. Armstrong (Ed.), *Microbeam Analysis Proc.*, San Francisco Press, San Francisco, 1985.
- [49] J.C. Bezdek, N.R. Pal, An index of topological preservation for feature extraction, *Pattern Recogn.* 28 (1995) 381–391.
- [50] C. Reimann, P. Filzmoser, R.G. Garrett, R. Dutter, *Statistical Data Analysis Explained: Applied Environmental Statistics with R*, Wiley, Chichester, 2008.
- [51] I.A. Abboud, Concentration effect of trace metals in Jordanian patients of urinary calculi, *Environ. Geochem. Health* 30 (2008) 11–20.
- [52] Available from <http://www.webmineral.com/> (last accessed May 30, 2014).
- [53] K. Proksová, K. Novotný, M. Galiová, T. Vaculovič, J. Kuta, M. Nováčková, V. Kanický, Studium distribuce prvků v močových kamenech technikou laserové ablace ve spojení s hmotnostní spektrometrií s indukčně vázaným plazmatem, *Chem. List.* 106 (2012) 229–235.
- [54] M. Elisa, R. Iordanescu, B.A. Sava, G. Aldica, V. Kuncser, C. Valsangiocom, G. Schintie, F. Nastase, C. Nastase, V. Bercu, A. Volceanov, S. Peretz, Optical and structural investigations on iron-containing phosphate glasses, *J. Mater. Sci.* 46 (2011) 1563–1570.
- [55] S.M. Abo-Naf, M.S. El-Amiry, A.A. Abdel-Khalek, FT-IR and UV-Vis optical absorption spectra of gamma-irradiated calcium phosphate glasses doped with Cr₂O₃, V₂O₅ and Fe₂O₃, *Opt. Mater.* 30 (2008) 900–909.
- [56] M. Guillong, H.R. Kuhn, D. Günther, Application of a particle separation device to reduce inductively coupled plasma-enhanced elemental fractionation in laser ablation-inductively coupled plasma-mass spectrometry, *Spectrochim. Acta B* 58 (2003) 211–220.
- [57] H.R. Kuhn, D. Günther, Laser ablation-ICP-MS: particle size dependent elemental composition studies on filter-collected and online measured aerosols from glass, *J. Anal. At. Spectrom.* 19 (2004) 1158–1164.
- [58] D. Günther, B. Hattendorf, Solid sample analysis using laser ablation inductively coupled plasma mass spectrometry, *TrAC Trends Anal. Chem.* 24 (2005) 255–265.
- [59] M. Guillong, D. Günther, Effect of particle size distribution on ICP-induced elemental fractionation in laser ablation-inductively coupled plasma-mass spectrometry, *J. Anal. At. Spectrom.* 17 (2002) 831–837.



Cite this: *J. Anal. At. Spectrom.*, 2015,
30, 1356

Preparation and testing of phosphate, oxalate and uric acid matrix-matched standards for accurate quantification of 2D elemental distribution in kidney stone sections using 213 nm nanosecond laser ablation inductively coupled plasma mass spectrometry

M. Vašinová Galiová,^{ab} K. Štěpánková,^a R. Čopjaková,^c J. Kuta,^d L. Prokeš,^{ae} J. Kynicky^f and V. Kanický^{*ab}

Matrix-matched calibration for quantitative elemental mapping of kidney stones by laser ablation-inductively coupled plasma-mass spectrometry (LA-ICP-MS) was developed with a 213 nm Nd:YAG laser ablation device and a quadrupole mass spectrometer. The method was applied to the imaging of P, Na, Sr, Zn, Ba and Pb distributions over a section of the kidney stone specimen containing phosphate and oxalate phases. Eighteen kidney stone specimens consisting of phosphate, oxalate and urate phases in various proportions were cut into halves for both preparation of calibration pellets and bulk analysis. Homogeneity of calibration pellets was examined by scanning electron microscopy (SEM) and LA-ICP-MS, concluding that areas of individual biominerals were thoroughly mixed and their size in units of micrometers was well below the size of the used laser spot. Calcium was employed as the internal reference element, being present in sufficient contents in the studied kidney stones. Mean values of calcium contents in oxalate and phosphate phases separately were determined using an electron microprobe (EMP) in the kidney stone section further subjected to the mapping. The actual (time- and space-resolved) Ca sensitivity was computed for each $^{44}\text{Ca}^+$ signal and used as the internal reference for LA-ICP-MS isotopic signals of P, Na, Sr, Zn, Ba and Pb when mapping. Dependences of particular isotopic signal intensity/Ca sensitivity ratios vs. average elemental contents by solution analysis were processed by ordinary least squares linear regression. Despite variable matrices the regression yielded calibration lines with insignificant intercepts, coefficients of determination $R^2 > 0.9955$, and relatively narrow prediction and confidence bands. However, in addition, the applicability of four-point calibration and four single-point calibrations as less time-consuming options was examined on the basis of the NIST SRM 1486 bone meal pellet analysis. Best fit was obtained for the four-point calibration and single-point calibration with the phosphate pellet. Quantitative elemental maps of the kidney stone section were recorded and computed for P, Na, Sr, Zn, Ba and Pb. The feasibility of quantification by matrix-matched single-point calibration was verified by determination of the median elemental contents in phosphate and oxalate phases by LA-ICP-MS and their arithmetic comparison mean values obtained over the same section area using EMP.

Received 16th October 2014

Accepted 9th March 2015

DOI: 10.1039/c4ja00347k

www.rsc.org/jaas

Introduction

Laser ablation-inductively coupled plasma-mass spectrometry (LA-ICP-MS) has already been employed in various fields of

scientific research such as biology,^{1–4} medicine,^{5–9} geology,^{10,11} archaeology,^{12–17} etc. The ability to focus the laser beam onto a sample area with size from units to thousands of square micrometers together with limits of detection down to units of

^aDepartment of Chemistry, Faculty of Science, Masaryk University, Kotlářská 2, 611 37 Brno, Czech Republic. E-mail: viktork@chemi.muni.cz

^bCentral European Institute of Technology (CEITEC), Masaryk University, Kamenice 5, 625 00 Brno, Czech Republic

^cDepartment of Geological Sciences, Faculty of Science, Masaryk University, Kotlářská 2, 611 37 Brno, Czech Republic

^dResearch Centre for Toxic Compounds in the Environment (RECETOX), Masaryk University, Kamenice 126/3, 625 00 Brno, Czech Republic

^eDepartment of Physical Electronics, Faculty of Science, Masaryk University, Kotlářská 2, 611 37 Brno, Czech Republic

^fDepartment of Pedology and Geology, Faculty of Forestry and Wood Technology, Mendel University in Brno, Zemědělská 3, 613 00 Brno, Czech Republic



milligrams per kilogram makes this method interesting for elemental mapping at the “microscale”. For example, elemental distribution was studied in archaeological findings, such as tooth and bone tissues, in order to reveal the diet and migration/mobility^{15–17} of ancient population. Results of analyses of recent samples are used in biomedicine and archaeology.^{18–21} Similarly, fish scales and otoliths as indicators of migration of fish, environmental pollution, water salinity and temperature were analyzed.^{22,23} LA-ICP-MS is a suitable technique to investigate phytoremediation where the knowledge about deposition of toxic elements is required.^{1–4} Considerable interest of the scientific community is focused on the monitoring of elemental distribution in soft tissues such as brain, muscle, kidney tissue, tumors *etc.*, or on a single cell analysis.^{24–27} Where elements of interest are stored, how their presence affects the distribution of other elements and how they relate to specific disease – are the questions that might be answered by LA-ICP-MS analysis.

The chemical and mineralogical composition of a kidney stone is related to a particular disease which is associated with a specific kidney stone formation, depends on the medical treatment and diet of a patient, metabolic conditions, and is influenced by environmental pollution in the patient's domicile and workplace. Chemical analysis might be helpful in understanding kidney stone formation, growth, and medical treatment. In general, kidney stone (urolith) has miscellaneous mineralogical composition, and phosphate, oxalate, carbonate, uric acid, cysteine, and xanthine are the main matrices. Correspondingly, several variants of minerals are present, *e.g.*, in the case of phosphate we find struvite $MgNH_4PO_4 \cdot 6H_2O$, brushite $CaHPO_4 \cdot 2H_2O$, whitlockite $Ca_9(MgFe)(PO_4)_6PO_3OH$, and apatite $(Ca_5(PO_4)_3(OH,F,Cl))$ with variable portions of OH^- (hydroxylapatite), F^- (fluorapatite) and CO_3^{2-} (carbonate-hydroxylapatite) anions. Oxalate occurs as whewellite $Ca(C_2O_4) \cdot H_2O$ and weddellite $Ca(C_2O_4) \cdot 2H_2O$. The urate matrix can be present as uric acid $C_5H_4N_4O_3$, or uric acid dihydrate $C_5H_4N_4O_3 \cdot 2H_2O$ and its salts, such as ammonium urate $NH_4C_5H_3N_4O_3$, and sodium urate monohydrate $NaC_5H_3N_4O_3 \cdot H_2O$. Usually, a urolith contains more than one mineral and therefore, direct analysis of solid samples is preferred in order to preserve spatial information.^{28–30}

Various techniques have been routinely employed in mineralogical and surface analysis of kidney stones, such as infrared spectroscopy,^{31,32} Raman spectroscopy,^{32,33} X-ray diffraction,^{34,35} tomography,³⁶ polarization optical crystallography, chemical microscopy, ultraviolet-visible spectroscopy and photomicroscopy, and light microscopy for macroscopic and microscopic examination. Besides, scanning electron microscopy (SEM/EDX)³⁷ or laser induced breakdown spectrometry (LIBS)^{38,39} has been used for surface analysis. An exploratory study focused on the possibilities of calibration using pressed pellets prepared from uroliths for bulk analysis and microanalysis by LIBS, laser ablation-laser induced breakdown spectrometry (LA-LIBS) and LA-ICP-MS/OES brought out a comparison of calibration curves in terms of linearity and coefficients of determination. However, no elemental mapping of uroliths was attempted.⁴⁰

However, when information on the spatial distribution of trace and minor elements is required, some of the above methods do not meet the requirements on limits of detection (LOD). LA-ICP-MS combines an appropriate resolution in tens of micrometers of the laser spot diameter with values of LOD in units of $mg\ kg^{-1}$ for most elements. So far only two papers have been published on qualitative surface analysis of kidney stones by LA-ICP-MS.^{41,42} A qualitative elemental mapping of uroliths by LA-ICP-MS and electron microprobe (EMP) imaging by means of backscattered electrons (BSE) were applied to distinguish particular mineral phases. Bulk analysis of selected elements in oxalate and phosphate phases by LA-ICP-MS was based on calibration with NIST SRM 1486 (bone meal) and confirmed by EMP analysis, however no quantitative elemental maps were created.⁴²

The major problem with LA-ICP-MS quantification consists in the lack of a reliable, commercially available calibration material. In such a case, effort is devoted to the preparation of laboratory-made standards. As examples, spiked gelatine,⁴³ agarose⁴⁴ or tissue freezing medium¹ is presented for calibration of the LA-ICP-MS determination of metals/metalloids in soft tissues. The calibration can be based on commercially available standards with a similar matrix, which are spiked with the required analytes.² If a suitable reference material is not available, and gelatine or agarose does not match the properties of the analyzed samples, real samples with a similar matrix, previously analyzed by independent methods, may be used with or without spiking.^{5,45,46} If material properties allow, the sample is crushed, milled, homogenized and the resulting powdered material is pressed into a pellet⁴⁷ or mixed with the matrix prepared by the sol-gel technique with subsequent homogenization and pelletization.^{48–50} Another approach consists in the pressing of the powdered sample with a suitable binder.^{17,50}

Uroliths are usually constituted by several mineral phases that are present in various proportions and differ in physical and physico-chemical properties. Consequently, different ablation rates exist in particular mineral zones and make quantitative elemental mapping by LA-ICP-MS difficult unless signal correction by a suitable internal reference is employed. Similarly, such a calibration is necessary which covers appropriately wide ranges of elemental contents and therefore, particular calibration standards would contain various proportions of minerals, and trace elements on various content levels. It is obvious that no compact calibration material is available and calibration has to be based on pressed powdered pellets.

The preparation of powdered calibration standards has been known for decades as it was being used for emission spectrography with electric arc excitation and X-ray fluorescence spectrometry. Calibration standards were typically prepared by mixing solid powdered reagents or natural previously analyzed materials with subsequent homogenization of the resulting mixtures. As both the spectral analytical methods exhibit non-spectral interferences, matrix-matched calibration with an internal reference was indispensable for quantitative analysis.

An easier way to prepare matrix-matched calibration standards for LA-ICP-MS elemental mapping of urolith sections is the use of already analyzed urolith samples, properly crushed,



milled, homogenized and pressed, instead of mixing of individual chemical reagents. In comparison with spectrography or X-ray fluorescence spectrometry of powdered materials, quantitative elemental mapping of uroliths by LA-ICP-MS comprises another factor, namely the difference between the properties of calibration standards and analyzed samples. Different ablation rates would exist not only between minerals, but also between pressed pellets and the surface of urolith sections. Therefore, a reliable internal reference is necessary to compensate for these multiple effects.

No quantitative LA-ICP-MS elemental maps of uroliths have been published so far. In a study,⁴⁰ calibration capabilities of laser ablation based techniques were studied for the purpose of bulk analysis and microanalysis of kidney stones. Intentionally the coarse-grained pellets were prepared from kidney stones instead of finely ground ones, thus respecting the original heterogeneity and multiphase matrix structure of uroliths consisting of several biominerals. This approach has been used because especially LIBS and LA-LIBS are more prone to matrix effects than LA-ICP-OES/MS. Thus, the urolith structure partially preserved in coarse-grained pellets might alleviate the differences between such pellets and kidney stone sections in the case of possible future elemental mapping. To eliminate coarse-grained pellet heterogeneity, a large ablated area and signal averaging were employed. As a result, a linear relationship between the content and signal was obtained, however, only loose correlation was observed, especially for LIBS. Moreover, the mineralogical composition influenced the preparation and mechanical properties of coarse-grained pellets. Pellet cohesion and strength depended on the prevailing phase (phosphate, oxalates, urates), which significantly influenced target material removal using laser beam. The study⁴⁰ focused only on the comparison of laser ablation based methods in terms of calibration and did not address elemental mapping. Hole drilling, from the viewpoint of mapping a time-consuming ablation mode, was employed for this calibration study.

In another study⁴² qualitative elemental distributions over urolith sections were obtained by LA-ICP-MS and particular biomineral zones were identified using EMP/BSE. The influence of different ablation rates on LA-ICP-MS signal magnitude in various mineral phases was compensated by applying the sensitivity of a calcium isotope as the internal reference, for which the average content of calcium was determined in individual phases by EMP analysis. Elemental associations with mineral phases distinguished by the Ca/P signal ratio were derived based on LA-ICP-MS signal distributions compensated for different ablation rates. Calibration with a single pressed pellet prepared from NIST SRM 1486 bone meal was employed for bulk analysis of oxalate and phosphate mineral phases and confirmed by the analysis of average composition by EMP analysis.

As already stated, only qualitative 2D distribution of isotope signals has been published^{41,42} or calibration based on pressed coarse-grained urolith pellets suited rather for LIBS has been developed but not tested for elemental mapping.⁴⁰ Single standard calibration with NIST SRM 1486 has been used for the determination of the average composition of mineral phases

but not for quantification of elemental maps.⁴² Although it appeared that NIST SRM 1486 can be used to quantify these distributions,⁴² there is still scope for increasing the reliability of the calibration.

Several reasons exist to substitute real matrix-matched calibration samples for NIST SRM 1486. Contents of some elements are significantly higher in uroliths than in NIST SRM 1486 which results in inappropriate extrapolation with respect to the calibrated range. This applies to most analytes considered in this work (SRM vs. sample: 0.47%_{m/m} Mg vs. 10%_{m/m} Mg, 0.50%_{m/m} Na vs. 1.50%_{m/m} Na, 264 mg kg⁻¹ Sr vs. 500 mg kg⁻¹ Sr, 147 mg kg⁻¹ Zn vs. 1000 mg kg⁻¹ Zn, 1.3 mg kg⁻¹ Pb vs. 20 mg kg⁻¹ Pb). In NIST SRM 1486 only contents of Ca, P, Mg, Fe, Pb, K, Sr and Zn are certified, while contents of Si, Na, C, Al, As, Cd, Cu, F, Mn and Se are provided as additional information. Therefore, especially in the case of traces (Al, As, Cd, Cu, Mn, and Se) it would be advisable to verify their contents in a particular SRM package by solution analysis. Available indicative values of elemental contents in the SRM are too low (mg kg⁻¹: <1 Al, 0.006 As, 0.003 Cd, 0.8 Cu, 1 Mn, 0.13 Se). Data on the level of contents of other important (potentially toxic) trace elements (Ni, Cr, Hg) are missing in the SRM certificate. Finally, NIST SRM 1486 represents only the calcium phosphate matrix, while kidney stones contain more minerals.

The aim of this study consists in developing a new, flexible matrix-matched calibration for LA-ICP-MS quantification of 2D elemental distributions in urolith sections. Fine-grained urolith pellets are considered for calibration to minimize heterogeneity and improve LA-ICP-MS signal stability. Eighteen urolith samples comprising concrements which consist of phosphate, oxalate and urate phases are included in the calibration study in order to encompass the major types of analyzed kidney stones and ranges of possible elemental contents. The maximum number of calibration samples is employed for the construction of calibration curves at first, and linearity as well as the presence of outliers due to the possible influence of the matrix is statistically tested. For practical reasons, one four-point calibration and four single-point calibrations are tested, too. The procedure consists in: (i) making of a calibration kit of pressed pellets prepared from uroliths, (ii) study of homogeneity and signal stability during laser ablation, (iii) construction of calibration curves of P, Na, Sr, Zn, Ba and Pb, (iv) verification of matrix-matched calibrations by the analysis of NIST SRM 1486, and finally (v) quantification of 2D elemental distributions and verification of results using EMP.

Experimental

Mineralogical composition of uroliths

A set of laboratory-made calibration standards and solid samples used for the testing of prepared standards consists of surgically removed human kidney stones obtained from a vast collection (more than eleven thousand uroliths) assembled by geologist Prof. Petr Martinec (Institute of Geonics, Academy of Sciences of the Czech Republic, Ostrava, Czech Republic). These uroliths have been obtained after the treatment of patients in the University Hospital Ostrava. The selection of uroliths



appropriate for matrix-matched calibration was based on information about their mineralogical composition which was determined by infrared spectrometry. The calibration should include prevailing urolith matrices, which are phosphates, oxalates and uric acid, and therefore uroliths containing mainly phosphates (9 samples), uroliths consisting essentially of oxalates (5 samples) and uroliths composed of a mixture of uric acid and oxalates (4 samples) were selected for the preparation of pressed powder pellets (Table 1). Sample no. 11605 was subjected to elemental quantification of 2D maps using matrix-matched pellets.

The phosphate matrix consists predominantly of apatite $\text{Ca}_5(\text{PO}_4)_3(\text{OH},\text{F},\text{Cl})$ and struvite $\text{NH}_4\text{MgPO}_4 \cdot 6\text{H}_2\text{O}$ in various proportions. The oxalate matrix comprises whewellite $\text{CaC}_2\text{O}_4 \cdot \text{H}_2\text{O}$ and weddellite $\text{CaC}_2\text{O}_4 \cdot 2\text{H}_2\text{O}$. A separate group includes mixed kidney stones containing a minor portion of oxalates (either whewellite or weddellite, exceptionally both) and uric acid ($\text{C}_5\text{H}_4\text{N}_4\text{O}_3$).

Elemental composition of uroliths

The average content of the elements of interest in the uroliths was determined using a wet digestion procedure followed by an ICP-MS measurement. The carbon content was determined by elemental analysis using a LiquiToc II device with Solids Module (Elementar Analysensysteme GmbH, Hanau, Germany). The elemental composition (Ca, Mg, C, P, Na, Sr, Zn, Ba and Pb) is summarized in Table 2. According to ref. 53 the examined urolith samples contain also trace contents of Al, K, Cr, Mn, Fe, Co, Ni, Cu, Se, Rb, Zr, Mo, Cd, Sn and Hg. The ICP-MS and carbon analyses were performed at the laboratory of Research

Centre for Toxic Compounds in the Environment, Faculty of Science, Masaryk University, Brno, Czech Republic. Both analytical procedures have already been reported elsewhere.^{51,53} The results of solution ICP-MS analysis slightly differ in some cases from those of IR screening, which probably results from the fact that each of the halves of a particular kidney stone was crushed and homogenized separately with the assumption that a kidney stone is approximately radially symmetric.

Making of pellets

Eighteen uroliths were employed for the preparation of matrix-matched calibration standards (Table 1, samples no. 5056–9130). The preparation of pellets presents an essential critical step in terms of precision and accuracy of LA-ICP-MS measurement. In particular, the homogeneity of the pellets and the grain size are crucial prerequisites to achieve a stable LA-ICP-MS signal. Besides, sufficient pellet cohesion is necessary to minimize cracking and crumbling of materials at ablation.

The use of pellets prepared from finely ground kidney stones was aimed at homogenizing the multiphase composition of uroliths to reduce the possible spread of calibration points. Kidney stones considered for pellet preparation were crushed in an agate bowl and subsequently milled and homogenized in a ball mill (Planetary Micro Mill Pulverisette 7, FRITSCH; Germany). One portion of each pulverized sample was pressed without adding any binder into pellets with a diameter of 12 mm and 2 mm thickness. Pelletization was performed for 30 s at the pressure of 1.3 GPa using a manual hydraulic press (Mobiko Company, Czech Republic). The remaining powdered sample was dissolved for subsequent ICP-MS analysis.

Table 1 Infrared spectrometry analysis of kidney stones employed for the preparation of calibration pellets and for elemental mapping of a urolith section (sample no. 11605)^a

Sample no.	Main matrix	Content of mineral (% _{m/m})				
		Apatite	Struvite	Whewellite	Weddellite	Uric acid
5056	Ph	50	40	~	10	~
5255		70	20	~	10	~
5397		5	95	~	~	~
5996		35	65	~	~	~
6489		50	50	~	~	~
6671		70	20	~	10	~
6686		60	40	~	~	~
8393		55	55	~	~	~
9130		50	50	~	~	~
5166	Ox	25	~	75	1	~
6275		10	~	80	10	~
7851		5	~	95	~	~
8365		15	0	60	25	~
9081		5	~	95	~	~
11605		30	~	40	30	~
6432	UA	~	~	40	~	60
6585		~	~	5	5	90
7301		~	~	~	10	90
8500		~	~	~	20	80

^a Ph = phosphate matrix, Ox = oxalate matrix, UA = uric acid.



Table 2 Contents of selected major, minor and trace elements in the studied kidney stones obtained by ICP-MS solution analysis^a

Sample no.	Main matrix	Elemental content				
		% _{m/m}				
Sample no.	Main matrix	Ca	Mg	C	P	Na
5056	Ph	23.6 ± 0.8	4.28 ± 0.09	3.29 ± 0.09	17.7 ± 0.4	0.63 ± 0.01
5255		23.8 ± 0.8	4.07 ± 0.09	3.02 ± 0.08	17.5 ± 0.4	0.96 ± 0.02
5397		0.35 ± 0.01	10.1 ± 0.2	1.06 ± 0.03	14.3 ± 0.3	0.0223 ± 0.0004
5996		12.8 ± 0.4	6.5 ± 0.1	2.84 ± 0.08	15.2 ± 0.3	0.69 ± 0.01
6489		18.3 ± 0.6	4.8 ± 0.1	2.92 ± 0.08	16.4 ± 0.3	0.91 ± 0.01
6671		27.5 ± 0.9	2.60 ± 0.05	3.6 ± 0.1	18.3 ± 0.4	1.52 ± 0.02
6686		21.1 ± 0.7	4.7 ± 0.1	3.52 ± 0.09	17.5 ± 0.4	0.81 ± 0.01
8393		20.1 ± 0.6	5.1 ± 0.1	2.29 ± 0.06	16.7 ± 0.4	0.67 ± 0.01
9130		23.2 ± 0.7	3.90 ± 0.08	2.82 ± 0.08	16.8 ± 0.4	0.62 ± 0.01
5166	Ox	26.5 ± 0.8	0.061 ± 0.001	11.5 ± 0.3	2.05 ± 0.04	0.223 ± 0.004
6275		26.4 ± 0.8	0.0404 ± 0.0008	11.4 ± 0.3	1.50 ± 0.03	0.151 ± 0.002
7851		24.5 ± 0.8	0.0280 ± 0.0006	11.9 ± 0.3	0.339 ± 0.007	0.135 ± 0.002
8365		25.9 ± 0.8	0.115 ± 0.002	8.6 ± 0.2	2.63 ± 0.06	0.111 ± 0.002
9081		24.5 ± 0.8	0.0231 ± 0.0005	10.9 ± 0.3	0.227 ± 0.005	0.086 ± 0.001
11605		27.3 ± 0.9	0.160 ± 0.003	9.8 ± 0.3	5.0 ± 0.1	0.258 ± 0.004
6432	UA	1.33 ± 0.04	0.00288 ± 0.00006	26.6 ± 0.7	0.0360 ± 0.0008	0.0214 ± 0.0003
6585		0.076 ± 0.002	0.00080 ± 0.00002	27.2 ± 0.7	0.0138 ± 0.0003	0.0133 ± 0.0002
7301		0.31 ± 0.01	0.00134 ± 0.00003	23.6 ± 0.7	0.0191 ± 0.0004	0.0428 ± 0.0007
8500		0.97 ± 0.03	0.00240 ± 0.00005	24.9 ± 0.7	0.0212 ± 0.0004	0.014 ± 0.0002

Sample no.	Main matrix	Elemental content			
		mg kg ⁻¹			
Sample no.	Main matrix	Sr	Zn	Ba	Pb
5056	Ph	314 ± 16	251 ± 5	10.1 ± 0.3	10.4 ± 0.3
5255		309 ± 15	939 ± 17	14.4 ± 0.4	67 ± 2
5397		4.4 ± 0.2	29.0 ± 0.5	0.72 ± 0.02	0.324 ± 0.008
5996		122 ± 6	373 ± 7	3.3 ± 0.1	9.7 ± 0.2
6489		180 ± 9	458 ± 8	4.1 ± 0.1	3.02 ± 0.08
6671		415 ± 21	711 ± 13	24.3 ± 0.8	13.8 ± 0.3
6686		329 ± 16	945 ± 17	12.3 ± 0.4	51 ± 1
8393		181 ± 9	477 ± 9	11.3 ± 0.4	19.0 ± 0.5
9130		517 ± 26	590 ± 11	22.4 ± 0.7	5.9 ± 0.1
5166	Ox	63 ± 3	137 ± 2	2.05 ± 0.06	9.6 ± 0.2
6275		38 ± 2	180 ± 3	0.84 ± 0.03	19.6 ± 0.5
7851		33 ± 2	31.0 ± 0.6	0.54 ± 0.02	5.1 ± 0.1
8365		102 ± 5	280 ± 5	9.7 ± 0.3	7.8 ± 0.2
9081		31 ± 2	45.4 ± 0.8	1.04 ± 0.03	5.4 ± 0.2
11605		116 ± 6	534 ± 10	5.0 ± 0.2	27.9 ± 0.7
6432	UA	1.72 ± 0.09	9.7 ± 0.2	0.17 ± 0.01	0.349 ± 0.009
6585		0.081 ± 0.004	7.0 ± 0.1	0.066 ± 0.002	0.58 ± 0.01
7301		1.17 ± 0.06	3.05 ± 0.05	0.052 ± 0.002	0.179 ± 0.004
8500		4.3 ± 0.2	6.7 ± 0.1	0.199 ± 0.006	0.83 ± 0.02

^a Ph = phosphate matrix, Ox = oxalate matrix, UA = uric acid.

In contrast to coarse-grained pellets, which were applied to the study of calibration capabilities in LIBS, LA-LIBS, and LA-ICP-OES/MS methods,⁴⁰ the fine grained ones eliminated the lack of pellet cohesion. The difference in particle size was significant. While scanning electron microscope (SEM) exposures of intact and ablated coarse-grained pellets in ref. 40 show particle size between 10 and 50 µm and in some cases even above 100 µm, SEM images in this work (Fig. 1) show particles

around 1 µm, *i.e.*, about one or two orders of magnitude smaller.

Preparation of the urolith section for elemental mapping

For LA-ICP-MS elemental mapping of the urolith section surface, sample no. 11605 was cut into two parts using a diamond saw and one part of the urolith was mounted onto polymethylmethacrylate (PMM) and polished. The other part was



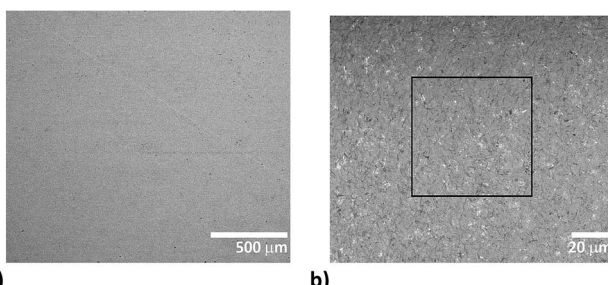


Fig. 1 BSE images of 7851 pressed pellet surface: (a) homogeneous character of the pellet in a large scale view, length of the scale 500 μm , (b) fine scale with evenly distributed phosphate (bright grains) within the fine-grained oxalate matrix (dark color), length of the scale 20 μm , while the square outline defines the size of the laser beam spot (65 \times 65 μm).

Table 3 Operating parameters of LA-ICP-MS, measured isotopes and acquisition times

Laser ablation system	New wave research UP213
Laser	Nd:YAG
Ablation chamber	SuperCell
Wavelength	213 nm
Pulse duration	4.2 ns
Fluence	7.5 J cm^{-2}
Repetition rate	5 Hz
Carrier gas flow rate	He 1.0 L min^{-1} + Ar 0.6 L min^{-1}
Ablation mode	Line scan
Ablation spot size	65 μm (square)
Scan speed	40 $\mu\text{m s}^{-1}$
Distance between lines	100 μm (for mapping only)
ICP-MS	ICP-QMS, Agilent 7500ce
Rf power input	1500 W
Plasma gas flow rate	Ar 15.0 L min^{-1}
Auxiliary gas flow rate	Ar 1.0 L min^{-1}
Sampling depth	8 mm
Collision cell	He 2.5 mL min^{-1}
Acquisition time and isotopes monitored	0.1 s: $^{12,13}\text{C}^+$, $^{23}\text{Na}^+$, $^{27}\text{Al}^+$, $^{31}\text{P}^+$, $^{39}\text{K}^+$, $^{55}\text{Mn}^+$, $^{56,57}\text{Fe}^+$, $^{63}\text{Cu}^+$, $^{66,68}\text{Zn}^+$, $^{85}\text{Rb}^+$, $^{86,88}\text{Sr}^+$, $^{118}\text{Sn}^+$, $^{135,137}\text{Ba}^+$, $^{208}\text{Pb}^+$ 0.05 s: $^{24,26}\text{Mg}^+$ 0.01 s: $^{42,43,44}\text{Ca}^+$

pulverized and left for the determination of the average composition.

Laser ablation-inductively coupled plasma-mass spectrometry procedures

Laser ablation experiments were performed at the Laboratory of Atomic Spectrochemistry, Department of Chemistry, Faculty of Science, Masaryk University. A pulsed Nd:YAG laser system UP 213 (New Wave Research, Inc., Fremont, CA, USA) working at 213 nm and a pulse duration of 4.2 ns was used. The ablation system is equipped with a SuperCell (New Wave Research) designed to enable rapid elution of the ablation-generated

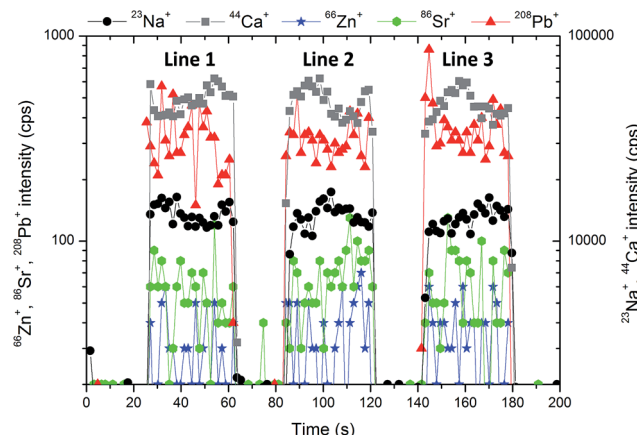


Fig. 2 The stability of the signal of $^{23}\text{Na}^+$, $^{44}\text{Ca}^+$, $^{66}\text{Zn}^+$, $^{86}\text{Sr}^+$, $^{208}\text{Pb}^+$ during the ablation of pellet no. 7851 within 3 lines with the length of 1.5 mm, approximately.

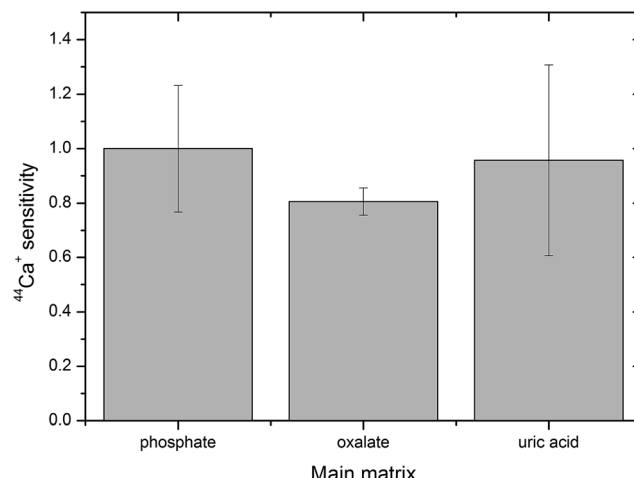


Fig. 3 Sensitivity of the calcium isotopic signal in oxalate and uric acid matrices normalized to the sensitivity in phosphate, error bars represent standard deviation.

aerosol in a large format cell. Helium was used as the carrier gas with a flow rate of 1 L min^{-1} . Aerosol was transported from the ablation cell using a 1 m long polyurethane transport tube (i.d. of 4 mm) to the ICP (ICP-MS Agilent 7500ce, Agilent Technologies, Santa Clara, CA, USA). The instrument was operated with a collision cell in He-mode for minimization of possible polyatomic interferences.

The urolith section (no. 11605) and calibration pellets were rastered with the square-shaped laser beam (65 μm) in line scanning mode at a scan speed of 40 $\mu\text{m s}^{-1}$ with a fluence of 7.5 J cm^{-2} and laser repetition rate of 5 Hz. Rasters composed of an appropriate number of parallel lines and spaced apart 100 μm were employed. The operating parameters are summarized in Table 3. Calibration sets were designed and statistically tested for P, Na, Sr, Zn, Ba and Pb, while Ca was employed as the internal reference. LA-ICP-MS data were collected also for carbon as the matrix element, for Mg as a medium/minor element, for K as a minor/trace element and for Al, Mn, Fe, Cu,

Table 4 Calibration kits, coefficients of determination, and limits of detection

Element	Calibration standards Ph/Ox/UA ^a	R ² outliers included	R ² outliers left out	Regression range % _{m/m}	LOD % _{m/m}
P	0/5/4	0.9991	0.9991	0.014–2.6	<0.1
Na	6/5/4	0.9936	0.9955	0.013–1.5	<0.1
Sr	6/4/4	0.9896	0.9960	0.0001–0.052	<0.004
Zn	6/4/4	0.9868	0.9966	0.0003–0.094	<0.007
Ba	7/4/4	0.9777	0.9957	0.05–24 ^b	<2 ^b
Pb	9/1/3	0.9861	0.9974	0.18–67 ^b	<4 ^b

^a Ph = phosphate matrix, Ox = oxalate matrix, UA = uric acid matrix. ^b LOD in mg kg⁻¹ calculated as the triple standard error of regression divided by the slope of the regression line, $3s_{y/x}/b$, considering the zero value intercept. For completeness of information, regression ranges are presented here while the actual calibrations are limited to values above LODs.

Rb, and Sn as trace elements. Significantly different contents of various types of uroliths were also found for Fe, Cu, and Sn by ICP-MS solution analysis⁵³ which corresponded to a range of LA-ICP-MS signals measured in this work.

Scanning electron microscopy study and electron microprobe analysis

The samples were examined by SEM and EMP analysis prior to LA-ICP-MS experiments. The sample surface was carbon coated for the SEM and EMP study. The quality of pellets in respect to the grain size and phase homogeneity was inspected using SEM. MIRA III SEM equipped with a back-scattered electron (BSE) detector (laboratories of TESCAN, a. s., Brno, Czech Republic) was employed. Back-scattered electron images (1024×1024 pixels) were acquired under the following analytical conditions: an accelerating voltage of 20 kV and a beam current of 20 nA.

The chemical composition (including major and trace elements) of specific phases within the kidney stone sample no. 11605 was determined using a Cameca SX100 electron microprobe (Department of Geological Sciences, Masaryk University, Brno) to check the trueness of results obtained by the quantification of 2D elemental distribution *via* LA-ICP-MS. The instrument was operated at an accelerating voltage of 15 kV, a beam current of 6 nA and scanning beam mode over the area $20 \times 15 \mu\text{m}$. The following calibration standards and analytical lines were used: (K α) lines: fluorapatite (Ca, P), albite (Na), sanidine (Si, Al, K), Mg₂SiO₄ (Mg), NaCl (Cl), hematite (Fe), gahnite (Zn), SrSO₄ (Sr) and topaz (F); (L α) lines: SrSO₄ (Sr), baryte (Ba). The peak counting times ranged from 10 to 20 s for major elements, and from 20 to 80 s for minor elements. The matrix effects were corrected using the PAP routine.⁵²

Results and discussion

Matrix-matched urolith standards

The homogeneity of pellets is of utmost importance for reliable LA-ICP-MS calibration. The critical case may be urolith containing a minor portion of a mineral which substantially differs in chemical composition from the matrix mineral. Therefore, the structure of pellets was inspected using SEM. As an example,

the pellet prepared from urolith no. 7851 containing 95%_{m/m} of oxalate and 5%_{m/m} of phosphate is discussed. The BSE large-scale image of the surface of this pellet does not indicate apparent lack of homogeneity, although bright grains consisting of phosphate and dark oxalate grains are easily distinguishable (Fig. 1a). The detailed image demonstrates almost uniform distribution of phosphate-rich grains characterized by bright spots ($\ll 1 \mu\text{m}$) within the dark oxalate area (Fig. 1b). As the ablation event occurs on the area of $(65 \times 65) \mu\text{m}^2$ (marked with a square in Fig. 1b), the inhomogeneity at a low micrometric scale is acceptable and would not result in isotopic signal instability and biased results. Indeed, as it is obvious from Fig. 2 where three line scans over the surface of pellet no. 7851 are recorded, the time-resolved signal of minor and trace elements such as Na (0.13%_{m/m}), Sr (0.003%_{m/m}), and Pb (0.0005%_{m/m}) exhibits a continuous course uninterrupted by any significant spike, which would otherwise indicate a time/space resolved ablation of a grain enriched with a particular element. This confirms a good “targeted” homogeneity, although these elements are predominantly associated with minor phosphates.⁵³

Compactness of pellets, their stability during ablation and relative insignificance of microinhomogeneity in comparison with the size of the ablation spot in Fig. 1b can also be assessed on the basis of signal variability of the main constituents. The major element present in both phosphate uroliths (with the exception of urolith no. 5397, which consists primarily of struvite) and oxalate uroliths is calcium ($\sim 12\text{--}27\%$ _{m/m} Ca), while one of the organic matrix elements in uric acid samples is carbon ($\sim 25\%$ _{m/m} C), as it follows from Tables 1 and 2.

As phosphate pellets contain apatite and struvite in various proportions and also include $\sim 10\%$ of weddelite in several cases, a fluctuation of $^{44}\text{Ca}^+$ signal along the line scans over the surface of a particular pellet indicates the degree of homogeneity of such a mixture and pellet compactness (presence of cracks, crumbling by the interaction with a laser beam). The RSD of the $^{44}\text{Ca}^+$ signal measured with all phosphate pellets falls within the range of 0.5–10.8% for three ablation tracks located at different areas of the pellet surface. As an example, development of the $^{44}\text{Ca}^+$ signal in time along the mentioned ablation lines is shown for urolith pellet no. 7851 in Fig. 2. The oxalate pellets contain predominantly whewellite, while



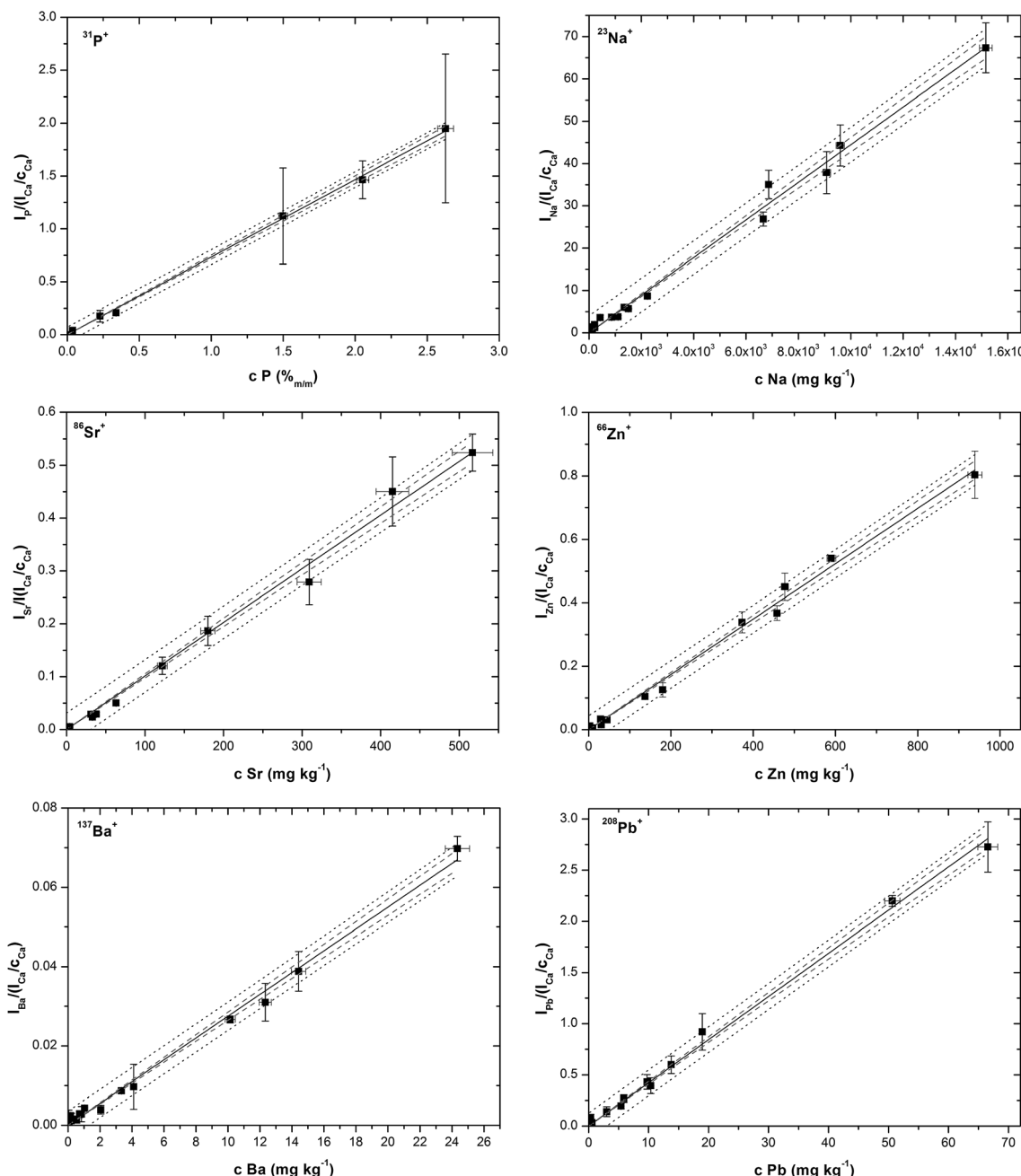


Fig. 4 Calibration lines for P, Na, Sr, Zn, Ba and Pb after statistical analysis and outliers exclusion.

weddellite content ranges up to 25% and the phosphate mineral group constitutes from 5 to 30% of the total. Signal variability of $^{44}Ca^+$ in oxalate pellets is characterized by RSD ranging from 0.6 to 4.9%. Calcium is a minor element (0.1–1.3%_{m/m}) in uric acid group uroliths, and therefore $^{44}Ca^+$ signal exhibits the most significant fluctuation with RSD between 4.4% and 51%. On the other hand, RSD of $^{12}C^+$ signal ranging from 3.3 to 7.1% documents quite a good stability and homogeneity of uric acid pellets. Nevertheless, urate-based pellets exhibit the highest fluctuation of $^{12}C^+$ signal in comparison with phosphate (0.4–2.0%) and oxalate (0.6–2.5%) groups, which is probably due to the presence of some fine cracks on the pellet surface. The

internal precision, which reflects the microscale homogeneity, is expressed as the median value of %RSD of $^{12}C^+$ isotopic signal fluctuation, and is equal to 4.5%, 4.1% and 9.9% for groups of uroliths with prevailing phosphate, oxalate and urate matrices, respectively. It should be generally noted that calcium and carbon signal fluctuation reflects, besides pellet compactness and homogeneity of their distributions in all kinds of pellets, also both the influence of ablation rate variability and overall instrumental precision of the LA-ICP-MS system. Obviously, Ca and C signal stability can be considered an appropriate common indicator of a particular pellet quality and suitability for calibration.

Table 5 Comparison of elemental contents with standard deviations in NIST SRM 1486 obtained with four-point and single-point calibrations after ablation of ten lines with the length of 2.8 mm, approximately

Element	Certified values	Four-point calibration	6686 Phosphate	8393 Phosphate	9130 Phosphate	6275 Oxalate
	mg kg ⁻¹					
P	12.30 ± 0.19 ^a	12.07 ± 0.68 ^a	12.06 ± 0.69 ^a	11.66 ± 0.66 ^a	12.19 ± 0.69 ^a	12.94 ± 0.74 ^a
Na	(0.50) ^{a,b}	0.48 ± 0.03 ^a	0.45 ± 0.02 ^a	0.34 ± 0.02 ^a	0.45 ± 0.02 ^a	0.32 ± 0.02 ^a
Sr	264 ± 7	273 ± 17	285 ± 18	274 ± 17	265 ± 16	269 ± 17
Zn	147 ± 16	148 ± 18	210 ± 17	153 ± 12	151 ± 12	128 ± 10
Ba	189–314 ^c	249 ± 12	235 ± 17	196 ± 14	227 ± 16	52.7 ± 3.8
Pb	1.335 ± 0.014	3.64 ± 0.48	2.68 ± 0.35	0.511 ± 0.068	0.99 ± 0.13	0.445 ± 0.059

^a In %_{m/m}. ^b Non-certified content. ^c The value is not included in the NIST SRM 1486 certificate; Ba content presented in Table 5 is taken from Georem.⁵⁴

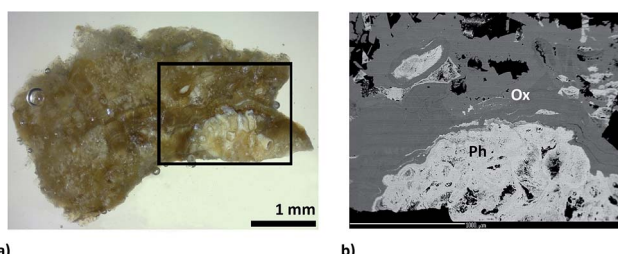


Fig. 5 (a) Photograph of no. 11605 kidney stone surface with the marked area analyzed via LA-ICP-MS and EMP imaging and (b) BSE image marked surface with the description of phases (Ph – phosphate and Ox – oxalate).

The occurrence of kidney stones with only one matrix is quite uncommon. It is not an exception that more than two matrices can be found in uroliths. Therefore, we attempted to create a single calibration which would be applicable to various types of kidney stones. The concept of matrix-matched calibration in our approach means that a single calibration would be able to cover phosphate, oxalate and urate matrices. A necessary prerequisite for application of the common calibration is the same or at least close sensitivity for these matrices.

The pellets were divided into three groups according to their mineralogical composition: (i) 9 pellets with a predominant phosphate matrix; (ii) 5 pellets with the prevailing oxalate matrix; and (iii) 4 pellets with the main content being uric acid (Table 1). The response in these three groups of uroliths was evaluated using the $^{44}\text{Ca}^+$ signal. Sensitivity was calculated for each pellet as the ratio of the $^{44}\text{Ca}^+$ net signal to the Ca content in the pellet, the values in each group were averaged and standard deviations were calculated and plotted (Fig. 3), while sensitivities in oxalate and uric acid matrices were normalized to the sensitivity in the phosphate group. Thus, the normalized sensitivity in the phosphate group is equal to one. The Ca contents in pellets with phosphate and oxalate as the main constituents are both high and close, while the pellets with uric acid/oxalates contain only 0.1–1.3%_{m/m} Ca. As observed, the highest sensitivity was obtained for the group of phosphate-based pellets while the sensitivity in oxalate and uric acid pellets reaches 81% and 96% of the maximum value (Fig. 3). However, non-parametric Kruskal-Wallis test indicated no statistically significant difference between sensitivities.

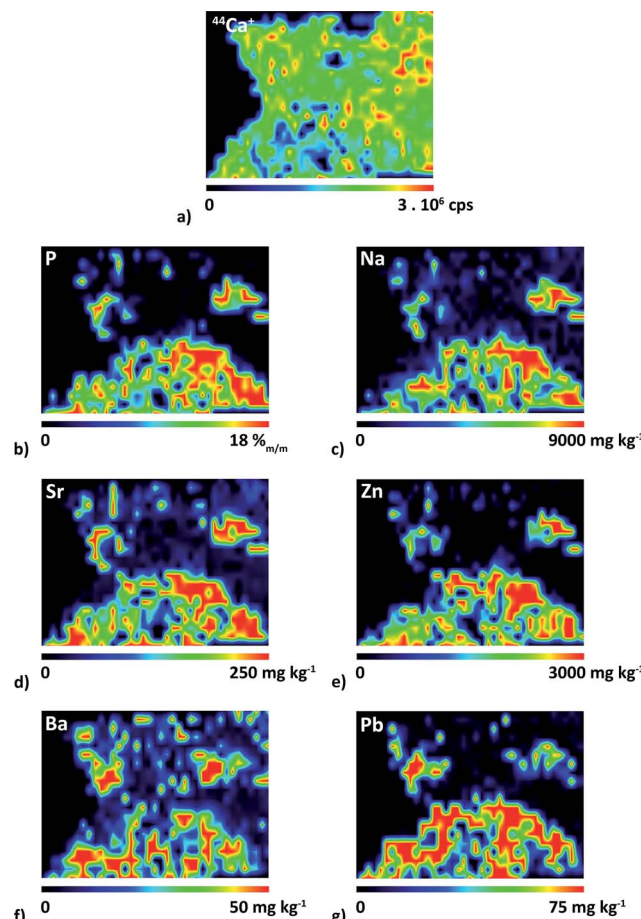


Fig. 6 Distributions of (a) $^{44}\text{Ca}^+$ and of elemental contents of (b) P, (c) Na, (d) Sr, (e) Zn, (f) Ba and (g) Pb which were quantified using the single-point calibration with pellet no. 9130.

Development of matrix-matched calibration kits

Eighteen pellets prepared from urolith specimens listed in Table 1 were used for the construction of calibration plots for P, Na, Sr, Zn, Ba and Pb. Calibration kits for particular analytes are listed in Table 4. Calibration for Mg of the same quality was obtained too (not presented in this work). The LA-ICP-MS measurement was repeated three times on each pellet using three parallel lines with



Table 6 Elemental contents in phosphate and oxalate matrices of urolith no. 11605 obtained by LA-ICP-MS and EMP analysis

Element	Median content range mg kg ⁻¹	Arithmetic mean of median contents	SD	Variability in content MAD	Arithmetic mean content
					EMP analysis
					mg kg ⁻¹
Phosphate area					
P	17.5–19.4 ^a	18.36 ^a	0.80 ^a	32	17.39 ± 0.22 ^a
Na	0.56–0.79 ^a	0.68 ^a	0.12 ^a	74	0.93 ± 0.06 ^a
Sr	244–262	251.7	7.8	71	<LOD
Zn	2303–3791	2890	630	47	2740 ± 630
Ba	7–30	23	11	49	<LOD
Pb	26–59	39	18	76	<LOD
Oxalate area					
P	1342–1489	1405	61	65	2400 ± 1200
Na	694–973	840	148	51	870 ± 330
Sr	39–41	39.8	1.2	82	<LOD
Zn	26–43	32.4	7.1	44	<LOD
Ba	2–11	8.3	4.0	55	<LOD
Pb	1–3	2.15	0.98	63	<LOD

^a %_{m/m}.

the length of 1.2 mm under conditions specified in the Experimental part. Background intensity was recorded prior to ablation and then subtracted from the signal measured during the ablation period. The sensitivity of the ⁴⁴Ca⁺ signal was applied as an internal reference for the correction of matrix effects.

Calibration points were plotted as analyte signals divided by ⁴⁴Ca⁺ sensitivities vs. elemental contents. Calibration curves were fitted using a computer program Origin. Linear regression models that resulted from the tests and two sets of coefficients of determination (R^2) were computed; one set with all data points included, and the other after outliers had been eliminated (Table 4). In Fig. 4, calibration curves of P, Na, Sr, Zn, Ba and Pb are plotted together with confidence and prediction bands without outliers. Ordinary least squares linear regression was applied and the regression line was fitted for calibration points representing arithmetic means of 3 replicates for each pellet. Each replicate represents the average value of all MS readings obtained during the line scan ablation measurement. Vertical error bars represent the combined uncertainty of replicates calculated based on the standard deviation of the signal of isotope (analyte) and standard deviation of calcium isotope signal (internal reference). Horizontal error bars represent uncertainty of ICP-MS solution analysis. Regression lines computed without outliers show tighter correlation, which is obvious from values of $R^2 > 0.99$, namely in the range 0.9955–0.9991 (Table 4). At this point it should be emphasized that calibrations for Sr, Mg, Ba, and Na obtained with coarse-grained pellets⁴⁰ exhibit worse values of R^2 (0.75–0.90). All calibration plots are described by the equation $y = bx$ with a zero value of the intercept at the level of confidence $(1 - \alpha) = 0.975$. The intercepts are not statistically significant regardless of whether the outliers are retained in the regression sets or excluded on the basis of statistical testing. The absence of intercepts together with the proved validity of linear models indicates that the

internal reference compensates for different ablation rates associated with the three various mineral matrices, and thus eliminates systematic error. The calibration line for phosphorus was fitted only with data points for oxalate and uric acid pellets, while phosphate data points were omitted as phosphorus is the main constituent in phosphate uroliths. In Fig. 4, calibration curves of P, Na, Sr, Zn, Ba and Pb are plotted together with confidence and prediction bands without outliers. Limits of detection were calculated as the triple standard error of regression divided by the slope of the regression line, $3s_{y/x}/b$, considering the zero value intercept. It has to be emphasized that limits of detection calculated through the calibration lines generally depend on both the number and distribution of calibration standards and are in principle higher than those (instrumental) obtained simply based on the triple standard deviation of the LA-ICP-MS blank signal recorded when ablation is off. Consequently, the LOD values in Table 4 follow from regression calculations performed in the presented regression ranges, and are associated with concrete calibration lines displayed in Fig. 4, while LOD values at a particular mapping may differ.

Verification of matrix-matched calibrations by the analysis of NIST SRM 1486

Practical application of the presented calibration kits is limited by the size of the ablation cell (SuperCell), which holds only five pellets because the PMM block with the urolith section occupies a relatively large space (~5 cm²). To minimize both the analysis time and the effect of handling the ablation cell on measurement stability, the calibration pellets and the urolith section should be inserted into the ablation cell at the same time. Based on the satisfactory results of the calibration dependence studies, we decided to explore the possibility of reducing the number of calibration points to four. In the extreme case, calibration with a



single pellet would bring, besides reducing the time of analysis, in particular the possibility to place more samples for mapping into the ablation cell. Therefore, four calibration pellets were selected to represent both the phosphate (3 pellets, 6686, 8393 and 9130) and the oxalate (1 pellet, 6275) matrices. The fifth pellet was NIST SRM 1486, the bone meal, which was employed to prove whether the calibration kit is really matrix-matched, in the first approximation as regards the analysis of the powdered material with the phosphate matrix.

The ablation pattern applied to pellets consisted of ten parallel lines 2.8 mm in length. Measurement was performed under conditions specified in the Experimental part. Two calibration procedures were examined: (i) the four-point calibration comprising three phosphate and one oxalate pellets; (ii) four single-point calibrations based on particular phosphate and oxalate pellets. Relative intensities representing ratios of signals of individual isotopes and the $^{44}\text{Ca}^+$ sensitivity were processed. Isotope $^{44}\text{Ca}^+$ sensitivity correlates reasonably with signals of analytes. This means that the internal reference follows analyte signal variations, which are due to both matrix-dependent ablation rate, and the fluctuations of instrumental operating conditions of the LA-ICP-MS system.

The NIST SRM 1486 elemental contents resulting from calibrations (i) and (ii) are shown together with the certified and published uncertified values in Table 5. Besides the four-point calibration with the coefficient of determination in the range of 0.990–0.999, best fit is obtained with single-point calibrations using phosphate pellets, while oxalate matrix calibration leads to an underestimation of Ba content due to the Ba content in pellet no. 6275 being below LOD (Table 4). Similarly, the Pb content in NIST 1486 is three times below LOD and cannot be determined under the method conditions used. Finally, the calibration with phosphate pellet no. 9130 was selected for mapping of the urolith section.

Quantification of 2D elemental distributions

Besides the sensitivities of particular analytes measured in calibration pellets, the sensitivities of analytes obtained for sections of uroliths play an important role in quantification. The section of kidney stone exhibits different physical properties than the pressed pellet. Ablation rate depends on the mineral phase and its density and hardness. Consequently, different ablation rates in various minerals can be expected in a given urolith section in comparison with the pressed pellet.

The elemental map of the part of the urolith no. 11605 section surface (1.4×1.9) mm² was quantified. The photograph of the whole sample surface with the analyzed area marked with a rectangle is presented in Fig. 5a. Sample no. 11605 contains 30%_{m/m} of phosphate and 70%_{m/m} of oxalate of which 40%_{m/m} is whewellite and 30%_{m/m} weddellite.

As shown in Fig. 5b, the analyzed area is composed mainly of oxalate (whewellite > weddellite) and fluorapatite according to EMP analysis. Fluorapatite predominates in the central part of the kidney stone. Calculation of the structural formula from the results of EMP analysis indicates a rather fine-grained mixture of predominant fluorapatite with a minor amount of Mg-rich

phosphate (probably struvite) compared to pure fluorapatite. The chemical heterogeneity of fluorapatite observed in the BSE image reflects a varying admixture of Mg-rich phosphate (a higher amount of Mg-rich phosphate decreases the brightness of the BSE image). Fluorapatite is overgrown by fine-grained, colomorph oxalate, possibly weddellite. Coarse-grained compact oxalate, probably whewellite, predominates in the kidney stone. The outermost part of the kidney stone is composed of intergrowths of both types of oxalate (whewellite and weddellite). Contents of minor elements in whewellite and weddellite are similar and generally decrease from the inner part of the kidney stone (close to the fluorapatite) to the rim.

A single-point calibration was used with respect to the low content of some elements in the oxalate matrix and with the aim to reduce the time of analysis. For this purpose, phosphate pellet no. 9130 was used as the calibration standard.

Elemental 2D maps are shown in Fig. 6, where Ca distribution is presented on the level of intensities (Fig. 6a), while P, Na, Sr, Zn, Ba and Pb (Fig. 6b–g) are quantified. It should be noted right at the beginning that the quantification of the inhomogeneous surface is hampered by the presence of defects (cracks) in phases. Besides, spatial resolution in the direction of *x*-axis is deteriorated by using the line scanning mode which induces overlapping of signals on the boundary of the phases. The spatial resolution of the elemental maps in the scanned area is also affected by the fact that lines are spaced 100 µm. As a result, the image of the boundary is not sharp.

The quantification procedure is as follows. Prior to quantification, the signal corresponding to PMM resin was removed and thus filtered values were divided into two groups characterizing section areas. The area comprising $^{31}\text{P}^+$ signal corresponds exclusively to the phosphate matrix whereas the area covered by the $^{44}\text{Ca}^+$ signal defines the whole sample section surface as calcium is common for both oxalate and phosphate phases. This distinction allows quantifying elemental contents separately in particular phases.

A correction for different ablation rates in oxalate and phosphate matrices of the urolith section and in calibration pellets is of utmost importance for obtaining quantitative elemental distributions. The average ablation rate in the phases of the sample section and in the pellet was determined on the basis of a large number of measurements. For this purpose, 50 and 80 values of $^{44}\text{Ca}^+$ signal in phosphate and oxalate phases were employed, respectively. Considering the Ca content in both phases obtained via EMP analysis and median intensity values of $^{44}\text{Ca}^+$ for each of the phases, the value of 1.3 was found which indicates that the Ca sensitivity in the phosphate phase is higher than that in the oxalate phase. In other words, the ablation rate in the oxalate phase reaches 80% of that in the phosphate phase. This is in good agreement with a comparison of Ca sensitivities for pellets (Fig. 3). As a result, $^{44}\text{Ca}^+$ distribution (Fig. 6a) corrected for the difference in the average ablation rate exhibits slightly higher intensity values in the phosphate-rich domain, and the intensity drops in small areas with material defects (cracks). The comparison of Ca (Fig. 6a) and P (Fig. 6b) distributions reveals that 42% of the examined part of the section surface corresponds to the phosphate matrix. It is apparent that the found elemental



distributions of Na, Sr, Zn, Ba and Pb (Fig. 6c–g) are concentrated to the area corresponding to the phosphate-based matrix (Fig. 6b).

Results of analyses of phosphate and oxalate phases in urolith no. 11605 are presented in Table 6. To verify that the quantification of 2D maps (Fig. 6), which is based on pellet no. 9130, is not distorted by this single-point calibration, median values of elemental contents in both phases were also determined using three other single-point calibrations with pellets no. 6686, 8393 and 6275, employed for the analysis of NIST SRM 1486. The range of thus obtained four median values is presented in Table 6 together with their arithmetic mean and corresponding standard deviation for each analyte. It is obvious from these low SD values that all the used single-pellet calibrations provide close results. Content variability over the phase area is expressed as the median absolute deviation (MAD), which is the median of the absolute deviations from the content's median. The median was selected in order to minimize the influence of the presence of cracks and distortion of signal by line scanning mode. For comparison, average values (arithmetic mean) with standard deviations are presented for EMP analyses of the studied phases. However, contents of Ba and Pb in phosphate and Sr, Zn, Ba and Pb in oxalate are below LOD of EMP analysis. The agreement between LA-ICP-MS and EMP analysis results is satisfactory when considering the fact that the variability in elemental contents within phosphate and oxalate area phases reaches at least 32% (P), 51% (Na) and 44% (Zn), respectively. As the quantification relies on the single-point calibration instead of the multi-point one, LODs of LA-ICP-MS measurement calculated as the triple standard deviation of background intensity divided by sensitivity were as follows: P 200 mg kg⁻¹, Na 20 mg kg⁻¹, Sr 4 mg kg⁻¹, Zn 0.7 mg kg⁻¹, Ba 0.05 mg kg⁻¹ and Pb 0.03 mg kg⁻¹.

Conclusions

The kidney stone investigation plays an important role in medical treatment when the process of formation and growth of uroliths as well as the influence of environmental pollution, for instance, have to be known. In this study, a new flexible matrix-matched calibration was designed, tested and used to quantify the distribution of elements in uroliths by laser ablation-inductively coupled plasma-mass spectrometry. Two-dimensional distributions of isotopic signals obtained from the selected area of the urolith section surface were converted to maps of elemental contents using the matrix-matched calibration. Calibration kits comprising 9–15 pressed pellets (depending on a particular element) were tested for homogeneity, signal stability and linear response with satisfactory results. Pellets were prepared without any binder from powdered uroliths consisting of phosphate, oxalate and urate phases. Despite the fact that the individual calibration pellets differ significantly in proportions of mineral phases and therefore also in physical and physico-chemical properties, a linear calibration model in the range of three orders of magnitude and with zero intercept was obtained for P, Na, Mg, Zn, Ba and Pb. The low scatter of calibration points is characterized by coefficients of determination >0.9955 and narrow confidence and prediction bands. This tight correlation was achieved through internal standardization. Correction of isotopic signals

for different ablation rates in phosphate, oxalate and urate matrices of calibration pellets was successfully accomplished by internal standardization with the response factor of $^{44}\text{Ca}^+$. For this purpose, calcium contents in particular uroliths employed for the preparation of calibration pellets were determined by solution analysis, while the average content of calcium in oxalate and phosphate phases of the mapped urolith section surface was determined using an electron microprobe.

To reduce the time of analysis, the four-point and four single-point calibrations were tested by the analysis of a pressed pellet of bone meal NIST SRM 1486. The four-point calibration with the coefficient of determination in the range of 0.990–0.999 and single-point calibrations with phosphate matrix pellets yielded better trueness than those for the oxalate pellet. This proved the feasibility of quantification of elemental maps using calibration with a single pellet. The trueness of quantitative elemental maps obtained by LA-ICP-MS was indirectly proved by comparison of averaged elemental contents in phosphate/oxalate phases with those determined by an electron microprobe. Limits of detection of minor or trace elements (Sr, Zn, Pb, and Ba) calculated from the standard error of regression (calibration) were found to be between units and hundreds of mg kg⁻¹.

The proposed calibration exhibits advantages over using the bone meal NIST SRM 1486. Unlike this SRM, calibration samples prepared from uroliths cover an existing wide range of elemental contents in the analyzed samples without extrapolation, which is on the other hand unavoidable in the case of Na, Mg, K, Pb, Sr and Zn quantification using NIST 1486. The number of calibration standards can be flexibly adapted to elemental contents in a particular urolith. Besides P, Na, Mg, Zn, Ba and Pb, urolith pressed pellets can also encompass linear multi-point calibrations for C, K, Al, Mn, Fe, Cu, Rb and Sn, while NIST SRM 1486 covers only Ca, Mg, P, Fe, K, Pb, Sr, and Zn with certified values. However, the real content of K, Pb, Sr, and Zn in analyzed uroliths is frequently above particular certified values.

Acknowledgements

The authors acknowledge the Czech Science Foundation for a grant to support the project 203/09/1394. This work was also supported by the European Regional Development Fund project "CEITEC" (CZ.1.05/1.1.00/02.0068). R. C. acknowledges support from Specific research programme MUNI/A/1005/2013 of the Masaryk University.

References

- M. Debeljak, J. T. van Elteren and K. Vogel-Mikus, *Anal. Chim. Acta*, 2013, **787**, 155–162.
- A. Hanc, A. Piechalak, B. Tomaszewska and D. Baralkiewicz, *Int. J. Mass Spectrom.*, 2014, **363**, 16–22.
- M. Galiova, J. Kaiser, K. Novotny, M. Hartl, R. Kizek and P. Babula, *Microsc. Res. Tech.*, 2011, **74**, 845–852.
- A. Kötschau, G. Büchel, J. W. Einax, C. Fischer, W. von Tümpling and D. Merten, *Microchem. J.*, 2013, **110**, 783–789.
- S. R. Ellis, A. L. Bruinen and R. M. A. Heeren, *Anal. Bioanal. Chem.*, 2014, **406**, 1275–1289.



- 6 J. Koelmel, T. Leland and H. Wang, *Environ. Pollut.*, 2013, **174**, 222–228.
- 7 A. Hanc, I. Komorowicz, M. Iskra, W. Majewski and D. Baralkiewicz, *Anal. Bioanal. Chem.*, 2011, **399**, 3221–3231.
- 8 S. Gruhl, F. Witte, J. Vogt and C. Vogt, *J. Anal. At. Spectrom.*, 2009, **24**, 181–188.
- 9 J. Chou, C. Austin, P. Doble, B. Ben-Nissan and B. Milthorpe, *J. Tissue Eng. Regener. Med.*, 2014, **8**, 515–520.
- 10 E. G. Grosch, J. Kosler, N. McLoughlin, K. Drost and J. Slama, *Precambrian Res.*, 2011, **191**, 85–99.
- 11 C. M. Fisher, H. P. Longerich, S. E. Jackson and J. M. Hanchar, *J. Anal. At. Spectrom.*, 2010, **25**, 1905–1920.
- 12 M. Bertini, A. Izmer, F. Vanhaecke and E. M. Krupp, *J. Anal. At. Spectrom.*, 2013, **28**, 77–91.
- 13 A. Nevin, G. Spoto and D. Anglos, *Appl. Phys. A: Mater. Sci. Process.*, 2012, **106**, 339–361.
- 14 C. Chataigner, M. Isikli, B. Gratuze and V. Cil, *Archaeometry*, 2014, **56**, 351–374.
- 15 C. Stadlbauer, C. Reiter, B. Patzak, G. Stingeder and T. Prohaska, *Anal. Bioanal. Chem.*, 2007, **388**, 593–602.
- 16 T. Prohaska, C. Latkoczy, G. Schultheis, M. Teschl-Nicola and G. Stingeder, *J. Anal. At. Spectrom.*, 2002, **17**, 887–891.
- 17 M. Vasinova Galiova, M. Nyvtova Fisakova, J. Kynicky, L. Prokes, H. Neff, A. Z. Mason, P. Gadas, J. Kosler and V. Kanicky, *Talanta*, 2013, **105**, 235–243.
- 18 A. E. Dolphin and A. H. Goodman, *Am. J. Phys. Anthropol.*, 2009, **140**, 399–409.
- 19 A. E. Dolphin, A. H. Goodman and D. D. Amarasinghe, *Am. J. Phys. Anthropol.*, 2005, **128**, 878–888.
- 20 D. Hare, C. Austin, P. Doble and M. Arora, *J. Dent.*, 2011, **39**, 397–403.
- 21 A. Arvidsson, B. Liedberg, K. Moller, B. Lyven, A. Sellen and A. Wennerberg, *J. Dent.*, 2002, **30**, 67–75.
- 22 Z. A. Doubleday, C. Izzo, S. H. Woodcock and B. M. Gillanders, *Aquat. Biol.*, 2013, **18**, 271–280.
- 23 A. D. Clarke, K. H. Telmer and J. M. Shrimpton, *Ecol. Freshwat. Fish*, 2007, **16**, 354–361.
- 24 B. Wu, J. S. Becker and J. Sabine, *Int. J. Mass Spectrom.*, 2012, **323**, 34–40.
- 25 S. D. Urgast, D. G. Ellingsen, B. Berlinger, E. Eilertsen, G. Friisk, V. Skaug, Y. Thomassen, J. H. Beattie, I. Kwun and J. Feldmann, *Anal. Bioanal. Chem.*, 2012, **404**, 89–99.
- 26 O. Reifschneider, C. A. Wehe, I. Raj, J. Ehmkke, G. Ciarimboli, M. Sperling and U. Karst, *Metalomics*, 2013, **5**, 1440–1447.
- 27 D. Drescher, C. Giesen, H. Traub, U. Panne, J. Kneipp and N. Jakubowski, *Anal. Chem.*, 2012, **84**, 9684–9688.
- 28 L. Prien and C. Frondel, *J. Urol.*, 1947, **57**, 949–994.
- 29 M. L. Stoller and M. V. Meng, *Urinary Stone Disease: the Practical Guide to Medical and Surgical Management*, Humana press, New Jersey, 2007.
- 30 N. Mandel, *Lab. Med.*, 1986, **17**, 449–458.
- 31 S. Tamasaityte, V. Hendrixson, A. Zelys, R. Tyla, Z. A. Kucinskaite, F. Jankevicius, M. Pucetaite, V. Jablonskiene and V. Sablinskas, *J. Biomed. Opt.*, 2013, **18**, 027011.
- 32 C. Conti, M. Casati, C. Colombo, M. Realini, L. Brambilla and G. Zerbi, *Spectrochim. Acta, Part A*, 2014, **128**, 413–419.
- 33 R. Selvaraju, A. Raja and G. Thiruppathi, *Spectrochim. Acta, Part A*, 2013, **114**, 650–657.
- 34 S. D. Blaschko, J. Miller, T. Chi, L. Flechner, S. Fakra, A. Kahn, P. Kapahi and M. L. Stoller, *J. Urol.*, 2013, **189**, 726–734.
- 35 K. Kaneko, Y. Matsuta, M. Moriyama, M. Yasuda, N. Chishima, N. Yamaoka, T. Fukuuchi, K. Miyazawa and K. Suzuki, *Int. J. Urol.*, 2014, **21**, 341–346.
- 36 E. S. Wisenbaugh, R. G. Paden, A. C. Silva and M. R. Humphreys, *Urology*, 2014, **83**, 1243–1247.
- 37 V. Uvarov, I. Popov, N. Shapur, T. Abdin, O. N. Gofrit, D. Pode and M. Duvdevani, *Environ. Geochem. Health*, 2011, **33**, 613–622.
- 38 B. G. Oztoprak, J. Gonzalez, J. Yoo, T. Gulecen, N. Mutlu, E. E. Russo, O. Gundogdu and A. Demir, *Appl. Spectrosc.*, 2012, **66**, 1353–1361.
- 39 J. Anzano and R. J. Lasheras, *Talanta*, 2009, **79**, 352–360.
- 40 K. Stepankova, K. Novotny, M. Vasinova Galiova, V. Kanicky, J. Kaiser and D. W. Hahn, *Spectrochim. Acta, Part B*, 2013, **81**, 43–49.
- 41 M. A. Chaudhri, J. Watling and F. A. Khan, *J. Radioanal. Nucl. Chem.*, 2007, **271**, 713–720.
- 42 M. Vasinova Galiova, R. Copjakova, R. Skoda, K. Stepankova, M. Vankova, J. Kuta, L. Prokes, J. Kynicky and V. Kanicky, *Spectrochim. Acta, Part A*, 2014, **100**, 105–115.
- 43 A. Izmer, D. Gholap, K. De Houwer, F. Cuyckens and F. Vanhaecke, *J. Anal. At. Spectrom.*, 2012, **27**, 413–418.
- 44 H. J. Stärk and R. Wennrich, *Anal. Bioanal. Chem.*, 2011, **399**, 2211–2217.
- 45 E. Moreno-Gordaliza, C. Giesen, A. Lazaro, D. Esteban-Fernandez, B. Humanes, B. Canas, U. Panne, A. Tejedor, N. Jakubowski and M. M. Gomez-Gomez, *Anal. Chem.*, 2011, **83**, 7933–7940.
- 46 D. J. Hare, J. Lear, D. Bishop, A. Beavis and P. A. Doble, *Anal. Methods*, 2013, **5**, 1915–1921.
- 47 D. Tabersky, N. A. Luechinger, M. Rossier, E. Reusser, K. Hametner, B. Aeschlimann, D. A. Frick, S. C. Halim, J. Thompson, L. Danyushhevsky and D. Guenther, *J. Anal. At. Spectrom.*, 2014, **29**, 955–962.
- 48 I. Hubova, M. Hola, J. Pinkas and V. Kanicky, *J. Anal. At. Spectrom.*, 2007, **22**, 1238–1243.
- 49 H. Sela, Z. Karpas, H. Cohen, Y. Zakon and Y. Zeiri, *Int. J. Mass Spectrom.*, 2011, **307**, 142–148.
- 50 J. A. T. Pugh, A. G. Cox, C. W. McLeod, J. Bunch, B. Whitby, B. Gordon, T. Kalber and E. White, *J. Anal. At. Spectrom.*, 2011, **26**, 1667–1673.
- 51 J. Kuta, J. Machát, D. Benova, R. Červenka and T. Kořistková, *Cent. Eur. J. Chem.*, 2012, **10**, 1475–1483.
- 52 J. L. Pouchou and F. Pichoir, in PAP, *Procedure for Improved Quantitative Microanalysis*, ed. J. T. Armstrong, Microbeam Analysis Proc. San Francisco Press, San Francisco, 1985, pp. 104–106.
- 53 J. Kuta, J. Machát, D. Benova, R. Červenka, J. Zeman and P. Martinec, *Environ. Geochem. Health*, 2013, **35**, 511–522.
- 54 http://georem.mpch-mainz.gwdg.de/sample_query.asp, 16/10/2014.





Laser ablation methods for analysis of urinary calculi: Comparison study based on calibration pellets

K. Štěpánková ^a, K. Novotný ^{a,b,*}, M. Vašinová Galiová ^{a,b}, V. Kanický ^{a,b}, J. Kaiser ^c, D.W. Hahn ^d

^a Department of Chemistry, Faculty of Science, Masaryk University, Kotlářská 2, 611 37 Brno, Czech Republic

^b CEITEC – Central European Institute of Technology, Masaryk University, Kamenice 5, 625 00 Brno, Czech Republic

^c X-ray micro CT and nano CT research group, CEITEC – Central European Institute of Technology, Brno University of Technology, Technická 2896/2, 616 69 Brno, Czech Republic

^d Department of Mechanical & Aerospace Engineering, University of Florida, Gainesville, FL 32611, USA

ARTICLE INFO

Article history:

Received 16 May 2012

Accepted 26 December 2012

Available online 8 January 2013

Keywords:

Laser ablation

LA-ICP-MS/OES

LIBS

LA-LIBS

Urinary calculi

ABSTRACT

Methods based on laser ablation, such as Laser-Induced Breakdown Spectroscopy (LIBS) and Laser-Ablation Inductively Coupled Plasma Mass/Optical Emission Spectrometry (LA-ICP-MS/OES) are particularly suitable for urinary calculi bulk and micro analysis. Investigation of spatial distribution of matrix and trace elements can help to explain their emergence and growth. However, quantification is still very problematic and these methods are often used only for qualitative elemental mapping. There are no commercially available standards, which would correspond to the urinary calculi matrix. Internal standardization is also difficult, mainly due to different crystalline phases in one kidney stone. The aim of this study is to demonstrate the calibration capabilities and examine the limitations of laser ablation based techniques. Calibration pellets were prepared from powdered human urinary calculi with phosphate, oxalate and urate matrix. For this comparative study, the most frequently used laser-ablation based analytical techniques were chosen, such as LIBS and LA-ICP-MS. Moreover, some alternative techniques such as simultaneous LIBS-LA-ICP-OES and laser ablation LA-LIBS were also utilized.

© 2013 Elsevier B.V. All rights reserved.

1. Introduction

Laser ablation based analytical techniques, namely Laser-Induced Breakdown Spectroscopy (LIBS) and Laser-Ablation Inductively Coupled Plasma Mass/Optical Emission Spectrometry (LA-ICP-MS/OES) are the subject of increasing popularity especially in the last two decades. Some of the many benefits offered by these techniques include the ability to analyze virtually any kind of solid material, high sensitivity and high spatial resolution, which enable scanning microanalysis of material surfaces [1–6]. However, limitations due to matrix effects and calibration difficulty are well known.

In the case of LIBS, different mechanical, physical and chemical properties of samples can result in serious matrix effects because the resulting laser-induced plasma is a product of the very complicated process of laser-matter interaction. LIBS can be highly sensitive to these undesirable effects also because of the high density of material in the plasma [4,5]. For these reasons reliable calibration is possible only if homogeneous samples of very similar composition and morphology are analyzed, all experimental conditions are unchanged, and standard reference samples of very similar composition and structure are available [7,8].

LA-ICP-MS/OES techniques require the transport of the dry aerosol formed in the ablation process into inductively coupled plasma via carrier gas. Therefore, the signal can be adversely affected not only by unwanted processes during laser-ablation but also by particle fractionation during transport of aerosol from the ablation chamber to ICP source [9,10]. The so-called fractionation effect origins of non-stoichiometric analysis may arise from different processes: particle production from laser ablation, particle transport from the ablation cell to the ICP plasma and particle vaporization process in the ICP plasma [11,12]. To overcome fractionation occurring throughout the whole LA-ICP system, many solutions have been studied [13]. Nevertheless to improve accuracy and precision, internal standards and matrix matching are very often used to obtain quantitative results.

LA-LIBS utilizes two independent laser processes to analyze the sample. The first laser pulse has a similar role as the LA laser in LA-ICP techniques and in contrary to the traditional LIBS or double-pulse (DP) LIBS [1–6] this laser is not used to create the atomic emission signal. The ablation plume is then passed using a carrier gas to second, analytical laser-induced plasma (LIP). The novelty of the proposed LA-LIBS approach is in the complete decoupling of the sampling LA process from the analytical LIBS plasma. This technique was proposed as a novel analytical scheme in order to minimize of the sample matrix effects and signal nonlinearities associated with traditional LIBS [14].

* Corresponding author at: Department of Chemistry, Faculty of Science, Masaryk University, Kotlářská 2, 611 37 Brno, Czech Republic.

E-mail address: cndl@sci.muni.cz (K. Novotný).

To understand the formation of urinary calculi and their growth, it is important to know their mineralogical structure and elemental composition. For these purposes, many analytical methods such as X-ray fluorescence spectrometry and X-ray powder diffraction [15–18], infrared spectroscopy with Fourier transform [19–22], PIXE and PIGE [23–25], Raman spectroscopy [26] or SIMS [27] were used. Surface analysis of urinary calculi was performed using polarizing microscopy, scanning electron microscope and electron microprobe [28–30]. For the total elemental composition, atomic absorption spectrometry (AAS) was used [31]. To accomplish these techniques, methods based on laser ablation are particularly suitable for investigation of spatial distribution of matrix and trace elements. This can help to explain the emergence and growth of urinary calculi. Formation of kidney stones is basically caused by elements in abundance dissolved in the urine. Urinary calculi are divided according to matrix type into four categories, namely a) oxalates, b) phosphates c) uric acid and d) cystine. The oxalate calculi are formed by whewellite ($\text{CaC}_2\text{O}_4 \cdot \text{H}_2\text{O}$) and weddellite ($\text{CaC}_2\text{O}_4 \cdot 2 \text{H}_2\text{O}$) and accounts about 70% [32]. The phosphate kidney stones are based on struvite ($\text{MgNH}_4\text{PO}_4 \cdot 6 \text{H}_2\text{O}$) and apatite ($\text{Ca}_5(\text{PO}_4)_3(\text{OH})$; $\text{Ca}_5(\text{PO}_4,\text{CO}_3)_3(\text{OH})$) that constitute about 15–20% and 5–10% respectively. Occurrence of the other uroliths represents 10% uric acid ($\text{C}_5\text{H}_4\text{N}_4\text{O}_3$), and 1% cystine calculi ($\text{C}_6\text{H}_{12}\text{N}_2\text{O}_4\text{S}_2$) [33]. The kidney stones are also frequently occurring in mixture. The most commonly emerging mineral in kidney stones in Czech Republic is whewellite (about 73.2%). The second most common mineral is uric acid (19.6%). The third group is a mixture of whewellite, weddellite, apatite, struvite and/or uric acid (about 7.2%) [34].

The article of Pineda et al. was focused on elemental mapping of urinary stones and creating the basic maps of elemental distribution [24]. Correlations were observed between Mn, Fe, Cu, Zn and Sr in relation to Ca. These correlations showed two possible ways in distribution of these trace elements among whewellite and weddellite. Some trace elements, like As, Se, Br and Pb were evenly distributed.

The spatial distribution of elements in urinary calculi has been also examined by LA-ICP-MS using line scans [35,36]. LIBS technique was used for qualitative analysis of kidney stones in different locations (nucleus, outer shell and surface stone). Quantitative estimation of the trace elements as Cu, Mg, Zn, and Sr contents in different parts of the calculi by LIBS was also described. This method was unusable for Ca line scanning, because calibration curves for Ca were nonlinear due to the high Ca content. Commercially available standards were used for calibration [37,38].

The main purpose of this article is to demonstrate the calibration capabilities and limitations of LA-based techniques applied for spatially-resolved elemental mapping on urinary calculi cross sections. The calibration difficulty of these techniques due to matrix effects and lack of appropriate reference materials is generally known. However, information about spatial distribution of investigated elements is very often much more important than accurate (average) content measurements and semi-quantitative estimation is sufficient. From this perspective calibration with an acceptable uncertainty can be performed using calibration pellets prepared from urinary calculi, for which the bulk analysis was performed by another technique. For this comparative study the most frequently used LA-based analytical techniques were chosen, such as LIBS and LA combined with mass or optical ICP spectrometry. Moreover, some alternative techniques such as simultaneous LIBS–LA-ICP-OES and LA-LIBS were also utilized.

2. Experimental

2.1. Simultaneous LIBS and LA-ICP-OES

The simultaneous LIBS and LA-ICP-OES setups were designed by utilizing a modified and commercially available laser ablation system

UP 266 MACRO (New Wave) that consists of a pulsed Nd:YAG laser operated at a wavelength of 266 nm. The original ablation chamber was replaced with a special laboratory made chamber, which is equipped with a window for collection of LIP emission. The radiation was transported by a fiber optic system onto the entrance slit of a Czerny-Turner monochromator (Jobin Yvon, TRIAX 320) equipped with an ICCD detector (Jobin Yvon, Horiba). This combination provides a spectral resolution about 0.1 nm. The detection delay time and gate width were optimized during preliminary experiments and were set for all measurements as 1 μs and 10 μs , respectively. The spectral data were collected using five spectral windows centered at 280, 315, 450 and 588 nm for detection of emission lines Mg I 285.2 nm, Ca II 315.9 nm, Sr I 460.6 nm, Ba I 458.0 nm and Na I 588.5 nm, respectively.

As a carrier gas for transport of ablated aerosol to laterally viewed ICP-OES spectrometer (JobinYvon, 170 Ultraice) argon was used, at a flow rate of 0.6 l. min^{-1} . The 40-MHz generator was operated at a forward power of 950 W. The ICP system was equipped with a polychromator Paschen Runge (measured emission lines Mg II 280.274 nm and Ca II 393.366 nm) and monochromator Czerny Turner (measured lines Sr II 407.771 nm, Ba II 455.403 nm and Na I 588.995 nm). Mode ON-PEAK and no background corrections were used.

The ablation experiments were performed at a laser pulse repetition rate of 10 Hz, pulse energy of 20 mJ and ablation spot size of 100 μm . The ablated area was enlarged by moving the laser beam on 1 mm diameter circle with duration of 120 s for each measurement. Due to ICCD throughput and integration time, ICP measurement signals integrated for 1 s from 100 measured values were chosen for analytical evaluation of LIBS and LA-ICP-OES techniques.

2.2. LA-LIBS

For the LA-LIBS measurements, the ablation laser was a Nd:YAG laser (Big Sky, CFR 400) operating at 355 nm, 40 mJ/pulse, with a focal lens of 100 mm, focused about 25 mm below the pellet surface.

The ablation chamber was custom made from a stainless-steel vacuum chamber of a diameter equal to 3.5 cm, and the pellets were mounted to a rotation stage, pellet rotation 0.25 s^{-1} . The laser beam was translated across the pellet surface, to produce ablation tracks of different radii, thereby sampling new material.

An approximately 3.2 mm inside diameter tube allowed the argon carrier gas to enter and exit the sample chamber on opposite sides, transporting the ablation particles directly to the free-standing LIP in the adjacent sample chamber. A 6.5 cm length of tubing was used to connect the ablation chamber to the analytical LIBS chamber, thereby minimizing any sample losses during transport. A vacuum pump was used to draw argon gas through the ablation chamber and the LIBS sample chamber, with a minimum pressure drop, leaving the LIBS chamber about 0.75 Torr below atmospheric pressure. The flow rate of Ar was 0.1 l min^{-1} .

For the analytical LIBS plasma, a Nd:YAG laser (Continuum Precision II) operating at 1064 nm, 200 mJ/pulse, and focused by lens 75 mm focal length was used to create the plasma. The plasma emission was then collected by pierced mirror 100 mm 2 , and a collimation lens of 100 mm focal length was used to collect and launch the emission into a fiber optic bundle, which was subsequently coupled to a Czerny Turner spectrometer and detected with an ICCD detector (0.15 nm spectral resolution).

The ablation and analytical plasma laser pulses were synchronized in time using a digital delay generator, and the carrier gas flow rate was adjusted for optimal transport from the ablation chamber to the analytical LIBS plasma. Optimization was realized by maximizing the analyte emission signal-to-noise ratio. It is noted that with the two laser pulse synchronized to fire at the same time, the analytical

LIBS plasma is actually analyzing the ablation plume from previous ablation pulses.

The spectral data were collected using five spectral windows centered at: 280 nm (delay 30 μ s, width 30 μ s), 315 nm (delay 40 μ s, width 60 μ s), 450 nm (delay 40 μ s, width 60 μ s) and 588 nm (delay 35 μ s, width 60 μ s) for detection of emission lines Mg I 285.2 nm, Ca II 315.9 nm, Sr I 460.6 nm, Ba I 458.0 nm and Na I 588.5 nm, respectively.

2.3. LA-ICP-MS

Laser ablation was performed by UP 213 (New Wave Research, Inc., Fremont, CA, USA) ablation system. The system consists of nanosecond laser Nd:YAG operating at 213 nm and SuperCell ablation chamber (volume 18 cm³). Carrier gas (He) flow rate was controlled by a mass flow controller (Brooks) and for all experiments was set to 1 min⁻¹.

Ablation chamber was connected by 1 m long polyurethane tube (i.d. 4 mm) to the injector of plasma torch ICP of the quadrupole mass spectrometer (Agilent 7500ce, Santa Clara, CA, USA) which was equipped with collision-reaction cell for suppression of polyatomic interferences. The collision gas flow rate (He) and flow rate of reaction gas (H₂) were set to 2.5 ml min⁻¹ and 1.0 ml min⁻¹, respectively.

For ablation experiments, the hole drilling mode was used. Five square shaped (65 × 65 μ m²) ablation craters were ablated on the surface of each pellet. The duration of the ablation was 60 s for each point with a 20 s measured background. Laser beam fluence was set to 8.84 J.cm⁻² and laser shot repetition rate was 5 Hz.

The measured isotopes were ²³Na, ²⁴Mg, ^{43,44}Ca, ⁸⁸Sr, ¹³⁵Ba, ¹³⁷Ba. The integration time was 0.1 s for these elements with exception of ^{43,44}Ca, with an integration time of 0.01 s.

2.4. Samples

The set of powdered kidney stone samples belongs to the large collection (about 15,000 samples) of the Institute of Geonics, v.v.i., Academy of Sciences of the Czech Republic in Ostrava. All original kidney stones of the collection were removed from patient's body surgically and then rinsed in distilled water and dried. Some of them were slit through the crystallization nucleus. One half of sample was embedded into the epoxy resin and the cut was polished. This part of the prepared sample was used for direct elemental mapping by LA based techniques (which is out of the scope of this paper).

Powdered kidney stone samples used in this study were homogenized by rubbing in a mortar to the coarser grained material (mm) and then spread in an agate mortar. The mortar was washed after each sample with distilled water and ethanol. Because the material was soft, this method of homogenization was sufficient.

Pellets were prepared by laboratory manual hydraulic press BSL pressing about 100 mg of the same homogenized material. Pellets with a diameter of 12 mm and thickness about 2 mm were pressed for 60 s at a pressure 15 MPa.

For solution analysis by ICP-MS, 100 mg of this homogenized material was dissolved in 2 ml of concentrated nitric acid. After dissolution, five drops of 30% hydrogen peroxide was added and the mixture was boiled. Then the solution was converted into a 100 ml volumetric flask and completed with distilled water.

For solution analysis ICP-MS spectrometer Agilent 7500ce (Agilent, Santa Clara, CA, USA) was used. Concentric nebulizer MicroMist G3266-65003 (Glass Expansion, Australia) was utilized for introduction of sample solution to the ICP. Collision-reaction cell was used only in helium mode with flow rate 5.5 ml min⁻¹. The flow rate for sample solution was 0.4 ml min⁻¹. Total carbon content in the powdered samples was determined by LiquiTIC II Analyzer (Elementar Analysensysteme GmbH, Hanau, Germany). Total carbon

content and results obtained by ICP-MS solution analysis are shown in Table 1.

Content of major mineral groups was calculated from the results of chemical analysis (Mg, Ca, P, C) based on stoichiometry: magnesium phosphate group (calculated as struvite), calcium phosphate group (calculated as hydroxylapatite from P content, which is not included in struvite), calcium oxalate group (calculated as a mixture of mono- and dihydrate 1:1) and uric acid group (calculated as uric acid anhydrous). Content of the last two mineral groups was calculated from carbon content and non-phosphate residue. Mineralogical composition calculated from chemical analysis of powdered samples used for preparing of pressed calibration pellets is shown in Table 2.

3. Results and discussion

Basic information about total content and content variation of selected elements in urinary stone samples was obtained by ICP-MS solution analysis. The results of this routine technique were used for comparison with data obtained by LA based techniques. It should be noted, however, that the experimental uncertainty of these results due to calculus inhomogeneity can be considerable. On the other hand, the expected uncertainty for laser techniques was significantly larger. For the same reason, no other reference material was used for a validation procedure.

For LA-based analytical techniques, coarse grained pellets were prepared, which respect the original heterogeneity of the kidney stone and different individual structures of the stone matrix (Fig. 1). The idea was to maintain in certain level the stone structure that could be completely destroyed in case of fine grinding. Although the SEM image of the pellet surface (Fig. 1a) shows particle with sizes below 10 μ m, after LA in the ablation crater larger crystal structures can be seen (Fig. 1b). Stone milling to finer particles leads to improving the standard deviation due to better pellet homogeneity. On the other hand, coarse grained pellets are more similar to the structure of real, compact urinary calculi. Enlarged ablation area and signal averaging were used for elimination of pellets heterogeneity. The same pellets were used for all techniques.

3.1. Comparison of different laser techniques

Five sets of LIBS and LA-LIBS spectra were measured as mentioned in Section 2. Measurements in three different spectral intervals were performed for each element, on different sites of the same pellet. For all measurements, the data were averaged and the standard deviation was calculated. In the case of LA-LIBS technique, the LA process is separated from the analytical LIBS plasma. In this context we expect a reduction of matrix effects associated with traditional LIBS. In addition, comparison of LA-LIBS signal and LA-ICP-OES signal can provide information about different properties of LIP and ICP source, because sampling processes (LA) for both techniques are similar. In the case of LA-LIBS and LIBS measurements, the ablation chamber was flushed with argon flow. Only during LIBS experiments ablated aerosol was transported to ICP-OES spectrometer and measured simultaneously by ICP-OES spectrometer. To allow a direct comparison of the analytical signal for the both techniques, synchronization of measurement was necessary. The corrections of unwanted time shifts were realized subsequently.

Fig. 2 shows the comparison of LIBS and LA-LIBS signals for spectral window centered at 450 nm. For LA-LIBS signal lower background and usually narrower emission lines (see Ca lines on Fig. 2) are its characteristics. On the other hand, although the absolute intensities for LA-LIBS were about an order of magnitude lower, RSD values were also lower. As we expected, the signal correlation of these two methods was significantly dependent on the matrix of pellet and the selected elements. Best correlation was obtained for phosphate matrix in case of Ca, Sr and Ba. Surprisingly, very poor correlation

Table 1

Contents of studied elements in the powdered samples obtained by ICP-MS solution analysis and elemental analyzer.

Element	C m _{w/w} [g·kg ⁻¹]	P m _{w/w} [g·kg ⁻¹]	Ca m _{w/w} [g·kg ⁻¹]	Mg m _{w/w} [g·kg ⁻¹]	Na m _{w/w} [g·kg ⁻¹]	Sr m _{w/w} [mg·kg ⁻¹]	Ba m _{w/w} [mg·kg ⁻¹]
Powder sample							
Phosphate matrix	5056	33	177	236	428	6.32	314
	5255	30	175	238	40.7	9.60	309
	5397	11	143	3.50	101	0.223	4
	5996	28	152	128	65.4	6.87	122
	6489	29	164	183	48.2	9.08	180
	6686	35	175	211	46.6	8.06	329
	8393	23	167	201	50.9	6.66	181
	9130	28	168	232	39.0	6.20	517
Mixed matrix	5166	115	21	265	0.607	2.23	63
	6275	114	15	264	0.403	1.51	38
	7301	236	0	3.08	0.013	0.428	1
	7851	119	3	245	0.279	1.35	33
	8365	86	26	259	1.15	1.11	102
	8500	249	0	9.75	0.024	0.140	4
	9081	109	2	245	0.231	0.860	31

was found for Mg and Na. A further evaluation of these results is discussed below.

Comparison of LIBS and LA-ICP-OES signals for Sr in phosphate matrix pellet is shown in Fig. 3. From temporal profiles of Sr emission it is evident that LA-ICP-OES signal is more stable probably due to the aerosol mixing during its transport to the ICP spectrometer. On the other hand, the LIBS signal is located to a specific ablation spot and it is therefore more influenced by the inhomogeneity of the calibration pellet. However, for both temporal signals, their mutual correlation is obvious. The signals correspond to the size of crystal structures in ablation craters (Fig. 1b). After averaging of both signals the differences were eliminated, but the RSD values for LIBS measurement were generally higher than for LA-ICP-OES.

Finally, the commercial LA-ICP-MS system, which is very often used for routine laser ablation technique, was used for comparison. Ablation was performed at five different locations of the pellet, while all selected isotopes were measured successively by quadrupole analyzer. All repetition data were also averaged and standard deviation was calculated.

3.2. Correlations in phosphate matrix

As mentioned above, results from solution analysis were taken as reference values. Calibration graphs were constructed separately for both, phosphate-matrix pellets and for pellets with mixed matrix

(phosphate, oxalate and urate). On the Figs. 4 and 5 the comparison of LIBS and LA-LIBS calibration curves for Sr in phosphate matrix pellets and comparison of LA-ICP-MS and LA-ICP-OES in phosphate matrix pellets are shown. The calibration curves were constructed for each element and each method. Surprisingly, some correlation coefficients were quite poor. This was most probably caused by different reasons (see Table 3). For example, deteriorated correlation coefficients were observed in case of sodium for all methods. Remarkably poor correlations for Ca and Mg in the case of LIBS (for Mg was

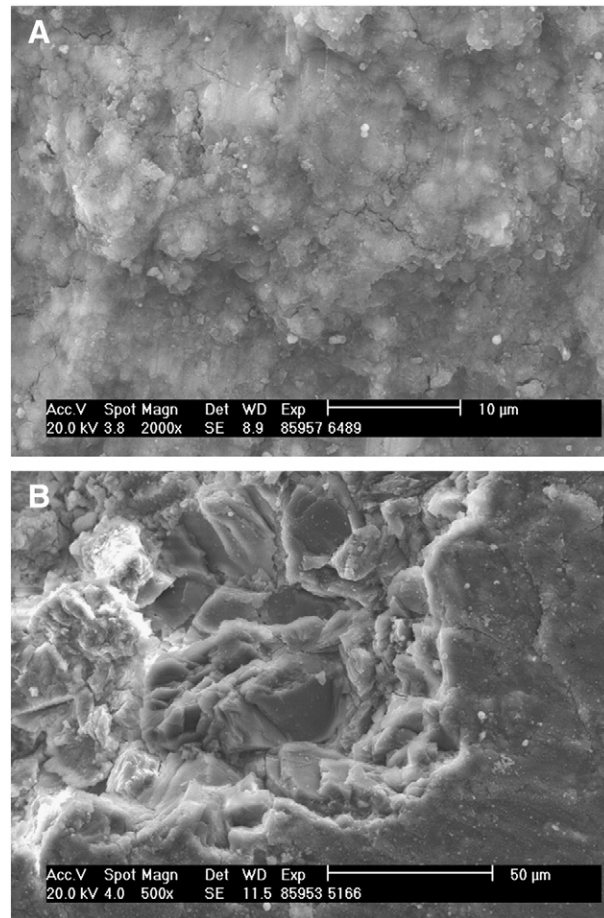


Fig. 1. SEM exposures of calibration pellets A) surface of calibration pellet (powdered sample 6489) before ablation, B) crater edge detail (powdered sample 5166).

Table 2

Mineralogical composition of studied powdered samples.

Mineral	Apatite	Struvite	Calcium oxalate	Uric acid
	Powder sample	[%]	[%]	[%]
Phosphate matrix	5056	60	40	0
	5255	61	39	0
	5397	6	94	0
	5996	35	65	0
	6489	53	47	0
	6686	56	44	0
	8393	51	49	0
	9130	61	39	0
Mixed matrix	5166	11	1	88
	6275	8	0	92
	7851	2	0	98
	8365	13	1	86
	9081	2	0	98
	7301	0	0	64
	8500	0	0	58
				42

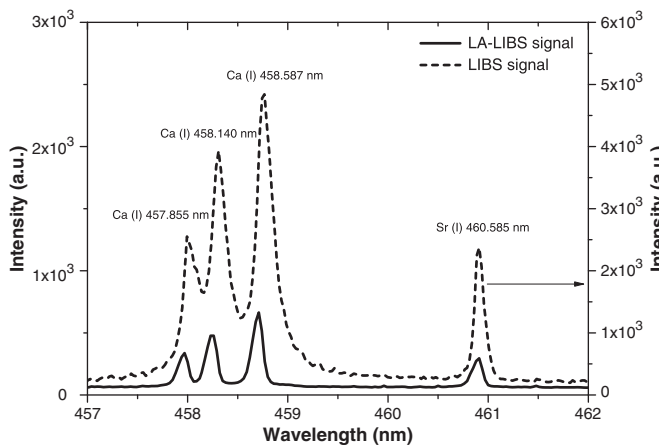


Fig. 2. Comparison of LIBS and LA-LIBS signals.

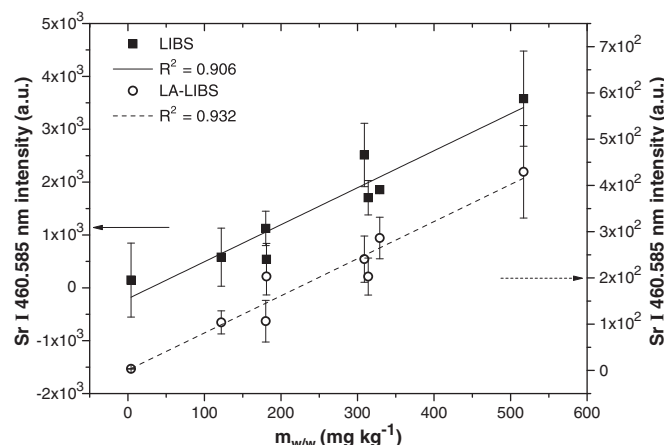


Fig. 4. Comparison of LIBS and LA-LIBS calibration curves for Sr in phosphate matrix pellets.

observed strong negative correlation for phosphate matrix) should be attributed to the high content of these elements. It should be noted, that these effects were observed even if another emission lines of Ca and Mg were used. Significant improvement was observed in case of LA-LIBS (Fig. 6). It can be deduced that problems with elements present in high content are related mainly to the LIBS technique and most probably they are connected to the processes in the LIP and self-absorption. On the other hand, in case of LA-LIBS technique where the analytical LIBS plasma is separated from LA, these undesirable effects are minimized. Also in case of methods with ICP sources these effects are suppressed.

Despite the effects mentioned above, the relatively high correlation between the LIBS and LA-LIBS methods was observed. On the other hand, somewhat unexpectedly, the correlation was worse in case of LIBS and LA-ICP-OES, despite the fact that the measurements were carried out simultaneously. This fact demonstrates that differences for individual techniques are more significant than the contribution of the pellets inhomogeneity. Slightly worse correlation between LA-ICP-OES and LA-ICP-MS techniques could be attributed to different laser ablation conditions (circle trajectory laser ablation in LA-ICP-OES measurement and ablation of five individual craters in case of LA-ICP-MS). However, in the case of ICP sources correlation coefficients for all study elements and all pellet matrixes were similar.

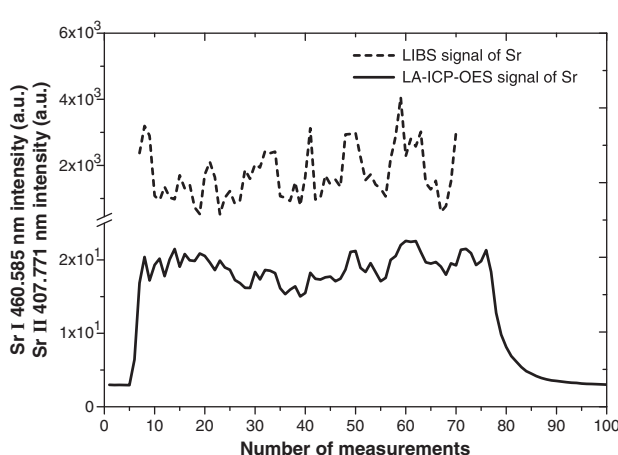


Fig. 3. Comparison of LIBS and LA-ICP-OES signals for Sr in phosphate matrix pellets. The LA-ICP-OES signal is more stable than the LIBS signal.

3.3. Influence of the mineralogical composition

The influence of the mineralogical composition was observed already during the pellets preparation. The strongest pellets were provided from powders of stones with phosphate matrix. Pellets prepared from mixed matrix stones were less rigid. The urate pressed pellets were fragile and crumbling. In this context, LA methods were most affected by increased pellet removal. In the ablation chamber large grains released from the pellets during ablation were often observed. These negative effects probably led to poorer results for calibration pellets containing oxalate and urate matrix. Some poor correlations can be attributed to the small content range of measured elements as in case of Ba in mixed matrix for LIBS (see Table 3). Due to the larger standard deviation of measurement, the correlation coefficients are very low; however, some other matrix effects deteriorated this correlation as well. In case of LA-LIBS significant improvement was observed again. In general, better results were observed for LA-LIBS than for LIBS, and ICP based techniques provided more precise results than LIBS based techniques. In this context, the very poor results for Na detection, especially in mixed matrix pellets, in the case of LA-ICP-OES and LA-ICP-MS are surprising. However, it should be noted, that most relevant improvement of correlation coefficients was observed using internal standardization for these results (see below).

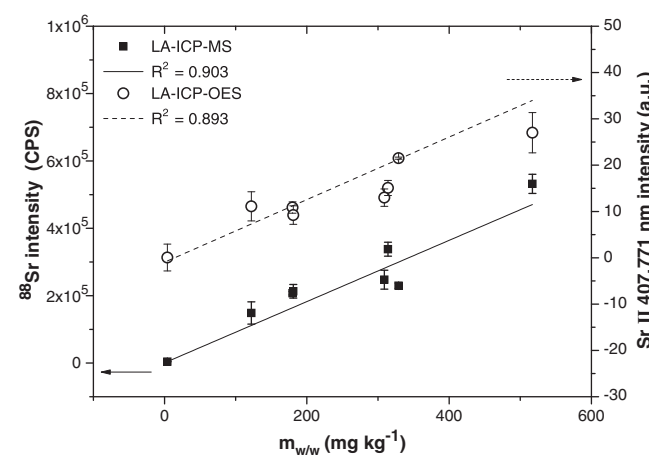


Fig. 5. Comparison of LA-ICP-MS and LA-ICP-OES calibration curves for Sr in phosphate matrix pellets.

Table 3Determination coefficients R^2 of calibration curves.

	Phosphate matrix				Mixed matrix			
	LIBS	LA-LIBS	LA-ICP-OES	LA-ICP-MS	LIBS	LA-LIBS	LA-ICP-OES	LA-ICP-MS
Ca	0.586	0.637	0.745	0.825	0.730	0.803	0.942	0.952
Sr	0.906	0.932	0.893	0.903	0.606	0.801	0.919	0.856
Ba	0.815	0.924	0.917	0.876	0.118	0.660	0.877	0.6101
Mg	—	0.907	0.930	0.738	0.459	0.884	0.766	0.600
Na	0.451	0.461	0.559	0.752	0.460	0.933	0.257	0.113

3.4. Mutual correlations of laser ablation methods

The cross-correlation study of LA based methods provides also interesting information. Pearson's correlation was used for this purpose, because it reflects the degree of linear relationship between two variables. Results for phosphate matrix and mixed matrix were combined together and used for construction of common correlation graphs for all elements. Cross correlation coefficients for Ca, Sr and Mg are shown in Table 4. The best mutual correlation coefficients for all elements were obtained for LA-ICP-OES with LA-ICP-MS. It is evident, from this point of view, that ICP sources are much more robust for these applications. Correlation coefficients for LIBS technique are strongly dependent on given element. This fact is probably due to various elemental compositions of different crystalline phases and different conditions in laser induced plasma during ablation of different crystalline structures. Good mutual correlation coefficients LIBS with LA-LIBS technique for Ca and Sr and relatively poor correlation for Mg show that LA-LIBS technique can eliminate some unwanted effects observed in traditional LIBS. These results indicate that the calibration for LIBS technique must be done with great circumspection especially in the case of elements that are present in high content.

3.5. Use of internal standardization

In order to improve the correlation coefficients, internal standardization was also used. The internal standard method was limited by the availability of a suitable reference species that must be measured simultaneously. This problem is particularly crucial for LIBS and LA-LIBS methods in the case of the spectrograph in the Czerny-Turner configuration, where only a limited spectral region of the spectrum is measured. For signal normalization, calcium as a matrix element was selected, because of its high content in all pellets. However, different calcium contents in different phases (especially in case of mixed matrix pellets) can be considerable. As

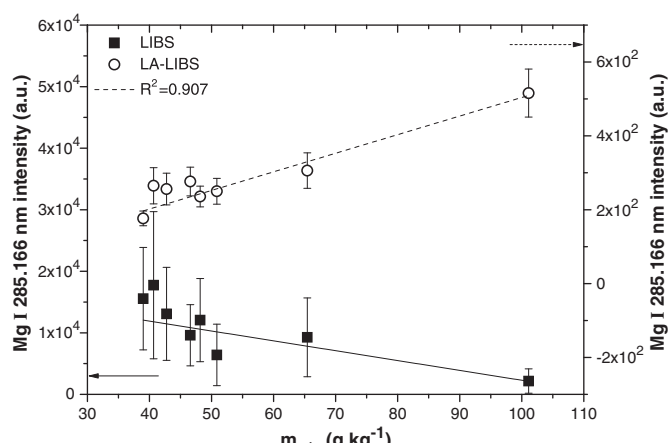
a "known", the content of reference calcium results obtained by solution analysis was used. A calibration curve was prepared so that the analyte signal was divided by the ratio of the Ca signal to the Ca known content and plotted vs. the analyte content in the pellet. In general, no improvements were observed in case of LIBS and LA-LIBS techniques. For example, in the case of LIBS regression coefficient deteriorated for all elements. In the case of LA-LIBS technique, correlation coefficients of calibration curves remained similar as in the case without internal standardization. Internal standard methods probably also degrade precision, because the overall precision depends on the reproducibility of measuring both the analyte and Ca. The reason for deterioration could be also caused by the fact that in the case of LA-LIBS and LIBS signals for all analytes and Ca could not be registered simultaneously. In the case of LA-ICP-OES and LA-ICP-MS techniques correlation coefficients have been improved in virtually all cases. Best improvement was observed in the case of Na (Fig. 7). On the other hand, it should be noted that routine use of internal standardization is limited. Accurate content of reference calcium is usually unknown and the distribution in the sample is uneven. For these reasons in the case of microanalysis or elemental mapping internal calibration is useless and can introduce significant errors.

4. Conclusions

Comparison study of laser ablation based methods was realized using urinary calculus calibration pellets. For this study, coarse grained pellets were prepared that represent the sample heterogeneity and different individual structures of matrix. Enlarged ablation area and signal averaging were used for elimination of pellet heterogeneity. Total content and content variation of selected elements in urinary calculi were obtained by ICP-MS solution analysis. The results show that LIBS technique is more affected by unwanted matrix effect than LA-LIBS and LA-ICP-OES/MS techniques. Remarkably poor calibration graphs for LIBS were obtained for matrix elements but

Table 4Laser methods cross-correlation coefficients R for: a) Ca b) Sr c) Mg.

a)	LIBS	LIBS	LIBS
	LIBS	1	LIBS
	LA-LIBS	0.7918	1
	LA-ICP-OES	0.5863	0.7521
	LA-ICP-MS	0.7502	0.8917
b)	LIBS	LIBS	LIBS
	LIBS	1	LIBS
	LA-LIBS	0.8905	1
	LA-ICP-OES	0.7752	0.8738
	LA-ICP-MS	0.8137	0.8567
c)	LIBS	LIBS	LIBS
	LIBS	1	LIBS
	LA-LIBS	0.3452	1
	LA-ICP-OES	0.0568	0.9137
	LA-ICP-MS	0.2719	0.9340

**Fig. 6.** Comparison of LIBS and LA-LIBS calibration curves for Mg in phosphate matrix pellets.

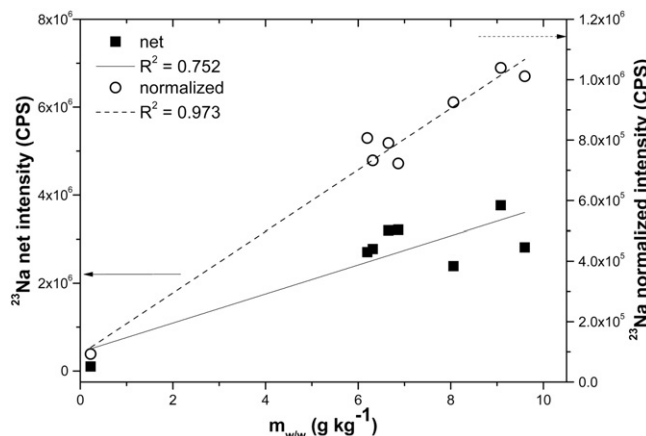


Fig. 7. Comparison of LA-ICP-MS calibration curves for Na in pellets with phosphate matrix constructed using net signal and normalized Na signal to Ca signal.

significant improvement was observed in case of LA-LIBS. In general, better results were observed for LA-LIBS than for LIBS and ICP based techniques provided more precise results than LIBS based techniques. Moreover, in the case of LA-ICP-OES and LA-ICP-MS techniques calibration correlation coefficients have been improved by using of an internal standardization.

Acknowledgment

We acknowledge the Ministry of Education, Youth and Sports of the Czech Republic for bestowing the research projects ME08002, ME10061 and the Czech Science Foundation for the project GA203/09/1394. This work was also supported by the project "CEITEC – Central European Institute of Technology" (CZ.1.05/1.1.00/02.0068) from the European Regional Development Fund. JK acknowledges the support of Brno University of Technology on the frame of grant FSI-S-11-22 (Application of advanced optical methods).

References

- [1] M. Galiova, J. Kaiser, K. Novotny, M. Ivanov, M.N. Fisarkova, L. Mancini, G. Tromba, T. Vaculovic, M. Liska, V. Kanicky, Investigation of the *Osteitis deformans* phases in snake vertebrae by double-pulse laser-induced breakdown spectroscopy, *Anal. Bioanal. Chem.* 398 (2010) 1095–1107.
- [2] M. Galiova, J. Kaiser, F.J. Fortes, K. Novotny, R. Malina, L. Prokes, A. Hrdlicka, T. Vaculovic, M.N. Fisarkova, J. Svoboda, V. Kanicky, J.J. Laserna, Multielemental analysis of prehistoric animal teeth by laser-induced breakdown spectroscopy and laser ablation inductively coupled plasma mass spectrometry, *Appl. Optics* 49 (2010) C191–C199.
- [3] M. Galiova, J. Kaiser, K. Novotny, M. Hartl, R. Kizek, P. Babula, Utilization of laser-assisted analytical methods for monitoring of lead and nutrition elements distribution in fresh and dried *Capsicum annuum* l. leaves, *Microsc. Res. Tech.* 74 (2011) 845–852.
- [4] D.A. Cremer, L.J. Radziemski, *Handbook of Laser-Induced Breakdown Spectroscopy*, Wiley, Chichester, 2006.
- [5] J.P. Singh, S.N. Thakur, *Laser-Induced Breakdown Spectroscopy*, Elsevier, Amsterdam, 2007.
- [6] J. Kaiser, K. Novotny, M.Z. Martin, A. Hrdlicka, R. Malina, M. Hartl, V. Adam, R. Kizek, Trace elemental analysis by laser-induced breakdown spectroscopy—biological applications, *Surf. Sci. Rep.* 67 (2012) 233–243.
- [7] K. Niemax, Laser ablation – reflection on a very complex technique for solid sampling, *Fresenius J. Anal. Chem.* 370 (2001) 332–340.
- [8] M. Pouzar, T. Kratochvíl, S. Kaski, J. Kaiser, P. Knotek, L. Capek, T. Cernohorsky, Effect of particle size distribution in laser-induced breakdown spectroscopy—analysis of mesoporous V-SiO₂ catalysts, *J. Anal. At. Spectrom.* 26 (2011) 2281–2288.
- [9] A. Monaster, D.W. Golightly, *Inductively Coupled Plasmas in Analytical Atomic Spectrometry*, Wiley, Hoboken, 1992.
- [10] R. Thomas, *Practical Guide to ICP-MS*, Marcel Dekker, 2004.
- [11] M. Hola, V. Konecna, P. Mikuska, J. Kaiser, V. Kanicky, Influence of physical properties and chemical composition of sample on formation of aerosol particles generated by nanosecond laser ablation at 213 nm, *Spectrochim. Acta Part B* 65 (2010) 51–60.
- [12] M. Hola, V. Konecna, P. Mikuska, J. Kaiser, K. Palenikova, S. Prusa, R. Hanzlikova, V. Kanicky, Study of aerosols generated by 213 nm laser ablation of cobalt-cemented hard metals, *J. Anal. At. Spectrom.* 23 (2008) 1341–1349.
- [13] R.E. Russo, X. Mao, H. Liu, J. Gonzales, S.S. Mao, Laser ablation in analytical chemistry – a review, *Talanta* 57 (2002) 425–451.
- [14] B.C. Windom, D.W. Hahn, Laser ablation-laser induced breakdown spectroscopy (LA-LIBS): a means for overcoming matrix effects leading to improved analyte response, *J. Anal. At. Spectrom.* 24 (2009) 1665–1675.
- [15] N.A. Pal'chik, T.N. Moroz, N.V. Maksimova, A.V. Dar'in, Mineral and microelement compositions of urinary stones, *Russ. J. Inorg. Chem.* 51 (2006) 1098–1105.
- [16] A. Abboud, Mineralogy and chemistry of urinary stones: patients from North Jordan, *Environ. Geochem. Health* 30 (2007) 445–463.
- [17] D. Bazin, P. Chevallier, G. Matzen, P. Jungers, M. Daudon, Heavy elements in urinary stones, *Urol. Res.* 35 (2007) 179–184.
- [18] A. Abboud, Analyzing correlation coefficients of the concentrations of trace elements in urinary stones, *Jordan J. Earth Environ. Sci.* 1 (2008) 73–80.
- [19] H. Perk, T.A. Serel, A. Kosar, N. Deniz, A. Sayin, Analysis of the trace element contents of inner nucleus and outer crust parts of urinary calculi, *Urol. Int.* 68 (2002) 286–290.
- [20] S. Ghosh, S. Basu, S. Chakraborty, A.K. Mukherjee, Structural and microstructural characterization of human kidney stones from eastern India using IR spectroscopy, scanning electron microscopy, thermal study and X-ray Rietveld analysis, *J. Appl. Crystallogr.* 42 (2009) 629–635.
- [21] R. Chandrajith, G. Wijewardana, C.B. Dissanayake, A. Abeygunasekara, Biomineralogy of human urinary calculi (kidney stones) from some geographic regions of Sri Lanka, *Environ. Geochem. Health* 28 (2006) 393–399.
- [22] J.R. Guerra – Lopez, J.A. Guida, C.O. Della Vedova, Infrared and Raman studies on renal stones: the use of second derivative infrared spectra, *Urol. Res.* 38 (2010).
- [23] C.A. Pineda, M. Peisach, Micro-analysis of kidney stones sequentially excreted from a single patient, *Nucl. Instrum. Meth. Phys. Res. B* 85 (1994) 896–900.
- [24] C.A. Pineda, A.L. Rodgers, V.M. Prozesky, W.J. Przybylowicz, Elemental mapping analysis of recurrent calcium oxalate human kidney stones, *Nucl. Instrum. Methods B* 104 (1995) 351–355.
- [25] M.N. Alkofahi, A.B. Hallak, Analysis of kidney stones by PIXE and RBS techniques, *X-Ray Spectrom.* 25 (1996) 225–228.
- [26] C.G. Kontoyannis, N.C. Bouropoulos, P.G. Koutsoukos, Urinary stone layer analysis of mineral components by Raman spectroscopy, IR spectroscopy, and X-ray powder diffraction: a comparative study, *Appl. Spectrosc.* 51 (1997) 1205–1209.
- [27] C.A.A. Ghuman, O.M.T. Carreira, A.M.C. Moutinho, A. Tolstogouzov, V. Vassilenko, O.M.N.D. Teodoro, Identification of human calculi with time-of-flight secondary ion mass spectrometry, *Rapid Commun. Mass Spectrom.* 24 (2010) 185–190.
- [28] Y.M.F. Marickar, P.R. Lekshmi, L. Varma, P. Koshy, Optical microscopy versus scanning electron microscopy in urolithiasis, *Urol. Res.* 37 (2009) 293–297.
- [29] Y.M.F. Marickar, P.R. Lekshmi, L. Varma, P. Koshy, Elemental distribution analysis of urinary crystals, *Urol. Res.* 37 (2009) 277–282.
- [30] Y.M.F. Marickar, P.R. Lekshmi, L. Varma, P. Koshy, EDAX versus FTIR in mixed stones, *Urol. Res.* 37 (2009) 271–276.
- [31] A. Abboud, Concentration effect of trace metals in Jordanian patients of urinary calculi, *Environ. Geochem. Health* 30 (2008) 11–20.
- [32] J. Kaiser, M. Hola, M. Galiova, K. Novotny, V. Kanicky, P. Martinec, J. Scucka, F. Brun, N. Sodini, G. Tromba, L. Mancini, T. Koristkova, Investigation of the microstructure and mineralogical composition of urinary calculi fragments by synchrotron radiation X-ray microtomography: a feasibility study, *Urol. Res.* 39 (2011) 259–267.
- [33] P.K. Pietrow, M.E. Karellos, Medical management of common urinary calculi, *Am. Fam. Physician* 74 (2006) 86–94.
- [34] J. Kuta, J. Machát, D. Benová, R. Červenka, T. Koříšková, Urinary calculi – atypical source of information on mercury in human biomonitoring, *Cent. Eur. J. Chem.* 10 (2012) 1475–1483.
- [35] K. Proksova, K. Novotny, M. Galiova, T. Vaculovic, J. Kuta, M. Novackova, V. Kanicky, Study of elemental distribution in urinary stones by laser ablation inductively coupled plasma mass spectrometry, *Chem. Listy* 106 (2012) 229–235.
- [36] M.A. Chaudhri, J. Watling, F.A. Khan, Spatial distribution of major and trace elements in bladder and kidney stones, *J. Radioanal. Nucl. Chem.* 271 (2007) 713–720.
- [37] X. Fang, S.R. Ahmad, M. Mayo, S. Iqbal, Elemental analysis of urinary calculi by laser induced plasma spectroscopy, *Lasers Med. Sci.* 20 (2005) 132–137.
- [38] V.K. Singh, A.K. Rai, P.K. Rai, P.K. Jindal, Cross-sectional study of kidney stones by laser-induced breakdown spectroscopy, *Lasers Med. Sci.* 24 (2009) 749–759.

STUDIUM DISTRIBUCE PRVKŮ V MOČOVÝCH KAMENECH TECHNIKOU LASEROVÉ ABLACE VE SPOJENÍ S HMOTNOSTNÍ SPEKTROMETRIÍ S INDUKČNĚ VÁZANÝM PLAZMATEM*

**KATEŘINA PROKSOVÁ^a, KAREL NOVOTNÝ^a,
MICHAELA GALIOVÁ^a, TOMÁŠ VACULOVIC^b,
JAN KUTA^c, MONIKA NOVÁČKOVÁ^a a VIKTOR KANICKÝ^a**

^aLaboratoř atomové spektrochemie, Ústav chemie, Přírodovědecká fakulta Masarykovy univerzity, Kotlářská 2, 611 37 Brno, ^bSředoevropský technologický institut, Masarykova univerzita, Kamenice 5, 625 00 Brno, ^cCentrum pro výzkum toxicických látek v prostředí, Přírodovědecká fakulta Masarykovy univerzity, Kotlářská 2, 611 37 Brno
viktork@chemi.muni.cz

Došlo 30.6.11, přijato 8.12.11.

Klíčová slova: laserová ablace, hmotnostní spektrometrie v indukčně vázaném plazmatu, LA-ICP-MS, biominerály, močové kameny

Úvod

Urolitiáza je bolestivé onemocnění, jehož podstatou je tvorba močových kamenů ve vylučovacím ústrojí. Tato choroba postihuje v Evropě 5 až 10 % obyvatelstva a vyznačuje se častou recidivou, což podle statistických průzkumů znamená, že se opakuje do desíti let od prvního onemocnění až u poloviny případů¹. Vznik močových kamenů má řadu příčin, včetně metabolických poruch. Zvýšení koncentrace kationtů některých prvků (Ca, Mg, K) nebo aniontů (např. šťavelanů nebo fosforečnanů) v moči má za následek vylučování mikrokryrstalů, které posléze vytvoří močový kámen. Vznik sraženin v moči závisí na pH a obsahu látek, které srážení potlačují¹. Proto je v souvislosti s tvorbou močových kamenů pozornost věnována právě sledování obsahu prvků v těle a jejich vlivu na biologické procesy.

Močové kameny jsou tvořeny anorganickými a organickými složkami. Anorganickou část představují „biokrystaly“, které jsou z fyzikálně-chemického hlediska totožné s krystaly v neživé přírodě. Organická část je tvo-

řena bílkovinami (především mukoproteiny a glykoproteiny), které vyplňují prostor mezi anorganickými krystaly^{2–4}.

Z mineralogického hlediska lze močové kameny rozdělit na šťavelany, fosforečnany či močany a jejich kombinace.

K identifikaci založené na zjištění struktury a elementárního složení močových kamenů se používá řada fyzikálně-chemických metod. Pro strukturní analýzu se uplatňuje zpravidla infračervená a Ramanova spektrometrie a rentgenová diffraktometrie^{5,6}. Pro analýzu se připraví drcením a mletím homogenní práškový vzorek. Měření analytického signálu se provádí s lisovanou tabletou nebo přímo s práškovým vzorkem. Pro prvkovou analýzu jsou využívány roztokové metody s využitím atomové absorpcní spektrometrie⁷ nebo metody hmotnostní či optické emisní spektrometrie v indukčně vázaném plazmatu. Společným rysem těchto metod je skutečnost, že se zkoumá homogenizovaný vzorek v pevném stavu nebo jako roztok a získá se tak pouze informace o průměrném prvkovém složení a zastoupení struktur (minerálů) v močovém kameni.

Pro poznání vzniku a růstu močových kamenů je důležitá historie ukládání vrstev materiálu v čase. Z tohoto důvodu je třeba doplnit informaci o průměrném mineralogickém a chemickém složení informací o prostorovém rozložení prvků a zejména minerálů. Pro mapování se používá technika laserové ablaci ve spojení s hmotnostní spektrometrií s indukčně vázaným plazmatem (LA-ICP-MS), která byla uplatněna například při studiu prostorové distribuce prvků v otolitech⁸, zubech⁹ či právě močových kamenech¹⁰.

Cílem této práce bylo ověření možnosti použití metody LA-ICP-MS pro sledování prostorové distribuce prvků na řezech močových kamenů a určení mineralogického složení vzorků. V práci je také diskutována možnost využití liniového skenu a bodové analýzy pro prvkové mapování.

Experimentální část

Laserový ablační systém

Do plazmového výboje hmotnostního spektrometru je zaváděn aerosol, který je generován ze vzorků močových kamenů zářením pulzního laseru Nd:YAG s šířkou pulsu 4,2 ns. Laser je jádrem ablačního systému UP 213 (New Wave Research, USA), který pomocí kombinace generátorů vyšších harmonických frekvencí poskytuje záření na úrovni páté harmonické frekvence (213 nm). Toto záření je fokusováno na vzorek umístěný v ablační cele (SuperCell) o objemu 33 cm³. Systém je vybaven počítačem řízeným motorizovaným posuvem ablační cely v osách x/y/z. Po výběru vzorku je snímán ve zvětšení kamerou (CCD) a zob-

* Tato práce byla úspěšně prezentována v soutěži O cenu firmy Merck 2011 za nejlepší studentskou vědeckou práci v oboře analytické chemie.

razován na monitoru.

Průtok nosného plynu (He) proudícího ablační celou je optimalizován na $1,0 \text{ dm}^3 \text{ min}^{-1}$. Nosný plyn s aerosolem je zaváděn z ablační cely do injektoru plazmové hlavice polyurethanovou hadicí o průměru 4 mm a délce 1 m. Před vstupem toku He s aerosolem do plazmové hlavice je přidáván do nosného plynu proud argonu o průtoku $0,6 \text{ dm}^3 \text{ min}^{-1}$.

ICP-MS

Aerosol je zaváděn do indukčně vázaného plazmového výboje hmotnostního spektrometru Agilent 7500ce (Agilent, Japonsko), který je vybaven kvadrupólovým analyzátorem, kolizně reakční celou a elektronovým násobičem sloužícím k detekci. Kolizně reakční cela je u přístroje Agilent 7500ce tvořena oktagónovým reakčním systémem. K odstranění polyatomických interferencí bylo využito heliového i vodíkového módu s průtoky $2,0 \text{ ml min}^{-1}$ He a $1,0 \text{ ml min}^{-1}$ H₂.

Podmínky měření pro laserovou ablaci s hmotnostní spektrometrií s indukčně vázaným plazmatem

Laserový ablační systém UP 213 umožňuje mapování povrchu ve dvou módech. Jeden mód spočívá v nepřerušované ablati s vhodnou opakovací frekvencí laserových pulsů při současném lineárním posunu vzorku optimalizovanou rychlostí. V průběhu ablacie se tedy vzorek kontinuálně posouvá, obvykle po přímce. Cílem optimalizace je dosažení pokud možno minimálního překryvu jednotlivých stop laserového paprsku na povrchu vzorku (kráterů), který je jednou z příčin omezujících laterální rozlišení metody. Volba rychlosti posunu je však omezena minimální dobou potřebnou na měření signálů, zejména v případě skenujícího hmotnostního spektrometru při měření většího počtu isotopů. Druhou příčinou zhoršující laterální rozlišení je mrtvý čas spojený s velikostí objemu ablační cely. Tento tzv. liniový sken (*line scan*) je kompromisem mezi laterálním rozlišením a rychlosťí pořízení mapy distribuce prvků. Plošná mapa se pak získá opakováním paralelních liniových skenů umístěných ve vhodné vzdálenosti od sebe. Ve srovnání s ablaci prováděnou v diskrétních bodech rozmístěných v určité vzdálenosti od sebe (rastr) je liniový sken rychlejší a je vhodný zejména pro mapování větších ploch.

Prvkové mapování pomocí diskrétních bodů pravidelně rozmístěných ve vhodné vzdálenosti (rastr bodů) se provádí tak, že je nejprve ablatováno zvolené místo po optimální době a poté je vzorek posunut o požadovanou vzdálenost. Tento mód je označován v anglosaské literatuře jako „raster mode“. Mapování pomocí rastru bodů má lepší laterální rozlišení a poskytuje dostatečnou dobu pro měření i většího počtu isotopů. Doba ablacie je však omezena zahľubováním kráteru, které způsobuje deformaci časového průběhu signálu i v případě homogenních vzorků. Močové kameny však představují složitý materiál z hlediska chemického složení, které se může měnit nejen

v rámci analyzované plochy, ale také dosažené hloubky během ablacie. Doba ablacie je volena podle počtu měřených isotopů a jejich integračních časů. Integrační čas se nastavuje podle obsahu prvku ve vzorku. Matriční prvky jsou měřeny s krátkým integračním časem (~0,01 s). U stopových prvků bývá čas delší (~0,1 s), aby zaznamenaný signál měl vyšší hodnotu intenzity. V případě, že každý isoton má být proměřen vícekrát, doba potřebná pro analýzu se dále zvyšuje. Mezi ablacemi jednotlivých bodů také vzniká další dostatečná časová prodleva pro vypláchnutí ablační cely nosným plynem. Měření v rastrovém módu klade větší nároky na čas, poskytuje však lepší laterální rozlišení.

V případě liniových skenů byla zvolena frekvence laseru 5 Hz s hustotou zářivé energie 7 J cm^{-2} . Vzorek byl posouván rychlosťí $40 \mu\text{m s}^{-1}$. Mapování bylo provedeno s průměrem laserového paprsku $65 \mu\text{m}$ a jednotlivé linie byly umístěny ve vzdálenosti $100 \mu\text{m}$.

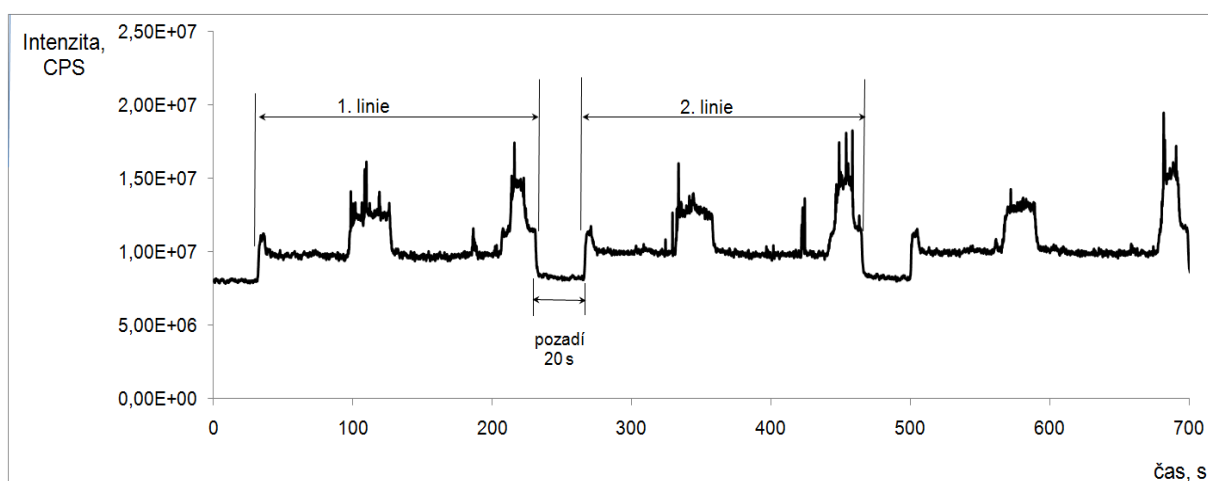
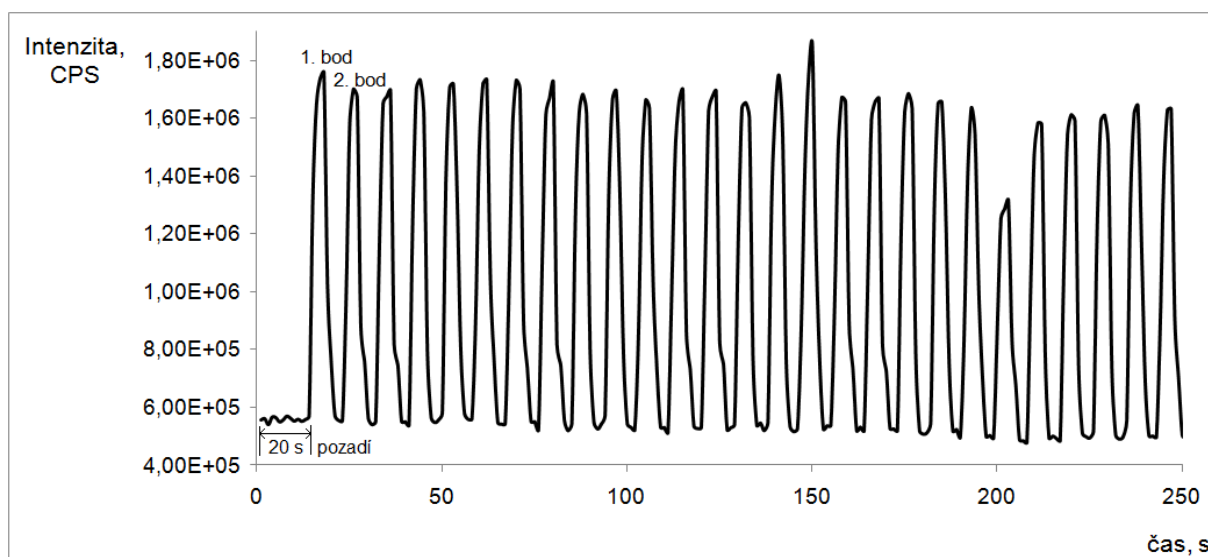
Mapování vzorků močových kamenů pomocí rastru bodů bylo provedeno s frekvencí laseru 10 Hz a průměrem laserového paprsku $65 \mu\text{m}$. Ablace do daného bodu probíhala po dobu 6 s a mezi body byla zvolena časová prodleva 8 s pro vypláchnutí ablační cely a dostatečný pokles signálu. Vzdálenost mezi krátery v ose x i y byla $65 \mu\text{m}$. Hustota zářivé energie byla nastavena na stejnou hodnotu jako v případě liniových skenů.

Vyhodnocování výsledků dosažených metodou LA-ICP-MS

Naměřená data jsou v podobě závislosti intenzity vybraných isotopů na čase. U prvkového mapování povrchu pomocí liniového skenu byla převedena závislost signálu intenzity vybraných isotopů na čase na signál odpovídající dané pozici na vzorku (obr. 1). Od každé hodnoty intenzity byla odečtena průměrná hodnota pozadí a vytvořena mapa rozložení daného isotopu na řezu (2D mapa).

Při použití módu rastru bodů je výstupem měření závislost intenzity na čase. Signál z hmotnostního spektrometru obsahuje celou řadu maxim, která musí být od sebe oddělena (obr. 2). Každé maximum odpovídá jednomu ablatovanému bodu. Problémy mohou nastat v oblastech, kde není analyzovaný prvek obsažen a místo maxim je patrný pouze signál odpovídající pozadí. V takovém případě musí být přesně určeno, kolik bodů se v takovém místě vyskytuje. Po oddělení a nalezení všech maximálních hodnot musí být proveden odečet průměrné hodnoty pozadí, které je zaznamenáváno před ablaci každého bodu (obr. 2). Celý tento proces je aplikován na všechny isotopy, které jsou předmětem studie. Po získání čistého signálu isotopů je možné na základě vzdáleností kráterů vytvořit 2D mapu rozložení daného isotopu.

Distribuce prvků ve vzorcích 11560 a 11727 byly vytvořeny pomocí liniových skenů a mapován byl celý vzorek. Pro vzorek 10806 byl použit liniový sken i rastr bodů s přesně definovanou vzdáleností, aby nedocházelo k překrývání ablatovaných ploch, a tím ke zhoršení plošného rozlišení.

Obr. 1. Závislost intenzity isotopu ^{12}C na čase při ablaci liniovým skenem povrchu vzorku 11727Obr. 2. Závislost intenzity isotopu ^{12}C na čase při bodové analýze řezu vzorku 10806

Zpracovaná data byla použita pro tvorbu 2D map rozložení isotopů Ca, P, C, Mg, Sr na řezech močových kamenů, k tomuto účelu byl použit program GRAMS 32.

Elektronová mikrosonda

Jako srovnávací metoda byla použita elektronová mikrosonda Cameca SX 100. Analýzou byl získán procentuální obsah prvků. Měření bylo provedeno na pracovišti Ústavu geologických věd Přírodovědecké fakulty Masarykovy univerzity.

Elektronová mikrosonda (EMPA) je vybavena optickým mikroskopem a sestavena z pěti vlnově-disperzních a jednoho energiově-disperzního detektoru, detektoru zpět-

ně odražených elektronů, sekundárních elektronů a katodoluminiscenčního detektoru. Optický mikroskop je napojen na CCD kameru, kterou je možno pozorovat vzorek.

Podmínky měření byly následující: urychlovací napětí 15 keV, proud svazku 10 nA a průměr paprsku 7 μm .

Vzorky

Vzorky močových kamenů pocházejí ze sbírky prof. Ing. Petra Martince, CSc. z Ústavu geoniky AV ČR v Ostravě. Ze vzorku byla odebrána reprezentativní část pro analýzu infračervenou spektrometrií, kterou byly určeny hlavní složky močového kamene. Pro analýzu LA-ICP-MS technikou byl močový kámen rozříznut nejlépe přes krys-

Tabulka I

Mineralogické složení močových kamenů získané metodou infračervené spektrometrie

Číslo vzorku	Složení vzorku
11560	25 % dahllit $[\text{Ca}_5(\text{PO}_4,\text{CO}_3)_3(\text{OH})]$
	25 % amorfní apatit $[\text{Ca}_5(\text{PO}_4)_3(\text{OH})]$
	50 % whewellit $[\text{Ca}(\text{C}_2\text{O}_4)_2 \cdot \text{H}_2\text{O}]$
11727	90 % whewellit $[\text{Ca}(\text{C}_2\text{O}_4)_2 \cdot \text{H}_2\text{O}]$
	10 % amorfní apatit $[\text{Ca}_5(\text{PO}_4)_3(\text{OH})]$
10806	90 % kyselina močová $[\text{C}_5\text{H}_4\text{N}_4\text{O}_3]$
	10 % whewellit $[\text{Ca}(\text{C}_2\text{O}_4)_2 \cdot \text{H}_2\text{O}]$

talizační jádro, aby zastoupení přírůstových linií bylo kompletní. Polovina vzorku byla zalita do epoxidové pryskyřice. Analyzované vzorky močových kamenů a jejich mineralogické složení je shrnuto v tab. I.

Výsledky a diskuse

Distribuce prvků na řezu vzorku 11560 s oválným tvarom, světle běžovým zbarvením a vrostlými světlými krystaly byla získána ablaci liniovými skeny. Tento vzorek je tvořen z 25 % dahllitem, 25 % amorfním apatitem a 50 % whewellitem. Z rozložení ^{12}C (obr. 3a) a ^{31}P (obr. 3b) lze pozorovat, že maximální hodnoty intenzity ^{31}P odpovídají minimálním hodnotám intenzity ^{12}C a naopak. Na základě mineralogického složení je možné usuzovat, že zvýšení intenzit ^{12}C v oblasti výskytu ve vzorku odpovídají přítomnosti šťavelanu vápenatého. Místa s nejvyšší intenzitou ^{12}C byla detegována v pryskyřici, kde je uhlík také obsažen. Zvýšení intenzity isotopu ^{12}C uvnitř vzorku je pravděpodobně způsobeno přítomností praskliny. Oblasti s maximálním signálem ^{31}P pak naznačují přítomnost fosforečnanu. Podle mineralogické analýzy se může jednat o dahllit nebo apatit, ale díky podobnému prvkovému složení není rozlišení těchto dvou fází pouze na základě laserové ablace jednoznačné.

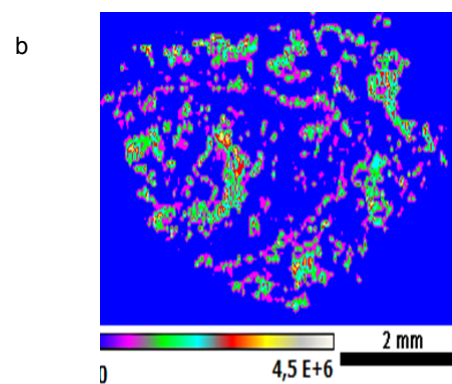
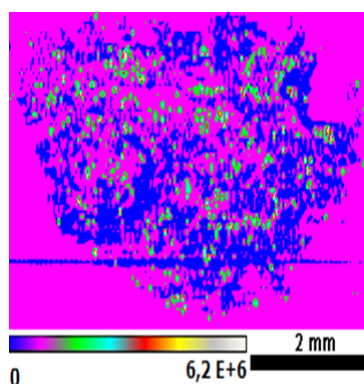
Prvkové mapování pomocí liniového skenu bylo také provedeno na řezu vzorku 11727 s hnědými úlomky a světlými krystaly. Z hlediska mineralogického složení se jedná o vzorek s 90 % šťavelanu vápenatého a 10 % amorfního apatitu. Rozložení ^{12}C (obr. 4a) ukazuje vyšší podíl šťavelanu v analyzované ploše vzorku. Z korelace mezi ^{12}C (obr. 4a) a ^{44}Ca (obr. 4b) lze vyvodit, že je zde obsažen šťavelan vápenatý. Výjimkou jsou oblasti se sníženou intenzitou ^{44}Ca , kde vzorek není na povrchu nábrusu a močový kámen je tak pomyslně rozdělen na dvě části. Menší část močového kamene je tvořena také fosforečnem, což potvrzuje distribuce ^{31}P . Nejvyšší hodnoty intenzit byly detegovány v malých oblastech. Na obr. 4d je jedna z oblastí vyznačená kruhem. Z 2D map lze potvrdit korelací hořčíku (obr. 4c), stroncia (obr. 4e), sodíku (obr. 4f) s fosforečnem (obr. 4d). Může se jednat o směsný fosforečnan, kde jsou ionty Ca^{2+} nahrazovány jinými nebo ionty mohou tvořit samostatné minerály. Distribuce isotopů ^{24}Mg (obr. 4c), ^{88}Sr (obr. 4e) a ^{23}Na (obr. 4f) ukazuje tedy na jejich asociaci s fosforečnany. Podobná asociace je pozorována i u ^{24}Mg a ^{88}Sr v oblasti šťavelanu.

Zvýšení intenzity měřených isotopů může být také způsobené rozdílnou tvrdostí a strukturou vzorku v daných místech. Ověření vyšší inzenzity a tedy i vyššího obsahu

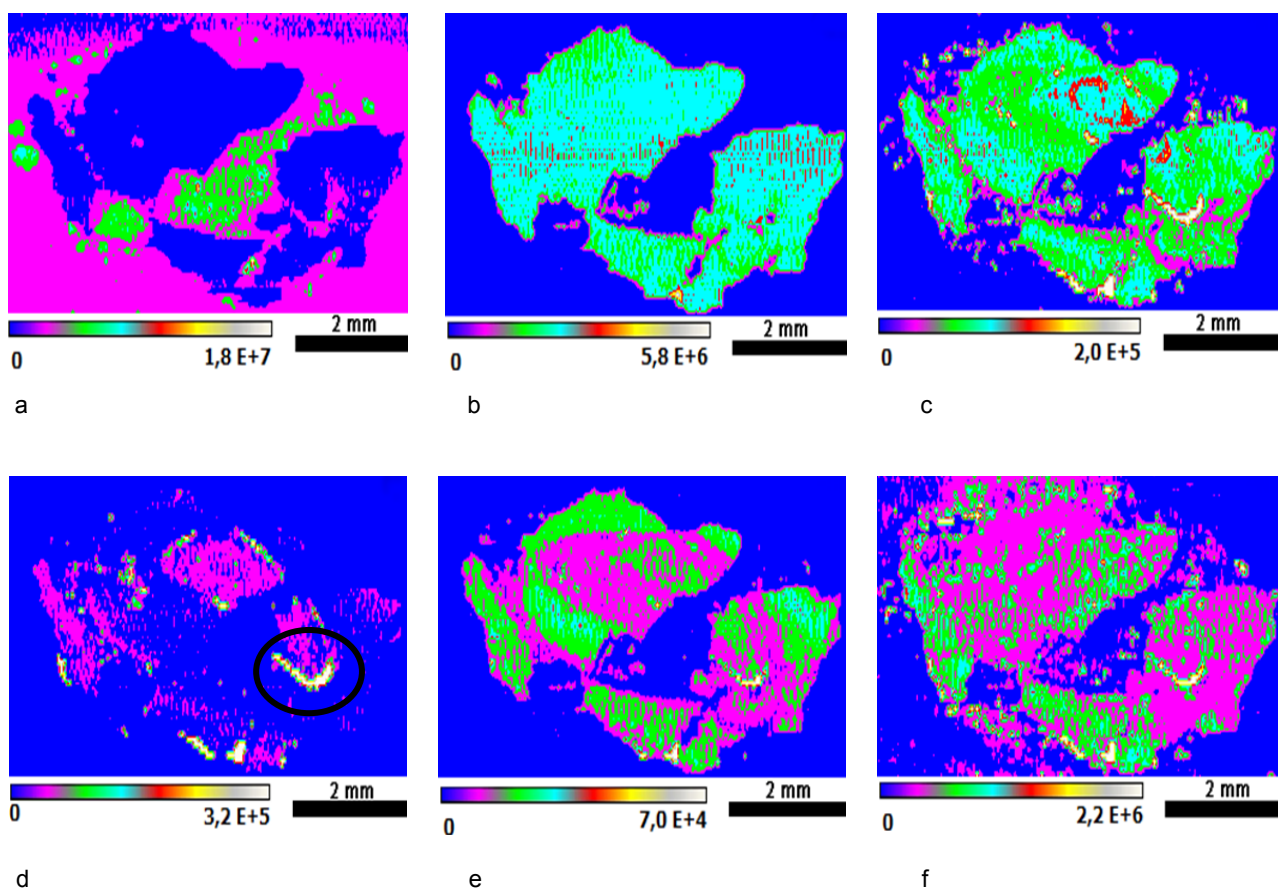
Tabulka II

Hodnoty obsahu prvků ve čtyřech bodech výbrusu vzorku 11727 (vyjádřené v hmotnostních procentech) stanovené měřením metodou EMPA

Prvek	Označení bodu [% m/m]			
	1	2	3	4
Na	0,44	0,56	0,96	neměřeno
Mg	0,22	0,26	0,44	0,03
Ca	29,18	27,74	33,18	28,78
K	0,07	0,08	0,12	0,03
P	14,03	13,6	17,67	0,37
Sr	< LOD	< LOD	0,05	0,04
Součet	76,52	74,16	92,01	41,59



Obr. 3. Distribuce isotopu a) ^{12}C , b) ^{31}P na povrchu vzorku 11560 po ablaci s liniovým skenem

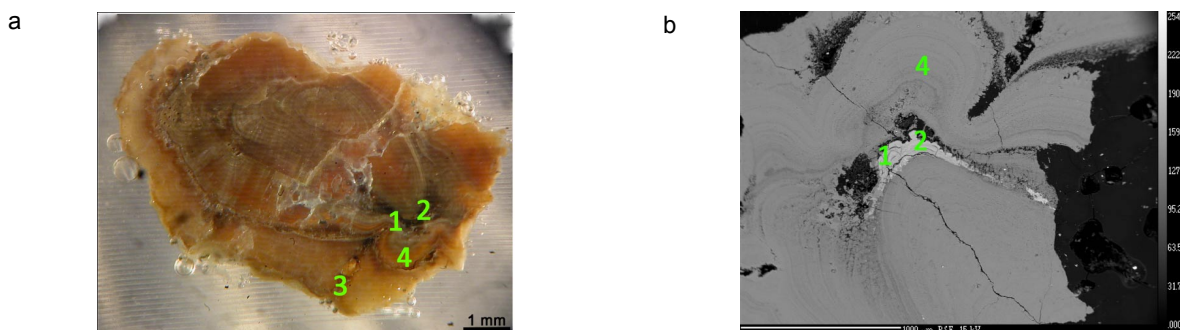


Obr. 4. Distribuce isotopu a) ^{12}C , b) ^{44}Ca , c) ^{24}Mg , d) ^{31}P , e) ^{88}Sr , f) ^{23}Na na povrchu vzorku 11727 po ablaci s liniovým skenem

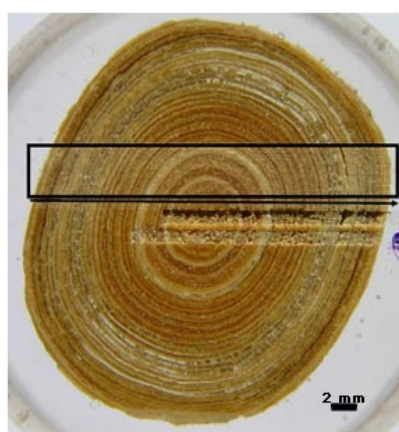
prvků v jednotlivých oblastech bylo provedeno metodou EMPA a tím mohla být potvrzena přítomnost štavelanu a fosforečnanu.

Analýza vzorku 11727 metodou EMPA byla provedena ve 4 různých bodech (obr. 5a, 5b) tak, aby byla zahrnuta fosforečnanová i štavelová fáze. Prvky byly vybrány s ohledem na možnost prokázání korelací pozorovaných

v mapách získaných pomocí LA-ICP-MS (viz tab. II). S výjimkou těchto prvků byly sledovány také obsahy prvků, které nebyly předmětem zájmu a nejsou tak zahrnutý do tab. II (Si, As, Al, Cl, Mn, Fe, Zn, V, F, S, Ba, Pb a O). Rozdílné fáze jsou patrné již ze snímku pořízeného pomocí zpětně odražených elektronů (obr. 5b). V bodech 1 a 2 byly zjištěny dvakrát nižší obsahy Na a Mg než v bodě 3.



Obr. 5. a) Místa analyzovaná elektronovou mikrosondou na řezu vzorku 11727, b) snímek povrchu vzorku 11727 získaný pomocí BSE



Obr. 6. Vzorek 10806 po ablaci s liniovým skenem

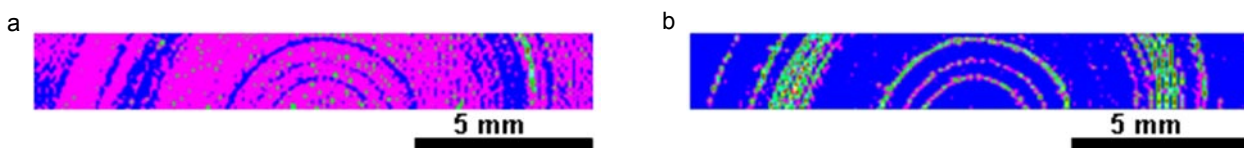
Zároveň v bodě 3 byl detegován vyšší obsah Ca až o 5 %. Ve všech případech se jedná podle obsahu P o fosforečnanovou fázi, ale suma všech prvků ukazuje na různý podíl OH^- a CO_3^{2-} skupin. Podle obsahu fosforu v bodě 4 lze usuzovat na přítomnost šťavelanu vápenatého jako hlavního minerálu. Dvakrát nižší intenzita signálu naměřená pomocí LA-ICP-MS metody v bodech 1 a 2 ve srovnání s intenzitami v bodě 3 není způsobena nižší ablaci rychlostí, tj. menším množstvím ablatovaného materiálu, ale nižším obsahem fosforu, jak potvrzuje výsledky EMPA.

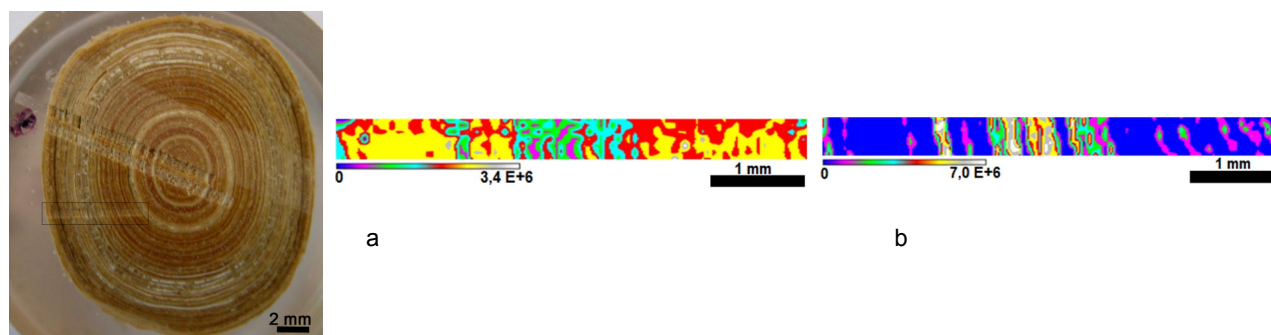
Močové kameny mohou být tvořeny kromě šťavelanu a fosforečnanu také kyselinou močovou a jejími solemi. Z důvodu porovnání byl pro další analýzu vybrán vzorek 10806, který obsahuje z 90 % kyselinu močovou a 10 % whewellit a apatit. Od ostatních vzorků se liší i strukturou, kdy při přípravě vzorku k analýze bylo přesně zachyceno krystalizační jádro a je patrné střídání vrstev jednotlivých minerálů, a to kyseliny močové a šťavelanu vápenatého (obr. 6). Tvar vzorku je oválný o velikosti 20×6 mm s hladkým povrchem a vyznačuje se zonalitou. Zbarvení kamene je světle žlutohnědá a kůra na další přírůstkové zóně okrově hnědá. Liniový sken byl proveden přes středovou část podél celého řezu vzorku (obr. 6). Rozložení ^{12}C (obr. 7a) naznačuje obsah kyseliny močové v oblastech s vyšším signálem ^{12}C . Oblasti, kde dochází k poklesu intenzity signálu ^{12}C , korespondují s místy, kde je patrný nárůst signálu isotopu vápníku (obr. 7b).

Ionty Ca^{2+} jsou obsaženy pouze ve šťavelanu. Z distribuce těchto dvou prvků je tedy patrná zonalita močového kamene a jeho postupný růst. Velikost jednotlivých zón je však velmi malá (desítky μm v závislosti na zóně) a veškeré změny ve složení nemusí být díky liniovému skenu zaznamenány.

Z tohoto důvodu byla část vzorku ablatována podle předem nastaveného rastru bodů (obr. 8). Velikost bodu byla zvolena stejně jako v případě liniového skenu ($65 \mu\text{m}$) a jejich vzdálenost byla nastavena tak, aby se jednotlivé ablaci krátery dotýkaly okrajovými částmi a tím byla minimalizována ztráta informací o prostorové distribuci prvků. Rozložení ^{12}C (obr. 8a) opět odhaluje oblasti s kyselinou močovou, a to především u okrajů ablaciho rastru. Mapa isotopu ^{44}Ca ukazuje vhodnou volbu vzdálenosti kráterů při prvkovém mapování, protože odhaluje nejen přítomnost šťavelanu vápenatého, ale také jeho velmi jemnou strukturu (obr. 8b). Z distribuce isotopu vápníku je patrné, že šťavelanová fáze není souvislá, ale je prorostlá velmi úzkými vrstvami kyseliny močové, což také potvrzuje fluktuace signálu isotopu uhlíku. Procentuální obsah uhlíku v kyselině močové je o 20 % vyšší než u whewellitu.

Při porovnání režimu měření liniového skenu či bodové analýzy jsou patrné výhody i nevýhody obou metod. V případě liniového skenu je značnou nevýhodou překryvání ablatovaných bodů, kde při zvolených podmínkách (rychllosť posunu vzorku $40 \mu\text{m s}^{-1}$) připadá 125 bodů na 1 mm vzorku a odpovídá překrytí ablaciho kráterů z 88 %. Tím dochází ke zhoršení plošného rozlišení a mapa se jeví jako rozmytá (obr. 3a). Při zvýšení rychlosti posunu vzorku je minimalizováno překrytí jednotlivých ablaciho kráterů, ale v závislosti na integračních dobách pro jednotlivé isotopy a jejich počtu může nastat zhoršení informace o jejich prostorovém rozložení v důsledku sekvenčního měření signálů. U bodové analýzy je hlavním problémem velká časová náročnost jak měření, tak i vyhodnocování. Rozlišení u bodové ablaci je dáno rozměry kráterů a jejich vzdálenostmi. V případě nastavení vzdáleností tak, že body budou těsně vedle sebe bez překryvu, je možné zachytit i velmi jemnozrnnou strukturu močového kamene. Vzhledem k tomu, že jsou vzorky močových kamenů často rozměrově velké, pro mapování celého řezu se jeví jako vhodné celý vzorek ablatovat liniovým skenem. U ploch, které se vyznačují zajímavými asociacemi mezi prvky, je třeba zvolit bodovou analýzu a preferovat zlepšení plošným rozlišením.

Obr. 7. Distribuce isotopu a) ^{12}C , b) ^{44}Ca na povrchu vzorku 10806 po ablaci s liniovým skenem



Obr. 8. Vzorek 10806 po bodové ablaci. a) Distribuce isotopu ¹²C, b) ⁴⁴Ca na povrchu vzorku 10806 po bodové ablaci

Závěr

Byly použity dva módy mapování, a to pomocí liniového skenu a bodové ablacie. Každá analýza má své výhody i nevýhody. Pro větší vzorky je z hlediska časové náročnosti vhodnější využití liniového skenu. V případě detekce jemné struktury je třeba dosáhnout vhodného plošného rozlišení a volit ablaci rastru bodů. Jednotlivé analytické úkoly musí být tedy řešeny v závislosti nejen na velikosti vzorku, ale také s ohledem na získání požadované informace a plošného rozlišení.

Pomocí LA-ICP-MS metody byly rozlišeny tři fáze (fosforečnan, šťavelan a kyselina močová) přítomné ve vzorcích močových kamenů a nalezeny asociace vybraných prvků podle změn signálu jejich isotopů.

Lze pozorovat korelace mezi Ca a C, která dokazuje na přítomnost whewellitu nebo weddellitu a korelace Ca a P na obsah apatitu. Byly zde potvrzeny i korelace mezi prvky Na a P, Sr a P, Mg a P a pravděpodobně se tedy jedná o prvky v asociaci s apatity. Výsledky byly potvrzeny měřením elektronovou mikrosondou.

Autoři děkují Grantové agentuře České republiky za podporu projektu GA203/09/1394 a Ministerstvu školství, mládeže a tělovýchovy České republiky za podporu výzkumného záměru MSM0021622412 a projektu ME08002 v programu KONTAKT.

Poděkování patří také Petru Martincovi za poskytnutí vzorků močových kamenů a analýzy infračervenou spektrometrií a Petru Gadasovi za pomoc při měření na elektronové mikrosondě.

LITERATURA

- Kasidas G. P., Samuell C. T., Weir T. B.: Ann. Clin. Biochem. 41, 91 (2004).
- Zvara V., Révusová V.: Močové konkrementy. Veda, Bratislava 1988.

- Giachelli C. M., Steitz S.: Matrix Biology 19, 615 (2000).
- Michalec Č.: Močový sediment a močové konkrementy. AVICENUM, Praha 1988.
- Carmona P., Bellanato J., Escolar E.: Biospectroscopy 3, 331 (1997).
- Tunney M. M., Bonner M. C., Keane P. F., Gorman S. P.: Biomaterials 17, 1025 (1996).
- Perk H., Serel T. A., Kosar A., Deniz N., Sayin A.: Urol. Int. 68, 286 (2002).
- Campana S. E., Thorrold S. R.: Can. J. Fish. Aquat. Sci. 58, 30 (2001).
- Lochner F., Appleton J., Keenan F., Cooke M.: Anal. Chim. Acta 401, 299 (1999).
- Chaudhri M. A., Watling J., Khan F. A.: J. Radioanal. Nucl. Chem. 271, 713 (2007).

K. Proksová, K. Novotný, M. Galiová, T. Vaculovič, J. Kuta, M. Nováčková, and V. Kanický (*Department of Chemistry, Faculty of Science, Masaryk University, Brno; Central European Institute of Technology (CEITEC), Masaryk University, Brno; Research Centre for Toxic Compounds in the Environment (RECETOX), Masaryk University, Brno*): **Study of Elemental Distribution in Urinary Stones by Laser Ablation Inductively Coupled Plasma Mass Spectrometry**

The title technique (LA-ICP-MS) is suitable for mapping of elemental distribution in urinary stones. Two ablation modes have been compared, namely line scan and raster of isolated ablation spots. The correlation between some elements made it possible to estimate the proportions of particular minerals in the urinary stones. The results will be used for comprehensive evaluation of the emergence and growth of urinary stones.

STUDIUM DISTRIBUCE PRVKŮ V MOČOVÝCH KAMENECH S VYUŽITÍM LASEROVÉ ABLACE VE SPOJENÍ S ICP-MS SPEKTROMETRIÍ

**KATEŘINA PROKSOVÁ, KAREL NOVOTNÝ,
MICHAELA GALIOVÁ, TOMÁŠ VACULOVIC
a VIKTOR KANICKÝ**

*Ústav chemie, Přírodovědecká fakulta, Masarykova univerzita, Kotlářská 2, 611 37 Brno
Katerina.Proksova@seznam.cz*

Úvod

Tvorba močových konkrementů ve vylučovacím ústrojí je nemoc známá jako urolitiáza. Jedná se o velmi bolestivé onemocnění, které postihuje v Evropě 5–12 % populace a často se opakuje, až z 50 % do deseti let¹. Formování kamenů většinou nastává v důsledku metabolické poruchy, kde jsou v nadměrně vysokém obsahu některé prvky, např. Ca, Mg, K, Pb a jiné². Ovšem některé kovy jsou přirozeně přítomny v lidském těle a jsou nezbytné pro jeho zdraví. Více než 40 chemických prvků má vliv na biologické funkce lidského těla. Tyto prvky mají různou koncentraci a funkci. Nízký obsah některých stopových prvků negativně ovlivňuje biologické procesy v těle. V poslední době je věnována pozornost právě studiu koncentrací stopových prvků v těle a jejich vlivu na procesy, mezi které patří i urolitiáza³.

Močové kameny se zařazují do několika skupin podle jejich polohy v močovém ústrojí a chemického složení. Podle rozmístění to jsou nefrolithiáza, kalikolithiáza, pyelolithiáza, ureterolithiáza, cystolithiáza, prostatolithiáza a uretrolithiáza. Mezi nejčastější typy kamenů patří vápenaté oxaláty a fosfáty. Dalším typem jsou méně časté struvitové kameny tvořeny při infekci močových cest. Mezi méně časté než struvitové se řadí urátové kameny a ke vzácným kamenům patří cystinové. Aby se zabránilo dalšímu tvoření ledvinových kamenů, je důležité zjistit jejich složení⁴.



Obr. 1. Neupravený močový konkrement

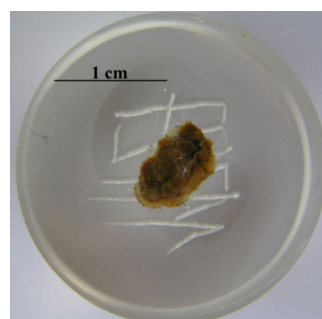
K identifikaci je možno použít řadu spektrometrických metod, jak pro zjištění struktury, tak i elementárního složení. Pro strukturální analýzu byla použita infracervená a Ramanova spektrometrie, rentgenová difrakce^{5,6}, zatímco pro prvkové složení byly použity metody indukčně vázaného plazmatu s hmotnostní nebo optickou emisní detekcí, dále pak atomová absorpční spektrometrie⁷. Nevýhodou metod je příprava a odběr reprezentativního vzorku a také velká spotřeba vzorku.

Nejvýznamnější nevýhodou je ztráta informací o prostorovém rozložení prvků v těchto kamenech. Znalost o prostorové distribuci elementárních složek ledvinových kamenů je nezbytné pro pochopení vzniku, mechanismu růstu a pro následnou diagnózu. Za tímto účelem byla použita metoda LA-ICP-MS (Laser Ablation Inductively Coupled Plasma Mass Spectrometry) pro detekci a určení korelace prostorově distribuovaných majoritních a stopových prvků přítomných v ledvinových konkrementech^{8,9}.

Experimentální část

Pro LA byl použit ablační systém UP213 (New Wave Research, USA) vybavený laserem Nd:YAG emitujícím záření 213 nm na páté harmonické frekvenci. Vytvořený aerosol byl vnášen pomocí He do indukčně vázaného plazmatu s hmotnostním kvadruplovým analyzátem a detektorem elektronovým násobičem Agilent 7500ce (Agilent, Japan). Optimalizované parametry, během měření byly neměnné: integrační čas 0,01 s, frekvence 5 Hz, rychlosť posuvu vzorku $40 \text{ } \mu\text{m s}^{-1}$, hustota zářivého toku $6,56 \text{ J cm}^{-2}$ a průměr laserového paprsku $65 \mu\text{m}$. Byla použita kolizní cela v heliovém a vodíkovém módu. Průtok H₂ byl 1 ml min^{-1} a He 2 ml min^{-1} .

Měřenými isotopy vybraných prvků byly: ^{12}C , ^{23}Na , ^{24}Mg , ^{31}P , ^{39}K , ^{43}Ca , ^{44}Ca , ^{55}Mn , ^{56}Fe , ^{63}Cu , ^{66}Zn , ^{88}Sr , ^{109}Ag , ^{118}Sn , ^{208}Pb .



Obr. 2. Vyleštěný řez močového konkrementu zalitého v epoxidové pryskyřici

Všechny vzorky močových kamenů analyzovaných LA-ICP-MS byly chirurgicky vyjmuty z těla pacienta. Poté, co je kámen vyjmut, je opláchnut vodou a osušen. Část vzorku je analyzována infračervenou spektroskopíí, díky které se zjistí hlavní složení močového konkrementu. Výsledky jsou zaevidovány a vzorek i s evidenčním číslem poslán na univerzitu. Všechny vzorky pocházejí ze sbírky prof. Petra Martince, ÚGN Ostrava. Pro analýzu pomocí LA-ICP-MS je nutné celé vzorky (obr. 1) rozříznout, nejlépe přes krystalizační jádro, aby složení přírůstových linií byla kompletní, dále zalít do epoxidové pryskyřice a vyleštít rez (obr. 2).

Byly vybrány vzorky 11726 a 11684.

Vzorek 11726 je močový konkrement běžové barvy. Na povrchu je whewellit pokrytý vrstvičkou apatitu. V průřezu nejsou viditelné koncentrické vrstvy, ani zde není viditelné krystalizační jádro, jsou zde viditelné póry na několika místech. Hlavními složkami je whewellit se stopami apatitu.

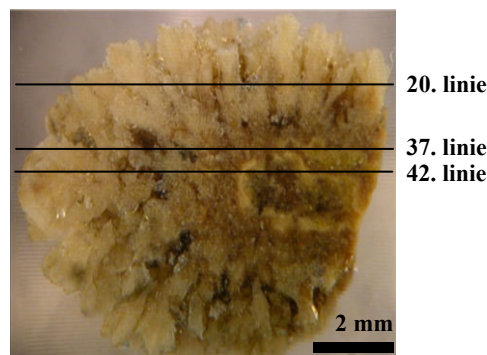
Vzorek 11684 má skořicové hnědé jádro, půrovité, s tmavším hnědým okrajem, ze kterého vyrůstají krystaly radiálně se světle krémovou barvou. Hlavními složkami je weddellit (95 %) a kyselina močová (5 %).

Výsledky a diskuse

Z rozložení matricových a stopových prvků a korelací mezi sebou lze pomocí LA-ICP-MS určit mineralogické složení.

Na vzorku 11684 (obr. 3) byla provedena analýza jednotlivých linií a určeno minerální složení.

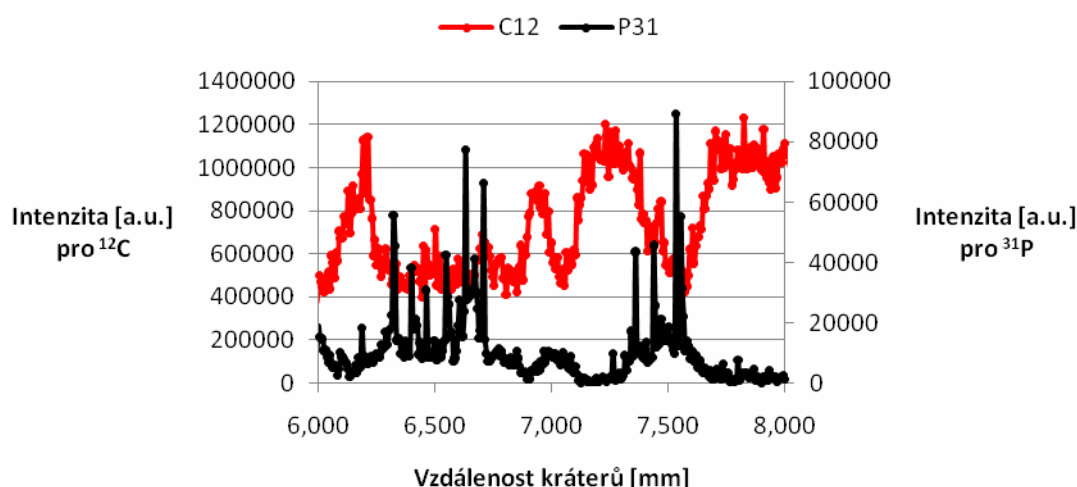
Z obr. 4 vyplývá, že maximální intenzita ^{12}C odpovídá



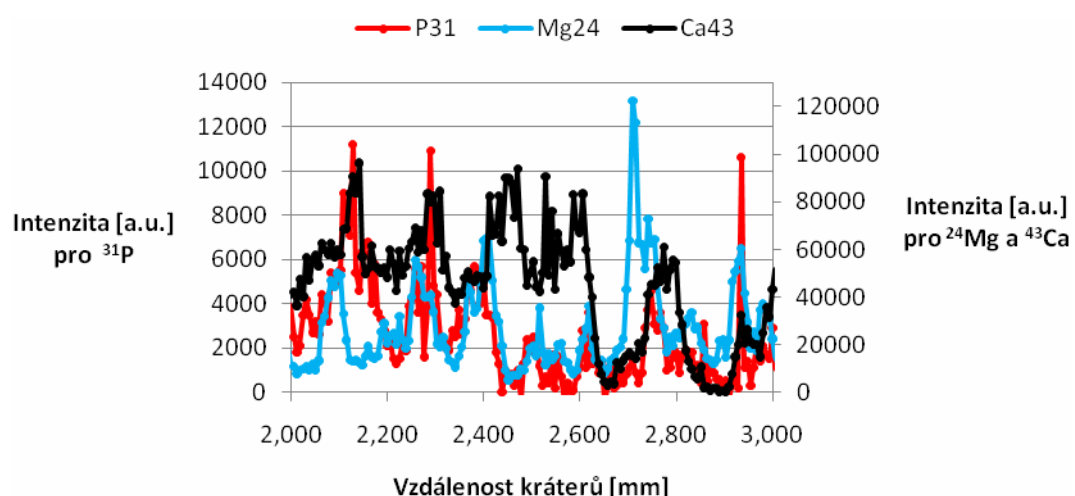
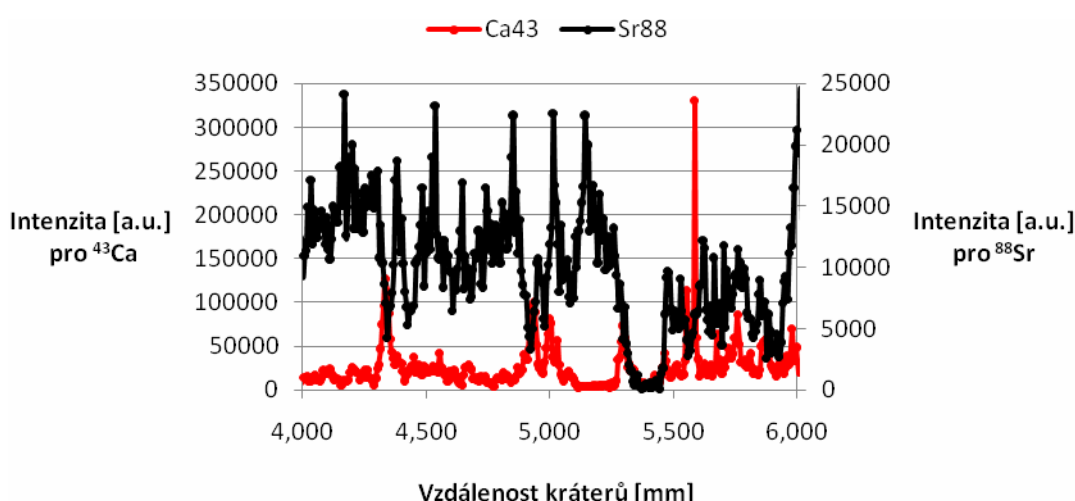
Obr. 3. Analyzovaný vzorek 11684

dá minimální intenzitě ^{31}P , což je způsobeno rozdílným složením močového konkrementu v příslušné linii. Maximální hodnoty intenzit ^{12}C odpovídají obsahu kyseliny močové nebo oxalátů a maximální hodnoty ^{31}P obsahu apatitu nebo struvitu. Je zde prokázána korelace mezi ^{43}Ca a ^{31}P , což dokazuje na přítomnost apatitu (obr. 5). Korelace mezi ^{24}Mg a ^{31}P ukazuje na obsah struvitu, ale je pouze jen v některých místech, proto bude pravděpodobně zařazena v nižším obsahu než apatit (obr. 5). Pokud srovnáme průběh intenzit pro ^{88}Sr a ^{43}Ca , zjistíme, že maxima ^{88}Sr odpovídají minimům ^{43}Ca a naopak. Pravděpodobným důvodem je nahrazen Ca^{2+} v krystalové mřížce za Sr^{2+} , který má podobný iontový poloměr a náboj (obr. 6).

Abychom získali lepší představu o prostorovém rozložení matricových a stopových prvků, byly vytvořeny 2D mapy pro jednotlivé měřené isotopy pro močový konkrem-



Obr. 4. Graf znázorňující rozložení isotopu ^{12}C a ^{31}P v 37. linii močového kamene 11684

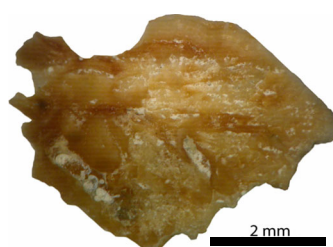
Obr. 5. Graf znázorňující rozložení isotopů ^{24}Mg , ^{43}Ca a ^{31}P v 42. linii močového kamene 11684Obr. 6. Graf znázorňující rozložení isotopů ^{88}Sr a ^{43}Ca v 20. linii močového kamene 11684

ment 11726 (obr. 7). Mapy jsou zhotoveny z 59 linií vzdálených od sebe 0,1 mm.

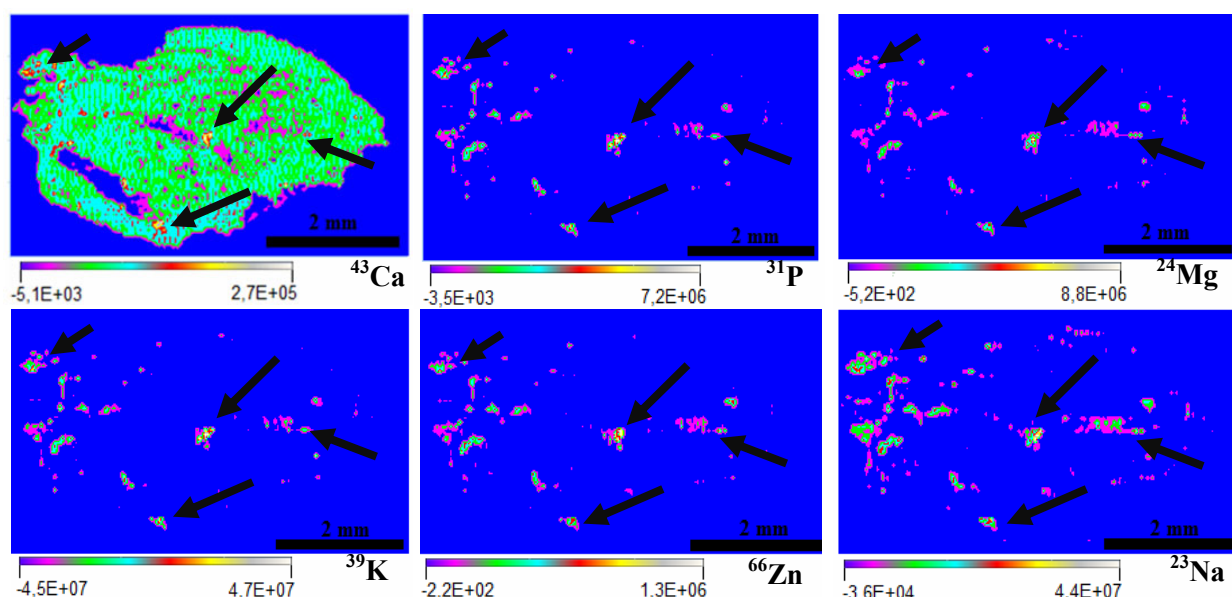
V úlomku tohoto močového konkrementu můžeme pozorovat korelace některých prvků.

Jako matricový prvek lze zvolit vápník, který je rozložen téměř homogenně. Pokles intenzit v 2D mapě vápníku je způsoben póravou strukturou vrstvy močového konkrementu.

Pokud se podíváme na rozložení jednotlivých prvků, je zde jistá korelace. Korelace mezi vápníkem a fosforem



Obr. 7. Analyzovaný vzorek 11726



Obr. 8. Intenzitní 2D mapy pro vzorek 11726

je lehce vysvětlitelná, protože se jedná o hlavní složky apatitů. Stejně je tomu i u korelace mezi hořčíkem a fosforem, což jsou složky struvitu. Ovšem je zajímavé, že bychom očekávali vyšší intenzitu u hořčíku. Pravděpodobně byla v moči vysoká koncentrace vápníku, což zapříčinilo vazbu na anion kyseliny fosforečné místo hořčíku. Z literatury¹⁰ se potvrzily korelace mezi isotopy prvků sodík-fosfor, sodík-draslík, sodík-zinek, zinek-fosfor, zinek-draslík. Pravděpodobně se jedná o prvky, které jsou v asociaci s apatyti (obr. 8).

Závěr

Metoda LA-ICP-MS se ukázala jako vhodná pro mapování prvků v biominerálech, jako jsou močové konkrementy. Je zkoumána závislost obsahu stopových prvků a těžkých kovů v závislosti na matricových prvcích. Výsledky získané metodou infračervené spektrometrie byly potvrzeny i 2D mapováním pomocí LA-ICP-MS. Tyto výsledky budou doplněny výsledky dalších metod, a to elektronové mikrosondy, Ramanovy spektrometrie a roztokových metod, a dle chorobopisu pacientů budou podkladem pro komplexní zhodnocení příčin vzniku a růstu močových konkrementů. Bylo zde ukázáno, že LA-ICP-MS může být použita přímo, nebo současně s jinou metodou, pro výzkum biominerálů.

Děkujeme Ministerstvu školství, mládeže a tělovýchovy České republiky za výzkumné projekty ME08002 a MSM0021622412.

LITERATURA

1. Fang X., Ahmad S. R., Mayo M., Iqbal S.: Lasers Med. Sci. 20, 132 (2005).
2. Kasidas G. P., Samuell C. T., Weir T. B.: Ann. Clin. Biochem. 41, 91 (2004).
3. Wandt M. A. E., Underhill L. G.: Br. J. Urol. 61, 474 (1988).
4. Moroz T. N., Palchik N. A., Dar'in A. V.: Nucl. Instrum. Methods Phys. Res., Sect. A 603, 141 (2009).
5. Carmona P., Bellanato J., Escolar E.: Biospectroscopy 3, 331 (1997).
6. Tunney M. M., Bonner M. C., Keane P. F.: Biomaterials 17, 1025 (1996).
7. Perk H., Serel T. A., Kosar A.: Urol. Int. 68, 286 (2002).
8. Singh V. K., Rai A. K., Rai P. K.: Lasers Med. Sci. 24, 749 (2009).
9. Chaudhri M. A., Watling J., Khan F. A.: J. Radioanal. Nucl. Chem. 271, 713 (2007).
10. Abboud I. A.: Jordan J. Earth Environ. Sci. 1, 73 (2008).



Study of metal accumulation in tapeworm section using laser ablation-inductively coupled plasma-mass spectrometry (LA-ICP-MS)



Simona Turková ^a, Michaela Vašinová Galiová ^{a,b}, Kristýna Štúlová ^a, Zuzana Čadková ^c, Jiřina Száková ^d, Vítězslav Otruba ^a, Viktor Kanický ^{a,b,*}

^a Department of Chemistry, Faculty of Science, Masaryk University, Kotlářská 2, 611 37 Brno, Czech Republic

^b Central European Institute of Technology, Masaryk University, Kamenice 5, 625 00 Brno, Czech Republic

^c Department of Zoology and Fisheries, Faculty of Agrobiology, Food and Natural Resources, Czech University of Life Sciences, Kamýcká 129, 165 21 Praha 6 - Suchdol, Czech Republic

^d Department of Agroenvironmental Chemistry and Plant Nutrition, Faculty of Agrobiology, Food and Natural Resources, Czech University of Life Sciences, Kamýcká 129, 165 21 Praha 6 - Suchdol, Czech Republic

ARTICLE INFO

Article history:

Received 25 October 2016

Received in revised form 5 April 2017

Accepted 5 April 2017

Available online 06 April 2017

Keywords:

Laser ablation

ICP mass spectrometry

Tapeworm

Elemental translocation

Calibration procedure

ABSTRACT

LA-ICP-MS method was utilized for the elemental mapping of *H. diminuta* tissue as possible bio-accumulating organism. Since no suitable commercial standards for analysis of *H. diminuta* sections are available, synthetic matrix similar standards containing 0, 5, 10, 20 and 30 mg kg⁻¹ of Fe and Pb as well as 0, 50, 100, 200, 300, 400 and 500 mg kg⁻¹ of Zn were prepared by spiking agarose gel with elements of interest. Two different laser ablation ICP-MS systems were used, namely 213 nm LA-ICP-(Q)MS and 193 nm LA-ICP-(SF)MS, and compared in terms of their detection limits and achievable goodness of fit of linear calibration dependencies. Carbon ¹²C⁺ was used as internal reference element to correct for the different tissue density and absorption rates. The prepared set of multi-elemental agarose gel standards was utilized for the quantitative elemental mapping of *H. diminuta* paraffin-embedded thin sections using the 213 nm solid state Nd:YAG coupled to ICP-(Q)MS. The content of Zn as biogenic element was found to be relatively homogeneously distributed within the cross section of proglottid, primarily in reproductive structures (uterus, fertilized eggs) while the Pb elemental distribution was found to be more concentrated in the tegument (surface).

© 2017 Elsevier B.V. All rights reserved.

1. Introduction

Some metallic elements, such as Fe, Cu and Zn, have an important role in biological systems as essential components that are involved in the regulation of intracellular functions. They are often bound to proteins in active sites of enzymes, and metal homeostasis is therefore vital for a living organism. On the other hand, some other metals such as Pb catalyze, already at relatively low concentrations, cytotoxic reactions and their occurrence is thus undesirable. Monitoring of both essential and toxic elements may facilitate evaluation of their pathways in the environment, their bioactivity and/or transport and distribution processes within tissue [1].

Compared to methods where the sample is transferred into solution (ICP-MS, ICP-AES), so called elemental imaging provides valuable information about spatial distribution of an element of interest in a tissue section.

Historically, the first methods used for visualization of metals in tissues were histological staining methods, which suffer from insufficient

sensitivity compared with the requirement for the determination of trace and ultra-trace elemental contents, the possible contamination from chemicals used for staining [2], possible metal species specificity to some chemical reactions [3], and also from the fact that only a single-elemental surficial distribution at a time can be obtained on a given tissue thin section. Multi-elemental imaging can be accomplished by various methods of surface analysis, such as scanning micro-X-ray fluorescence spectrometry [4,5], micro-proton-induced X-ray emission [6–8], and secondary ion mass spectrometry [9–11].

One of the most promising methods for elemental bioimaging is laser ablation-inductively coupled plasma-mass spectrometry (LA-ICP-MS). Main advantages of LA-ICP-MS in terms of the requirements for a multi-elemental imaging method applicable to soft tissues consist in: *i*) a quasi-simultaneous ICP-MS data acquisition in terms of temporal resolution of an ablation system; *ii*) acceptable spatial resolution of a laser beam sampling procedure; and in *iii*) sufficiently high sensitivity, which allows determination of elemental contents, otherwise undetectable by traditionally used tissue staining methods, as LA-ICP-MS detection limits for elemental mapping span from sub mg kg⁻¹ level down to the µg kg⁻¹ in the µm range [12–14]. Over the last few years LA-ICP-MS method has been applied for the analysis of various tissues (e.g. brain

* Corresponding author.

E-mail address: viktork@chemi.muni.cz (V. Kanický).

[15,16], kidney [17], tumor tissue [18]) and the resulting data helped to better understand the biological processes (e.g. abnormal metal accumulation has been observed in the brains of a transgenic mouse model of Alzheimer's neurodegenerative dinase [19], or the distribution of the cis-platin in the tumor tissue [20]).

Despite all the benefits of LA-ICP-MS method, there is a major problem with the calibration of soft tissue LA-ICP-MS data as the ablated mass flow of biological tissue is not constant and is water content dependent [21]. An ideal soft tissue calibration standard should fulfill several practical criteria: easy standard preparation, applicability to wide range of elements and its homogeneity and stability both during the analysis and during the long-term storage in the laboratory [22]. Several calibration approaches have been employed up to date to overcome problematic soft tissue calibration and to obtain quantitative images of metal distributions in thin section tissues. Most of the laboratories rely on the use of in-house prepared standards. Use of certified reference materials (CRM) is possible as well, but only limited number of standards for soft tissue calibration is available up to date to fit the wide range of biological soft tissue materials [1,23]. The most frequently used soft tissue calibration strategies are:

i) Matrix-matched calibration as relatively one of the most reliable calibration method that corrects for different ablation characteristics caused by different sample and standard matrix. Most of the laboratories rely on the in-house prepared standards from various biological tissues (e.g. human brain tissue for the study of metals influence as possible triggers of Alzheimer's and Parkinson's diseases [24], thin sections of rat tissues [12], internal organs of domestic animals [25], drug treated tumor rat tissue [26]).

ii) Synthetic "matrix-similar" standards are used since it is not always possible or convenient to use matrix matched tissue material to produce calibration standards. For this purpose, spiking of synthetic high-purity materials such as gelatin, which was recently used for quantification of both biological samples and inorganic carbon [12,26], agarose used for the analysis of cell cultures [27] or spiked tissue freezing medium for quantification of Hg in plant root cross sections prepared by cryostat sectioning, has been reported [28]. The preparation procedure of these standards is relatively convenient and fast. Both single and multi-element standards might be prepared in this way. However, accurate quantification of elements of interest remains to be quite challenging due to different forms of organic compounds forming the matrix of the sample and standard. Corrections must be therefore applied to obtain correct results (e.g. normalization of the signal using suitable internal standard element).

iii) Another way of data quantification in the case that the solid standard material is not available or difficult to be produced is the solution-based calibration. In this approach, the micronebulizer can be inserted either directly into the ablation chamber or the two aerosol streams are introduced separately into the injector tube inside a special ICP torch [16,29]. The preparation of standard solutions is easy, but there might be a problem with different forms of the sample (ablated particles) and standard matter (liquid aerosol) entering the plasma. This can result in serious matrix effects. Problems arising from different sample and standard matrix may be corrected by direct ablation of liquid standard with modified absorption coefficient by addition of a suitable chromophore [30,31]. Introduction of water vapor may also lead to elevated oxide formation and other molecular interferences. This method also does not account for variations that may occur during the laser sampling process and the dilution of the ablation stream by nebulized solution, which may decrease sensitivity of analysis [32]. One possible solution for this problem is desolvation of the solution aerosol before it reaches the plasma [33].

In practice, the first two mentioned calibration approaches are employed most frequently. However, neither the matrix-matched nor the matrix-similar calibration take into account different tissue density and water content across the tissue sample and standard, which may result in different ablation behavior of the sample and calibration

standard during the laser ablation and subsequent processes in the plasma [34]. Another problem resulting from matrix effects are the different ablation rates between the used reference material and sample. Normalization of the signal (referred also as "internal standardization"(IS)) is therefore needed to correct for these different ablation efficiencies due to matrix effects, laser energy fluctuation, surface roughness, differences in tissue density and thickness across the sample and/or differences in absorption coefficients of the ablated material [13,21,35]. Internal standard also improves the precision of the measurement since it compensates for the shot-to-shot variation. Given that the use of an IS should lead to reliable results; the need for matrix matching might thus be regarded as questionable [30]. Appropriate element used for normalization must meet several requirements, particularly homogeneous spatial distribution and equal affection of normalizing element and analyte by laser sampling, meaning fractionation index of the analyte and IS should be similar. Carbon, as the matrix element of biological tissues, is the most frequently used as normalizing element for soft tissue analysis since its distribution is supposed to be relatively constant across the sample [36] and its use leads to improved reproducibility [13]. Nevertheless, the normalization of signal using carbon is still quite challenging as neither ¹²C nor ¹³C are sufficiently sensitive to instrumental fluctuations of signal compared to elements of interest [37]. Furthermore, the LA-ICP-MS analysis of carbon is considered prone to problems including high background signal and unfavorable transport properties. Taking into account high first ionization potential as well, the detectability of less abundant carbon isotopes is contingent on high content in investigated sample [38]. The carbon as a matrix predominately of soft tissue is linked with the analysis of thin slice and the elemental distribution can vary not only within the surface, but with depth as well. In this context, the sampling of as thin slices as possible results in high quality bioimaging, and using ¹²C as internal reference isotope benefits in better signal/background ratio. However, both ¹²C and ¹³C isotopes have been recently confirmed as effective internal standards [39].

Another factor limiting thin section tissue analysis next to the process of data quantification is the process of thin sections preparation itself, since the water content in tissues can often exceed 30%_{m/m} and it is not constant across the tissue. As the laser radiation heats the sample the water evaporates from the sample surface [25]. The abundance of atomized hydrogen and oxygen in the ablated material is high and therefore these consume the energy of the plasma at the expense of the analyte ionization. Therefore, it is advisable to analyze well dried samples. Several approaches are being employed to prepare soft tissue sections for LA-ICP-MS analysis: i) Paraffin-embedding using microtome is the traditional method for thin section preparation in histology based on water removal from the tissue by dipping the sample in the increasing EtOH series. ii) Another approach of water removal consists in the use of *cryogenically cooled microtome* [28]. Use of cryostat eliminates the risk of tissue section contamination from chemicals. However, the rate of water removal is supposed to be depending on the type of soft tissue. iii) Use of cryogenically cooled laser ablation cell, which was first described in Feldmann et al. [25] enables direct analysis of fresh soft tissues. The temperature in the ablation cell can be controlled within the range from –20 °C to –100 °C using liquid nitrogen stored in Dewar container connected with the ablation cell. Several commercially available cryo-chambers are now available (e.g. CryoLAC™ developed by AWI, Germany). Several studies using cryogenically cooled ablation cell have been published [13,29,37].

Another crucial aspect of elemental mapping by LA-ICP-MS is the laser ablation conditions. Mapping is usually performed using the spot mode ablation or the line scan, both of them having their advantages and disadvantages. Use of spot mode analysis enables improved lateral resolution compared to the line scan if the distance between the ablation spots is adjusted to the diameter of the laser beam. However, the spot mode analysis is in general more time consuming compared to the line scan. Depending on the laser spot size and area to be ablated

the total analysis time to obtain 2D maps using spot mode LA-ICP-MS analysis may reach even tens of hours [40]. On the other hand, line scan enables significant reduction of the total analysis time and related analysis cost if the scan speed is optimized [41]. The value of the scan speed is typically set to more or less to the value of the laser beam diameter to obtain optimal resolution. However, Lear et al. reported that the scan speed can be increased up to five times to the value of the laser beam without the significant variation in image resolution and resulting calculated contents [41]. Crucial parameter linked to the scan speed is also the washout time since increasing washout time increases the mixing of the signal from a previous data point on following data points. This can result in image blurring [41]. Care must be also taken to avoid surface contamination if line scan is employed since during the line scan just the surface of the sample, which is prone to contamination, is ablated.

Laser fluence is another important working parameter for LA-ICP-MS imaging. In general, lower laser fluence is recommended for thin section analysis of soft tissues. However, the use of higher laser energy may lead to the total consumption of the thin layer (with usual thickness of 5–20 µm). The total consumption of the thin layer may be advantageous for the subsequent data evaluation because defined analyte mass flow is generated by laser ablation upon condition that the thickness of the sample and standard is constant, which is often difficult to accomplish [28]. The commercially available lasers enable analysis using spot diameter starting from 4 µm for high resolution elemental mapping. However, the use of small laser beam diameters leads to increase of limits of detection and long acquisition times. Compromise must be therefore made between the LOD, time of analysis and the optimal resolution [42].

The present study explores the use of LA-ICP-MS to study elemental translocation within *H. diminuta* helminthes as a possible bioaccumulating organism. Since *H. diminuta* are supposed to be bioaccumulators of heavy metals from the hosting animal tissue, their monitoring, namely Pb, may help in tracing the pathways of these elements in the system plant-animal-parasite. Several helminthes were already confirmed to be able to accumulate considerable levels of toxic elements [43–46], but it still remains unclear if the accumulation of risk metals in helminthes affects the metal levels in the hosting organism. The distribution of specific elements within the individual proglottid sections should be determined to get better understanding on the process and preferential storing locations of risk elements within the helminthes tissue.

Primary objective of this study was to develop reliable synthetic calibration standards for 2D elemental mapping of paraffin-embedded *H. diminuta* thin sections by LA-ICP-MS. Since no suitable commercial standards for analysis of *H. diminuta* sections are available, synthetic matrix similar standards prepared by spiking of agarose gel with elements of interest were tested and used. Besides Pb, the metal distribution was also studied for Zn and Fe as essential elements naturally present in biological tissues. The applicability of the developed calibration procedure was tested for elemental mapping of a paraffin-embedded *H. diminuta* thin section. Problems arising from different tissue density, different ablation rate and different absorption coefficients of sample and standard needed to be solved using appropriate normalization technique. In this context, carbon was used as internal reference element. Other factors influencing data quantification including absorption of laser light and thickness of the sample and calibration standard are also discussed.

2. Experimental

2.1. Biological material

2.1.1. Pb exposure of testing rats, isolation and treatment of tapeworm strobilae

H. diminuta strobilae were obtained from male rats (Wistar strain, commercial supplier Velaz, Czech Republic) experimentally inoculated

at 2 months of age by *H. diminuta* larvae (cysticercoids). After inoculation, the tapeworms were allowed to grow for 6 weeks. During this period, host rats were fed at standard pellet diet (ST-1; Velaz, Czech Republic) and were allowed to drink water ad libitum. The Pb exposed animal was given repeated per oral doses of lead nitrate. Each rat received a total of 36 mg of Pb during a 6-week period and the accumulated amount and preferring storing locations of Pb in the *H. diminuta* were studied in the present work. At the end of exposure period, rats were euthanized and *H. diminuta* strobilae were immediately removed from the small intestines using Teflon® dissecting instruments. Tapeworm tissues were thoroughly rinsed in double distilled water, fixed in solution of boiling 4% formaldehyde for several minutes, and finally stored at –20 °C in 70% ethyl alcohol until subsequent procedures. All chemicals used in these procedures were of the analytical grade purity and were obtained from commercial supplier (Lach-Ner, s.r.o., Czech Republic).

2.1.2. Thin section preparation for morphological observation and LA-ICP-MS analysis

For the paraffin wax-embedding the segments of the tapeworm strobilae were dehydrated in an increasing ethanol series (70%, 80% and finally absolute ethanol) and embedded in paraffin wax (Paraplast plus, Sigma-Aldrich). Both the cross sections and the longitudinal sections were prepared using a microtome device (Leica Microsystems GmbH, Germany). The 40 µm thin slices (for LA-ICP-MS analysis) and the 10 µm thin slices (for morphological observation) were alternately sectioned and fixed on Adhesion Microscope Slides HistoBond® + (Paul Marienfeld GmbH & Co. KG, Laboratory Glassware, Germany). Subsequently, samples for morphological description were stained with Weigert's haematoxylin, counterstained with a 1% eosin B solution and covered with glass slides. Samples for LA-ICP-MS analyses were left unstained and uncovered for further procedures.

2.2. Calibration standards

2.2.1. Preparation of spiked agarose gels and elemental content verification

Single element aqueous calibration ASTASOL® solutions of Fe, Zn and Pb in 2% HNO₃ containing 1 g l⁻¹ of the element (Analytika spol. s r.o., Czech Republic) were used for the spiking of agarose (Sigma-Aldrich®, USA). Since agarose is pH sensitive and in acidic environment arising from ASTASOL® solutions the prepared spiked agarose gel would possibly not settle down, the acid from the standard stock solutions was evaporated prior to spiking of agarose and the metal residues were re-dissolved in Milli-Q water (Simplicity® Water Purification System, Merck Millipore, USA) so the buffering, which would be a possible source of contamination, was not needed. Standard single stock solutions containing 500 mg kg⁻¹ of Zn and 100 µg g⁻¹ of Fe and Pb were prepared that way.

Multi-elemental standards containing 0, 5, 10, 20 and 30 mg kg⁻¹ of Fe and Pb and 0, 50, 100, 200, 300, 400 and 500 mg kg⁻¹ of Zn were prepared by mixing different weights of "acid free" standard solutions and 0.5 g of agarose powder with Milli-Q water which was added to the total mass of 50 g (1% agarose gel). The mixture was homogenized using magnetic stirrer for about one hour and heated to 90 °C until the agarose was completely dissolved. About 10 g of the melted agarose solution was poured onto the Petri dish with a diameter of 10 cm and let to solidify on a flat surface and then dried under clean conditions at laboratory temperature (around three days). Complete water evaporation was assumed for metal concentration calculations. After drying a thin film of spiked agarose has been formed. Agarose standard square pieces (approx. 1 × 1 cm) were fixed on their margins onto the clean microscopic slide using double-sided adhesive tape and subjected to LA-ICP-MS analysis. The laser ablation measurements were done on the central area of the standard piece placed directly on the glass surface without the adhesion tape layer.

Table 1

Operating conditions of LA-ICP-MS measurement using two different laser ablation ICP-MS systems.

LA-ICP-MS operating conditions		Laser ablation (Analyte G2)	
Laser ablation (New Wave Research UP 213)		Laser ablation (Analyte G2)	
Wavelength	213 nm	Wavelength	193 nm
Pulse length	~4 ns	Pulse length	~4 ns
Sample chamber	SuperCell™	Sample chamber	Helex™
He flow rate	1.0 l min ⁻¹	He flow rate	0.65 l min ⁻¹
Make-up Ar flow rate	0.6 l min ⁻¹	Make-up Ar flow rate	~1 l min ⁻¹
ICP-MS (Agilent 7500 CE)		ICP-MS (Element 2)	
RF power	1500 W	RF power	1200 W
Plasma gas flow rate	15 l min ⁻¹ Ar	Cooling gas flow rate	15.50 l min ⁻¹ Ar
Auxiliary gas flow rate	1 l min ⁻¹ Ar	Auxiliary gas flow rate	1.12 l min ⁻¹ Ar
Collision gas flow rate	1 ml min ⁻¹ He	Mass resolution	Low resolution
Isotopes measured	¹² C, ²⁸ Si, ⁵⁷ Fe, ⁶⁶ Zn, ²⁰⁸ Pb	Isotopes measured	¹³ C, ²⁸ Si, ²⁹ Si, ⁵⁷ Fe, ⁶⁶ Zn, ²⁰⁸ Pb

To check the actual spiked concentrations in the prepared set of calibration standards a SN-ICP-MS analysis was done. Standards (~0.1 g of the dry mass) were digested using 5% HNO₃ (Merck, USA) at 120 °C for about 1.5 h on a hotplate. Procedural blank was prepared using the same procedure and resulting solutions were analyzed using SN-ICP-(Q)MS.

2.3. Instrumentation

Two LA-ICP-MS systems: *i*) a quadrupole-based spectrometer, ICP-(Q)MS, coupled to Nd:YAG 213 nm laser ablation system; *ii*) sector field instrument, ICP-(SF)MS, coupled to ArF* 193 nm laser ablation device were used and compared in terms of limits of detection and achievable tightness of linear calibration dependences of studied elements in prepared set of spiked agarose standards.

Instrumentation for the LA-ICP-(Q)MS consisted of a laser ablation system UP 213 (New Wave Research, USA) and an ICP-MS spectrometer Agilent 7500 CE (Agilent Technologies, USA). A commercial Q-switched Nd:YAG laser ablation device working at a wavelength of 213 nm is equipped with XY-stages to move the sample along a programmed trajectory during ablation and a CCD camera to monitor sample during laser ablation. The samples were placed into the SuperCell™ (New Wave Research, USA) and the ablated material was transported using a 1 m long polyurethane tubing (i.d. of 4 mm). Make up gas flow of argon (0.6 l min⁻¹) was admixed to the helium carrier gas flow (1 l min⁻¹) before entering the ICP-MS. The ICP-MS was operated in the collision mode to reduce possible interferences with the He flow of 1 ml min⁻¹.

Optimization of the LA-ICP-MS parameters (gas flow rates, sampling depth, voltage of ion optic) was performed using the glass reference material NIST SRM 612 with respect to maximum signal to background ratio and minimum oxide formation (ThO⁺/Th⁺ counts ratio < 0.2%, U⁺/Th⁺ counts ratio < 1.1%). Following isotopes were measured: ¹²C, ²⁸Si, ⁵⁷Fe, ⁶⁶Zn, and ²⁰⁸Pb. The silicone isotope was measured to indicate the ablation through the sample onto the glass support. Background-subtracted signals of isotopes of interest were normalized to ¹²C signal.

The second facility consisted of a Photon Machines Analyte G2 laser ablation platform equipped with the two-volume Helex™ ablation chamber and the ATLEX 193 nm excimer laser source (ATL-Lasertechnik GmbH, Wermelskirchen, Germany). The 193 nm laser ablation system was coupled to the sector field ICP-MS instrument (ELEMENT 2, Thermo Scientific, Germany), which was tuned to maximum sensitivity and operated under optimized conditions in low resolution mode. Following isotopes were measured: ¹³C, ²⁸Si, ⁵⁷Fe, ⁶⁶Zn, and ²⁰⁸Pb. The data were processed in the same way as the ICP-(Q)MS data. Operating conditions of both LA-ICP-MS systems are summarized in Table 1.

2D mapping of tapeworm tissue was done under optimized laser ablation conditions at line scan mode: 65 µm laser spot size (square), scan speed of 91 µm s⁻¹, fluence 2 J cm⁻², and repetition rate of 10 Hz using the 213 nm Nd:YAG laser coupled to ICP-(Q)MS.

Agilent 8453 UV-Visible Spectroscopy System (Agilent Technologies, USA) with deuterium discharge lamp for the UV wavelength range has been used to measure the absorbance spectra of the prepared calibration standard and soft tissue sample. The paraffin-embedded soft tissue section and film of agarose standard have been fixed to the surface of quartz cuvette and measured in the UV region.

3. Results and discussion

3.1. Verification of prepared set of agarose standards

The spiked agarose standards (0–500 mg kg⁻¹ of Zn and 0–30 mg kg⁻¹ of Fe and Pb) were digested using the procedure described above and subjected to the SN-ICP-MS analysis for the recoveries to check the efficiency of agarose spiking procedure. The actual contents determined using SN-ICP-(Q)MS were compared with the theoretical elemental contents. The recoveries of the spiked elements were in the range of 82–117%. The actual and theoretical concentrations of the spiked elements with respective recoveries are in Table 2. In Fig. 1 are the actual SN-ICP-MS contents of Fe, Zn and Pb plotted against the theoretical elemental contents.

3.2. Characterization of the spiked agarose standards

The in-house prepared calibration standards made by spiking of agarose gel with Fe, Zn and Pb were tested as a calibration material for the quantification of the 2D elemental maps of *H. diminuta* thin sections since no suitable commercial standards matching the sample matrix were available. Such custom-made standards provide the advantage of unlabeled spiking with the elements of interest.

3.2.1. Homogeneity of standards

Spatial homogeneity of the prepared set of calibration standards was estimated using LA-ICP-(Q)MS measurement performed at the following optimized laser (213 nm) ablation conditions: line scan ablation with 65-µm square laser spot, scan speed of 91 µm s⁻¹, fluence of 2 J cm⁻² and laser repetition rate of 10 Hz. Three parallel 3-mm line tracks spaced apart by 100 µm were ablated on the square-shaped piece of 200/20 (Zn/Fe, Pb) mg kg⁻¹ agarose standard fixed on the glass microscopic slide. The stability of the ⁵⁷Fe, ⁶⁶Zn and ²⁰⁸Pb signal

Table 2

Theoretical and actual elemental contents (c) determined by SN-ICP-MS with the recovery values of the measured elements.

Fe Theoret. content (c) (mg kg ⁻¹)	SN-ICP-MS c ± SD (mg kg ⁻¹)	Recovery %	Zn Theoret. content (c) (mg kg ⁻¹)	SN-ICP-MS c ± SD (mg kg ⁻¹)	Recovery %	Pb Theoret. content (c) (mg kg ⁻¹)	SN-ICP-MS c ± SD (mg kg ⁻¹)	Recovery %
4.470	4.304 ± 0.076	96	46.83	47.21 ± 0.77	101	4.66	4.325 ± 0.041	93
8.82	10.36 ± 0.13	117	98.2	107.9 ± 1.6	110	9.83	10.81 ± 0.19	110
19.54	18.87 ± 0.67	97	207.1	185.6 ± 3.3	90	19.55	16.44 ± 0.22	84
29.31	28.49 ± 0.21	97	295.7	283.1 ± 3.9	96	29.51	24.04 ± 0.12	82
			396.4	448.2 ± 4.2	113			
			480	512 ± 11	107			

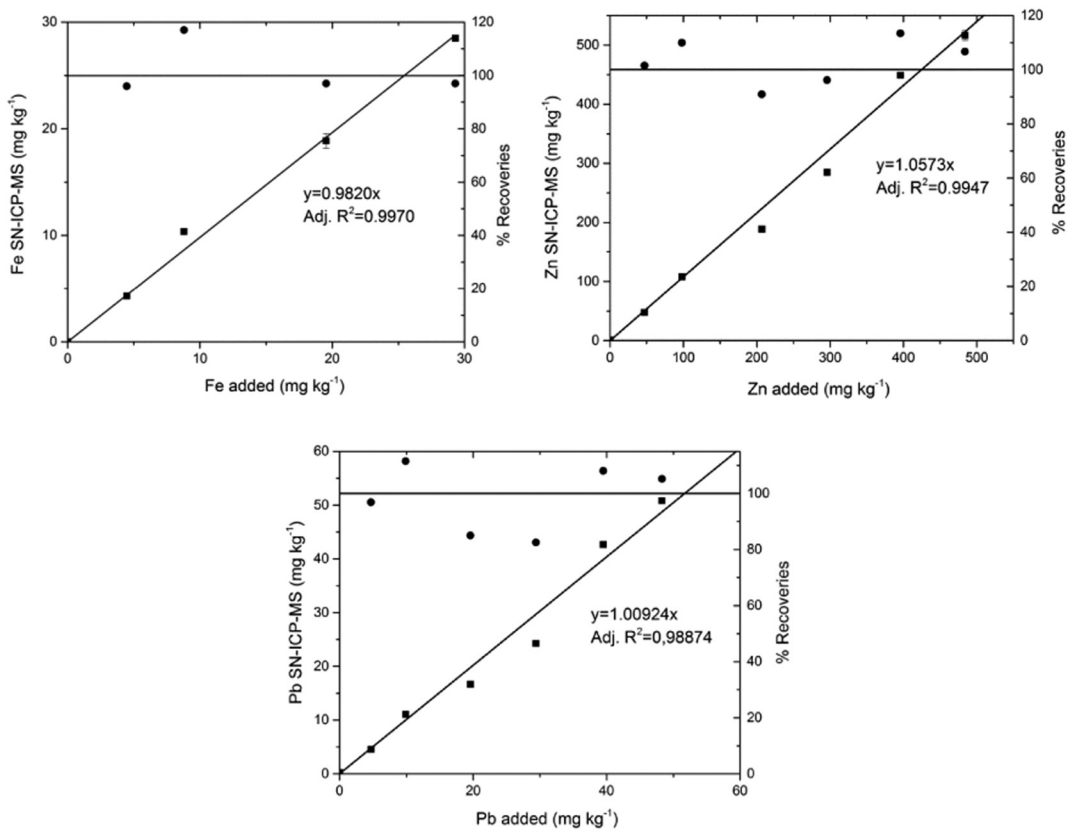


Fig. 1. Recovery values of Fe, Zn and Pb determined using SN-ICP-(Q)MS. The recovery values are in the range from 82% (for 30 mg kg⁻¹ of Pb) to 117% (for 10 mg kg⁻¹ of Fe) being randomly scattered around the 100% recovery line. There is statistically non-measurable bias as a function of the concentration, and thus it would suggest no systematic sample contamination or elemental losses during the standard preparation.

after exclusion of spikes is evident from records in Fig. 2. The precision of the measurement calculated by averaging the RSD values of the three parallel lines of the background-subtracted signal was: 2.6%, 26%, 12% and 13% for ¹²C, ⁵⁷Fe, ⁶⁶Zn and ²⁰⁸Pb, respectively.

3.2.2. Influence of laser parameters

Laser sampling conditions were tested and optimized using the solid state Nd:YAG 213 nm laser coupled to ICP-(Q)MS with the prepared set of spiked agarose calibration standards in terms of limits of detection at various spot sizes and goodness of fit of linear calibration dependences. Carbon ¹²C as matrix element was used as internal standard to correct for any variation in the ablated material amount due to laser energy fluctuation, layer thickness and changes of absorption coefficient of the ablated material. ¹²C isotope was preferred over the ¹³C, since it enables higher sensitivity compared to minor ¹³C isotope. This is crucial especially when quadrupole mass analyser was employed, which yields in general lower sensitivity compared to the sector field instruments in low resolution mode. Two modes of laser ablation were tested, namely the spot mode and line scan.

3.2.2.1. Spot mode ablation. Spot mode ablation was tested using three different spot sizes of 25, 40 (μm) and 65 (μm) with 5 s ablation time, 10 s background acquisition, laser fluence of 2 J cm^{-2} and repetition rate of 10 Hz. Ten spots were ablated on the central area of each standard with distance of 100 μm between the spots. Based on the signal of silicone, which was acquired to indicate the laser ablation through the standard onto the glass support, the laser ablation during the 5 s spot mode analysis at the laser fluence of 2 J cm^{-2} did not lead to the ablation through the standard. The ¹²C normalized ²⁰⁸Pb intensities for the three tested laser spot sizes of 25, 40 and 65 μm acquired by the spot analysis of the agarose standard with the content of 5 mg kg⁻¹ of Pb, which was supposed to be matching the actual Pb content in the

analyzed soft *H. diminuta* tissue are in Fig. 3. Rapid decrease of the ²⁰⁸Pb/¹²C signal intensity was registered at the spot sizes of 25 and 40 μm rendering to higher limits of detection compared to the 65 μm spot size. The stability of the signal at 65 μm was relatively stable with the plateau area. Based on the normalized peak areas of ²⁰⁸Pb signal the homogeneity of the prepared standards is satisfactory with the RSD value of 10% for the ²⁰⁸Pb/¹²C signal areas using 65 μm spot size. The calibration graphs obtained using the laser spot size of 25, 40 and 65 μm are presented for Zn and Pb in Fig. 4, while signal intensities are normalized to the signal of ¹²C. The data were evaluated as integrated peak areas. The points were tested for outliers using Grubbs' test. No

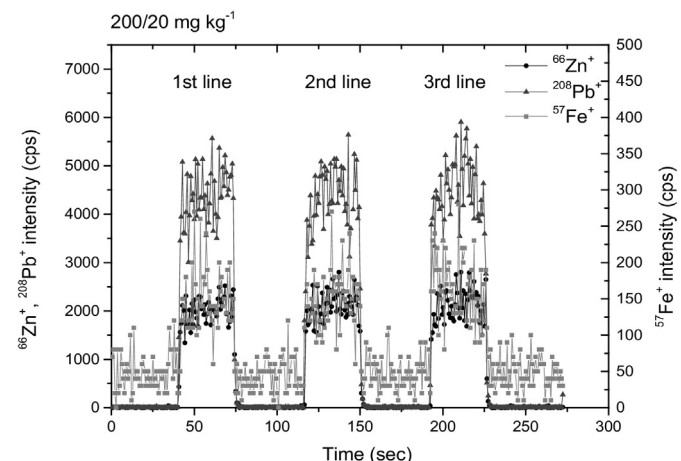


Fig. 2. The signal stability of ⁵⁷Fe⁺, ⁶⁶Zn⁺ and ²⁰⁸Pb⁺ during the line scan ablation of 200/20 mg kg⁻¹ (Zn/Fe and Pb) agarose standard.

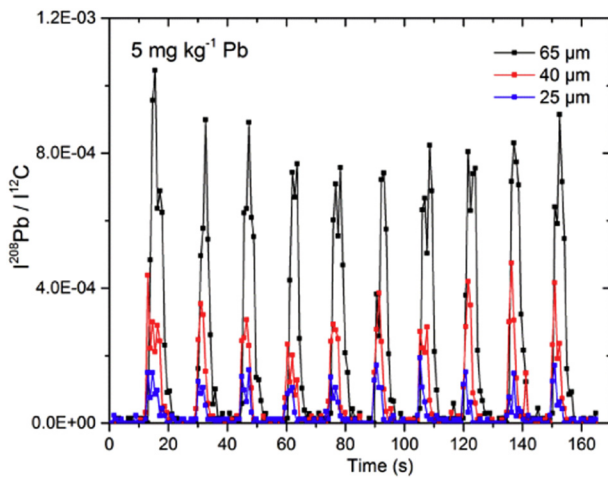


Fig. 3. Time resolved 10 spot analysis of $^{208}\text{Pb}/^{12}\text{C}$ normalized data in spiked agarose standard with Pb content of 5 mg kg^{-1} using three laser spot sizes of 25, 40 and 65 μm . Laser ablation was done using 50 laser pulses and intersite pause of 10 s.

significant outlier has been found at the p-value of 0.01. In case of Pb, the decrease of laser spot size from 65 μm to 25 μm had no effect on the coefficients of determination (Adj. R^2 values were used), which were in the range of 0.9950 (65 μm) to 0.9956 (25 μm). Conversely, the decrease of the laser spot size from 65 μm to 25 μm led to deterioration of coefficients of determination for Zn from 0.9788 (65 μm) to 0.6897 (25 μm) and also the intercept was found to be statistically significant for the 25 μm spot size. In case of Fe, the use of laser spot sizes of 25 and 40 μm led to insufficient signal/background ratio, as minor ^{57}Fe isotope was measured instead of ^{56}Fe to avoid ArO^+ interference. Compared to that the signal/background ratio of all analyzed spiked elements obtained using 65 μm laser spot size was satisfactory and enabled acceptable analysis time and resolution for elemental 2D mapping of *H. diminuta* tissue.

3.2.2.2. Line scan mode ablation. Line scan mode was tested using the laser spot size of 65 μm and two laser fluences of 2 J cm^{-2} and 8 J cm^{-2} . During the line scan less material in depth is released compared to spot mode ablation, therefore the higher of the two tested energies was used to ensure sufficient amount of the material to be ablated. Three parallel 3-mm line tracks spaced apart by 100 μm were ablated in line scan mode. The value of scan speed ($91 \mu\text{m s}^{-1}$) was adjusted to the total mass cycle time of the method.

The laser fluence of 8 J cm^{-2} led to increased amounts of ablated material, and in case of the multi-elemental calibration standard with

content of 100/10 mg kg^{-1} of Zn/Fe and Pb the total ablation through the standard onto the glass support was observed on basis of the elevated Si signal. This was caused probably by slightly lower thickness of the 100/10 mg kg^{-1} standard compared to other standards. By laser ablation of the microscopic glass slide, which was used as the support material for the agarose standard, it was found that the signal at the m/z 57 was increased, while the signal at m/z 66 and 208 for Zn and Pb was under LOD calculated as 3σ of the background signal. This glass-associated signal at m/z 57, which might origin either from ^{57}Fe isotope and possible interferences (e.g. Ca-O), caused deterioration of the calibration dependence of Fe spiked agarose standards. A correction for the signal at m/z 57 originating from the glass support that contributed to the total intensity of an analyte in agarose standard should have been therefore applied using the following equation:

$$I_{\text{Fe}_{\text{St}}}^{\text{C}} = I_{\text{Fe}_{\text{St}}} - \left(\frac{I_{\text{Si}_{\text{St}}}}{I_{\text{Si}_{\text{G}}}} \times I_{\text{Fe}_{\text{G}}} \right)$$

where $I_{\text{Fe}_{\text{St}}}^{\text{C}}$ is the corrected signal intensity of iron in the agarose standard normalized to ^{12}C , $I_{\text{Fe}_{\text{St}}}$ is the net intensity of iron normalized to ^{12}C in agarose standard, $I_{\text{Si}_{\text{St}}}$ is the net intensity of Si normalized to ^{12}C in agarose standard placed on supporting glass slide, $I_{\text{Si}_{\text{G}}}$ is the net signal intensity of Si normalized to ^{12}C in the glass support and $I_{\text{Fe}_{\text{G}}}$ is the net signal intensity of iron normalized to ^{12}C in the glass support (abbr. G-glass, St-Standard).

The correction of signal of elements present in the supporting glass matrix led to increase of the Adj. R^2 value of Fe calibration dependence from 0.8116 to 0.9754. The glass supporting material was also tested using the laser fluence of 2 J cm^{-2} , but this relatively low fluence in combination with the use of 213 nm laser wavelength was not sufficient either to ablate through the standard layer or for the ablation of the transparent glass. Use of this energy thus did not cause signal increase at mass m/z 57 originating from supporting glass material so the term $I_{\text{Fe}_{\text{G}}}$ was equal to zero value and the $I_{\text{Fe}_{\text{St}}}^{\text{C}}$ value was equal to $I_{\text{Fe}_{\text{St}}}$ value.

The limits of detection based on the signal of blank agarose standard were generally lower for the higher of the two tested fluences since more material was ablated using the higher of the two tested laser fluences (see Table 3). Calibration curves are not shown for these experimental conditions but the goodness of fit of linear model is expressed by Adj. R^2 values in Table 3. The tightness of linear calibration dependences (after outlier exclusion in the case of Zn with content of 295.7 mg kg^{-1}) for measured elements using the two tested laser fluences of 2 and 8 J cm^{-2} was found to be satisfactory with values above 0.98 except Fe calibration dependence at 8 J cm^{-2} (Adj. R^2 value 0.9754). In the case of Fe the use of laser fluence of 2 J cm^{-2} led to better correlation with linear model compared to the laser fluence of 8 J cm^{-2} . This loosened correlation of Fe calibration dependence at

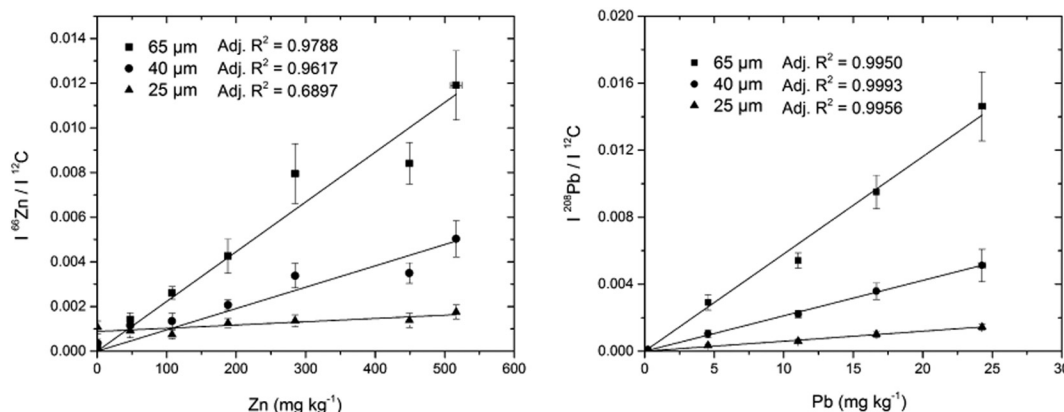


Fig. 4. Calibration curves for Zn (a) and Pb (b) obtained using three laser spot sizes of 25, 40 and 65 μm with resulting Adj. R^2 values.

Table 3

The coefficients of determination for calibration dependences (not shown) of Fe, Zn and Pb obtained using line scan at two laser fluences of 2 and 8 J cm⁻² with respective limits of detection (¹²C normalized data were used, * value obtained using the glass signal correction).

2 J cm ⁻²		8 J cm ⁻²	
Adj. R-square	LOD (mg kg ⁻¹)	Adj. R-square	LOD (mg kg ⁻¹)
Fe	0.9948	0.9754*	4.4
Zn	0.9887	0.9946	2.5
Pb	0.9987	0.9847	0.18

laser fluence of 8 J cm⁻² was caused most probably by the previously mentioned deteriorated signal at *m/z* 57 arising from the glass supporting material, that was not possible to completely correct for even if the previously described glass signal related correction procedure has been used. Hence, the lower of the two tested fluences that was not sufficient to ablate through the prepared standards has been used for the elemental mapping.

Line scan was further used for the subsequent elemental mapping of Pb doped *H. diminuta* thin sections since it enables faster acquisition of data for elemental 2-D mapping compared to spot mode analysis.

3.2.3. Goodness of fit of the linear calibration dependences

The optimized laser ablation conditions for elemental mapping (line scan using 65 μm laser spot size, scan speed of 91 μm s⁻¹, fluence of 2 J cm⁻² and repetition rate of 10 Hz) were used to obtain calibration dependences using both the 213 nm Nd:YAG laser coupled to ICP-(Q)MS and 193 nm ArF* laser ablation device coupled to the ICP-(SF)MS. The SF instrument was employed since it enables lower limits of detection of measured elements compared to (Q)MS and both instruments were thus compared in terms of their LOD and resulting correlation with linear model of calibration dependences.

The obtained data were subjected to linear regression analysis. The background subtracted signal of an element of interest was normalized to the background subtracted signal of ¹²C. Carbon was selected as internal reference to correct possible matrix effects and signal drift. Average values of ¹²C normalized signal intensities of an element of interest with

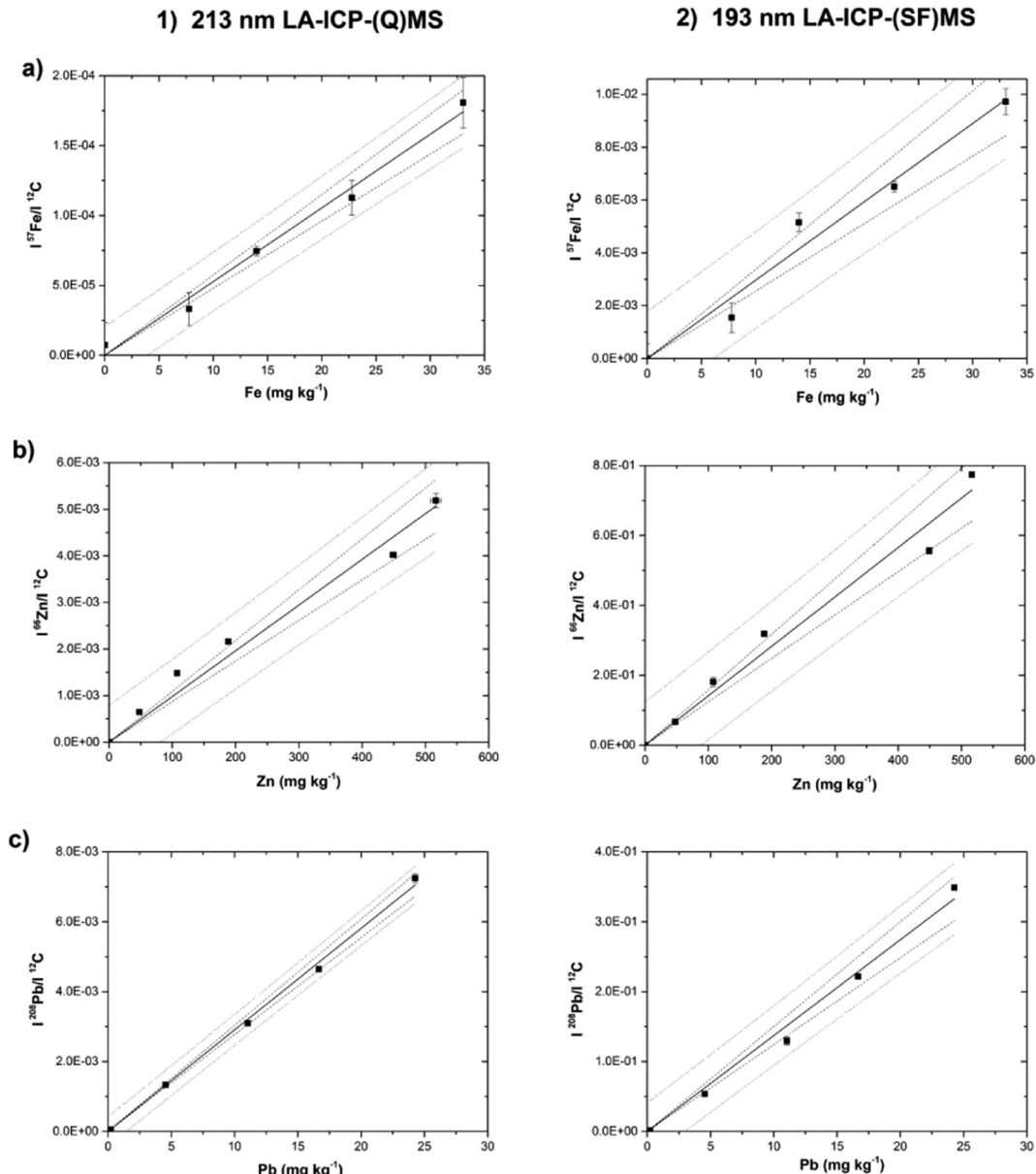


Fig. 5. Calibration lines for Fe (a), Zn (b) and Pb (c) using (1) 213 nm LA coupled to ICP-(Q)MS and (2) 193 nm LA with ICP-(SF)MS after Zn outlier exclusion.

the respective standard deviations (calculated as the sample variance) were plotted against the elemental contents determined by SN-ICP-(Q)MS. The resulting calibration data were subjected to linear regression analysis, which has been done using Origin software. Firstly, the intercepts were tested using the *t*-test at the level of significance ($1-\alpha$) = 0.975. The intercepts were found to be insignificant in all cases. The calibration curves forced through zero value were then tested for the presence of outliers using Grubbs' test (*p*-value 0.01). There was found only one outlier for the agarose standard with the content of 295.7 mg kg^{-1} of Zn.

Final calibration dependences of Fe, Zn and Pb obtained using both the ICP-(Q)MS coupled to 213 nm Nd:YAG laser and ICP-(SF)MS instrument with 193 nm ArF* laser are presented in Fig. 5. The calibration graphs also contain the prediction and confidence bands. The vertical error bars represent the sample variance of normalized signal intensity of three ablated lines on each standard and the horizontal error bars represent the uncertainties of the SN-ICP-MS analysis ($n = 5$), which were overlapped by the data symbols. In case of the use of laser fluence of 2 J cm^{-2} , no elevated ^{28}Si signal from the supporting glass material was recorded; therefore the glass signal correction of the measured elements described above was not needed at this laser fluence.

The LOD values of elements of interest calculated based on 3σ of the agarose gel blank standard measurements were used as the criterion to compare both LA-ICP-MS systems. Calculated LOD (Table 4) for the 213 nm laser coupled to ICP-(Q)MS system were: 27 mg kg^{-1} (Fe), 5.2 mg kg^{-1} (Zn) and 0.31 mg kg^{-1} (Pb). The LOD's for Fe were relatively high since minor isotope ^{57}Fe has been measured. Limits of detection for Fe and other elements obtained using the 193 nm ArF* coupled to LA-ICP-(SF)MS were considerably lower: 8.7 mg kg^{-1} (Fe), 0.57 mg kg^{-1} (Zn) and 0.07 mg kg^{-1} (Pb). This might have been caused by higher sensitivity of the (SF)MS instrument compared to (Q)MS and also by the use of 193 nm laser wavelength coupled to LA-ICP-(SF)MS, which is in general more effective for the laser ablation of transparent materials.

3.3. LA-ICP-MS quantitative mapping of *H. diminuta* thin sections using agarose standards

3.3.1. Absorption of radiation by soft tissue and calibration standards at laser wavelengths

The laser beam interaction with the sample and thus related amount of ablated material strongly depends on the absorbed portion of laser beam energy. Therefore, absorption coefficients of calibration and analyzed samples should be ideally close each other at lasing wavelength to provide similar ablation rates thus enabling quantification with minimum bias. The aim of the following measurement was to estimate sample/standard absorption at 193 and 213 nm.

For the absorption measurement both the soft tissue section and agarose standard were transferred onto the outer surface of quartz cuvettes enabling the absorbance measurement in the UV-region. It is also necessary to note that absorption of the soft tissue section embedded in the paraffin might be affected by possible presence of wax in tissue pores. It should also be emphasized that the absorbance value averaged over the whole section area is thus obtained, which does not take into account the tissue density local variation within the section area. For that reasons the measured absorbance gives only rough estimate.

The absorbance spectrum in Fig. 6 shows that spiked agarose standard (red line) has lower absorbance compared to the paraffin-embedded soft tissue for both the 193 nm and 213 nm wavelengths. The absorption of radiation by both materials is in general higher in the deeper UV region thus preferring laser ablation using 193 nm over 213 nm laser. The standard and tissue differ in thickness which requires relating of measured absorbance to unit optical path. The absorbance values normalized to the thickness of $100 \mu\text{m}$ for standard and tissue were 1.445 and 2.365 at 193 nm, and 1.100 and 1.753 at 213 nm,

Table 4

The coefficients of determination and LOD values for the 213 nm LA-ICP-(Q)MS and 193 nm LA-ICP-(SF)MS of Fe, Zn and Pb.

	213 nm LA-ICP-(Q)MS Adj. R-square	LOD (mg kg^{-1})	193 nm LA-ICP-(SF)MS Adj. R-square	LOD (mg kg^{-1})
Fe	0.9948	27	0.9918	8.7
Zn	0.9887	5.2	0.9867	0.57
Pb	0.9987	0.31	0.9943	0.07

respectively. In other words, agarose is more transparent and transmits at 193 nm radiant flux 8.3 times higher compared to tissue. Similarly, at 213 nm agarose transmits radiant flux 4.5 times higher than tissue. It is supposed that this ratio is reflected in different ablation rates, although absorption itself is not the only influencing material property. At the same time, it is assumed that this effect is compensated by internal standardization.

The maximum absorbance of the soft tissue in paraffin wax was observed at the laser wavelength of 193 nm while the maximum absorbance of the agarose standard was moved to lower UV region that was outside the measuring range. The use of 213 nm LA has been associated with the decrease of the absorbance of 24% for the agarose standard compared to the 193 nm laser. However, the difference in the absorbance between soft tissue and agarose standard was slightly lower for the 213 nm laser and thus the 213 nm laser ablation was preferred over the 193 nm laser.

3.3.2. LA-ICP-MS mapping of tapeworm thin section

The optimized procedure for quantitative elemental mapping based on the use of in-house prepared set of spiked agarose calibration standards with content range of $0\text{--}500 \text{ mg kg}^{-1}$ of Zn and $0\text{--}30 \text{ mg kg}^{-1}$ of Pb and Fe was demonstrated by LA-ICP-MS imaging of *H. diminuta* thin sections using 213 nm laser coupled to LA-ICP-(Q)MS. The hosting rat organism was exposed to total of 36 mg of Pb. The Pb preferred storing locations in the resulting paraffin wax-embedded tapeworm cross sections originating from the terminal part of the tapeworm were studied together with Zn and Fe distributions as biogenic elements. The thin section for the morphological observation (Fig. 7a) stained with Weigert's hematoxylin and counterstained with 1% eosin B solution shows the morphology of the sample with the areas where the ovules (dark spots) are stored.

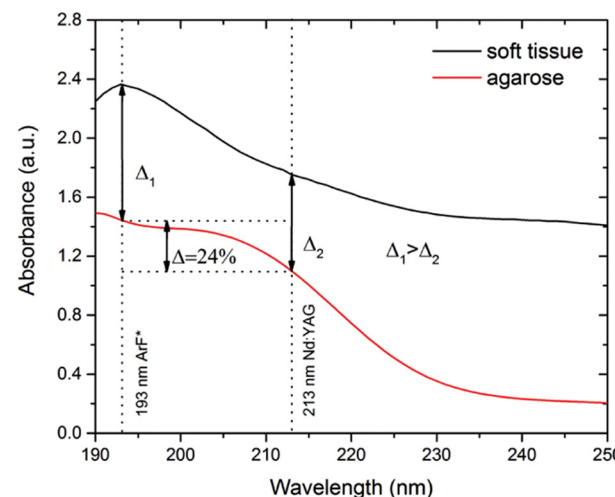


Fig. 6. Absorbance spectrum of the paraffin-embedded *H. diminuta* soft tissue and agarose calibration standard in the UV region (absorbance was normalized to the thickness of $100 \mu\text{m}$). Δ - difference in the absorbance at 193 nm and 213 nm laser wavelengths of the agarose standard. (For interpretation of the references to color in this figure legend, the reader is referred to the web version of this article.)

During the LA analysis the prepared set of spiked agarose standards was placed into the ablation cell together with the *H. diminuta* cross thin section. Tapeworm tissue was analyzed using the optimized conditions. In total 45 lines with the length of 5.1 mm and 100 μm spacing between the lines (ablated area 5.1 mm \times 4.5 mm) were ablated on the *H. diminuta* cross section (Fig. 7b). Standards were analyzed both prior and after the data acquisition from the soft tissue section. Three lines with the length of 3 mm were ablated on each of the standards using the same laser ablation conditions as in the case of thin section. ^{12}C was used as normalizing element and the resulting 2D quantitative mapping was performed using the Thermo Scientific™ GRAMS/3D Spectroscopy Software.

In Fig. 7 are the resulting ^{56}Fe , ^{66}Zn , and ^{208}Pb elemental distributions. The quantified elemental distributions of Fe and Zn (Fig. 7c, d) as biogenic elements that are naturally incorporated into many coenzymes were found to be more or less uniform across the thin section. Fe was uniformly distributed across the whole area of the thin section including both the tegument and the inner area while Zn was concentrated more in the inner part of the section. The content of Zn in the

tegument was depleted. The quantified distribution of Pb (Fig. 7e) shows distinct areas of localization concentrated more on the margins of the thin section.

Areas, where the higher Zn concentrations were detected using LA-ICP-MS, correspond well with regions formed by uterus and fertilized eggs in gravid proglottids of *H. diminuta*. This finding is not surprising with regards to Zn essential functions in reproduction, embryogenesis, development and growth processes including protein synthesis, DNA replication and its integrity. On the other hand, the tegument, cortical structures and longitudinal muscle show lower Zn concentration when compared to that of reproductive structures and eggs.

Fe seems to be distributed homogeneously across the whole area of thin section including either the surface (tegumental) or inner (parenchymal) parts of gravid proglottids. The highest Fe concentration was detected in the region, where the histological section passes through cortical area and longitudinal muscles. Therefore, higher Fe levels may be associated with muscle structures or non-heme Fe in mitochondria. However, laser spot size used for analyses and bioimaging does not allow us to define Fe-rich structure more precisely.

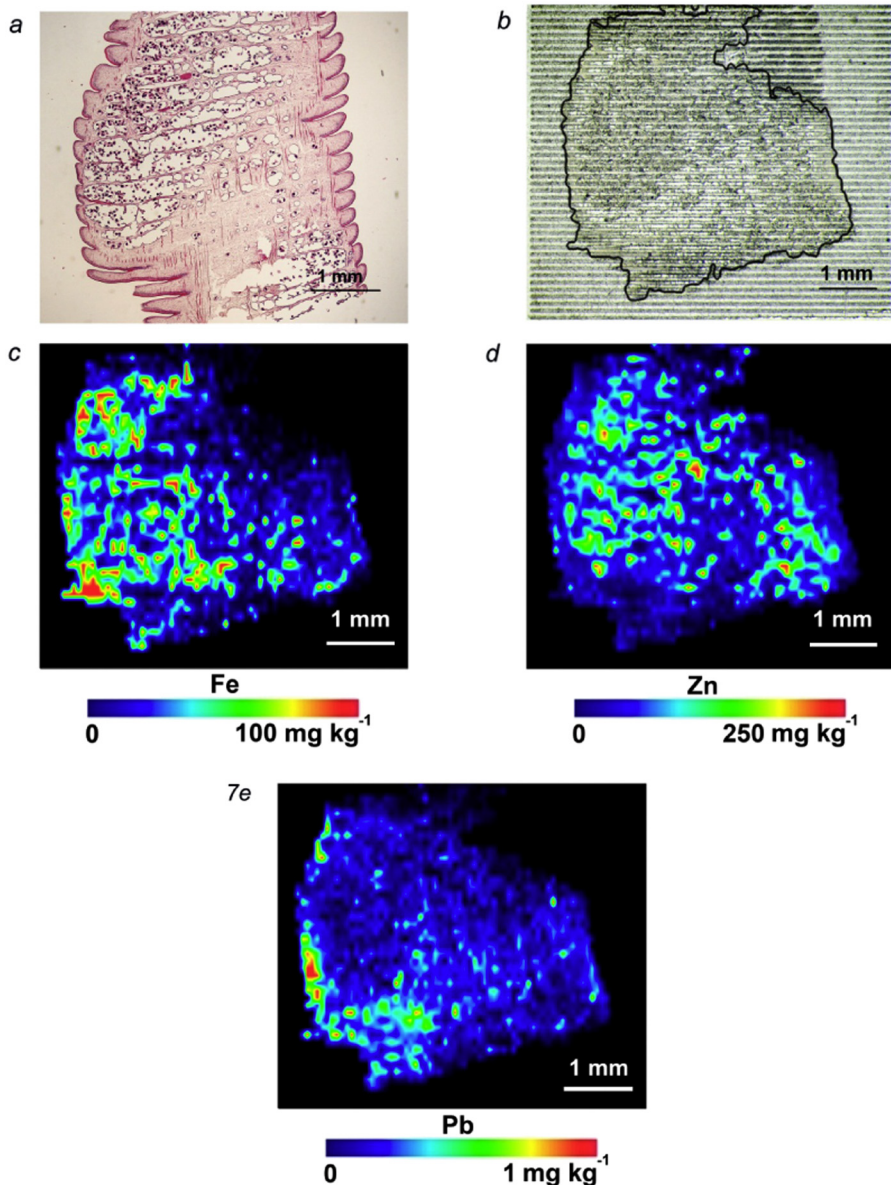


Fig. 7. (a) Thin section for morphological observation; (b) picture of the thin section subjected to LA-ICP-(Q)MS analysis after laser ablation using 213 nm line scan mode where the soft tissue area is highlighted by black perimeter line; (c) Fe, (d) Zn, (e) Pb are the quantitative elemental maps.

Concerning Pb, LA-ICP-MS results indicate that this toxic heavy metal, which lacks any biogenic function, may be concentrated only in surface layer – the tegument. Presented results indicate, Pb not to be actively absorbed and distributed within internal structures of cestode strobila. However, it should be mentioned, that Pb-hot spot was detected only in one side of histological section, whereas on the opposite side (in the tegument of the same proglottids) higher Pb levels are not evident. Therefore, with regard to Pb, results of our study should be considered as preliminary and an unambiguous Pb localization has yet to be proven by specific analysis with higher resolution.

Generally taking into account previously published results focusing only on bulk elemental analysis of parasitic platyhelminthes soft tissues, the specification of elemental distribution within the thin slice of tapeworm in micrometric scale provides the additional but detailed information. The storage of biogenic elements (Zn and Fe) inside of proglottid confirms function of these elements in tapeworm metabolic process. Contrarily, toxic lead is not probably absorbed into inner structure.

4. Conclusions

This study has demonstrated the utilization of in-house prepared set of matrix similar standards based on spiked agarose with elements of interest for multi-elemental quantitative mapping of metals in *H. diminuta* thin sections as a possible bio-accumulating organism. Such custom made standards have advantage they may be spiked with elements of interest in the range that fit the actual contents of studied elements within the soft tissue subjected to LA-ICP-MS.

The influence of laser operating conditions including ablation mode, spot size and laser fluence on limits of detection, resolution and analysis time has been studied using 213 nm laser ablation coupled to (Q)MS. Two modes of laser ablation were tested including spot mode and line scan analysis. Line scan was favored due to reduction of total analysis time needed to obtain data for quantitative elemental maps. Laser fluences of 2 and 8 J cm⁻² were tested using the line scan. Use of the higher of the two tested fluences led to the total ablation through one of the measured standards onto the glass support and related deterioration of calibration dependence for Fe caused by the increased signal at the *m/z* 57 arising from the supporting glass slide. Correction procedure for this signal has been proposed. The correction procedure led to better tightness of correlation of the calibration dependence of Fe based on the Adj. R² values (from 0.8116 to 0.9754). Nevertheless, the correction procedure for the glass related signal did not remove the influence of the signal from glass supporting material entirely. Therefore use of lower laser energy of 2 J cm⁻², that was not sufficient to ablate either through the agarose standard onto the glass support or the transparent glass material using the laser wavelength of 213 nm, was preferred for the subsequent elemental mapping procedure.

The optimized laser ablation conditions were tested using two LA-ICP-MS systems including 213 nm Nd:YAG laser coupled to ICP-(Q)MS and 193 nm ArF* laser coupled to ICP-(SF)MS. The limits of detection based on the 3σ of agarose blank standard replicate measurements were significantly lower in the case of LA-ICP-(SF)MS. The tightness of correlation of the calibration dependence for all measured elements using both instruments was satisfactory (starting with 0.9867 for Zn up to 0.9987 for Pb).

The prepared set of multi-elemental agarose gel standards was tested and successfully utilized for the quantitative elemental mapping of *H. diminuta* paraffin-embedded thin sections using the 213 nm solid state Nd:YAG coupled to ICP-(Q)MS upon optimized laser ablation conditions using line scan mode at the laser spot size of 65 μm, scan speed of 91 μm s⁻¹, fluence of 2 J cm⁻² and repetition rate of 10 Hz. Carbon ¹²C⁺ was used as internal standard to correct for the different tissue density and absorption rates. The content of Fe and Zn as biogenic elements was found to be homogeneously distributed within the cross section

of the tissue while the Pb elemental distribution was found to be more concentrated in the tegument.

Acknowledgements

This project was supported by Czech Science Foundation GA13-18154S. The results of this research have been acquired within CEITEC 2020 (LQ1601) project with financial contribution made by the Ministry of Education, Youth and Sports of the Czech Republic within special support paid from the National Programme for Sustainability II Funds.

References

- [1] M.C. Santos, M. Wagner, B. Wu, J. Scheider, J. Oehlmann, S. Cadore, J.S. Becker, *Talanta* 80 (2009) 428–433.
- [2] F. Watt, *Cell. Mol. Biol.* 42 (1996) 17–26.
- [3] I.C. Fuentealba, S. Haywood, J. Trafford, *Liver* 7 (1987) 277–282.
- [4] D.S. Gholap, A. Izmer, B. De Samber, J.T. van Elteren, V.S. Selih, R. Evens, K. De Schampelaere, C. Janssen, L. Balcaen, I. Lindemann, L. Vincze, F. Vanhaecke, *Anal. Chim. Acta* 664 (2010) 19–26.
- [5] B. De Samber, G. Silversmit, R. Evens, K. De Schampelaere, C. Janssen, B. Masschaele, L. Van Hoorebeke, L. Balcaen, F. Vanhaecke, G. Falkenberg, L. Vincze, *Anal. Bioanal. Chem.* 390 (2008) 267–271.
- [6] F.J. Ager, M.D. Ynsa, J.R. Dominguez-Solis, C. Gotor, M.A. Respaldiza, L.C. Romero, *Nucl. Instrum. Methods B* 189 (2002) 494–498.
- [7] I.M. Weiersbye, C.J. Straker, W.J. Przybylowicz, *Nucl. Instrum. Methods B* 158 (1999) 335–343.
- [8] J. Mesjasz-Przybylowicz, W.J. Przybylowicz, *Nucl. Instrum. Methods B* 189 (2002) 470–481.
- [9] S. Chandra, G.H. Morrison, *Biol. Cell.* 74 (1992) 31–42.
- [10] J.L. Guerquin-Kern, T.D. Wu, C. Quintana, A. Croisy, *Biochim. Biophys. Acta Gen. Subj.* 1724 (2005) 228–238.
- [11] D. Touboul, F. Kollmer, E. Niehuis, A. Brunelle, O. Laprevote, *J. Am. Soc. Mass Spectrom.* 16 (2005) 1608–1618.
- [12] A. Izmer, D. Gholap, K. De Houwer, F. Cuyckens, F. Vanhaecke, *J. Anal. Atom. Spectrom.* 27 (2012) 413–418.
- [13] A. Kindness, C.N. Sekaran, J. Feldmann, *Clin. Chem.* 49 (2003) 1916–1923.
- [14] J.S. Becker, M. Zoriy, V.L. Dressler, B. Wu, J.S. Becker, *Pure Appl. Chem.* 80 (2008) 2643–2655.
- [15] J.S. Becker, *Int. J. Mass Spectrom.* 289 (2010) 65–75.
- [16] D. Pozebon, V.L. Dressler, M.F. Mesko, A. Matusch, J.S. Becker, *J. Anal. Atom. Spectrom.* 25 (2010) 1739–1744.
- [17] M. Zoriy, A. Matusch, T. Spruss, J.S. Becker, *Int. J. Mass Spectrom.* 260 (2007) 102–106.
- [18] S. Theiner, E. Schreiber-Brynzak, M.A. Jakupc, M. Galanski, G. Koellensperger, B.K. Keppler, *Metallooms* 8 (2016) 398–402.
- [19] R.W. Hutchinson, A.G. Cox, C.W. McLeod, P.S. Marshall, A. Harper, E.L. Dawson, D.R. Howlett, *Anal. Biochem.* 346 (2005) 225–233.
- [20] T. Van Acker, S.J.M. Van Malderen, M. Van Heerden, J.E. McDuffie, F. Cuyckens, F. Vanhaecke, *Anal. Chim. Acta* 945 (2016) 23–30.
- [21] M.V. Zoriy, M. Dehnhardt, A. Matusch, J.S. Becker, *Spectrochim. Acta B* 63 (2008) 375–382.
- [22] J.A.T. Pugh, A.G. Cox, C.W. McLeod, J. Bunch, B. Whitby, B. Gordon, T. Kalber, E. White, *J. Anal. Atom. Spectrom.* 26 (2011) 1667–1673.
- [23] T. Narukawa, S. Willie, *J. Anal. Atom. Spectrom.* 25 (2010) 1145–1148.
- [24] J.S. Becker, A. Matusch, C. Palm, D. Salber, K.A. Morton, S. Becker, *Metallooms* 2 (2010) 104–111.
- [25] J. Feldmann, A. Kindness, P. Ek, *J. Anal. Atom. Spectrom.* 17 (2002) 813–818.
- [26] D. Gholap, J. Verhulst, W. Ceelen, F. Vanhaecke, *Anal. Bioanal. Chem.* 402 (2012) 2121–2129.
- [27] H.J. Staerk, R. Wennrich, *Anal. Bioanal. Chem.* 399 (2011) 2211–2217.
- [28] M. Debeljak, J.T. van Elteren, K. Vogel-Mikus, *Anal. Chim. Acta* 787 (2013) 155–162.
- [29] J.S. Becker, M.V. Zoriy, C. Pickhardt, N. Palomero-Gallagher, K. Zilles, *Anal. Chem.* 77 (2005) 3208–3216.
- [30] F. Boué-Bigne, B.J. Masters, J.S. Crighton, B.L. Sharp, *J. Anal. Atom. Spectrom.* 14 (1999) 1665–1672.
- [31] B.J. Masters, B.L. Sharp, *Anal. Commun.* 34 (1997) 237–239.
- [32] D. Gunther, S.E. Jackson, H.P. Longerich, *Spectrochim. Acta B* 54 (1999) 381–409.
- [33] J.J. Leach, L.A. Allen, D.B. Aeschliman, R.S. Houk, *Anal. Chem.* 71 (1999) 440–445.
- [34] I. Konz, B. Fernandez, M. Luisa Fernandez, R. Pereiro, A. Sanz-Medel, *Anal. Bioanal. Chem.* 403 (2012) 2113–2125.
- [35] D. Hare, F. Burger, C. Austin, F. Fryer, R. Grimm, B. Reedy, R.A. Scolyer, J.F. Thompson, P. Doble, *Analyst* 134 (2009) 450–453.
- [36] A. Limbeck, P. Galler, M. Bonta, G. Bauer, W. Nischkauer, F. Vanhaecke, *Anal. Bioanal. Chem.* 407 (2015) 6593–6617.
- [37] B. Jackson, S. Harper, L. Smith, J. Flinn, *Anal. Bioanal. Chem.* 384 (2006) 951–957.
- [38] D.A. Frick, D. Gunther, *J. Anal. Atom. Spectrom.* 27 (2012) 1294–1303.
- [39] G.D. Pessoa, J.L. Capelo-Martinez, F. Fdez-Riverola, H. Lopez-Fernandez, D. Glez-Pena, M. Reboiro-Jato, M.A.Z. Arruda, *J. Anal. Atom. Spectrom.* 31 (2016) 832–840.
- [40] M. Vasinova Galiova, M.N. Fisakova, J. Kynicky, L. Prokes, H. Neff, A.Z. Mason, P. Gadas, J. Kosler, V. Kanicky, *Talanta* 105 (2013) 235–243.

- [41] J. Lear, D. Hare, P. Adlard, D. Finkelstein, P. Doble, *J. Anal. Atom. Spectrom.* 27 (2012) 159–164.
- [42] T. Vaculovic, T. Warchilova, Z. Cadkova, J. Szakova, P. Tlustos, V. Otruba, V. Kanicky, *Appl. Surf. Sci.* 351 (2015) 296–302.
- [43] K. MacKenzie, *Mar. Pollut. Bull.* 38 (1999) 955–959.
- [44] B. Sures, *Parasitology* 126 (2003) S53–S60.
- [45] B. Sures, *Trends Parasitol.* 20 (2004) 170–177.
- [46] J. Torres, J. Peig, C. Eira, M. Borras, *Environ. Pollut.* 143 (2006) 4–8.

Utilization of Laser-Assisted Analytical Methods for Monitoring of Lead and Nutrition Elements Distribution in Fresh and Dried *Capsicum annuum* L. Leaves

MICHAELA GALIOVÁ,¹ JOZEF KAISER,^{2*} KAREL NOVOTNÝ,¹ MARTIN HARTL,³
RENÉ KIZEK,⁴ AND PETR BABULA⁴

¹Department of Chemistry, Faculty of Science, Masaryk University, Kotlářská 2, 611 37 Brno, Czech Republic

²Institute of Physical Engineering, Brno University of Technology, Technická 2896/2, 616 69 Brno, Czech Republic

³Institute of Machine and Industrial Design, Brno University of Technology, Technická 2896/2, 616 69 Brno, Czech Republic

⁴Department of Chemistry and Biochemistry, Mendel University in Brno, Žemědělská 1, 613 00 Brno, Czech Republic

KEY WORDS LIBS; LA-ICP-MS; elemental mapping

ABSTRACT Laser induced breakdown spectroscopy (LIBS) and laser ablation inductively coupled plasma mass spectrometry (LA-ICP-MS) have been applied for high-resolution mapping of accumulation and distribution of heavy metal (lead) and nutrition elements (potassium, manganese) in leaves of *Capsicum annuum* L. samples. Lead was added in a form of Pb(NO₃)₂ at concentration up to 10 mmol L⁻¹ into the vessels that contained tap water and where the 2-months old *Capsicum annuum* L. plants were grown another seven days. Two dimensional maps of the elements are presented for both laser-assisted analytical methods. Elemental mapping performed on fresh (frozen) and dried *Capsicum annuum* L. leaves are compared. *Microsc. Res. Tech.* 74:845–852, 2011. © 2010 Wiley-Liss, Inc.

INTRODUCTION

In the recent years, the effort to develop and utilize methods that enable to detect contamination by toxic elements and compounds has increased, due to high mobility of the heavy elements and their ability to get into the animal and human body through the food chain. The content of heavy metals in soil, water, or biological tissues is increasing mainly in industrially developed countries (Liu et al., 2007). The mostly dangerous and for this reason also intensively tracked elements are Pb, Cd, Ag, Hg, As etc.

One of the most “natural” ways to subtract hazardous compounds or elements from soil or water is by using plants with high uptake ability. This process is called phytoremediation (Fig. 1). The aim of phytoremediation is to achieve maximum accumulation of potentially toxic compounds to hyperaccumulator plants (Krämer, 2005). Several authors deal with a different kind of remediation technologies (Chen et al., 2000; Mulligan et al., 2001). It was shown, that the concentration and form of the toxic metal in the soil solution affect the amounts of metal absorbed by a plant (Patra et al., 2004).

Finding proper plant species for phytoremediation is a complex task that includes extensive studies of selected plants in controlled environment. At laboratory condition, heavy metals are added to growth solutions in various forms. They affect the mobility of monitored nutrition elements, interaction with the other species, and try to simulate a soil solution of field scale (Adriano et al., 2004). The level of heavy metal accumulation is dependent on a lot of factors like presence of another compounds or elements [e.g., Fe, ethylenediaminetetraacetic acid (EDTA), ethylenediamine-N, N'-disuccinic acid (EDDS), tartrate, glutamate], pH, kind of plants. Phytoremediation process is affected by change of mobility of investigated elements and enables increasing of

effectivity of cleaning phase. As an example, for chelated-assisted phytoremediation, increasing content of heavy metals in plant samples were observed after addition of EDTA caused by increased mobility of investigated elements (Doumett et al., 2008; January et al., 2008; Núñez-López et al., 2008; Römkens et al., 2002).

In this study as a typical heavy metal, lead was chosen for all experiments. This element is highly toxic and it is dangerous already in a small content, ~30–300 µg g⁻¹ (Liu et al., 2007). In some cases, lower concentrations of lead might stimulate metabolic processes due to its similarity with calcium(II) ions, which may be replaced by lead(II) ions. It is well known that toxicity of heavy metals ions depend on their concentration, kind of salts and plant species (higher toxicity was demonstrated in the case of organic forms of heavy metals). The major processes, which may be affected, are seed germination, seedling growth, photosynthesis, plant water status, mineral nutrition, and enzymatic activities (Chen et al., 2000). Toxic elements are stored in various plants tissues and organs (root, stem, leaves, flowers, fruits, or seeds) at different concentrations. Lead is accumulated mainly in roots in comparison with its content in the other parts of plant. However, it is possible to increase the lead content in aerial parts by translocation of element from roots to these aerial parts by adding EDTA into the soil (Doumett et al.,

*Correspondence to: Jozef Kaiser, Institute of Physical Engineering, Brno University of Technology, Technická 2896/2, 616 69 Brno, Czech Republic. E-mail: kaiser@fme.vutbr.cz

Received 12 August 2010; accepted in revised form 18 October 2010

Contract grant sponsor: Ministry of Education of the Czech Republic; Contract grant numbers: ME09015, ME10061, MSM0021622412, MSM 0021622411; Contract grant sponsor: Czech Grant Agency; Contract grant number: GACR 522/07/0692

DOI 10.1002/jemt.20967

Published online 16 December 2010 in Wiley Online Library (wileyonlinelibrary.com).

2008). This can be caused by influence of ATPases function of specialized membrane transporters (Hong et al., 2007). Increasing lead transport through xylem from roots to stem is reported in (Piechalaka et al., 2003). The same effect was monitored in *Pinus radiata* D. Don. Plants of this species were exposed to $\text{Pb}(\text{NO}_3)_2$ with and without EDTA or H-EDTA. Without addition of chelating reagent, Pb content was measured mainly in cell walls of root tissues. After application of (H) EDTA, Pb accumulation was observed inside of adjacent to cell walls and in intercellular spaces of needles (Jarvis and Leung, 2002). Similar experiment is described in the article, where authors deal with influence of EDTA to distribution of Pb, Ni, and Zn (Barona et al., 2001). Determination of the effect of NaCl irrigation on displacement of heavy metals with and without EDTA is shown in (Wahla and Kirkham, 2008).

In (Antosiewicz, 2005), regulated lead deposition in cell walls of plants was studied in four different plant species. It was observed that lead toxicity increases with decreasing calcium content. The influence of Pb content on total amount and distribution of potassium and manganese was also studied (Galiová et al., 2007).

The uptake ability of different plant species is intensively investigated. As an example, monitoring of distribution of Pb, Cd, and Zn into various parts of twelve different species and removal efficiency was studied in (Liu et al., 2007). The distribution of Pb, Ba, and Cd in different plants is investigated in (Pichtel et al., 2000). The uptake can be dependent on pH and concentration of heavy metals in contaminated soil (Komárek et al., 2007). In (Liu et al., 2000), lead was added in a form of $\text{Pb}(\text{NO}_3)_2$ at different concentrations. The influence of lead nitrate on root, hypocotyl and shoot growth and its accumulation in each part was studied. It was showed that the amount of Pb in roots increases with increasing Pb content. Lead-exposed plants showed reduction in root calcium, zinc and copper contents. The total Pb content was measured by ICP-MS (Brunet et al., 2008).

In the work (Brunet et al., 2009) the study of the lead nitrate impact on steady-state accumulation of messengers corresponding to stress responsive genes in grass pea (*L. sativus L.*) plants is presented. The plants accumulated the pollutant mostly in their roots. Direct effects of lead on these tissues included growth arrest and variations in target gene transcript accumulation.

The presence of heavy metal in plant affected by enzyme activities was studied in (Verma et al., 2003).

Regarding the analytical techniques, the total amount of toxic elements present in the plant after the phytoremediation process can be measured by several techniques, for example by atomic absorption spectrometry (AAS), inductively coupled plasma optical emission or mass spectrometry (ICP-MS/OES) (Pereira et al., 2004; Suleiman et al., 2008; Masson et al., 2010). Dissolution of samples for analysis is however a time consuming process, moreover by using this technique information on distribution of observed ions are lost. In general, there is a lack of information where monitored toxic ions are stored in various parts of hyperaccumulator plants. In order to obtain data about trafficking and storage of these ions, methods enable mapping the chemical composition of sample in solid state should be applied.

Laser-assisted analytical methods offer simple and fast tool for chemical mapping (Kaiser et al., 2009; Galiová et al., 2008; Becker et al., 2010a,b). These techniques can be applied without any or with simple and straightforward sample preparation such as ablation of impurities from the sample surface by applying "cleaning" pulses. Both, LA-ICP-MS and LIBS allow qualitative and semiquantitative direct analysis, profiling, and mapping of elements distribution. Basically, the achievable spatial resolution of these methods depends only on the diameter of ablation crater created by the focused laser beam (Kaiser et al., 2009; Galiová et al., 2008; Becker et al., 2010a,b; Novotný et al., 2008). The main disadvantage of techniques that uses laser ablation for sampling is a lack of certified reference materials for calibration. The typical detection limits (LOD) for LA-ICP-MS analyses of plant samples are approximately $\mu\text{g g}^{-1}$ (Becker et al., 2010; Santos et al., 2009). The detection limits of LIBS analysis are in general 10 times worse ($10 \times \mu\text{g g}^{-1}$) (Vadillo et al., 1999). It should be also noted that the LOD for LIBS can be improved by applying modified LIBS techniques as double-pulse (DP) LIBS or combining LIBS by laser-induced fluorescent spectrometry (LIFS) (Samek et al., 1998; Telle et al., 2001; Laville et al., 2009).

Here we report on a pilot study focused on monitoring of effects of lead(II) ions on important field crop—*Capsicum annuum L.* (pepper). In the case of improvement of its features, the usage of this plant in field conditions is relatively undemanding. Laser-assisted analytical methods (LIBS, LA-ICP-MS) were utilized for mapping of lead and nutrition elements distribution in pepper leaves treated by lead. The influence of water present in sample on results of LIBS and LA-ICP-MS analysis was investigated. The LIBS results are compared with outcomes obtained by LA-ICP-MS.

EXPERIMENTAL

Plants Cultivation and Sample Preparation

C. annuum L. seeds were germinated on wet filter paper in special vessels at $23^\circ\text{C} \pm 2^\circ\text{C}$ in dark. After 7 days, the pepper seedlings were placed into vessels containing Richter solution and cultivated in aeroponic system for 2 months with 14-h long daylight per day (maximal light intensity was about 5,400 lx) at a temperature $21\text{--}23^\circ\text{C}$. When the roots reached ~ 2 cm, the seedlings were placed into vessels contained 25 L modified aerated Richter's nutrient solution. The concentrations of macroelements per 1 L were 3 mmol $\text{Ca}(\text{NO}_3)_2$, 2 mmol KNO_3 , 1.5 mmol KH_2PO_4 , 1 mmol $\text{MgSO}_4 \cdot 7 \text{H}_2\text{O}$. Iron in the form of Fe-EDTA was added to the nutrient solution (0.18 mol L^{-1} Fe). Micro-elements were added to the nutrient solution in the form of Hoagland's AZ solution.

After that, the selected very vital, well-growing, uniform 2-month old pepper plants were placed in the vessels that contained tap water with addition of $\text{Pb}(\text{NO}_3)_2$ (0, 0.5, 1, 2, and 10 mmol L^{-1}), where they were grown for 7 days. Plants cultivated without the presence of lead served as a control.

First changes in physiology of experimental plants were well evident already after 24 h of treatment in the highest applied lead(II) concentration; these

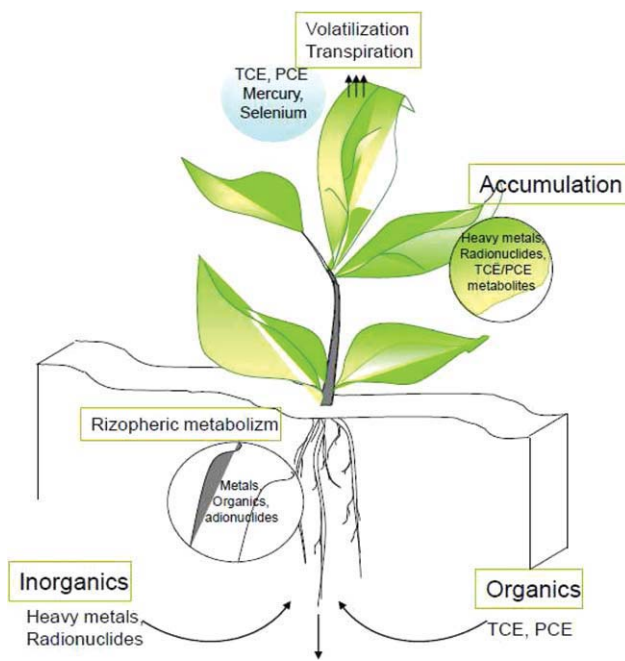


Fig. 1. Phytoremediation can occur through a series of complex interactions between plants, microbes, and the soil, including accumulation, hyperaccumulation, exclusion, volatilization, and degradation. Plants also stabilize mobile contaminated sediments by forming dense root mats under the surface. [Color figure can be viewed in the online issue, which is available at wileyonlinelibrary.com.]

changes included especially reduction of experimental solution uptake. After 30 h of treatment, also morphological changes resulting from water uptake reduction were well evident. After 72 h, these changes were well evident also in the case of other experimental variants—plants treated by lead(II) ions at concentrations 0.5 and 1 mmol L⁻¹. After 168 h, plants treated by highest lead(II) ions concentration (10 mmol L⁻¹) demonstrated very significant nonphysiological changes including chlorophyll degradation, necroses with leaves browning and significant reduction of water content; these changes were not so accentuated in two lower concentrations (Fig. 2). Control plants and plants treated by lead(II) ions in lowest concentration (0.5 mmol L⁻¹) did not embody growth depression (Fig. 2a).

Ontogenetically oldest leaves ($n = 6$) were sampled from each variant at certain time intervals (0, 48, 96, 144, and 168 h) during the experiment. After sampling, the leaves were rinsed three times in distilled water and 0.5 mol L⁻¹ EDTA. In addition, each harvested leave was divided onto halves. One half was stored in deep freezer at -80°C (Sanyo, Japan) and the second one was dried for 12 h at 45°C (Memmert, Germany) (Fig. 2b).

From this relatively large set of samples for LIBS and LA-ICP-MS mapping, the representative leaves from untreated (control) sample and leaves from samples treated by 10 mmol L⁻¹ Pb(NO₃)₂ for 2 days were used.

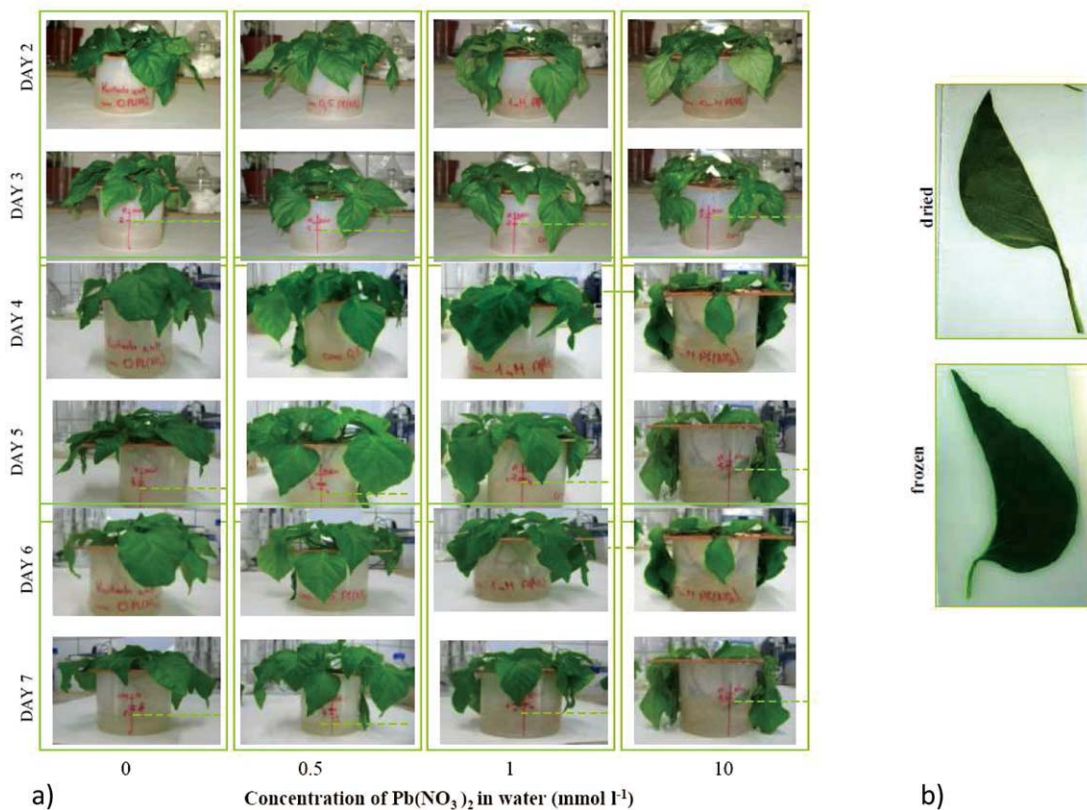


Fig. 2. (a) Set of *C. annuum* L. samples used for monitoring effects of lead(II) ions. (b) Example of the investigated *C. annuum* L. leaves. [Color figure can be viewed in the online issue, which is available at wileyonlinelibrary.com.]

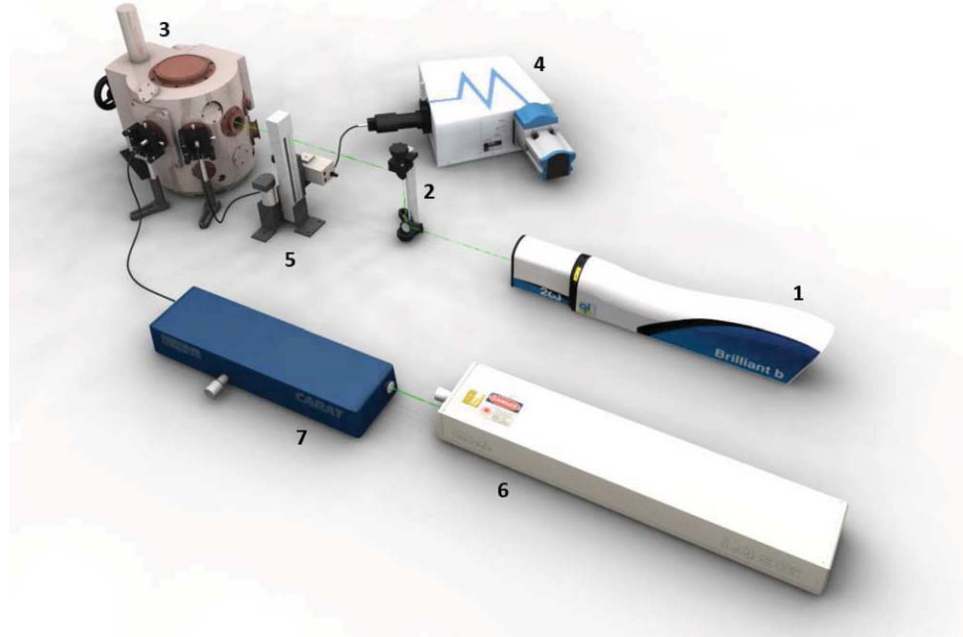


Fig. 3. Computer rendering of the LIBS experimental setup: 1. Nd:YAG ablation laser with a module for second harmonic (532 nm) generation (Quantel Brilliant B, France), 2. Periscope, 3. Interaction chamber (TESCAN s.r.o., Czech Republic), 4. Spectrograph (LOT Oriel 260i, USA) equipped with ICCD camera (Andor

IStar 734i, UK), 5. CCD camera for sample alignment, 6. Nd: YAG laser (Solar LS LQ529A, Belarus), and 7. Ti: Sa laser (Solar LS LX325, Belarus) for further developments (LIBS+LIFS). [Color figure can be viewed in the online issue, which is available at wiley.onlinelibrary.com.]

LIBS Setup

The LIBS setup utilized in our experiments is shown in Figure 3. For creating the microplasma, Nd:YAG laser system (Brilliant B, Quantel, France) working on its second harmonics frequency (532 nm) was used. The laser pulse width was ~ 5 ns and beam diameter 8 mm. LIBS signals were obtained using the energy of the laser pulse 10 mJ at the sample that was set and controlled by an energy meter (Field Master LM-P10, Coherent, USA). The samples with sample holder were placed inside the ablation chamber (TESCAN s.r.o., Czech Republic) to the stage with precision movements ($2\text{ }\mu\text{m}$ in x , y , and z direction). The LIBS measurements were realized in air at atmospherics pressure. CCD camera placed outside of the chamber was used for targeting and controlling of each ablation spot (Novotný et al., 2009). Laser beam was focused with 16 mm focal-length glass doublet (Sill Optics, Germany) and emitted radiation was collected by objective and transported with a 3-m fiber optics system onto the entrance slit of the 1/4 m monochromator (LOT Oriel 260i, USA). For LIBS measurements, the grating 2,400 g mm^{-1} of the monochromator and 10 μm entrance slit were used. As a detector an ICCD camera (Andor IStar 734i, UK) was employed. The camera was triggered by the Q-switch signal of the laser. The ICCD detector was gated 1 μs after the Q-switch signal and the integration time was 10 μs .

Analytical lines of Pb (I) 405.78 nm, Mn (I) 403.07 nm, 403.31 nm, and K (I) 404.41 nm, 404.72 nm were observed in the selected spectral interval. The LIBS ablation patterns had a spacing of 500 μm and the diameter of ablation craters was $\sim 200\text{ }\mu\text{m}$. To obtain two-

dimensional maps, background was subtracted for each shot and the area under the selected peak (for appropriate chemical element) was calculated.

LA-ICP-MS Device

Instrumentation for LA-ICP-MS consists of a laser ablation system UP 213 (New Wave, USA) and an ICP-MS spectrometer Agilent 7500 CE (Agilent, Japan). A Q-switched Nd:YAG laser ablation device works at the 5th harmonic frequency (213 nm). The ablation device is equipped with programmable xy -stages to move the sample along a programmed trajectory during ablation. Target visual inspection is accomplished by means of built-in microscope/CCD-camera system. A sample was enclosed in the SuperCell (New Wave, USA) and was ablated by the laser beam, which was focused onto the sample surface through a quartz window. The ablation cell (volume 20 cm^3) was flushed with helium (carrier gas), which transported the laser-induced aerosol to the inductively coupled plasma. A sample gas flow of argon was admixed to the helium carrier gas flow after the laser ablation cell. Therefore, the total gas flow was 1.6 L min^{-1} . Optimization of LA-ICP-MS conditions (gas flow rates, sampling depth, electrostatic lenses voltages of the MS) was performed with the glass reference material NIST SRM 612 with respect to maximum S/N ratio and minimum oxide formation (ThO^+/Th^+ counts ratio 0.2%, U^+/Th^+ counts ratio 1.1%). The optimized ICP-MS parameters are summarized in Table 1.

To analyze specific locations in the sample, for LA-ICP-MS line scanning and 2D mapping the ablation laser was used in hole drilling mode (fixed sample

position during laser ablation), for the duration of 1 s for each spot. The LA-ICP-MS ablation pattern consisted of ablation craters of $\sim 100 \mu\text{m}$ in diameter, placed in distances of $\sim 200 \mu\text{m}$. Both ablation patterns (LIBS and LA-ICP-MS) were placed near to each other. Time delay between end of laser ablation of one spot and initiation of laser ablation of following spot was 1 s. Laser ablation was performed with laser spot diameter $100 \mu\text{m}$, laser fluency 3 J cm^{-2} and repetition rate 10 Hz. The isotopes ^{208}Pb , ^{55}Mn , and ^{39}K were measured with integration time 0.1 s/isotope.

RESULTS AND DISCUSSION

Laser Ablation Measurements

In this study, the elemental mapping using the comparison of potassium (404.41 and 404.72 nm), manganese (403.07 and 403.31 nm), and lead (405.78 nm) LIBS signals measured on fresh (frozen) sample and on dried samples was realized. All results were compared with outcomes obtained by LA-ICP-MS. Typical single-shot LIBS spectra taken at two different positions on the pepper leaf samples and temporal LA-ICP-MS signals for Pb and K of *C. annuum* L. leaf samples are shown in Figure 4. Potassium was mapped as a nutrition element present in the LIBS spectral window suitable for the lead detection.

For elemental mapping, LIBS signals were recorded for each shot on the area $7.5 \times 9.5 \text{ mm}^2$ for fresh (frozen) and $7 \times 14 \text{ mm}^2$ for dried control leaf sample of *C. annuum* L. Size of LA-ICP-MS ablation pattern was $2 \times 6 \text{ mm}^2$ for all samples. In Figure 5, maps of potassium obtained from the studied area of the control (untreated) leaf measured by both techniques Figure 5a LIBS and Figure 5b LA-ICP-MS are shown. There is a comparison of potassium distribution in fresh (frozen) and dried samples. Potassium as a nutrition

element is spread homogenously within area of the control sample similar to manganese distribution (not shown). The distribution of potassium (and manganese) is not affected by presence of water in the case of fresh sample.

In Figure 6b, results of leaf sample analysis obtained after 2 days of lead (10 mmol L^{-1}) treatment, are demonstrated. The area investigated by LIBS was $6.5 \times 7.5 \text{ mm}^2$ for fresh (frozen), $6 \times 12.5 \text{ mm}^2$ for dried leaf and $2 \times 6 \text{ mm}^2$ was measured by LA-ICP-MS. Maps of potassium distribution in the studied area by laser ablation based methods are shown in Figure 6b. As it is evident from obtained experimental data, there are nonsignificant differences between control and treated plants.

We should note that also in the case of lower applied concentrations (0.5 and 1 mmol L^{-1}), there were no changes detected in potassium accumulation in comparison with potassium distribution in untreated leaf sample, in both cases of fresh and dried samples. The same results were obtained for manganese distribution in leaf samples.

The important difference was observed for lead distribution in the 2 days 10 mmol L^{-1} lead treated *C. annuum* L. leaf sample. The maps of lead obtained by LIBS and LA-ICP-MS analyses (Fig. 7) show that lead is accumulated mainly in the central vein and in surrounding area. Distribution of potassium is not affected by accumulation of the toxic element. No influence of frozen water present in the sample for analytical outcomes was detected. The results obtained by LIBS are the same for fresh and dried samples. Moreover, LA-ICP-MS analyses confirmed LIBS outcomes.

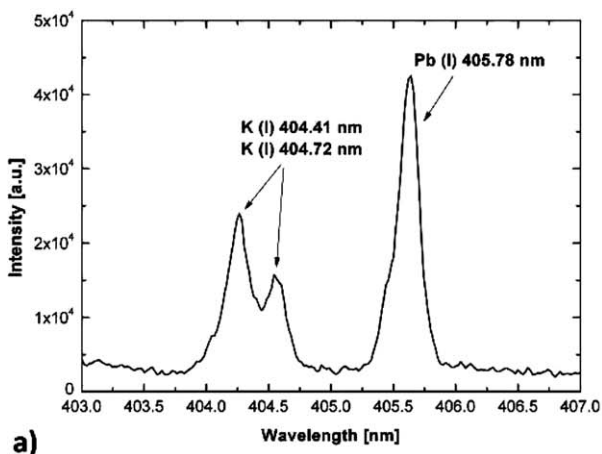
On the base of this study, we can conclude that both, fresh and dried samples can be used for monitoring of nutrition and toxic elements distribution in plant tissue. The distribution of investigated elements is not affected by the drying process.

Statistical Analysis

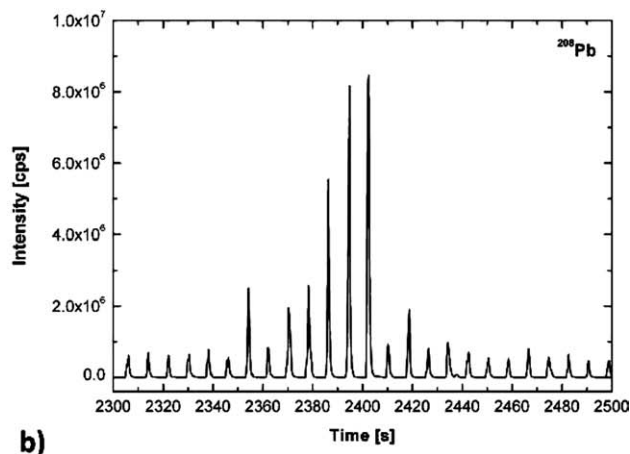
Peak area of potassium and lead from each investigated leaf derived from LIBS measurement and intensity of selected elements recorded by LA-ICP-MS were analyzed by statistical software. It was obtained that

TABLE 1. ICP-MS optimized parameters

RF power	1,350 W
Carrier gas flow	1.00 L min^{-1} He
Makeup gas	0.6 L min^{-1} Ar
Plasma gas	15.0 L min^{-1} Ar
Sampling depth	8.0 mm



a)



b)

Fig. 4. (a) Typical single shot LIBS spectra taken at two different position and (b) temporal LA-ICP-MS signal for Pb and K of the *C. annuum* L. leaf sample.

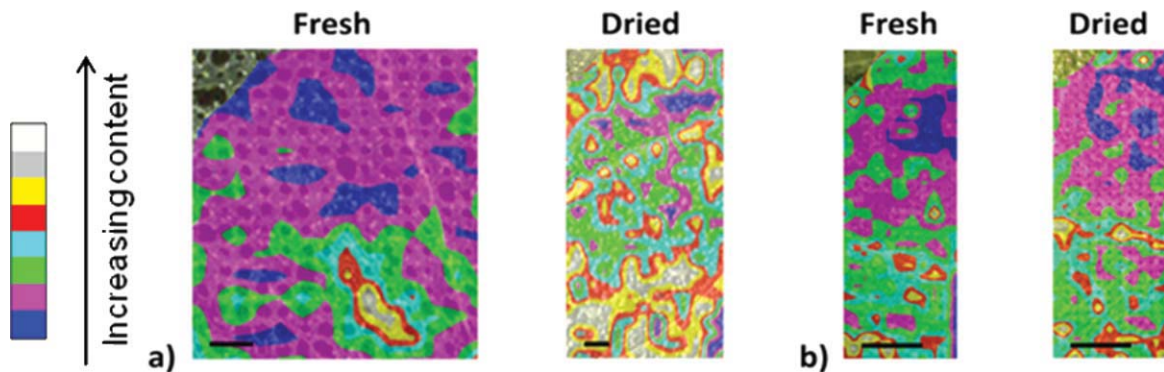


Fig. 5. The maps of K obtained from the studied area of the control (untreated) *C. annuum* L. leaf. The K distribution in fresh (frozen) and dried leaf measured by (a) LIBS and (b) LA-ICP-MS. The maps are shown together with the photos of the samples. In the upper left corners, the part of the photograph is uncovered. The length of bar is 1 mm.

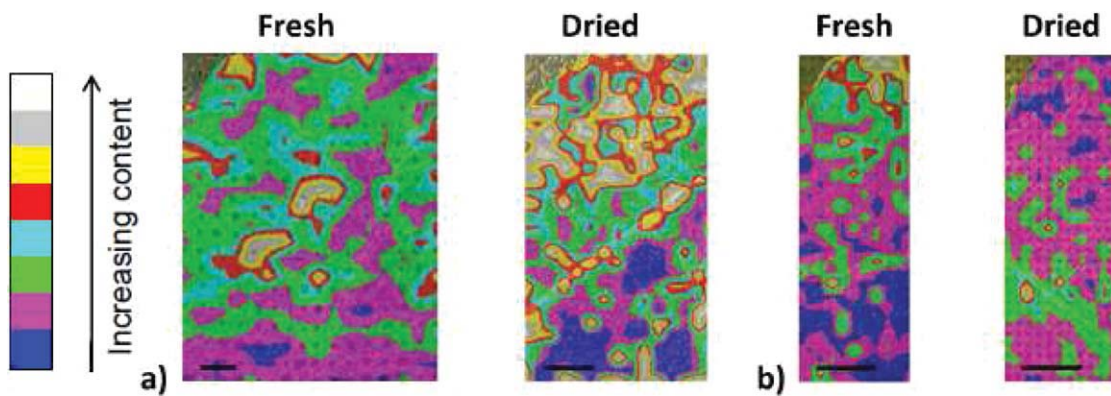


Fig. 6. The maps of K obtained from the studied area of the 2 days 10 mmol L⁻¹ Pb(NO₃)₂ treated *C. annuum* L. leaf. The K distribution in fresh (frozen) and dried samples measured by (a) LIBS and (b) LA-ICP-MS. The maps are shown together with the photos of the samples. In the upper left corners, the part of the photograph is uncovered. The length of bar is 1 mm.

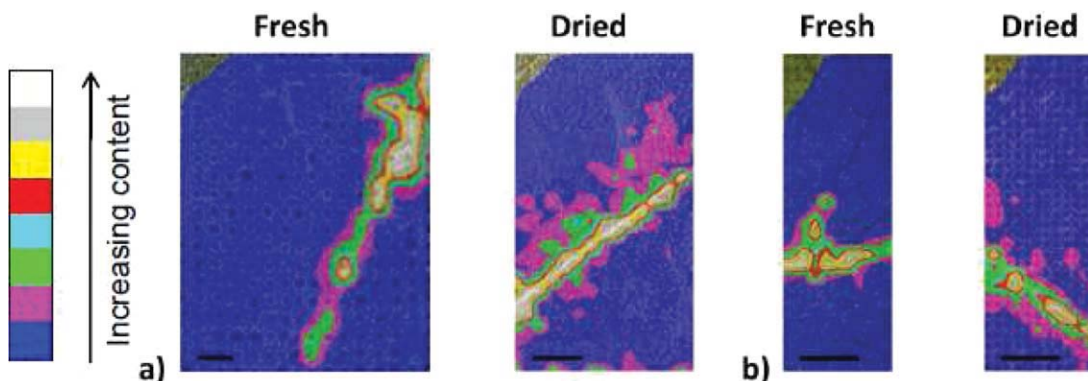


Fig. 7. The maps of Pb obtained from the studied area of the 2 days 10 mmol L⁻¹ Pb(NO₃)₂ treated *C. annuum* L. leaf. The K distribution in fresh (frozen) and dried leaf measured by (a) LIBS and (b) LA-ICP-MS. The maps are shown together with the photos of the samples. In the upper left corners, the part of the photograph is uncovered. The length of bar is 1 mm.

data of these values had the Log-normal distribution (Reimann et al., 1999) of these values was revealed. The average of the logarithm of intensity values or

peak area was calculated (Limpert et al., 2001). The comparison of the lead signal obtained by LIBS and LA-ICP-MS analyses of 2 days 10 mmol L⁻¹ lead

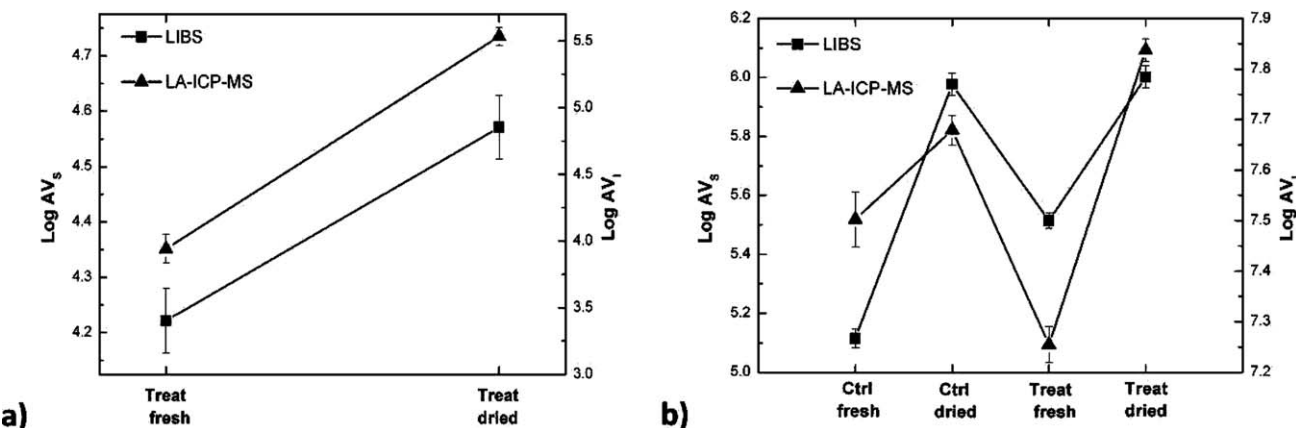


Fig. 8. The logarithm of average value of the peak areas (LogAV_s) and the logarithm of average value of the intensities (LogAV_i) for (a) K and (b) Pb on untreated (Ctrl) and 2 days 10 mmol L^{-1} $\text{Pb}(\text{NO}_3)_2$ treated *Capsicum annuum* L. samples measured by LIBS and LA-ICP-MS.

treated *C. annuum* L. fresh and dried leaf is shown in Figure 8a). The results of this simple statistical analysis shows the logarithm of average value of the peak areas (Log AV_s) and the logarithm of average value of the intensities (Log AV_i) for the appropriate element (potassium manganese and lead) in the case of LIBS and LA-ICP-MS, respectively.

The increase in the intensity of the MS signal and on the peak areas for LIBS in the case of dried sample is evident for both elements. It should be noted, that however the presence of the water decreases the LIBS/LA-ICP-MS signal intensity; the frozen samples are much less fragile than the dried one, thus denser ablation patterns can be created on them. It means that frozen samples are more suitable for analysis with high spatial resolution.

Figure 8b demonstrates the capability of LIBS and LA-ICP-MS to record the changes in accumulation of nutrition element (K) in different areas of untreated (control) and 10 mmol L^{-1} lead treated leaf sample. For LIBS and LA-ICP-MS measurement, higher signal of investigated element was observed for dried leaves on contrary to the fresh (frozen) samples. In comparison of logarithm of average value of the intensities and logarithm of average value of the peak areas obtained by LIBS with values measured by LA-ICP-MS, lower value of Log AV_i was calculated for fresh 10 mmol L^{-1} lead treated leaf sample than for untreated sample measured by LA-ICP-MS. In the case of LIBS measurement, decreased amount of potassium was determined for untreated leaf sample. These differences can be explained by different position of LIBS and LA-ICP-MS ablation patterns on the sample. The Log AV_i and Log AV_s for dried samples are similar. The same behavior was observed for manganese.

CONCLUSION

In summary, by utilizing two laser-ablation based diagnostic methods, namely LIBS and LA-ICP-MS, the accumulation mechanism of lead pollutant in *C. annuum* L. plant species was revealed. The lead is accumulated preferably in the vein structure of leaves. Moreover, the LIBS and LA-ICP-MS signal on dried

and fresh samples were compared, and the possibility to achieve lower detection limits on dried samples demonstrated. It should be noted that despite the number of advantages of laser-ablation based methods, the major drawback of these techniques in the case of analysis of environmental samples in their natural form is the difficult standardization. The measurements presented in this work gave the map of the intensity (or area) of a spectral line, which may be proportional to the local concentration, but there was not attempt to calibration or a demonstration of linearity of response. In the ongoing work complimentary techniques, mainly X-ray microradiography and microtomography (Kaiser et al., 2005, 2007) will be applied for validation of LIBS and LA-ICP-MS outcomes.

ACKNOWLEDGMENTS

The authors acknowledge the help of T. Vaculovič in realization of LA-ICP-MS measurements and Violetta Shevtitska for technical assistance.

REFERENCES

- Adriano DC, Wenzel WW, Vangronsveld J, Bolan NS. 2004. Role of assisted natural remediation in environmental cleanup. *Geoderma* 122:121–142.
- Antosiewicz DM. 2005. Study of calcium-dependent lead-tolerance on plants differing in their level of Ca-deficiency tolerance. *Environ Pollut* 134:23–34.
- Barona A, Aganguiz I, Elías A. 2001. Metal associations in solid before and after EDTA extractive decontamination: Implications for the effectiveness of further clean-up procedures. *Environ Pollut* 113: 79–85.
- Brunet J, Repellin A, Varraud G, Terryn N, Zuly-Fodil Y. 2008. Lead accumulation in the roots of grass pea (*Lathyrus sativus* L.): A novel plant for phytoremediation systems? *Comptes Rendus Biol* 331:859–864.
- Brunet J, Varraud G, Zuly-Fodil Y, Repellin A. 2009. Accumulation of lead in the roots of grass pea (*Lathyrus sativus* L.) plants triggers systemic variation in gene expression in the shoots. *Chemosphere* 77:1113–1120.
- Becker JS, Zorić M, Matusch A, Wu B, Salber D, Palm C, Becker JS. 2010a. Bioimaging of metals by laser ablation inductively coupled plasma mass spectrometry. *Mass Spectrometry Rev* 29:156–175.
- Becker JS, Niehren S, Matusch A, Wu B, Hsieh H-F, Kumtabtim U, Hamester M, Plaschke-Schlüter A, Salber D. 2010b. Scaling down the bioimaging of metals by laser microdissection inductively coupled plasma mass spectrometry (LMD-ICP-MS). *Int J Mass Spectrometry* 294:1–6.

- Chen HM, Zheng CR, Tu C, Shen ZG. 2000. Chemical methods and phytoremediation of soil contaminated with heavy metals. *Chemosphere* 41:229–234.
- Doumett S, Lamperi L, Checchini L, Azzarello E, Mugnai S, Mancuso S, Petruzzelli G, Del Bubba M. 2008. Heavy metal distribution between contaminated soil and *Paulownia tomentosa*, in a pilot-scale assisted phytoremediation study: Influence of different complexing agents. *Chemosphere* 72:1481–1490.
- Galiová M, Kaiser J, Novotný K, Samek O, Reale L, Malina R, Páleníková K, Liška M, Čudek V, Kanický V, Otruba V, Poma A, Tucci A. 2007. Utilization of laser induced breakdown spectroscopy for investigation of the metal accumulation in vegetal tissues. *Spectrochim Acta B* 62B:1597–1605.
- Galiová M, Kaiser J, Novotný K, Novotný J, Vaculovič T, Liška M, Malina R, Stejskal K, Adam V, Kizek R. 2008. Investigation of heavy-metal accumulation in selected plant samples using laser induced breakdown spectroscopy and laser ablation inductively coupled plasma mass spectrometry. *Appl Phys A* 93:917–922.
- Hong-Qi W, Si-Jin L, Hua L, Zhi-Hua Y. 2007. EDTA-enhanced phytoremediation of lead contaminated soil by *Bidens maximowicziana*. *J Environ Sci* 19:1496–1499.
- January MC, Cutright TJ, Van Keulen H, Wei R. 2008. Hydroponic phytoremediation of Cd, Cr, Ni, As, and Fe: Can *Helianthus annuus* hyperaccumulate multiple heavy metals? *Chemosphere* 70:531–537.
- Jarvis MD, Leung DWM. 2002. Chelated lead transport in *Pinus radiata*: An ultrastructural study. *Environ Exp Bot* 48:21–32.
- Kaiser J, Reale L, Ritucci A, Tomassetti G, Poma A, Spano L, Tucci A, Flora F, Lai A, Faenov A, Pikuz T, Mancini L, Tromba G, Zanini F. 2005. Mapping of the metal intake in plants by large-field X-ray microradiography and preliminary feasibility studies in microtomography. *Eur Phys J D* 32:113–118.
- Kaiser J, Samek O, Reale L, Liška M, Malina R, Ritucci A, Poma A, Tucci A, Flora F, Lai A, Mancini L, Tromba G, Zanini F, Faenov A, Pikuz T, Cinque G. 2007. Monitoring of the heavy-metal hyperaccumulation in vegetal tissues by X-ray radiography and by femto-second laser induced breakdown spectroscopy. *Microsc Res Technol* 70:147–153.
- Kaiser J, Galiová M, Novotný K, Červenka R, Reale L, Novotný J, Liška M, Samek O, Kanický V, Hrdlička A, Stejskal K, Adam V, Kizek R. 2009. Mapping of the heavy-metal pollutants in plant tissues by laser-induced breakdown spectroscopy. *Spectrochim Acta B* 64:67–73.
- Komárek M, Tlustoš P, Száková J, Chrastný V, Ettler V. 2007. The use of maize and poplar in chelant enhanced phytoextraction of lead from contaminated agricultural soils. *Chemosphere* 67:640–651.
- Krämer U. 2005. Phytoremediation: Novel approaches to cleaning up polluted soils. *Curr Opin Biotechnol* 16:133–141.
- Laville S, Goueguel C, Loudy H, Vidal F, Chaker M, Sabsabi M. 2009. Laser-induced fluorescence detection of lead atoms in a laser-induced plasma: An experimental analytical optimization study. *Spectrochim Acta B* 64:347–353.
- Limpert E, Stahel WA, Abbt M. 2001. Log-normal distributions across the sciences: Keys and clues. *BioScience* 51:341–352.
- Liu D, Jiang W, Liu C, Xin C, Hou W. 2000. Uptake and accumulation of lead by roots, hypocotyls and shoots of Indian mustard *Brassica juncea* (L.). *Bioresource Technol* 71:273–277.
- Liu J, Dong Y, Xu H, Wang D, Xu J. 2007. Accumulation of Cd, Pb and Zn by 19 wetland plant species in constructed wetland. *J Hazard Mater* 147:947–953.
- Masson P, Dalix T, Bussiere S. 2010. Determination of major and trace elements in plant samples by inductively coupled plasma-mass spectrometry. *Commun Soil Sci Plant Anal* 41:231–243.
- Mulligan CN, Yong RN, Gibbs BF. 2001. Remediation technologies for metal-contaminated soil and groundwater: An evaluation. *Eng Geol* 60:193–207.
- Novotný K, Kaiser J, Galiová M, Konečná V, Novotný J, Malina R, Liška M, Kanický V, Otruba V. 2008. Mapping of different structures on large area of granite sample using laser-ablation based analytical techniques, an exploratory study. *Spectrochim Acta B* 63B:1139–1144.
- Novotný J, Malina R, Kaiser J, Liška M, Galiová M, Novotný K. 2009. Implementation of an autofocus algorithm based on searching the best in-focus image into a table-top laser-induced breakdown spectroscopy setup. *Opt Eng* 10:48–58.
- Núñez-López RA, Measa Y, Gamaa SC, Borges RO, Olgún EJ. 2008. Leaching of lead by ammonium salts and EDTA from *Salvinia minima* biomass produced during aquatic phytoremediation. *J Hazard Mater* 154:623–632.
- Patra M, Bhowmik N, Bandopadhyay B, Sharma A. 2004. Comparison of mercury, lead and arsenic with respect to genotoxic effects on plant systems and the development of genetic tolerance. *Environ Exp Bot* 52:199–223.
- Pereira MG, Pereira-Filho ER, Berndt H, Arruda MAZ. 2004. Determination of cadmium and lead at low levels by using preconcentration at fullerene coupled to thermospray flame ionization atomic absorption spectrometry. *Spectrochim Acta B* 59:515–521.
- Pichtel J, Kuroiwa K, Sawyerr HT. 2000. Distribution of Pb, Cd and Ba in soils and plants of two contaminated sites. *Environ Pollut* 110:171–178.
- Piechalaka A, Tomaszecka B, Baralkiewicz D. 2003. Enhancing phytoremediative ability of *Pisum sativum* by EDTA application. *Phytochemistry* 64:1239–1251.
- Reimann C, Filzmoser P. 1999. Normal and lognormal data distribution in geochemistry: Death of a myth. Consequences for the statistical treatment of geochemical and environmental data. *Environ Geol* 39:1001–1014.
- Römkens P, Bouwman L, Japenga J, Draisma C. 2002. Potentials and drawbacks of chelate-enhanced phytoremediation of soils. *Environ Pollut* 116:109–121.
- Samek O, Liška M, Kaiser J. 1998. Využití laserových ablací pro materiálovou analýzu: Integrace LIFS a LIBS. *Fine Mech Opt* 43:123–129 (in Czech).
- Santos MC, Wagner M, Wu B, Scheider J, Oehlmann J, Cadore S, Becker JS. 2009. Biomonitoring of metal contamination in a marine prosobranch snail (*Nassarius reticulatus*) by imaging laser ablation inductively coupled plasma mass spectrometry (LA-ICP-MS). *Talanta* 80:428–433.
- Suleiman JS, Hu B, Huang C, Zhang N. 2008. Determination of Cd, Co, Ni and Pb in biological samples by microcolumn packed with black stone (*Pierre noire*) online coupled with ICP-OES. *J Hazard Mater* 157:410–417.
- Telle HH, Beddoes DCS, Morris GW, Samek O. 2001. Sensitive and selective spectrochemical analysis of metallic samples: The combination of laser-induced breakdown spectroscopy and laser-induced fluorescence spectroscopy. *Spectrochim Acta B* 56:947–960.
- Vadillo JM, Cardell K, Cremers DA, Laserna JJ. 1999. Rapid screening method for heavy metals in contaminated soils using LIBS. *Quim Anal* 18:169–174.
- Verma S, Dubey RS. 2003. Lead toxicity induces lipid peroxidation and alters the activities of antioxidant enzymes in growing rice plants. *Plant Sci* 164:645–655.
- Wahla IH, Kirkham MB. 2008. Heavy metal displacement in salt water-irrigated soil during phytoremediation. *Environ Pollut* 155: 271–283.



Variability of trace element distribution in *Noccea* spp., *Arabidopsis* spp., and *Thlaspi arvense* leaves: the role of plant species and element accumulation ability

Michaela Vašinová Galiová · Jiřina Száková · Lubomír Prokeš · Zuzana Čadková · Pavel Coufalík · Viktor Kanický · Vítězslav Otruba · Pavel Tlustoš

Received: 20 November 2018 / Accepted: 15 February 2019
© Springer Nature Switzerland AG 2019

Abstract Laser ablation-inductively coupled plasma-mass spectrometry (LA-ICP-MS) was applied for the determination of Cd and Zn distributions within the leaves of Cd- and Zn-hyperaccumulating plants, *Noccea caerulescens*, *N. praecox*, and *Arabidopsis halleri*, in contrast to nonaccumulator species, *Thlaspi arvense* and *A. thaliana*. The elemental mapping of the selected leaf area was accomplished via line scans with a

110-μm-diameter laser beam at a 37-μm s⁻¹ scan speed and repetition rate of 10 Hz. The lines were spaced 180 μm apart and ablated at an energy density of 2 J cm⁻². The elemental imaging clearly confirmed that Cd was predominantly distributed within the parenchyma of the *T. arvense*, whereas in the *Noccea* spp. and *A. halleri*, the highest intensity Cd signal was observed in the veins of the leaves. For Zn, higher intensities were observed in the veins for all the plant species except for *A. thaliana*. Close relationships between Zn and Ca were identified for the *Noccea* spp. leaves. These relationships were not confirmed for *A. halleri*. Significant correlations were also proved between the Cd and Zn distribution in *A. halleri*, but not for the *Noccea* spp. For both *T. arvense* and *A. thaliana*, no relevant significant relationship for the interpretation of the results was observed. Thus, the LA-ICP-MS imaging is proved as a relevant technique for the description and understanding of the elements in hyperaccumulating or highly accumulating plant species, although its sensitivity for the natural element contents in nonaccumulator plant species is still insufficient.

Electronic supplementary material The online version of this article (<https://doi.org/10.1007/s10661-019-7331-5>) contains supplementary material, which is available to authorized users.

M. V. Galiová · L. Prokeš · P. Coufalík · V. Kanický · V. Otruba
Department of Chemistry, Faculty of Science, Masaryk University,
Kotlářská 2, 611 37 Brno, Czech Republic

M. V. Galiová · V. Kanický · V. Otruba
Central European Institute of Technology, Masaryk University,
Kamenice 5, 625 00 Brno, Czech Republic

J. Száková · P. Tlustoš
Department of Agro-Environmental Chemistry and Plant
Nutrition, Faculty of Agrobiology, Food and Natural Resources,
Czech University of Life Science Prague, Kamýcká 129, 165
21 Prague-Suchdol, Czech Republic
e-mail: szakova@af.czu.cz

Z. Čadková
Department of Zoology and Fisheries, Faculty of Agrobiology,
Food and Natural Resources, Czech University of Life Science
Prague, Kamýcká 129, 165 21 Prague-Suchdol, Czech Republic

P. Coufalík
Institute of Analytical Chemistry, The Czech Academy of
Sciences, v.v.i., Veveří 97, 602 00 Brno, Czech Republic

Keywords Laser ablation · Elemental mapping · Hyperaccumulating plants · Brassicaceae · Trace elements

Introduction

Various analytical methods have already been tested for the spatial distribution of elements and/or important

bioactive compounds that determine the biochemical and physiological processes in plants. Wu and Becker (2012), Bartels and Svatoš (2015), and Boughton et al. (2016) reviewed the available techniques for elemental imaging and speciation analysis that allow more detailed knowledge about the elemental distribution in plants to be obtained. In this context, mass spectrometric methods, i.e., secondary ionization mass spectrometry (SIMS), laser ablation-inductively coupled plasma-mass spectrometry (LA-ICP-MS), and synchrotron-based X-ray fluorescence spectroscopy, have been discussed (Bartels and Svatoš 2015; Boughton et al. 2016). Laser ablation-electrospray ionization-mass spectrometry imaging was tested for metabolic mapping of living tissues of various plant species (Etalo et al. 2015). Lobinski et al. (2006) reviewed the available techniques for the determination of elemental distributions within biological tissues. From their comparison, the detection limits of measurements decreased in the following order: X-ray microanalysis on a transmission electron microscope > ion beam microprobe using particle-induced X-ray emission (μ -PIXE) > synchrotron radiation microanalysis (μ -SXRF) > SIMS > LA-ICP-MS.

LA-ICP-MS is frequently used for the detailed description of the nutrients and/or trace element distributions in various plant compartments. This makes it possible to elucidate the fate of elements and their uptake by plants in more detail, compared to the conventional analytical techniques requiring sample decomposition. Wu et al. (2013) showed differences in the spatial distribution of nutrients (Fe, K, Cu, Zn, Ca), in developing wheat grain. The distribution of nutrients in seeds of Zn-treated plants of *Kosteletzkyia virginica* was investigated by Han et al. (2013). Polatajko et al. (2011) applied LA-ICP-MS for the screening of Cd-binding proteins in Cd-exposed *Spinacia oleracea* plants. LA-ICP-MS was also applied for an assessment of micronutrient mobility in the root zone of *Lupinus albus* to estimate the bioavailability of the nutrients under various soil treatments (Valentinuzzi et al. 2015). Similarly, the radial distribution of Al along the root tips of *Fagopyrum esculentum* for a better understanding of Al uptake and translocation was investigated Klug et al. (2011). Kaiser et al. (2009) confirmed the higher concentrations of Pb, Mg, and Cu in the central vein of the *Helianthus annuus* leaves using LA-ICP-MS with a resolution up to 200 μ m in an up to centimeter by centimeter area of a leaf. Hu et al. (2012) found that Cd was distributed mainly in the trichomes, upper and lower epidermis, and bundle sheath cells of

the Zn/Cd hyperaccumulator *Picris divaricata*, whereas the levels of Cd in mesophyll cells were low.

Concerning the spatial distribution of trace elements, such as Cd and Zn, previous studies have focused on hyperaccumulator plants, i.e., plant species are able to accumulate large concentrations of elements, namely metals (Zhao et al. 2014). For non-hyperaccumulator plants, determination is difficult because of the low tissue element concentrations. Thus, researchers often use artificially enhanced concentrations of target elements (Cd) in plant tissues that can cause severe phytotoxicity symptoms and the physiologically based element distribution can be altered by the high trace element uptake (Zhao et al. 2014). Similarly, Galiová et al. (2011) enriched the growth medium for *Capsicum annuum* cultivation with various concentrations of $Pb(NO_3)_2$ to enhance the Pb contents in leaves and to achieve Pb levels detectable by LA-ICP-MS.

The variations in plant uptake of the trace elements can also result in alterations in the uptake and accumulation of other elements, regardless of their toxicity or essentiality. In this context, both synergistic and antagonistic relationships can occur, potentially resulting in an imbalance of the nutrient status of the plants. The stimulatory effect of Fe deficiency on Cd uptake by *N. caerulescens* was observed by Lombi et al. (2002) where the results indicated that these relationships are connected with Fe-regulated transporter-like protein genes. Among the nutrient elements, similarities between the distribution of Cd and Ca was observed in *B. juncea* and *S. alfredii* tissues (Tian et al. 2011, Yang et al. 2014). Basic et al. (2006) observed that the Cd concentration in the *N. caerulescens* plants was positively correlated with plant Zn, Fe, and Cu concentrations. Decreasing the Zn uptake by *N. caerulescens* in excess copper in soil was reported by Walker and Bernal (2004), whereas no interrelationships among Zn, P, and S in the vacuoles of *N. caerulescens* were observed by Frey et al. (2000). Thus, the potential similarities and/or differences in spatial distribution among Cd, Zn, and other elements can be useful for improved interpretation of the role of these elements in hyperaccumulating plants.

Noaccaea spp., particularly *N. caerulescens* (Brassicaceae), is the most intensively investigated Cd- and Zn-hyperaccumulating plant (Milner and Kochian 2008), suitable for the research of hyperaccumulation principles as a model plant. An excellent Cd hyperaccumulation ability was confirmed in this plant, whereas another Cd- and Zn-hyperaccumulating plant, *Arabidopsis halleri*

(Brassicaceae), showed a lower Cd concentration, but similar or higher Zn accumulation in the aboveground biomass (McGrath et al. 2006; Tlustoš et al. 2016). However, substantial differences were reported among the Cd and Zn accumulation ability of this plant species originating from different populations (Verbruggen et al. 2013; Stein et al. 2016; Sitko et al. 2017; Meyer et al. 2015). Some evidence indicates the potential physiological role of Cd in *N. caerulescens* (Liu et al. 2008). Hyperaccumulating plants are characterized by a predominant translocation of the target element into the aboveground biomass. Lovy et al. (2013) showed that 86% of the Cd taken up by *N. caerulescens* is allocated to the shoots. Whereas Cd in non-hyperaccumulators is associated with the sulfur ligands, Cd in hyperaccumulators is bound only by weak oxygen ligands (Leitenmaier and Küpper 2013). Detailed explanation of the molecular biology of metal hyperaccumulation was presented by Maestri et al. (2010) and Hanikenne and Nouet (2011). In addition to *N. caerulescens*, *N. praecox* is also an often investigated hyperaccumulation plant. Likar et al. (2010) demonstrated that internally transcribed spacer rDNA sequences from eight *N. praecox* populations from Slovenia showed 99% similarity and formed a sister group to *N. caerulescens*. Pongrac et al. (2009) compared the hyperaccumulation capacity of *N. caerulescens* and *N. praecox*. They found that the two species hyperaccumulated Cd in their shoots to a similar extent, whereas *N. caerulescens* accumulated more Zn in the shoots than *N. praecox*. Moreover, *N. praecox* showed lower tolerance to Cd application than *N. caerulescens*.

The main objectives of this study were (i) to verify the usefulness of LA-ICP-MS mapping for the assessment of the element distribution in plant leaves differing in their element accumulation ability, (ii) to describe the potential differences between hyperaccumulating and nonaccumulator species within one family (genus) planted on long-term contaminated and uncontaminated soils, and (iii) to establish the limitations of the LA-ICP-MS analytical method for the detailed description of the elemental compartmentalization within the plant tissues. The novel approach of the investigation was a direct comparison of the plants with different Cd and Zn accumulation ability by using the hyperaccumulating and nonaccumulator plant species coming from one family, both growing in non-stressed conditions. Additionally, the important task is whether the LA-ICP-MS is able to reflect the differences in Cd and Zn localization among hyperaccumulating plants growing in the same conditions.

Material and methods

Plant cultivation and sampling

Among Cd- and Zn-hyperaccumulating plants, two species of *Nothocalais* genus were used: *N. caerulescens* from Ganges, southern France, and *N. praecox* from Mežica, Slovenia. *Arabidopsis halleri* was sampled in the heavy metal-contaminated area in the vicinity of Příbram, Czech Republic. For comparison, similar, but nonaccumulator plant species, were chosen for the experiment, namely, *Thlaspi arvense* and *A. thaliana*. The hyperaccumulating plants were cultivated in long-term Cd- and Zn-contaminated Luvisol containing 11 mg Cd kg⁻¹ and 1022 mg Zn kg⁻¹. The soil was characterized by pH 7.3, cation exchange capacity (CEC) 333 mmol₍₊₎ kg⁻¹, and total organic carbon (TOC) content 2.7%. Uncontaminated chernozem with a CEC of 230 mmol₍₊₎ kg⁻¹, TOC of 2.31%, and soil pH of 8.5, containing 0.69 mg Cd kg⁻¹ and 120 mg Zn kg⁻¹ was used for cultivation of the nonaccumulator species. The soils were sampled at the individual locations from the upper layer (0–25 cm), passed through a 5-mm plastic sieve, and air-dried. The pH values of the soils were determined in a 0.01 mol/L CaCl₂ extract (1:10 w/v). The CEC value was calculated as the sum of Ca, Mg, K, Na, Fe, Mn, and Al extractable in 0.1 mol/L BaCl₂ (1:10 w/v, shaken for 2 h) (ISO 1994). The TOC values were determined using the dichromate oxidation method proposed by Mingorance et al. (2007). Different soils for the hyperaccumulators and nonaccumulator plants were chosen to keep the plants in their “natural” soil conditions to avoid potential stress able to shift the element distribution within the leaves, and to obtain “normal” element levels in the plant leaves of both species groups. More details concerning the physicochemical characteristics of the soils are published elsewhere (Kulhánek et al. 2016; Vondráčková et al. 2014).

The plants were cultivated in 6-L plastic pots with 5 kg of air-dried soil, and the detailed description of the cultivation conditions was presented elsewhere (Tlustoš et al. 2016). In the flowering stage, the fully developed mature leaves were sampled from the rosette, carefully washed by deionized water, and fresh leaves were mounted on glass slides. Different approaches were described regarding the plant sample mounting on the glass slide (Dong et al. 2016), where the application of adhesive tape seems to be the suitable method for the mounting of whole leaves. Since the literature (Dong

et al. 2016) paid attention to the potential contamination of the sample via the tape, direct contact of the analyzed leaf section with the tape was avoided. Thus, in this experiment, the whole leaves were mounted using adhesive tape at the ends of the leaves, and the central part of the leaves was covered with a cover slip mounted with the glass slide with the tape. The samples were then frozen at -18°C and subsequently freeze-dried. Before the LA-ICP-MS measurements, the cover slips were removed and the leaf was fixed using double-sided tape on a glass surface on both parts, the tip and base of the sample, respectively. The ablated area was localized centrally on each sample surface to minimize variability in the elemental distribution within the tip and base of the leaf, and to avoid ablation of the tape.

Determination of total cadmium and zinc content

The ablated leaves were separated from the glass slide and used for the determination of the total Cd and Zn contents. The samples of leaves were mineralized in sub-boiling HNO_3 prepared just before the decomposition. Each sample was weighed directly into a mineralization quartz tube and digested in 1 mL of HNO_3 by means of an UltraWAVE mineralizer (Milestone, Italy) at 250°C for 20 min. After the decomposition, the samples were quantitatively transferred together with 3 mL of deionized water ($0.055\ \mu\text{s cm}^{-1}$) into polyethylene scintillation vials (Kartel, Italy). Blanks were prepared according to the same procedure as the samples. The sample handling was carried out on a clean bench in the laboratory with HEPA filters. Quartz tubes were decontaminated using a traceCLEAN cleaning system (Milestone, Italy). The Astasol-certified reference materials (Analytika, Czech Republic) were used for the preparation of standards, namely, $\text{Cd } 1 \pm 0.002\ \text{g L}^{-1}$ in 2% HNO_3 and $\text{Zn } 1 \pm 0.002\ \text{g L}^{-1}$ in 2% HCl.

The determination of Cd and Zn was performed by graphite furnace atomic absorption spectrometry (GF-AAS) by using an AAnalyst 600 atomic absorption spectrometer (PerkinElmer, USA) with a longitudinal Zeeman effect background correction. Hollow cathode lamps of Cd (228.8 nm) and Zn (213.9 nm) were used as the source of radiation with a slit width of 0.7 nm. An internal gas flow of argon was $250\ \text{mL min}^{-1}$. The temperature programs for the determination of metals are summarized in Table 1. A matrix modifier of $50\ \mu\text{g NH}_4\text{H}_2\text{PO}_4 + 3\ \mu\text{g Mg}(\text{NO}_3)_2$ was dosed into the graphite furnace for the determination of Cd. The sampling

Table 1 Experimental conditions for the determination of Cd and Zn by GF-AAS

Step	Temperature ($^{\circ}\text{C}$)/ramp ($^{\circ}\text{C s}^{-1}$)/hold (s)	
	Cd	Zn
Drying 1	110/1/30	110/1/30
Drying 2	130/15/30	130/15/30
Pyrolysis	500/20/20	500/20/20
Atomization ^a	1600/0/3	1800/0/3
Cleaning	2450/1/2	2450/1/2

^a Internal gas flow during the atomization of Zn was $250\ \text{mL min}^{-1}$

volume for the measurement was $20\ \mu\text{L}$. Three parallel analyses were performed for each sample and element. The limits of quantification of the method, including all operations with samples, were 0.67 and $27.8\ \mu\text{g g}^{-1}$ for Cd and Zn, respectively. The limit of quantification is defined as ten times the standard deviation of experimental blanks.

LA-ICP-MS

The investigation of the elemental distribution was performed using an Analyte G2 (Teledyne CETAC Technologies, Omaha, USA) 193 ArF* excimer laser ablation system equipped with a two-volume cell HelEx coupled to an Element 2 (Thermo Scientific, Bremen, Germany) double-focusing sector field ICP mass spectrometer. The instrument was operated in low-mass resolution mode ($m/\Delta m = 300$) and was tuned to the maximum sensitivity response with respect to low double charge ions and oxide formation using glass SRM NIST 612. The elemental mapping of the selected leaf area was accomplished via line scans with a $110\text{-}\mu\text{m}$ laser beam in diameter, at a $37\text{-}\mu\text{m s}^{-1}$ scan speed and repetition rate of 10 Hz (Turková et al. 2017). The lines were spaced $180\ \mu\text{m}$ apart and ablated at an energy density of $2\ \text{J cm}^{-2}$. The ablated material was transported from the sample chamber using helium carrier gas (total He flow rate of $0.65\ \text{L min}^{-1}$) and mixed with argon ($\sim 1\ \text{L min}^{-1}$) prior to the torch (Vašinová Galiová et al. 2013). More details concerning the operational conditions are summarized in Table 2. The correction of time-dependent instrumental drift was based on glass standards analysis under the identical working parameters as leaf samples. To suppress the potential impact of ablated mass on signal inhomogeneity in laser

Table 2 Operating conditions of LA-ICP-MS elemental mapping

Laser ablation (Analyte G2)	
Wavelength	193 nm
Pulse length	< 5 ns
Sample chamber	HelEx™
He flow rate	0.65 L min ⁻¹
Make-up Ar flow rate	~0.9–1 L min ⁻¹
ICP-MS (Element 2)	
RF power	1200 W
Cooling gas flow rate	15.50 L min ⁻¹ Ar
Auxiliary gas flow rate	1.12 L min ⁻¹ Ar
Mass resolution	Low resolution
Isotopes measured	¹³ C, ²⁴ Mg, ³¹ P, ²⁸ Si, ⁴⁴ Ca, ⁵⁵ Mn, ⁵⁷ Fe, ⁶⁵ Cu, ⁶⁶ Zn, ¹¹² Cd, ²⁰⁸ Pb

ablation, ¹³C was used as an internal element for normalization of the intensity of each measured isotope (Wu et al. 2009; Yang et al. 2014; Nunes et al. 2016).

Data processing

Data analysis was made using the freely available R statistical package (<https://www.r-project.org/>) with carbon-normalized data. Despiking of the line scans was made using a three-point median Tukey filter (Rittner and Müller 2012), and subsequently, a 15-point Hampel filter (Pearson 2002) was employed to remove outliers. Visualization of the filtered data was made via two-dimensional elemental maps. The spatial homogeneity/heterogeneity of elements in the leaves was explored using LISA (Local Indicators of Spatial Association), mean Moran I autocorrelation of a particular point with the neighboring points (Anselin 1995). Through the extent of significant spatial clustering of similar values, LISA gives an indication of areas of spatial non-homogeneity. The distributions of particular elements were visualized using kernel density estimators (Silverman 1986). Because of the non-Gaussian data distribution, the correlation between elemental distributions was calculated using non-parametrical coefficient Spearman ρ (de Siqueira Santos et al. 2014) and visualized as rank variation graphs (Friendly 2002).

Differences in the total concentrations of Zn and Cd between the two *Noccaea* species (*Noccaea caerulescens*, 13 specimens; *Noccaea praecox*, 6 specimens), and *Thlaspi arvense* (14 specimens) were performed using the Kruskal-Wallis rank test combined

with multiple comparison procedures based on the Dunn test. Differences in the total concentrations of Zn and Cd between the two *Arabidopsis* species (*A. halleri*, 6 specimens; *A. thaliana*, 3 specimens) were tested with the one-sample Wilcoxon rank test. Non-parametric tests were employed because of non-normal distribution of the data. Quantile-based boxplots were also used for visualization of the concentration data (Zar 1999). For samples grown in the same pot, pooled values of arithmetic means and standard deviations (Cochran 1977) were calculated.

Results and discussion

Comparison of Cd and Zn distributions in hyperaccumulating and nonaccumulator plant species

The total concentrations of Cd in the individual leaves were $92 \pm 47 \text{ mg kg}^{-1}$ for *N. praecox*, $285 \pm 134 \text{ mg kg}^{-1}$ for *N. caerulescens*, and $37 \pm 8 \text{ mg kg}^{-1}$ for *A. halleri*, confirming the exceptional hyperaccumulation capacity of the *Noccaea* spp., particularly, the Ganges ecotype of *N. caerulescens* (Lombi et al. 2000). On the contrary, the *A. halleri* population from Příbram location indicated belongs to the populations with limited accumulation ability for Cd (Corso et al. 2018). The Zn concentrations in the leaves were $2160 \pm 736 \text{ mg kg}^{-1}$ for *N. praecox*, $3350 \pm 428 \text{ mg kg}^{-1}$ for *N. caerulescens*, and $3600 \pm 606 \text{ mg kg}^{-1}$ for *A. halleri*. The total element concentrations in the nonaccumulator plant species were $2.43 \pm 0.01 \text{ mg kg}^{-1}$ of Cd, and $360 \pm 13 \text{ mg kg}^{-1}$ of Zn for *A. thaliana*, and $0.80 \pm 0.13 \text{ mg kg}^{-1}$ of Cd, and $52.1 \pm 7.0 \text{ mg kg}^{-1}$ of Zn for *T. arvense*. For both Cd and Zn, the results indicate statistically significant (at a significance level of $\alpha = 0.05$) differences between *N. caerulescens* and *T. arvense*, between *N. praecox* and *T. arvense*, and between *A. halleri* and *A. thaliana*. No statistically significant difference (at a significance level of $\alpha = 0.05$) was found between *N. caerulescens* and *N. praecox* (Fig. 1).

The distributions of Cd and Zn in the leaves of the individual plant species are summarized in Figs. 2 and 3. The results showed that Cd predominantly distributed within the whole leaves of the *T. arvense*, whereas in *N. caerulescens* and *N. praecox*, the highest intensity of Cd signal was observed in the veins of the leaves. A similar pattern was observed in the case of *A. halleri*. It

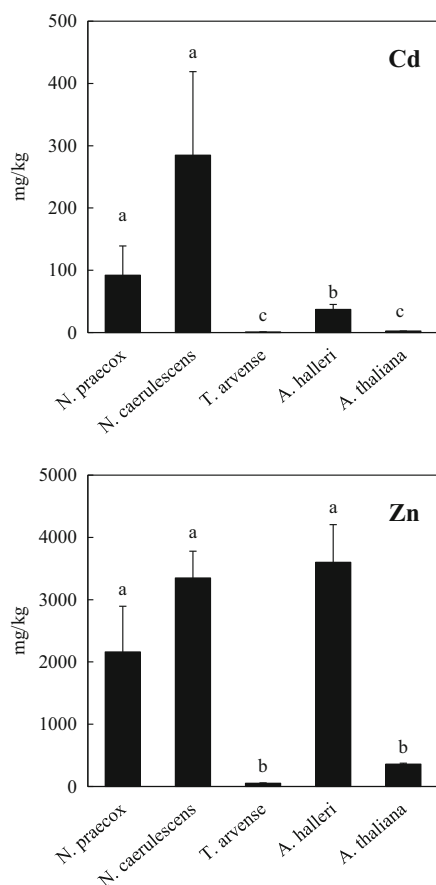


Fig. 1 The total contents of Cd and Zn in the element hyperaccumulating *Noccaea* spp. in contrast to the nonaccumulator *T. arvense*; the bars marked by the same letter did not significantly differ at $\alpha=0.05$ within individual plant species

should be noted that *T. arvense* and *A. thaliana* represent nonaccumulator plant species and a higher $^{112}\text{Cd}/^{13}\text{C}$ ratio can be partially blurred by polyatomic interferences, for instance, $^{42}\text{Ca}^{42}\text{Ca}^{28}\text{Si}$ originating from the glass slide. For Zn, the intensities tended to increase in the veins of the leaves of *T. arvense*, *N. caerulescens*, and *N. praecox*, whereas the Zn distribution within whole leaves were observed for *A. halleri* and *A. thaliana*. However, as apparent from the photograph of leaf tissue after the laser sampling, the vein system of the analyzed leaf of *A. halleri* was poor, and the central vein was finer in comparison with other samples. The Cd accumulation in the veins was confirmed according to Callahan et al. (2016), but the Zn accumulation differed. These authors observed Zn concentrated in the leaf tip. However, they cultivated the plants in Zn-enriched hydroponic culture, where the plants reached

the concentrations up to 7900 mg kg⁻¹, exceeding those reached in our experiment (Fig. 1). Thus, different Zn distribution at the extremely high Zn levels can be speculated in this case, although no differences between the Zn localization within the *N. caerulescens* leaves cultivated in soil and/or hydroponic culture were observed by Kozhevnikova et al. (2017). For nonaccumulator *A. thaliana*, the intensities were not so low, but the sample thickness and poor vein structure did not allow for the estimation of the differences in the Cd and Zn localization within the leaf itself and complicated a comparison of Cd and Zn behavior in the hyperaccumulating and nonaccumulator species, as apparent from the mapping of *A. halleri* and *A. thaliana* leaves (Fig. 3). The results confirmed all the advantages and limitations of LA-ICP-MS. The method seems to be suitable for the estimation of the elemental distribution within the plant leaves, but it is not able to unambiguously characterize the elemental fate at the cellular level.

The enrichment of elements in nonaccumulator plants via the enhancement of these elemental concentrations in soil is questionable. These plants are stressed by the presence of the enhanced trace element uptake and do not represent the balanced physiological status of the plants. Thus, the elemental distribution within these plants can be altered by the enhanced elemental content in the plant tissues and by the subsequent response of the plant in the stress conditions. In this experiment, uncontaminated soil was used for the cultivation of the nonaccumulator species (*T. arvense*, *A. thaliana*) and the interpretation of the spatial distribution of the elements is ambiguous. The cluster analysis separating the artificial side effects originating from glass slide-leaf tissue crossing and the residues of the glass base (Supplementary material, Figures S1 and S2) also more clearly improve the leaf-related intensities of isotopes from interfering signals.

As reviewed by Zhao et al. (2014), the spatial resolution of common laser ablation instrumentations usually ranges from 50 to 300 mm. For high resolution, a laser beam with a smaller spot size is necessary. Cizdziel et al. (2012) used the laser ablation technique at the full energy setting ($> 4.0 \text{ mJ/pulse}$), with a repetition rate of 20 Hz, a spot size of 100 μm and a scan rate of 50 $\mu\text{m}/\text{min}$ for direct determination of both nutrients and risk elements in plant leaves. Yang et al. (2014) applied LA-ICP-MS with a laser beam diameter of 20 μm for the determination of elemental distribution in Cd-enriched *Brassica juncea* stems. In this experiment, low-mass

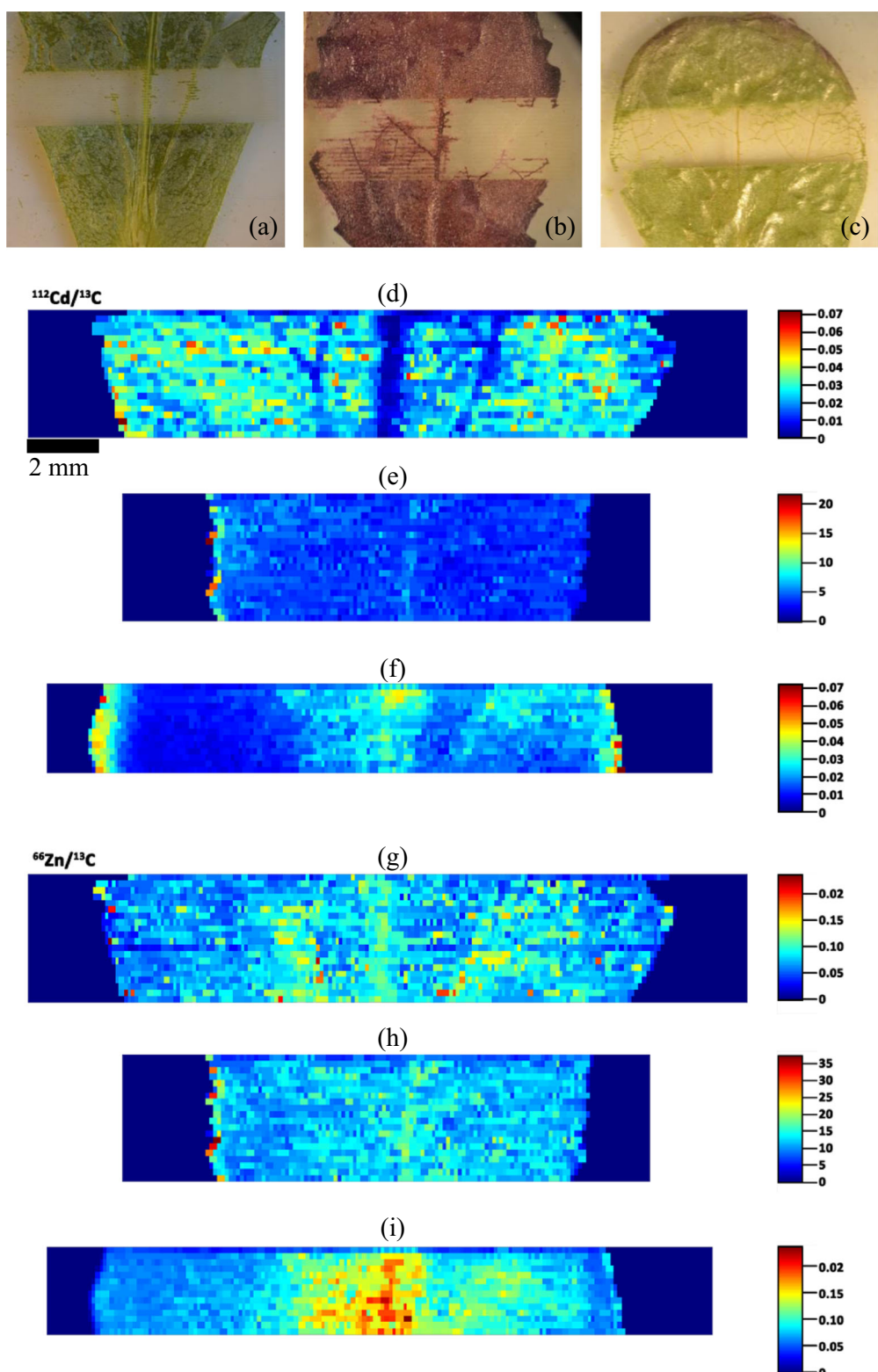


Fig. 2 Distribution of $^{112}\text{Cd}/^{13}\text{C}$ (d, e, f) and $^{66}\text{Zn}/^{13}\text{C}$ (g, h, i) in the *T. arvense* (a, d, g), *N. caerulescens* (Ganges) (b, e, h), and *N. praecox* (c, f, i) leaves derived from laser ablation ICP-MS analysis

resolution mode ($m/\Delta m = 300$), a laser spot diameter of 110 μm and a repetition rate of 10 Hz, was applied. Thus, the experimental conditions used in this experiment fall within the range of values of experimental parameters used by other authors. Therefore, the coupling of the LA-ICP-MS method with other techniques is able to discriminate, in more detail, the localization of the elements within the plant tissues and organelles. For instance, Hanč et al. (2016) combined LA-ICP-MS with energy dispersive X-ray microanalysis spectroscopy (EDX) for imaging of the distribution of elements in pea seedlings. The EDX was applied to confirm results obtained by LA-ICP-MS and to identify the exact localization of metal deposits in root tissue. The coupling of LA-ICP-MS with other techniques is able to discriminate the cell compartments within the leaves and can be helpful for better elucidation of the fate of trace elements in different plant species.

The related literature shows variable findings concerning the spatial distribution of elements in plant leaves of individual species. Cosio et al. (2005) found cadmium in *N. caerulescens* leaves inside the cells and also in the cell walls (especially in large epidermal cells). They assumed that Cd is stored predominantly in the less metabolically active compartments of leaf cells. This experiment showed lower Cd concentrations in the veins of *T. arvense*, as compared with the hyperaccumulators, again indicating the storage of Cd in the peripheral cells (Fig. 2). Yang et al. (2014) proved that Cd was predominantly accumulated in the epidermis, cortex, and vascular tissues of *B. juncea* stems, while lower proportions of Cd were contained in parenchyma cells. Similarly, high concentrations of Cd were determined in the vascular system of the hyperaccumulators (Figs. 2 and 3). Vogel-Mikuš et al. (2008a) determined the spatial distribution of Cd in *N. praecox* leaves using μ -PIXE, where Cd was preferentially localized in the epidermis and vascular bundles, whereas the concentrations lower by about 50% were found in the mesophyll. However, because the mesophyll represents a higher volume of biomass compared to the epidermis, the mesophyll seems to be the important sink of Cd. Isaure et al. (2015) determined using X-ray absorption spectroscopy and microfocused X-ray fluorescence that Cd in *A. halleri* leaves was located in the mesophyll tissue, as well. The differences in element distribution within the leaves could be also affected by the time of exposition and leaf maturity (Huguet et al. 2012). Within this study, the missing resolution between

the mesophyll and epidermis did not allow us to state which part of the leaves were Cd and Zn predominantly accumulated. Alternatively, the spatial distribution of these elements lead to similar conclusions as in published articles in case of the hyperaccumulators.

Although *N. caerulescens* and *A. halleri* are both Cd and Zn hyperaccumulators, the previous investigations indicated that their mechanisms of Cd accumulation are different, where the Cd-permeable transport proteins are differentially regulated (Cosio et al. 2004). The large variation in the total Cd and Zn concentrations was already observed among the different ecotypes of *N. caerulescens* (Assunção et al. 2003; Callahan et al. 2016). Similarly, differences in the adaptation of *A. halleri* plants to high Zn contents in soils was recently demonstrated by Schwartzman et al. (2018) by a comparison of various *A. halleri* populations originating from Poland and Italy. Similarly, the differences in the Cd tolerance and accumulation among the various populations of *A. halleri* were shown for instance by Meyer et al. (2015). Previous investigations showed Cd accumulation in the trichomes of *A. halleri* by micro X-ray fluorescence imaging (Fukuda et al. 2008), or Zn in the epidermal cells of the leaves of *N. praecox* using μ -PIXE (Vogel-Mikuš et al. 2008b). However, Sarret et al. (2002) applied synchrotron-based X-ray microfluorescence (μ -SXRF) for Zn speciation in *A. halleri* originating from contaminated and/or non-contaminated areas at different Zn levels. Their results showed no significant differences between the plants of different origins, and no effect of the Zn exposure regarding the Zn pattern in the plants, where this element was present as a malate complex in the aboveground biomass.

Spatial interrelationships of elemental distribution within plant leaves

The results of rank correlation analyses of the inter-elemental relationships are presented as rank variation graphs (Figs. 4 and 5), and the levels of Spearman ρ coefficients are summarized in the Supplementary table S1. For *A. thaliana*, no relevant significant relationship for the interpretation of the results was observed, where the ρ values only occasionally exceeded 0.5 (Fig. 5, Supplementary table S1). Significant correlations were proved by Spearman ρ coefficients between Cd and Zn distributions in *A. halleri* with $\rho = 0.81, p < 0.05$ (Fig. 5, Supplementary table S1), whereas for *Nothaea* spp.,

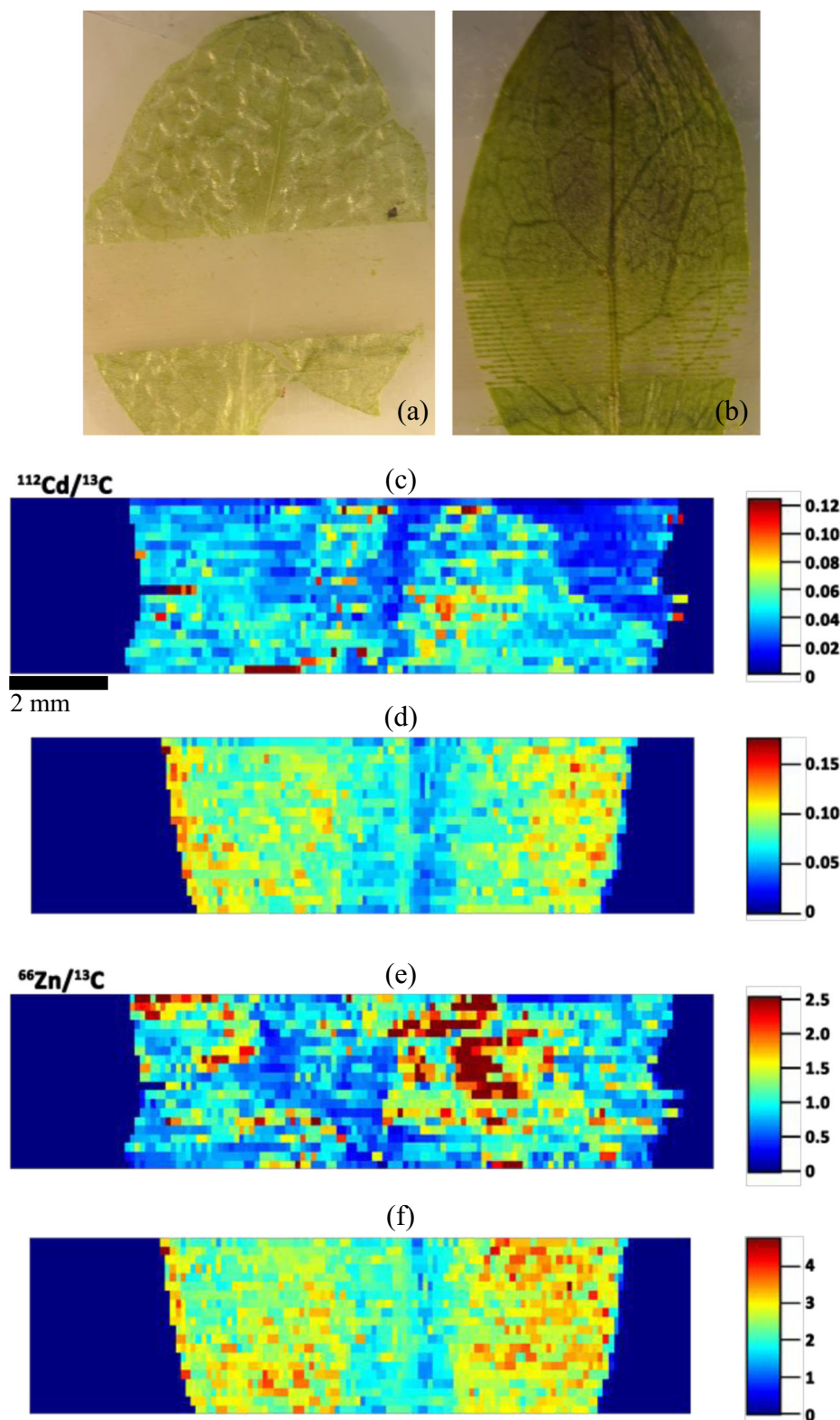


Fig. 3 Distribution of $^{112}\text{Cd}/^{13}\text{C}$ (c, d) and $^{66}\text{Zn}/^{13}\text{C}$ (e, f) in the *A. thaliana* (a, c, e), and *A. halleri* (b, d, f) leaves derived from laser ablation ICP-MS analysis

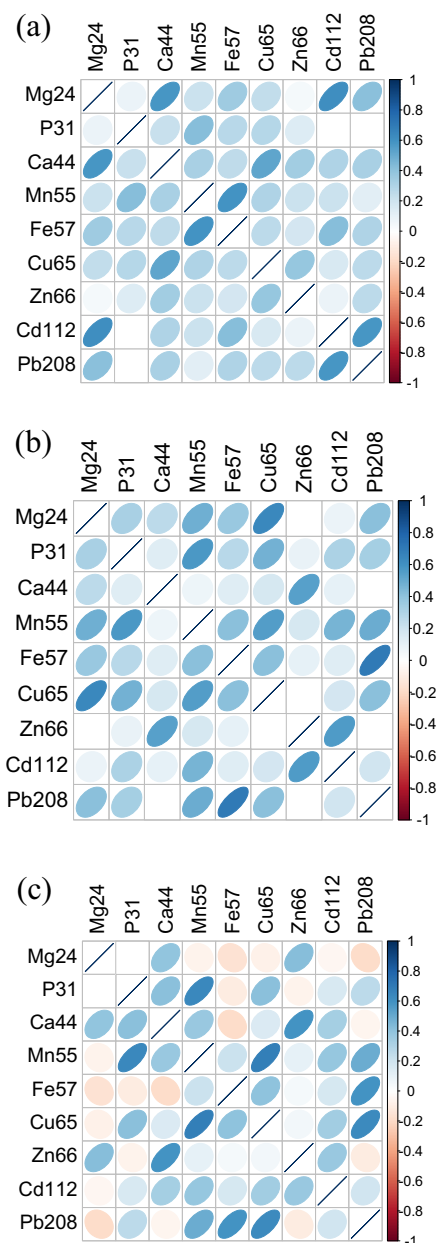


Fig. 4 The rank variation graphs of Spearman ρ correlations among element distributions in *Thlaspi arvense* (a), *Noccaea caerulescens* (b), and *Noccaea praecox* (c); particular ellipse shape and its color intensity are dependent on the correlation coefficient value. Statistically non-significant correlation coefficients are whitened in the plot

these relationships did not occur and the ρ values varied between 0.43 and 0.59, and similar value ($\rho = 0.55$, $p < 0.05$) was determined for *T. arvense* (Fig. 4, Supplementary table S1). Different mechanisms of the plant response on the enhanced Cd concentrations for

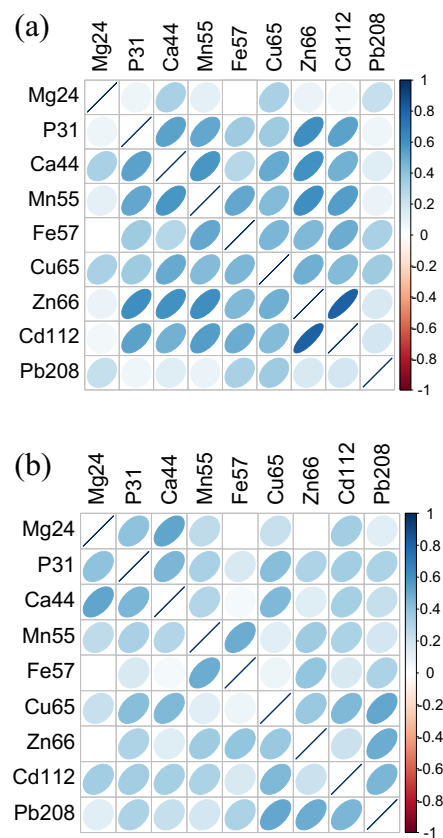


Fig. 5 The rank variation graphs of Spearman ρ correlations among element distributions in *Arabidopsis halleri* (a), and *Arabidopsis thaliana* (b); particular ellipse shape and its color intensity are dependent on the correlation coefficient value. Statistically non-significant correlation coefficients are whitened in the plot

N. caerulescens and *A. halleri* were described by Zemanová et al. (2013). As mentioned above, the analyzed *A. halleri* phenotype showed better Zn accumulation ability than the *Noccaea* spp. (Tlustoš et al. 2016; Kashem et al. 2010). These findings also indicate differences in the Cd and Zn accumulation mechanisms of the *Noccaea* spp. and *A. halleri*, resulting in different spatial distribution of both elements. Similarly, as the case of Cd and Zn in this experiment, high concentrations of macro- and micronutrients in the veins of *Elsholtzia splendens* leaves were reported by Wu et al. (2009). Oliveira and Arruda (2015) compared the alterations in spatial distribution of Fe in the transgenic and non-transgenic soybean (*Glycine max*) leaves. Although no significant differences were observed in the total Fe concentrations, in the transgenic soybean leaves, Fe was homogenously distributed, while in the non-transgenic leaves, this element was concentrated in the main and

minor veins. Thus, the differences in the spatial distribution of Fe among the *Noccaea* spp., *A. halleri*, and *A. thaliana* could be related to the alterations among the individual species and/or phenotypes. Although the possible relationships between Cd and Fe accumulation ability of *Arabidopsis* spp. were described (Verbruggen et al. 2013), weak correlations between these elements were observed in this experiment (Fig. 5). Hanć et al. (2016) reported Cd, Pb, and Zn deposits in the cell wall, cell membrane, vacuoles, cytoplasm, and organelles (mitochondria, peroxisomes) as determined by electron microscopy of *Pisum sativum* seedlings cultivated in a hydroponic culture. However, weaker relationships were observed in all the analyzed plant leaves of the *Noccaea* spp., and *A. halleri* for both Cd and Zn related to P, Mn, Fe, Cu, and Pb (Figs. 4 and 5, Supplementary table S1).

For the *Noccaea* spp. leaves, a close relationship between Zn and Ca was identified, where Spearman ρ coefficients varied between 0.82 and 0.93, $p < 0.05$ (Fig. 4, supplementary table S1). Similarly, close relationship between Zn and Mg was observed for these species, where ρ values varied between 0.69–0.72, $p < 0.05$. Weaker Zn and Ca relationships were observed for *A. halleri*, where $\rho = 0.60$, $p < 0.05$ (Fig. 5, supplementary table S1). Concerning the Ca-Zn interrelationship, antagonism in the uptake of these elements in plants was frequently reported (Kizilgos 2016). The protective role of Ca against the Zn toxicity in plants was discussed in this context (Pellegrini et al. 1993), where increasing the Ca content in plants grown in Zn-contaminated soil indicated the possible role of this element in detoxification mechanisms (Turnau et al. 2010). Close positive relationships of Ca and Zn in the shoots of *N. caerulescens* was verified by Sterckeman et al. (2017) at the large set of samples representing 60 populations. Thus, this experiment suggested the protective role of Ca against the extremely high concentrations of Zn in the *Noccaea* spp. plants, whereas this effect was not so predominantly apparent in *A. halleri* with better Zn accumulation ability and the likelihood is that *A. halleri* is more tolerant to the extremely high Zn concentrations in the soil.

Przedpełska-Wąsowicz et al. (2012) confirmed the presence of various Cd-binding low molecular weight proteins in Cd-treated *A. halleri* plants, where these compounds were not present in the untreated plants. Alvarez-Fernandez et al. (2014) reviewed the identified metal-ligand species in the xylem and phloem saps.

They found that the metal carboxylate complexes have always been found in xylem, whereas metals associated with proteins or other high molecular weight compounds have been determined in the phloem. However, these compounds were not identified as phytochelatin and/or metallothionein-like proteins. Thus, the chemical speciation identifying the proportions of elements associated with the particular chemical compounds or structures can support the findings concerning potential differences in Cd and Zn uptake and the accumulation between hyperaccumulating and nonaccumulator plant species, and/or among different hyperaccumulating plant species. In this experiment, the sulfur distribution in the leaves was determined, as well (data not shown), but no significant correlations were observed for both Cd-S and Zn-S relationships for all the analyzed plant species. According to Isaure et al. (2015), Cd in *A. halleri* was predominantly connected with O ligands, whereas in nonaccumulator *A. lyrata*, Cd was coordinated by S atoms.

Conclusions

The LA-ICP-MS analysis was able to describe clearly the Cd and Zn distribution in the leaves of hyperaccumulating plants, *Noccaea* spp. and *A. halleri*, and to estimate the differences in the element translocation in the leaves of the hyperaccumulating plants. However, the results clearly showed the limitations of the method, where (i) the spatial resolution does not allow for the assessment of the element localization at the plant cell level and (ii) is insufficient for an assessment of the element distribution in the nonaccumulator plants at low element levels. However, the method represents excellent approach for estimation of the interrelationships among the elements to predict their potential synergism/antagonism. The description of trace element localization in the leaves of nonaccumulator plants remains as a challenge for further research: the experimental increase of the trace element uptake by plants via soil or medium amendment can lead to (i) antioxidative response of plant organism on the trace element-induced stress and (ii) shifts in the accumulation and/or distribution of the essential elements within the plant leaves. Thus, the trace element amendment cannot give relevant information concerning the fate of low levels of elements taken up by plants growing in uncontaminated soil. Therefore,

the improvement of the analytical techniques and methods will be the most reasonable way for better understanding of the fate of trace elements in “common” plants.

Funding information This study was financially supported by the GAČR project 13-18154S. The results of this research have also been acquired within CEITEC 2020 (LQ1601) project with financial contribution made by the Ministry of Education, Youth and Sports of the Czech Republic within special support paid from the National Programme for Sustainability II Funds.

Publisher's note Springer Nature remains neutral with regard to jurisdictional claims in published maps and institutional affiliations.

References

- Alvarez-Fernandez, A., Diaz-Benito, P., Abadia, A., Lopez-Millan, A. F., & Abadia, J. (2014). Metal species involved in long distance metal transport in plants. *Frontiers in Plant Science*, 5, 105.
- Anselin, L. (1995). Local indicators of spatial association – LISA. *Geographical Analysis*, 27, 93–115.
- Assunção, A. G. L., Ten Bookum, W. M., Nelissen, H. J. M., Vooijis, R., Schat, H., & Ernst, W. H. O. (2003). Differential metal-specific tolerance and accumulation patterns among *Thlaspi caerulescens* populations originating from different soil types. *New Phytologist*, 159, 411–419.
- Bartels, B., & Svatoš, A. (2015). Spatially resolved in vivo plant metabolomics by laser ablation-based mass spectrometry imaging (MSI) techniques: LDI-MSI and LA-ESI. *Frontiers in Plant Science*, 6, 471.
- Basic, N., Keller, C., Fontanillas, P., Vittoz, P., Besnard, G., & Galland, N. (2006). Cadmium hyperaccumulation and reproductive traits in natural *Thlaspi caerulescens* populations. *Plant Biology*, 8, 64–72.
- Boughton, B. A., Thinagaran, D., Sarabia, D., Bacic, A., & Roessner, U. (2016). Mass spectrometry imaging for plant biology: a review. *Phytochemistry Reviews*, 15, 445–488.
- Callahan, D. L., Hare, D. J., Bishop, D. P., Doble, P. A., & Roessner, U. (2016). Elemental imaging of leaves from the metal hyperaccumulating plant *Noccaea caerulescens* shows different spatial distribution of Ni, Zn and Cd. *RSC Advances*, 6, 2337–2344.
- Cizdziel, J., Bu, K. X., & Nowinski, P. (2012). Determination of elements in situ in green leaves by laser ablation ICP-MS using pressed reference materials for calibration. *Analytical Methods*, 4, 564–569.
- Cochran, W. G. (1977). *Sampling techniques* (Third ed.). New York: Wiley.
- Corso, M., Schwartzman, M. S., Guzzo, F., Souard, F., Małkowski, E., Hanikenne, M., & Verbruggen, N. (2018). Contrasting cadmium resistance strategies in two metalloids populations of *Arabidopsis halleri*. *New Phytologist*, 218, 283–297.
- Cosio, C., Martinoia, E., & Keller, C. (2004). Hyperaccumulation of cadmium and zinc in *Thlaspi caerulescens* and *Arabidopsis halleri* at the leaf cellular level. *Plant Physiology*, 134, 716–725.
- Cosio, C., DeSantis, L., Frey, B., Diallo, S., & Keller, C. (2005). Distribution of cadmium in leaves of *Thlaspi caerulescens*. *Journal of Experimental Botany*, 56, 765–775.
- de Siqueira Santos, S., Takahashi, D. Y., Nakata, A., & Fujita, A. (2014). A comparative study of statistical methods used to identify dependencies between gene expression signals. *Briefings in Bioinformatics*, 15, 906–918.
- Dong, Y., Li, B., Malitsky, S., Rogachev, I., Aharoni, A., Kaftan, F., Svatoš, A., & Franceschi, P. (2016). Sample preparation for mass spectrometry imaging of plant tissues: a review. *Frontiers in Plant Science*, 7, 60.
- Etalo, D. W., De Vos, R. C. H., Joosten, M. H. A. J., & Hall, R. D. (2015). Spatially resolved plant metabolomics: some potentials and limitations of laser-ablation electrospray ionization mass spectrometry metabolite imaging. *Plant Physiology*, 169, 1424–1435.
- Frey, B., Keller, C., Zierold, K., & Schulin, R. (2000). Distribution of Zn in functionally different leaf epidermal cells of the hyperaccumulator *Thlaspi caerulescens*. *Plant, Cell & Environment*, 23, 675–687.
- Friendly, M. (2002). Corgrams: exploratory displays for correlation matrices. *American Statistician*, 56, 316–324.
- Fukuda, N., Hokura, A., Kitajima, N., Terada, Y., Saito, H., Abe, T., & Nakai, I. (2008). Micro X-ray fluorescence imaging and micro X-ray absorption spectroscopy of cadmium hyperaccumulating plant, *Arabidopsis halleri* ssp. *gummifera*, using high-energy synchrotron radiation. *Journal of Analytical Atomic Spectrometry*, 23, 1068–1075.
- Galiová, M., Kaiser, J., Novotný, K., Hartl, M., Kizek, R., & Babula, P. (2011). Utilization of laser-assisted analytical methods for monitoring of lead and nutrition elements distribution in fresh and dried *Capsicum annuum* L. leaves. *Microscopy Research and Technique*, 74, 845–852.
- Han, R., Quinet, M., André, E., van Elteren, J. T., Destrebecq, F., Vogel-Mikuš, K., Cui, G., Debeljak, M., Lefèvre, I., & Lutts, S. (2013). Accumulation and distribution of Zn in the shoots and reproductive structures of the halophyte plant species *Kosteletzkya virginica* as a function of salinity. *Planta*, 238, 441–457.
- Hanć, A., Malecka, A., Kutrowska, A., Bagiewska-Zadworna, A., Tomaszewska, B., & Baralkiewicz, D. (2016). Direct analysis of elemental biodistribution in pea seedlings by LA-ICP-MS, EDX and confocal microscopy: imaging and quantification. *Microchemical Journal*, 128, 305–311.
- Hanikenne, M., & Nouet, C. (2011). Metal hyperaccumulation and hypertolerance: a model for plant evolutionary genomics. *Current Opinion in Plant Biology*, 14, 252–259.
- Hu, P. J., Gan, Y. Y., Tang, Y. T., Zhang, Q. F., Jiang, D., Yao, N., & Qiu, R. L. (2012). Cellular tolerance, accumulation and distribution of cadmium in leaves of hyperaccumulator *Picris divaricata*. *Pedosphere*, 22, 497–507.
- Huguet, S., Bert, V., Laboudigue, A., Barthes, V., Isaure, M. P., Llorens, I., Schat, H., & Sarret, G. (2012). Cd speciation and localization in the hyperaccumulator *Arabidopsis halleri*. *Environmental and Experimental Botany*, 82, 54–65.
- Isaure, M. P., Huguet, S., Meyer, C. L., Castillo-Michel, H., Testemale, D., Vantelon, D., Saumitou-Laprade, P., Verbruggen, N., & Sarret, G. (2015). Evidence of various mechanisms of Cd sequestration in the hyperaccumulator

- Arabidopsis halleri*, the non-accumulator *Arabidopsis lyrata*, and their progenies by combined synchrotron-based techniques. *Journal of Experimental Botany*, 66, 3201–3214.
- ISO 11260. (1994). *Standard of soil quality - determination of effective cation exchange capacity and base saturation level using barium chloride solution*. Geneve: International Organization for Standardization.
- Kaiser, J., Galiová, M., Novotný, K., Červenka, R., Reale, L., Novotný, J., Liška, M., Samek, O., Kanický, V., Hrdlička, A., Stejskal, K., Adam, V., & Kizek, R. (2009). Mapping of lead, magnesium and copper accumulation in plant tissues by laser-induced breakdown spectroscopy and laser-ablation inductively coupled plasma mass spectrometry. *Spectrochimica Acta Part B*, 64, 67–73.
- Kashem, M. A., Singh, B. R., Kubota, H., Sugawara, R., Kitajima, N., Kondo, T., & Kawai, S. (2010). Zinc tolerance and uptake by *Arabidopsis halleri* ssp. *gummifera* grown in nutrient solution. *Environmental Science and Pollution Research*, 17, 1174–1176.
- Kizilgoz I (2016) Effects of increasing soil calcium application on growth and uptake of calcium, phosphorus, zinc and boron in durum wheat (*Triticum durum* L.). *Oxid Commun* 39: 258–265.
- Klug, B., Specht, A., & Horst, W. J. (2011). Aluminium localization in root tips of the aluminium accumulating plant species buckwheat (*Fagopyrum esculentum* Moench). *Journal of Experimental Botany*, 62, 5453–5462.
- Kozhevnikova, A. D., Seregin, I. V., Gosti, F., & Schat, H. (2017). Zinc accumulation and distribution over tissues in *Noccaea caerulescens* in nature and in hydroponics: a comparison. *Plant and Soil*, 411, 5–16.
- Kulhánek, M., Balík, J., Černý, J., Sedlář, O., & Vašák, F. (2016). Evaluating of soil sulfur forms changes under different fertilizing systems during long-term field experiments. *Plant, Soil and Environment*, 62, 408–415.
- Leitenmaier, B., & Küpper, H. (2013). Compartmentation and complexation of metals in hyper- accumulator plants. *Frontiers in Plant Science*, 4, 374.
- Likar, M., Pongrac, P., Vogel-Mikuš, K., & Regvar, M. (2010). Molecular diversity and metal accumulation of different *Thlaspi praecox* populations from Slovenia. *Plant and Soil*, 330, 195–205.
- Liu, M. Q., Yanai, J., Jiang, R. F., Zhang, F., McGrath, S. P., & Zhao, F. J. (2008). Does cadmium play a physiological role in the hyperaccumulator *Thlaspi caerulescens*? *Chemosphere*, 71, 1276–1283.
- Lobinski, R., Moulin, C., & Ortega, R. (2006). Imaging and speciation of trace elements in biological environment. *Biochimie*, 88, 1591–1604.
- Lombi, E., Zhao, F. J., Dunham, S. J., & McGrath, S. P. (2000). Cadmium accumulation in populations of *Thlaspi caerulescens* and *Thlaspi goesingense*. *New Phytologist*, 145, 11–20.
- Lombi, E., Tearall, K. L., Howarth, J. R., Zhao, F. J., Hawkesford, M. J., & McGrath, S. P. (2002). Influence of iron status on cadmium and zinc uptake by different ecotypes of the hyperaccumulator *Thlaspi caerulescens*. *Plant Physiology*, 128, 1359–1367.
- Lovy, L., Latt, D., & Sterckeman, T. (2013). Cadmium uptake and partitioning in the hyperaccumulator *Noccaea caerulescens* exposed to constant Cd concentrations throughout complete growth cycles. *Plant and Soil*, 362, 345–354.
- Maestri, E., Marmiroli, M., Vissoli, G., & Marmiroli, N. (2010). Metal tolerance and hyperaccumulation: cost and trade-offs between traits and environment. *Environmental and Experimental Botany*, 68, 1–13.
- McGrath, S. P., Lombi, E., Gray, C. W., Caille, N., Dunham, S. J., & Zhao, F. J. (2006). Field evaluation of Cd and Zn phytoextraction potential by the hyperaccumulators *Thlaspi caerulescens* and *Arabidopsis halleri*. *Environmental Pollution*, 141, 115–125.
- Meyer, C. L., Juranić, M., Huguet, S., Chaves-Rodriguez, E., Salis, P., Isaure, M. P., Goormaghtigh, E., & Verbruggen, N. (2015). Intraspecific variability of cadmium tolerance and accumulation, and cadmium-induced cell wall modifications in the metal hyperaccumulator *Arabidopsis halleri*. *Journal of Experimental Botany*, 66, 3215–3227.
- Milner, M. J., & Kochian, L. V. (2008). Investigating heavy-metal hyperaccumulation using *Thlaspi caerulescens* as a model system. *Annals of Botany*, 102, 3–13.
- Mingorance, M. D., Barahona, E., & Fernandez-Galvez, J. (2007). Guidelines for improving organic carbon recovery by the wet oxidation method. *Chemosphere*, 68, 409–413.
- Nunes, M. A. G., Voss, M., Corazza, G., Flores, E. M. M., & Dressler, V. L. (2016). External calibration strategy for trace element quantification in botanical samples by LA-ICP-MS using filter paper. *Analytica Chimica Acta*, 905, 51–57.
- Oliveira, S. R., & Arruda, M. A. Z. (2015). Application of laser ablation (imaging) inductively coupled plasma mass spectrometry for mapping and quantifying Fe in transgenic and non-transgenic soybean leaves. *Journal of Analytical Atomic Spectrometry*, 30, 389–395.
- Pearson R.K. (2002) Outliers in process modeling and identification. *IEEE Transactions on Control Systems Technology* 10, 55–63.
- Pellegrini, M., Laugier, A., Sergent, M., Phantanluu, R., Valls, R., & Pellegrini, L. (1993). Interactions between the toxicity of the heavy-metals cadmium, copper, zinc in combinations and the detoxifying role of calcium in the brown alga *Cystoseira barbata*. *Journal of Applied Phycology*, 5, 351–361.
- Polatajko, A., Feldmann, I., Hayen, H., & Jakubowski, N. (2011). Combined application of a laser ablation-ICP-MS assay for screening and ESI-FTICR-MS for identification of a Cd-binding protein in *Spinacia oleracea* L. after exposure to Cd. *Metallomics*, 3, 1001–1008.
- Pongrac, P., Zhao, F. J., Razinger, J., Zrimec, A., & Regvar, M. (2009). Physiological responses to Cd and Zn in two Cd/Zn hyperaccumulating *Thlaspi* species. *Environmental and Experimental Botany*, 66, 479–486.
- Przedpelska-Wąsowicz, E., Polatajko, A., & Wierzbicka, M. (2012). The influence of cadmium stress on the content of mineral nutrients and metal-binding proteins in *Arabidopsis halleri*. *Water, Air, and Soil Pollution*, 223, 5445–5458.
- Rittner M., Müller W. (2012) 2D mapping of LA-ICPMS trace element distributions using R. *Computers & Geosciences* 42, 152–161.
- Sarret, G., Saumitou-Laprade, P., Bert, V., Proux, O., Hazemann, J. L., Traverse, A., Marcus, M. A., & Manceau, A. (2002). Forms of zinc accumulated in the hyperaccumulator *Arabidopsis halleri*. *Plant Physiology*, 130, 1815–1826.

- Schvartzman, M. S., Corso, M., Fataftah, N., Scheepers, M., Nouet, C., Bosman, B., Carnol, M., Motte, P., Verbruggen, N., & Hanikenne, M. (2018). Adaptation to high zinc depends on distinct mechanisms in metalloous populations of *Arabidopsis halleri*. *New Phytologist*, 218, 269–282.
- Silverman, B. W. (1986). *Density estimation for statistics and data analysis*. London: Chapman & Hall.
- Sitko, K., Rusinowski, S., Kalaji, H. M., Szopiński, M., & Małkowski, E. (2017). Photosynthetic efficiency as bioindicator of environmental pressure in *A. halleri*. *Plant Physiology*, 175, 290–302.
- Stein, R. J., Höreth, S., de Melo, J. R. F., Syllwasschy, L., Lee, G., Garbin, M. L., Clemens, S., & Krämer, U. (2016). Relationships between soil and leaf mineral composition are element-specific, environment-dependent and geographically structured in the emerging model *Arabidopsis halleri*. *New Phytologist*, 213, 1274–1286.
- Sterckeman, T., Cazes, Y., Gonneau, C., & Sirguey, C. (2017). Phenotyping 60 populations of *Noccaea caerulescens* provides a broader knowledge of variation in traits of interest for phytoextraction. *Plant and Soil*, 418, 523–540.
- Tian, S., Lu, L., Labavitch, J., Yang, X., He, Z., Hu, H., Sarangi, R., Newville, M., Commissio, J., & Brown, P. (2011). Cellular sequestration of cadmium in the hyperaccumulating plant species *Sedum alfredii*. *Plant Physiology*, 157, 1914–1925.
- Tlustoš, P., Břendová, K., Száková, J., Najmanová, J., & Koubová, K. (2016). The long-term variation of Cd and Zn hyperaccumulation by *Noccaea* spp. and *Arabidopsis halleri* plants in both pot and field conditions. *International Journal of Phytoremediation*, 18, 110–115.
- Turková, S., Vašinová Galiová, M., Štúlová, K., Čadková, Z., Száková, J., Otruba, V., & Kanický, V. (2017). Study of metal accumulation in tapeworm section using laser ablation-inductively coupled plasma-mass spectrometry (LA-ICP-MS). *Microchemical Journal*, 133, 380–390.
- Turnau, K., Ostachowicz, B., Wojtczak, G., Anielska, T., & Sobczyk, Ł. (2010). Metal uptake by xerothermic plants introduced into Zn-Pb industrial wastes. *Plant and Soil*, 337, 299–311.
- Valentinuzzi, F., Cesco, S., Tomasi, N., & Mimmo, T. (2015). Influence of different trap solutions on the determination of root exudates in *Lupinus albus* L. *Biology and Fertility of Soils*, 51, 757–765.
- Vašinová Galiová, M., Fišáková Nývlťová, M., Kynický, J., Prokeš, L., Neff, H., Mason, A. Z., Gadas, P., Kosler, J., & Kanický, V. (2013). Elemental mapping in fossil tooth root section of *Ursus arctos* by laser ablation inductively coupled plasma mass spectrometry (LA-ICP-MS). *Talanta*, 105, 235–243.
- Verbruggen, N., Juraniec, M., Baliardini, C., & Meyer, C. L. (2013). Tolerance to cadmium in plants: the special case of hyperaccumulators. *Biometals*, 26, 633–638.
- Vogel-Mikuš, K., Simcic, J., Pelicon, P., Budnar, M., Kump, P., Necemer, M., Mesjasz-Przybyłowicz, J., Przybyłowicz, W. J., & Regvar, M. (2008a). Comparison of essential and non-essential element distribution in leaves of the Cd/Zn hyperaccumulator *Thlaspi praecox* as revealed by micro-PIXE. *Plant, Cell & Environment*, 31, 1484–1496.
- Vogel-Mikuš, K., Regvar, M., Mesjasz-Przybyłowicz, J., Przybyłowicz, W. J., Simcic, J., Pelicon, P., & Budnar, M. (2008b). Spatial distribution of cadmium in leaves of metal hyperaccumulating *Thlaspi praecox* using micro-PIXE. *New Phytologist*, 179, 712–721.
- Vondráčková, S., Hejčman, M., Száková, J., Müllerová, V., & Tlustoš, P. (2014). Soil chemical properties affect the concentration of elements (N, P, K, Ca, Mg, As, Cd, Cr, Cu, Fe, Mn, Ni, Pb, and Zn) and their distribution between organs of *Rumex obtusifolius*. *Plant and Soil*, 379, 231–245.
- Walker, D. J., & Bernal, M. P. (2004). The effects of copper and lead on growth and zinc accumulation of *Thlaspi caerulescens* J. and C. Presl: implications for phytoremediation of contaminated soils. *Water, Air, and Soil Pollution*, 151, 136–372.
- Wu, B., & Becker, J. S. (2012). Imaging techniques for elements and element species in plant science. *Metalomics*, 4, 403–416.
- Wu, B., Chen, Y., & Becker, J. S. (2009). Study of essential element accumulation in the leaves of a Cu-tolerant plant *Elsholtzia splendens* after Cu treatment by imaging laser ablation inductively coupled plasma mass spectrometry (LA-ICP-MS). *Analytica Chimica Acta*, 633, 165–172.
- Wu, B., Andersch, F., Weschke, W., Weber, H., & Becker, J. S. (2013). Diverse accumulation and distribution of nutrient elements in developing wheat grain studied by laser ablation inductively coupled plasma mass spectrometry imaging. *Metalomics*, 5, 1276–1284.
- Yang, H. X., Zhao, L. H., Liu, W., & Li, B. (2014). Bioimaging and distribution of Cd, P, S, K, Ca, Cu and Zn elements in Indian Mustard stem. *Chinese Journal of Analytical Chemistry*, 42, 355–359.
- Zar, J. H. (1999). *Biostatistical analysis* (Fourth ed.). Upper Saddle River: Prentice Hall.
- Zemanová, V., Pavlik, M., Pavliková, D., & Tlustoš, P. (2013). The changes of contents of selected free amino acids associated with cadmium stress in *Noccaea caerulescens* and *Arabidopsis halleri*. *Plant, Soil and Environment*, 59, 417–422.
- Zhao, F. J., Moore, K. L., Lombi, E., & Zhu, Y. G. (2014). Imaging element distribution and speciation in plant cells. *Trends in Plant Science*, 19, 183–192.



CHAPTER 9

Laser Ablation Inductively Coupled Plasma Mass Spectrometry as a Tool in Biological Sciences

MICHAELA VASINOVA GALIOVA and VIKTOR KANICKÝ

Department of Chemistry, Faculty of Science, and Central European Institute of Technology, Masaryk University, Brno, Czech Republic

JAN HAVLIS

National Centre for Biomolecular Research, Faculty of Science, and Central European Institute of Technology, Masaryk University, Brno, Czech Republic

9.1 INTRODUCING ELEMENTAL ANALYSIS OF BIOGENIC MATERIALS CONTAINING HETEROELEMENTS

When considering *inductively coupled plasma mass spectrometry* as a tool for elemental analysis in biological sciences, there are basically two types of samples: (*semi)solid* (e.g., biominerals, soft and hard tissues, polyacrylamide gels) and *liquid* (solutions). This contribution concerns only the direct analysis of solid or semisolid samples and comprises neither solution analysis as a means of determination of elemental content after sample dissolution, nor speciation analysis based on coupling of a separation technique with ICP-MS *via* any nebulization device.

Analysis of materials containing metal or heteroelements may be used in a number of research fields. The prime task is either to identify the presence of the elements or to identify the sample according to the presence of specific element(s). Samples containing proteins constitute a special case, and their analysis requires identifying both the protein part and the heteroelement part. The next task is to quantify the content of metal or heteroelements, and the ultimate aim is to study the contextual distribution of metal or heteroelements in samples (e.g., tumor tissues), by means of

Natural Products Analysis: Instrumentation, Methods, and Applications, First Edition.

Edited by Vladimír Havlíček and Jaroslav Špižek.

© 2014 John Wiley & Sons, Inc. Published 2014 by John Wiley & Sons, Inc.

imaging. As regards biogenic materials, we propose using the term *heteroelements* for minor elements composing their structures alongside their major components (e.g., carbon, oxygen, and nitrogen). These could be further divided into three categories: *metals*, *metalloids* (selenium), and *nonmetals* (e.g., phosphorus, sulfur). Proteins naturally contain *sulfur* in their primary structure; *phosphorus* incorporation is one of the most frequent post-translational modifications (phosphoproteins), and *selenium* (selenoproteins) is an important functional part of different proteins in prokaryotes and animals [1–3].

9.2 LASER ABLATION INDUCTIVELY COUPLED PLASMA MASS SPECTROMETRY IN BIOLOGICAL SCIENCES

For solid samples, the method of *Laser Ablation* followed by *Inductively Coupled Plasma Mass Spectrometry* (LA-ICP-MS) can be performed on various kinds of materials as analysis of individual spots (“standard LA-ICP-MS”) or as two-/three-dimensional analysis, referred to as “LA-ICP-MS imaging,” which, in case of soft tissues, is defined as bioimaging. LA-ICP-MS may be done qualitatively to identify the presence of heteroelement species, or else quantitatively to define, for example, specific markers. We may also apply LA-ICP-MS on gels, mostly polyacrylamide (PAGE LA-ICP-MS). This approach can be used for heteroelement-containing biogenic species after separation by gel electrophoresis.

These approaches rely on the significance of signal intensity, its reproducibility, and relevance to the amount of the element in the sample. There are a few basic factors that influence these parameters: the planarity of the sample, the particle size distribution after laser ablation, and the content of matrix elements. Planarity controls which material will be ablated and what the spatial distribution of the ablation will be; the less planar the surface of the sample, the greater the variability and fluctuation of the signal intensity. The particle size distribution in the ablated material influences the efficiency of vaporization and ionization, for example in the plasma plume, and thus it affects the proportionality of the elemental content in different particles. Moreover, ionization efficiency and thus signal intensity is influenced by ionization reactions of constituents other than the elements of interest—that is, those in the matrix, mostly carbon, which are abundant and compete for ionization energy. These reactions also make any signal normalization difficult because the ionization process is not proportional for all elements under the same function of ionization efficiency.

LA-ICP-MS (Figure 9.1) belongs to a group of sensitive analytical methods that have been undergoing a rapid development. The sampling by laser beam, together with highly efficient ionization and sensitive ion detection, represents an outstanding combination of principles and devices for efficient qualitative and quantitative analysis of a wide range of types of solid samples. Moreover, the high precision and accuracy attainable by high-resolution mass instruments, together with careful sample preparation and optimization of experimental conditions, make it possible to determine isotope ratios that carry important information for various biological and geological applications. The particles, complexes, and agglomerates released from

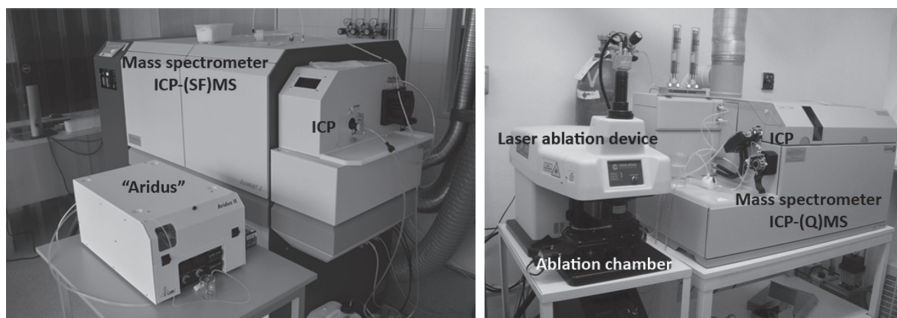


FIGURE 9.1 Instrumentation used for laser ablation with ICP-MS: Sector field ICP-MS with a device for drying of aerosol (**left**) and quadrupole-based ICP-MS connected with laser ablation device Nd:YAG 213 nm (**right**). For color detail, please see color plate section.

the sample surface during the target–laser beam interaction (LA) are introduced *via* a carrier gas into inductively coupled plasma (ICP). The argon ICP ideally provides complete particle vaporization, atomization and ionization. The resulting ions are subsequently separated in an analyzer according to their mass to charge ratio [4].

Low MS spectral background, together with high sensitivity, yields exceptionally low limits of detection (LOD). Direct investigation of solid samples minimizes the risk of contamination or loss of volatile elements that would otherwise usually occur during decomposition when performing solution analysis. Furthermore, laser ablation requires minimal or no sample preparation.

LA-ICP-MS is widely used for bulk analysis as well as for investigating a specific area on a sample surface. In contrast to solution analysis, solid sampling offers the benefit of obtaining information on the spatial distribution of elements in the samples. The advantages of solid sampling are employed in various branches such as medicine, geology, archaeology, and biology. The great variability of the samples, their compositions, and various chemical and physical properties have given rise to different approaches in terms of experimental parameters and calibration procedures.

As with all analytical methods, many studies were accomplished before LA-ICP-MS could be routinely utilized. Many optimization experiments are still necessary due to the significant physicochemical differences in materials that induce production of aerosols with different compositions. For instance, different particle size distributions can arise depending on the equipment used, laser radiation wavelength, or laser pulse duration. The aerosol transport efficiency is influenced by the shape and volume of the ablation chamber, the diameter and length of the transport tubing, and the type and flow rate of the carrier gas. In the ICP, aerosol particles are vaporized, atomized, and ionized with different efficiencies with respect to their composition and size. Apart from the solid sampling and ionization, the quality of ion beam spectral separation and isolation also contributes to overall accuracy and precision of analysis. To assess all these factors, some fundamental investigations have to be first performed.

As a result of the ablation, transport, and vaporization/atomization/ionization processes, the composition of the ion flow entering the mass spectrometer differs

from the elemental composition of the original sample. The measured elemental/isotope ratios therefore differ from those of the target. This change is called elemental fractionation [5]. If all aspects are taken into account and suitable working conditions of the instrumentation are chosen, then the appropriate LOD, limits of quantification (LOQ), and sensitivity are achieved. It should be noted that LA-ICP-MS is a powerful method for the determination of elements but not their chemical species (e.g., Se (IV) and Se (VI)) or compounds. For this purpose, separation methods should be implemented prior to LA-ICP-MS or the selected species must be bound with compounds stored in specific compartments.

9.2.1 Fundamental Aspects of Spot Analysis and Imaging via Laser Ablation-ICP-MS

When using laser ablation inductively coupled plasma mass spectrometry for hard and soft tissue imaging and/or analysis individual spots, one should be aware that the method has a number of pitfalls that should be taken into account. First of all, the major limitation on achieving an accurate result with low uncertainty lies in sample preparation. Little or no sample preparation is often undertaken, especially in the case of hard tissue. The unevenness of the sample surface results in variations in the amount of ablated material and thus in the intensity of the isotope signal and determined elemental content/concentration. Imaging of soft tissues such as plants, tissue slices of brain, kidney, and liver, or electrophoretic gel containing metal-bearing proteins is complicated by the presence of water. There are several approaches on how to suppress the presence of water. The first approach relies on drying the gel, but this leads to a reduction in the gel thickness; moreover, a planar surface is not guaranteed. The second possibility is based on laser ablation at a low temperature, requiring a cooled ablation cell. In the case of gel, electroblotting offers concentration and immobilization of the proteins on the membrane surface. If the gel is analyzed without any modification and standard equipment is used, normalization of the isotope signal of interest to that originating from the matrix (usually $^{13}\text{C}^+$) eliminates the influence of the presence of water and its influence on the time-resolved mass spectrometric signal. The selection of a sampling regime suitable for the investigated material represents another crucial point in the laser-assisted method (Figure 9.2).

The software supplied with commercially delivered ablation systems enables an optimization of many important parameters such as variations in the diameter of the laser beam spot, shape of the ablation imprint, scan speed, the settings of laser beam fluence, and laser shot frequency. These parameters are important when both line scanning and spot analysis are used. The use of the line scanning mode, during which the laser ablation and movement of the sample take place simultaneously, leads to poorer spatial resolution in comparison with spot analysis. The extent of the reduced spatial resolution depends on all the above experimental parameters, especially on the laser spot diameter, scan speed, and frequency. At slow scan speeds and high frequencies, an overlap of ablation craters increases and therefore lateral resolution decreases. Lear *et al.* [6] reported on an easy method to calculate scan speed to reduce total measuring time. A different approach to improving the sensitivity and subsequent resolution of the imaging consists in the enhancement of the signal-to-background ratio. Usually, this parameter is limited

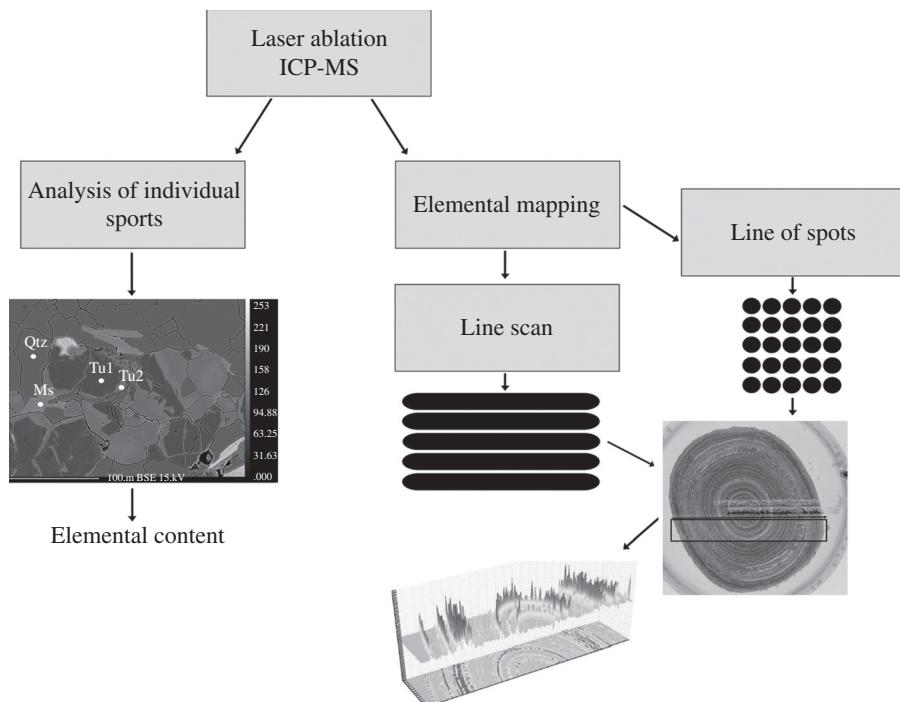


FIGURE 9.2 Scheme of LA-ICP-MS method and strategies. For color detail, please see color plate section.

by high values of background due to spectral interference [7]. The advantage of line scan is that it traces a thin layer on the sample surface [8]. On the other hand, if no pre-ablation and/or cleaning laser pulses are applied, the recorded signal can be distorted. For instance, metal-binding proteins are concentrated within the volume of the gel rather than on its surface. In this context, the sampling of the surface does not necessarily represent the true elemental concentration. Moreover, particle size distribution depends on the selected laser sampling regime. In comparison with spot analysis, larger particles are produced, which results in lower vaporization, atomization, and ionization efficiency in the ICP and a higher matrix effect [8]. The combination of the sample surface deteriorated planarity and the reduction in the ionization efficiency might lead to higher detection limits and distorted results with higher uncertainties.

Overlap of ablation craters can be easily eliminated using spot analysis. Positioning of spots at precisely defined distances improves lateral resolution. Sample translation to the next position occurs until the laser ablation event is completed. The laser spot diameter should be in relation to the size of the investigated area. In contrast to a line scan, the spot analysis method is able to compensate for variations in sample surface planarity by focusing the laser beam on a particular spot, and it additionally produces smaller particles due to the formation of a deeper crater. The ratio of small-to-large particle numbers increases with the depth by a factor of 3 [8, 9]. In contrast, a deeper ablation crater poses limitations on the ablation of thin layers and causes a decrease

in the signal. The time of interaction between the laser beam and the investigated spot should be adapted so as to reach a compromise between a stable signal and particle size. The depth of a crater should not be greater than its diameter (aspect ratio) [10, 11]. The diameter and distance of ablation spots are usually adjusted according to the distance and dimensions of the particular zones. If spots of appropriate size are placed close to each other, no spatial information is lost. On the other hand, a more precise spot ablation regime is time-consuming and costly, especially when the area to be investigated is large [12, 13]. Due to the fact that the elemental contents in biological tissues are usually very low, experimental parameters such as spot diameter and fluence should be set with respect to the demand of low LOD. The diminishing of the laser spot diameter as well as lower fluence lead to an increase in LOD. High energy produces a deeper ablation pit and a steeper drop in the signal-time dependence.

9.2.2 LA-ICP-MS Setup and Its Influence on Analytical Outcomes

Not only the laser ablation sampling regime but also aerosol transport, vaporization, atomization, and ionization in the ICP lead to fractionation—that is, changes in stoichiometry in the aerosol particles with respect to that of the target. To some extent, laser beam wavelength is responsible for particle size distribution. As a rule, the portion of larger particles in the aerosol increases with a longer wavelength. Laser ablation by a 193-nm laser beam produces aerosols with a higher percentage of small particles in comparison with 266 nm, which is beneficial for the efficiency of aerosol transport as well as for vaporization and following processes in the ICP discharge. Consequently, lower elemental fractionation is thus observed for 193 nm [14]. When larger particles are filtered off in the transport tubing, stoichiometric vaporization and ionization is assured, but a reduction in the total signal by about 50–80% is observed [8].

The average ablation rate (AAR) has been introduced for characterizing the laser beam interaction with matter. The AAR is expressed as the amount of material released per single laser shot. It was found that the AAR at two wavelengths (193 nm and 266 nm) was almost the same and independent of the carrier gas type for two different standard reference glass materials (NIST 612 and AGV-1). In general, the AAR drops with deepening of the crater, but the reduction in the ablation rate is more pronounced for a 266-nm laser beam compared to 193 nm [14].

Chemical transformations occur as a result of ablation, which may influence the stoichiometry of the aerosol particles. This modification reduces the chance for quantitative analysis even using relatively close calibration materials. For instance, during the first 250 s of ablation by the 266-nm laser beam, the NIST 612 glass standard reference material and zircon both provide particles with a diameter less than 2.5 μm . Then the diameter drops to less than 0.3 μm , but production of 0.2–0.5 μm and 0.005 μm particles in the case of zircon is accompanied by its thermal decomposition to baddeleyite and SiO_2 , as both were identified on the wall of the ablation crater [15].

The employed carrier gas influences the formation of aerosol particles and their transport efficiency. Argon and/or helium are usually employed as aerosol carrier gases. Of the three noble gases (He, Ne, and Ar) tested, helium provides the highest

sensitivity [16]. Helium exhibits greater thermal conductivity than argon and, consequently, faster cooling of the sample vapor, resulting in the production of smaller particles by condensation; the same applies for particle formation by coalescence. This effect is more pronounced at 193 nm than at the 266-nm laser wavelength because the shorter wavelength radiation produces a larger portion of the vapor phase. As He increases the transport efficiency by about 30% compared to Ar, the signal per unit ablated volume is higher in He [16]. As a result, He exhibits greater sensitivity and lower LOD for 193 nm than for 266 nm—in contrast to Ar, where the signal per unit ablated volume is the same for both laser wavelengths [14].

Processes in the ICP discharge associated with excitation/ionization are influenced by the addition of certain substances. The addition of hydrogen into the carrier gas flow enhances the sensitivity by a factor of 2–7 [17]; similar results were obtained with nitrogen [18]. This improvement is related to the charge transfer reaction and a higher electron temperature in the plasma. On the other hand, it should be kept in mind that the addition of gases or compounds into the plasma discharge may induce the formation of polyatomic ions and thus bring about a certain risk of increase in spectral interference.

Besides elemental and isotopic fractionation brought about by laser ablation and transport phenomena, it is the spectral interferences which lower the precision and accuracy of the measurement. Both parameters are important, especially in trace and isotope analysis. Spectral or isobaric interferences can be classified as (i) spectral coincidence of an analyte signal with a signal of a monoatomic isobaric ion; (ii) molecular or polyatomic (AB^+) products which comprise, for example, oxides (MO^+), resulting from the presence of argon, water, and some concomitants; and (iii) doubly charged ions (M^{2+}). The number and magnitude of spectral overlaps and signal coincidences generally depend on the sample composition, plasma operating conditions, ICP/MS interface, ion optics settings, and the type of mass spectrometer and its resolving power. Molecular ions result from (i) reactions of plasma gas ions (Ar) with sample constituents, (ii) sample and solvent, and (iii) from chemical ionisation of residual gases in the vacuum part of the mass spectrometer [19–21]. In the context of laser ablation, the influence of solvents (and acids) is of less significance than when analyzing wet aerosols produced by the nebulization of a solution. Nevertheless, the presence of water and its participation in the formation of polyatomic interferents is to be considered in the case of laser ablation of water-containing tissues and with some approaches applied in isotopic ratio measurement. Mathematical formulae, currently used for corrections of spectral interference in atomic emission spectrometry, are not very helpful in ICP-MS because the limits of detection are usually deteriorated and the correction factor depends on the analyzed matrix.

The most widespread mass spectrometers are based on quadrupole mass filters (Q-MS), which suffer from spectral interferences more than some other types of MS constructions. Quadrupole-based mass spectrometers are equipped with a collision-reaction cell (CRC) or dynamic reaction cell (DRC), allowing a reduction in the occurrence of interfering species. Both types of cells precede the quadrupole analyzer and are filled with collision and/or reaction gases and may differ from each other in technical design.

The CRC is equipped with a multipole (quadrupole, hexapole, octopole) and is flushed with a suitable working gas at low pressure. The multipole serves to transport ions through the CRC and focus the ion beam. The CRC is included between the ion extraction lenses and the analyzer (quadrupole). Unlike the collision cell employed in organic mass spectrometry for collision-induced dissociation, CRC in the ICP-MS system serves to eliminate interfering ions [19, 22]. The principle of polyatomic ion elimination consists of collisions of ions from the plasma with particles of the working gas. Depending on the ion and working gas properties, the polyatomic ions are eliminated by two basic mechanisms: (i) kinetic energy discrimination and (ii) chemical reaction.

The first mechanism for elimination of interferents consists of kinetic energy discrimination (KED). The CRC is operated as a collision cell, and the inert gas (He, Ne, Ar, Xe) serves as a working gas. Molecular ions collide with atoms of the working gas and lose part of their kinetic energy. As collisional cross sections of analyte ions are smaller than those of interfering molecular ions, the probability of collisions is lower and the kinetic energy of the analyte ions drops to less than the kinetic energy of the polyatomic ions. When the appropriate potential is applied at the output of a collision (retardation potential) cell, the potential barrier lets only the analyte ions pass, while the low-energy interfering polyatomic ions do not leave the collision cell [20]. The advantage of KED lies in the fact that the formation of new ions is minimized due to the inert working gas and, therefore, practically no further interferents are formed.

The second mechanism of interference elimination is based on chemical reactions of the interfering molecular ion with a working gas particle in the CRC. H₂, NH₃, CH₄, and O₂ are used as reactive working gases; interfering ions react with the working gas and the resulting particles differ in *m/z* value from the analyte ions. The kinetic energy of the product ions is considerably lower than the kinetic energy of the analyte ions; therefore, the output of new ions from the CRC can be reduced by the selection of an appropriate retardation potential. Analyte ions are further separated from product ions in the following quadrupole analyzer. The probability of ion-molecular transfers of small particles (electron, proton, hydrogen atom) depends on the difference in ionization energies between the reactants and the products. Thus the signal of the interferent can be suppressed by several orders of magnitude, while the signal of the analyte may remain the same or is slightly attenuated. The following reactions may occur in the CRC and can be used to minimize interference: neutralization of interferent, association of interferent, condensation of interferent, and fragmentation of interferent. Frequently, hydrogen is used as a reaction gas responsible for the elimination of interferents, especially by the transfer of a hydrogen atom or a proton and charge transfer [23]. Ion-molecular reactions can be employed to eliminate interference in two ways. The first approach is based on suppression or elimination of the interfering ion; the other consists of conversion of the analyte ion by reaction with an appropriate reaction gas to an ion with a different *m/z* that is not interfered with and can be measured [24]. Details on the functioning of DRC and CRC can be found in references [19–29].

Among the commonly used reaction and collision gases, helium and hydrogen are most frequently employed. Compared with hydrogen, helium yields better LOD and

sensitivity. Hydrogen is efficient at suppressing polyatomic ions which contain argon, and the yield of this reaction rises with increasing electronegativity of the element included in the interfering species [30]. De Muynck and Vanhaecke [31] optimized NH₃ flow rate through a DRC and determined the DRC quadrupole conditions for simultaneous determination of P, Ca, and Sr in hydroxyapatite. ArCa⁺, Ca₂⁺, and N-, O-, and Ar-based interferences with ^{86,88}Sr⁺ and ^{42,43,44}Ca⁺, respectively, were almost eliminated. Interference-free determination of Ca and Sr content in tooth samples for selected isotopes was achieved at an optimal flow rate of 0.8 mL min⁻¹ and a rejection parameter *q* (RPq) of the cell quadrupole of 0.65 [31].

Additionally, a reduction in spectral background and thus in interference could be achieved *via* ambient helium ICP-MS; however, it is more expensive than hydrogen [32]. It should be noted that to understand polyatomic and metal-oxide interference better and achieve precise and accurate results, a study of these effects is required for each matrix investigated in dry plasma in the case of laser ablation.

Concerning *mass analyzers*, the Q-MS provides less precise results in terms of mass resolving power and sequential data acquisition; but if all pitfalls are investigated, the outcome can be comparable to that of analyzers with a higher resolving power. Time-of-flight (TOF) MS is not equipped with additional devices enabling attenuation of interference but offers faster data acquisition and simultaneous measurement of the whole mass spectrum [33]. Vanhaecke *et al.* [34] reported that the relative standard deviation (RSD) of precision in isotope ratio by ICP-TOF-MS is less than 0.05%. The most efficient solution to spectral interference lies in the use of spectrometers with high resolving power. Sector field mass spectrometers (SF-MS) eliminate a large majority of the interferences. However, an increase in the resolving power (*R*) results in lower signal sensitivity. An increase in *R* from 300 (Q-MS) to 3000 means a signal attenuation of one order of magnitude [20]; an increase in *R* from 300 to 7200 reduces sensitivity by 99% [35].

As for *ablation cell size and shape*, line scan as well as spot analysis requires sufficient washout time to let the signal drop to background level, which depends on the size and shape of the ablation cell and the carrier gas flow rate (Figure 9.3).

Several studies have been devoted to modeling the trajectory of ablated particles in various types of ablation cells. Bleiner and Bogaerts [36] reported on the influence of ablation cell size and geometry on gas velocity pattern and extraction efficiency, which was found to be in the range of 5–15% (number of particles) for a conventional cell with a volume of 3–100 cm³. A study of ablation cells with volumes in the range of 0.25–63 cm³ and various transfer tubes differing in diameter and length proved that, with volume reduction, the structure of the signal was modified and the washout time was reduced. On the other hand, utilization of a 0.25 cm³ cell gave rise to a reduction in transport efficiency and an increase in rinse time. The diameter and length of the transport tubes were not found to affect the amount of material transported but only the structure of the signal [37]. The development of an ablation cell enabling a repetition rate of more than 10 Hz has also been described [38]. As reported, a cylindrical cell with a small volume ~1 cm³ provides better figures in comparison with a cuboid chamber. Signal intensity increases linearly with the laser ablation scan speed [39].

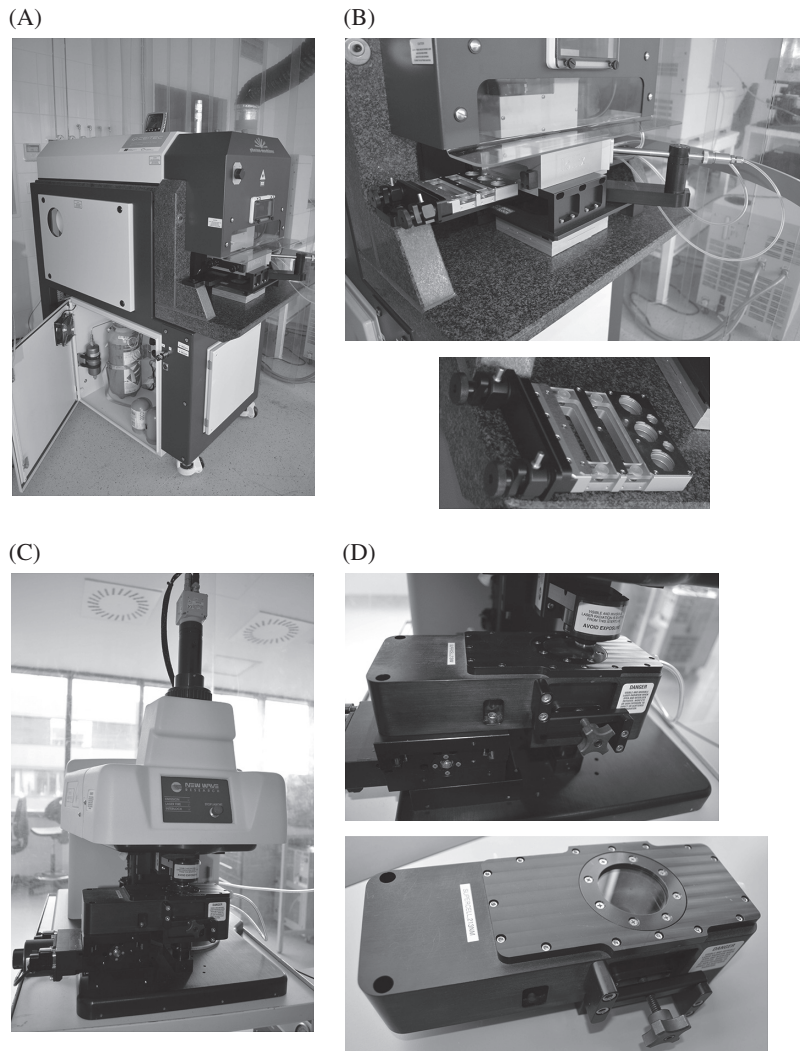


FIGURE 9.3 Photographs of laser ablation devices: (A) Excimer laser 193 nm with (B) detail of ablation chamber and (C) Nd:YAG 213 nm with (D) detail of ablation chamber. For color detail, please see color plate section.

9.2.3 Normalization of the Isotope Signal and Internal Reference Element

Matrix effects and instrumental drift lower the precision and accuracy of measurement. To compensate for the influence of these effects and low-frequency noise, a suitable internal reference element is frequently employed for analytical signal normalization. The behavior of the internal reference signal of a selected isotope, as governed by ablation rate, dissociation energy, and ionization energy, has to correlate as tightly

as possible with the signals from the isotopes of interest. Therefore, simultaneous measurement is the first prerequisite of a successful “internal standardization.”

Due to their water content, natural materials represent matrices that significantly influence analytical signals. Laser ablation of fresh samples or materials containing water such as plant/animal tissues leads to a reduction in the amount of mobilized material in the form of aerosol. In the context of elemental mapping, local variability in the water content in a studied target may distort the image of elemental distribution obtained by LA-ICP-MS. Moreover, water content results in deterioration of LOD. The $^{13}\text{C}^+$ isotope is frequently proposed as a suitable internal reference for natural materials with organic matrix, as carbon constitutes a significant part of many substances of interest, such as electrophoretic gel and plants. Similarly, carbon can serve as an internal reference for some inorganic natural substances. On the other hand, carbon is responsible for enhanced ionization of elements with first ionization energy in the range of 9–11 eV (Se, Te, As, Hg, Au), first observed by Allain *et al.* [40] and described in the ICP-MS analysis of biological samples [41–43] and in the ICP-OES analysis [44]. The mechanism of ionization enhancement was explained by Abou-Shakra as being due, for instance, to a charge transfer from C^+ to Se [45]. On the one hand, this enhanced ionization improves sensitivity but, on the other hand, it represents a serious element-dependent matrix effect. Moreover, depending on the type of matrix, laser ablation of carbon-containing materials results in the formation of various species that can be classified into two categories, namely carbon-containing gaseous species and carbon-containing particles [46]. This fact has to be considered when carbon is to be determined or used as the internal reference, as this phenomenon represents a significant type of fractionation. Besides, this kind of carbon speciation has not yet been fully explored and therefore internal standardization with carbon is not as straightforward as it might seem [46, 47]. $^{13}\text{C}^+$ has been used as an internal reference to compensate for signal fluctuations associated with laser ablation, transport, and ionization processes in the determination of iodine and arsenic in a sheep horn by surface tracing with LA-ICP-MS [48]. Wu *et al.* [49] used the $^{13}\text{C}^+$ signal to reduce the influence of the presence of water in LA-ICP-MS analysis of leaf samples.

Similar to carbon, sulfur (isotopes $^{32}\text{S}^+$ and $^{34}\text{S}^+$) is used to correct for the influence of water content. The benefit of correction *via* the sulfur signal consists in obtaining a sulfur-to-metal ratio, which is an important characteristic of metalloproteins [50]. Prior to normalization, careful suppression of spectral interference must be ensured, as the signals of sulfur isotopes are overlapped with signal of polyatomic species such as $^{16}\text{O}^{16}\text{O}^+$, $^{14}\text{N}^{18}\text{O}^+$ due to the presence of N and O in tissues and, moreover, $^{32}\text{S}_2^+$ overlaps the ion signal at mass 64, where $^{64}\text{Zn}^+$ is present. The successful application of $^{34}\text{S}^+$ for quantification of mercury in hair strands has been reported [51]. The utilization of sulfur to characterize metalloproteins after separation of proteins *via* SDS-PAGE was described by Becker *et al.* [52]. The tracing of separated Zn-, Fe-, and Fe-bearing proteins in gel was performed using LA-ICP-(SF)MS at a mass resolution $m/\Delta m$ of 4400, which eliminated potential interference. In the case of hard biological tissues (e.g., teeth, bones, and fish scales), signals of calcium isotopes are usually employed as an internal reference [53].

For normalization, the content or concentration of an internal reference element has to be known in advance; therefore, its determination by a complementary method is necessary. Generally, normalization is based on the application of one internal reference element. De Ridder *et al.* [54] reported on multiple normalization leading to a reduction in RSD by 30% when two internal reference signals were used, and either 42% or 50% of its original value when three or four elements were employed, respectively. Furthermore, normalization of elemental content on bulk components (100%) has been developed [55].

9.2.4 Quantification Approaches

Although LA-ICP-MS is widely reported as a quantitative method for bulk analysis and elemental mapping in a large variety of materials, truly reliable determinations cannot usually avoid the use of a strictly individual approach to particular matrices. The LA-ICP-MS method generally suffers from a lack of appropriate calibration standards and/or certified reference materials (SRM, CRM), which are necessary for calibration and method validation. Suitable SRM/CRM must exhibit properties that enable compensation for several types of matrix effects and consequently the achievement of bias-free quantitative results. Most SRM/CRM based on a biological matrix are primarily designed and prepared for solution analysis. As laser ablation represents a so-called “microsampling” technique, the homogeneity of such SRM/CRM, which otherwise safely meets the requirements in terms of solution analysis, should be checked.

SRMs/CRMs with biological matrices are commercially available, mostly for food commodities. They are specifically intended for the determination of total content of toxic elements and in some cases also for their speciation (As, Hg, and Sn). For plant tissue analysis, various herbal materials (rice/wheat flour, NIST SRM 1568a and 1567a; peach, NIST SRM 1547; tomato, NIST SRM 1573a; orchard, NIST SRM 1571; apple, NIST SRM 1515; pine, NIST SRM 1575; spinach, NIST SRM 1570; citrus, NIST SRM 1572; and tobacco, CTA-VTL-2) [49, 56–58] are available as an SRM. Elemental contents in animal tissue can be quantified with material prepared from pig liver (CRM LGC 7112), kidney (CRM ERM -BB186), bovine liver (SRM 1577b), muscle tissue (NIST RM 8414, DORM-2), mussel (CRM BCR 668), or fish tissue (BCR SRM 278) [58–62]. Some of these SRM/CRM could be used for quantification in solids. Frozen human urine (NIST SRM 2669), human/bovine blood (CRM BCR 635 and NIST SRM 966), or serum (NIST SRM 1598) diluted and/or spiked with some elements has been also employed [63–65]. Quantification in hard tissues with a hydroxyapatite matrix, such as bones or teeth, usually relies on calibration with an SRM prepared from bone meal (NIST SRM 1486) or bone ash (NIST SRM 1400) [31–66]. As they are available in powdered form, it is necessary to prepare compact targets for laser ablation by pressing them into pellets, using a sol–gel technique or embedding the SRM into epoxy resin or a carboxymethyl cellulose block [67–70].

As the choice of SRMs suitable for LA-ICP-MS is insufficient, preparation of matrix-matched, fine-grained, and homogeneous in-house standard materials from

real samples is of utmost importance. Powdered homogenized samples can be spiked with standard solutions containing the elements of interest. If there are solid materials with the same matrix and, at the same time, with appropriate concentration ranges of the elements of interest, they can be used as calibration samples. Another approach employs spiked gelatine or electrophoretic gel. Nebulization of a standard solution can be used for LA-ICP-MS calibration, but the correction factor for different sensitivities between dry and wet plasma has to be calculated [23–71].

If a well-defined reference material with an appropriate matrix is not available, isotope dilution can provide very precise and accurate quantitative results in comparison with external calibration [72, 73]. Isotope dilution is mostly used for solution analysis, combined with separation methods [74–76]. In the case of analysis of solids, a solution standard with an isotope-enriched tracer is nebulized into the flow of ablated material to guarantee matrix matching *via* online isotope dilution [77].

9.2.5 Imaging *via* LA-ICP-MS

The quite sharply localized region of a beam–target interaction with the spot diameter of the order of several hundred micrometers to several micrometers makes the laser an ideal tool for the measurement of elemental distribution in a sample. Whether the analysis is carried out in discrete spots positioned in precisely defined locations of *x* and *y* axes or as line scan, investigation of sample surface results in two- or three-dimensional images. The term of imaging LA-ICP-MS is generally used in this context.

This section is devoted to elemental imaging of the surface of various biomaterials which can be divided into two groups according to their physical properties. Much research has been focused on the investigation of hard tissues such as carbonate (e.g., shells or otoliths) [78–84], phosphate (fish scale [83, 84], teeth and bones [53, 85–88]), and organic matrix constituting bark and tree rings [89–91], hair [92, 93], dried blood [63], urine [94], and so on. Leaves and animal/human tissues, which offer the opportunity to study the bioavailability and accumulation of essential or toxic metals and metalloids, bonds of metals and proteins, and their characterization, are categorized into the group of soft tissues [56, 95–99]. These studies include direct analysis of tissue slices or the examination of electrophoretic gels after a separation procedure. LA-ICP-MS analysis of electrophoretic gel is described in an individual subsection of ‘Imaging *via* LA-ICP-MS.’

Relevant data about elemental distribution can be obtained only by using proper sample preparation and proper ablation procedure including suitable calibration. Studies published [100, 101] deal with an approach to interpreting the transient data in laser ablation scanning mainly by taking into consideration the geometry of the arrangement. A few other articles describe the influence of the particle size distribution of an ablated material after laser ablation on LA-ICP-MS analysis, as these parameters dictate the quality of the data [102, 103]. Lateral and depth resolution also plays a significant role in interpreting the spatial distribution of elements; the lower the resolution, the less true the maps and thus the less reliable are any conclusions drawn [104]. Modern techniques such as near-field laser ablation inductively

coupled plasma mass spectrometry are able to go down to hundreds of nanometers in lateral resolution, and perspectives with improved instrumentation are even an order of magnitude better [105].

9.2.5.1 Monitoring the Distribution of Elements in Hard Tissue As mentioned, teeth, bones, or fish scales constitute a group of hard tissue materials. The investigation of recent and/or fossil skeletal parts and parts of a fish's integumentary system is frequently focused on identifying spatial elemental distribution. The matrix of bones and teeth is made up of hydroxyapatite, a biomimetic with calcium and phosphorus as its major elements. Both tissues are metabolically active and their composition reveals dietary status and the migration/mobility of humans and animals, and it also yields data for the reconstruction of palaeoclimate, economic development, social status of humans, and historical processes occurring in any geographical location of interest.

Tooth represents a hard tissue comprising several different parts. Tooth crown consists of enamel and dentine. The enamel is the hardest part of the human body and begins to form in the prenatal stage. Thereafter, its composition remains unchanged throughout life. But, as opposed to enamel, dentin is active and its composition changes; therefore, the dietary input and mobility of subjects can be ascertained. Various parts of the sample can be distinguished by the LA-ICP-MS method [53]. Sr, Ba, Zn, and Ca are predominantly accumulated in the bone structure, but small portions of these elements are also deposited in tooth tissue and therefore they belong to elements of interest [85]. They are incorporated into the hydroxyapatite structure and cause changes in the elemental ratios, for instance Sr/Ca, Ba/Sr, and Zn/Sr. The level of chemical changes relates to the composition of the diet. It is well known that seafood is rich in strontium and barium. By contrast, meat consumption is reflected in a higher content of zinc and low level of Sr. The interpretation of LA-ICP-MS data is, however, complicated by postmortem processes when elemental depletion and enrichment in hydroxyapatite structure may take place, and the final content of the element of interest may not reflect the amount that is decisive for categorization according to dietary input. Nevertheless, alteration can be revealed on the basis of Ca/P ratio or the presence of rare earth elements (REE) in the matrix. The high content of REE is typical for ancient findings, in which $\Sigma\text{REE} + \text{Y}$ may reach up to units of m/m . Another application may concern, for example, the study of milk-teeth, which provides information on the pregnancy, health status, and dietary input of a mother and child.⁸⁷ The milk-tooth enamel is divided by neonatal line (NL) into postnatal and prenatal enamel. The chemical composition, position and thickness of NL have been studied by LA-ICP-MS [106, 107]. In view of the low thickness of NL, LA-ICP-MS experimental parameters must be carefully optimized with respect to required high spatial resolution and low LOD.

Skeletal tissue changes have been monitored using LA-ICP-MS, and quantification has been accomplished by bone meal (NIST SRM 1486) or bone ash (NIST SRM 1400) standards [53]. Calcium as an internal reference element permits the compensation for laser beam fluence fluctuation, ablation rate differences over the

investigated area, and instrument drift. Homogeneous distribution of an internal reference element over a rastered area is necessary for normalization.

Because hard tissues can accumulate heavy and toxic elements, otoliths (fish ear bones) and fish scales with carbonate and phosphate matrices have been analyzed to evaluate the exposure of the species to environmental pollution and the environmental history of a specific location [81–84]. Moreover, the chemistry of both tissues is affected by salinity, temperature, chemical composition of environment (e.g., water, soil), and dietary input [108]. The otolith in inner ear represents the carbonate indicator (aragonite) of fish age and it continuously accrues by growing incremental layers. Concentric layers enclose the core of otoliths, which is characterized by a higher content of Mn in case of some kind of fish. Sr, Ba, and Zn are also present beside Ca as matrix element, but their amount depends on many factors. The contribution of environment to Sr and Ba levels in otoliths represents more than 60% and is thus higher than the contribution of the diet [109]. The fact that the elemental content reflects the composition of the environment makes it possible to assess the mobility of fish population and differences between marine or fresh-water sources. It can also aid in determining the pollution of the environment or occurrence of fish in such a polluted environment [110]. Fish scales are investigated for the same purpose, but the environmental contribution to the level of Sr has not been found as significant as in the case of otoliths [111]. Comparative LA-ICP-MS analysis of fish scales and otoliths shows that fish can be classified according to their elemental fingerprints into groups related to capture sites. Both fish scale and otolith provide sorting 87% and 89% of fish population, respectively [112]. The variability in elemental contents has not been observed only on the sample surface, but the elemental distribution was also found to change with depth [84]. Significant differences were observed when sample surface rastering was followed by depth profiling.

The above materials belong to the group of biominerals that includes others such as kidney or bladder stones. Analysis of uroliths, especially their elemental mapping, may provide information on their initiation, formation, and growth and can facilitate medical treatment. The chemical composition of uroliths reflects many factors such as diet or disease and can reflect environmental pollution. Phosphate, oxalate, and uric acid belong to the most common matrices of uroliths, but their major portion consists of more than one phase; this gives rise to mixed kidney stones [113]. LA-ICP-MS analysis makes it possible to distinguish these various phases as well as elemental association [114]. Like in other cases, the analysis is often complicated by the lack of standard/certified reference material for quantification. For this purpose, Stepankova *et al.* [115] prepared laboratory-made matrix-matched calibration pellets.

Dendrochemical studies performed by LA-ICP-MS analysis on wood samples were aimed at determining changes in elemental contents within the spring and winter incremental rings that may provide information on the pollution history of studied locality. This again necessitates the development of suitable standard material for quantification. Also, the type of element and complex studies must be taken into account [89]. Su *et al.* [116], who studied the elemental distribution in single wood fibers, developed also the calibration strategy. On comparing calibration dependences of selected elements contained in doped cellulose pellets and single wood

fibers, they concluded that a higher amount of material is ablated from the surface of cellulose pellets. This resulted in the use of a mass coefficient, when the elemental content in a single wood fiber is determined *via* spiked cellulose pellets as standard materials [116].

The skeletal remains such as bones, teeth, fish scales, and otoliths are not the only sources of information about the diet, migration/mobility, and environment pollution. Hair can also serve as an information archive, though only on a short timescale. The study of elemental distribution along a hair can reveal, for example, intoxication due to the consumption of various drugs, food, and drinking water. The main interest is devoted to analysis of heavy metals such as Pb [117], Hg [118], Pt [93], and As [119] in relation to exogenous contamination and/or cytostatic drug exposure and the amount of elements of interest deposited in hair. Various calibration strategies have been developed for quantification. When the authenticity of Mozart remains was studied, the simplest way involved using as a calibration standard hair powder (CRM 397) pressed into a pellet [119]. Another approach giving a linear response (correlation coefficient of at least 0.97 for 24 elements) consists in simultaneous nebulization of calibration solution and laser ablation of the sample [118].

Utilization of the LA-ICP-MS technique in an analysis of solid samples is connected not only with elemental mapping within the hard tissue, but also with bulk analysis of biological liquids fixed on a solid carrier. In this case, changes in elemental distribution are expected only as the result of different distribution of the sample itself over the solid carrier. The deposition of liquid samples leads to the reduction in the amount of the material for analysis, and it requires a sensitive analytical technique. This type of application includes, for instance, analysis of dried blood droplets fixed on the surface of a hydrophobic filter membrane. Standard/certified reference materials (bovine and human blood) were utilized as samples to validate the concentration data. Accurate results were established for almost all measured elements, with reproducibility in the range of 4–8.5% [63]. A similar study has been carried out by Aramendia *et al.* [94] with human urine fixed on pre-cut filter paper disc as the investigated sample. Two external calibrations, in which internal standard was added in various sequence, and isotope dilution were tested.

9.2.5.2 Elemental Imaging in Soft Tissue This section is focused on analysis of soft tissue such as plant samples and human or animal tissue. In contrast to hard tissue analysis, the term “soft tissue” is usually connected with the study of interaction between heteroelements elements and proteins. It should be noted that LA-ICP-MS analysis provides information only on elements but not on compounds or elemental species. However, the bond of an element or ion in a certain oxidation state to a specific compound permits us to form conclusions about elemental speciation or occurrence of a compound. Detailed studies can be performed, for example, *via* separation of proteins by gel electrophoresis and subsequent determination of heteroelements in separated components. As this section is devoted to direct analysis of soft tissues, the discussion concerning this topic is in another section (see Section 9.2.5.3). Metallomic studies in plant tissues aid in elucidating the role of metals and metalloids in plant functions and metabolism and provide important

information that can be either (a) used for development in fields such as food chemistry and agriculture or (b) implemented into genetic engineering research. The study of plants, meat, and seafood is important for proposing and reaching a healthy and balanced diet. Similar to other biological materials, concentration levels of essential as well as toxic elements are investigated. For instance, seafood is known to accumulate high levels of toxic elements, and ICP-MS was successfully used to assess the bioaccessibility of Al, Cd, Hg, and Pb [120].

Elemental content determined by solution analysis can vary in individual plant organs (leaf, stem, and root), but it need not reflect availability and toxicity of these elements in the food chain—that is, for animals or humans [121]. Still, only methods for analysis of solids can answer questions such as where the elements are stored and how the transport of elemental species takes place. Lateral resolution must be adapted to suit the specific area to be characterized. Based on the analysis, one can depict two- or three-dimensional distribution [95]. In addition to high lateral resolution, quantification is the crucial point in revealing elemental distribution for which CRM or SRM mentioned in Section 9.2.4 are utilized [91]. Nevertheless, similar to other LA-ICP-MS studies, many researchers have been trying to prepare laboratory-made standards [56, 96]. In spite of the possibility to prepare suitable matrix-matched calibration materials, the analysis of fresh samples of soft tissues is usually complicated by the presence of water and by the inequality of sample surface of dried samples. Imaging of tissues characterized by different tissue density requires finding an appropriate normalization factor [96].

Bioimaging is an old technique originating in staining tissues for histology and anatomy research since the time of Camillo Golgi [122]. Currently [123], LA-ICP-MS plays an important role as a bioimaging tool [124, 125] along with traditional fluorescence confocal microscopy or atmospheric pressure surface sampling/ionization techniques [126]. Applied either on gels or on microsections of frozen tissue, the purpose of bioimaging by LA-ICP-MS is to obtain qualitative and quantitative information on the planar or spatial distribution of different elements. Elemental imaging of soft tissues such as liver, kidney, and brain tissue represents a more difficult analysis in comparison with hard tissues due to the higher water content, instability of the signal, and exacting optimization of the experimental parameters and equipment. To minimize the influence of the presence of water, the laser ablation is carried out at a lower temperature. Ablation at -60°C leads to better results but requires utilization of a cryogenically cooled ablation cell. As reported, a cryogenic cell assists in achieving better reproducibility and detection limits in tens of $\mu\text{g kg}^{-1}$ for Cd, Cu, and Zn or in units of $\mu\text{g kg}^{-1}$ for Pb [62].

Many studies have been performed on thin sections of brain tissue. The research group of Becker has been devoted to the imaging of brain tumors using mass spectrometry. One of the published papers concerns a study of elemental distribution (Cu, Zn, P, and S) in rat brain tissue for the detection of small-sized tumors. The sample surface was traced by a 213-nm laser beam with a diameter of $50\text{ }\mu\text{m}$ at a frequency of 20 Hz. The rat brain tissue was placed into a cooled ablation chamber. Mass spectrometric analysis showed an inhomogeneous distribution of elements, with decreasing content around the tumor. Quantification was performed via

matrix-matched laboratory-made standard samples (brain tissue slices) spiked with a standard solution [97].

A study of the distribution of Cu, Zn, Pb, and U in human tumor tissue was also described. Imaging was accomplished with a 266-nm Nd:YAG laser. The spot size diameter and frequency were the same as in the above study, and the setting of the scan speed was $30\text{ }\mu\text{m s}^{-1}$. In this paper, the dependence of the ICP-MS signal for the investigated element on laser beam spot diameter was shown. The contents of all elements were established using a spiked matrix-matched standard as in the previous case. Under the experimental parameters, LODs of Cu and Zn were 0.34 and 0.14 mg kg^{-1} , respectively. Values of 12.5 and $6.9\text{ }\mu\text{g kg}^{-1}$ were calculated for Pb and U [99]. Reproducibility expressed as a relative standard deviation of concentration was tested on five adjacent slices of human brain tissue and was equal to 5.4–6.5% for $^{13}\text{C}^+$, and 5.8–8.2% for copper, and the reproducibility for Zn was in the range of 5.1–6.7 % [127]. A similar calibration strategy was developed by Sela *et al.* [69], but the key difference was in encapsulation of spiked brain tissue into sol-gel matrix. A different approach for laboratory-made standards was applied in reference [70]. Treated as matrices, whole blood and blood serum were spiked with elements of interest, subsequently frozen and embedded into a carboxymethyl cellulose block. The signal stability was verified based on the fluctuation in the Fe and Zn response. The linear response and good reproducibility ensured LODs in the range of $\mu\text{g kg}^{-1}$ for Sr, Pt, and Gd.

Gholap *et al.* [128] used the LA-ICP-MS to study the penetration of platinum into tumors in rat tissue after the application of metallodrugs (oxaliplatin and bevacizumab). 2D maps of different isotopes ($^{194}\text{Pt}^+$, $^{31}\text{P}^+$, $^{13}\text{C}^+$) were constructed based on a line raster ablated by means of a 193-nm Nd:YAG laser beam with a 70- μm diameter and a 70- $\mu\text{m s}^{-1}$ scan speed. Phosphorus was used as a reference element for depicting the size and shape of the investigated material. A higher signal for Pt was observed on the sample/drug borderline. The quantification approach was not based on matrix-matched standards prepared from the investigated tissue but on a gelatine matrix spiked with Pt, as this organic substance mimicked the matrix. When using gelatine-based standards with sufficient homogeneity, the LOD of Pt was 0.25 ng g^{-1} . Isotope dilution as a quantification technique was also used for determining Cu concentration with the aim of analyzing small volumes of biological samples such as human brain fluids [129]. In the field of biological tissue imaging, Becker's group developed a methodology to determine the distribution and concentration of various elements (Cu, Zn, Fe, Mn, Na, Ca, K, Mg, Cd, Hg, Pb, U, Th, C, S, P, Cl, I, etc.) [130, 131]. To study the anatomy of brain tissue, a U and Nd containing solution was used for staining, resulting in LODs in the sub- $\mu\text{g g}^{-1}$ range [132].

One of the best examples of where bioimaging is heading is shown in the 3D bio-imaging of murine brain presented in reference 133. A 3D atlas of metal (Fe, Cu, Zn) content and distribution in cerebral tissue may serve to correlate these features to functional and, more practically, dysfunctional aspects of the tissue, although little is as yet known about particular cases beyond the general toxicity of some heteroelements (mostly metal ions) and the widely discussed Alzheimer's and Parkinson's diseases, where this technique may be utilized. Also, any bioimaging will chiefly



serve for fundamental research studies following pathological anatomy, because, as an invasive technique, it can hardly be applied as a diagnostic tool.

As the methodology of soft tissue elemental mapping is already well established, improvements in spatial resolution for small-sized samples and single-cell analyses are the next logical steps. The possibility of analyte signal enhancement exists for near-field laser ablation coupled with ICP-MS. This technique utilizes the near-field enhancement effect on the tip of a thin silver needle positioned in the laser beam on the target surface, which improves spatial resolution and increases the efficiency of the laser beam's energy delivery onto the sample surface [105]. The reproducibility was estimated to be 16% (RSD) [134].

9.2.5.3 PAGE LA-ICP-MS Both essential and toxic metals and metalloids are present in almost 40% of proteins, and they play an important role in their function. Polyacrylamide gel electrophoresis (PAGE), as the most appropriate technique for separating proteins, is also frequently applied to metalloproteins. PAGE is still the most popular protein separating method, although it has its well-known drawbacks, especially when separating metal-binding proteins/metalloproteins. The main drawback is the stability of metal-binding proteins/metalloproteins during separation; published data agree that non-denaturing, also known as native PAGE, is more suitable than denaturing, or SDS-PAGE [135]. However, both these methods have been successfully used to separate metalloproteins in the form of SDS PAGE [136], PAGE with decreased content of SDS [137] and native PAGE [138]. Another influential parameter playing a role in laser ablation efficiency on gels seems to be gel visualization by means of staining, because it is reasonable to suppose that such a staining process may disrupt protein–metal bonds [139]. Data show that silver staining is the most appropriate method of gel visualization for LA-ICP-MS [136, 140]. Last, but not least, the high water content (up to 90%) in electrophoretic gels, which evaporates during the ablation process, causes deformations and ruptures of gels and has to be decreased significantly. This is achieved either by drying, possibly in a gel drier without further processing [137, 141] or between cellophane foils [142], or by exchanging water for a more suitable liquid (such as glycerol) [136]. The drying process, besides lowering the water content, has to ensure proper geometric properties.

A solution to the need of applying laser ablation to gel slabs prior to ICP-MS is to connect the gel electrophoresis online *via* column elution gel electrophoresis (CEGE). This approach was recently reviewed in Raab *et al.* [136]. Although the method is described in the above review as “a promising analytical tool,” to date only one article has been published, which deals with an experimental examination of CEGE followed by elemental analysis of the metalloproteins cytochrome C and hemoglobin or the metal-binding proteins ferritin and human transferrin [143]. Also, general metallomic applications are rather rare [144]. However, successful separation of metalloproteins by PAGE without their disruption is hindered in some cases by the very nature of the technique, because some metal complexes with proteins are labile and can disintegrate during separation. In order to prevent this process, non-denaturing separation protocols must be used. The presence of metal impurities in the gels has to be avoided and ultrapure staining reagents are highly recommended,

unless they are completely omitted, because the loss of some metal may occur in each of the steps (separation, fixing, and staining) [145]. For correctly separated metalloproteins, LA-ICP-MS represents an efficient tool for *in situ* probing of a gel with metalloprotein spots to prove the presence of metals and metalloids, determine their content, and study the metal–protein bonds and their mechanisms [146].

One of the tasks that may be solved by PAGE LA-ICP-MS is the quantification of proteins *via* their heteroelement content. The source of the heteroelement is either extrinsic in metal containing mass tags, or intrinsic, like with sulfur, the content of which is proportional to the content of the protein according to sulfur-amino acids (cysteine, methionine) present in its structure [52]. Jiménez *et al.* [147] studied the presence of Cu, Zn, and I contained in superoxide dismutase and thyroglobulin proteins using a 1 D SDS-glycine method. For quantification purposes, matrix-matched standards consisting of dried gel spiked with a well-defined solution of the element of interest were prepared and $^{13}\text{C}^+$ was selected as an internal reference element for normalization. The gel was ablated using the line scanning mode at a scan speed of $60\text{ }\mu\text{m s}^{-1}$, a frequency of 20 Hz, and a laser beam $100\text{ }\mu\text{m}$ in diameter. The concentration of I using PAGE LA-ICP-MS was 8.5 g kg^{-1} , which was in good agreement with solution analysis (9.3 g kg^{-1}). The achieved RSD was equal to 7%. On the contrary, no signal for Cu was detected and in the case of Zn the signal was very low, probably due to loss of the metal during SDS-PAGE. The method was substituted by native PAGE but without any changes in the signal for Cu and Zn [147].

Different approaches to the preparation of gels for laser ablation were applied in Ballihaut *et al.* [148]. The aim of this study was to detect selenoproteins after SDS-PAGE. The authors compared the signal of $^{78}\text{Se}^+$ after (a) ablation of the gel with selenoproteins and (b) electroblotting onto a polyvinylidene fluoride (PVDF) membrane. From the viewpoint of sensitivity, sample preparation by electroblotting linked to nebulization of the organic solution was found to be 80 times more sensitive than classical LA-ICP-MS. The laser ablation ICP-MS method is also convenient, for example, for visualization of proteins tagged by iodine. BSA, b-casein, cytochrome c, and lysozyme proteins were separated by SDS-PAGE and subsequently transported onto a membrane. Their distribution through the membrane was subsequently determined by means of $^{127}\text{I}^+$ intensity [149].

9.2.6 Comparison with Other Methods for Analysis of Solids

The utilization of LA-ICP-MS in the field of elemental mapping is evident; but the question concerning comparison with other methods, not merely those serving for imaging but those used for solid sample analysis in general, still remains. The comparison of these methods in terms of LODs, spatial resolution, sensitivity, capability to detect most of the elements in the periodic table, linear dynamic range, calibration strategies, availability of SRM/CRM, and their application for various matrices requires a complex approach and not an individual appraisal of the enumerated factors. Generally, solid samples are analyzed by neutron activation analysis (NAA), electron microprobe analysis (EMPA), infrared and Raman spectroscopy (IR/RS), proton-induced X-ray analysis (PIXE), micro-X-ray fluorescence and

absorption (XRF and XRA), and secondary ion mass spectrometry (SIMS). One of the characteristics of solids is the type of structure organization, that is, the presence of amorphous or crystalline phase and a type of this crystal structure including lattice parameters, which is the task for X-ray diffraction (XRD). The aim of a target mapping consists not only in elemental distribution, but also in attribution of elements to particular solid phases. Infrared and Raman spectrometry are also tools for the speciation of elements in solid phase. Contrary to XRD, IR, and RS, LA-ICP-MS does not allow this speciation. The methods differ from each other in the specific information they provide. Therefore, the selection of a suitable method must be performed with respect to the aim of the study and thus the required results.

In the case of analysis of hard tissues such as bone, teeth, otoliths, fish scale, and kidney stones, NAA and EMPA techniques are convenient, for example, for an investigation of specific elements (fluorine, chlorine, etc.) that cannot be detected by elemental/inorganic mass spectrometry. Moreover, spatial resolution of most methods reaches better values in comparison with laser beam sampling. On the other hand, the LODs of, for example, EMPA are higher, and trace elements thus cannot be detected.

Similar to what was done in Proksova *et al.* [114], X ray fluorescence and absorption were employed in the analysis of various kinds of human kidney stones and the “speciation” of Sr was investigated [150]. The main objective consisted in identification of particular phases and compounds in which strontium was incorporated. The presence of Sr was studied with respect to the type of kidney stones (cystine, oxalate, carbonate, and phosphate). Predictably, Sr was not found in cystine uroliths, but its presence was associated with the occurrence of calcium. Moreover, an XRA study of oxalate stone revealed the presence of Sr in the form of phosphate (80%) and carbonate (20%). The LA-ICP-MS technique cannot offer equally high spatial resolution, but the “elemental speciation” can also be studied. Synchrotron-based XRF was also utilized for the analysis of Ca, Sr, and Pb in hydroxyapatite matrix, which is the main component of fossil bones [151]. Elemental mapping was carried out with a resolution of 10 µm and the beam spot size of 5 µm. LA-ICP-MS can provide spatial resolution of ~5 µm under optimal experimental conditions but at the expense of LOD and the information on the distribution of ultra-trace elements. For instance, the LA-ICP-MS has been used for the study of incremental layers in dental enamel with the beam diameter set to 10 µm [106]. Moreover, this method can be used to study the formation of new bony tissue in medical research [152]. Similarly, an “ultrastructural” study of bone tissue was carried out in Ramirez-Fernandez *et al.* [153], where the Ca/P ratio was determined by energy-dispersive X-ray spectrometry. The aim of this study was to determine the Ca/P ratio in the biomaterial, in the interface, and in the newly formed bone tissue. In this case, the utilization of LA-ICP-MS could be complicated by worse spatial resolution, especially when the interface between the biomaterial and the newly formed tissue is examined. The size of the new bone part reached up to 75 µm and its analysis was easily performed. Not only two-dimensional imaging, but also 3D maps of elemental distribution, can be obtained by dual-energy K-edge subtraction (KES). In this case, Sr distribution was investigated in a bony animal tissue, and EMPA and KES were combined with a resolution better than 2 µm [154]. However, strontium was not selected in order to reveal

the dietary input or migration/mobility like in the case of fossil samples, but instead was chosen as a potential tracer allowing the newly bone tissue to be visualized. Moreover, it made it possible to study the influence of Sr on morphology and mechanical properties. As mentioned, PIXE has also found the application in a high-resolution quantitative elemental imaging of otoliths [155] and teeth [156]. In the case of LA-ICP-MS measurement, the samples were analyzed with micrometric scale resolution. But when studying the correlation between changes in elemental composition and daily increment, the LA-ICP-MS technique does not provide the sufficient spatial resolution achieved by PIXE. The octopus stylets were analyzed by PIXE at a spatial resolution of about $2.5\text{ }\mu\text{m}$, with LOD equal to tens and thousands of mg kg^{-1} for trace and major elements, respectively. Broad-beam PIXE or μ -PIXE provides information on the distribution in units of micrometer scale and can be used for most elements that are important in the study of tooth and bone mineralization [157, 158]. The achieved LODs are lower units of mg kg^{-1} or below the 1 mg kg^{-1} for trace elements. In another study devoted to the analysis of dental enamel, the LOD was in the range of $10\text{--}0.1\text{ mg kg}^{-1}$ and the attained accuracy was better than 5% [159].

Comparison of SIMS and LA-ICP-MS as imaging mass spectrometry techniques for hard tissues shows that SIMS is superior to LA-ICP-MS in terms of lateral resolution, because the beam-target interaction area is substantially smaller, and the achievable lateral resolution therefore varies in the range of a nanometer scale. In Lodding *et al.* [160], SIMS was used for the imaging of individual apatite crystallites in tooth tissue, with a resolution of 20 nm . Infrared or Raman spectrometry exhibits an advantage over LA-ICP-MS, SIMS, and synchrotron-based methods due to their ability to distinguish different structures and their changes. In other words, it is easy to detect elemental changes with respect to the presence of various phases, medical treatment, dietary input, environment, and so on, but there is no information on the bond of an element to a specific position in the main component.

All of the above methods have been used in the analysis of hair and plants. PIXE-tomography and simultaneous on/off axis scanning transmission ion microscopy-tomography were utilized in hair analysis and investigation of 3D distribution of S, K, Cl, Ca, Fe, and Zn on the quantitative level [161]. The nanoSIMS and EMPA were utilized for the analysis of leaves and monitoring of Zn, Mn, Ni, Co, Cu, Se, Cd, and As [162].

Based on the number of articles dealing with elemental imaging of various matrices, the techniques of choice are PIXE, SEM/EMPA, and synchrotron radiation-based methods, which are widely used for the study of elemental distribution. However, it is not merely the applicability in terms of analytical and chemometric parameters which is a decisive criterion for a method selection. The requisite instrumentation is characterized by high purchase and operation costs and measurements, and data evaluation is usually time-consuming.

Besides LA-ICP-MS, micro-X-ray fluorescence is widely used as an imaging technique of soft tissues. Comparative testing of these two methods with respect to spatial resolution and detection power has been carried out on thin sections of the organism *Daphnia magna* [163]. The comparison was based on the measurement of Ca, P, S, and Zn. Micro-XRF measurement was characterized by a longer analysis

time than LA-ICP-MS, by a factor of 2–3. The determination of LOD changes with beam diameter and measuring time in the case of LA-ICP-MS and micro-XRF, respectively, prevented the comparison of LODs. At a fixed diameter of 15 µm and live time of 5 s, better LODs were determined using bovine liver (NIST SRM 1577B) by micro-XRF for all elements except P and Zn. The critical factor resulting in poorer LOD by LA-ICP-MS was found to be spectral interference. In the conclusion of this study, it was noted that each technique is applicable for one unique element (e.g. sulfur) and they could be considered as complementary.

The competitiveness of LA-ICP-MS with other imaging techniques was described in Pugh *et al.* [164], where LA-ICP-MS was compared with magnetic resonance imaging (MRI). The objective of the study was to monitor the distribution of Gd and Pt in histological sections of rat brain. The time of analysis, number of measurable elements, isotope determination, sensitivity, resolution, and sample preparation were the compared parameters. Even though better spatial resolution (in the range of µm), quantification, and sensitivity (in the range of µg kg⁻¹) were achieved by LA-ICP-MS, MRI is used for living tissues (*in vivo* analysis) [164].

The ion beam microprobe technique benefits from single-cell quantitative analysis. In the case of a proton beam, 100-fold higher sensitivity is attainable when compared to an electron beam. The typical LOD is equal to 0.01 mg kg⁻¹. A synchrotron radiation microprobe offers detection limits in the range of 0.1–1 mg kg⁻¹. SIMS, similar to LA-ICP-MS, provides multielemental and isotope analysis but with higher spatial resolution [165].

Electron energy-loss spectroscopy (EELS) and energy-filtered transmission electron microscopy (EFTEM) are characterized by a very high spatial resolution of 2 nm. However, most of the imaging techniques (X-ray microanalysis, electron probe X-ray microanalysis, proton microprobe, and synchrotron X-ray microprobe) require sample preparation in the form of dried or frozen thin sections [166].

9.3 THE CRITICAL VIEW OF UTILIZATION OF LA-ICP-MS

Metrological parameters constitute important attributes of quantitative analysis. The repeatability and reproducibility of measurements by means of LA-ICP-MS, especially in the case of bioimaging, represent fundamental topics, as reported experimental values frequently have nothing to do with quantitative analysis. There is as yet no work available which would comprehensively evaluate these metrological parameters, although it is clear that they are essential and critical. It is important to be aware of the fact that there are many issues concerning the repeatability and reproducibility of LA-ICP-MS procedures. Among other noteworthy factors, there are the influence of laser energy on ablation, sample geometry, stability of aerosol flow into the ICP, or efficiency of transmission of the real content to the detected signal. Some studies mention validation [e.g., 98, 167, 168], which is in fact not validation but either calibration or normalization of measured signals. Additionally, the results are frequently expressed in a way difficult to interpret. For example, one work actually presents the results of such validation, called in a later paper *reproducibility*

(instead of the correct term *repeatability*, which is what they really did), in an $X \pm Y$ format, where Y is *relative standard deviation*, used instead of *confidence limits* [169]. Proper statistical evaluations of analytical characteristics within bioimaging protocols, which would define the relevance of such analyses, are still missing.

ACKNOWLEDGMENTS

This work was supported by the project CEITEC—Central European Institute of Technology (CZ.1.05/1.1.00/02.0068)—from European Regional Development Fund and by the project EVOGEN from European Social Fund (CZ.1.07/2.3.00/20.0189).

REFERENCES

1. Kryukov, G. V., Gladyshev, V. N. (2004). The prokaryotic selenoproteome. *EMBO Reports* **5**, 538–543.
2. Hatfield, D. L., Gladyshev, V. N. (2002). How selenium has altered our understanding of the genetic code. *Molecular and Cellular Biology* **22**, 3565–3576.
3. Faria, N., Winship, P. D., Weiss, D. J., Coles, B. J., Schoenberg, R., Hutchison, C., Pereira, D. I. A., Powell, J. J. (2011). Development of DRC-ICP-MS methodology for the rapid determination of Fe-58 erythrocyte incorporation in human iron absorption studies. *Journal of Analytical Atomic Spectrometry* **26**, 1648–1652.
4. Mokgalaka, N. S., Gardea-Torresdey, J. L. (2006). Laser ablation inductively coupled plasma mass spectrometry: Principles and applications. *Applied Spectroscopy Reviews* **41**, 131–150.
5. Koch, J., Gunther, D. (2011). Review of the State-of-the-Art of Laser Ablation Inductively Coupled Plasma Mass Spectrometry. *Applied Spectroscopy* **65**, 155A–162A.
6. Lear, J., Hare, D., Adlard, P., Finkelstein, D., Doble, P. (2012). Improving acquisition times of elemental bio-imaging for quadrupole-based LA-ICP-MS. *Journal of Analytical Atomic Spectrometry* **27**, 159–164.
7. Lear, J., Hare, D. J., Fryer, F., Adlard, P. A., Finkelstein, D. I., Doble, P. A. (2012). High-Resolution Elemental Bioimaging of Ca, Mn, Fe, Co, Cu, and Zn Employing LA-ICP-MS and Hydrogen Reaction Gas. *Analytical Chemistry* **84**, 6707–6714.
8. Guillong, M., Gunther, D. (2002). Effect of particle size distribution on ICP-induced elemental fractionation in laser ablation-inductively coupled plasma-mass spectrometry. *Journal of Analytical Atomic Spectrometry* **17**, 831–837.
9. Eggins, S. M., Kinsley, L. P. J., Shelley, J. M. G. (1998). Deposition and element fractionation processes during atmospheric pressure laser sampling for analysis by ICP-MS. *Applied Surface Science* **127**, 278–286.
10. Mank, A. J. G., Mason, P. R. D. (1999). A critical assessment of laser ablation ICP-MS as an analytical tool for depth analysis in silica-based glass samples. *Journal of Analytical Atomic Spectrometry* **14**, 1143–1153.
11. Mason, P. R. D., Mank, A. J. G. (2001). Depth-resolved analysis in multi-layered glass and metal materials using laser ablation inductively coupled plasma mass spectrometry (LA-ICP-MS). *Journal of Analytical Atomic Spectrometry* **16**, 1381–1388.

12. Ulrich, T., Kamber, B. S., Jugo, P. J., Tinkham, D. K. (2009). Imaging element-distribution patterns in minerals by laser ablation – inductively coupled plasma – mass spectrometry (LA-ICP-MS). *Canadian Mineralogist* **47**, 1001–1012.
13. Sanborn, M., Telmer, K. (2003). The spatial resolution of LA-ICP-MS line scans across heterogeneous materials such as fish otoliths and zoned minerals. *Journal of Analytical Atomic Spectrometry* **18**, 1231–1237.
14. Gunther, D., Heinrich, C. A. (1999). Comparison of the ablation behaviour of 266 nm Nd: YAG and 193 nm ArF excimer lasers for LA-ICP-MS analysis. *Journal of Analytical Atomic Spectrometry* **14**, 1369–1374.
15. Kosler, J., Wiedenbeck, M., Wirth, R., Hovorka, J., Sylvester, P., Mikova, J. (2005). Chemical and phase composition of particles produced by laser ablation of silicate glass and zircon – implications for elemental fractionation during ICP-MS analysis. *Journal of Analytical Atomic Spectrometry* **20**, 402–409.
16. Horn, I., Gunther, D. (2003). The influence of ablation carrier gasses Ar, He and Ne on the particle size distribution and transport efficiencies of laser ablation-induced aerosols: implications for LA-ICP-MS. *Applied Surface Science* **207**, 144–157.
17. Guillong, M., Heinrich, C. A. (2007). Sensitivity enhancement in laser ablation ICP-MS using small amounts of hydrogen in the carrier gas. *Journal of Analytical Atomic Spectrometry* **22**, 1488–1494.
18. Hu, Z. C., Gao, S., Liu, Y. S., Hu, S. H., Chen, H. H., Yuan, H. L. (2008). Signal enhancement in laser ablation ICP-MS by addition of nitrogen in the central channel gas. *Journal of Analytical Atomic Spectrometry* **23**, 1093–1101.
19. Feldmann, I., Jakubowski, N., Stuewer, D. (1999). Application of a hexapole collision and reaction cell in ICP-MS Part I: Instrumental aspects and operational optimization. *Fresenius Journal of Analytical Chemistry* **365**, 415–421.
20. Feldmann, I., Jakubowski, N., Thomas, C., Stuewer, D. (1999). Application of a hexapole collision and reaction cell in ICP-MS Part II: Analytical figures of merit and first applications. *Fresenius Journal of Analytical Chemistry* **365**, 422–428.
21. Eiden, G. C., Barinaga, C. J., Koppenaal, D. W. (1999). Analytical performance of the plasma source RF quadrupole ion trap in elemental and isotopic MS. *Journal of Analytical Atomic Spectrometry* **14**, 1129–1132.
22. Rowan, J. T., Houk, R. S. (1989). Attenuation of polyatomic ion interferences in inductively coupled plasma mass-spectrometry by gas-phase collisions. *Applied Spectroscopy* **43**, 976–980.
23. Hattendorf, B., Gunther, D. (2000). Characteristics and capabilities of an ICP-MS with a dynamic reaction cell for dry aerosols and laser ablation. *Journal of Analytical Atomic Spectrometry* **15**, 1125–1131.
24. Tanner, S. D., Baranov, V. I., Bandura, D. R. (2002). Reaction cells and collision cells for ICP-MS: a tutorial review. *Spectrochimica Acta Part B-Atomic Spectroscopy* **57**, 1361–1452.
25. Tanner, S. D., Baranov, V. I. (1999). Theory, design, and operation of a dynamic reaction cell for ICP-MS. *Atomic Spectroscopy* **20**, 45–52.
26. Baranov, V. I., Tanner, S. D. (1999). A dynamic reaction cell for inductively coupled plasma mass spectrometry (ICP-DRC-MS) – Part 1. *The rf-field energy contribution in thermodynamics of ion-molecule reactions*. *Journal of Analytical Atomic Spectrometry* **14**, 1133–1142.



27. Mason, P. R. D., Kaspers, K., van Bergen, M. J. (1999). Determination of sulfur isotope ratios and concentrations in water samples using ICP-MS incorporating hexapole ion optics. *Journal of Analytical Atomic Spectrometry* **14**, 1067–1074.
28. Tanner, S. D., Baranov, V. I., Vollkopf, U. (2000). A dynamic reaction cell for inductively coupled plasma mass spectrometry (ICP-DRC-MS) - Part III. Optimization and analytical performance. *Journal of Analytical Atomic Spectrometry* **15**, 1261–1269.
29. Bandura, D. R., Tanner, S. D. (1999). Effect of collisional damping in the dynamic reaction cell on the precision of isotope ratio measurements. *Atomic Spectroscopy* **20**, 69–72.
30. Mason, P. R. D., Kraan, W. J. (2002). Attenuation of spectral interferences during laser ablation inductively coupled plasma mass spectrometry (LA-ICP-MS) using an rf only collision and reaction. *Journal of Analytical Atomic Spectrometry* **17**, 858–867.
31. De Muynck, D., Vanhaecke, F. (2009). Development of a method based on inductively coupled plasma-dynamic reaction cell-mass spectrometry for the simultaneous determination of phosphorus, calcium and strontium in bone and dental tissue. *Spectrochimica Acta Part B-Atomic Spectroscopy* **64**, 408–415.
32. Jin, X. Z., Li, L. F., Hang, W., Chen, J. G., Huang, B. L. (2010). Inductively coupled plasma mass spectrometry with ambient helium surrounding ion source. *Spectrochimica Acta Part B-Atomic Spectroscopy* **65**, 1052–1055.
33. Kozlov, B., Saint, A., Skroce, A. (2003). Elemental fractionation in the formation of particulates, as observed by simultaneous isotopes measurement using laser ablation ICP-oa-TOFMS. *Journal of Analytical Atomic Spectrometry* **18**, 1069–1075.
34. Vanhaecke, F., Moens, L., Dams, R., Allen, L., Georgitis, S. (1999). Evaluation of the isotope ratio performance of an axial time-of-flight ICP mass spectrometer. *Analytical Chemistry* **71**, 3297–3303.
35. Du, Z. Y., Houk, R. S. (2000). Attenuation of metal oxide ions in inductively coupled plasma mass spectrometry with hydrogen in a hexapole collision cell. *Journal of Analytical Atomic Spectrometry* **15**, 383–388.
36. Bleiner, D., Bogaerts, A. (2007). Computer simulations of sample chambers for laser ablation-inductively coupled plasma spectrometry. *Spectrochimica Acta Part B-Atomic Spectroscopy* **62**, 155–168.
37. Bleiner, D., Gunther, D. (2001). Theoretical description and experimental observation of aerosol transport processes in laser ablation inductively coupled plasma mass spectrometry. *Journal of Analytical Atomic Spectrometry* **16**, 449–456.
38. Gurevich, E. L., Hergenroder, R. (2007). A simple laser ICP-MS ablation cell with wash-out time less than 100 ms. *Journal of Analytical Atomic Spectrometry* **22**, 1043–1050.
39. Wu, B., Becker, J. S. (2012). Bioimaging of metals in rat brain hippocampus by laser micro-dissection inductively coupled plasma mass spectrometry (LMD-ICP-MS) using high-efficiency laser ablation chambers. *International Journal of Mass Spectrometry* **323**, 34–40.
40. Allain, P., Jaunault, L., Mauras, Y., Mermet, J. M., Delaporte, T. (1991). Signal enhancement of elements due to the presence of carbon-containing compounds in inductively coupled plasma mass-spectrometry. *Analytical Chemistry* **63**, 1497–1498.
41. Campbell, M. J., Demesmay, C., Olle, M. (1994). Determination of total arsenic concentrations in biological matrices by inductively-coupled plasma-mass spectrometry. *Journal of Analytical Atomic Spectrometry* **9**, 1379–1384.
42. Larsen, E. H., Sturup, S. (1994). Carbon-enhanced inductively-coupled plasma-mass spectrometric detection of arsenic and selenium and its application to arsenic speciation. *Journal of Analytical Atomic Spectrometry* **9**, 1099–1105.

43. Gammelgaard, B., Jons, O. (1999). Determination of selenium in urine by inductively coupled plasma mass spectrometry: interferences and optimization. *Journal of Analytical Atomic Spectrometry* **14**, 867–874.
44. Machat, J., Otruba, V., Kanicky, V. (2002). Spectral and non-spectral interferences in the determination of selenium by inductively coupled plasma atomic emission spectrometry. *Journal of Analytical Atomic Spectrometry* **17**, 1096–1102.
45. AbouShakra, F. R., Rayman, M. P., Ward, N. I., Hotton, V., Bastian, G. (1997). Enzymatic digestion for the determination of trace elements in blood serum by inductively coupled plasma mass spectrometry. *Journal of Analytical Atomic Spectrometry* **12**, 429–433.
46. Frick, D. A., Gunther, D. (2012). Fundamental studies on the ablation behaviour of carbon in LA-ICP-MS with respect to the suitability as internal standard. *Journal of Analytical Atomic Spectrometry* **27**, 1294–1303.
47. Todoli, J. L., Mermet, J. M. (1998). Study of polymer ablation products obtained by ultra-violet laser ablation inductively coupled plasma atomic emission spectrometry. *Spectrochimica Acta Part B-Atomic Spectroscopy* **53**, 1645–1656.
48. Caumette, G., Ouypornkochagorn, S., Scrimgeour, C. M., Raab, A., Feldmann, J. (2007). Monitoring the arsenic and iodine exposure of seaweed-eating North Ronaldsay sheep from the gestational and suckling periods to adulthood by using horns as a dietary archive. *Environmental Science & Technology* **41**, 2673–2679.
49. Wu, B., Zoriy, M., Chen, Y. X., Becker, J. S. (2009). Imaging of nutrient elements in the leaves of Elsholtzia splendens by laser ablation inductively coupled plasma mass spectrometry (LA-ICP-MS). *Talanta* **78**, 132–137.
50. Yin, X. B., Li, Y., Yan, X. P. (2008). CE-ICP-MS for studying interactions between metals and biomolecules. *TRAC-Trends in Analytical Chemistry* **27**, 554–565.
51. Legrand, M., Lam, R., Passos, C. J. S., Mergler, D., Salin, E. D., Chan, H. M. (2007). Analysis of mercury in sequential micrometer segments of single hair strands of fish-eaters. *Environmental Science & Technology* **41**, 593–598.
52. Becker, J. S., Zoriy, M., Krause-Buchholz, U., Pickhardt, C., Przybylski, M., Pompe, W., Rodel, G. (2004). In-gel screening of phosphorus and copper, zinc and iron in proteins of yeast mitochondria by LA-ICP-MS and identification of phosphorylated protein structures by MALDI-FT-ICR-MS after separation with two-dimensional gel electrophoresis. *Journal of Analytical Atomic Spectrometry* **19**, 1236–1243.
53. Hare, D., Austin, C., Doble, P., Arora, M. (2011). Elemental bio-imaging of trace elements in teeth using laser ablation-inductively coupled plasma-mass spectrometry. *Journal of Dentistry* **39**, 397–403.
54. De Ridder, F., Pintelon, R., Schoukens, J., Navez, J., Andre, L., Dehairs, F. (2002). An improved multiple internal standard normalisation for drift in LA-ICP-MS measurements. *Journal of Analytical Atomic Spectrometry* **17**, 1461–1470.
55. Chen, L., Liu, Y. S., Hu, Z. C., Gao, S., Zong, K. Q., Chen, H. H. (2011). Accurate determinations of fifty-four major and trace elements in carbonate by LA-ICP-MS using normalization strategy of bulk components as 100%. *Chemical Geology* **284**, 283–295.
56. Cizziel, J., Bu, K. X., Nowinski, P. (2012). Determination of elements in situ in green leaves by laser ablation ICP-MS using pressed reference materials for calibration. *Analytical Methods* **4**, 564–569.
57. Ward, N. I., Durrant, S. F., Gray, A. L. (1992). Analysis of biological standard reference materials by laser ablation inductively coupled plasma mass-spectrometry. *Journal of Analytical Atomic Spectrometry* **7**, 1139–1146.



58. Nardi, E. P., Evangelista, F. S., Tormen, L., SaintPierre, T. D., Curtius, A. J., de Souza, S. S., Barbosa, F. (2009). The use of inductively coupled plasma mass spectrometry (ICP-MS) for the determination of toxic and essential elements in different types of food samples. *Food Chemistry* **112**, 727–732.
59. Tibi, M., Heumann, K. G. (2003). Isotope dilution mass spectrometry as a calibration method for the analysis of trace elements in powder samples by LA-ICP-MS. *Journal of Analytical Atomic Spectrometry* **18**, 1076–1081.
60. Kirby, J., Maher, W. (2002). Measurement of water-soluble arsenic species in freeze-dried marine animal tissues by microwave-assisted extraction and HPLC-ICP-MS. *Journal of Analytical Atomic Spectrometry* **17**, 838–843.
61. Locatelli, C. (2000). Proposal of new analytical procedures for heavy metal determinations in mussels, clams and fishes. *Food Additives and Contaminants* **17**, 769–774.
62. Feldmann, J., Kindness, A., Ek, P. (2002). Laser ablation of soft tissue using a cryogenically cooled ablation cell. *Journal of Analytical Atomic Spectrometry* **17**, 813–818.
63. Hsieh, H. F., Chang, W. S., Hsieh, Y. K., Wang, C. F. (2011). Using dried-droplet laser ablation inductively coupled plasma mass spectrometry to quantify multiple elements in whole blood. *Analytica Chimica Acta* **699**, 6–10.
64. Davis, W. C., Zeisler, R., Sieber, J. R., Yu, L. L. (2010). Methods for the separation and quantification of arsenic species in SRM 2669: arsenic species in frozen human urine. *Analytical and Bioanalytical Chemistry* **396**, 3041–3050.
65. Nixon, D. E., Neubauer, K. R., Eckdahl, S. J., Butz, J. A., Burritt, M. F. (2003). Evaluation of a tunable bandpass reaction cell inductively coupled plasma mass spectrometer for the determination of selenium in serum and urine. *Spectrochimica Acta Part B-Atomic Spectroscopy* **58**, 97–110.
66. Bellis, D. J., Hetter, K. M., Jones, J., Amarasiriwardena, D., Parsons, P. J. (2006). Calibration of laser ablation inductively coupled plasma mass spectrometry for quantitative measurements of lead in bone. *Journal of Analytical Atomic Spectrometry* **21**, 948–954.
67. Ito, K., Hasebe, N., Hasebe, A., Arai, S. (2011). The matrix effect on U-238 and Th-232 measurements using pressed powder pellets by LA-ICP-MS. *Geochemical Journal* **45**, 375–385.
68. Hubova, I., Hola, M., Pinkas, J., Kanicky, V. (2007). Examination of sol-gel technique applicability for preparation of pellets for soil analysis by laser ablation inductively coupled plasma optical emission spectrometry. *Journal of Analytical Atomic Spectrometry* **22**, 1238–1243.
69. Sela, H., Karpas, Z., Cohen, H., Zakon, Y., Zeiri, Y. (2011). Preparation of stable standards of biological tissues for laser ablation analysis. *International Journal of Mass Spectrometry* **307**, 142–148.
70. Pugh, J. A. T., Cox, A. G., McLeod, C. W., Bunch, J., Whitby, B., Gordon, B., Kalber, T., White, E. (2011). A novel calibration strategy for analysis and imaging of biological thin sections by laser ablation inductively coupled plasma mass spectrometry. *Journal of Analytical Atomic Spectrometry* **26**, 1667–1673.
71. Pozebon, D., Dressler, V. L., Mesko, M. F., Matusch, A., Becker, J. S. (2010). Bioimaging of metals in thin mouse brain section by laser ablation inductively coupled plasma mass spectrometry: novel online quantification strategy using aqueous standards. *Journal of Analytical Atomic Spectrometry* **25**, 1739–1744.
72. Becker, J. S., Dietze, H. J. (1998). Inorganic trace analysis by mass spectrometry. *Spectrochimica Acta Part B-Atomic Spectroscopy* **53**, 1475–1506.

73. Compernolle, S., Wambeke, D., De Raedt, I., Vanhaecke, F. (2012). Evaluation of a combination of isotope dilution and single standard addition as an alternative calibration method for the determination of precious metals in lead fire assay buttons by laser ablation-inductively coupled plasma-mass spectrometry. *Spectrochimica Acta Part B-Atomic Spectroscopy* **67**, 50–56.
74. Meermann, B., Hulstaert, A., Laenen, A., Van Looveren, C., Vliegen, M., Cuyckens, F., Vanhaecke, F. (2012). HPLC/ICP-MS in Combination with “Reverse” Online Isotope Dilution in Drug Metabolism Studies. *Analytical Chemistry* **84**, 2395–2401.
75. Chung, S. W. C., Chan, B. T. P. (2011). A reliable method to determine methylmercury and ethylmercury simultaneously in foods by gas chromatography with inductively coupled plasma mass spectrometry after enzymatic and acid digestion. *Journal of Chromatography A* **1218**, 1260–1265.
76. Konig, S., Luguet, A., Lorand, J. P., Wombacher, F., Lissner, M. (2012). Selenium and tellurium systematics of the Earth’s mantle from high precision analyses of ultra-depleted orogenic peridotites. *Geochimica Et Cosmochimica Acta* **86**, 354–366.
77. Pickhardt, C., Izmer, A. V., Zoriy, M. V., Schaumloffel, D., Becker, J. S. (2006). On-line isotope dilution in laser ablation inductively coupled plasma mass spectrometry using a microflow nebulizer inserted in the laser ablation chamber. *International Journal of Mass Spectrometry* **248**, 136–141.
78. Jochum, K. P., Scholz, D., Stoll, B., Weis, U., Wilson, S. A., Yang, Q. C., Schwalb, A., Borner, N., Jacob, D. E., Andreae, M. O. (2012). Accurate trace element analysis of speleothems and biogenic calcium carbonates by LA-ICP-MS. *Chemical Geology* **318**, 31–44.
79. Schone, B. R., Zhang, Z. J., Radermacher, P., Thebault, J., Jacob, D. E., Nunn, E. V., Maurer, A. F. (2011). Sr/Ca and Mg/Ca ratios of ontogenetically old, long-lived bivalve shells (*Arctica islandica*) and their function as paleotemperature proxies. *Palaeogeography Palaeoclimatology Palaeoecology* **302**, 52–64.
80. Dunphy, B. J., Millet, M. A., Jeffs, A. G. (2011). Elemental signatures in the shells of early juvenile green-lipped mussels (*Perna canaliculus*) and their potential use for larval tracking. *Aquaculture* **311**, 187–192.
81. Hoover, R. R., Jones, C. M., Grosch, C. E. (2012). Estuarine ingress timing as revealed by spectral analysis of otolith life history scans. *Canadian Journal of Fisheries and Aquatic Sciences* **69**, 1266–1277.
82. Webb, S. D., Woodcock, S. H., Gillanders, B. M. (2012). Sources of otolith barium and strontium in estuarine fish and the influence of salinity and temperature. *Marine Ecology Progress Series* **453**, 189–199.
83. Ugarte, A., Unceta, N., Pecheyran, C., Goicolea, M. A., Barrio, R. J. (2011). Development of matrix-matching hydroxyapatite calibration standards for quantitative multi-element LA-ICP-MS analysis: application to the dorsal spine of fish. *Journal of Analytical Atomic Spectrometry* **26**, 1421–1427.
84. Hola, M., Kalvoda, J., Novakova, H., Skoda, R., Kanicky, V. (2011). Possibilities of LA-ICP-MS technique for the spatial elemental analysis of the recent fish scales: Line scan vs. depth profiling. *Applied Surface Science* **257**, 1932–1940.
85. Galiova, M., Kaiser, J., Fortes, F. J., Novotny, K., Malina, R., Prokes, L., Hrdlicka, A., Vaculovic, T., Fisakova, M. N., Svoboda, J., Kanicky, V., Laserna, J. J. (2010). Multielemental analysis of prehistoric animal teeth by laser-induced breakdown spectroscopy and laser ablation inductively coupled plasma mass spectrometry. *Applied Optics* **49**, C191–C199.



86. Austin, C., Hare, D., Rozelle, A. L., Robinson, W. H., Grimm, R., Doble, P. (2009). Elemental bio-imaging of calcium phosphate crystal deposits in knee samples from arthritic patients. *Metalomics* **1**, 142–147.
87. Dolphin, A. E., Goodman, A. H. (2009). Maternal Diets, Nutritional Status, and Zinc in Contemporary Mexican Infants' Teeth: Implications for Reconstructing Paleodiets. *American Journal of Physical Anthropology* **140**, 399–409.
88. Kepa, M., Kozlowski, T., Szostek, K., Drozd, A., Walas, S., Mrowiec, H., Stepanczak, B., Glab, H., Grupa, M. (2012). Analysis of mercury levels in historical bone material from syphilitic subjects - pilot studies (short report). *Anthropologischer Anzeiger* **69**, 367–377.
89. Monticelli, D., Di Iorio, A., Ciceri, E., Castelletti, A., Dossi, C. (2009). Tree ring micro-analysis by LA-ICP-MS for environmental monitoring: validation or refutation? Two case histories. *Microchimica Acta* **164**, 139–148.
90. Bukata, A. R., Kyser, T. K. (2008). Tree-ring elemental concentrations in oak do not necessarily passively record changes in bioavailability. *Science of the Total Environment* **390**, 275–286.
91. Siebold, M., Leidich, P., Bertini, M., Deflorio, G., Feldmann, J., Krupp, E. M., Halmschlager, E., Woodward, S. (2012). Application of elemental bioimaging using laser ablation ICP-MS in forest pathology: distribution of elements in the bark of *Picea sitchensis* following wounding. *Analytical and Bioanalytical Chemistry* **402**, 3323–3331.
92. Stadlbauer, C., Prohaska, T., Reiter, C., Knaus, A., Stingeder, G. (2005). Time-resolved monitoring of heavy-metal intoxication in single hair by laser ablation ICP-DRCMS. *Analytical and Bioanalytical Chemistry* **383**, 500–508.
93. Pozebon, D., Dressler, V. L., Matusch, A., Becker, J. S. (2008). Monitoring of platinum in a single hair by laser ablation inductively coupled plasma mass spectrometry (LA-ICP-MS) after cisplatin. *International Journal of Mass Spectrometry* **272**, 57–62.
94. Aramendia, M., Rello, L., Vanhaecke, F., Resano, M. (2012). Direct Trace-Elemental Analysis of Urine Samples by Laser Ablation-Inductively Coupled Plasma Mass Spectrometry after Sample Deposition on Clinical Filter Papers. *Analytical Chemistry* **84**, 8682–8690.
95. Galiova, M., Kaiser, J., Novotny, K., Hartl, M., Kizek, R., Babula, P. (2011). Utilization of Laser-Assisted Analytical Methods for Monitoring of Lead and Nutrition Elements Distribution in Fresh and Dried Capsicum annuum L. Leaves. *Microscopy Research and Technique* **74**, 845–852.
96. Becker, J. S., Dietrich, R. C., Matusch, A., Pozebon, D., Dressler, V. L. (2008). Quantitative images of metals in plant tissues measured by laser ablation inductively coupled plasma mass spectrometry. *Spectrochimica Acta Part B-Atomic Spectroscopy* **63**, 1248–1252.
97. Becker, J. S., Zoriy, M. V., Pickhardt, C., Zilles, K. (2005). Copper, zinc, phosphorus and sulfur distribution in thin section of rat brain tissues measured by laser ablation inductively coupled plasma mass spectrometry: possibility for small-size tumor analysis. *Journal of Analytical Atomic Spectrometry* **20**, 912–917.
98. Becker, J. S., Zoriy, M. V., Pickhardt, C., Palomero-Gallagher, N., Zilles, K. (2005). Imaging of copper, zinc, and other elements in thin section of human brain samples (Hippocampus) by laser ablation inductively coupled plasma mass spectrometry. *Analytical Chemistry* **77**, 3208–3216.

99. Zoriy, M. V., Dehnhardt, M., Reifenberger, G., Zilles, K., Becker, J. S. (2006). Imaging of Cu, Zn, Pb and U in human brain tumor resections by laser ablation inductively coupled plasma mass spectrometry. *International Journal of Mass Spectrometry* **257**, 27–33.
100. Plotnikov, A., Vogt, C., Wetzig, K. (2002). An approach to the reconstruction of true concentration profile from transient signal in spatially resolved analysis by means of laser ablation ICP MS. *Journal of Analytical Atomic Spectrometry* **17**, 1114–1120.
101. Plotnikov, A., Vogt, C., Wetzig, K., Kyriakopoulos, A. (2008). A theoretical approach to the interpretation of the transient data in scanning laser ablation inductively coupled plasma mass spectrometry: Consideration of the geometry of the scanning area. *Spectrochimica Acta Part B-Atomic Spectroscopy* **63**, 474–483.
102. Schmitz, T. A., Koch, J., Gunther, D., Zenobi, R. (2010). Characterization of aerosol plumes in nanosecond laser ablation of molecular solids at atmospheric pressure. *Applied Physics B-Lasers and Optics* **100**, 521–533.
103. Hu, Z. C., Liu, Y. S., Gao, S., Hu, S. H., Dietiker, R., Gunther, D. (2008). A local aerosol extraction strategy for the determination of the aerosol composition in laser ablation inductively coupled plasma mass spectrometry. *Journal of Analytical Atomic Spectrometry* **23**, 1192–1203.
104. Becker, J. S., Zoriy, M., Dobrowolska, J., Matusch, A. (2007). Laser ablation inductively coupled plasma mass spectrometry (LA-ICP-MS) in elemental imaging of biological tissues and in proteomics. *Journal of Analytical Atomic Spectrometry* **22**, 736–744.
105. Becker, J. S., Gorbunoff, A., Zoriy, M., Izmer, A., Kayser, M. (2006). Evidence of near-field laser ablation inductively coupled plasma mass spectrometry (NF-LA-ICP-MS) at nanometre scale for elemental and isotopic analysis on gels and biological samples. *Journal of Analytical Atomic Spectrometry* **21**, 19–25.
106. Kang, D., Amarasinghe, D., Goodman, A. H. (2004). Application of laser ablation-inductively coupled plasma-mass spectrometry (LA-ICP-MS) to investigate trace metal spatial distributions in human tooth enamel and dentine growth layers and pulp. *Analytical and Bioanalytical Chemistry* **378**, 1608–1615.
107. Arora, M., Hare, D., Austin, C., Smith, D. R., Doble, P. (2011). Spatial distribution of manganese in enamel and coronal dentine of human primary teeth. *Science of the Total Environment* **409**, 1315–1319.
108. Elsdon, T. S., Gillanders, B. M. (2004). Fish otolith chemistry influenced by exposure to multiple environmental variables. *Journal of Experimental Marine Biology and Ecology* **313**, 269–284.
109. Doubleday, Z. A., Izzo, C., Woodcock, S. H., Gillanders, B. M. (2013). Relative contribution of water and diet to otolith chemistry in freshwater fish. *Aquatic Biology* **18**, 271–280.
110. Ranaldi, M. M., Gagnon, M. M. (2008). Trace metal incorporation in otoliths of black bream (*Acanthopagrus butcheri munro*), an indicator of exposure to metal contamination. *Water Air and Soil Pollution* **194**, 31–43.
111. Clarke, A. D., Telmer, K. H., Shrimpton, J. M. (2007). Elemental analysis of otoliths, fin rays and scales: a comparison of bony structures to provide population and life-history information for the Arctic grayling (*Thymallus arcticus*). *Ecology of Freshwater Fish* **16**, 354–361.
112. Ramsay, A. L., Milner, N. J., Hughes, R. N., McCarthy, I. D. (2011). Comparison of the performance of scale and otolith microchemistry as fisheries research tools in a



- small upland catchment. *Canadian Journal of Fisheries and Aquatic Sciences* **68**, 823–833.
113. Chaudhri, M. A., Watling, J., Khan, F. A. (2007). Spatial distribution of major and trace elements in bladder and kidney stones. *Journal of Radioanalytical and Nuclear Chemistry* **271**, 713–720.
 114. Proksova, K., Novotny, K., Galiova, M., Vaculovic, T., Kuta, J., Novackova, M., Kanicky, V. (2012). Study of Elemental Distribution in Urinary Stones by Laser Ablation Inductively Coupled Plasma Mass Spectrometry. *Chemicke Listy* **106**, 229–235.
 115. Stepankova, K., Novotny, K., Galiova, M. V., Kanicky, V., Kaiser, J., Hahn, D. W. (2013). Laser ablation methods for analysis of urinary calculi: Comparison study based on calibration pellets. *Spectrochimica Acta Part B-Atomic Spectroscopy* **81**, 43–49.
 116. Su, P., Ek, P., Ivaska, A. (2012). Determination of metal ions in single wood fiber by LA-ICP-MS. *Holzforschung* **66**, 833–840.
 117. Bartkus, L., Amarasinghe, D., Arriaza, B., Bellis, D., Yanez, J. (2011). Exploring lead exposure in ancient Chilean mummies using a single strand of hair by laser ablation-inductively coupled plasma-mass spectrometry (LA-ICP-MS). *Microchemical Journal* **98**, 267–274.
 118. Dressler, V. L., Pozebon, D., Mesko, M. F., Matusch, A., Kumtabtim, U., Wu, B., Becker, J. S. (2010). Biomonitoring of essential and toxic metals in single hair using on-line solution-based calibration in laser ablation inductively coupled plasma mass spectrometry. *Talanta* **82**, 1770–1777.
 119. Stadlbauer, C., Reiter, C., Patzak, B., Stigeder, G., Prohaska, T. (2007). History of individuals of the 18th/19th centuries stored in bones, teeth, and hair analyzed by LA-ICP-MS—a step in attempts to confirm the authenticity of Mozart's skull. *Analytical and Bioanalytical Chemistry* **388**, 593–602.
 120. Leufroy, A., Noel, L., Beauchemin, D., Guerin, T. (2012). Use of a continuous leaching method to assess the oral bioaccessibility of trace elements in seafood. *Food Chemistry* **135**, 623–633.
 121. Lombi, E., Scheckel, K. G., Kempson, I. M. (2011). In situ analysis of metal(loid)s in plants: State of the art and artefacts. *Environmental and Experimental Botany* **72**, 3–17.
 122. Golgi, C. (1889). Sul ciclo evolutivo dei parassiti malarici nella febbre terzana : diagnosi differenziale tra i parassiti endoglobulari malarici della terzana e quelli della quartana. *Archivio per le Scienze Mediche* **13**, 173–196.
 123. Adams, F., Barbante, C. (2012). History and present status of imaging analysis. *Talanta* **102**, 16–25.
 124. Konz, I., Fernandez, B., Fernandez, M. L., Pereiro, R., Sanz-Medel, A. (2012). Laser ablation ICP-MS for quantitative biomedical applications. *Analytical and Bioanalytical Chemistry* **403**, 2113–2125.
 125. Hare, D., Reedy, B., Grimm, R., Wilkins, S., Volitakis, I., George, J. L., Cherny, R. A., Bush, A. I., Finkelstein, D. I., Doble, P. (2009). Quantitative elemental bio-imaging of Mn, Fe, Cu and Zn in 6-hydroxydopamine induced Parkinsonism mouse models. *Metallomics* **1**, 53–58.
 126. Pasilis, S. P., Van Berkel, G. J. (2010). Atmospheric pressure surface sampling/ionization techniques for direct coupling of planar separations with mass spectrometry. *Journal of Chromatography A* **1217**, 3955–3965.

127. Zoriy, M. V., Becker, J. S. (2007). Imaging of elements in thin cross sections of human brain samples by LA-ICP-MS: A study on reproducibility. *International Journal of Mass Spectrometry* **264**, 175–180.
128. Gholap, D., Verhulst, J., Ceelen, W., Vanhaecke, F. (2012). Use of pneumatic nebulization and laser ablation-inductively coupled plasma-mass spectrometry to study the distribution and bioavailability of an intraperitoneally administered Pt-containing chemotherapeutic drug. *Analytical and Bioanalytical Chemistry* **402**, 2121–2129.
129. Becker, J. S., Sela, H., Dobrowolska, J., Zoriy, M. (2008). Recent applications on isotope ratio measurements by ICP-MS and LA-ICP-MS on biological samples and single particles. *International Journal of Mass Spectrometry* **270**, 1–7.
130. Becker, J. S., Matusch, A., Wu, B., Palm, C., Becker, A. J., Salber, D. (2011). Mass spectrometric imaging (MSI) of metals using advanced BrainMet techniques for biomedical research. *International Journal of Mass Spectrometry* **307**, 3–15.
131. Becker, J. S., Kumtabtim, U., Wu, B., Steinacker, P., Otto, M., Matusch, A. (2012). Mass spectrometry imaging (MSI) of metals in mouse spinal cord by laser ablation ICP-MS. *Metalomics* **4**, 284–288.
132. Becker, J. S., Dobrowolska, J., Zoriy, M., Matusch, A. (2008). Imaging of uranium on rat brain sections using laser ablation inductively coupled plasma mass spectrometry: a new tool for the study of critical substructures affined to heavy metals in tissues. *Rapid Communications in Mass Spectrometry* **22**, 2768–2772.
133. Hare, D. J., George, J. L., Grimm, R., Wilkins, S., Adlard, P. A., Cherny, R. A., Bush, A. I., Finkelstein, D. I., Doble, P. (2010). Three-dimensional elemental bio-imaging of Fe, Zn, Cu, Mn and P in a 6-hydroxydopamine lesioned mouse brain. *Metalomics* **2**, 745–753.
134. Zoriy, M. V., Mayer, D., Becker, J. S. (2009). Metal Imaging on Surface of Micro- and Nanoelectronic Devices by Laser Ablation Inductively Coupled Plasma Mass Spectrometry and Possibility to Measure at Nanometer Range. *Journal of the American Society for Mass Spectrometry* **20**, 883–890.
135. Prange, A., Profrock, D. (2005). Application of CE-ICP-MS and CE-ESI-MS in metalloproteomics: challenges, developments, and limitations. *Analytical and Bioanalytical Chemistry* **383**, 372–389.
136. Raab, A., Ploselli, B., Munro, C., Thomas-Oates, J., Feldmann, J. (2009). Evaluation of gel electrophoresis conditions for the separation of metal-tagged proteins with subsequent laser ablation ICP-MS detection. *Electrophoresis* **30**, 303–314.
137. Becker, J. S., Zoriy, M., Przybylski, M. (2007). High resolution mass spectrometric brain proteomics by MALDI-FTICR-MS combined with determination of P, S, Cu, Zn and Fe by LA-ICP-MS. *International Journal of Mass Spectrometry* **261**, 68–73.
138. Lustig, S., Lampaert, D., De Cremer, K., De Kimpe, J., Cornelis, R., Schramel, P. (1999). Capability of flatbed electrophoresis (IEF and native PAGE) combined with sector field ICP-MS and autoradiography for the speciation of Cr, Ga, In, Pt and V in incubated serum samples. *Journal of Analytical Atomic Spectrometry* **14**, 1357–1362.
139. Binet, M. R. B., Ma, R. L., McLeod, C. W., Poole, R. K. (2003). Detection and characterization of zinc- and cadmium-binding proteins in Escherichia coli by gel electrophoresis and laser ablation-inductively coupled plasma-mass spectrometry. *Analytical Biochemistry* **318**, 30–38.



140. Jimenez, M. S., Rodriguez, L., Gomez, M. T., Castillo, J. R. (2010). Metal-protein binding losses in proteomic studies by PAGE-LA-ICP-MS. *Talanta* **81**, 241–247.
141. Becker, J. S., Zoriy, M., Pickhardt, C., Damoc, E., Juhacz, G., Palkovits, M., Przybylski, M. (2005). Determination of phosphorus-, copper-, and zinc-containing human brain proteins by LA-ICPMS and MALDI-FTICR-MS. *Analytical Chemistry* **77**, 5851–5860.
142. Becker, J. S., Pozebon, D., Dressler, V. L., Lobinski, R. (2008). LA-ICP-MS studies of zinc exchange by copper in bovine serum albumin using an isotopic enriched copper tracer. *Journal of Analytical Atomic Spectrometry* **23**, 1076–1082.
143. Haider, S. R., Sharp, B. L., Reid, H. J. (2011). On-line coupling of gel electrophoresis and inductively coupled plasma-mass spectrometry. *Trac-Trends in Analytical Chemistry* **30**, 1793–1808.
144. Anorbe, M. G., Messerschmidt, R., Feldmann, I., Jakubowski, N. (2007). On-line coupling of gel electrophoresis (GE) and inductively coupled plasma-mass spectrometry (ICP-MS) for the detection of Fe in metalloproteins. *Journal of Analytical Atomic Spectrometry* **22**, 917–924.
145. Lobinski, R., Becker, J. S., Haraguchi, H., Sarkar, B. (2010). Metallomics: Guidelines for terminology and critical evaluation of analytical chemistry approaches (IUPAC Technical Report). *Pure and Applied Chemistry* **82**, 493–504.
146. Neilsen, J. L., Abildtrup, A., Christensen, J., Watson, P., Cox, A., McLeod, C. W. (1998). Laser ablation inductively coupled plasma-mass spectrometry in combination with gel electrophoresis: a new strategy for speciation of metal binding serum proteins. *Spectrochimica Acta Part B-Atomic Spectroscopy* **53**, 339–345.
147. Jimenez, M. S., Gomez, M. T., Rodriguez, L., Martinez, L., Castillo, J. R. (2009). Some pitfalls in PAGE-LA-ICP-MS for quantitative elemental speciation of dissolved organic matter and metalomics. *Analytical and Bioanalytical Chemistry* **393**, 699–707.
148. Ballihaut, G., Kilpatrick, L. E., Kilpatrick, E. L., Davis, W. C. (2011). Detection and characterization of selenoproteins by tandem mass spectrometry assisted by laser ablation inductively coupled plasma mass spectrometry: application to human plasma selenoproteins. *Journal of Analytical Atomic Spectrometry* **26**, 383–394.
149. Waentig, L., Jakubowski, N., Hayen, H., Roos, P. H. (2011). Iodination of proteins, proteomes and antibodies with potassium triiodide for LA-ICP-MS based proteomic analyses. *Journal of Analytical Atomic Spectrometry* **26**, 1610–1618.
150. Blaschko, S. D., Chi, T., Miller, J., Flechner, L., Fakra, S., Kapahi, P., Kahn, A., Stoller, M. L. (2013). Strontium Substitution for Calcium in Lithogenesis. *Journal of Urology* **189**, 735–739.
151. Swanston, T., Varney, T., Coulthard, I., Feng, R. F., Bewer, B., Murphy, R., Hennig, C., Cooper, D. (2012). Element localization in archaeological bone using synchrotron radiation X-ray fluorescence: identification of biogenic uptake. *Journal of Archaeological Science* **39**, 2409–2413.
152. Mahamid, J., Sharir, A., Addadi, L., Weiner, S. (2008). Amorphous calcium phosphate is a major component of the forming fin bones of zebrafish: Indications for an amorphous precursor phase. *Proceedings of the National Academy of Sciences of the United States of America* **105**, 12748–12753.
153. Ramirez-Fernandez, M. P., Calvo-Guirado, J. L., Delgado-Ruiz, R. A., del Val, J., Negri, B., Diago, M. P. (2013). Ultrastructural study by backscattered electron imaging and elemental microanalysis of biomaterial-to-bone interface and mineral degradation of



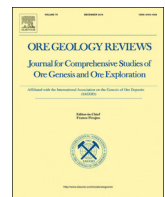
- bovine xenografts in maxillary sinus floor elevation. *Clinical Oral Implants Research* **24**, 645–651.
154. Cooper, D. M. L., Chapman, L. D., Carter, Y., Wu, Y., Panahifar, A., Britz, H. M., Bewer, B., Zhouping, W., Duke, M. J. M., Doschak, M. (2012). Three dimensional mapping of strontium in bone by dual energy K-edge subtraction imaging. *Physics in Medicine and Biology* **57**, 5777–5786.
155. Zheng, Y., Guo, H., Tang, W., Wei, K., Shen, H., Yang, M., Mi, Y. (2011). Micro-PIXE line-scan measurements of the yellow eel's otolith. *Nuclear Instruments & Methods in Physics Research Section B-Beam Interactions with Materials and Atoms* **269**, 2303–2306.
156. Rautray, T. R., Das, S., Rautray, A. C. (2010). In situ analysis of human teeth by external PIXE. *Nuclear Instruments & Methods in Physics Research Section B-Beam Interactions with Materials and Atoms* **268**, 2371–2374.
157. Preoteasa, E. A., Preoteasa, E., Kuczumow, A., Gurban, D., Harangus, L., Grambole, D., Herrmann, F. (2008). Broad-beam PIXE and mu-PIXE analysis of normal and in vitro demineralized dental enamel. *X-Ray Spectrometry* **37**, 517–535.
158. Rautray, T. R., Mishra, S., Patnaik, S. K., Vijayan, V., Panigrahi, S. (2007). Analysis of human bone and teeth. *Indian Journal of Physics and Proceedings of the Indian Association for the Cultivation of Science* **81**, 99–102.
159. Oprea, C., Kobzev, A. P., Oprea, I. A., Szalanski, P. J., Buzguta, V. (2007). PIXE detection limits for dental enamel from some human teeth by excitation with protons and He-4(2+) ions from a 3 MeV Van der Graaff accelerator. *Vacuum* **81**, 1167–1170.
160. Lodding, A. R., Fischer, P. M., Odelius, H., Noren, J. G., Sennerby, L., Johansson, C. B., Chabala, J. M., Levisetti, R. (1990). Secondary ion mass-spectrometry in the study of biominerizations and biomaterials. *Analytica Chimica Acta* **241**, 299–314.
161. Beasley, D., Gomez-Morilla, I., Spyrou, N. (2008). Elemental analysis of hair using PIXE-tomography and INAA. *Journal of Radioanalytical and Nuclear Chemistry* **276**, 101–105.
162. Smart, K. E., Kilburn, M. R., Salter, C. J., Smith, J. A. C., Grovenor, C. R. M. (2007). NanoSIMS and EPMA analysis of nickel localisation in leaves of the hyperaccumulator plant Alyssum lesbiacum. *International Journal of Mass Spectrometry* **260**, 107–114.
163. Gholap, D. S., Izmer, A., De Samber, B., van Elteren, J. T., Selih, V. S., Evens, R., De Schampelaere, K., Janssen, C., Balcaen, L., Lindemann, I., Vincze, L., Vanhaecke, F. (2010). Comparison of laser ablation-inductively coupled plasma-mass spectrometry and micro-X-ray fluorescence spectrometry for elemental imaging in *Daphnia magna*. *Analytica Chimica Acta* **664**, 19–26.
164. Pugh, J. A. T., Cox, A. G., McLeod, C. W., Bunch, J., Writer, M. J., Hart, S. L., Bienemann, A., White, E., Bell, J. (2012). Elemental imaging of MRI contrast agents: benchmarking of LA-ICP-MS to MRI. *Analytical and Bioanalytical Chemistry* **403**, 1641–1649.
165. Lobinski, R., Moulin, C., Ortega, R. (2006). Imaging and speciation of trace elements in biological environment. *Biochimie* **88**, 1591–1604.
166. Twining, B. S., Baines, S. B., Vogt, S., de Jonge, M. D. (2008). Exploring ocean biogeochemistry by single-cell microprobe analysis of protist elemental composition. *Journal of Eukaryotic Microbiology* **55**, 151–162.



348 LASER ABLATION INDUCTIVELY COUPLED PLASMA MASS SPECTROMETRY

167. Becker, J. S., Lobinski, R. (2009). Metal imaging in non-denaturating 2D electrophoresis gels by laser ablation inductively coupled plasma mass spectrometry (LA-ICP-MS) for the detection of metalloproteins. *Metallomics* **1**, 312–316.
168. Becker, J. S., Zoriy, M., Matusch, A., Wu, B., Salber, D., Palm, C. (2010). BIOIMAGING OF METALS BY LASER ABLATION INDUCTIVELY COUPLED PLASMA MASS SPECTROMETRY (LA-ICP-MS). *Mass Spectrometry Reviews* **29**, 156–175.
169. Ross, S. (2010). Introductory Statistics, 3rd edn., Academic Press, San Diego, USA.





Diversity of lithium mica compositions in mineralized granite–greisen system: Cínovec Li-Sn-W deposit, Erzgebirge



Karel Breiter^{a,*}, Michaela Hložková^b, Zuzana Korbelová^a, Michaela Vašinová Galiová^{c,d}

^a Institute of Geology of the Czech Academy of Science, Rozvojová 269, CZ-165 00 Praha 5, Czech Republic

^b Department of Chemistry, Faculty of Science, Masaryk University, Kotlářská 2, CZ-611 37 Brno, Czech Republic

^c Institute of Chemistry and Technology of Environmental Protection, Faculty of Chemistry, Brno University of Technology, Purkyňova 118, 61200 Brno, Czech Republic

^d Central European Institute of Technology, Brno University of Technology, Purkyňova 123, 61200 Brno, Czech Republic

ARTICLE INFO

Keywords:

Li-mica
Trace elements
Granite
Greisen
Cínovec/Zinnwald
Krušné Hory/Erzgebirge

ABSTRACT

The Li-Sn-W deposit Cínovec/Zinnwald in the eastern Erzgebirge (Czech Republic and Germany) represents one of the worldwide best known examples of complex rare-metal plutons with pervasive greisenization. Mica from altogether 38 samples representing all granite and greisen varieties from the present surface to the depth of 1596 m was analysed using electron microprobe (EMPA) and laser-ablation inductively-coupled plasma mass spectrometry (LA-ICP-MS) for major (including F, Rb) and trace (Li, Sc, Ga, Ge, Nb, In, Sn, Cs, Ta, Ti, W) elements, respectively. All primary micas at Cínovec are trioctahedral Li-Fe micas close to the annite–zinnwaldite–trilithionite series. Biotite from granites in the deeper part of the pluton (depth of 735–1596 m) contains 33.9–39.6 wt% SiO₂, 19.6–23.8 wt% FeO, 0.5–0.7 wt% Rb₂O, 0.9–1.8 wt% Li₂O, 3.4–4.8 wt% F, 381–937 ppm Nb, 34–134 ppm Ta, 20–46 ppm W, and 93–617 ppm Sn. Zinnwaldite from granites in the upper part of the pluton (depth of 0–735 m) contains 41.2–48.5 wt% SiO₂, 8.9–15.2 wt% FeO, 0.9–1.9 wt% MnO, 2.0–4.4 wt% Li₂O, 0.8–1.9 wt% Rb₂O, 7.0–8.6 wt% F, 43–464 ppm Nb, 101–213 ppm Sn, 6–80 ppm Ta, and 28–52 ppm W. Zinnwaldite from bodies of pervasive greisen and quartz-zinnwaldite veins is, compared to zinnwaldite from granites, relatively slightly enriched in Si, Mn and Ga, and depleted in Fe, F, Rb, Sn, W and Nb; Li and Ta contents are similar. Contents of Li, Rb and F, and the Fe/Mn and Nb/Ta values in mica closely positively correlate with those in the bulk rock, illustrating an upwards fractionation of parental melt. In contrast, the contents of high-field-strength elements in mica do not correspond to their contents in the bulk rock (melt); they were controlled by the order of crystallization of mica vs. accessory oxide minerals. Therefore, biotite generally contains distinctly higher Sn, Nb, Ta, and W than zinnwaldite. Dioctahedral micas of the muscovite–phengite series were found only as a late product of alteration of primary trioctahedral mica. Replacement of greisen-stage zinnwaldite by muscovite is chemically expressed in a strong depletion in Fe, F, and Li, and an enrichment in Sn. The share of trioctahedral mica in the bulk-rock budget of Sn decreases from 40–70% in biotite granite to less than 5% in greisen; in the case of Nb and Ta from 20–50% to less than 10%. The share of mica in the budget of W, mostly in the range of 2–15%, is stable through the whole pluton.

1. Introduction

Micas are chemically the most variable mineral group among all rock-forming minerals. Due to their specific layered crystal structure, micas are able to accommodate relatively high contents of many minor and trace elements (Bailey, 1984; Wise, 1995; Xie et al., 2015; Li et al., 2015). Chemical composition of magmatic micas, such as an enrichment in lithophile elements (Li, Rb and F), may indicate chemical composition of parental melt (Černý et al., 1985; Monier et al., 1987; Roda et al., 1995; Roda-Robles et al., 2012). To the contrary, micas

easily equilibrate with hydrothermal fluids, changing their major- and trace-element compositions considerably (Van Lichervelde et al., 2008; Petrik et al., 2014). Nevertheless, a careful evaluation of mica chemistry may help in the interpretation of the evolution of complex granitic plutons and associated mineral deposits (Brigatti et al., 2000; Van Lichervelde et al., 2008; Johan et al., 2012; Legros et al., 2016).

The present work is aimed at proving the significance of Li-micas for the concentration of volatiles and trace elements during pronounced magmatic fractionation and following metasomatic greisenization. The well-known greisen-type Cínovec Li-Sn-W deposit in the eastern

* Corresponding author.

E-mail address: breiter@gli.cas.cz (K. Breiter).

Erzgebirge was chosen as a typical object for this purpose, including the 1.6 km deep borehole CS-1 in its center.

First data on the chemical composition of mica from the Li-Sn-W Cínovec deposit were published by [Johan et al. \(2012\)](#) and later in a comprehensive study on granitic micas from the Bohemian Massif ([Breiter et al., 2017b](#)). The data set was now complemented with a detailed study of mica from the mineralized parts of the granite cupola. All data will be treated from three main points: (i) to decipher the vertical zoning of mica composition through an ore-bearing granite pluton, (ii) to check differences in the composition between magmatic and hydrothermal (greisen-stage) mica, and (iii) to evaluate the share of mica in the budget of ore elements Sn, W, Nb, Ta, and Sc throughout the mineralized granite–greisen system.

2. Geological background and samples

The Cínovec rare-metal granite cupola is situated on both sides of the Czech–German state border in the eastern part of the Krušné Hory/Erzgebirge Mts. as the youngest evolutionary member of the late Variscan Altenberg–Teplice rhyolite caldera ([Hoth et al., 1995](#); [Breiter, 1997](#); [Mlčoch and Skácelová, 2010](#); [Walther et al., 2016](#)).

The caldera is transected from NW to SE by mostly hidden subsurface ridge of A-type granites, with several local elevations rising to the present surface ([Fig. 1](#)). One of them is the Cínovec/Zinnwald (Czech and German synonyms) cupola with an exposure of 1.4×0.3 km. A specific feature of the rare-metal granites (RMGs) in the Erzgebirge is their intrusion to a subvolcanic level, as proved by the formation of explosive breccia pipes ([Seltmann et al., 1987](#)). From the viewpoint of geochemistry, the Cínovec pluton represents strongly fractionated A-type granite: it is only slightly peraluminous, enriched in F, Li, Rb, Zr, Th, HREE, Sc, Sn, W, Nb, and Ta, and depleted in P, Ti, Mg, and Ca ([Breiter et al., 2017a](#)).

The RMG plutons often show a distinct vertical stratification (e.g., [Beskin et al., 1994](#); [Raimbault et al., 1995](#); [Yin et al. 1995](#); [Syritso et al., 2001](#)), with the Cínovec being an excellent example ([Štemprok and Šulcuk, 1969](#); [Breiter et al., 2017a](#)) ([Fig. 2](#)):

- A fine-grained, strongly porphyritic variety of zinnwaldite granite, locally known as zinnwaldite microgranite (ZiGm, [Fig. 3a](#)), forms a hem up to several tens of meters thick along the upper part of the cupola. It is composed of euhedral quartz and perthite and subhedral albite phenocrysts (up to 5–10 mm across), cemented by fine-grained (< 0.5 mm) matrix of the same composition. Macroscopically black poikilitic zinnwaldite is common; topaz, fluorite, zircon, rutile and thorite are accessory. This facies represents the first portion of melt, fast crystallized along the upper contact of the intrusion. This carapace granite was partially destructed shortly after crystallization, and large xenoliths plunged into underlying melt.
- The upper part of the cupola, the “canopy”, to a depth of 260 m is composed of mostly leucocratic equigranular fine-grained albite-zinnwaldite granite (ZiGC, [Fig. 3b](#)). The granite consists of albite, quartz, zinnwaldite and sericitized K-feldspar. Typical accessory minerals are fluorite, topaz, zircon, cassiterite and columbite.
- Banded quartz-zinnwaldite veins (QZV, ± topaz, K-feldspar, wolframite, cassiterite), form a well-known onion-like structure in the central part of the cupola. The veins 20–200 cm thick are rimmed by a cm- to m-sized selvage of quartz-zinnwaldite metasomatic greisen mineralized by cassiterite and scheelite. Steep quartz-zinnwaldite veins, striking SW–NE and texturally similar to the previous type, are rare.
- Bodies termed “massive greisen” by the miners (GR) are flat zones of pervasive metasomatic greisenization tens to hundreds meters in size; they were typically formed 20–200 m beneath the granite/rhyolite contact. The combination of predominantly irregular steep joints with flat L-shaped joints enabled fluid migration and intensive

replacement of feldspars by quartz, zinnwaldite, topaz and fluorite. Mineralization is irregularly distributed in the greisens: cassiterite strongly prevails over scheelite.

- Mica-free granite (MfG) was encountered at a depth of 260–369 m as a medium-grained porphyritic rock composed of up to 10 mm-sized perthite phenocrysts in quartz-K-feldspar-albite groundmass. Zinnwaldite is present only incidentally. Fluorite, zircon, rutile, thorite, cassiterite and columbite are typical accessories. Potassium-dominated fine- to medium-grained feldspathites (FSP) form several layers up to 5 m thick within the MfG body.
- A zone of large xenoliths of ZiGm ([Fig. 3a](#)) with local mingling with the ZiG appears at a depth of 369–530 m.
- Medium- to coarse-grained albite-zinnwaldite granite (ZiG, [Fig. 3c](#)) at the depth of 530–740 m is almost white and is texturally and mineralogically homogeneous. It is composed of perthite, quartz, albite and macroscopically black zinnwaldite. The granite further comprises topaz, fluorite, zircon, xenotime, thorite, monazite, rutile, cassiterite, columbite, scheelite and pyrochlore.
- The suite of biotite granites at the depth of 735–1596 m is homogeneous in its mineral and chemical compositions but exhibits various textures. Slightly porphyritic medium-grained biotite granite prevails (BtG, [Fig. 3d](#)). A fine-grained, distinctly porphyritic facies (“biotite microgranite”, BtGm, [Fig. 3e](#)) is subordinate. The pink color of the rocks is characteristic. All textural varieties of BtG contain accessory amounts of zircon, xenotime, thorite, monazite and rutile.

Altogether 38 samples covering all granite and greisen facies in a vertical section of the pluton to the depth of 1.6 km were collected ([Table 1](#)). Polished thin slabs 250–300 μm thick were prepared from all samples. Bulk-rock chemical analyses of all samples were available from the previous stage of the deposit investigation ([Breiter et al., 2017a](#)), and the complete dataset is available as an electronic supplement to the aforementioned paper.

3. Methods

Major elements in micas were analyzed using a CAMECA SX100 electron microprobe housed in the Institute of Geology of the Czech Academy of Sciences, Praha. We used an accelerating voltage of 15 kV, a beam current of 10 nA, and a beam diameter of 2 μm . The following standards were used: Na, Al – jadeite, Mg, Si, Ca – diopside, K – leucite, Ti – rutile, P – apatite, Mn – MnCr_2O_4 , Fe – magnetite, F – fluorite, Rb – RbCl. The counting times on each peak were optimized for individual elements according to their expected concentrations (10–60 s), and half that time was used to obtain background counts. X-ray lines and background offsets were selected to minimize interference. The X-Phi correction procedure ([Merlet, 1994](#)) was applied. Chemical analyses of micas were recalculated to the proposed structural formulae based on 44 negative charges.

The trace elements in the micas were analyzed at the Laboratory of Atomic Spectrochemistry (LAS), Department of Chemistry, Faculty of Science, Masaryk University Brno. Besides Li, we decided to analyze another 10 elements: Sn, W, Nb and Ta as rare metals which are enriched and potentially mineable at the deposit, Cs and Tl as rare elements geochemically similar to K and potentially concentrating in micas (Rb was already analyzed by the EMPA), Ga and Ge as potential indicators of magma fractionation (as decreasing Al/Ga and Si/Ge values, [Argollo and Schilling, 1978](#); [Breiter et al., 2013](#)), and Sc and In as rare elements enriched at mineral deposits across the eastern Erzgebirge ([Seifert and Sandmann, 2006](#); [Kempe and Wolf, 2006](#)). A pulsed Nd:YAG-based laser ablation system UP 213 (New Wave Research, Inc., Fremont, CA, USA) operating at 213 nm and equipped with a SuperCell was used for sampling. The ablation-generated aerosol was transported using helium carrier gas (1l min^{-1}) into the ICP source of the quadrupole-based mass spectrometer Agilent 7500ce (Agilent Technologies,

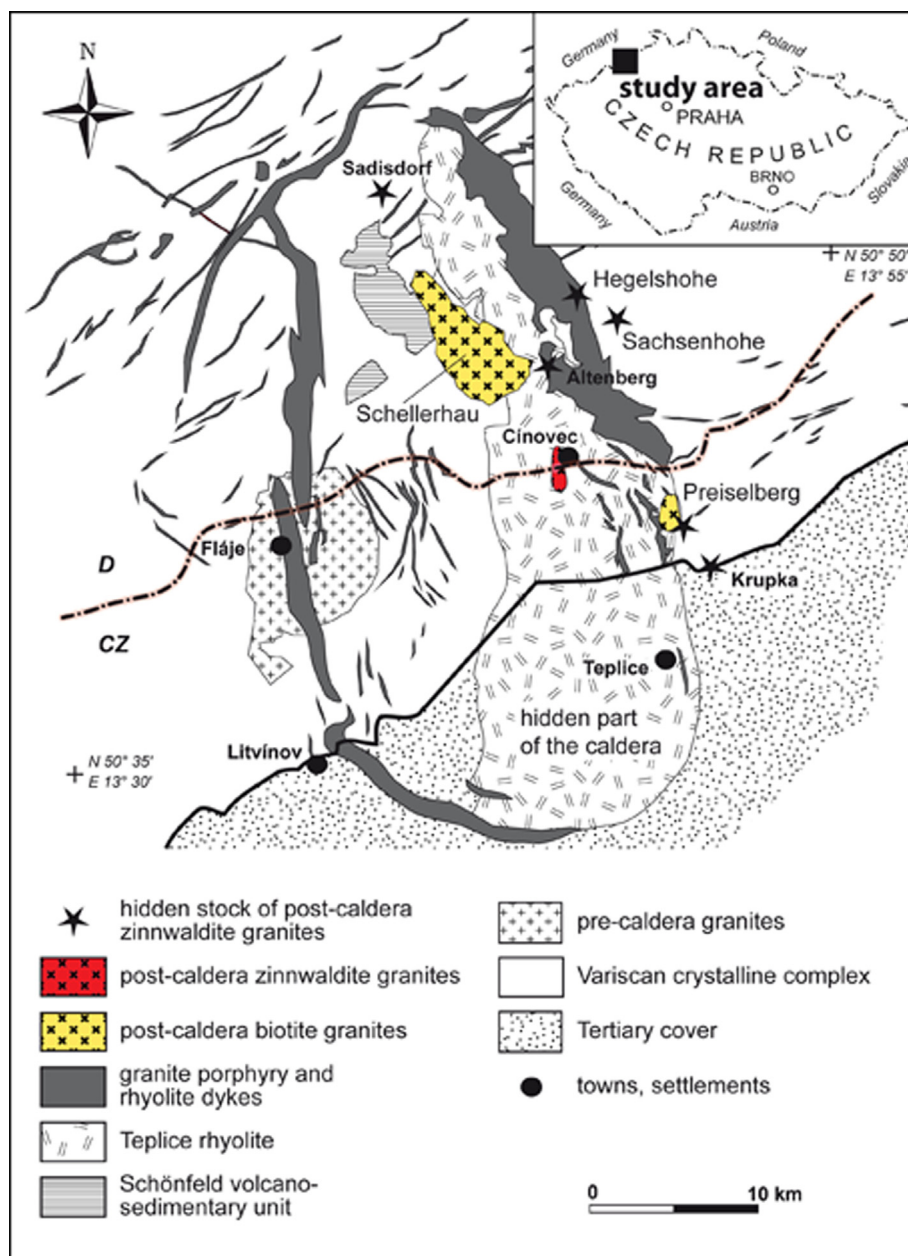


Fig. 1. Simplified geological map of the Altenberg-Teplice caldera. Modified according to Hoth et al. (1995) and Mlčoch and Skácelová (2010).

Santa Clara, CA, USA). The He carrier gas was mixed with argon make-up gas via a Y-connector prior to the ICP. To minimize potential polyatomic interferences, a collision-reaction cell in He mode (1 ml min^{-1}) was used. Time-resolved signals for the following isotopes were recorded: $^{7}\text{Li}^+$, $^{27}\text{Al}^+$ and $^{28}\text{Si}^+$ as matrix elements, and $^{45}\text{Sc}^+$, $^{69}\text{Ga}^+$, $^{72}\text{Ge}^+$, $^{93}\text{Nb}^+$, $^{115}\text{In}^+$, $^{118}\text{Sn}^+$, $^{133}\text{Cs}^+$, $^{181}\text{Ta}^+$, $^{182}\text{W}^+$ and $^{205}\text{Tl}^+$ as trace elements. An integration time of 0.1 s was used except for Ge (0.5 s) and In (0.7 s). A fluence of 13 J cm^{-2} was found to be optimal, and a spot diameter of $50 \mu\text{m}$ and a repetition rate of 10 Hz were fixed. Each spot analysis incorporates approximately 30 s of background (Ar-He gas blank) followed by 40 s of data acquisition from the sample. Contents were calculated from the background-corrected peak areas using NIST SRM 612 and NIST SRM 610 and Si as the internal reference element. The detection limits were calculated as three times the standard deviation of the background divided by the sensitivity (defined as the isotope intensity to elemental content ratio). The average detection limits under the operating conditions were as follows: 1.8 ppm Li; 1.5 ppm Al; 170 ppm Si; 0.70 ppm Sc; 0.18 ppm Ga; 1.0 ppm

Ge; 0.08 ppm Nb; 0.04 ppm In; 2.1 ppm Sn; 0.15 ppm Cs; 0.08 ppm Ta; 0.21 ppm W and 0.41 ppm Tl.

To calculate the share of mica in the budget of rare metals in the bulk rock (Fig. 11), modal contents of mica in the rock sample should be determined with the highest possible precision. While mica is the only host of Li in the studied rocks, modal contents of mica in rock samples were calculated based on the bulk-rock Li contents (data published in Breiter et al., 2017a) and Li contents in the particular mica analyzed by LA-ICP-MS.

4. Terminological remark

According to the IMA rules, only so-called “end member” mineral names are valid. Actual nomenclature of micas (Rieder et al., 1999) is based on this rule. Nevertheless, in the case of rock-forming minerals important for igneous rock classification, practical petrology typically uses more detailed mineral classifications. In this paper, therefore, we use the traditional name zinnwaldite (Haidinger, 1845; Rieder et al.,

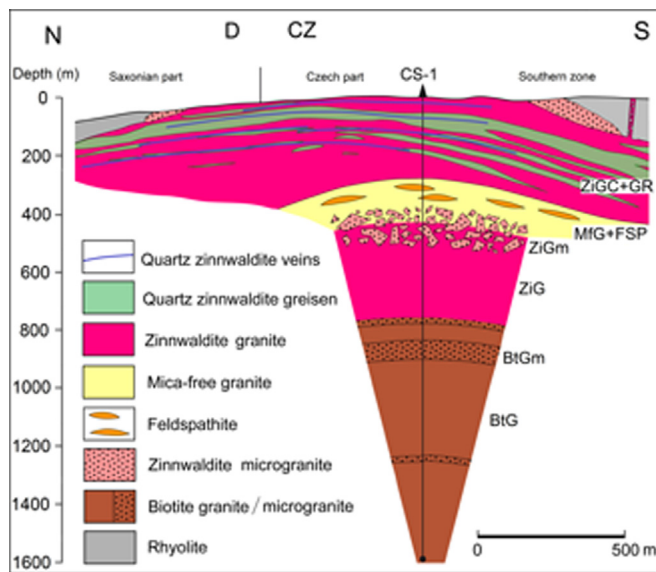


Fig. 2. A cross-section through the Cínovec granite pluton and greisen deposit (according to Breiter et al., 2017a, modified).

1996) for Li-rich micas that are close to the intersection of the siderophyllite–polylithionite and the annite–trilithionite join with preferred formula $K_2Li_2Fe_2Al_2(Al_2Si_6O_{20})F_4$. Micas close to this composition are common not only in the granites and greisens at Cínovec, but also in Sn- and W-bearing granites worldwide (Stone et al., 1988; du Bray, 1994). In the older literature, also the name protolithionite has been used for mica from deeper parts of the Cínovec cupola (Štemprok and Šulc, 1969; Johan et al., 2012). Protolithionite (*sensu* Weiss et al., 1993) with

preferred formula $K_2LiFe_4Al(Al_2Si_6O_{20})(F, OH)_4$ situated on the zinnwaldite–annite join is common in relatively less evolved facies of rare-metal granite systems. Nevertheless, the usage of this name was not recommended by IMA (Rieder et al., 1999).

For simplicity, this paper adheres to the name “zinnwaldite” for micas containing more than 1.2 apfu Li, and the name “biotite” for the Li-poorer micas (Fig. 4). Such classification is in accord with geological structure of the Cínovec pluton, composed of the deeper intrusion of “biotite granite” and the upper intrusion of “zinnwaldite granite” including greisen bodies and quartz-zinnwaldite veins. This simplified classification is also corroborated by two styles in Li substitution mechanism in mica crystal lattice (Breiter et al., 2017b).

5. Results

We studied micas in polished slabs from 38 granite and greisen samples. Typical shapes of mica grains are shown in Figs. 5 and 6.

Zinnwaldite from the middle part of the cupola (ZiG, ZiGm) is macroscopically black (Figs. 3a, c, 5a), forming grains 2–5 mm in size with numerous inclusions of fluorite, zircon, monazite, xenotime and Nb,Ta-enriched rutile. Zinnwaldite from the uppermost part of the cupola is silvery (in greisen, Fig. 5b) or light-brown to colorless (disseminated in granite, Figs. 3b, 5c). In veins, monomineral bands up to 5 cm thick and several m^2 in size with individual flakes larger than 10 cm^2 are common. This zinnwaldite is poor in mineral inclusions (Fig. 5b, c). Local muscovitization of zinnwaldite was encountered in some greisen bodies (Fig. 6). The contents of zinnwaldite in ZiG and ZiGm are about 5 vol%, decreasing to 2 vol% in albite-rich ZiGC, but increasing up to 40 vol% in greisens. Late muscovitization, locally developed in greisen bodies, is connected with the post-greisen Sn-transfer and will be discussed later.

Macroscopically black biotite constitutes 2–4 vol% of biotite

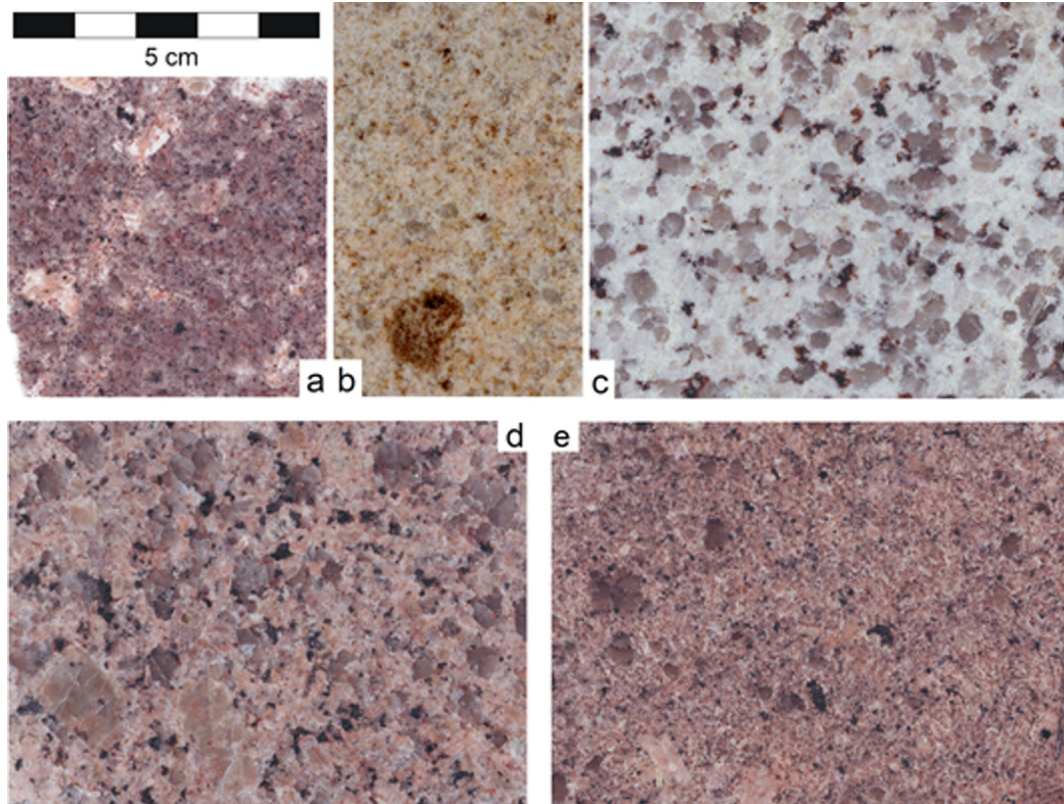


Fig. 3. Macroscopic photographs of typical granites from the Cínovec cupola: a, zinnwaldite microgranite with black zinnwaldite (a xenolith, CS-1, depth 413 m); b, zinnwaldite granite of the upper part of the cupola with light brown zinnwaldite (CS-1, depth 87 m); c, zinnwaldite granite from the middle part of the cupola with black zinnwaldite (CS-1, 608 m); d, biotite granite (CS-1, depth 1400 m); e, biotite microgranite (CS-1, depth 914 m).

Table 1

List of analyzed samples.

Sample	Borehole	Depth (m)	Rock type	Symbol	Description
4970	CS-1	35	quartz-zinnwaldite vein	QZV	thin flat quartz-zinnwaldite vein with greisen selvages
4674	CS-1	40	zinnwaldite granite	ZiGC	fine-grained albite-zinnwaldite leucogranite with strong sericitization of Kfs
4683	CS-1	97	zinnwaldite granite	ZiGC	medium-grained zinnwaldite leucogranite
4971	CS-1	130	quartz-zinnwaldite vein	QZV	thin flat quartz-zinnwaldite vein in granite
4972A	CS-1	149	greisen	GR	quartz-zinnwaldite greisen with miaroles and with selective muscovitization of rims of the zinnwaldite flakes, mica-rich part
4972B	CS-1	149	greisen	GR	quartz-zinnwaldite greisen with miaroles and with selective muscovitization of rims of the zinnwaldite flakes, quartz-rich part
4973	CS-1	163	greisen	GR	quartz-zinnwaldite greisen with miaroles filled by clay minerals
5048	CS-1	182	zinnwaldite granite	ZiGC	altered medium-grained zinnwaldite granite
4974	CS-1	193	greisen	GR	quartz-zinnwaldite greisen
4685	CS-1	205	zinnwaldite granite	ZiGC	medium-grained zinnwaldite granite with strongly sericitized feldspars
4975	CS-1	213	zinnwaldite granite	ZiGC	slightly greisenized zinnwaldite granite
5064	CS-1	244	zinnwaldite granite	ZiGC	medium-grained zinnwaldite granite
4687	CS-1	413	zinnwaldite microgranite	ZiGm	fine-grained porphyritic zinnwaldite granite
4936	CS-1	477	zinnwaldite microgranite	ZiGm	fine-grained porphyritic zinnwaldite granite
4688	CS-1	559	zinnwaldite granite	ZiG	medium-grained zinnwaldite granite, fresh
4938	CS-1	653	zinnwaldite granite	ZiG	medium-grained zinnwaldite granite, fresh
4689	CS-1	735	zinnwaldite granite	ZiG	medium-grained zinnwaldite granite, fresh
4690	CS-1	741	biotite microgranite	BtGm	fine-grained strongly porphyritic biotite granite
4691	CS-1	749	biotite granite	BtG	fine- to medium-grained porphyritic granite
4801	CS-1	774	biotite granite	BtG	medium-grained porphyritic biotite granite
5171	CS-1	800	biotite granite	BtG	medium-grained porphyritic biotite granite
4802	CS-1	860	biotite microgranite	BtGm	fine-grained strongly porphyritic biotite granite
4692	CS-1	988	biotite granite	BtG	medium-grained porphyritic biotite granite
4940	CS-1	1025	biotite granite	BtG	medium-grained porphyritic biotite granite
4941	CS-1	1245	biotite microgranite	BtGm	fine-grained strongly porphyritic biotite granite
4942	CS-1	1400	biotite microgranite	BtGm	fine-grained strongly porphyritic biotite granite
4693	CS-1	1579	biotite granite	BtG	medium-grained porphyritic biotite granite
5423	Cis-2	180	zinnwaldite granite	ZiGC	fine-grained fine-porphyritic zinnwaldite granite
5425	Cis-2	186	zinnwaldite granite	ZiGC	fine-grained equigranular zinnwaldite granite
5427	Cis-2	190	greisen	GR	zinnwaldite-rich greisen
5428	Cis-2	191	greisen	GR	quartz-zinnwaldite greisen
5429	Cis-2	280	zinnwaldite granite	ZiGC	altered medium-grained zinnwaldite granite
5430	Cis-2	374	zinnwaldite granite	ZiGC	altered medium-grained zinnwaldite granite
5438	PSn07	332	greisen	GR	quartz-rich greisen with zinnwaldite
5436	PSn07	343	zinnwaldite granite	ZiGC	medium-grained zinnwaldite granite
5434	PSn07	412	zinnwaldite granite	ZiGC	medium-grained granite with scarce zinnwaldite
4981	Bunau Stollen		greisen	GR	quartz-rich greisen with zinnwaldite
5412	Bunau Stollen		quartz-zinnwaldite vein	QZV	flat quartz vein with zinnwaldite rims

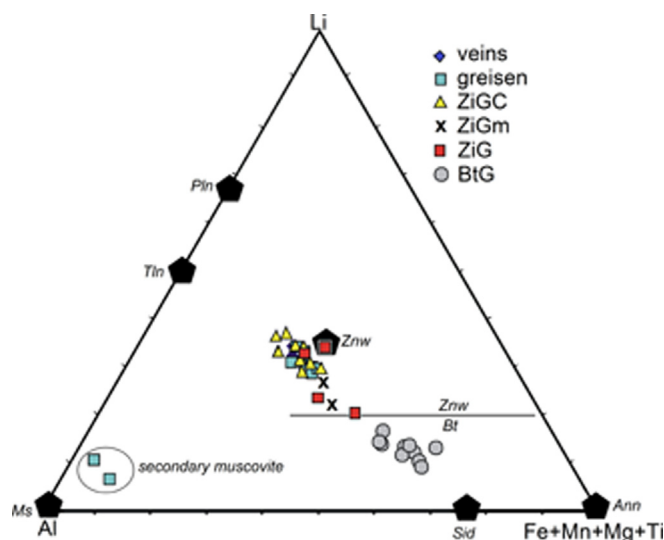


Fig. 4. Classification of Li-micas according to Foster (1960) showing the occupancy of the hexahedral site in coordinates Li-Fe + Mn + Mg + Ti-Al. Ideal IMA endmembers: Ann – annite, Sid – siderophyllite, Ms – muscovite, Znw – zinnwaldite, Tln – trilithionite, Pln – polylithionite. Empirical discrimination between biotite and zinnwaldite from Cínovec at Li = 1.2 apfu is shown. Figurative points near the muscovite apex represent a product of late muscovitization of greisen zinnwaldite (compare also with Fig. 6).

granites. Individual subhedral to anhedral flakes, mostly 0.5–2 mm across, often contain common inclusions of monazite, xenotime, zircon and Ti-oxides, sometimes associated with fluorite (Fig. 5d, e). Only a slight chloritization was encountered in some biotite grains from the deeper part of the cupola (depth of 1000–1596 m, Fig. 5f); this late style of alteration was not studied in detail. From each rock sample, 4–6 mica grains with 2 EMPA spots (core and rim) and 4–5 LA spots were analyzed, e.g., 8–12 EMPA and 15–25 LA spots in each sample in average. After elimination of ca. 10% of outliers (mainly occasional hits of mineral inclusions or cleavage), the primary database contains 364 EMPA and 814 LA spot analyses. The data presented in the tables represent average values of major elements (Table 2), structural formulae (Table 3) and medians and median absolute deviations of trace elements (Table 4) of all samples.

All primary micas at Cínovec are trioctahedral Li-Fe micas close to the annite–zinnwaldite–trilithionite series (Fig. 4). Dioctahedral micas of the muscovite–phengite series were found only as late products of alteration of primary trioctahedral micas, and as very fine-grained late alterations of K-feldspar (sericite).

With respect to major elements including Li, Rb and F, the trioctahedral micas can be classified into two distinct groups: zinnwaldite and Li-enriched biotite. Zinnwaldite contains 41.2–48.5 wt% SiO₂, 8.9–15.2 wt% FeO, 0.9–1.9 wt% MnO, 2.0–4.4 wt% Li₂O, 0.8–1.9 wt% Rb₂O and 7.0–8.6 wt% F. The contents of TiO₂ and MgO are very low, usually less than 0.3 and 0.1 wt%, respectively. In contrast, biotite contains 33.9–39.6 wt% SiO₂, 19.6–23.8 wt% FeO, 0.4–1.2 wt% MgO, 0.5–1.4 wt% TiO₂, 0.5–0.7 wt% MnO, 0.5–0.7 wt% Rb₂O, 0.9–1.8 wt%

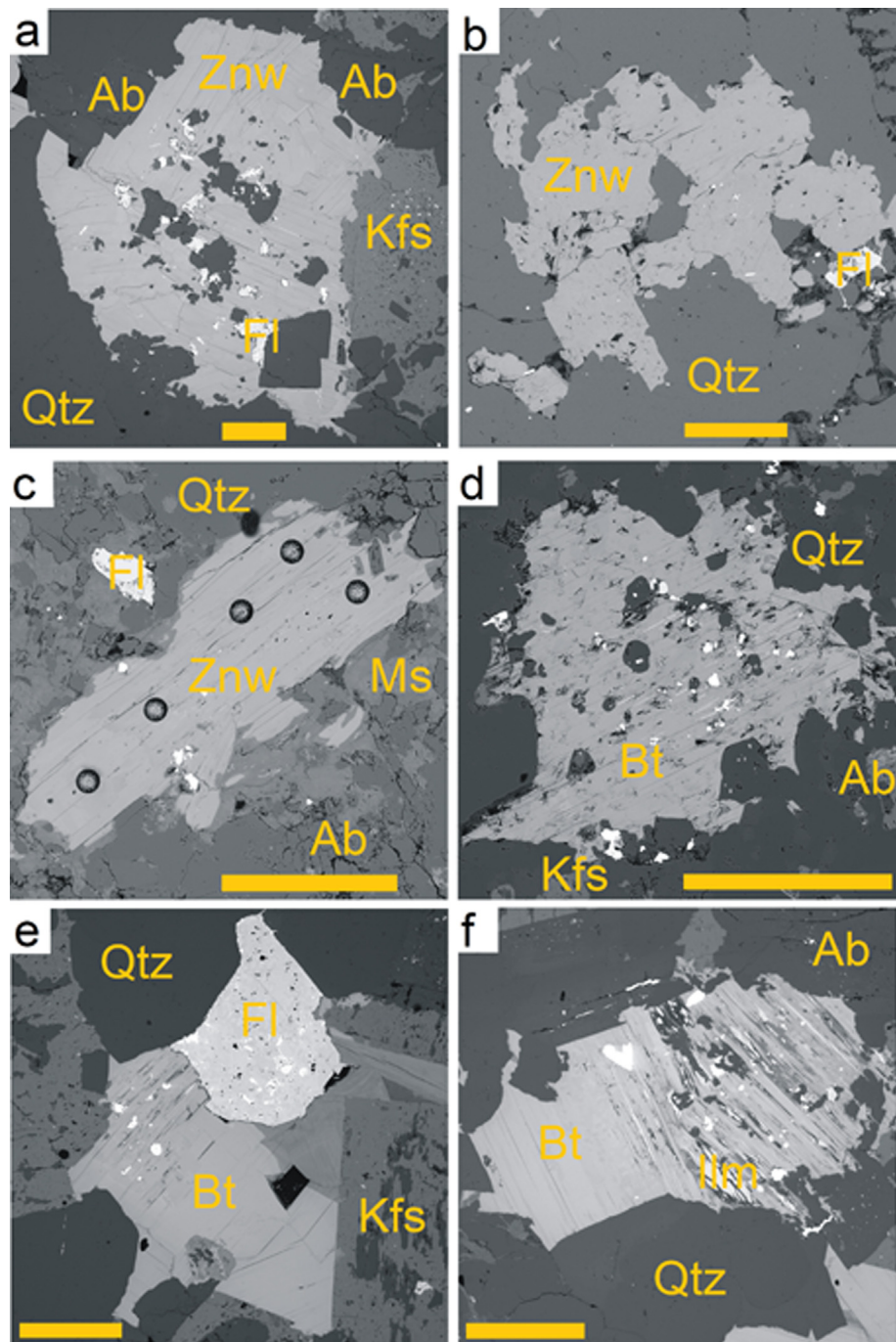


Fig. 5. Back-scattered electron (BSE) images of typical mica grains: a: mica from the deeper part of the albite-zinnwaldite granite (#4689, borehole CS-1, depth of 735 m), 2.02 wt% Li₂O (on the zinnwaldite–protolithionite join), typically contains inclusions of quartz and fluorite and small inclusions of zircon, monazite, xenotime and thorite; b: mica from the quartz-zinnwaldite greisen (#4974, borehole CS-1, depth of 193 m) with 3.43 wt% Li₂O, near “ideal” zinnwaldite; c: mica from the albite-zinnwaldite granite in the uppermost part of the cupola (#4674, borehole CS-1, depth of 40 m) with 4.20 wt% Li₂O (on the zinnwaldite–trilithionite join), laser-ablations spots 50 μm in diameter are visible; d: mica from biotite microgranite (#4690, borehole CS-1, depth of 741 m), contains 1.80 wt% Li₂O, near ideal protolithionite with inclusions of quartz and small inclusions of zircon and thorite; e: mica from medium-grained porphyritic biotite granite (#4692, borehole CS-1, depth of 988 m), contains 1.10 wt% Li₂O, positioned on the protolithionite–annite join; in association with a large grain of fluorite f: slightly chloritized mica from coarse-grained biotite granite (#4693, borehole CS-1, depth of 1579 m), contains 1.49 wt% Li₂O, positioned on the protolithionite–annite join. Scale bars in all cases equal to 500 μm. Mineral abbreviations: Qtz – quartz; Ab – albite; Kfs – K-feldspar; Znw – zinnwaldite; Ms – muscovite; Bt – biotite; Fl – fluorite; Ilm – ilmenite.

Li₂O and 3.4–4.8 wt% F. The contents of Al₂O₃, K₂O and Na₂O are homogeneous in all mica types, attaining 18.7–21.2 wt%, 9.1–10.3 wt% and 0.2–0.3 wt%, respectively. The distribution of trace elements is more complicated, varying across broad intervals not only within a distinct mica type, but also within particular sample and grain. Nevertheless, no systematic differences between cores and rims were found.

Within the group of zinnwaldite, noticeable difference was found between samples from different facies of granite and greisen. For example, the contents of Nb decrease from 158–464 ppm in zinnwaldite from the lower part of the cupola (ZiG) to 45–91 ppm in zinnwaldite from the upper part of the cupola (ZiGC) and 36–70 ppm in zinnwaldite from greisen and veins. Similarly, Ta decreases from 80 ppm in zinnwaldite from the ZiG to 6–28 ppm in zinnwaldites from greisens and the ZiGC. The contents of Sn are scattered mostly between 100 and 200

(occasionally up to 530) ppm in zinnwaldite from the ZiG and 65–155 ppm in zinnwaldite from greisens, with no clear vertical trend. The contents of W are slightly higher in zinnwaldite from granites (28–74 ppm) than in zinnwaldite from greisen (13–39 ppm, in one sample only 2.9 ppm). Also the contents of Cs are slightly higher in zinnwaldite from granites (370–630 ppm) than in zinnwaldite from greisen (360–500 ppm). The contents of other analyzed trace elements in zinnwaldite from both rock types are similar: 42–100 ppm Sc, 32–55 ppm Tl, 66–160 ppm Ga, mostly 2.7–8 ppm Ge (in one case 14.5 ppm Ge) and mostly < 1 ppm In (occasionally up to 1.4 ppm In).

In comparison with zinnwaldite, biotite from all facies of the BtG contains generally higher Nb (381–937 ppm), Ta (34–134 ppm), and Sn (93–617 ppm), while the contents of Cs (356–655 ppm), Sc (51–130 ppm), Ga (84–128 ppm), Ge (mostly 5.5–9.2 ppm) and In (mostly < 1 ppm) are similar. The contents of W (20–46 ppm) and Tl

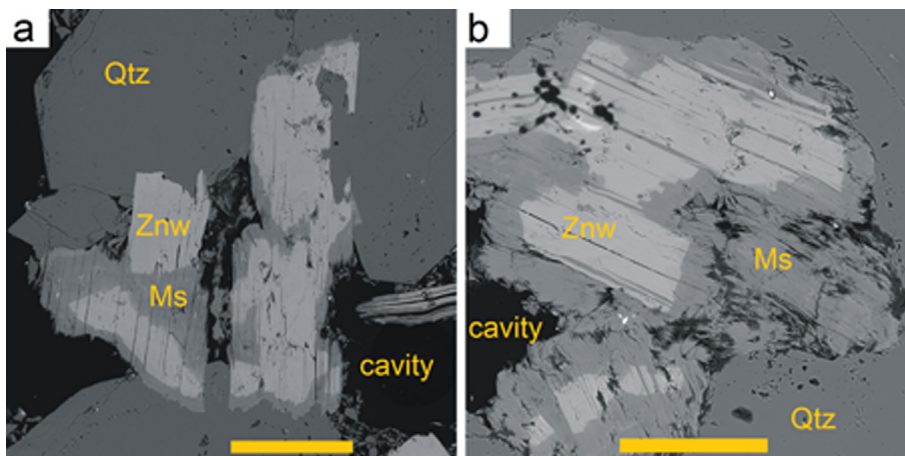


Fig. 6. Back-scattered electron (BSE) images of muscovitized micas: a: muscovitized zinnwaldite from zinnwaldite-rich greisen (#4972A, borehole CS-1, depth of 149 m); b: muscovitized zinnwaldite from quartz-rich greisen (#4972B, borehole CS-1, depth of 149 m). Scale bars 200 μm . Mineral abbreviations as in Fig. 5.

Table 2

Chemical composition (means) of micas (wt%). Li₂O analyzed via LA-ICP-MS, other via microprobe. Content of water computed on the basis of full occupation of the (F, OH) site (compare Table 3). For rock symbols see Table 1. Symbol “O = F” means the oxygen equivalent of fluorine.

Sample	Location	Depth (m)	Rock symbol	Mica	n	SiO ₂	TiO ₂	Al ₂ O ₃	FeO	MnO	MgO	Rb ₂ O	Li ₂ O	Na ₂ O	K ₂ O	F	H ₂ O	O = F	Total
4970	CS-1	35	QZV	Znw	8	46.74	0.03	20.10	11.32	1.42	0.01	1.02	3.69	0.18	10.22	8.45	0.20	-3.56	99.82
4674	CS-1	40	ZiGC	Znw	14	47.80	0.13	19.78	8.91	1.33	0.03	1.86	4.20	0.23	9.89	8.56	0.17	-3.61	99.29
4683	CS-1	97	ZiGC	Znw	12	47.88	0.01	19.31	10.05	1.26	0.02	1.23	4.39	0.17	10.04	8.10	0.39	-3.42	99.43
4971	CS-1	130	QZV	Znw	8	46.07	0.15	20.02	11.97	1.22	0.02	1.11	4.01	0.19	9.74	8.07	0.36	-3.41	99.54
4972A	CS-1	149	GR	Znw	7	46.33	0.03	19.53	12.72	1.01	0.03	1.17	3.90	0.18	9.72	6.92	0.90	-2.91	99.54
4972A	CS-1	149	GR	Ms	7	48.63	0.00	31.31	2.08	1.05	0.09	0.39	0.60	0.03	10.08	0.88	4.03	-0.37	98.81
4972B	CS-1	149	GR	Znw	7	46.13	0.03	20.08	13.21	0.96	0.02	1.23	3.51	0.17	9.82	7.07	0.83	-2.98	100.09
4972B	CS-1	149	GR	Ms	5	48.33	< 0.01	34.34	1.17	0.14	0.09	0.26	1.02	0.05	10.02	0.41	4.36	-0.17	100.03
4973	Cs-1	163	GR	Znw	12	45.72	0.03	20.17	13.54	1.01	0.03	1.22	3.81	0.18	9.97	8.14	0.63	-3.43	101.02
5048	CS-1	182	ZiGC	Znw	7	45.93	0.22	19.89	12.53	0.91	0.09	1.36	3.79	0.23	9.58	7.95	0.41	-3.35	99.55
4974	CS-1	193	GR	Znw	8	45.17	0.18	20.39	13.91	0.93	0.04	1.89	3.43	0.23	9.69	8.12	0.32	-3.42	100.89
4685	CS-1	205	ZiGC	Znw	6	45.60	0.07	19.63	12.54	0.77	0.02	1.01	3.59	0.22	10.14	7.64	0.50	-3.22	98.52
4975	CS-1	213	ZiGC	Znw	8	45.46	0.24	20.39	13.00	0.81	0.10	0.98	3.25	0.23	9.72	8.01	0.35	-3.38	99.17
5064	CS-1	244	ZiGC	Znw	8	45.90	0.23	20.22	12.64	0.70	0.11	1.48	4.05	0.26	9.59	8.32	0.26	-3.51	100.25
4687	CS-1	413	ZiGm	Znw	12	42.88	0.53	20.64	16.38	0.77	0.18	0.82	2.42	0.23	9.79	6.94	0.78	-2.93	99.43
4936	CS-1	477	ZiGm	Znw	10	43.99	0.41	20.85	15.24	0.70	0.10	0.91	3.02	0.23	9.69	7.84	0.42	-3.30	100.10
4688	CS-1	559	ZiG	Znw	6	45.88	0.22	20.22	12.84	0.82	0.07	1.35	3.86	0.23	9.84	7.93	0.44	-3.35	100.36
4938	CS-1	653	ZiG	Znw	8	43.30	0.32	20.89	15.01	0.71	0.09	1.12	2.53	0.32	9.60	8.17	0.19	-3.44	98.81
4689	CS-1	735	ZiG	Znw	4	41.21	0.42	20.32	18.70	0.66	0.14	0.83	2.02	0.26	9.82	6.08	1.10	-2.56	99.00
4690	CS-1	741	BtGm	Bt	28	39.56	1.06	21.02	21.18	0.66	0.42	0.73	1.81	0.31	9.25	4.35	1.94	-1.83	100.46
4691	CS-1	749	BtG	Bt	4	39.58	0.75	19.93	20.11	0.59	0.70	0.71	1.41	0.29	9.64	3.78	2.11	-1.59	98.01
4801	CS-1	774	BtG	Bt	6	37.77	1.32	20.85	22.08	0.52	0.93	0.55	1.41	0.32	9.64	3.54	2.25	-1.49	99.70
5171	CS-1	800	BtG	Bt	12	37.80	1.37	19.98	22.66	0.50	1.00	0.49	1.26	0.31	9.29	4.72	1.65	-2.00	99.04
4802	CS-1	860	BtGm	Bt	6	37.93	1.21	20.46	22.43	0.57	0.44	0.62	1.19	0.30	9.59	3.44	2.26	-1.45	99.00
4692	CS-1	988	BtG	Bt	14	37.92	0.92	20.02	23.10	0.60	1.29	0.47	1.10	0.31	9.48	4.72	1.66	-1.99	99.61
4940	CS-1	1025	BtG	Bt	6	36.93	1.33	19.34	23.84	0.64	0.80	0.51	1.35	0.28	9.14	4.31	1.79	-1.81	98.45
4941	CS-1	1245	BtGm	Bt	9	37.40	1.20	19.88	23.78	0.64	0.72	0.50	0.94	0.28	9.35	4.22	1.86	-1.78	98.99
4942	CS-1	1400	BtGm	Bt	10	39.21	1.45	20.02	21.93	0.57	1.25	0.52	1.47	0.27	9.34	4.84	1.68	-2.04	100.52
4693	CS-1	1579	BtG	Bt	4	39.57	0.50	19.93	19.64	0.75	0.88	0.49	1.49	0.29	9.77	3.93	2.04	-1.65	97.64
5423	Cis-2	180	ZiGC	Znw	8	48.42	0.08	19.06	8.96	1.92	0.02	2.22	3.67	0.21	9.65	8.45	0.20	-3.56	99.30
5425	Cis-2	186	ZiGC	Znw	10	48.52	0.07	19.42	9.61	1.43	0.02	2.24	3.73	0.24	9.70	8.48	0.22	-3.58	100.10
5427	Cis-2	190	GR	Znw	3	45.92	0.03	18.69	13.27	1.38	0.01	1.07	3.13	0.23	10.12	7.83	0.39	-3.30	98.77
5428	Cis-2	191	GR	Znw	6	46.28	0.01	18.15	13.60	1.42	< 0.01	0.98	3.31	0.16	10.33	7.87	0.38	-3.32	99.18
5429	Cis-2	280	ZiGC	Znw	14	44.97	0.12	20.35	13.65	1.02	0.01	2.14	3.54	0.19	9.63	7.98	0.37	-3.37	100.60
5430	Cis-2	374	ZiGC	Znw	10	44.84	0.14	20.20	14.98	1.01	0.02	1.13	3.45	0.23	9.66	8.00	0.37	-3.37	100.66
5438	PSn07	332	GR	Znw	10	47.56	0.07	19.09	11.50	1.14	0.01	1.19	3.97	0.21	10.13	7.29	0.76	-3.07	99.85
5434	PSn07	412	ZiGC	Znw	12	46.52	0.20	19.72	12.47	0.78	0.07	1.31	3.58	0.25	10.13	7.16	0.80	-3.01	99.98
5436	PSn07	343	ZiGC	Znw	10	47.57	0.11	19.37	11.71	0.89	0.02	1.54	4.01	0.23	10.06	7.34	0.75	-3.09	100.51
4981	Bunau Stollen		GR	Znw	8	47.29	0.01	19.49	11.46	1.24	0.01	1.07	3.45	0.19	10.16	8.48	0.17	-3.57	99.46
5412	Bunau Stollen		QZV	Znw	10	47.97	0.02	19.45	11.20	1.35	0.01	0.91	4.03	0.15	10.05	8.44	0.25	-3.56	100.27

(17–33 ppm) in biotite are lower than those in zinnwaldite. Along basic division of trioctahedral micas to zinnwaldite and biotite, systematic chemical changes in vertical direction along borehole CS-1 are noticeable (Figs. 7, 8). The contents of major elements Si, Al, Fe, Li and F show a regular trend with principal change at the depth of 735 m, corresponding to the contact between biotite and zinnwaldite granites

(Fig. 7). The contents of major elements are scattered within the BtG with no obvious trend but their systematic evolution within the intrusion of zinnwaldite granites corroborates the general petrological-geochemical trend of upwards fractionation (Breiter et al., 2017a): the contents of Fe and Al decrease, whereas the contents of Si, Li, Rb and F increase in upward direction. The most intensive variations can be seen

Table 3

Structural formulae of micas (apfu) on the basis of 44 negative charges.

Sample	Si	Al ^{IV}	Total T	Ti	Al ^{VI}	Fe	Mn	Mg	Li	Total Y	Na	K	Rb	Total Z	F	OH
4970	6.669	1.331	4	0.003	2.049	1.351	0.172	0.002	2.117	5.694	0.050	1.860	0.094	2.003	3.813	0.187
4674	6.786	1.214	4	0.014	2.095	1.058	0.160	0.006	2.398	5.731	0.063	1.791	0.170	2.024	3.843	0.157
4683	6.787	1.213	4	0.001	2.013	1.191	0.151	0.004	2.502	5.863	0.047	1.815	0.112	1.974	3.631	0.369
4971	6.596	1.404	4	0.016	1.974	1.433	0.148	0.004	2.309	5.884	0.053	1.779	0.102	1.934	3.653	0.347
4972A	6.646	1.354	4	0.003	1.947	1.526	0.123	0.006	2.250	5.855	0.050	1.779	0.108	1.936	3.139	0.861
4972A	6.557	1.443	4	0.000	3.532	0.235	0.120	0.018	0.325	4.229	0.008	1.734	0.034	1.775	0.375	3.625
4972B	6.608	1.392	4	0.003	1.998	1.582	0.116	0.004	2.022	5.726	0.047	1.794	0.113	1.955	3.202	0.798
4972B	6.360	1.640	4	0.000	3.686	0.129	0.016	0.018	0.540	4.387	0.013	1.682	0.022	1.717	0.171	3.829
4973	6.534	1.466	4	0.003	1.930	1.618	0.122	0.006	2.190	5.870	0.050	1.817	0.112	1.929	3.678	0.322
5048	6.598	1.402	4	0.024	1.966	1.505	0.111	0.019	2.190	5.815	0.064	1.756	0.126	1.945	3.612	0.388
4974	6.493	1.507	4	0.019	1.947	1.672	0.113	0.009	1.983	5.743	0.064	1.777	0.175	2.015	3.691	0.309
4685	6.626	1.374	4	0.008	1.987	1.524	0.095	0.004	2.098	5.715	0.062	1.879	0.094	2.036	3.510	0.490
4975	6.566	1.434	4	0.026	2.037	1.570	0.099	0.022	1.888	5.642	0.064	1.791	0.091	1.946	3.658	0.342
5064	6.548	1.452	4	0.025	1.948	1.508	0.085	0.023	2.324	5.912	0.072	1.745	0.136	1.953	3.753	0.247
4687	6.320	1.680	4	0.059	1.906	2.019	0.096	0.040	1.434	5.553	0.066	1.841	0.078	1.984	3.235	0.765
4936	6.379	1.621	4	0.045	1.943	1.848	0.086	0.022	1.761	5.704	0.065	1.792	0.085	1.942	3.595	0.405
4688	6.551	1.449	4	0.024	1.954	1.533	0.099	0.015	2.216	5.841	0.064	1.792	0.124	1.980	3.580	0.420
4938	6.386	1.614	4	0.035	2.016	1.851	0.089	0.020	1.500	5.512	0.091	1.806	0.106	2.004	3.810	0.190
4689	6.200	1.800	4	0.048	1.803	2.353	0.084	0.031	1.222	5.541	0.076	1.885	0.080	2.041	2.893	1.107
4690	5.927	2.073	4	0.119	1.638	2.653	0.084	0.094	1.091	5.679	0.090	1.768	0.070	1.928	2.061	1.939
4691	6.073	1.927	4	0.087	1.678	2.580	0.077	0.160	0.870	5.451	0.086	1.887	0.070	2.043	1.834	2.166
4801	5.764	2.236	4	0.151	1.514	2.818	0.067	0.212	0.865	5.628	0.095	1.877	0.054	2.025	1.708	2.292
5171	5.825	2.175	4	0.159	1.453	2.920	0.065	0.230	0.781	5.607	0.093	1.826	0.049	1.967	2.300	1.700
4802	5.846	2.154	4	0.140	1.562	2.890	0.074	0.101	0.738	5.505	0.090	1.885	0.061	2.036	1.676	2.324
4692	5.831	2.169	4	0.106	1.458	2.970	0.078	0.296	0.680	5.589	0.092	1.859	0.046	1.998	2.295	1.705
4940	5.775	2.225	4	0.156	1.338	3.117	0.085	0.186	0.849	5.732	0.085	1.823	0.051	1.959	2.131	1.869
4941	5.813	2.187	4	0.140	1.455	3.091	0.084	0.167	0.588	5.525	0.084	1.854	0.050	1.988	2.074	1.926
4942	5.907	2.093	4	0.164	1.462	2.763	0.073	0.281	0.891	5.633	0.079	1.795	0.050	1.924	2.306	1.694
4693	6.080	1.920	4	0.058	1.690	2.524	0.098	0.202	0.921	5.491	0.086	1.915	0.048	2.050	1.910	2.090
5423	6.906	1.094	4	0.009	2.109	1.069	0.232	0.004	2.105	5.528	0.058	1.756	0.203	2.017	3.811	0.189
5425	6.869	1.131	4	0.007	2.110	1.138	0.171	0.004	2.124	5.554	0.066	1.752	0.204	2.021	3.796	0.204
5427	6.712	1.288	4	0.003	1.931	1.622	0.171	0.002	1.840	5.569	0.065	1.887	0.100	2.052	3.619	0.381
5428	6.745	1.255	4	0.001	1.862	1.657	0.175	0.000	1.940	5.635	0.045	1.920	0.092	2.057	3.627	0.373
5429	6.487	1.513	4	0.013	1.946	1.646	0.125	0.002	2.053	5.786	0.053	1.772	0.198	2.023	3.640	0.360
5430	6.460	1.540	4	0.015	1.890	1.805	0.123	0.004	1.999	5.837	0.064	1.775	0.105	1.944	3.645	0.355
5438	6.768	1.232	4	0.007	1.970	1.368	0.137	0.002	2.272	5.757	0.058	1.839	0.109	2.006	3.280	0.720
5434	6.658	1.342	4	0.022	1.984	1.492	0.095	0.015	2.060	5.668	0.069	1.849	0.120	2.039	3.240	0.760
5436	6.738	1.262	4	0.012	1.971	1.387	0.107	0.004	2.284	5.765	0.063	1.818	0.140	2.021	3.288	0.712
4981	6.771	1.229	4	0.001	2.060	1.372	0.150	0.002	1.986	5.572	0.053	1.856	0.098	2.007	3.839	0.161
5412	6.773	1.227	4	0.002	2.009	1.322	0.161	0.002	2.288	5.785	0.041	1.810	0.083	1.934	3.768	0.232

in the case of Fe, Li and F contents. Systematic evolution of mica composition is disturbed only in the zone of xenoliths of ZiGm at a depth of 369–530 m: zinnwaldite within the ZiGm is chemically less evolved (1.43–1.75 apfu Li) than zinnwaldite from the surrounding medium-grained ZiG (2.32 and 2.44 apfu Li).

Different patterns were encountered in vertical distribution of rare metals in mica: the contents of Sn, Nb and Ta decrease strongly upward: 620 → 70 ppm Sn, 550 → 50 ppm Nb and 70 → 20 ppm Ta (Fig. 8a, b, c). Local enrichment disturbing this trend was found in the upper part of the BtG (depth of ca. 740–750 m) and in the ZiGm (depth of 413 m), in both cases in coincidence with some enrichment of Sn in the bulk-rock. In case of biotite from BtG, the enrichment may be explained by influence of fluids from neighboring ZiG, in case of zinnwaldite from ZiGm the lack of Ti-oxide minerals pushed all Sn to the mica.

In contrast, the contents of W vary only slightly between 20 and 70 ppm, showing no trend (Fig. 8d). The highest contents of Sc (80–130 ppm) were found in the upper part of the BtG at a depth of 740–1000 m (Fig. 8e). The contents of all mentioned trace elements in mica do not correlate with their contents in the bulk rock; the entry of particular element into mica crystal lattice was controlled in particular namely by the associated mineral assemblage, i.e., with saturation of Ti, Sn, W, Nb and Ta-bearing oxide minerals.

Thallium is the only trace element the contents of which systematically increase upwards with maxima in the range of 40–60 ppm in the uppermost part of the ZiG. The contents of Tl in mica correlate well with Tl contents in the bulk rock, with $Tl_{\text{mica}}/Tl_{\text{rock}} \sim 5$ (Fig. 8f).

Of the elemental ratios proposed as indicators of magma

fractionation (Černý et al., 1985), the Nb/Ta values decrease upwards (7 → 2) with disturbances in the uppermost part of the BtG and in the ZiGm. The Nb/Ta values in the whole rock decrease in a similar way: from 6.5 in the BtG through 3.5 in the ZiG to 2.7 in greisen and 2.5 in the ZiGC (Fig. 8g). Similarly, the Fe/Mn values, stable within the BtG, decrease systematically upwards in the ZiG, showing a perfect coincidence between the mica values and bulk-rock values (Fig. 8h). Concordance in the evolution of Nb/Ta and Fe/Mn values in columbite and bulk rock (Breiter et al., 2017c) and in micas and bulk rock (this paper) indicates an intensive equilibration of the whole mineral assemblage during the late magmatic/hydrothermal stage.

Dioctahedral mica of the muscovite–phengite series was found only locally as a product of late alteration of zinnwaldite flakes. Muscovite contains ca. 47.5–49.0 wt% SiO₂, 30.6–35.2 wt% Al₂O₃, 0.9–2.1 wt% FeO, 0.1–1.5 wt% MnO, 0.3–0.4 wt% Rb₂O, less than 0.1 wt% TiO₂, MgO and Na₂O, 0.1–1.6 wt% Li₂O, and 0.3–1.0 wt% F. Chemical boundary between muscovite and zinnwaldite is sharp without any visible transition zone (Fig. 6). The contents of Sn increase from 27–300 ppm to 600–1500 ppm during muscovitization (Fig. 9), while the contents of other trace elements are scattered with no distinct trends.

6. Discussion

6.1. Reliability of Li computation from microprobe analyses (Fig. 10)

Lithium as the only major constituent of micas from evolved

Table 4

Contents of trace elements (medians and median absolute deviations) in micas (ppm) analyzed via LA-ICP-MS.

Sample	Rock		Li	Sc	Ga	Ge	Nb	In	Sn	Cs	Ta	W	Tl
Detection limit			1.8	0.7	0.18	1.0	0.08	0.04	2.1	0.15	0.08	0.21	0.41
4970	QZV	median	17,154	56	115	6.8	39	0.47	109	231	20	19	44
		MAD	335	6	9	0.8	12	0.08	31	39	5	6	2
4674	ZiGC	median	19,472	76	67	4.8	55	0.36	123	631	26	48	55
		MAD	1536	4	6	0.9	12	0.23	41	80	4	7	4
4683	ZiGC	median	20,390	49	75	2.6	45	1.19	112	350	6	28	35
		MAD	860	2	2	0.3	9	0.20	15	13	2	6	0
4971	QZV	median	18,637	84	76	6.4	70	0.61	114	423	34	39	39
		MAD	456	2	5	0.3	6	0.07	16	58	3	4	2
4972A-Zin	GR	median	18,752	65	96	5.6	42	0.45	103	180	10	15	39
		MAD	793	4	11	0.6	12	0.24	45	38	5	4	2
4972A-Ms	GR	median	2640	66	78	1.2	9	2.33	1165	192	7	2	46
		MAD	2311	2	7	0.1	1	1.21	208	11	1	1	5
4972B-Znw	GR	median	15,778	62	77	3.1	24	1.16	145	273	10	13	45
		MAD	54	10	0	0.0	2	0.04	30	54	1	6	3
4972B-Ms	GR	median	5282	85	62	2.1	37	3.56	1408	182	26	10	37
		MAD	2071	3	3	0.1	19	0.09	213	28	15	5	4
4973	GR	median	17,715	71	125	19.0	54	0.37	68	448	18	19	53
		MAD	1062	9	15	2.0	9	0.09	13	108	5	5	5
5048	GR	median	17,617	83	71	7.1	85	0.42	101	467	29	45	39
		MAD	525	2	6	0.5	25	0.08	19	63	6	6	6
4974	GR	median	15,920	79	66	6.7	69	0.43	79	362	29	29	32
		MAD	644	6	4	0.7	11	0.06	15	26	7	7	2
4685	ZiGC	median	16,660	69	69	2.8	98	1.03	149	435	34	33	33
		MAD	1253	4	3	1.1	9	0.16	19	54	5	4	1
4975	ZiGC	median	15,084	81	70	13.1	41	0.77	80	399	14	18	35
		MAD	366	5	2	1.5	13	0.06	13	40	4	6	1
5064	ZiGC	median	18,817	86	82	6.7	91	0.31	118	472	22	40	42
		MAD	449	2	16	0.5	20	0.07	30	72	10	10	8
4687	ZiGm	median	11,255	62	94	6.3	313	0.38	238	467	41	36	46
		MAD	287	4	6	0.5	99	0.04	37	30	10	2	2
4936	ZiGm	median	14,033	78	86	5.9	172	0.26	139	528	29	39	34
		MAD	401	3	7	0.3	59	0.05	13	43	6	5	2
4688	ZiG	median	17,909	67	87	2.8	119	0.89	150	449	41	52	46
		MAD	1290	13	14	2.2	34	0.12	26	159	9	4	4
4938	ZiG	median	11,751	62	73	4.6	158	0.22	106	322	26	36	35
		MAD	363	10	11	0.3	37	0.03	24	46	4	7	2
4689	ZiG	median	9405	100	109	14.5	464	1.43	213	981	80	37	33
		MAD	809	12	5	1.3	155	0.20	28	158	6	9	2
4690	BtG	median	8406	83	104	6.5	631	2.22	444	400	41	46	33
		MAD	399	7	5	0.5	120	0.19	35	71	15	15	2
4691	BtG	median	6555	89	106	7.1	486	3.23	623	395	31	28	29
		MAD	233	7	4	0.8	41	0.33	40	65	8	5	1
4801	BtG	median	6560	83	115	9.2	517	0.17	93	481	71	38	27
		MAD	546	7	6	0.7	110	0.04	9	99	35	12	2
5471	BtG	median	5876	94	115	8.4	588	0.18	140	436	44	34	25
		MAD	547	6	6	0.9	43	0.06	16	109	19	15	1
4802	BtG	median	5527	129	129	22.4	937	0.21	99	356	134	40	29
		MAD	405	4	6	2.2	87	0.03	9	82	42	4	1
4692	BtG	median	5111	92	110	7.3	506	0.41	239	655	123	26	25
		MAD	521	6	8	0.8	56	0.05	31	85	35	6	2
4940	BtG	median	6265	51	84	5.5	402	1.37	232	530	78	20	17
		MAD	249	3	7	1.4	93	0.20	32	69	14	2	1
4941	BtG	median	4365	62	107	8.6	495	0.23	311	470	62	33	23
		MAD	606	11	13	1.4	152	0.13	68	126	21	13	2
4942	BtG	median	6823	76	114	8.5	381	0.30	477	581	47	33	22
		MAD	520	8	8	1.1	74	0.08	36	101	30	8	1
4693	BtG	median	6941	65	97	8.4	472	3.08	541	460	76	31	22
		MAD	289	6	7	1.4	69	0.25	22	89	16	5	2
5423	ZiGC	median	17,062	77	92	4.7	150	0.28	628	388	55	81	46
		MAD	989	8	14	1.2	91	0.13	419	118	26	27	6
5425	ZiGC	median	17,312	69	83	5.3	96	0.20	181	327	24	64	48
		MAD	2216	6	9	1.0	37	0.11	48	99	7	16	6
5427	GR	median	14,521	53	146	2.8	37	0.48	150	373	28	13	43
		MAD	1206	7	10	0.3	6	0.11	37	33	9	3	4
5428	GR	median	15,380	54	161	2.7	42	0.53	155	401	19	13	44
		MAD	790	7	25	0.7	10	0.11	32	42	9	3	4
5429	ZiGC	median	16,438	64	83	13.4	65	0.61	84	390	33	31	34
		MAD	336	3	6	1.2	12	0.07	12	26	7	4	2
5430	ZiGC	median	16,046	74	79	16.7	82	0.35	75	439	26	29	36
		MAD	1079	4	12	1.9	16	0.11	18	78	6	4	4
5438	GR	median	18,456	58	97	5.4	69	0.80	118	496	22	39	45
		MAD	906	5	8	0.7	14	0.10	30	29	13	5	3

(continued on next page)

Table 4 (continued)

Sample	Rock		Li	Sc	Ga	Ge	Nb	In	Sn	Cs	Ta	W	Tl
5434	ZiGC	median	16,620	74	77	4.7	66	0.24	44	366	31	28	34
		MAD	1408	9	12	0.7	20	0.06	16	101	12	8	7
5436	ZiGC	median	18,607	65	81	5.9	69	0.33	69	375	16	31	41
		MAD	988	14	8	0.9	32	0.14	25	96	7	12	5
4981	GR	median	16,024	61	160	5.6	45	5.79	176	477	17	20	40
		MAD	615	4	8	0.6	6	4.55	35	42	3	2	2
5412	QZV	median	18,688	46	105	4.3	37	0.90	121	382	10	29	39
		MAD	1185	3	6	0.3	3	0.10	24	35	2	5	2

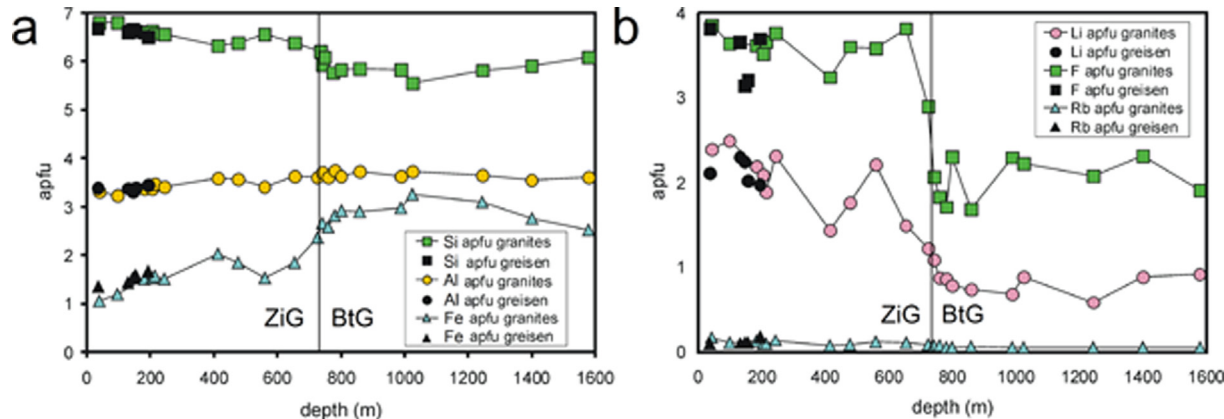


Fig. 7. Vertical zoning of mica composition in the borehole CS-1 (in apfu): a, Si, Al, Fe; b, Li, Rb, F.

granites and pegmatites cannot be analyzed using electron microprobe. To solve this problem, several methods of Li calculation from other elements, easily analyzed by the microprobe, have been suggested (Stone et al., 1988; Tindle and Webb, 1990; Tischendorf et al., 1997). In mineralogical practice, the Tischendorf's method [Li_2O (wt. %) = 0.298* SiO_2 (wt. %)–9.658] has been frequently applied (Li et al., 2015; Legros et al., 2018).

While Li enters the mica crystal lattice along several competing substitution schemes (annite–trilithionite, siderophyllite–polylithionite, muscovite–lepidolite), the Li content cannot be easily calculated based on formula stoichiometry; all suggested methods are based on statistical evaluation of large datasets of published chemical and microprobe analyses. This approach is useful for a first approximation but can result in significant errors in a particular case. Fig. 10a shows that, in the case of the studied Li–Fe micas from Cínovec, the values calculated according to Tischendorf are overestimated by 0.5–1 wt% in most samples. The real micas from Cínovec contain, at a given content of SiO_2 , less Li than expected by ideal trioctahedral substitutions and also less Li than calculated using the Tischendorf's formula (Fig. 10b). This is caused by the higher-than-ideal content of Al in the trioctahedral layer: micas from Cínovec, and probably a large majority of Li–Fe micas worldwide, are not ideal trioctahedral micas containing some vacancies.

6.2. The share of mica in the bulk-rock budget of ore elements

Knowing the modal content of mica in the rock, the bulk-rock chemical composition, and the contents of particular elements in mica, we are able to compute the share of mica in the bulk-rock budget of these elements. This will be later used as a supporting argument for the discussion of processes forming the deposit.

Mica is the only host of Li in the Cínovec magmatic system, and an important host of F, Rb, Cs, Tl, Ga, Sn, W, Nb, Ta and Sc (Fig. 11). The actual F content in mica and the share of mica in F budget increase from the BtG to greisen (Fig. 11a): biotite accommodates 25–35% and zinnwaldite 25–100% of the present F, the rest being hosted especially by fluorite and topaz. While the contents of Ca available for fluorite

crystallization decrease upwards, fluorine dominantly enters the crystal lattice of mica up to a 95% occupancy of the (F, OH)-site. A similar trend was also found in the case of Rb (Fig. 11b), Cs and Tl, all hosted also by K-feldspar. While the contents of Kfs decrease from BtG to ZiGC (Breiter et al., 2017a), all elements geochemically following potassium are dominantly accommodated in mica in ZiG and greisens. A different trend was found in the budget of Nb: the share of mica in Nb budget during the pluton evolution generally decreases from ca. 20–80% in the BtG to 2–10% in most samples of the ZiG and ZiGC. This means that in the less evolved BtG the major part of Nb was incorporated in mica and only a subordinate part into rutile. In the ZiG and ZiGC, the major part of Nb was hosted by accessory Nb-rich rutile and columbite, respectively (Breiter et al., 2017c), and the influence of later crystallizing mica on Nb distribution was minimized (Fig. 11c). The Nb share of zinnwaldite from greisen samples scattered: Nb-rich samples contain columbite and the share of mica in Nb budget is small. In unmineralized Nb-poor samples, however, it increases up to 50%. The shares of mica in the budget of Ta (Fig. 11d) and Sn (Fig. 11e) are similar to those in the budget of Nb. The share of mica in the budget of tungsten is only about 10% in the BtG and between 4 and 30% in the ZiG + ZiGC (Fig. 11f); a major part of W is probably hosted by an oxide mineral. The shares of mica in W budget in mineralized greisen samples containing wolframite and scheelite are always negligible.

6.3. Mica in the mineralizing process

Based on the vertical zoning of mica, its mineral assemblage, and the share of mica in the budget of F, Li and rare metals, we may try to interpret the role of mica in the origin of the deposit.

Zinnwaldite grains in greisen are homogeneous in BSE, which indicates their homogeneous chemical composition as regards the distribution of major elements. The contents of trace elements are scattered, but no regular zoning was identified. Consequently, remnants of primary magmatic zinnwaldite and later hydrothermal zinnwaldite grooving in the greisen stage cannot be distinguished. We conclude that all zinnwaldite in greisen was fully re-equilibrated in a reaction with

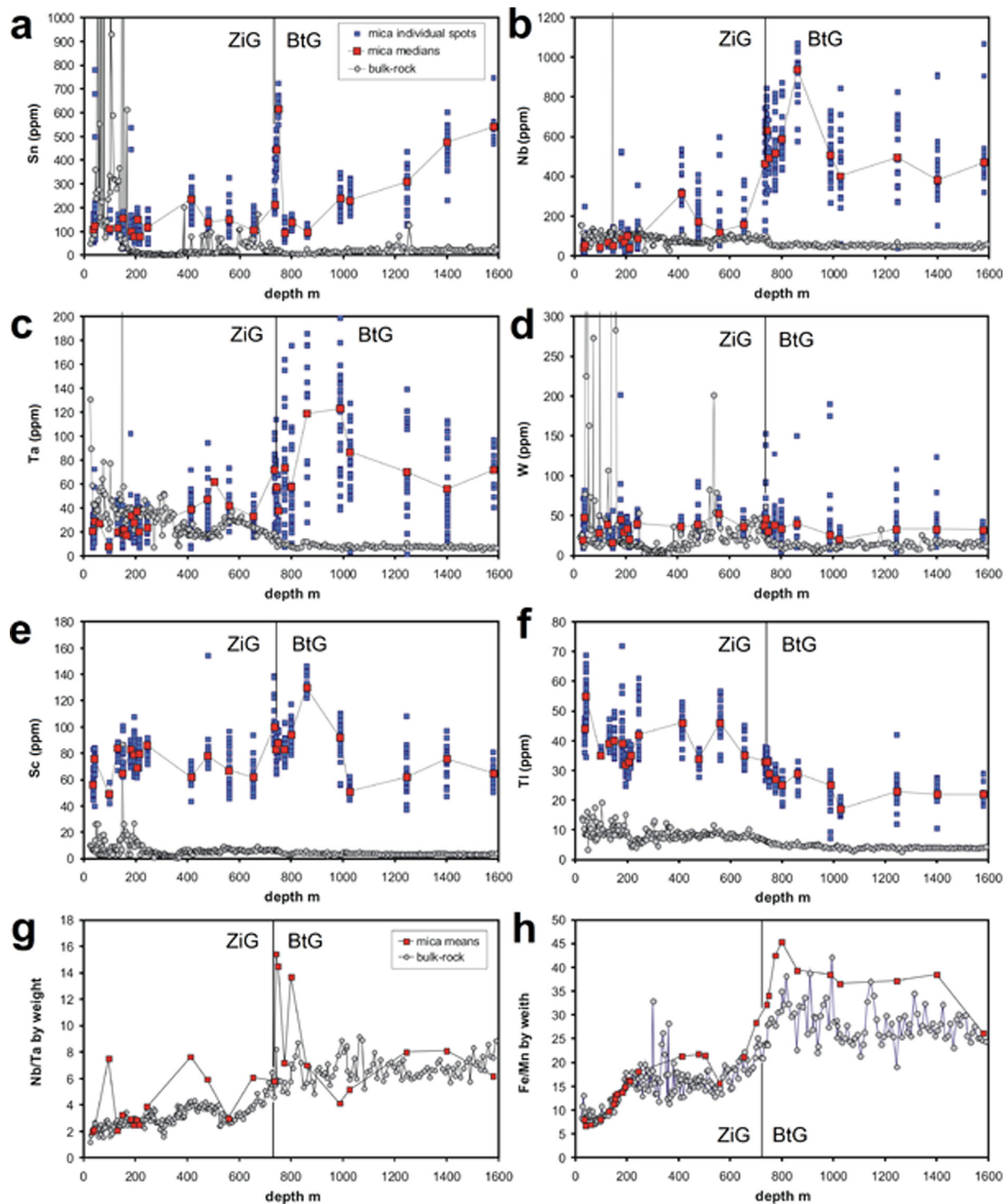


Fig. 8. Vertical zoning of mica composition in the borehole CS-1 (in ppm) compared with bulk-rock composition. All analyses (blue points) and medians (red points) are shown in diagrams a-f, while only medians are shown in diagrams g-h. Bulk-rock data are shown in gray: a, Sn; b, Nb; c, Ta; d, W; e, Sc; f, Tl; g, Nb/Ta; h, Fe/Mn. (For interpretation of the references to colour in this figure legend, the reader is referred to the web version of this article.)

the greisenizing fluid. This is different from quartz, where magmatic cores and hydrothermal overgrowths can be easily distinguished using cathodoluminescence (Breiter et al., 2017d).

Comparing zinnwaldite from granite and these from greisen and veins, the latter is slightly poorer in FeO (means 11.5 vs. 12.8 wt%), Rb₂O (means 1.1 vs. 1.4 wt%) and F (means 7.2 vs. 7.8 wt%), and enriched in SiO₂ (means 46.8 vs. 45.8 wt%) and MnO (means 1.15 vs. 1.0 wt%). The contents of Li₂O are almost identical, about 3.6 wt%. The variability in trace element contents is higher: zinnwaldite from greisen

and veins in borehole CS-1 is, compared to zinnwaldite from neighbouring granites, relatively depleted in Nb (54 vs. 63 ppm), W (26 vs. 41 ppm), Sn (86 vs. 115 ppm) and Cs (370 vs. 472 ppm), and enriched in Ga (94 vs. 72 ppm, in all cases means of all analyzed samples from the depth of 0–250 m). The contents of other measured trace elements differ insignificantly. In other words, mica crystallizing from fluid during greisenization was relatively enriched in Ga and, at the same time, impoverished in Rb, F, Sn and W in comparison with mica in granite.

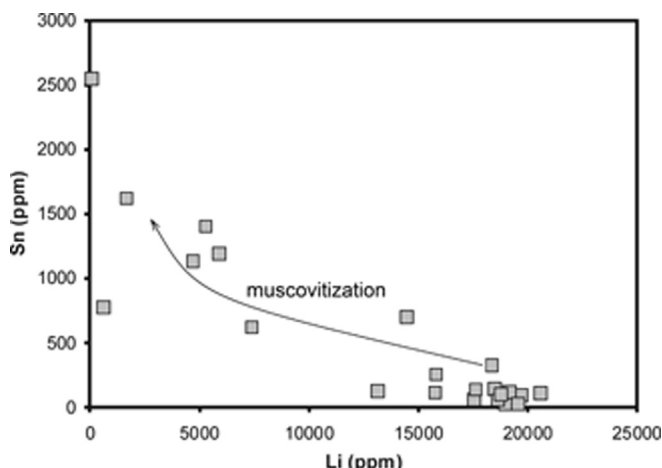


Fig. 9. Input of tin during muscovitization: contents of Li vs. Sn in muscovite.

Comparing zinnwaldite from greisen in the central part of the deposit (greisen selvages of quartz veins, altogether 165 analytical spots) with zinnwaldite from greisen in the southern part of the deposit (massive greisen bodies, 119 analytical spots), the former is slightly enriched in Li (17.350 vs. 16.640 ppm), Cs (437 vs. 390 ppm), Sn (197 vs. 130 ppm), W (46 vs. 29 ppm), Nb (133 vs. 107 ppm), Ta (31 vs. 24 ppm), and Sc (73 vs. 65 ppm). Zinnwaldite from the southern greisen is slightly enriched in Ga (112 vs. 81 ppm), while the contents of Ge and Tl are nearly the same (9 vs. 7 and 43 vs. 41 ppm, respectively, means of all available analyses in all cases). In relation with this difference, it is worth mentioning that the major greisen bodies in the south were described as geologically younger than greisen selvages along veins in the centre, having a different structural position in detail (Fengl et al., 1991; unpublished results of actual revision of the deposit by Geomet Co.). The systematic shift in the zinnwaldite composition from granites through greisen selvages to major greisen bodies corresponds to their relative age and thus to the expected decrease in their crystallization temperature.

Johan et al. (2012), studying micas from Cínovec, found that biotite is generally Sn-richer than zinnwaldite. This finding, although based on a very limited number of analyses, has led these authors to an opinion that Sn-rich biotite was the primary host of Sn; later, during the process of “lithionation”, biotite in the whole upper rock packet (depth interval 0–735 m) was transformed to Sn-poor zinnwaldite + cassiterite. Our

much larger dataset shows the following relation between the contents of Li vs. contents of rare metals and other trace elements (Fig. 12):

Among the analyzed elements, only Tl is well positively correlated with Li (Fig. 12a); this is consistent with the incompatible behaviour of these two elements in granitic melt (Shaw, 1957). In contrast, the contents of Nb, Ta and Sn (Fig. 12b, c, d) generally decrease with increasing Li, while no correlation was found between Li and Cs (Fig. 12e), W (Fig. 12f), Sc, Ga, and Ge. So, our data confirmed the negative correlation between Li and Sn mentioned by Johan et al. (2012), although we provide a different explanation for this fact.

In our opinion, Sn-rich biotite in biotite granites as well as Sn-poor zinnwaldite in zinnwaldite granites are primary magmatic minerals. The only documented hydrothermal alteration of zinnwaldite within the complex of zinnwaldite granites is muscovitization locally found in greisens (Fig. 6). This process, insignificant in its volume, led to the enrichment of mica in Sn and its depletion in Li (Fig. 9). This means that the process was the opposite to the Johan's et al. (2012) assumption.

The paradox that biotite from only slightly Sn-enriched biotite granites (usually 10–30 ppm Sn) shows higher Sn contents than zinnwaldite from strongly Sn-enriched zinnwaldite granites (usually 50–200 ppm Sn) can be explained by evaluating the whole mineral assemblages of both granite types and the order of crystallization of particular minerals. Biotite is, besides relatively scarce Ti-oxides, the major host of rare metals in biotite granites, while the generally low contents of Sn, Nb, and Ta in zinnwaldite from all facies of zinnwaldite granites should be explained by its relatively late crystallization when a substantial part of rare metals was already bound in disseminated magmatic cassiterite and columbite. During the greisen stage, rare metals preferably formed oxide minerals (Breiter et al., 2017c), and the associated zinnwaldite is Sn, Nb, Ta-poor.

The probable source of rare metals and Li and F necessary for the greisen formation was in the middle part of the complex of zinnwaldite granites, at depths of 260–369 m in borehole CS-1. Here, a body of quartz-feldspathic rocks about 130 thick, extraordinarily poor in volatiles and metals (“mica-free granite”), is explained as alkali-rich remnant after fluid segregation from the residual melt. The released fluid rich in F and Li effectively sequestered Sn and W from the melt and transported those upwards forming zinnwaldite-rich greisen + oxide minerals (cassiterite, scheelite > wolframite, columbite, pyrochlore), while the residual silicate melt crystallized as volatile- and metal-poor mica-free granite (Breiter et al. 2017a,c).

Late muscovitization indicates the second, although spatially limited, episode of tin transfer to the upper part of the cupola. In Beauvoir, France, similar Sn-rich late muscovite in greisen is interpreted to

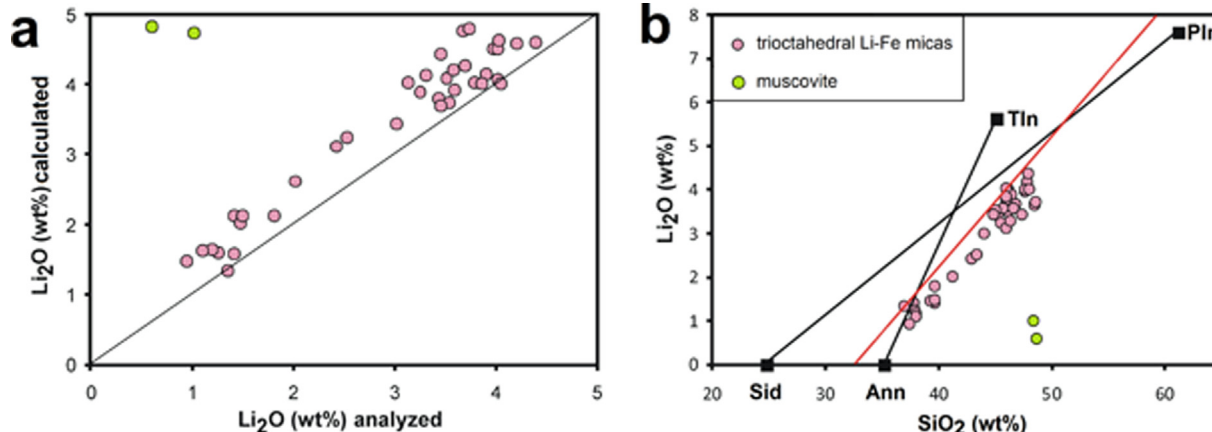


Fig. 10. Comparison of real Li contents in mica with those calculated according to Tischendorf et al. (1997): a, comparison of analyzed and calculated Li values of micas from Cínovec; b, A relation between the contents of SiO₂ and Li₂O along ideal substitution series siderophyllite (Sid)-polyliithionite (Pln) and annite (Ann)-trilithionite (Tln) is shown in black lines. Tischendorf's formula Li₂O (wt%) = 0.298*SiO₂ (wt%)-9.658 is shown in a red line. Note that nearly all calculated Li values are overestimated. (Keep on mind that the shown ideal substitution will be in reality slightly variable depending on F/OH- and Fe/Mn + Mg-values of the analyzed micas.)

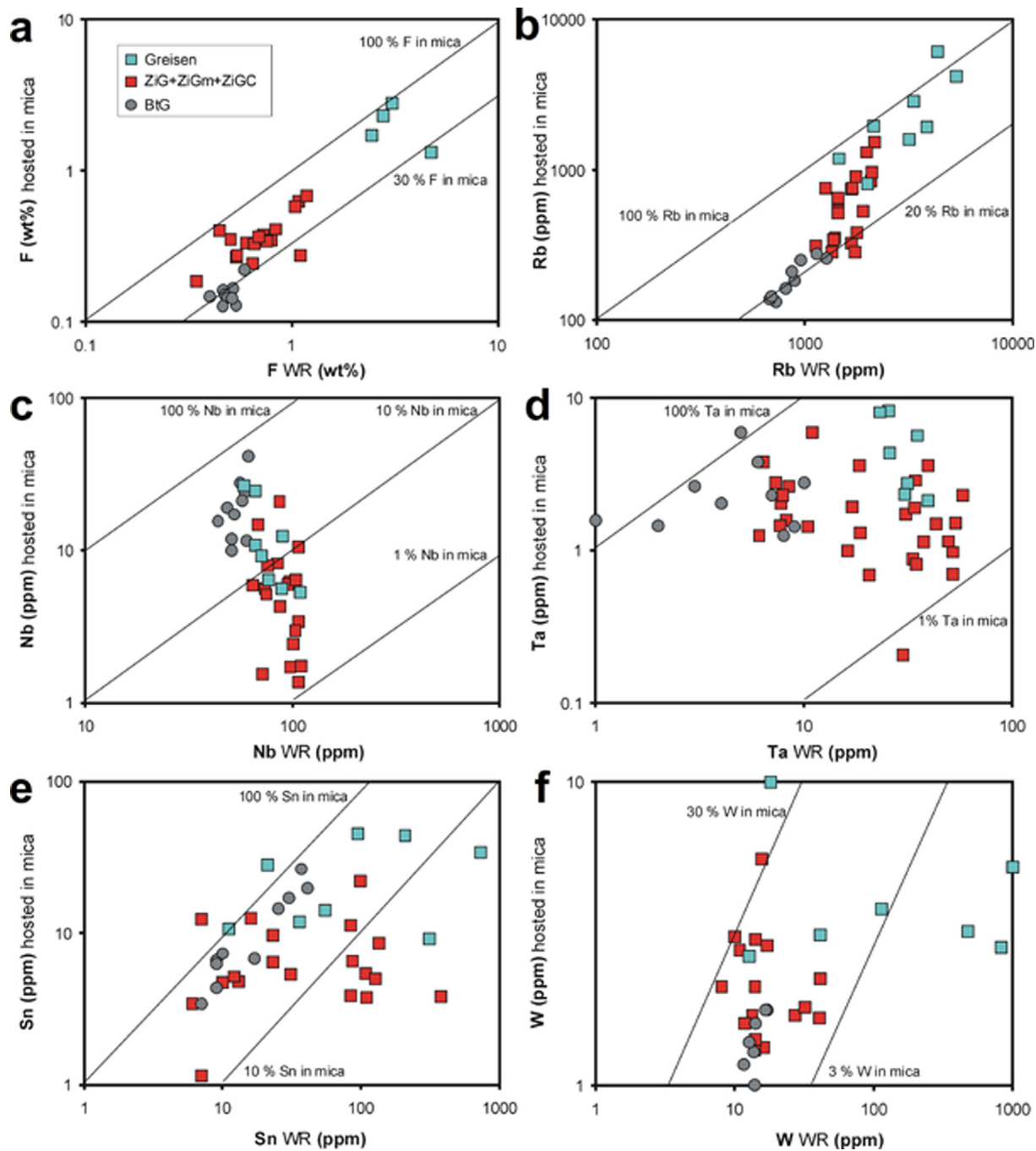


Fig. 11. The share of mica in the whole-rock (WR) budget of some elements: a, F; b, Rb; c, Nb; d, Ta; e, Sn; f, W.

incorporate tin from altered magmatic cassiterite (Monnier, 2018). At Cínovec, there is no evidence for cassiterite dilution in the cupola. The source of this fluid, poor in F and Li in this case, cannot be precisely localized; nevertheless, signs of muscovitization are limited to the uppermost part of the cupola above the zone of mica-free granites.

6.4. Comparison with Li-micas from other rare-metal granites

Despite of huge volumes of mica-related literature, papers with reliable datasets of major, Li, and trace element analyses of Li-rich micas from rare-metal granites or pegmatites are as yet scarce. Papers using modern spot analyses (EPMA + LA-ICP-MS) are effectively limited to Van Lichtervelde et al. (2008), Roda-Robles et al. (2012), Xie et al. (2015), Legros et al. (2016) and Breiter et al. (2017b). The contents of

Li and trace elements in mica concentrates from pegmatites analyzed by a combination of chemical methods (XRF, AAS, ICP-OES) were published by Wise (1995). Identical methods were used by Monier et al. (1987) in Beauvoir, Stone et al. (1988) in Cornwall, du Bray (1994) in Saudi Arabia, Roda-Robles et al. (1995) and Vieira et al. (2011), both in Spain, and by Martins et al. (2012) in Portugal. All these data including author's unpublished LA-ICP-MS data from Beauvoir granite and western Erzgebirge are used for comparison with micas from Cínovec (Fig. 13). Among the compared granitic micas, all plutons except Beauvoir contain trioctahedral Li-Fe micas of the biotite-zinnwaldite series. In contrast, all referred LCT pegmatites contain dioctahedral micas of the muscovite-lepidolite series (Rieder et al., 1999). In the Beauvoir granite, trioctahedral Fe-poor micas of the zinnwaldite-trilithionite series prevail. These differences must be taken into account

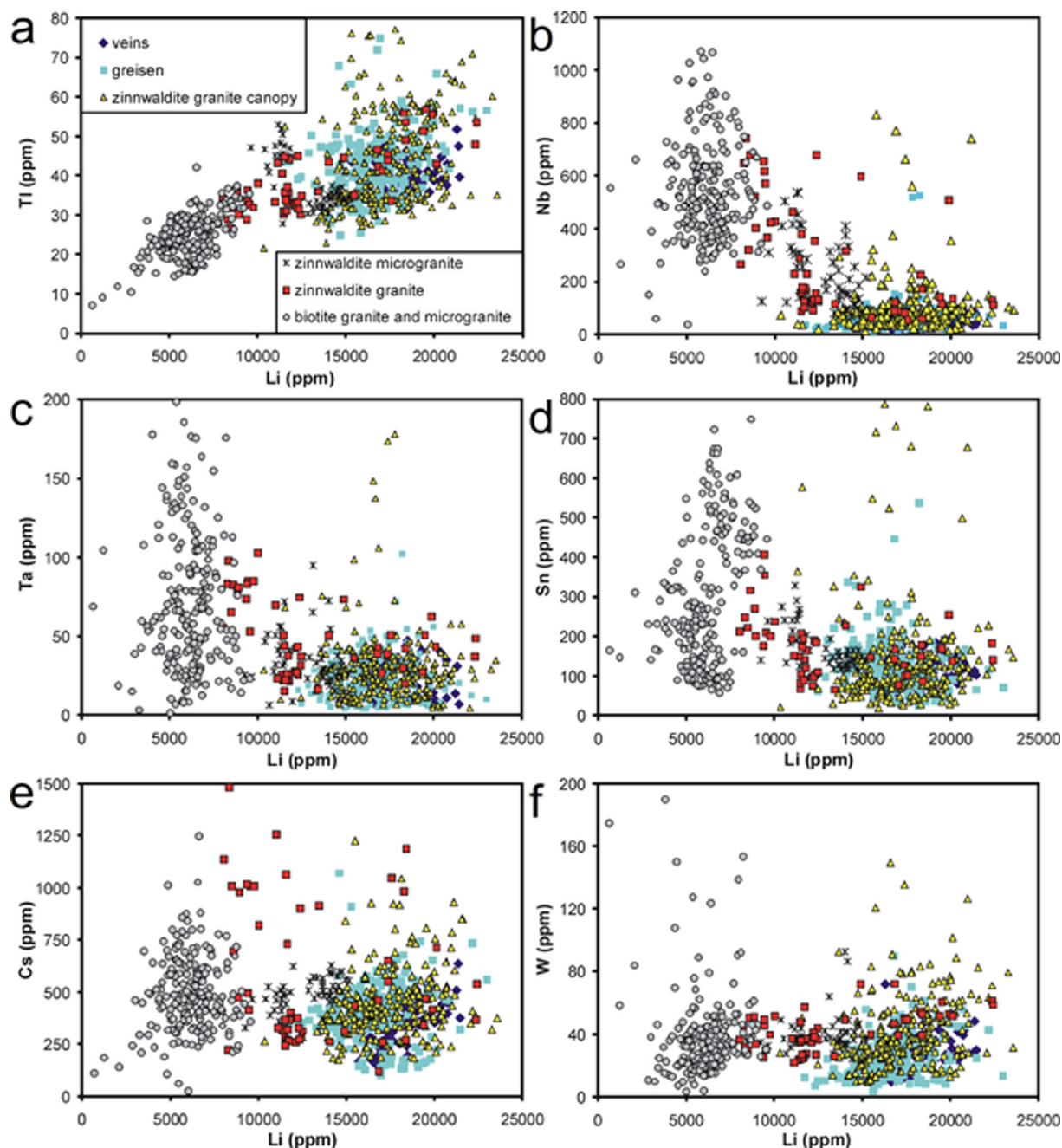


Fig. 12. A relation between the contents of Li and trace elements in trioctahedral micas: a, Li vs. Tl; b, Li vs. Nb; c, Li vs. Ta; d, Li vs. Sn; e, Li vs. Cs; f, Li vs. W.

discussing the contents of trace elements, as scarce studies comparing associated biotite and muscovite indicate higher potential of muscovite to accommodate Sn and probably also other HFSE (Koller and Breiter, 2003). In both, granite and pegmatitic micas, Li closely positively correlates with fluorine: the equation $F(\text{wt}\%) \div 2 \cdot \text{Li}_2\text{O}(\text{wt}\%)$ is valid up to ca. 4 wt% of Li_2O (nearly ideal zinnwaldite), where a nearly full F saturation is reached. With further increase in Li (zinnwaldite → lepidolite), F contents cannot increase any further (Fig. 13a). Several points located outside this trend (samples too poor in F) represent micas from amblygonite-spodumene pegmatites of the Fregeneda area in western Spain (Roda et al., 1995); these micas were analyzed as monomineral concentrates using AAS (Li) and XRF (F), which may indicate somewhat lower accuracy of data.

The contents of Nb in mica is relatively high and systematically decrease during the evolution of some granite plutons (Saudi Arabia, Cínovec) or are generally low in others (< 350 ppm: western

Erzgebirge, Cornwall, China). Low Nb contents (mostly < 200 ppm) were found also in all referred pegmatic muscovites (Fig. 13b). The behavior of W differs in individual plutons: W positively correlates with Li (from < 20 ppm in biotites to 150–300 ppm in zinnwaldite and lepidolite) in strongly peraluminous plutons like Beauvoir and western Erzgebirge and also in majority of referred pegmatites. In contrast, W contents remained comparatively low during the whole evolution of the Cínovec and Maoping plutons, and were highly variable in Yashan granites (Fig. 13c). The most complicated distribution was found for Sn (Fig. 13d). The only statement can be generally made for granites and pegmatites: Li-poor to moderately Li-enriched micas may be strongly enriched in Sn up to 1000 ppm, while Li-rich micas (> 3 wt% Li_2O) usually contain less than ca. 350 ppm Sn.

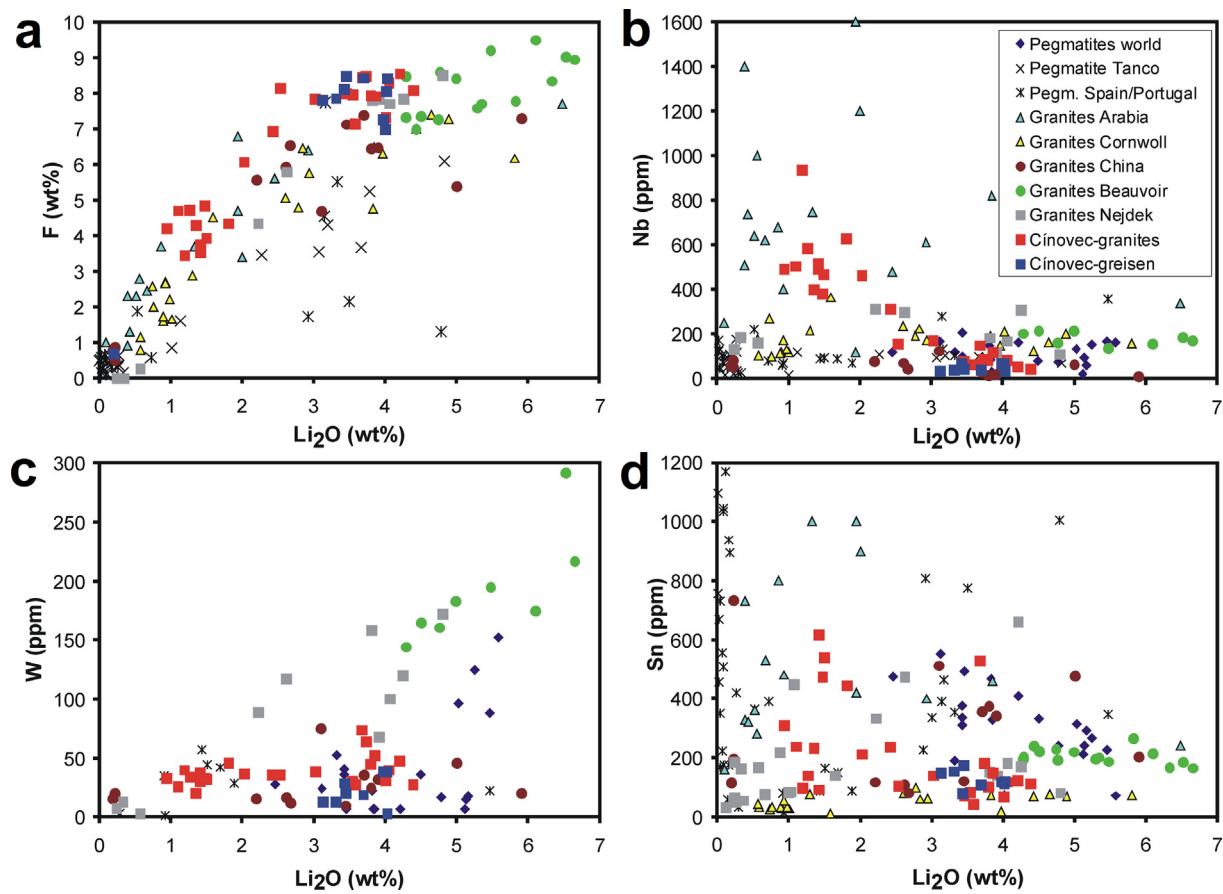


Fig. 13. Comparison of ore-element contents in micas from different granites and pegmatites: a, Li₂O vs. F; b, Li₂O vs. Nb; c, Li₂O vs. W; d, Li₂O vs. Sn. Source of data: Wise (1995) – Li-pegmatites worldwide; Van Lichtervelde et al. (2008) – Tanco pegmatite, Canada; Roda et al. (1995), Martins et al. (2012), Roda-Robles et al. (2012) and Vieira et al. (2011) – pegmatites from western Spain and eastern Portugal; du Bray (1994) – granites from Saudi Arabia; Monier et al. (1987) – Beauvoir granite, France; Stone et al. (1988) – granites from Cornwall; Xie et al. (2015) and Legros et al. (2016) – Yashan granites, China; author's data from the Nejdek pluton (western Erzgebirge) and Beauvoir, France.

7. Summary

Chemical composition of magmatic and hydrothermal micas along with whole-rock chemistry provide important information about the evolution of strongly fractionated rare-metal granite system necessary to formulate a reliable genetic scenario. In the case of the Cínovec deposit, the micas yielded following constraining information:

- all primary micas are trioctahedral micas of the annite–zinnwaldite–lepidolite series.
- vertical zoning (fractionation) of lithophile elements in mica including Li, Rb, and F well corroborate zoning of these elements in the bulk rock.
- the contents of HFSE in mica do not correspond to those in the bulk rock (melt). Generally, biotite associated only with Ti-oxides displays distinctly higher contents of Sn, Nb, Ta and W than zinnwaldite associated with cassiterite, columbite, and pyrochlore.
- the share of mica in the bulk-rock budget of Sn decreases from 40–70% in biotite granite to less than 5% in mineralized greisen; the shares of mica in budgets of Nb and Ta are lower but have identical trends. The entry of the HFSE to mica is mainly controlled by the order of crystallization of mica vs. accessory oxide minerals.
- during hydrothermal greisenization, primary magmatic zinnwaldite was fully re-equilibrated: slightly enriched in Si, Mn and Ga, and depleted in Fe, Rb, F, Cs and ore elements Sn, Nb, Ta and W.
- late local muscovitization in the upper part of the cupola was accompanied by an input of Sn. Late muscovite is Li, F-poor, and

chemically strongly differs from remnants of greisen-stage zinnwaldite; no transitional composition between zinnwaldite and muscovite was found.

– we do not recommend to calculate Li contents in mica from microprobe data. Such calculation is subject to a large error.

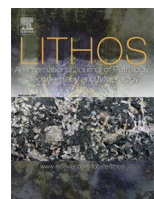
Acknowledgements

This work was supported by the Czech Science Foundation, Czech Republic, project No. P210/14/13600S and conducted with institutional support RVO 67985831 of the Institute of Geology of the Czech Academy of Sciences. One anonymous reviewer is thanked for detail inspiring review.

References

- Argollo, R.D., Schilling, J.G., 1978. Ge–Si and Ga–Al fractionation in Hawaiian volcanic rocks. *Geochim. Cosmochim. Acta* 42, 623–630.
- Bailey, S.W., (ed.), 1984. Micas. *Reviews in Mineralogy* 13, 584 pp.
- Beskin, S.M., Grebennikov, A.M., Matias, V.V., 1994. The Khangilai granite pluton and related Orlovskoye tantalum deposit in Transbaikalia. *Petrology* 2, 68–87.
- du Bray, E.A., 1994. Compositions of micas in peraluminous granitoids of the eastern Arabian Shield. *Contrib. Mineral. Petrol.* 116, 381–397.
- Brigatti, M.F., Lugli, C., Poppi, L., Ford, E.E., Kile, D.E., 2000. Crystal chemical variations in Li- and Fe-rich micas from Pikes Peak batholith (central Colorado). *Am. Mineral.* 85, 1275–1286.
- Breiter, K., 1997. Teplice rhyolite (Krušné hory Mts., Czech Republic) chemical evidence of a multiply exhausted stratified magma chamber. *Bull. Czech Geol. Surv.* 72, 205–213.
- Breiter, K., Gardenová, N., Kanický, V., Vaculovič, T., 2013. Gallium and germanium geochemistry during magmatic fractionation and post-magmatic alteration in

- different types of granitoids: a case study from the Bohemian Massif, Czech Republic. *Geol. Carpathica* 64, 171–180.
- Breiter, K., Ďurišová, J., Hrstka, T., Korbelová, Z., Hložková, Vaňková M., Vašinová, Galiová M., Kanický, V., Rambousek, P., Kněsl, I., Dobeš, P., Dosbaba, M., 2017a. Assessment of magmatic vs. metasomatic processes in rare-metal granites: a case study of the Cínovec/Zinnwald Sn-W-Li deposit, Central Europe. *Lithos* 292–293, 198–217.
- Breiter, K., Vaňková, M., Vašinová Galiová, M., Korbelová, Z., Kanický, V., 2017b. Lithium and trace element concentrations in trioctahedral micas from granites of different geochemical types measured via laser ablation ICP-MS. *Mineral. Mag.* 81, 15–33.
- Breiter, K., Korbelová, Z., Chládek, Š., Uher, P., Kněsl, I., Rambousek, P., Honig, S., Šešulka, V., 2017c. Diversity of Ti-Sn-Nb-Ta oxide minerals in the classic granite-related magmatic-hydrothermal Cínovec/Zinnwald Sn-W-Li deposit (Czech Republic). *Eur. J. Mineral.* 29, 727–738.
- Breiter, K., Ďurišová, J., Dosbaba, M., 2017d. Quartz chemistry – a step to understanding magmatic-hydrothermal processes in ore-bearing granites: Cínovec/Zinnwald Sn-W-Li deposit, Central Europe. *Ore Geol. Rev.* 90, 25–35.
- Cerný, P., Meintzer, R.E., Anderson, A.J., 1985. Extreme fractionation in rare-element granitic pegmatites: selected examples of data and mechanisms. *Can. Mineral.* 23, 381–421.
- Fengl, M. et al., 1991. Final shut down report of Cínovec mining. Manuscript, Archive of the Czech Geological Survey- Geofond. (in Czech).
- Foster, M.D., 1960. Interpretation of the composition of Li-micas. *U.S. Geol. Surv. Prof. Pap.* 354E, 113–147.
- Haidinger, W., 1845. Handbuch der bestimmenden Mineralogie. Braumüller & Seidel, Wien, pp. 625.
- Hořík, K., Wasternack, J., Berger, H.-J., Breiter, K., Mlčoch, B., Schovánek, P., 1995. Geologische Karte Erzgebirge/Vogtland 1:100 000. Sachsisches Landesamt für Umwelt und Geologie Freiberg.
- Johan, Z., Strnad, L., Johan, V., 2012. Evolution of the Cínovec (Zinnwald) granite cul-pola, Czech Republic: composition of feldspars and micas, a clue to origin of W, Sn mineralization. *Can. Mineral.* 50, 1131–1148.
- Kempe, U., Wolf, D., 2006. Anomalously high Sc contents in ore minerals from Sn-W deposits: possible economic significance and genetic implications. *Ore Geol. Rev.* 28, 103–122.
- Koller, F., Breiter, K., 2003. Variation of Li-, Be-, Rb-, and Sn-contents in micas from Variscan granites of the South Bohemian Pluton. In: International Symposium on Light Elements in Rock-forming Minerals. Nové Město na Moravě, Czech Republic, June 20–25, pp. 40–41.
- Legros, H., Marignac, Ch., Mercadier, J., Cuney, M., Richard, A., Wang, R.-Ch., Charles, N., Lespinasse, M.-Y., 2016. Detailed paragenesis and Li-mica compositions as recorders of the magmatic-hydrothermal evolution of the Maoping W-Sn deposit (Jiangxi, China). *Lithos* 264, 108–124.
- Legros, H., Marignac, C., Tabary, T., Mercadier, J., Richard, A., Cuney, M., Wang, R., Charles, N., Lespinasse, M., 2018. The ore-forming magmatic-hydrothermal system of the Piaotang W-Sn deposit (Jiangxi, China) as seen from Li-mica geochemistry. *Am. Mineral.* 103, 39–54.
- Li, J., Huang, X.-L., He, P.-L., Li, W.-X., Yu, Y., Chen, L., 2015. In situ analyses of micas in the Yashan granite, South China: constraints on magmatic and hydrothermal evolutions of W and Ta-Nb bearing granites. *Ore Geol. Rev.* 65, 793–810.
- Martins, T., Roda-Robles, E., Lima, A., Parseval, P., 2012. Geochemistry and evolution of micas in the Barroso-Alvao pegmatite field, Northern Portugal. *Can. Mineral.* 50, 1117–1129.
- Merlet, C., 1994. An accurate computer correction program for quantitative electron probe microanalysis. *Microchim. Acta* 114 (115), 363–376.
- Mlčoch, B., Skácelová, Z., 2010. Geometry of the Altenberg-Teplice caldera revealed by the borehole and seismic data in its Czech part. *J. Geosci.* 55, 217–229.
- Monier, G., Charoy, B., Cuney, M., Ohnenstetter, D., Robert, J.L., 1987. Évolution spatiale et temporelle de la composition des micas du granite albítique à topaze-lepidolite de Beauvois. *Geol. France* 1987, 179–188.
- Monnier, L., 2018. Utilisation de la signature LA-ICPMS des quartz et des micas pour la reconstitution du fonctionnement d'un système magmatique et hydrothermal polyphasé. Application au complexe Sn-1 d'Échassières (Massif Central, France). Doctoral thesis. University Paul Sabatier, Toulouse.
- Petrík, I., Čík, Š., Miglierini, M., Vaculovič, T., Dianiška, I., Ozdiň, D., 2014. Alpine oxidation of lithium micas in Permian S-type granites (Gemicic unit, Western Carpathians, Slovakia). *Mineral. Mag.* 78, 507–533.
- Raimbault, L., Cuney, M., Azencott, C., Duthou, J.L., Joron, J.L., 1995. Geochemical evidence for a multistage magmatic genesis of Ta-Sn-Li mineralization in the granite at Beauvois, French Massif Central. *Econ. Geol.* 90, 548–596.
- Rieder, M., Hybler, J., Smrčok, L., Weiss, Z., 1996. Refinement of the crystal structure of zinnwaldite 2M₁. *Eur. J. Mineral.* 8, 1241–1248.
- Rieder, M., Cavazzini, G., Dyakonov, Y.S., Frank-Kamenetskii, V.A., Gottardi, G., Guggenheim, S., Kovář, P.V., Müller, G., Neiva, A.M.R., Radoslovich, E.W., Robert, J.L., Sassi, P.F., Takeda, H., Weiss, Z., Wones, D.R., 1999. Nomenclature of micas. *Mineral. Mag.* 73, 267–279.
- Roda, E., Pesquera, A., Velasco, F., 1995. Micas of the muscovite-lepidolite series from the Fregeneda pegmatites (Salamanca, Spain). *Mineral. Petrol.* 55, 145–157.
- Roda-Robles, E., Pesquera, A., Gil-Grespo, P., Torres-Ruiz, J., 2012. From granite to highly evolved pegmatite: a case study of the Pinilla de Fermoselle granite-pegmatite system (Zamora, Spain). *Lithos* 153, 192–207.
- Seifert, T., Sandmann, D., 2006. Mineralogy and geochemistry of indium-bearing polymetallic vein-type deposits: Implications for host minerals from the Freiberg district Eastern Erzgebirge, Germany. *Ore Geol. Rev.* 28, 1–31.
- Seltmann, R., Wetzel, H.-U., Felix, M., Schilka, W., 1987. Brekzien der Altenberger Scholle. Exkursion Führer 34. Jahrestagung der Gesellschaft für geologische Wissenschaften DDR, Berlin.
- Shaw, D.M., 1957. The geochemistry of gallium, indium, thallium – a review. *Phys. Chem. Earth* 2, 548–596.
- Stone, M., Exley, C.S., George, M.C., 1988. Composition of trioctahedral micas in the Cornubian batholith. *Mineral. Mag.* 52, 175–192.
- Syrtsos, L.F., Tabuns, E.V., Volkova, E.V., Badanina, E.V., Vysotskii, Yu.A., 2001. Model for the genesis of Li-F granites in the Orlovka Massif, Eastern Transbaikalia. *Petrology* 9, 313–336.
- Štempruk, M., Šulcuk, Z., 1969. Geochemical profile through an ore-bearing lithium granite. *Econ. Geol.* 64, 392–404.
- Tindle, A.G., Webb, P.C., 1990. Estimation of lithium contents in trioctahedral micas using microprobe data: application to micas from granitic rocks. *Eur. J. Mineral.* 2, 595–610.
- Tischendorf, G., Gottesmann, B., Förster, H.J., Trumbull, R.B., 1997. On Li-bearing micas: estimating Li from electron microprobe analyses and an improved diagram for graphical representation. *Mineral. Mag.* 61, 809–834.
- Van Lichervelde, M., Grégoire, M., Linnen, R.L., Béziat, D., Salvi, S., 2008. Trace element geochemistry by laser ablation ICP-MS of micas associated with Ta mineralization in the Tanco pegmatite, Manitoba, Canada. *Contrib. Mineral. Petrol.* 155, 791–806.
- Vieira, R., Roda-Robles, E., Pesquera, A., Lima, A., 2011. Chemical variation and significance of micas from the Fregeneda-Almendra pegmatitic field (Central-Iberian Zone, Spain and Portugal). *Am. Mineral.* 96, 637–645.
- Walther, D., Breitkreuz, C., Rapprich, V., Kochergina, Y.V., Chlupáčová, M., Lapp, M., Stanek, K., Magna, T., 2016. The Late Carboniferous Schönfeld-Altenberg Depression on the NW margin of the Bohemian Massif (Germany/Czech Republic): volcanosedimentary and magmatic evolution. *J. Geosci.* 61, 371–393.
- Weiss, Z., Rieder, M., Smrčok, L., Petříček, V., Bailey, S.W., 1993. Refinement of the crystal structures of two "protolithionites". *Eur. J. Mineral.* 5, 493–502.
- Wise, M.A., 1995. Trace element chemistry of lithium-rich micas from rare-element granitic pegmatites. *Mineral. Petrol.* 55, 203–215.
- Xie, L., Wang, R.C., Groat, L.A., Zhu, J.C., Huang, F.F., Cempírek, J., 2015. A combined EMPA and LA-ICP-MS study of Li-bearing mica and Sn-Ti oxide minerals from the Qiguling topaz rhyolite (Qitianling District, China): the role of fluorine in origin of tin mineralization. *Ore Geol. Rev.* 65, 779–792.
- Yin, L., Pollard, P.J., Shouxi, H., Taylor, R.G., 1995. Geologic and geochemical characteristics of the Yichun Ta-Nb-Li deposit, Jiangxi province, South China. *Econ. Geol.* 90, 577–585.



The transition from granite to banded aplite-pegmatite sheet complexes: An example from Megiliggar Rocks, Tregonning topaz granite, Cornwall



K. Breiter ^{a,*}, J. Ďurišová ^a, T. Hrstka ^a, Z. Korbelová ^a, M. Vašinová Galiová ^{b,1}, A. Müller ^{c,d}, B. Simons ^e, R.K. Shail ^f, B.J. Williamson ^f, J.A. Davies ^f

^a Institute of Geology of the Czech Academy of Sciences, Rozvojová 269, CZ-16500 Praha, Czech Republic

^b Department of Chemistry, Faculty of Science, Masaryk University, Kotlářská 2, CZ-611 37 Brno, Czech Republic

^c Natural History Museum, University of Oslo, P.O. Box 1172, Blindern, 0318 Oslo, Norway

^d Natural History Museum, Cromwell Road, London SW7 5BD, United Kingdom

^e 14 Park an Fenten, St. Agnes, Cornwall TR5 0AS, United Kingdom

^f Camborne School of Mines, College of Engineering, Mathematics and Physical Sciences, University of Exeter, Penryn Campus, Cornwall TR10 9FE, United Kingdom

ARTICLE INFO

Article history:

Received 22 September 2017

Accepted 13 January 2018

Available online 31 January 2018

Keywords:

Granite

Aplite

Pegmatite

Magmatic layering

Megiliggar Rocks

Cornwall

ABSTRACT

The genetic relationship between a granite pluton and adjacent complex of rare-metal pegmatite-aplite-banded sheets (Megiliggar Sheet Complex - MSC) has been studied at the border of the Tregonning topaz granite at Megiliggar Rocks, Cornwall, SW England. Similarities in whole-rock chemical and mineralogical compositions, together with a gradual change in textures away from the granite margin, provide strong evidence for a genetic link between the Tregonning Granite and MSC. The sheets are likely to represent apophyses of residual melt which escaped from the largely crystallized roof of the granite pluton. The escaping melt was peraluminous, had a composition near the F, B, Li slightly enriched granite minimum, and, in comparison with other Cornish granites, was enriched in F, Li, Rb, Cs, Sn, W, Nb, Ta, and U, and depleted in Fe, Mg, Ca, Sr, Th, Zr, and REE. With increasing distance from the Tregonning Granite, the silicate melt crystallized as homogeneous leucogranite sheets and banded complex sheets (i.e. combinations of bands with granitic, aplitic and pegmatitic textures), then layered aplite-pegmatites; this sequence becoming progressively more depleted in the fluxing and volatile elements F, Li, Rb, and Cs, but showing no change in Zr/Hf ratios. The fixed Zr/Hf ratio is interpreted as indicating a direct genetic link (parental melt) between all rock types, however the melt progressively lost fluxing and volatile elements with distance from the granite pluton, probably due to wall-rock reaction or fluid exsolution and migration via fractures.

Differentiation of the primary melt into Na-Li-F-rich and separate K-B-rich domains was the dominant chemical process responsible for the textural and mineral diversity of the MSC. On a large (cliff-section) scale, the proximal Na-Li-F-rich leucogranite passes through complex sheets into K-B-rich aplite-pegmatites, whilst at a smaller (<1 m) scale, the K-B-rich bands are interspersed (largely overlain) by Na-Li-F-rich segregations. The grain size differences between the aplite and pegmatite could be related to pressure fluctuations and/or undercooling.

© 2018 Elsevier B.V. All rights reserved.

1. Introduction

The genetic relationship between granitic pegmatites and adjacent or enclosing granites has long been debated, particularly whether such pegmatites form from residual, volatile-rich melts sourced from the granites (London, 2008, chapter 5). In the case of pericontact pegmatites, e.g. stockscheider in tin granites in the Erzgebirge (Breiter et al., 2005), and intragranitic pegmatites, e.g. Black Hills, South Dakota

(Norton, 1994) or Pikes Peak, Colorado (Simmons and Heinrich, 1975), a direct genetic link is generally accepted. Stockscheider represent an early product of volatile enrichment at the upper or lateral contacts of a granite melt with non-granite host rocks or a previously emplaced melt batch (Breiter et al., 2005). Intragranitic pegmatites represent late segregations of residual water-rich melt (Shearer et al., 1992). These pegmatite types are commonly found in both strongly peraluminous and subaluminous (S- and A-type) granite plutons.

In the case of typical "classic pegmatites", i.e. large dykes or bodies with strong internal zoning and enrichment of rare minerals/elements, typically intruded into metamorphic rocks distal from granite plutons of appropriate composition, the source of the pegmatitic melt is often inferred (London, 2008, chapter 10). Goad and Černý (1981) introduced

* Corresponding author.

E-mail address: breiter@gli.cas.cz (K. Breiter).

¹ Actual address: Department of Geology and Pedology, Faculty of Forestry and Wood Technology, Mendel University in Brno, Zemědělská 1, 613 00 Brno, Czech Republic.

the term “fertile granite” for the mainly leucocratic granitic plutons which lie proximal to pegmatite fields (mainly of LCT-type). These fulfil the theoretical expectations for fertile starting compositions coupled with long fractionation processes, forming bodies of complex pegmatites (Breaks and Moore, 1992; Černý, 1991). Nevertheless, despite an intensive search, localities enabling the direct study of the transition from a granite pluton to rare-element pegmatite dykes in the host rock are scarce (Autunes et al., 2013; Neiva and Ramos, 2010).

We describe here a superb example from Megiliggars Rocks in Cornwall, SW England. A subhorizontal sheet complex, showing the transition from leucogranites to aplites and pegmatites, is spectacularly displayed over 500 m of coastal cliff exposures at the SE margin of the Tregonning Granite. Although the locality is well-known, published mineralogical investigations and data are relatively sparse (Badham, 1980; Breiter et al., 2016; Bromley, 1989; Duchoslav et al., 2017; Exley and Stone, 1982; Floyd et al., 1993; George et al., 1981; Hall, 1930; Henderson et al., 1989; Hosking, 1952; Simons et al., 2017; Stone, 1969, 1975, 1992; Stone et al., 1988; Stone and George, 1978); the most comprehensive study of aplite-pegmatite banding is that of Stone (1969). The aims of this study are to describe the mineralogy, mineral chemistry and whole-rock geochemistry of the entire range of granitic rocks within the Megiliggars sheets (granites, aplites, pegmatites) and ascertain their relationship(s) with each other and the adjacent Tregonning Granite.

2. Geological setting

The Early Permian Cornubian Batholith of SW England is a classic location for the study of rare-metal granites (e.g. Chappell and Hine, 2006; Charoy, 1986; Manning and Exley, 1984; Müller et al., 2006; Simons et al., 2016; Stone and Exley, 1985; Willis-Richards and Jackson, 1989). These Variscan post-collisional peraluminous granites can be subdivided into five major types (Fig. 1a): two mica (G1), muscovite (G2), biotite (G3), tourmaline (G4) and topaz (G5) granites. The topaz granites are typically medium-grained, equigranular and aphyric alkali feldspar granites (<An₅), and are characterized by lithium-rich micas and up to 3 vol% topaz (Manning et al., 1996; Manning and Hill, 1990; Simons et al., 2016; Stone, 1992). Topaz granites occur principally in the Tregonning Granite and the Nanpean and Hensbarrow stocks within the composite St Austell Granite; the Meldon Dyke, north of the Dartmoor Granite, is a topaz aplite (Simons et al., 2016).

The Tregonning-Godolphin Granite (Stone, 1975, 1992) contains the fine- to medium-grained porphyritic two mica Godolphin Granite in the north, and the Tregonning Granite in the central and southern parts of the pluton which is exposed on the coast. Hall (1930) attributed these coastal exposures to the Godolphin Granite, following early Geological Survey usage (Reid and Flett, 1907), but the composite nature of the pluton was recognised by Stone (1960) and the Tregonning Granite has been distinguished separately in most subsequent work (e.g. Stone, 1975, 1992; Floyd et al., 1993; Simons et al., 2016).

The host rocks to the Tregonning Granite are low-grade regionally- and contact-metamorphosed metasedimentary rocks of the Mylor Slate Formation (Goode and Taylor, 1988; Leveridge and Shail, 2011). Field relations indicate that granite emplacement and contact-metamorphism post-dated the development of folds and cleavages related to both Variscan thrusting (D1 and D2) and post-Variscan extension (D3) (Alexander and Shail, 1996; Pownall et al., 2012; Stone, 1966, 1975). The dominant fabric in the host rocks is a gently SE-dipping S3 crenulation cleavage (S2 of Stone, 1966) that commonly transposes earlier fabrics and locally contains variably boudinaged veins of metamorphic quartz (Alexander and Shail, 1996). The history of pre- and post-granite vein development and the associated fluid characteristics has been described by Wilkinson (1990, 1991) and Gleeson et al. (2000).

A series of leucocratic, partly layered granites, termed the “roof complex” (Stone, 1975), lies along the horizontal upper contact of the

Tregonning Granite with the Mylor Slate Formation. At the SE margin of the Tregonning Granite, the roof complex is represented by gently SE-dipping leucogranite and aplite-pegmatite sheets within the Mylor Slate Formation that are continuously exposed in a 30–50 m high cliff section over a distance of c. 500 m between Legereath Zawn (“zawn” is a Cornish term meaning a deep and narrow sea-inlet cut by erosion into sea-cliffs, and with steep or vertical side-walls) and Tremearne Par (“Megiliggars Rocks” 50°04'26.4" N, 5°24'42.6" W) (Fig. 2a). We hereafter refer collectively to these sheets as the “Megiliggars Sheet Complex” (MSC). The geometrical relations of these sheets, and their relations to the Tregonning Granite, have been variably represented in sketch cross-sections (Hall, 1930; Stone, 1975; Badham, 1980; Exley and Stone, 1982; Bromley, 1989; Floyd et al., 1993; Fig. 1b in this work).

The easternmost exposure of the Tregonning Granite occurs around Legereath Zawn where it post-dates an earlier biotite granite porphyry (“elvan”) dyke (Hall, 1930), the ‘Legereath granite porphyry’ of Stone (1975) or ‘Legereath Zawn Elvan’ of Breiter et al. (2016). The uppermost part of the Tregonning Granite is exposed in the western, northern and eastern walls of Legereath Zawn. In the northern wall it occupies the full cliff height (50 m) but moving eastwards passes, at an elevation of c. 15 m, into the lowermost sheet of the MSC within the Mylor Slate Formation. We concur with Hall (1930), that there is also a magmatic linkage, via a short sheet segment, between this lowermost sheet and the uppermost part of the Tregonning Granite towards the base of the cliff on the eastern side of Legereath Zawn. Although the contacts between the more easterly MSC sheets and the Tregonning Granite are not exposed, we infer that all the MSC was sourced in a comparable manner from the upper parts of the Tregonning Granite.

3. Analytical methods

The whole-rock (WR) major element oxide determinations (using wet techniques, for detail see <http://www.geology.cz/extranet-eng/services/laboratories/inorganic-analysis>) were carried out at the Czech Geological Survey, Praha. Replicate analyses of an international reference material (JG-3; Geological Survey of Japan) yielded an average error (1 sigma) of ±1% with respect to the recommended values (Govindaraju, 1994). Trace elements were determined by ICP mass spectrometry following lithium metaborate/tetraborate fusion or nitric acid digestion in the laboratories of the Bureau Veritas, Vancouver, Canada (For details including limits of detection see http://acmelab.com/wp-content/uploads/2009/03/BVM_2017-Fee-Schedule_v4_14Sep2017.pdf, laboratory codes LF100 and MA200, and the Supplementary Table 11.).

A TESCAN Integrated Mineral Analyzer (TIMA) was used for automated mineralogical, modal and textural analysis employing Liberation Analysis mode (Gottlieb et al., 2000). Liberation Analysis mode, with ‘high-resolution mapping’, includes the collection of backscattered electron (BSE) and EDS data on a regular grid (10 µm point spacing in our case). At each point, the BSE level is determined. If the BSE level is above a certain threshold, the beam is kept directed on this spot until a predefined number of X-ray counts (1000 in our case) from the spectrometer are collected. The individual points are grouped based on a similarity search algorithm and areas of coherent BSE and EDS data merged to produce segments (i.e. mineral grains). Individual spectra from points within each segment are summed. The average BSE value is also calculated. Data from each segment are then compared against a classification scheme to identify the mineral and assign its chemistry and density (Hrstka et al., in prep.). The results are plotted in the form of a map showing the distribution of minerals within the sample.

Minerals were chemically analyzed using a Cameca SX 100 electron microprobe, in wavelength-dispersive mode, at the Institute of Geology CAS. Analytical conditions for silicates were: accelerating voltage 15 kV, beam current 10 nA, beam diameter 2 µm. The following calibration standards were used: Na, Al – jadeite, Mg, Si, Ca – diopside, K – leucite, Ti – rutile, P – apatite, Mn – MnCr₂O₄, Fe – magnetite, F – fluorite, and Rb – RbCl. The matrix correction procedure X-Phi (Merlet, 1994) was

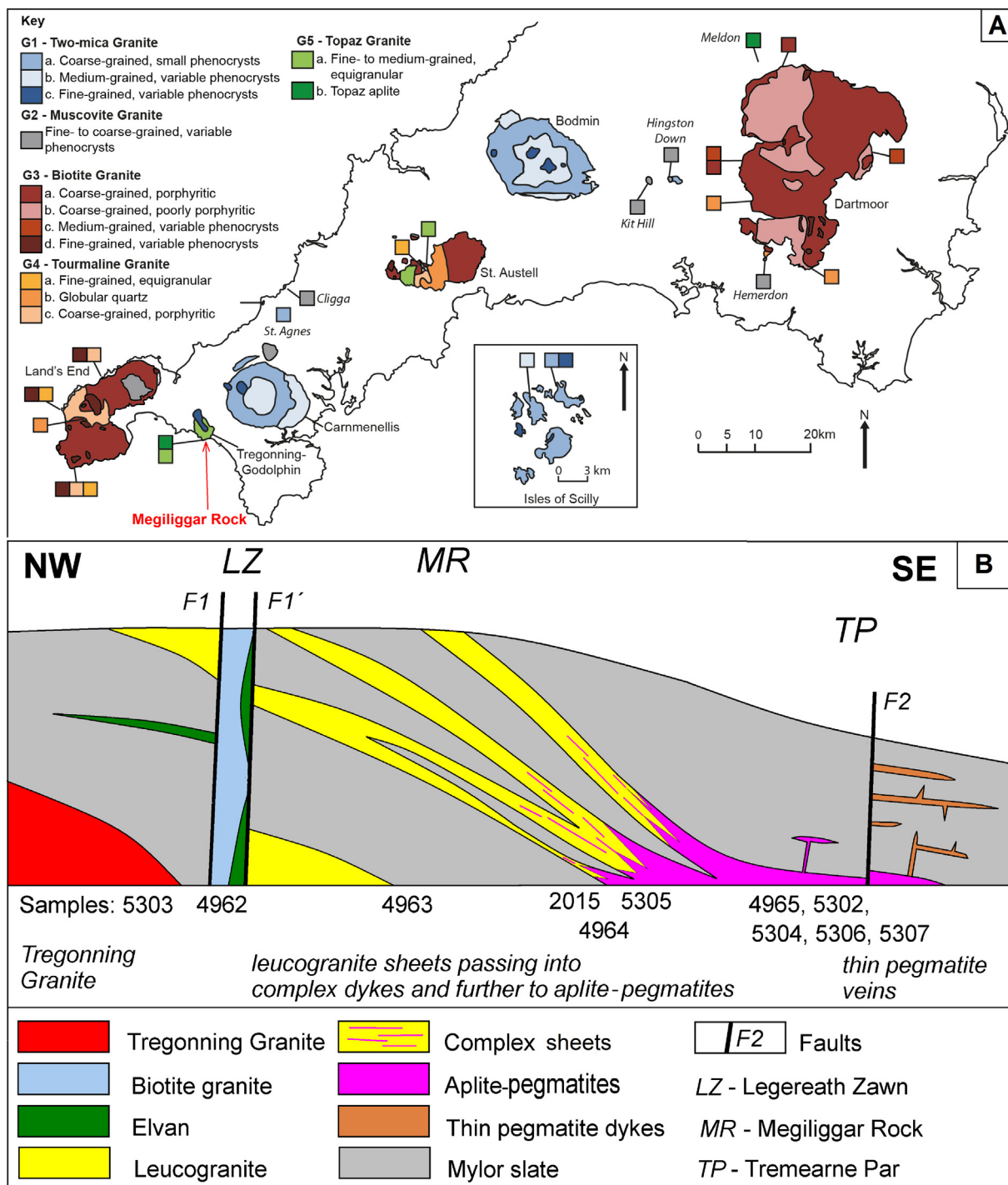


Fig. 1. A - Geological sketch map of Cornwall (acc. to Simons et al., 2016); B - Schematic section through Megiliggar Rocks showing the location of samples (not to scale). The total length of the section is ca. 600 m. The sheets are likely to represent apophyses of residual melt which escaped from the largely crystallized roof of the granite pluton. With increasing distance from the Tregonning Granite, the silicate melt crystallized as homogeneous leucogranite sheets, banded complex sheets (i.e. combinations bands with granitic, aplite and pegmatic textures), and layered aplite-pegmatites. A gradual change in textures away from the granite margin, together with similarities in whole-rock chemical compositions, provide strong evidence for a genetic link between the Tregonning Granite and Megiliggar Sheet Complex.

applied. The empirical formulae of the feldspars were calculated based on 8 oxygen atoms per formula unit (8 O apfu); the empirical formulae of the micas were calculated based on 44 negative charges. The empirical formulae of the tourmaline were calculated based on 24.5 oxygen atoms per formula unit (boron excluded).

The Sn, W, Nb, Ta-oxide minerals and zircon were analyzed at an accelerating voltage and beam current of 15 kV and 7 nA, and 15 kV and 10 nA, respectively, with a beam diameter of 1 to 3 μm . The counting times on each peak were optimized for individual elements according

to their expected concentrations (10–60 s), and half that time was used to obtain background counts. X-ray lines and background offsets were selected to minimize interference.

Lithium and trace elements in micas and tourmalines were determined using LA-ICP-MS at the Masaryk University, Brno. Micas were analyzed using a Nd:YAG-based laser ablation system at a wavelength of 213 nm (New Wave Research, Inc., Fremont, CA, USA), which was coupled to a ICP-QMS instrument with quadrupole mass spectrometer (Agilent 7500ce, Agilent Technologies, Santa Clara, CA, USA). Tourmaline

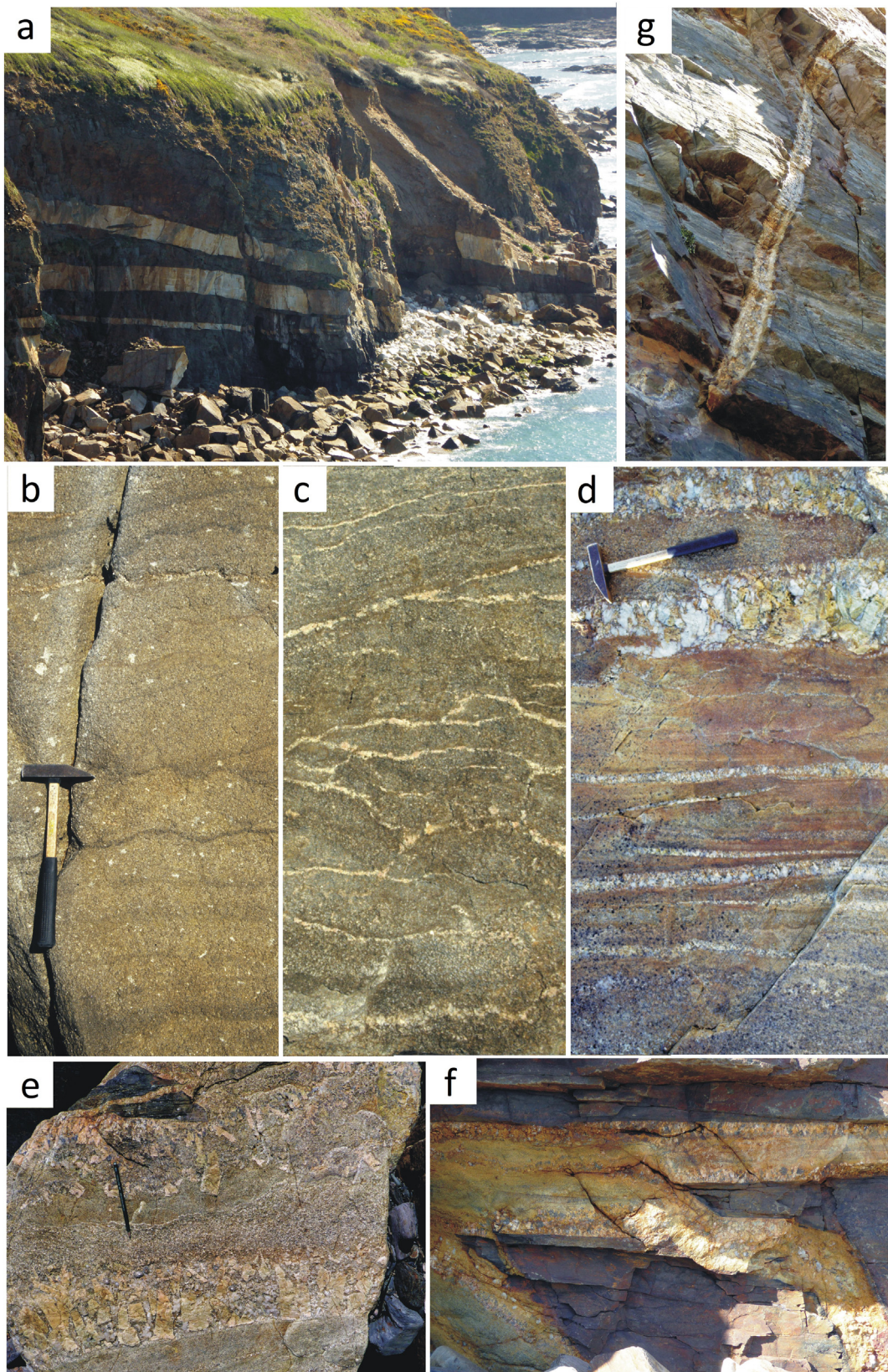


Fig. 2. Field photographs: a, cliff at Megiliggar Rocks, western part of the major leucogranite sheets (up to 2.5 m thick) laterally (to the right) passing into 'complex sheets'; b–e, the textural evolution of the sheets with increasing distance from the Tregonning Granite (from West to East): Close to the granite the sheets are more or less homogeneous (leucocratic sheet granite). About 50 m from the contact the first layered structures can be traced caused by a local enrichment in mica (b). Further on (c, 75 m) grain-size differences between individual layers start to develop, in addition to the local mica enrichments, and about 100 m away the first thin veinlets with pegmatitic textures appear within the sheet (c). Further east the borders between the layers become more distinct; the differences in the grain sizes of the aplitic, granitic and pegmatitic layers increases together with the thickness in particular of the pegmatitic layers (d to e). f, bifurcation of a thin (~30 cm) aplite-pegmatite sheet, showing comb K-feldspar crystals along both the contact in the upper sheet vs. central position in the lower sheet; g, steeply inclined, thin (~10–15 cm) aplite-pegmatite sheet cutting the slate in the eastern part of the cliff.

grains were analyzed with an ArF* excimer-based laser ablation system Analyte G2 (Teledyne CETAC Technologies) at a wavelength of 193 nm, which was coupled to an Element2 (Thermo Fischer Scientific) ICP-MS instrument with double focusing electrostatic and magnetic sectors. Operating conditions of both the LA-ICP-QMS and LA-ICP-SFMS were optimized with the aim of obtaining maximum signal-to-background ratios and sensitivity, minimum spectral and non-spectral interferences and best signal stability, and then kept constant throughout the analyses. Micas were ablated under optimal conditions of: fluence ($13 \text{ J} \cdot \text{cm}^{-2}$), frequency (10 Hz), ablation dwell time (40 s), duration of Ar-He gas blank measurement (40 s) and laser beam spot diameter ($80 \mu\text{m}$). For tourmaline, a spot diameter of $30 \mu\text{m}$, fluence of $3 \text{ J} \cdot \text{cm}^{-2}$, frequency of 10 Hz, 60 s ablation dwell time and 60 s Ar-He gas blank measurement were applied. Silica was employed as the internal reference element having been previously determined in samples by electron microprobe. The systems were calibrated using artificial glass NIST610 and NIST612 to quantify the concentrations of Li, Al, Sc, Ga, Ge, Nb, In, Sn, Cs, Ta, W and Tl in mica, and Li, Be, B, Al, Sc, Zn, Ga, Ge, Rb, Nb, In, Sn, Cs, W, and Tl in tourmaline.

Trace element concentrations (Al, B, Be, Fe, Ge, Li, Mn, P, Rb, Sn, Sr, and Ti) in quartz were determined by LA-ICP-MS at the Institute of Geology CAS. This utilized a Thermo-Finnigan Element 2 sector field mass spectrometer coupled to an Analyte Excite 193 nm excimer laser (Photon Machines). Analyses were conducted using a repetition rate of 10–20 Hz, laser fluence of $3\text{--}5 \text{ J} \cdot \text{cm}^{-2}$, beam size of $40\text{--}80 \mu\text{m}$; all parameters were optimized against the intensity of signals. The ablated material was transported by high purity He gas from the laser ablation cell. Time-resolved signal data were processed using Glitter software (<http://www.gleiter-gemoc.com/>). The isotopes ^{29}Si and ^{30}Si were used as internal standards based on the assumption that the analyzed quartz contains 99.95 wt% SiO_2 . The data were calibrated using artificial glass NIST612. For more details see Breiter et al. (2013).

4. Petrology of the Megiliggar Sheet Complex (MSC)

4.1. Textural varieties of MSC samples studied

The Tregonning Granite is a medium-grained equigranular granite, light in colour and composed of quartz, albite, perthitic K-feldspar, zinnwaldite/lepidolite micas, and Li-F-rich schorl. Apatite is minor, while rutile, Fe-columbite, and zircon are accessory (typical sample #5303, Fig. 3a).

A small body of fine-grained equigranular granite with macroscopic black mica, termed a biotite granite dyke, was found within the faulted zone at Legereath Zawn, in association with a typical granite-porphyry ("elvan") dyke. The biotite granite is composed of quartz, albite, K-feldspar, strongly muscovitized Li-Fe-mica (primarily siderophyllite-zinnwaldite in composition) and schorl. Apatite is minor; rutile, zircon and monazite are accessory minerals (sample #4962).

SE from Legereath Zawn, the following principal types (facies) can be defined within the sheets of the MSC (Fig. 1b):

- Homogeneous leucogranite which forms three major sheets, each up to 3 m thick and 200 m long (Fig. 2a). This rock is fine- to medium grained, equigranular and nearly white in colour. It is composed of quartz, albite > K-feldspar, zinnwaldite-trilithionite mica, and Li-enriched fluoro-schorl. Sub-parallel dark layers up to 3 cm thick that are enriched in mica are locally conspicuous (Fig. 2b, c). Amblygonite and apatite are minor; zircon, Mn-columbite, and uraninite are accessory (typical sample #4963).
- These fine-to medium grained leucogranite sheets also contain a fine-layered aplitic facies and minor pods and laminae of pegmatitic facies. Further SE, the proportions of granitic, aplitic and pegmatitic facies became nearly equal forming "complex sheets" (Fig. 2d, e). Some aplitic and pegmatitic layers form rhythmic structures; textural borders are smooth and gradational. The direction of crystallization, i.e. relative

age of layers, may be inferred from orientation of feldspar crystals in unidirectional solidification textures (UST) (London, 2008). In some cases, the layering is a product of repeated injection (compare Bromley, 1989) with symmetrical zoning. These sheets are enriched in Li and F; they contain pinkish Li-bearing zinnwaldite-trilithionite micas and Li-enriched (deep green) tourmaline in some laminae, but muscovite and black schorl in others. Albite dominates over K-feldspar. Manganese-rich apatite is minor; fluorite, monazite, xenotime, zircon, columbite, rutile, cassiterite, wolframite, uraninite, pyrite, arsenopyrite, molybdenite and native Bi are accessory minerals. Typical samples are #2015 (fine layered aplite), 4964 (fine-grained granite with pegmatitic laminae), 5304 (fine-grained granite rich in tourmaline), 5305 (layered combination of granite, pegmatite and aplite, Fig. 3b).

- Major bodies of aplite/coarse-grained granite/pegmatite and abundant thinner aplite/pegmatite sheets with very different textures and scales of layering appear mainly in flat outcrops on the beach, and are subordinate in the cliff. They are composed of irregular and locally interpenetrative domains (layers, nests, dykes) of <1 mm-sized (aplitic), 1–2 cm-sized (granitic) and coarser (pegmatitic) matter. Contacts are both sharp and gradational; in-situ fractionation is combined here with repeated injection of similar magma (thin laminas crystallizing from both contacts inwards cross an older layering with upwards oriented crystallization). All textural varieties within these sheets contain more K-feldspar than albite, and are rich in tourmaline (schorl to foitite). Mica is in all cases muscovite/phengite in composition. Apatite is minor, and zircon, monazite, xenotime, uraninite, sphalerite, pyrite, molybdenite, and native Bi are accessory. Rocks are Li- and F-poor. Typical samples are #4965 (layered aplite from centre of a thick sheet), #5306 (aplite at the border of a sheet), and #5307 (granitopegmatite, i.e. very coarse grained rock with granitic texture, centre of the sheet next to #5306, Fig. 3c). Quartz-cored tourmaline is also present (very coarse-grained granite, #5302).
- Thin pegmatite or aplite/pegmatite dykes (usually <20 cm, Fig. 3c, d) occur in the eastern part of the cliff. These dykes often change orientation (horizontal vs. vertical), diverge and coalesce. The pegmatite-like textures appear mainly along the contacts (Fig. 3d), but locally change laterally to pericontact and central positions (Fig. 2f). These dykes are tourmaline and muscovite-dominant, and Li- and F-poor. Occasionally, texturally similar, but steeply-inclined sheets occur (Fig. 2g).
- Quartz veins, variably developed throughout the study area, but conspicuous in the easternmost part around Tremearne Par (Badham, 1980; Bromley, 1989; Hosking, 1952). These are deformed (folded and/or boudinaged) within the S3 cleavage and pre-date granite emplacement; they were sourced from Variscan metamorphic fluids and are not part of the MSC.

For further description and interpretation, samples have been classified into three principal groups, based on a combination of textures, whole-rock chemistry, and mineral abundances and compositions: (i) granites, i.e. fine- to medium-grained homogeneous rocks (Tregonning Granite #5303, leucogranite sheet #4963), (ii) Li-mica-dominated complex sheets (#2015, 4964, 5305, 5304), and (iii) muscovite-tourmaline-dominated aplite-pegmatites (#4965, 5302, 5306, 5307) [The term aplite-pegmatite is hereafter used for intimate banding of fine-grained (aplitic) and coarse-grained (pegmatitic) layers (Jahns and Tuttle, 1963; London, 2008)]. This classification is somewhat simplistic, as combinations of textural types and transitional facies are common, but is necessary to allow further description, interpretation, and discussion.

4.2. Detail zoning of the sheets

Two samples of fine-layered rock were chosen for a detailed study of mineralogical and geochemical zoning: a Li-mica dominated sample

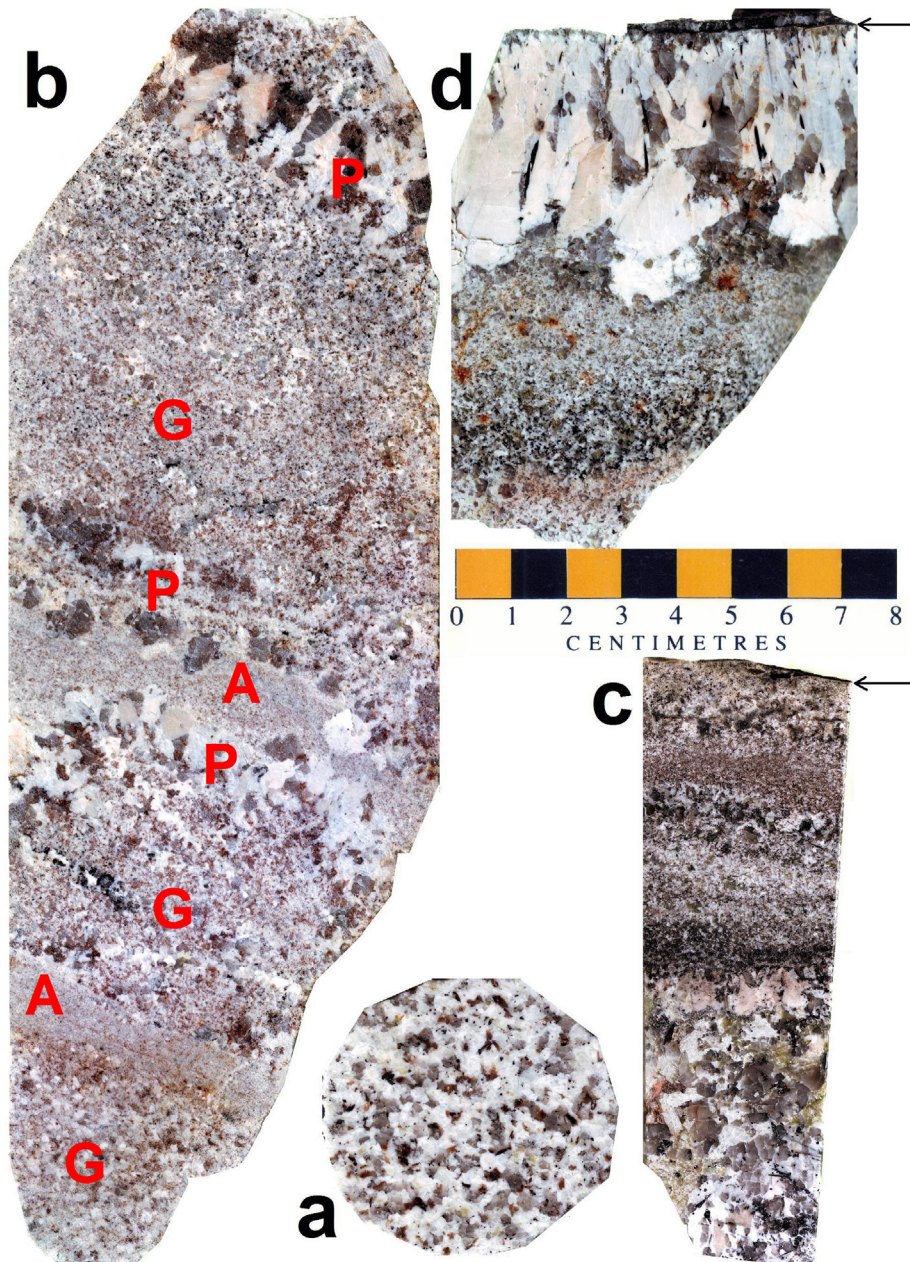


Fig. 3. Rock textures: a, Tregonning granite (#5303); b, typical layering in the 'complex sheets' composed of granitic (G), pegmatitic (P) and aplitic (A) layers (#5305); c, aplite-pegmatite sheet with aplitic layer near the contact and coarse-grained granite to pegmatite in the centre (#5306 resp. #5307); d, aplite-pegmatite sheet with pegmatitic (stockscheider-like) rim and aplitic centre. Contact plane between the sheets and Mylor Slates is highlighted by arrows.

from a complex sheet (#2015, Fig. 4), and a muscovite-tourmaline-dominated aplite domain of an aplite-pegmatite sheet (#4965, Fig. 5). Mineral maps across the zoning were constructed and mineral compositions in texturally distinct layers (laminae) were computed using TIMA-technology. Approximate chemical compositions of individual layers and WR (Fig. 6, Supplementary Tables 1, 2) were computed from modal compositions of layers and chemical composition of rock-forming minerals determined by electron microprobe, with Li by the LA-ICP-MS.

The texture of sample #2015, from a Li, F-enriched complex sheet, is composite and can be divided into three sections. The lower part of the sequence, termed layers #1 → 7, evolved systematically with a decrease in the modal abundance of K-feldspar (28 → 6.5 vol%), quartz (33 → 25 vol%), and tourmaline (8 → 4 vol%), along with a strong increase in the modal abundance of albite (16 → 74 vol%, Fig. 4). In the middle section, lines 8 → 11, the modal abundance of minerals is much more variable,

as it is in the upper part of the sample, layers #12 → 22, which is also rich in albite (38–74 vol%), zinnwaldite (mostly 5–6 vol%) and topaz (up to 11 vol% in lines 19 and 20), and poor in K-feldspar (mostly <10 vol%), tourmaline (mostly <1 vol%) and muscovite (mostly <2 vol%). Additionally, the grain size of the albite-dominated layers is significantly finer than that of K-feldspar dominated layers.

Distinctive chemical changes appear between layers #11 and 12: K and B decrease, while F increases (Fig. 6a). Mineralogically, this is due to muscovite and tourmaline giving way to zinnwaldite and topaz. The pairs Na–K and F–B are negatively correlated (Fig. 6b, c) due to mineralogical antagonism of albite vs. K-feldspar and lepidolite vs. tourmaline. Boron and Fe show a positive trend (Fig. 6d), both hosted dominantly in tourmaline, and F with Mn, as F-rich micas are relatively enriched in Mn. The relationship between F and B vs. the Ab–Kfs ratio is more complex; nevertheless, F- (resp. B-) enrichment in Ab- (resp. Kfs-) dominated layers is clear.

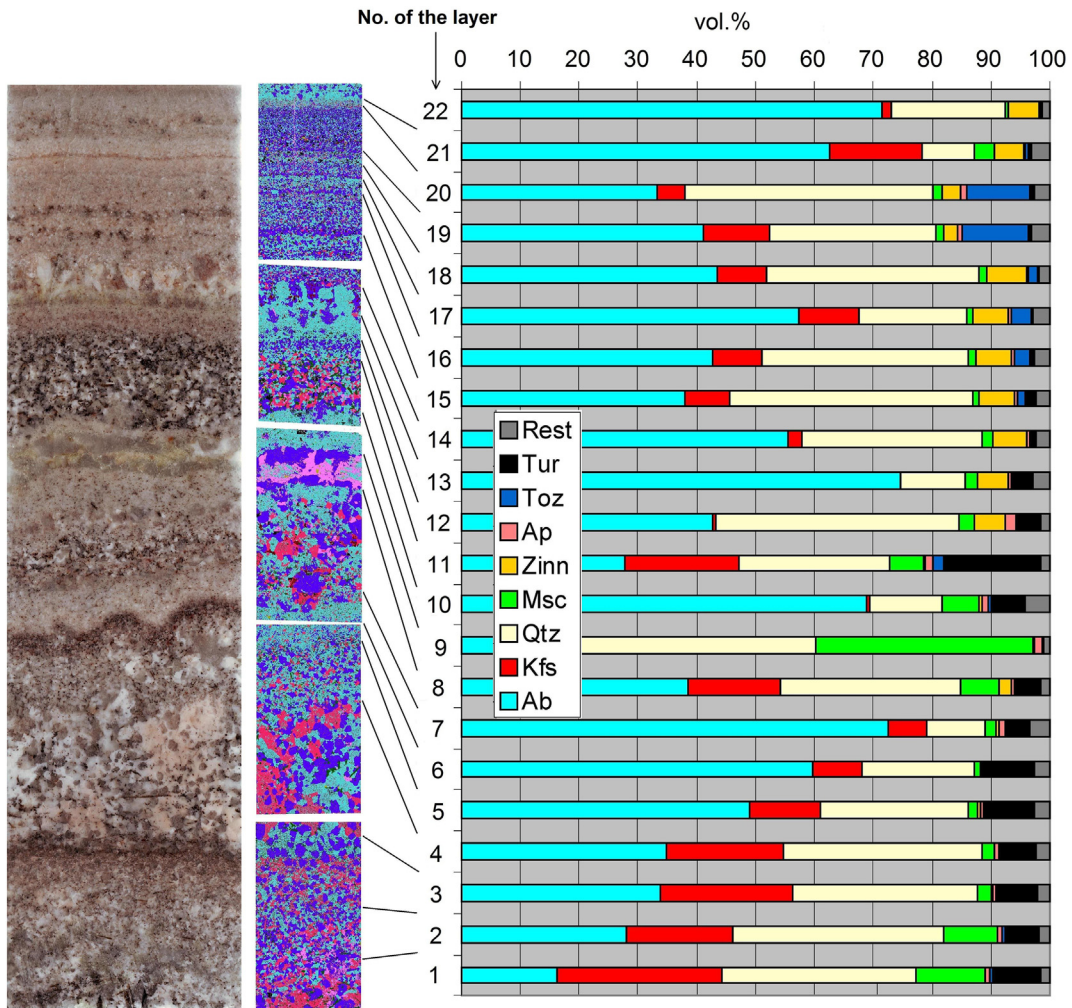


Fig. 4. Detailed investigation of a finely-banded portion of a complex sheet (sample 2015): left - photo of an 18 cm wide cut sample face; Central - mineral map determined by TIMA (in the middle, Kfs (K-feldspar) – red, Ab (Albite) – light blue, Qtz (Quartz) – dark blue, Msc (Muscovite) – pink, Zin (Zinnwaldite) – brown, Tur (Tourmaline) – green), Rest – other accessory minerals; Right - mineral composition of individual bands (vol%). Crystallization of the rock proceeded upwards.

The tourmaline-muscovite aplite-pegmatite is dominated by aplite (#4965, Fig. 5) and shows only moderate variability in mineral compositions in layers #1–5, with 23–42 vol% K-feldspar, 12–26 vol% albite, 30–47 vol% quartz, 4–8 vol% muscovite and 4–10 vol% schorl. The zoning is visually apparent from a variation in grain size and orientation of tourmaline grains. There is no general trend in composition from layers #1 → 5. Layer #6 differs remarkably and is rich in topaz and muscovite (22.4 and 32.4 vol% resp.), representing a vug filled with residual melt/fluid. Surprisingly, even though sample #4965 contains F-poor tourmaline and mica, the WR content of fluorine is, due to the high topaz vol% in layer #6, higher than that in sample #2015 (Fig. 6c).

5. Whole-rock chemical compositions

All rock types forming the MSC are chemically similar, being rich in silica (69–76 wt% SiO₂), leucocratic, and strongly peraluminous (ASI = 1.23–1.46, (molar Al₂O₃ / CaO + K₂O + Na₂O)) (Table 1, Fig. 7). All rock types are, in comparison with other Cornubian granites, rich in alumina (mostly 14–16 wt% Al₂O₃), phosphorus (0.3–0.7 wt% P₂O₅), Li, Nb, Ta and Sn, but poor in iron (mostly <1 wt% FeO_{tot}), magnesium (mostly <0.2 wt% MgO), calcium (with one exception ≤0.6 wt% CaO), Zr and REE (Chappell and Hine, 2006; Simons et al., 2016).

Comparing the three main groups of rocks, the granites (comprising the Tregonning Granite and leucogranite sheet) are relatively poor in silica (69.2–71.1 wt% SiO₂) and potassium (4.2–5.3 wt% K₂O), but rich in sodium (3.4–4.3 wt% Na₂O), lithium (ca. 0.40 wt% Li₂O), fluorine (0.9–1.4 wt% F), Rb (1400–1830 ppm), and Cs (200–250 ppm). In contrast, the aplite/pegmatite sheets are rich in silica (72.1–76.3 wt% SiO₂) and potassium (mostly >5 wt% K₂O), but poor in sodium (1.9–2.9 wt% Na₂O), lithium (<0.03 wt% Li₂O), fluorine (0.2–0.64 wt% F), Rb (356–755 ppm), and Cs (17–33 ppm). High-field strength trace elements (HFSE) are highly variable in their concentrations: Sn (13–80 ppm), W (4–46 ppm), Nb (17–69 ppm), Ta (6–50 ppm), and Zr (9–29 ppm). The chemical composition of the ‘complex sheets’ usually lies between the “granites” and “aplite-pegmatites”.

Within the WR data, there is a strong positive correlation between Li, Rb, F, and Na (i.e. elements hosted in Li-mica and albite), and among all these elements and the Mn/Fe value. All rock types, excluding biotite granite, have very low contents of all REEs, flat REE distribution pattern, and a distinct tetrad effect (Fig. 7e). The extremely low REE-content of the sample 4963 probably indicates strong interaction with a late- or post-magmatic fluid. The biotite granite has an REE pattern typical of common granitoids with a relative enrichment of LREE over HREE. The granites and sheets from Megiliggar show an extreme enrichment in Li, Nb, Ta, Sn and W relative to other Cornubian granites, and show

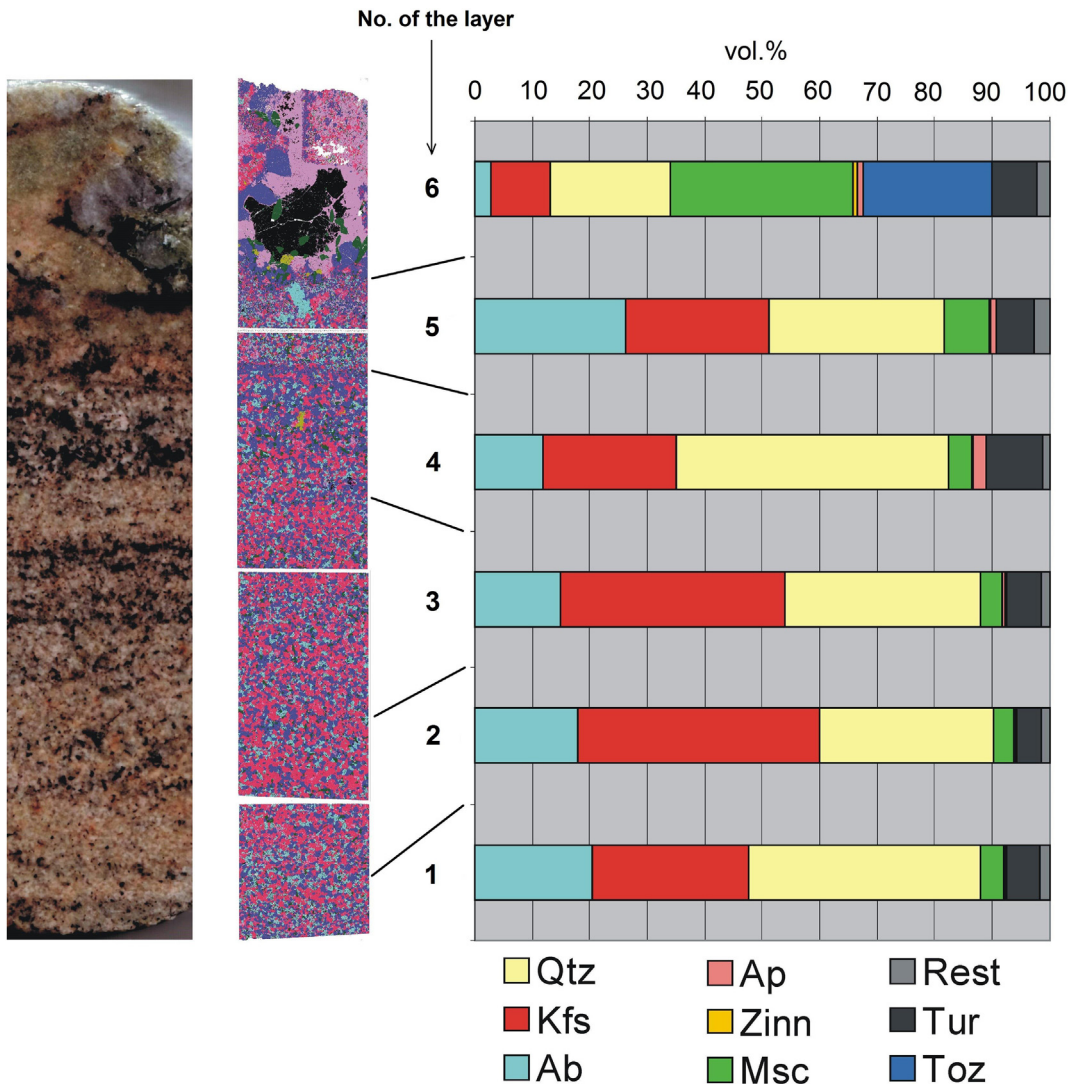


Fig. 5. Detail investigation of a tourmaline aplite (sample 4965): left - photo of a 12.5 cm wide sample cut face; middle - mineral map determined by TIMA (K-feldspar) – red, Ab (Albite) – light blue, Qtz (Quartz) – dark blue, Msc (Muscovite) – pink, Tur (Tourmaline) – dark green, Toz (Topaz) – black, Ap (Apatite) – yellow-green), Rest – other accessory minerals; Right – mineral composition of individual bands (vol%). The crystallization proceeded upwards.

significantly lower Zr and REE (e.g. Chappell and Hine, 2006; Müller et al., 2006; Simons et al., 2016, 2017).

The biotite granite differs from all the above mentioned rock types in being slightly enriched in FeO_{tot} (1.37 wt%), MgO (0.26 wt%) and strongly enriched in U (39 ppm), Th (7 ppm) and all REEs (for example Ce 25 ppm).

6. Minerals

Quartz typically has consistent primary abundances of trace elements and therefore gives reliable information about the composition of the magma from which it crystallized (e.g. Jacamon and Larsen, 2009). The chemical composition of quartz in samples from Megiliggar is characterized both by a relatively large scatter of trace elements in each sample, and, conversely, by similarity in composition across all samples (Fig. 8, Supplementary Table 3). Surprising is the strong positive correlation between Ti and Al, which is very different to the usual negative correlation between these elements in common granites, with Ti decreasing with increasing Al during fractionation (Breiter et al., 2014; Müller et al., 2010). The Al/Ti ratio, usually a good indicator of magma fractionation, has a narrow interval of 10–40. Quartz from all samples is very rich in Li,

but poor in Ge. In comparison with a large dataset for Variscan granites and pegmatites (Breiter et al., 2013, 2014), quartz from the MSC shows trace element trends which are more like those of granites than pegmatites. Indications of a hydrothermal origin, low contents of Ti (<5 ppm) coupled with very high Al (>1000 ppm) (Rusk et al., 2008) were not found.

K-feldspar (Kfs) is present in two textural varieties: (i) as perthite which appears in rock facies with typical pegmatite textures, usually enriched in schorl, and (ii) as small phenocrysts (<25 mm) in the Tregonning Granite. Homogeneous Kfs, often with abundant inclusions of albite (but not admixtures), prevails in other rock types (groundmass in the Tregonning Granite, leucogranite sheet, aplites). In layered rock, the tourmaline-rich sample #4965 contains only homogeneous Kfs, while sample #2015 contains perthite in the layer #4 and homogeneous Kfs in all other layers.

Chemically, two groups of K-feldspars may be distinguished (Supplementary Table 4): (i) relatively more evolved P-enriched (>0.3 wt% P_2O_5) grains with 0.2–0.6 wt% Rb_2O were found in the granites (incl. biotite granite from Legereath Zawn) and complex sheets, and (ii) less evolved crystals, with $\text{P}_2\text{O}_5 < 0.3$ wt% and $\text{Rb}_2\text{O} < 0.3$ wt%, in the aplite-pegmatites. The abundance of P and Rb does not relate to whether the K-feldspar has a homogeneous or perthitic texture.

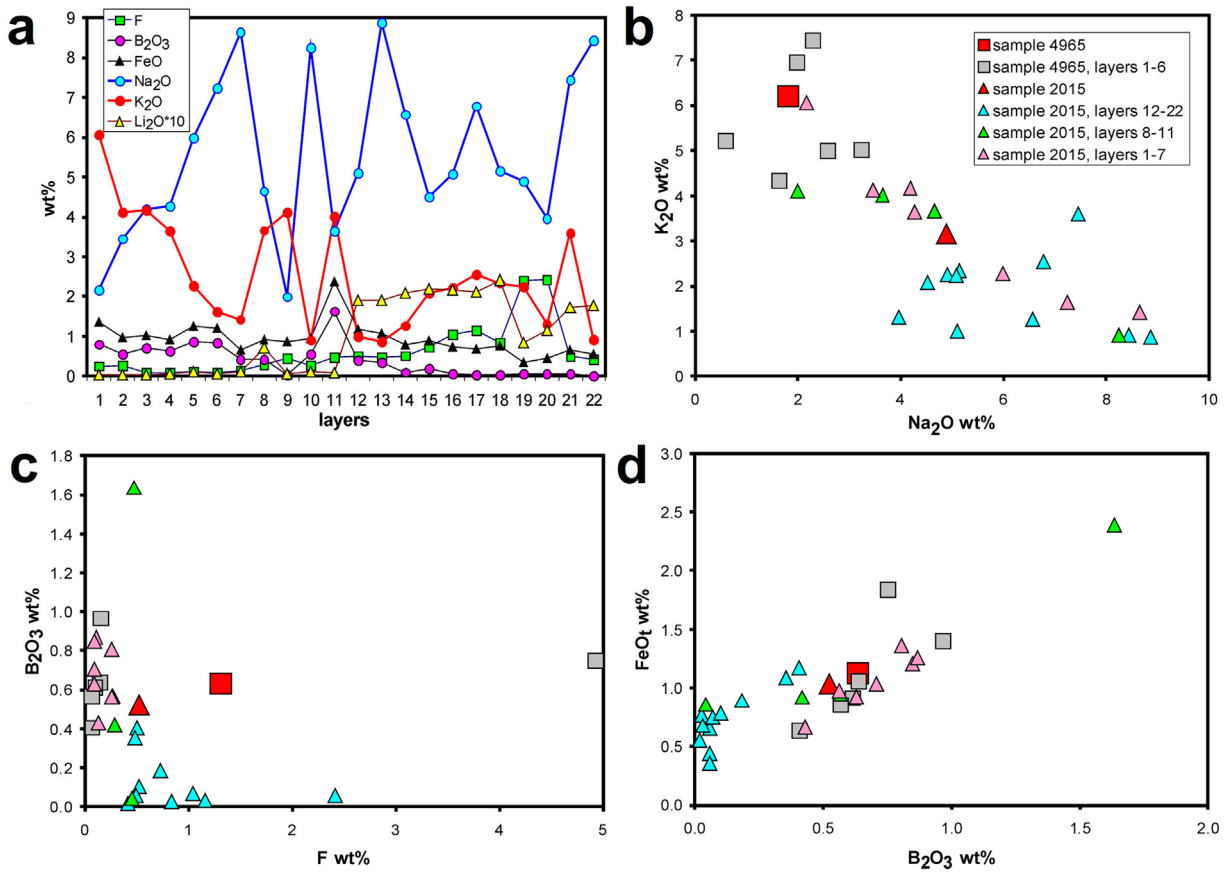


Fig. 6. Approximate chemical composition of individual layers in finely banded rocks computed from modal compositions and chemical analyses of minerals: a, distribution of selected elements across the layering (#2015); b, K₂O vs. Na₂O; c, B₂O₃ vs. F; d, FeO vs. B. Mean values of the whole samples are highlighted by red marks in diagrams b–d.

Albite is the main plagioclase phase containing <1.2 wt% CaO (<0.06 apfu Ca, Supplementary Table 2), in line with previous studies (Simons et al., 2017; Stone, 1992). The highest content of Ca was found in albite from the biotite granite dyke (0.47–1.18 wt% CaO), while nearly all grains from the other rock types contain albite with <0.4 wt% CaO. The Li-mica bearing complex sheets contain P-enriched albite (0.4–0.6 wt% P₂O₅, 0.015–0.022 apfu P), while albite from the Tregonning Granite and from the tourmaline-bearing facies of the sheets usually contains <0.1 wt% P₂O₅ (<0.004 apfu P).

Micas usually form small grains (<1 mm across) that are evenly distributed through the samples. Aggregates of larger muscovite flakes were only found in some thin laminae within complex sheets, e.g. layer #9 in sample 2015 (Fig. 4), and layer #6 in sample 4965 (Fig. 5). Three types of mica can be distinguished in the rocks studied: (i) zinnwaldite-trilithionite group (hereafter “lepidolite”), (ii) muscovite-phengite group (hereafter “muscovite”), and (iii) mica slightly enriched in Li within the siderophyllite–muscovite–zinnwaldite space (hereafter “Li-Fe-Al-mica”). This mica subdivision is represented on binary plots of mineral composition (Fig. 9a, b).

Lepidolite dominates in granites (e.g. outcrops of the Tregonning Granite and leucogranite sheets) and has also been found in the complex sheets. It is rich in Li (4–5 wt% Li₂O), Rb (0.8–1.1 wt% Rb₂O) and F (7.8–9 wt% F) (Supplementary Table 5); all these elements show a positive correlation. Muscovite is present in complex sheets and dominates in aplite-pegmatites. It is enriched in Fe (typically containing 2 wt% FeO, occasionally up to 4 wt%), but poor in Li, Rb and F (<0.1 wt% Li₂O, <0.2 wt% Rb₂O, <0.1 wt% F). In the fine-layered parts of complex sheets, muscovite and lepidolite micas alternate (Fig. 9c).

‘Li-Fe-Al-mica’ was found dominantly in the biotite granite dyke and occasionally also in the complex sheets. Macroscopically, this mica is

black, resembling common biotite, which strongly differs from the light beige to pink colour of zinnwaldite–trilithionite. In comparison to the Li-micas of the zinnwaldite–trilithionite series, this mica is lower in Li (0.8–2.15 wt% Li₂O), Rb (0.3–0.6 wt% Rb₂O) and F (3–4 wt% F) and strongly variable in Al and Fe (22–31 wt% Al₂O₃, 4–18 wt% FeO), with an approximate mean formula of K₂Li_{1.6}Fe₁Al_{2.7}(Si₆Al₂O₂₀)F_{1.5}(OH)_{2.5}.

Of the trace elements, Cs is mainly present in lepidolite (500–6000 ppm, Supplementary Table 6), whilst it does not exceed 100 ppm in muscovite and Li-Fe-Al-mica. Similarly, Ta (Fig. 9d) and W have a positive correlation with Li, reaching 25–75 ppm Ta and 300–600 ppm W in lepidolite from the Tregonning Granite and leucogranite sheet. Conversely, the highest content of Sn was found in muscovite from the complex sheets (180–340 ppm) and the highest Nb in the Li-Fe-Al-mica from the biotite granite dyke (120–350 ppm, Fig. 9e). Micas are the major host of Cs and W in all Megiliggar Rocks, while their importance for the Sn-, Nb-, and Ta-budget of the rock is limited, consistent with the findings for topaz granites across the region (Simons et al., 2017).

Tourmaline was found, with variable modal abundances, in all examined varieties of granite and sheet rocks. It forms elongate grains <1 mm long in granites and aplites, but also up to 5–10 cm long and 1–2 mm wide thin needles in pegmatites. Higher abundances of tourmaline were found in rock types and laminae relatively rich in K-feldspar and muscovite, while samples relatively enriched in albite and lepidolite are usually tourmaline-poor. The tourmaline is mainly schorl and more rarely foitite (Fig. 10a). The most Li-rich tourmaline, which was found in the leucogranite sheet is dark green in colour, contains up to 0.7 apfu F (Supplementary Table 7, Fig. 10b). Li is likely to occupy the Y-site in the following proportions: □_{0.1}Li_{0.7}(Fe + Mg + Mn)_{1.2}Al₁ apfu (Fig. 10c). This tourmaline is alkaline and poor in vacancies; it should

Table 1

Chemical composition of studied rocks (wt%, trace elements in ppm).

Sample	Granites			Complex sheets (Li-mica bearing)			Aplite-pegmatites (Tourmaline dominated)			
	Tregonning Granite	Leuco-granite sheet	Biotite granite dyke	Layered granite-pegmatite	Fine grained aplite	Layered granite-pegmatite	Granite-pegmatite	Layered aplite	Layered sheet	
	5303	4963	4962	4964	5304	5305	5302	4965	5306	5307
SiO ₂	69.23	71.11	69.49	70.58	70.25	73.40	73.14	73.31	72.11	76.31
TiO ₂	0.05	0.01	0.10	0.04	0.10	0.11	0.04	0.03	0.02	0.03
Al ₂ O ₃	16.66	15.57	16.84	15.52	15.18	14.03	15.09	14.36	16.30	13.75
Fe ₂ O ₃	0.28	0.14	0.55	0.21	0.56	0.25	0.54	0.50	0.45	0.67
FeO	0.58	0.37	0.87	1.04	0.33	0.63	0.14	0.25	0.18	0.20
FeOt _{tot}	0.83	0.50	1.37	1.23	0.84	0.85	0.63	0.70	0.58	0.80
MgO	0.12	0.07	0.26	0.09	0.19	0.07	0.08	0.21	0.14	0.19
MnO	0.04	0.09	0.05	0.07	0.06	0.04	0.01	0.02	0.01	0.03
CaO	0.39	0.23	0.54	0.61	1.54	0.44	0.40	0.55	0.60	0.48
Li ₂ O	0.38	0.41	0.14	0.28	0.26	0.23	0.03	0.01	0.01	0.01
Na ₂ O	3.37	4.33	3.83	3.21	3.66	3.78	2.71	1.88	2.46	2.93
K ₂ O	5.28	4.23	4.13	4.39	3.28	4.54	5.30	6.09	5.79	3.45
P ₂ O ₅	0.41	0.52	0.31	0.48	0.77	0.45	0.38	0.33	0.42	0.31
F	1.13	1.33	0.47	1.44	1.27	0.89	0.64	0.37	0.32	0.21
L.O.I.	1.20	1.00	1.37	1.27	1.60	0.96	0.76	0.91	0.84	0.84
H ₂ O(–)	0.11	0.16	0.37	0.22	0.15	0.09	0.07	0.40	0.08	0.12
F(ekv)	–0.47	–0.56	–0.20	–0.61	–0.53	–0.37	–0.27	–0.15	–0.13	–0.09
Total	99.23	99.56	99.32	99.46	99.20	99.90	99.33	99.21	99.73	99.52
Ba	12	5	25	11	35	19	16	128	63	45
Be	7	9	9	4	10	2	1	10	4	<1
Cs	199	253	74	107	182	88	33	23	25	17
Ga	42	45	39	44	48	43	40	24	33	29
Hf	1.1	1.1	2.7	0.8	1.6	0.9	0.7	1.6	1.4	0.9
Nb	40	52	33	68	69	57	38	34	26	17
Rb	1401	1832	898	1201	885	1091	755	538	613	356
Sn	22	80	26	17	61	13	13	14	15	13
Sr	24	17	20	11	116	17	11	59	40	27
Ta	17.3	16.7	6.6	10.1	50	12.4	8.2	20.4	9.1	5.8
Th	1	1	7	1	1	1	1	2	2	1
U	16	9	39	6	21	7	3	16	25	14
V	<8	<8	9	<8	14	9	<8	<8	<8	<8
W	30	37	19	28	46	21	10	4	5	8
Zr	17	13	62	9	23	12	11	26	29	15
Y	5.6	0.6	14.4	7.7	5.0	5.0	4.2	4.4	11.4	7.5
La	2.0	1.0	11.0	1.9	1.9	1.7	1.2	2.5	2.6	1.7
Ce	4.6	0.6	25.0	4.6	3.7	3.0	3.2	5.7	6.3	4.2
Pr	0.6	0.1	2.7	0.5	0.4	0.5	0.4	0.6	0.7	0.5
Nd	2.1	<0.3	9.5	1.5	1.6	1.7	1.4	2.2	2.8	1.8
Sm	1.0	<0.05	2.8	0.7	0.7	0.7	0.6	0.8	1.1	0.8
Eu	0.04	<0.02	0.07	0.03	0.06	0.04	0.04	0.19	0.13	0.12
Gd	0.87	<0.05	2.63	0.76	0.71	0.70	0.74	0.72	1.44	1.07
Tb	0.20	0.01	0.53	0.20	0.15	0.16	0.15	0.14	0.34	0.24
Dy	1.19	0.08	2.82	1.25	0.83	0.89	0.85	0.82	1.99	1.42
Ho	0.17	<0.02	0.53	0.16	0.13	0.12	0.12	0.15	0.33	0.19
Er	0.43	0.04	1.41	0.52	0.33	0.33	0.31	0.47	0.88	0.60
Tm	0.07	0.01	0.21	0.09	0.06	0.05	0.05	0.07	0.14	0.09
Yb	0.50	0.09	1.41	0.79	0.40	0.49	0.42	0.51	0.98	0.60
Lu	0.06	0.01	0.19	0.10	0.07	0.05	0.06	0.06	0.14	0.09
Mo	0.3	<0.1	0.3	<0.1	2.3	<0.1	<0.1	1.0	1.9	1.7
Cu	1.9	0.8	2.8	1.3	0.8	0.8	1.0	1.6	0.6	1.2
Pb	10	7	13	5	6	7	12	19	13	7
Zn	41	35	61	47	27	31	19	30	40	77
As	10	24	60	33	75	59	23	6	53	363
Bi	1.0	0.2	1.9	1.1	1.0	1.8	1.3	15.9	1.6	3.8
Sc	4	5	3	9	6	5	4	2	2	3
Tl	7.5	10.3	5.1	6.4	4.4	5.4	5.1	4.5	3.8	2.2
K/Rb	31	19	38	30	31	34	58	94	78	80
Zr/Hf	15	12	23	11	14	14	16	16	21	16
Nb/Ta	2.3	3.1	5.0	6.7	1.4	4.6	4.6	1.7	2.9	2.9

Rem.: major elements in wt%, trace elements in ppm, elemental ratios by weight.

be termed Li-rich fluor-schorl. Tourmaline in other rocks is mostly black Li-F-poor schorl up to F-poor foitite. Tourmaline in the Tregonning Granite is usually zoned with relatively F-Na-Al-Mn-rich and Fe-Mg-depleted rims. These data are consistent with previous studies (Duchoslav et al., 2017; London and Manning, 1995).

In the finely banded rock domains (both #2015 and #4965), the contents of Fe, Mn, and Na in tourmaline increase, while Mg, Ca, and vacancies decrease from the oldest to the youngest layers. Some crystals are slightly zoned, often with schorl cores and slightly Li-F-enriched rims.

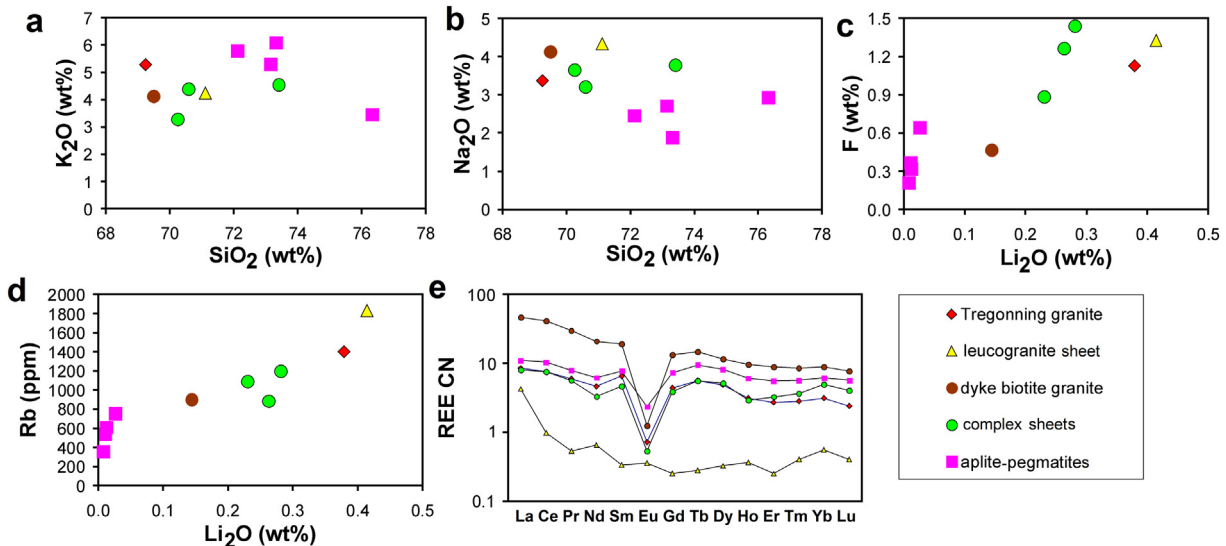


Fig. 7. Whole-rock compositions of studied rocks. Note the tetrad effect in Fig. e! Contents of some of the REE in the sheet leucogranite are below the detection limits of ICP-MS.

Schorl crystals with quartz cores were found in some aplite/pegmatite sheets in the central part of the MSC (see images in the Supplementary material). Similar textures have been described from Roche Rock, St. Austell (Müller et al., 2005). This tourmaline is slightly chemically zoned (with relatively Fe-rich and Mg-poor rims), but is generally low in Li and F. The Li and F contents of tourmaline generally show a positive correlation with those in mica.

Among the trace elements (Supplementary Table 8) in the tourmaline, Sn correlates strongly with Li reaching 60–130 ppm in fluor-schorl from the leucogranite sheet (Fig. 10d), and Ta attains 5–8 ppm in the leucogranite sheets. In contrast, the concentrations of W and Nb are generally very low: <0.5 ppm and <5 ppm, respectively, consistent with recent studies by Duchoslav et al. (2017) and Simons et al. (2017). Niobium and Ta in tourmaline, as in micas, are decoupled: Ta is preferentially enriched in fluor-schorl from the leucogranite sheets and in schorl from the youngest layer #6 in the fine-layered aplite #4965, while Nb prevails in tourmaline from all other locations. Levels of Zn in tourmaline vary mostly between 400 and 600 ppm with some outliers down to 150 and up to 700 ppm, but with little systematic difference between rock types. Gallium concentrations are highly variable (70–350 ppm), with the highest concentrations (>200 ppm) found in tourmaline from the leucogranite sheets and in the latest layer #6 of the sample #4965. The concentration of Be is usually <10 ppm, except in tourmaline from leucogranite sheets where it reaches 30–50 ppm. Contents of Cs, Ge and In are low in tourmaline from all rock types: <3 ppm, <5 ppm, <1 ppm, respectively.

Fluoroapatite appears to have crystallized relatively late in all rock types as it is interstitial and anhedral. Apatite is enriched in Mn in the granites, reaching 0.2–0.3 apfu, and in the albite-rich laminae of the layered rocks, with up to 0.52 apfu Mn (7.18 wt% MnO). Amblygonite, which shows limited alteration to montebrasite along cleavage planes, was found occasionally in the leucogranite sheets as aggregates of anhedral grains several mm across. Monazite and xenotime form scarce small grains (usually ~20 µm, occasionally up to 100 µm) in all rock types. They are the major carriers of REE.

Rutile forms small anhedral grains which show irregular or patchy zonation (in SEM-BSE mode) and contain inclusions of columbite, ixiolite or tantalite (Fig. 11a,b,c). Rarely, intergrowths of rutile and cassiterite were found (Fig. 11d). Rutile, which is enriched in W and slightly in Nb (up to 6.1 wt% WO₃ and 1.6 wt% Nb₂O₅), was often found as inclusions in micas in the biotite granite dyke. It is the only Nb, W-bearing mineral in this rock. Rutile, which is strongly enriched in Nb and Ta

(up to 17 wt% Nb₂O₅, 36 wt% Ta₂O₅), and appears together with Fe-columbite in the Tregonning Granite, complex sheets and aplite-pegmatites (Fig. 12a), locally contains up to 0.7 wt% Sc₂O₃ and 1 wt% WO₃ (Supplementary Table 9).

Columbite-group minerals form 100–200 µm long needle-like crystals (Fig. 11e, f) or smaller (<30 µm) anhedral inclusions in rutile (Fig. 11a, c). They typically have a Ta / (Nb + Ta) ratio < 0.5, i.e. the mineral can be classified as columbite. The Mn / (Fe + Mn) value strongly varies not only among samples, but also within a single grain. Generally, columbite-Mn is more common in the granites and complex sheets, while columbite-Fe prevails in aplite-pegmatite sheets (Fig. 12b). Fe-columbite contains 0.5–1 wt% Sc₂O₃ and 2–10 wt% WO₃. Columbite-like grains with >10 wt% WO₃ (up to 30.7 wt% WO₃) are classified as “ixiolite”, however it is difficult to confirm this without more crystal-chemical information. The W-rich grains (domains in complex grains) are relatively Nb- and Fe-rich (Fig. 12b, c). Tantalite-Mn was found only as one small crystal included in rutile in the Tregonning Granite (Fig. 11b).

Cassiterite occurs as scarce subhedral grains in complex sheets (#5304), locally associated with rutile (Fig. 11d). It is poor in minor elements (>97.8 wt% SnO₂) containing only traces of Nb and Fe.

Wolframite forms small (~20 µm) anhedral grains in some samples from complex sheets (#2015, 5304). It is poor in minor elements (usually <1 wt% Nb₂O₅ + Ta₂O₅ + Sc₂O₃), with only one grain containing 4.3 wt% Nb₂O₅, 2.6 wt% Ta₂O₅ and 1 wt% SnO₂.

Monazite and xenotime (Fig. 11g), major hosts of REE, are scarce, but were found in all rock types. Uraninite, which forms both euhedral and anhedral grains up to 50 µm across, is quite common and is usually rimmed by pyrite (Fig. 13h, i). Within the finely banded aplite (#4965) it was found as inclusions in columbite and zircon (Fig. 11j).

Zircon is a rare accessory mineral in all rock types, as indicated from low WR Zr values, but rare euhedral grains, 10–20 µm across, were found in all samples (Fig. 11f). Numerous inclusions of uraninite were found in some zircon grains from the fine-layered aplite (Fig. 11j, k). Zircon is relatively poor in trace elements (usually Y₂O₃ < 0.6 wt%, Yb₂O₃ < 0.3 wt%, ThO₂ < 0.3 wt%, Supplementary Table 10), with unique values of 5.46 wt% UO₂, 0.40 wt% ThO₂, 1.89 wt% Y₂O₃ and 0.49 wt% Yb₂O₃ (Fig. 13). Hf contents are highly variable, ranging from 1.5–8.9 wt% HfO₂ (0.013–0.082 apfu Hf); the highest values were found within the rims of some crystals from the leucogranite sheets (Fig. 11k). Zircon from the aplite-pegmatite sheets has generally lower Zr/Hf values and lower contents of trace elements than zircon from the complex sheets

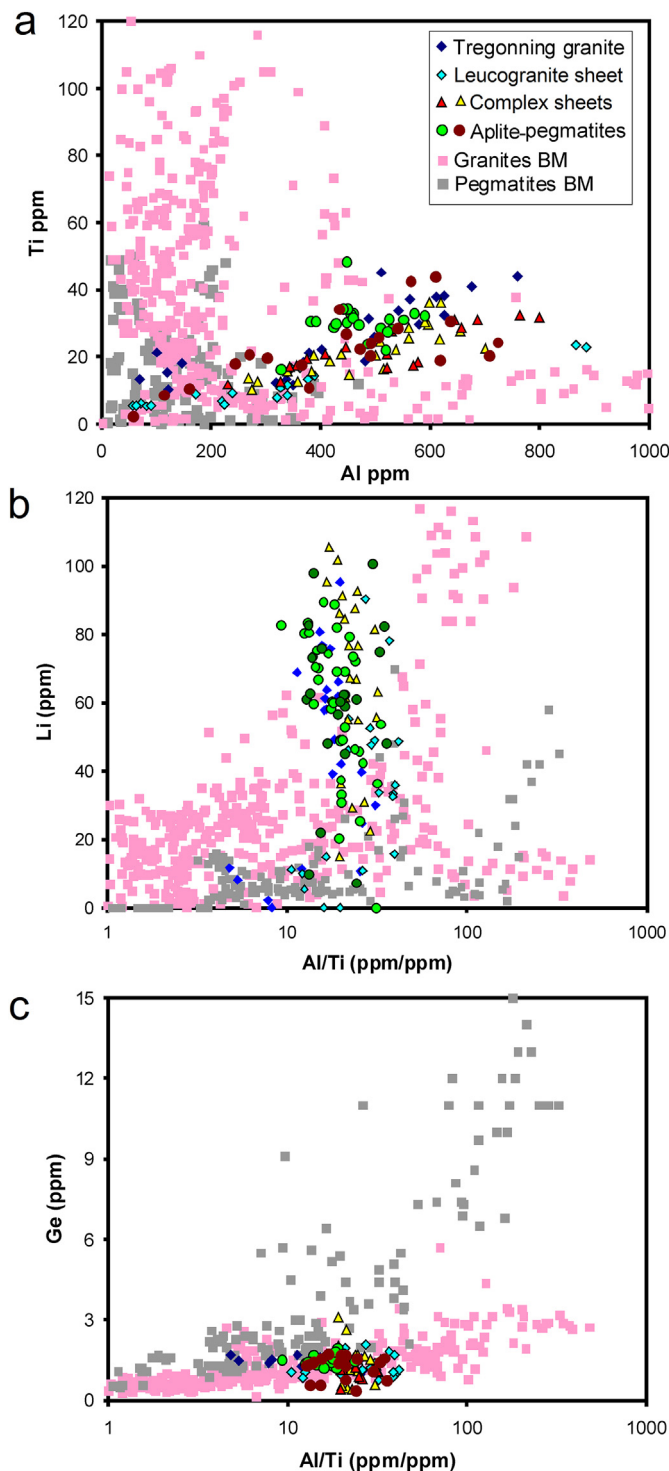


Fig. 8. Trace elements in quartz: a, Al vs. Ti; b, Al/Ti vs. Li; c, Al/Ti vs. Ge. Data from Variscan granites (I-, S-, A-types, Breiter et al., 2013) and pegmatites (muscovite to lepidolite types, Breiter et al., 2014) from the Bohemian Massif are shown for comparison.

(Fig. 13). Zircon from the biotite granite dyke is chemically uniform having intermediate Zr/Hf values (≈ 50) and low contents of all trace elements. All zircon types are free of the “ore elements” Nb, Ta, W, Bi, and Cu.

Magmatic fluorite was found occasionally in some finely banded rock samples. Sulphides (arsenopyrite (Fig. 11) \gg sphalerite, galena, bismuthinite, molybdenite) and native Bi were found in some aplite-pegmatite sheets.

7. Discussion

The origin of layered albite-pegmatite sheets, which can include finely-banded aplites (line rock, Schaller, 1925), is an intriguing petrogenetic question which has broad implications for the genesis of pegmatites. Sheets containing fine-grained “albitic” (usually in the lower half) and coarse-grained “pegmatitic” textures (usually in the upper half) have been explained previously as having both metasomatic (Schaller, 1925; Stone, 1969), and magmatic origins (Jahns and Tuttle, 1963; London, 2014; Webber et al., 1997). The MSC exposures at Megiligar Rocks provide an excellent locality for testing these hypotheses. Our discussions focus on the relationship between the sheets and the nearby Tregonning Granite, mainly whether the sheets were formed from relatively evolved melt segregations within the roof of the Tregonning Granite. Differentiation of initially homogeneous granitic melt to Na-Li-F- and K-B-enriched portions was the main process determining the diversity of sheet rocks. This Na-Li-F vs. K-B differentiation was manifested at two scales: (i) between the Tregonning Granite and MSC; and (ii) within the aplite-pegmatite banding of individual sheets.

7.1. MSC rocks as fractionated equivalents of the Tregonning Granite; large-scale Na-Li-F vs. K-B differentiation

All previous authors agree unequivocally that there is a link between the Tregonning Granite and the MSC. Hosking (1952) interpreted the MSC as having a purely magmatic origin, with aplite and pegmatite sheets (including layers or laminae in the sheets) forming by repeated injections of the same primary magma which varied episodically in its water and volatile contents. Later, Stone (1969, 1975, 1992) proposed a combination of magmatic and metasomatic processes, with initial formation of the aplites by crystallization of residual melts from the Tregonning Granite, followed by subsolidus metasomatic recrystallization of the aplites to pegmatites and replacement of albite by K-feldspar. This view was based on the observation that the aplite parts of the sheets were more mineralogically and chemically similar to the Tregonning Granite than the pegmatic portions. The development of banded aplite-pegmatite sheets has also been interpreted to be a consequence of repeated melt decompression during fracture propagation accompanying xenolith separation (Bromley, 1989; Bromley and Holl, 1986). During decompression, volatile exsolution drove the residual melt towards the solidus, resulting in rapid nucleation and crystallization of aplite; the exsolved hydrous fluid trapped above the aplite contributed to the development of a complementary pegmatite layer.

From our textural and chemical data we suggest a dominantly magmatic origin for all MSC rock types; however, interpretation of the WR chemical data is not straightforward. Nevertheless, the Na vs. K differentiation, mineralogically expressed in albite vs. K-feldspar enriched domains is well documented. In an eastwards traverse from the margin of the Tregonning Granite, through the leucogranite sheets and complex sheets to the aplite-pegmatite sheets, there are conspicuous changes in some major and trace element concentrations (Table 1): Na₂O decreases from 3.3–4.3 to 1.9–2.9 wt%, F decreases from 0.9–1.4 to 0.2–0.6 wt%, Li₂O decreases from 0.23–0.41 to 0.01–0.03 wt%, Rb decreases from 530–1830 ppm to 360–760 ppm, and Cs from 88–253 ppm to 17–33 ppm. In contrast, K₂O in the same direction increases from 3.3–4.5 to 3.5–6.1 wt%. The concentration of B, as evident from the abundance of tourmaline, also increases eastwards, but chemical data for this element are not available. The contents of Si, Al, Fe and P remain fairly constant, and the HFSE are variable but show no obvious trends.

According to the K/Rb ratio, the most common index for magmatic fractionation, the leucogranite sheets (K/Rb = 19) are more evolved than the Tregonning Granite (K/Rb = 31), which is consistent with their interpretation as a product of crystallization of residual melt sourced from the Tregonning Granite roof zone. The lepidolite-bearing complex sheets show K/Rb values only slightly higher than the leucogranites (K/Rb = 21).

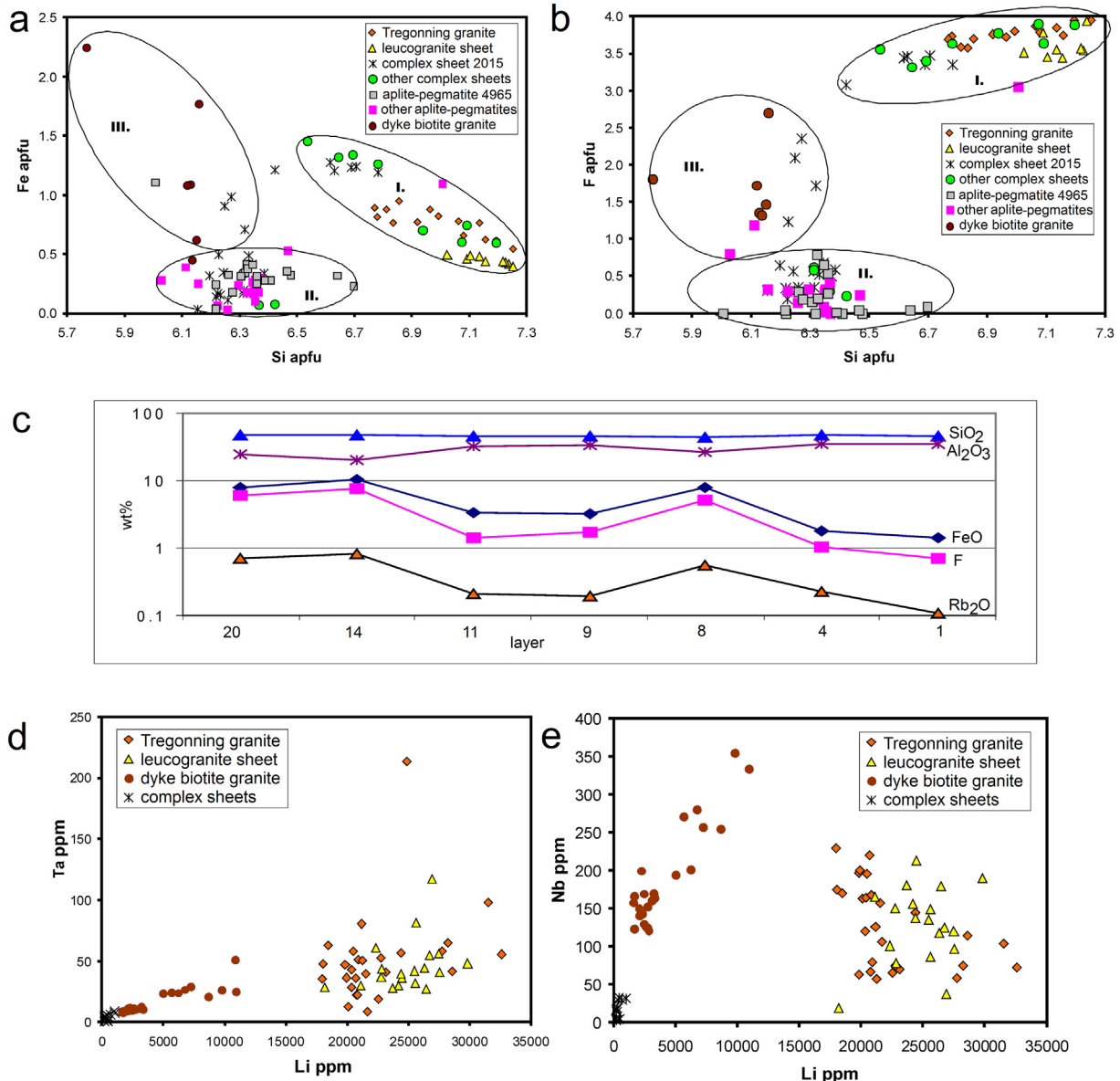


Fig. 9. Chemical composition of micas: a, Si vs. Fe; b, Si vs. F; c, composition of micas (means of 4–5 EMPA analyses) across the finely banded portion of a complex sheet (sample#2015); d, Li vs. Ta; e, Li vs. Nb. In diagrams a–b, three groups of micas are highlighted: I, zinnwaldite–trilithionite series; II, muscovite–phengite series; III, altered (?) Li–Fe–Al mica.

Rb = 30–44), and have slightly lower contents of Li, Rb, and F, indicating that they may also represent fractionated equivalents of the Tregonning Granite melt, notwithstanding fracture-controlled partial escape of Li-F-bearing fluids into the surrounding host rocks. Conversely, the chemical composition of tourmaline-muscovite dominated aplite-pegmatite sheets is less evolved than the Tregonning Granite having relatively low Rb-contents (high K/Rb = 58–94) and extremely low F, Li, and Cs abundances.

The complex sheets and aplite-pegmatite sheets have highly variable mobile alkalis and fluorine compositions. Lower contents of the rare alkalis in the distal parts of the sheet system may be explained by variable fluid escape from the crystallizing melt. Enrichment of the Mylor Slate Formation in the exocontact, previously noted by Stone and Awad (1988), may have been controlled by fractures now represented by steeply dipping aplite/pegmatite sheets (Fig. 2g). However, this does not explain the relative B enrichment in the distal aplite-pegmatite sheets. In the proximal part of the MSC (Fig. 1b), both Li-F-bearing tourmaline and mica crystallized late in the leucogranites, due to low levels of Fe in the melt. In the middle part of the MSC, in the complex sheets, crystallization of tourmaline precedes the crystallization of

Li-F-micas. Tourmaline was the first Fe-bearing mineral in which the melt became saturated; this demonstrates a relatively high abundance of B and Fe in the melt at the beginning of the crystallization. Mica crystallized later, when F was sufficiently concentrated in the residual melt. In the distal MSC, within the aplite-pegmatite sheets, B predominates over F, even though its fluid/melt partition coefficient is distinctly higher than that of fluorine. Thus, the eastwards proximal to distal decrease in F was not a result of its partitioning into a fluid and escape to the slates, but a consequence of its consumption by the relatively late crystallization of F-minerals (topaz?) in the proximal and central parts of the MSC. The last portion of melt, filling the distal parts of the sheet system, was F-poor, but still had sufficient B for tourmaline saturation, with Fe scavenged from the slate host rocks.

Variations in Nb- and Ta-contents and Nb/Ta ratios are often used as indicators of the degree of granite and pegmatite melt evolution and/or zoning (Ballouard et al., 2016). Tantalite has a higher solubility in peraluminous granite melts at low temperature relative to columbite (e.g. Linnen and Kepler, 1997; Linnen, 1998), which commonly results in the melt evolving from Fe-Nb- to Mn-Ta-enriched end-members of the columbite group (Černý et al., 1985; London, 2008). Moreover, the

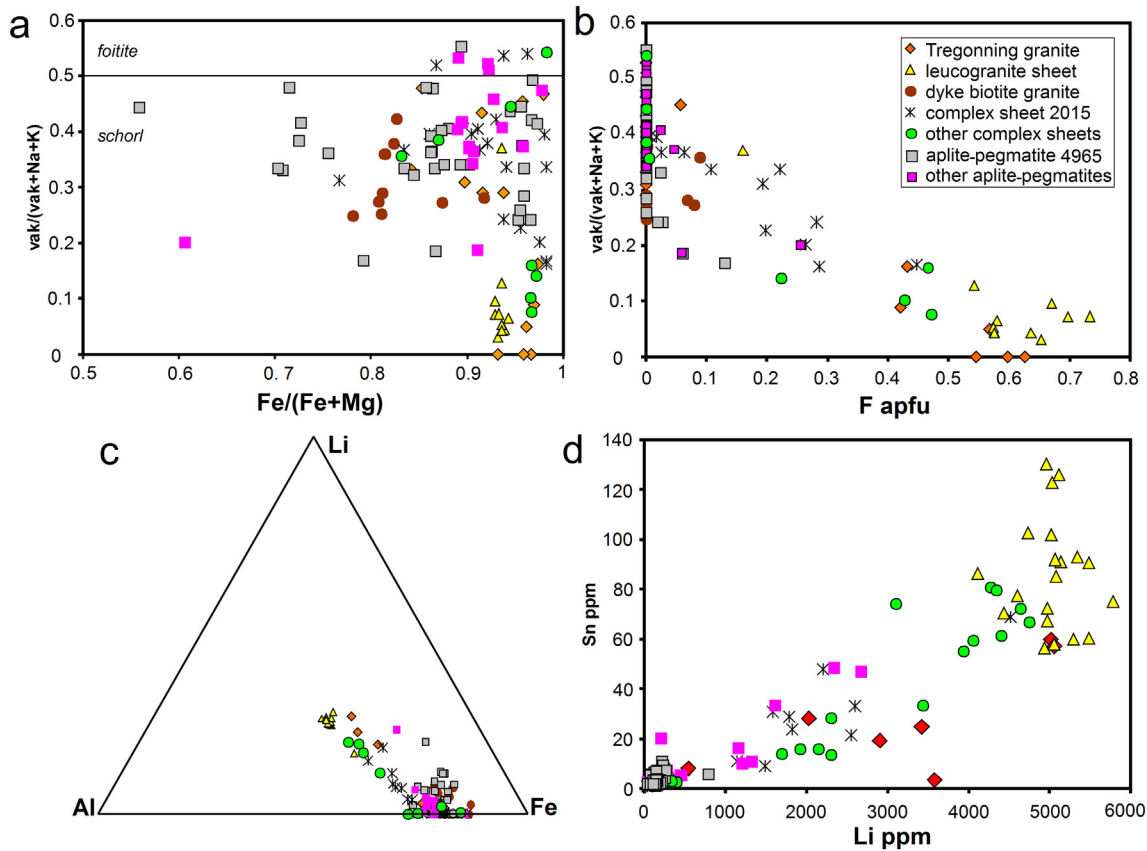


Fig. 10. Chemical composition of tourmaline: a, $\text{Fe}/(\text{Mg}+\text{Fe})$ vs. $\square/(\square+\text{Na}+\text{K})$ (apfu); b, F vs. $\square/(\square+\text{Na}+\text{K})$ (apfu); c, occupation of the Y-site (apfu); d, Li vs. Sn (ppm).

crystallization of micas also aids in the decoupling of Nb and Ta within a peraluminous melt, with Nb preferentially partitioning into biotite compared with Ta; the latter is strongly partitioned into residual F-bearing melts (e.g. Stepanov and Hermann, 2013). Nevertheless, changes in the Nb/Ta ratio are also influenced by a succession of coprecipitating minerals (oxides, micas, tourmaline) and the combined effects of Li, Na, B, F, and P in the melt or fluid phase (e.g., Belkasmi et al., 2000; Johan and Johan, 1994; Novák et al., 2003; Van Lichtervelde et al., 2006; Wise et al., 2012). In the MSC, fluorine presumably remained in pockets of residual melt until the crystallization of topaz (e.g. Figs. 4, 5), with Ta therefore concentrated within the last layers to crystallize, while Nb is more evenly distributed throughout the rocks. However, in examining larger volume WR samples (Fig. 14a, b), the Nb/Ta ratio is scattered between 1 and 7 independent of rock type and Li- and F-content. In micas and tourmaline (Fig. 14c-f) the Nb- and Ta-contents and the Nb/Ta ratio are highly variable within individual samples, but the general trend is to relative Ta-enrichment in Li-enriched grains and/or the outer zones of crystals. We conclude that WR Nb/Ta ratios in Megiliggar Rocks were controlled by the order of crystallization and relative amounts of oxides vs. silicate carriers and, in this case, cannot serve as a marker of melt fractionation.

The mineralogy of the different MSC rock types reflects their WR compositions, with the leucogranite sheets and complex sheets containing lepidolite, relatively high P-contents in both feldspars and Rb in K-feldspar, and higher Li and Fe/Mg in tourmaline. These signatures are characteristic of “evolved” or “highly fractionated” rocks, comparable with peraluminous tin granites in the Erzgebirge (Breiter et al., 2005; Förster et al., 1999) and France (Raimbault et al., 1995), and LCT pegmatites (London, 2008). In contrast, the aplite-pegmatite sheets, which contain Li-F-poor muscovite, and often schorl, are chemically and mineralogically more primitive. However, all rock-types show nearly identical and low (12–21) WR Zr/Hf values, which are generally indicative

of high degrees of fractionation (Breiter and Škoda, 2017; Hanchar and Hoskin, 2003). The zircon Zr/Hf value (Fig. 13) is consistent with WR Zr/Hf data and zircon from the aplite/pegmatite sheets is at least as strongly differentiated as zircon from the complex sheets and is more fractionated than zircon from the Tregonning Granite.

The field relations and geochemical similarity indicate a direct link between the Tregonning Granite and the MSC. The textural and mineral diversity in the sheets, from proximal to distal, eastwards across the study area, was caused by Na-Li-F vs. K-B fractionation, where the K-B-rich portion of melt (fluid) could migrate more effectively to the distal part of the crystallizing magmatic system. However, the Zr/Hf value, unaffected by this fractionation, is similar across the whole MSC, demonstrating a uniform magmatic source.

The composition of the biotite granite dyke is distinctive and does not follow the aforementioned trends; this lithology does not appear to form part of the MSC. Instead, it is likely to be an expression of earlier magmatism petrogenetically linked to the Godolphin Granite (two mica) or biotite granite porphyry (“elvan”) dykes (see Simons et al., 2016).

The suggestion that the easternmost distal expression of the MSC is represented by quartz veins linked directly to aplite-pegmatite sheets (Badham, 1980; Bromley, 1989; Hosking, 1952) is refuted; we think that this assertion was based on miscorrelation of the easternmost MSC sheets with pre-granite subhorizontal quartz veins contained within the S3 cleavage. The similar orientation of the MSC sheets and these quartz veins reflects the influence of the mechanical anisotropy imparted by the S3 cleavage on the propagation of fractures controlling emplacement of the MSC.

7.2. Local Na-Li-F vs. K-B fractionation within layered sheets

The complex sheets and aplite-pegmatite sheets within the MSC differ from the majority of common pegmatite sheets having a more

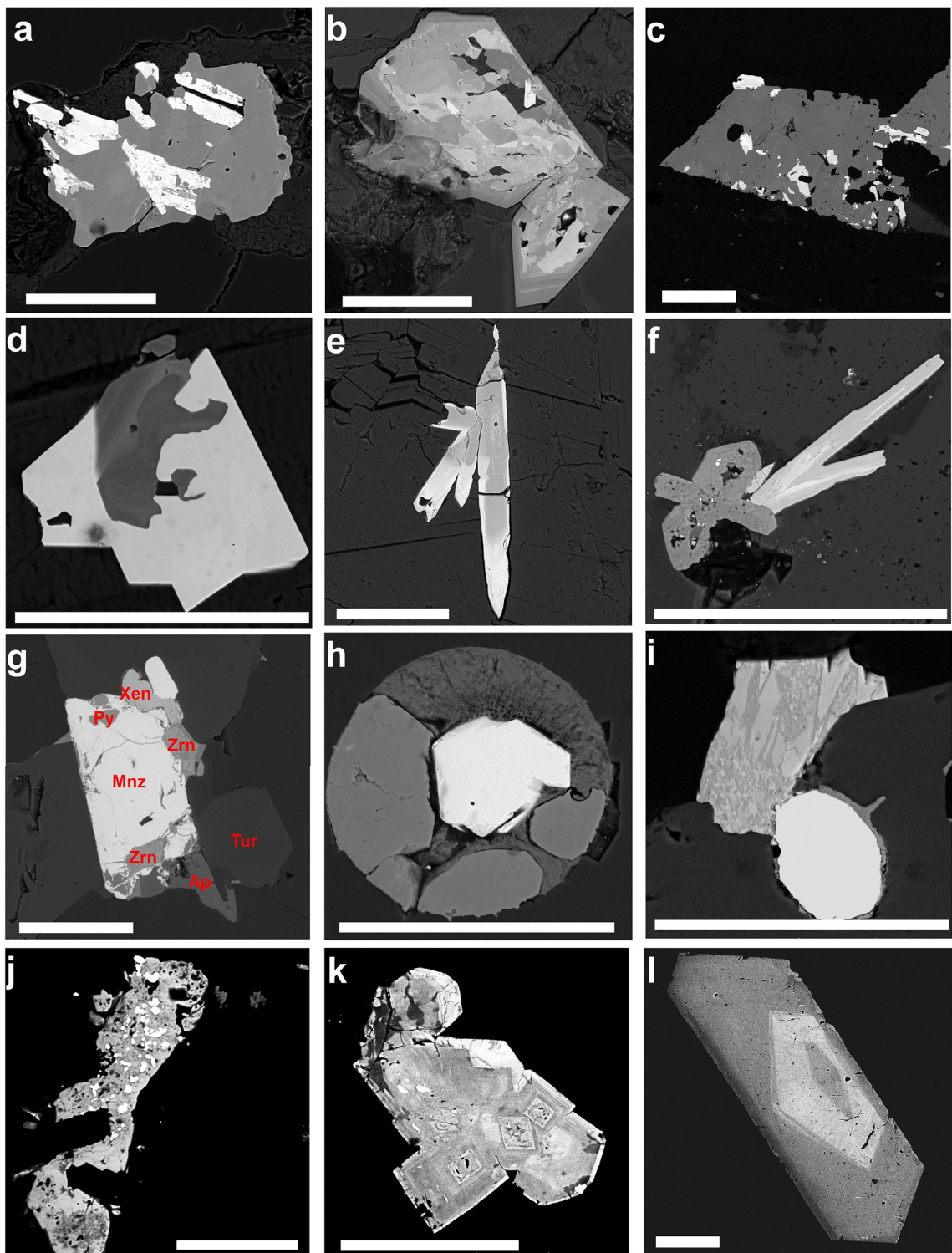


Fig. 11. BSE-images of minerals: a, Nb-Ta-rich rutile (grey) with inclusions of W-rich Fe-columbite (bright), #2015, in banded rock; b, patchy zoned Nb-Ta-enriched rutile (grey) with small crystals of tantalite (bright), #5303, in Tregonning granite; c, rutile with inclusions of columbite and ixiolite, #4964, in composite granite/pegmatite sheet; d, intergrowth of cassiterite (bright) and rutile (dark grey), #5304, in granitic part of the composite granite/pegmatite sheet; e, needle-like crystals of Mn-columbite with Ta-enriched rims in Li-mica, #4963, in leucocratic sheet granite; f, crystals of Fe-columbite (light grey with bright zones) in association with two colander-like zircon crystals, #5302, in coarse grained tourmaline-bearing sheet granite; g, monazite (Mnz) associated with xenotime (Xen), zircon (Zrn), Mn-rich apatite (Ap), pyrite (Py) and tourmaline (Tur) in quartz, #2015, in banded rock; h, crystal of uraninite (bright) rimmed by pyrite in quartz, #2015, in banded rock; i, grain of uraninite (bright) with thin rim of pyrite associated with a Nb, Y-phase, #5307, in pegmatic core of composite aplite/pegmatite sheet; j, central part of an altered zircon grain contains numerous inclusions of uraninite while its rim is inclusions free, #4965, in tourmaline-rich banded rock; k, zoned zircon with Hf-enriched rim, in leucocratic sheet granite, #4963; l, zoned crystal of arsenopyrite, #2015, in banded rock. White scale bars in all cases 50 µm.

complex structure, often appearing to have formed as a result of multiple melt injections. The banding almost certainly originated via in situ fractionation, as crystals grew upwards; in combination with the

emplacement of younger narrow melt injections which crystallized from both contacts inwards (compare Hosking, 1952). This feature was encountered in both complex sheets and aplite-pegmatites.

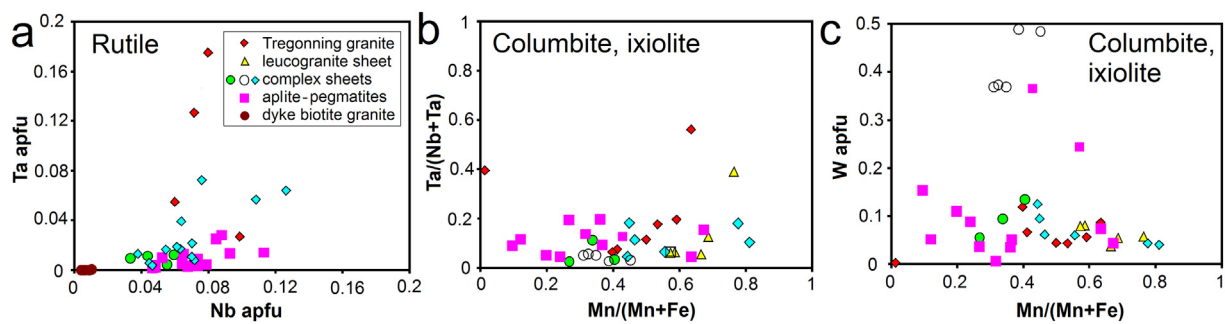


Fig. 12. Nb-Ta-Sn-W-oxide cross plots: a, Nb vs. Ta in rutile; b, columbite classification diagram; c, W vs. Mn/(Mn + Mn) in columbite and 'ixiolite'. Coloured symbols = columbite, empty symbols = ixiolite.

Crystallization within most single sheets (or sheet domains), i.e. formed from a single injection of melt, is comparable with other examples of pegmatite sheets (London et al., 2012; Webber et al., 1997).

Samples #4965 and #2015 represent parts of in situ crystallized layered sequences, at an appropriate layer scale for detailed investigation. Sample #4965 (Fig. 5, Supplementary Table 2) represents a fine-grained (aplitic) part of an aplite-pegmatite sheet which is albite-poor and dominated by quartz, K-feldspar, muscovite and tourmaline. The composition of individual laminae can be traced effectively from the Qtz-Kfs ratio, but without any general evolutionary trend (Fig. 15a). The abundance of tourmaline varies between 4.1 and 9.8 vol% (ca. 0.4–1.0 wt% B₂O₃). The younger laminae #4 → 6 contain 1–2 vol% apatite (up to 1 wt% P₂O₅). The melt, from which layers #1 → 5 crystallized, was B- and P-rich, but relatively F-poor (<0.15 wt%), and only the youngest lamina #6 reaches nearly 5 wt% F due to crystallization of common topaz from the residual liquid or from a new injection of F-rich melt/fluid. In any case, the crystallized rock composition lies away from the granite minima (Johannes and Holz, 1996) (Fig. 15b).

Sample #2015 (Fig. 4, Supplementary Table 1) represents a finely banded portion of a Li-F-bearing complex sheet. Its mineral composition is more complex than in the previous case, with bands dominated by K-feldspar, tourmaline and muscovite alternating with those strongly enriched in albite and zinnwaldite. The oldest portion of the layered sequence, lines #1 → 7, evolved systematically from a Qtz-Kfs-rich composition towards the Ab-apex of the Qtz-Ab-Kfs diagram (16 → 72 wt% Ab, Figs. 4, 15a). The bands have variable compositions, but the general trend towards Ab-enrichment is obvious. The computed volatile content varies between 0 → 1.6 wt% B₂O₃, 0.2 → 0.8 wt% P₂O₅, and 0.1 → 2.4 wt% F. Although B generally decreases along this trend, P levels remain unchanged and F, Li and Rb increase (Fig. 9c). Here, it should be noted that the sample does not really represent the mean of the whole banded

sheet, but only a partial section; the real composition of the injected melt may be different.

7.3. Comparison with similar aplite-pegmatite sheets

The first model for the generation of layered aplite-pegmatite sheets was developed by Jahns and Tuttle (1963), which was based on a study of mafic pegmatites in San Diego County, California. The authors described a typical arrangement of "sodic aplite" in lower, and "potassic pegmatite" in the upper parts of horizontal sheets with inward crystallization of both facies which finished in the central pocket zone. Later, London et al. (2012) and London (2014) confirmed the common position of (often layered) aplitic domains in the lower part, and pegmatic domains in the upper part of many horizontal pegmatite sheets, but questioned their dominantly sodic vs. potassic character. Another, rhythmic style of layering, expressed as alternations of 0.5–2 m thick K-feldspar and tourmaline-dominated pegmatite and albite-rich aplite layers, has been reported from the B-rich Calamity Peak layered pluton (Duke et al., 1992).

The evolution of the banded sequences in the MSC is comparable with the George Ashley Block (GAB) pegmatite, Pala district, California (Webber et al., 1997). The mean composition of the granite sheet and complex sheets from Megiliggar is only slightly Ab-enriched in comparison with the mean of the GAB pegmatite, which may be explained by a higher content of F in the Megiliggar sheets (Fig. 15b). The composition of the oldest band in the sample #2015 and the WR #4965 is nearly identical to the composition of the K-rich portions of the GAB pegmatite, located in its central-upper parts, while the mean of the late finely banded aplitic portion of sample #2015 is equal to the composition of the finely banded aplitic portion of the GAB pegmatite (Webber et al., 1997) (Fig. 15b). Therefore, the banded portions of the MSC we have studied experienced the same differentiation as the whole George Ashley Block pegmatite dyke. In both localities, both contrasting rock facies (Na + F + Li vs. K + B-enriched) are adjacent in a single sheet, together having logically expected compositions near the "granitic minimum" of a slightly B-, resp. F-enriched melt (Manning, 1981; Pichavant, 1987) (Fig. 15b).

Webber et al. (1999) and London et al. (2012) concluded that crystallization of finely banded aplite ("line rock") to give a water- and fluxes-poor mineral assemblage near the lower contact of the sheets was likely due to undercooling, whereas accumulation of volatiles in the upper parts of the sheet decreased the degree of undercooling and promoted crystallization from a flux-enriched boundary-layer, i.e. crystallization of rare minerals and grainsize coarsening. At Megiliggar, this process is expressed in complex sheets which show a transition from muscovite-bearing aplite through to Li-F-mica-bearing aplite to coarse-grained sheet domains bearing Li-F-mica and tourmaline. In the aplite-pegmatites, the increase in F and Li during crystallization of the aplite unit was minimal, but their influence was superseded by increasing abundances of water and boron. Repeated sudden decompression followed by exsolution of fluid driving such grainsize changes

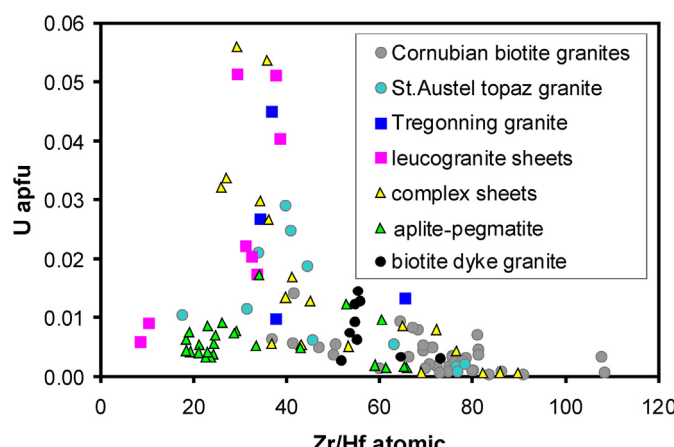


Fig. 13. Relation between the Zr/Hf ratios in zircon (using data also from Breiter et al., 2016).

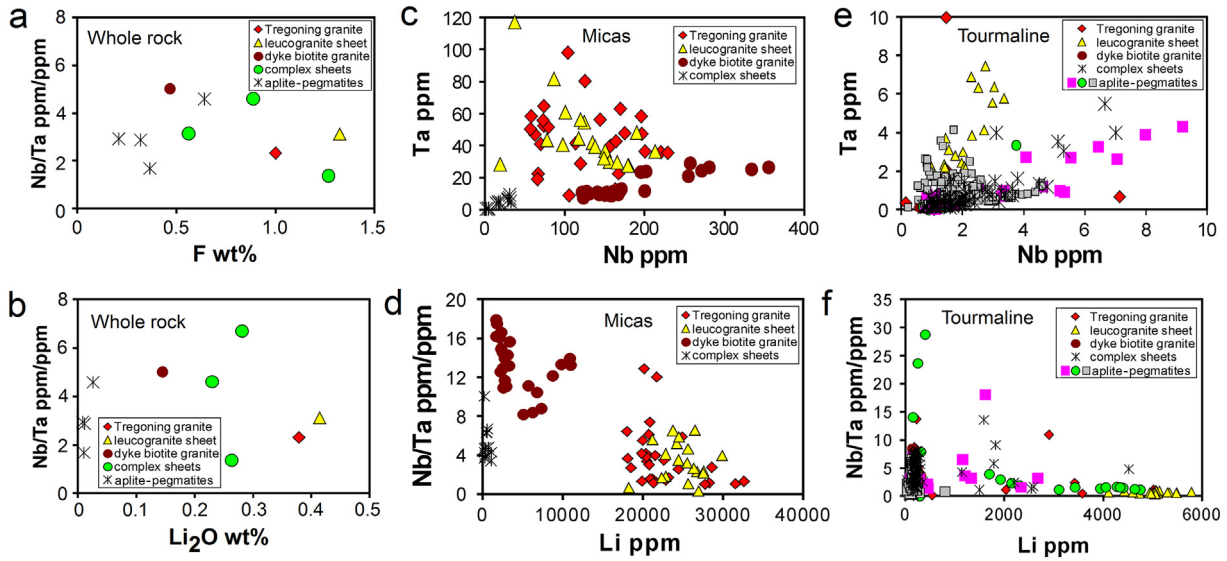


Fig. 14. Variation in the Nb/Ta ratio at Megiliggar Rocks: a, Nb/Ta vs. F in whole rocks; b, Nb/Ta vs. Li₂O in whole rocks; c, Nb vs. Ta in micas; d, Li vs. Nb/Ta in micas; e, Nb vs. Ta in tourmaline; f, Li vs. Nb/Ta in tourmaline.

might be driven by repeated fracture propagation during the lateral growth and inflation of the MSC (London, 2008; Webber et al., 1997) rather than xenolith separation (Bromley, 1989; Bromley and Holl, 1986). In such conditions, the growth rate of K-feldspar is higher than that of quartz and albite (Swanson, 1977): this is well demonstrated in layers 1 → 7 of sample #2015, although the initial dominance of K-feldspar was superseded, in a stepwise fashion, by albite. Similar, although not so significant, is the evolution in lines 11 → 13, 15 → 17 and 20 → 22.

7.4. Possible implications for models of pegmatite genesis

Among recent models for the genesis of pegmatites, the complex model by London (for example London, 2008, 2014) and model based on the study of melt inclusions by Thomas (for example Thomas et al., 2006; Thomas and Davidson, 2012, 2013) are the best constrained and often discussed, including mutual discussion of both authors (London,

2015; Thomas and Davidson, 2015). In a very simplistic way, London explained the specific features of pegmatites as crystallization products of peraluminous water-undersaturated melts via the boundary layer effect, while Thomas and Davidson prefer crystallization from immiscible hydrous peralkaline melt. Detail discussion of the mentioned models is beyond the scope of this article, but we would like to stress the importance of our findings from Megiliggar, which we feel should be considered in any future models for pegmatite genesis.

The evidence from outcrops at Megiliggar, and our detail mineralogical studies, suggests an intimate coexistence of “granite”, “aplite” and “pegmatite” rocks of similar mineral and chemical composition, differing only in grain size and texture. We did not find any evidence of abrupt changes in mineral and chemical composition, though sudden changes in texture, from pegmatitic to aplitic varieties, and vice versa, are common. In other words, an evolved peraluminous granitic melt may repeatedly change in its style of crystallization from granitic to aplitic and pegmatitic without any abrupt changes in chemical or mineral

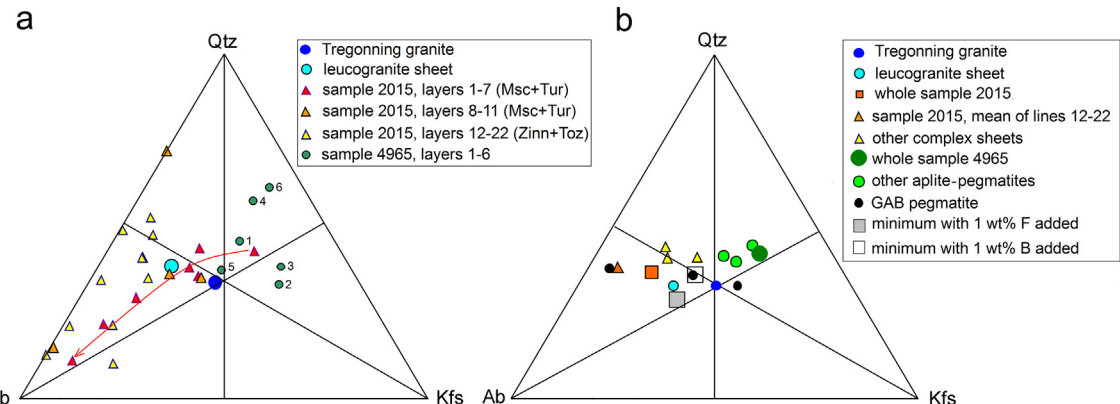


Fig. 15. a Composition of whole rocks and individual bands in banded rocks in the Qtz-Ab-Kfs triangle. Note systematic evolution of the lower (older) part of the sample #2015: systematic shift to the Ab-apex from line 1 to 7 (red arrow). Later zones, poorer in Kfs, scatter along the Qtz-Ab join. Sample #4965 represents the aplite-pegmatite melt with rather chaotic zoning; b Composition of proposed starting melt (Tregonning granite) and the Megiliggar sheet rocks computed according to whole-rock chemical data and EMPA of rock-forming minerals (sample 2015 acc. to modal analyse by TIMA). Three typical compositions of the George Ashley pegmatite (layered aplite rich in Ab, whole dyke, granular pegmatite rich in Kfs) acc. to Webber et al. (1997) and water-saturated leucogranitic solidus with 1 wt% added F, resp. B (Manning, 1981 resp. Pichavant, 1987) are also shown for comparison.

composition. The factors controlling granitic or pegmatitic styles of evolution (water and volatile contents? undercooling? fluctuation of pressure?) changed gradually, smoothly, are were reversible.

8. Conclusions

Chemical and mineralogical data together with a gradual change in prevailing textures suggests a strong genetic link between the Tregonning Granite and MSC. The lithologies within the MSC formed from residual melt escaping from the Tregonning Granite. This melt was strongly peraluminous and, in comparison with other Cornish granites, rich in F, Li, Rb, Cs, Sn, W, Nb, Ta, and U, and poor in Fe, Mg, Ca, Sr, Th, Zr, and REE.

During crystallization, the melt underwent differentiation into Na-Li-F-enriched vs. K-B-enriched domains, which may be traced at two scales: (i) in finely banded sequences where the K-B-enriched layers evolved into more Na-Li-F-enriched ones, and (ii) generally, the Na-Li-F-enriched proximal leucogranite sheets pass gradually into K-B-dominated distal aplite-pegmatites. The mean composition of the sheets is similar to the eutectic composition of leucocratic granitic melts saturated in water and slightly enriched in F and B. Differentiation to fine-grained (i.e. aplitic) and coarse-grained (i.e. pegmatitic) layers was most probably forced by repeated decompression and undercooling due to fracture propagation during the lateral growth and inflation of the MSC system.

With distance from the contact with the parental Tregonning Granite, the melt became depleted in the fluxing and volatile elements F, Li, Rb, and Cs, probably due to escape of fluid to surrounding slates or via fractures, but the Zr/Hf value in all rock types remains virtually unchanged indicating derivation from a single parental magma source.

Knowledge gained at Megiliggar Rocks may help to better understand the chemical and mineralogical evolution of large aplite-pegmatite systems and their relation to parental granite plutons. Mineral and textural zoning, usually evolving from the contacts to the core of the pegmatite bodies, is at Megiliggar combined with a lateral transition from dominantly granitic to aplitic and pegmatitic textures, chemically expressed in Na-F-Li vs. K-B differentiation. The combination of transversal and longitudinal zoning in the Megiliggar sheets may provoke similar studies in other well-exposed aplite-pegmatite systems.

Acknowledgements

Laser-ablation ICP-MS analyses of micas and tourmaline in Masaryk University Brno were supported by the Czech Science Foundation project No. GA14-13600S. All other analytical work for this contribution was supported by the RVO 67985831 in the Institute of Geology of the Czech Academy of Sciences, Praha. We are grateful to P. Davidson and an anonymous referee for their reviews.

Appendix A. Supplementary data

Additional rock and mineral images in electronic form are available as a "Supplementary image pdf-file". Supplementary data associated with this article can be found in the online version, at <https://doi.org/10.1016/j.lithos.2018.01.010>.

References

- Alexander, A.C., Shail, R.K., 1996. Late-to post-Variscan structures on the coast between Penzance and Pentewan, south Cornwall. *Proceedings of the Ussher Society* 9, 72–78.
- Autunes, I.M.H.R., Neiva, A.M.R., Ramos, J.M.F., Silva, P.B., Silva, M.M.V.G., Corfu, F., 2013. Petrogenetic links between lepidolite-subtype aplite-pegmatite, aplite veins and associated granites at Segura (central Portugal). *Chemie der Erde* 73, 323–341.
- Badham, J.P.N., 1980. Late magmatic phenomena in the Cornish batholith – useful field guide for tin mineralization. *Proceedings of the Ussher Society* 5, 44–53.
- Ballouard, C., Poujol, M., Boulvais, P., Branquet, Y., Tartese, R., Vigneresse, J.-L., 2016. Nb-Ta fractionation in peraluminous granites: a marker of the magmatic-hydrothermal transition. *Geology* 44, 231–234.
- Belkasmı, M., Cuney, M., Pollard, P.J., Bastoul, A., 2000. Chemistry of the Ta-Nb-Sn-W oxide minerals from the Yichun rare metal granite (SE China): genetic implications and comparison with Moroccan and French Hercynian examples. *Mineralogical Magazine* 64, 507–523.
- Breaks, F.W., Moore Jr., J.M., 1992. The Ghost Lake batholith, Superior Province of north-western Ontario: a fertile, S-type, peraluminous granite – rare-element pegmatite system. *Canadian Mineralogist* 30, 835–875.
- Breiter, K., Škoda, R., 2017. Zircon and whole-rock Zr/Hf ratios as markers of the evolution of granitic magmas: examples from the Teplice caldera (Czech Republic/Germany). *Mineralogy and Petrology* 111, 435–457.
- Breiter, K., Müller, A., Leichmann, J., Gabašová, A., 2005. Textural and chemical evolution of a fractionated granitic system: the Podlesí stock, Czech Republic. *Lithos* 80, 323–345.
- Breiter, K., Ackerman, L., Svojtka, M., Müller, A., 2013. Behavior of trace elements in quartz from plutons of different geochemical signature: a case study from the Bohemian Massif, Czech Republic. *Lithos* 175–176, 54–67.
- Breiter, K., Ackerman, L., Řurišová, J., Svojtka, M., Novák, M., 2014. Trace element composition of quartz from different types of pegmatites: a case study from the Moldanubian Zone of the Bohemian Massif (Czech Republic). *Mineralogical Magazine* 78, 703–722.
- Breiter, K., Müller, A., Shail, R., Simons, B., 2016. Composition of zircons from the Cornubian Batholith of SW England and comparison with zircons from other European Variscan rare-metal granites. *Mineralogical Magazine* 80, 1273–1289.
- Bromley, A.V., 1989. Field guide - the Cornubian orefield. 6th International Symposium on Water-Rock Interaction, Malvern (UK). International Association of Geochemistry and Cosmochemistry, Camborne School of Mines, UK, p. 111.
- Bromley, A.V., Holl, J., 1986. Tin mineralisation in southwest England. In: Wills, B.A., Barley, R.W. (Eds.), *Mineral Processing at a Crossroads*. NATO ASI Ser. No. 117. Martinus Nijhoff, Dordrecht, pp. 195–262.
- Černý, P., 1991. Fertile granites of Precambrian rare-element pegmatite fields: is geochemistry controlled by tectonic setting or source lithologies? *Precambrian Research* 51, 429–468.
- Černý, P., Meintzer, R.E., Anderson, A.J., 1985. Extreme fractionation in rare-element granitic pegmatites: selected examples of data and mechanisms. *Canadian Mineralogist* 23, 381–421.
- Chappell, B.W., Hine, R., 2006. The Cornubian Batholith: an example of magmatic fractionation on a crustal scale. *Resource Geology* 56, 203–244.
- Charoy, B., 1986. The genesis of the Cornubian Batholith (South-West England): the example of the Carmmenellis Pluton. *Journal of Petrology* 27, 571–604.
- Duchoslav, M., Marks, M.A.W., Drost, K., McCammon, C., Marschall, H.R., Wenzel, T., Markl, G., 2017. Changes in tourmaline composition during magmatic and hydrothermal processes leading to tin-ore deposition: The Cornubian Batholith, SW England. *Ore Geology Reviews* 83, 215–234.
- Duke, E.F., Papike, J.J., Laul, J.C., 1992. Geochemistry of a boron-rich peraluminous granite pluton: the Calamity Peak layered granite-pegmatite complex, Black Hills, South Dakota. *American Mineralogist* 30, 811–833.
- Exley, C.S., Stone, M., 1982. Hercynian intrusive rocks. In: Sutherland, D.S. (Ed.), *Igneous rocks of the British Isles*. Wiley, Chichester, pp. 287–320.
- Floyd, P.A., Exley, C.S., Styles, M.T., 1993. Igneous Rocks of South-West England. *Geological Conservation Review Series*. Chapman and Hall, London.
- Förster, H.-J., Trumbull, R.B., Gottesmann, B., 1999. Late-collisional granites in the Variscan Erzgebirge, Germany. *Journal of Petrology* 40, 1613–1645.
- George, M.C., Stone, M., Fejer, E.E., Symes, R.F., 1981. Triplite from the Megiliggar Rocks, Cornwall. *Mineralogical Magazine* 44, 236–238.
- Gleeson, S.A., Wilkinson, J.J., Shaw, H.F., Herrington, R.J., 2000. Post-magmatic hydrothermal circulation and the origin of base metal mineralization, Cornwall, UK. *Journal of the Geological Society* 157, 589–600.
- Goad, B.E., Černý, P., 1981. Peraluminous pegmatitic granites and their pegmatite aureoles in the Winnipeg River district, southeastern Manitoba. *Canadian Mineralogist* 19, 177–194.
- Goode, A.J.J., Taylor, R.T., 1988. *Geology of the country around Penzance (Sheet 351/358). Memoir of the British Geological Survey*. HMSO, London.
- Gottlieb, P., Wilkie, G., Sutherland, D., Ho-Tun, E., Suthers, S., Perera, K., Jenkins, B., Spencer, S., Butcher, A., Rayner, J., 2000. Using quantitative electron microscopy for process mineralogy applications. *JOM* 52, 24–25.
- Govindaraju, K., 1994. Compilation of working values and sample description for 383 geo-standards. *Geostandards Newsletter* 18, 1–158.
- Hall, S., 1930. The geology of the Godolphin Granite. A study of the coastal geology between Perranuthnoe and Looe Pool. *Proceedings of the Geologists' Association* 42, 117–147.
- Hanchar, J.M., Hoskin, P.W.O. (Eds.), 2003. *Zircon. Reviews in Mineralogy and Geochemistry* 53.
- Henderson, C.M.B., Martin, J.S., Mason, R.A., 1989. Compositional relations in Li-micas from SW England and France: an ion- and electronmicroprobe study. *Mineralogical Magazine* 53, 427–449.
- Hosking, K.F.G., 1952. Cornish pegmatites and bodies with pegmatite affinities. *Transactions. Royal Geological Society of Cornwall* 18, 411–455.
- Jacamon, F., Larsen, R.B., 2009. Trace element evolution of quartz in the charnockitic Kleivan granite, SW Norway: the Ge/Ti ratio of quartz as an index of igneous differentiation. *Lithos* 107, 281–291.
- Jahns, R.H., Tuttle, O.F., 1963. Layered pegmatite-aplite intrusives. *Mineralogical Society of America Special Paper* 1, 78–92.
- Johan, V., Johan, Z., 1994. Accessory minerals of the Cinovec (Zinnwald) granite cupola, Czech Republic. Part 1: Nb-, Ta- and Ti-bearing oxides. *Mineralogy and Petrology* 51, 323–343.
- Johannes, W., Holz, F., 1996. Petrogenesis and Experimental Petrology of Granitic Rocks. *Minerals and Rocks* 22. Springer (335 pp.).
- Leveridge, B.E., Shail, R.K., 2011. The Gramscatho Basin, south Cornwall, UK: Devonian active margin successions. *Proceedings of the Geologists' Association* 122, 568–615.

- Linnen, R.L., 1998. The solubility of Nb-Ta-Zr-Hf-W in granitic melts with Li and Li+F: constraints for mineralization in rare metal granites and pegmatites. *Economic Geology* 93, 1013–1025.
- Linnen, R.L., Keppler, H., 1997. Columbite solubility in granitic melts: consequence for the enrichment and fractionation of Nb and Ta in the Earth's crust. *Contributions to Mineralogy and Petrology* 128, 213–227.
- London, D., 2008. Pegmatites. Canadian Mineralogist Special Publication 10 (347 pp.).
- London, D., 2014. A petrologic assessment of internal zonation in granitic pegmatites. *Lithos* 184–187, 74–104.
- London, D., 2015. Reply to Thomas and Davidson on "A petrologic assessment of internal zonation in granitic pegmatites". *Lithos* 212–215, 469–484.
- London, D., Manning, D.A.C., 1995. Chemical variation and significance of tourmaline from South West England. *Economic Geology* 90, 495–519.
- London, D., Morgan VI, G.B., Paul, K.A., Guttry, B.M., 2012. Internal evolution of miarolitic granitic pegmatites at the Little Three mine, Ramona, California, USA. *Canadian Mineralogist* 50, 1025–1054.
- Manning, D.A.C., 1981. The effect of fluorine on liquidus phase relationships in the system Qz-Ab-Or with excess water at 1 kbar. *Contributions to Mineralogy and Petrology* 76, 206–215.
- Manning, D.A.C., Exley, C.S., 1984. The origins of late-stage rocks in the St. Austell granite – a reinterpretation. *Journal of the Geological Society* 141, 581–591.
- Manning, D.A.C., Hill, P.I., 1990. The petrogenetic and metallogenetic significance of topaz granite from the southwest England orefield. *Geological Society of America Special Papers* 246, 51–69.
- Manning, D.A.C., Hill, P.I., Howe, J.H., 1996. Primary lithological variation in the kaolinized St Austell granite, Cornwall, England. *Journal of the Geological Society of London* 153, 827–838.
- Merlet, C., 1994. An accurate computer correction program for quantitative electron probe microanalysis. *Microchimica Acta* 114 (115), 363–376.
- Müller, A., Williamson, B.J., Smith, M., 2005. Origin of quartz cores in tourmaline from Roche Rock, SW England. *Mineralogical Magazine* 69, 381–401.
- Müller, A., Seltmann, R., Halls, C., Siebel, W., Dulski, P., Jeffries, T., Spratt, J., Kronz, A., 2006. The magmatic evolution of the Land's End pluton, Cornwall, and associated pre-enrichment of metals. *Ore Geology Reviews* 28, 329–367.
- Müller, A., van den Kerkhof, A.M., Behr, H.-J., Kronz, A., Koch-Müller, M., 2010. The evolution of late-Hercynian granites and rhyolites documented by quartz – a review. *Geological Society of America Special Papers* 472, 185–204.
- Neiva, A.M.R., Ramos, J.M.F., 2010. Geochemistry of granitic aplite-pegmatite sills and petrogenetic links with granites, Guarda-Belmonte area, central Portugal. *European Journal of Mineralogy* 22, 837–854.
- Norton, J.J., 1994. Structure and bulk composition of the Tin Mountain pegmatite, Black Hills, South Dakota. *Economic Geology* 89, 1167–1175.
- Novák, M., Černý, P., Uher, P., 2003. Extreme variation and apparent reversal of Nb-Ta fractionation in columbite-group minerals from the Scheibengraben beryl-columbite granitic pegmatite, Maršíkov, Czech Republic. *European Journal of Mineralogy* 15, 565–574.
- Pichavant, M., 1987. Effect of B and H₂O on liquidus phase relations in the haplogranite system at 1 kbar. *American Mineralogist* 72, 1056–1070.
- Pownall, J.M., Waters, D.J., Searle, M.P., Shail, R.K., Robb, L.J., 2012. Shallow laccolithic emplacement of the Land's End and Tregonning granites, Cornwall, UK: evidence from aureole field relations and P-T modelling of cordierite-anthophyllite hornfels. *Geosphere* 8, 1467–1504.
- Rainbault, L., Cuney, M., Azencott, C., Duthou, J.L., Joron, J.L., 1995. Geochemical evidence for a multistage magmatic genesis of Ta-Sn-Li mineralization in the granite at Beauvoir, French Massif Central. *Economic Geology* 90, 548–596.
- Reid, C., Flett, J.S., 1907. The geology of the Land's End District. Memoir of the British Geological Survey, Sheets 351/358 (England and Wales).
- Rusk, B.G., Lowers, H.A., Reed, M.H., 2008. Trace elements in hydrothermal quartz: relationship to cathodoluminescent textures and insights into vein formation. *Geology* 36, 547–550.
- Schaller, W.T., 1925. The genesis of lithium pegmatites. *American Journal of Science* 10, 269–279.
- Shearer, C.K., Papike, J.J., Jollieff, B.L., 1992. Petrogenetic links among granites and pegmatites in the Harney Peak rare-element granite-pegmatite system, Black Hills, South Dakota. *Canadian Mineralogist* 30, 785–809.
- Simmons, W.B., Heinrich, E.W., 1975. A summary of the petrogenesis of the granite-pegmatite system in the northern end of the Pikes Peak batholith. *Fortschritte der Mineralogie* 52, 251–264.
- Simons, B., Shail, R.K., Andersen, C.Q., 2016. The petrogenesis of the Early Permian granites of the Cornubian Batholith: lower plate post-collisional peraluminous magmatism in the Rhenohercynian Zone of the SW England. *Lithos* 260, 76–94.
- Simons, B.J., Andersen, J., Shail, R.K., Jenner, F.E., 2017. Fractionation of Li, Be, Ga, Nb, Ta, In, Sn, Sb, W and Bi in the peraluminous Early Permian Variscan granites of the Cornubian Batholith: precursor processes to magmatic-hydrothermal mineralisation. *Lithos* 278–281, 491–512.
- Stepanov, A.S., Hermann, J., 2013. Fractionation of Nb and Ta by biotite and phengite: implications for the "missing Nb paradox". *Geology* 41, 303–306.
- Stone, M., 1960. The Tregonning-Godolphin granite. In: Robson, J., Simpson, S. (Eds.), *Proceedings of the Conference of Geologists and Geomorphologists Working in South West England*. Royal Geological Society of Cornwall, Penzance, Bristol, pp. 14–16.
- Stone, M., 1966. Fold structures in the Mylor Beds, near Porthleven, Cornwall. *Geological Magazine* 103, 440–460.
- Stone, M., 1969. Nature and origin of banding in the granitic sheets Tremarne, Porthleven, Cornwall. *Geological Magazine* 106, 142–158.
- Stone, M., 1975. Structure and petrology of the Tregonning-Godolphin granite, Cornwall. *Proceedings of the Geologists' Association* 86, 155–170.
- Stone, M., 1992. The Tregonning granite: petrogenesis of Li-mica granites in the Cornubian batholith. *Mineralogical Magazine* 56, 141–155.
- Stone, M., Awad, N.T.I., 1988. Behaviour of trace-alkali and other elements at Tregonning granite – pelite contacts. *Proceedings of the Ussher Society* 7, 47–51.
- Stone, M., Exley, C.S., 1985. High heat production granites of southwest England and their associated mineralization: a review. *High Heat Production (HHP) Granites, Hydrothermal Circulation and Ore Genesis*, pp. 571–593.
- Stone, M., George, M.C., 1978. Amblygonite in the leucogranites of the Tregonning-Godolphin granite, Cornwall. *Mineralogical Magazine* 42, 151–152.
- Stone, M., Exley, C.S., George, M.C., 1988. Compositions of trioctahedral micas in the Cornubian batholith. *Mineralogical Magazine* 52, 175–192.
- Swanson, S.E., 1977. Relation of nucleation and crystal-growth to the development of granitic textures. *American Mineralogist* 62, 966–978.
- Thomas, R., Davidson, P., 2012. Water in granite and pegmatite-forming melts. *Ore Geology Reviews* 46, 32–46.
- Thomas, R., Davidson, P., 2013. The missing link between granites and granitic pegmatites. *Journal of Geosciences* 58, 183–200.
- Thomas, R., Davidson, P., 2015. Comment on "A petrologic assessment of internal zonation in granitic pegmatites" by David London (2014). *Lithos* 212–215, 462–468.
- Thomas, R., Webster, J.D., Rhede, D., Seifert, W., Rickers, K., Förster, H.-J., Heinrich, W., Davidson, P., 2006. The transition from peraluminous to peralkaline granitic melts: evidence from melt inclusions and accessory minerals. *Lithos* 91, 137–149.
- Van Lichtervelde, M., Linnen, R., Salvi, S., Beziat, D., 2006. The role of metagabbro rafts on tantalum mineralization in the Tanco granitic pegmatite, Manitoba. *Canadian Mineralogist* 44, 625–644.
- Webber, K.L., Falster, A.U., Simmons, W.B., Foord, E.E., 1997. The role of diffusion-controlled oscillatory nucleation on the formation of line rock in pegmatite-aplite dikes. *Journal of Petrology* 38, 1777–1791.
- Webber, K.L., Simmons, W.B., Falster, A.U., Foord, E.E., 1999. Cooling rates and crystallization dynamics of shallow level pegmatite-aplite dikes, San Diego County, California. *American Mineralogist* 84, 708–717.
- Wilkinson, J.J., 1990. The role of metamorphic fluids in the development of the Cornubian ore field: fluid inclusion evidence from south Cornwall. *Mineralogical Magazine* 54, 219–230.
- Wilkinson, J.J., 1991. Volatile production during contact metamorphism: the role of organic matter in pelites. *Journal of the Geological Society, London* 148, 731–736.
- Willis-Richards, J., Jackson, N.J., 1989. Evolution of the Cornubian ore field, southwest England: part 1. Batholith modelling and ore distribution. *Economic Geology* 84, 1078–1100.
- Wise, M.A., Francis, C.A., Černý, P., 2012. Compositional and structural variations in columbite-group minerals from granitic pegmatites of the Brunswick and Oxford fields, Maine: differential trends in F-poor and F-rich environments. *Canadian Mineralogist* 50, 1515–1530.

Milarite-group minerals from the NYF pegmatite Velká skála, Písek district, Czech Republic: sole carriers of Be from the magmatic to hydrothermal stage

MILAN NOVÁK¹, JAROSLAV CÍCHA², RENATA ČOPJAKOVÁ¹, RADEK ŠKODA^{1,*} and
MICHAELA VAŠINOVÁ GALIOVÁ^{1,3,4}

¹ Department of Geological Sciences, Faculty of Science, Masaryk University, 611 37 Brno, Czech Republic

*Corresponding author, e-mail: rskoda@sci.muni.cz

² Prácheň Museum, Velké náměstí 114, 397 24 Písek, Czech Republic

³ Department of Chemistry, Faculty of Science, Masaryk University, Kotlářská 2, 611 37 Brno, Czech Republic

⁴ Central European Institute of Technology, Masaryk University, Kamenice 5, 625 00 Brno, Czech Republic

Abstract: Four distinct paragenetic, morphological and compositional types of milarite-group minerals were distinguished in the NYF pegmatite Velká skála, Písek district, Czech Republic (Moldanubian Zone). The simply zoned (Kfs, Plg, Ab, Qz > Bt > Ap > Tur) pegmatite dike, ~60 cm thick, is enclosed in durbachite (K, Mg-rich melasyenite). The milarite-group minerals include: yellowish, subhedral, prismatic grains of homogeneous milarite I (milarite s.s.); prismatic subparallel aggregates of white to grayish milarite II (zoned milarite s.s. to Sc-rich milarite, up to ~20 mol% of the oftedalite component) from small pockets; colorless hexagonal prismatic crystals of milarite III (milarite s.s.) lining open fractures and microscopic fillings in recrystallized K-feldspar locally associated with REE-bearing minerals (allanite, aeschynite, titanite); very rare milarite IV (milarite s.s. to agakhanovite) as prismatic crystals and thin overgrowths with complex oscillatory zoning, ≤200 µm in size, on crystals of milarite II and milarite III. Their mineral assemblages, textures and compositions suggest primary (magmatic) for milarite I and hydrothermal origin for milarite II, III, and IV. The simplified compositional evolution in these milarites is: Al + Ca → Be + Sc → Be + Y, HREE → Be + LREE. Milarite-group minerals are the sole carriers of Be in the pegmatite, no relics or pseudomorphs after other Be-rich minerals were found; thus milarite is now established as an additional primary Be-rich mineral in granitic pegmatites. Mineral assemblages, chemical composition of minerals and close relation to the host durbachite suggest an NYF affinity of the Velká skála pegmatite as well as a close relation to euxenite-type pegmatites of the Třebíč Pluton. Milarite-group minerals from Velká Skála exhibit very similar compositional evolution to those found in the Heftetjern pegmatite, Tørdal, Norway.

Key-words: milarite; agakhanovite-(Y); EPMA; LA-ICP-MS; CL; compositional trends; beryllium; NYF pegmatite.

1. Introduction

Due to its very small ionic size and low ionic charge, Be is a highly incompatible element; consequently, in spite of its low crustal concentration of 5 ppm (Wedepohl, 1995), a large number of mineral species with nominally high Be content occur in nature (Grew, 2002; Grew & Hazen, 2014). Complex mineral assemblages of Be-rich phases that originated in the magmatic to hydrothermal stage are particularly common in granitic pegmatites and are very sensitive to their environments (Barton & Young, 2002; Černý, 2002; London & Evensen, 2002). Primary (magmatic) Be minerals in granitic pegmatites (both LCT and NYF families) contain beryl as the most abundant mineral by far, along with several other Be-bearing phases whose abundances range from common to very rare: e.g., chrysoberyl, Be-bearing cordierite, gadolinite-group minerals, phenakite, bazzite, hambergite, hurlbutite, beryllonite, helvite- and rhodizite-group minerals (e.g., Černý,

2002; Cooper *et al.*, 2006). Typically, one primary Be-rich mineral is present alone in a single pegmatite body or pegmatite district in most LCT (lithium–cesium–tantalum) and NYF (niobium–yttrium–fluorine) pegmatites (Černý, 2002); only sporadically two or more primary Be-rich phases may occur (e.g., Bjørlykke, 1934; Bergstøl & Juve, 1988; Novák *et al.*, 1998a; Cooper *et al.*, 2006). The assemblages of secondary Be-rich minerals are mostly pseudomorphs of beryl containing two or more Be minerals (Černý, 2002), but some late hydrothermal Be-rich minerals occurring in pockets show no evident relations to alteration of any primary Be-bearing mineral (Černý, 2002).

Milarite *stricto sensu* (s.s.), ideally $\text{Ca}_2\text{K}(\text{Be}_2\text{Al})\text{Si}_{12}\text{O}_{30}(\text{H}_2\text{O})$, is the most common member of the osumilite supergroup. These minerals are known from very different geological environments: peralkaline to alkaline intrusive to effusive rocks and their pegmatites, high-grade metamorphic rocks, meteorites, hydrothermal

veins, Alpine veins and granitic pegmatites of the LCT and NYF families (*e.g.*, Hawthorne *et al.*, 1991, 2014; Černý *et al.*, 1991; Černý, 2002; Cooper *et al.*, 2006). Milarite-group minerals (milarite s.s. and its Sc- and Y-rich analogs, oftedalite and agakhanovite-(Y)) are considered late minerals that mostly occur as hydrothermal alteration products of beryl and Be-bearing cordierite or as late hydrothermal minerals in pockets with no evident relationships to alteration of any primary Be-bearing mineral (Černý, 2002). Milarite-group minerals crystallize in alkaline conditions at low pressure ($P < \sim 2$ kbar) and temperature ($T < \sim 300$ °C; Hawthorne *et al.*, 1991; Černý, 2002). Milarite is not considered a primary (magmatic) mineral, although some members of the osumilite group may crystallize at high $P-T$ conditions (*e.g.*, osumilite, Holland *et al.*, 1996).

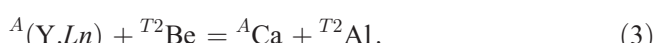
The granitic pegmatites of the Písek district have been known since the 1880s (*e.g.*, Scharizer, 1888; Vrba, 1895). Ježek & Krejčí (1920) described beryl crystals from the Velká skála locality with a density of $D = 2.54$ and 2.57 g cm^{-3} , values that are lower than those of beryl ($D \geq 2.65 \text{ g cm}^{-3}$) but very close to those of milarite ($D = 2.51\text{--}2.56 \text{ g cm}^{-3}$; Černý *et al.*, 1980). A detailed study of recently collected samples revealed that beryl reported by Ježek & Krejčí (1920) was very likely milarite; however, the original samples were not available. Milarite-group minerals present in several paragenetically, morphologically, and compositionally distinct types at this pegmatite were studied in detail to reveal their mineral assemblages, compositional variations and position in the crystallization sequence from the magmatic to hydrothermal stage.

2. Crystal chemistry of the osumilite group

The osumilite group belongs to the framework silicates with the general formula: $A_2B_2CDT_2Tl_{12}O_{30}(H_2O)$, where $A = \text{Al, Fe}^{3+}, \text{Sn, Mg, Zr, Fe}^{2+}, \text{Ca, Na, Y, Sc, lanthanides (Ln)}$; $B = \square, \text{Na, H}_2\text{O, K, Ca}$; $C = \text{K, Na, Ba, } \square$; $D = \square$; $T2 = \text{Li, Be, B, Mg, Al, Si, Mn, Zn}$; $Tl = \text{Si, Al}$ (Hawthorne *et al.*, 1991, 2014). We will focus on Be-bearing minerals of the milarite subgroup. Milarite s.s. with the ideal formula ${}^A\text{Ca}_2{}^B\square{}^C\text{K}{}^{T2}(\text{Be}_2\text{Al}){}^{Tl}\text{Si}_{12}\text{O}_{30}(\text{H}_2\text{O})$ was used to derive the substitutions, and the most common one:



yields two hypothetical milarite end-members, Be-rich “alkaline milarite” and Be-poor “aluminous milarite”, with the ideal formulae ${}^A\text{Ca}_2{}^B\text{Na}{}^C\text{K}{}^{T2}(\text{Be}_3){}^{Tl}\text{Si}_{12}\text{O}_{30}(\text{H}_2\text{O})$ and ${}^A\text{Ca}_2{}^B\square{}^C\square{}^{T2}(\text{BeAl}_2){}^{Tl}\text{Si}_{12}\text{O}_{30}(\text{H}_2\text{O})$, respectively; milarite s.s. is half way between both end-members (Černý, 2002). The substitutions:



are heading from milarite s.s. toward oftedalite ${}^A(\text{ScCa})_2{}^B\square{}^C\text{K}{}^{T2}(\text{Be}_3){}^{Tl}\text{Si}_{12}\text{O}_{30}(\text{H}_2\text{O})$, a Sc-analog of milarite (Cooper *et al.*, 2006), and agakhanovite-(Y) ${}^A(\text{YCa})_2{}^B\square{}^C\text{K}{}^{T2}(\text{Be}_3){}^{Tl}\text{Si}_{12}\text{O}_{30}(\text{H}_2\text{O})$, a Y-analog of milarite (Hawthorne *et al.*, 2014).

3. Granitic pegmatites of the Písek district

Pegmatites from the Písek district, which are enclosed in migmatised gneisses and amphibole-biotite durbachites (K,Mg-rich melasyenites to melagranites) of the Mehelník Massif, Moldanubian Zone (Fig. 1), are part of the Variscan Moldanubian pegmatite province (Novák *et al.*, 1998a and b, 2013; Melleton *et al.*, 2012). Two distinct types of granitic pegmatites were distinguished: (i) common beryl–columbite pegmatites, typical of the Písek district, were dated at 336 ± 3 Ma (U/Pb dating of monazite; Novák *et al.*, 1998b) and at 338 ± 11 Ma (U–Th–Pb dating of xenotime; Švecová *et al.*, 2016). They vary from small and simple dikes to large, texturally highly differentiated and geochemically more fractionated pegmatite bodies, up to 25 m in thickness, which commonly contain tourmaline, minor beryl, muscovite, and numerous accessory minerals, *e.g.*, fluorapatite, niobian rutile, ilmenite, monazite-(Ce), xenotime-(Y), zircon, and cordierite–sekaninaite. These mineral assemblages suggest the LCT signature; however, common REE-oxide minerals (*e.g.*, Bouška & Johan, 1972; Škoda *et al.*, 2011) from the most evolved pegmatites indicate some NYF affinity. Along with common beryl and rare Be-bearing cordierite–sekaninaite numerous secondary/hydrothermal Be-rich phases occur in these pegmatites: bertrandite, milarite, phenakite, danalite, helvite, and secondary beryl (Vrba, 1895; Novák & Cempírek, 2010; unpubl. data of the authors). (ii) Rare NYF pegmatites closely related to the host durbachites dated at 335–342 Ma (Janoušek & Holub, 2007; Kotková *et al.*, 2010) were found at the Velká skála locality and in the Kamenné doly quarry $\sim 3\text{--}4$ km NE of Písek. These simply zoned dikes, commonly $<\sim 1$ m thick with transitional contacts to host durbachite, contain minor chloritised biotite, accessory allanite-(Ce), titanite, ilmenite, and tourmaline. The examined Velká skála pegmatite with several paragenetic types of milarite is described in detail in Section 5.

4. Methods

4.1. Electron-probe microanalysis (EPMA)

The internal textures and chemical compositions of milarite and associated phases were investigated by a combination of back-scattered electron (BSE) images, cathodoluminescence imaging (EPMA-CL), EPMA and X-ray element mapping using the wavelength-dispersion mode of a CAMECA SX100 system. Operating conditions for EPMA were: accelerating voltage 15 kV, beam current 10–30 nA, and beam diameter 2–5 µm. Peak-counting times varied from 10 to 80 s in order to optimize the

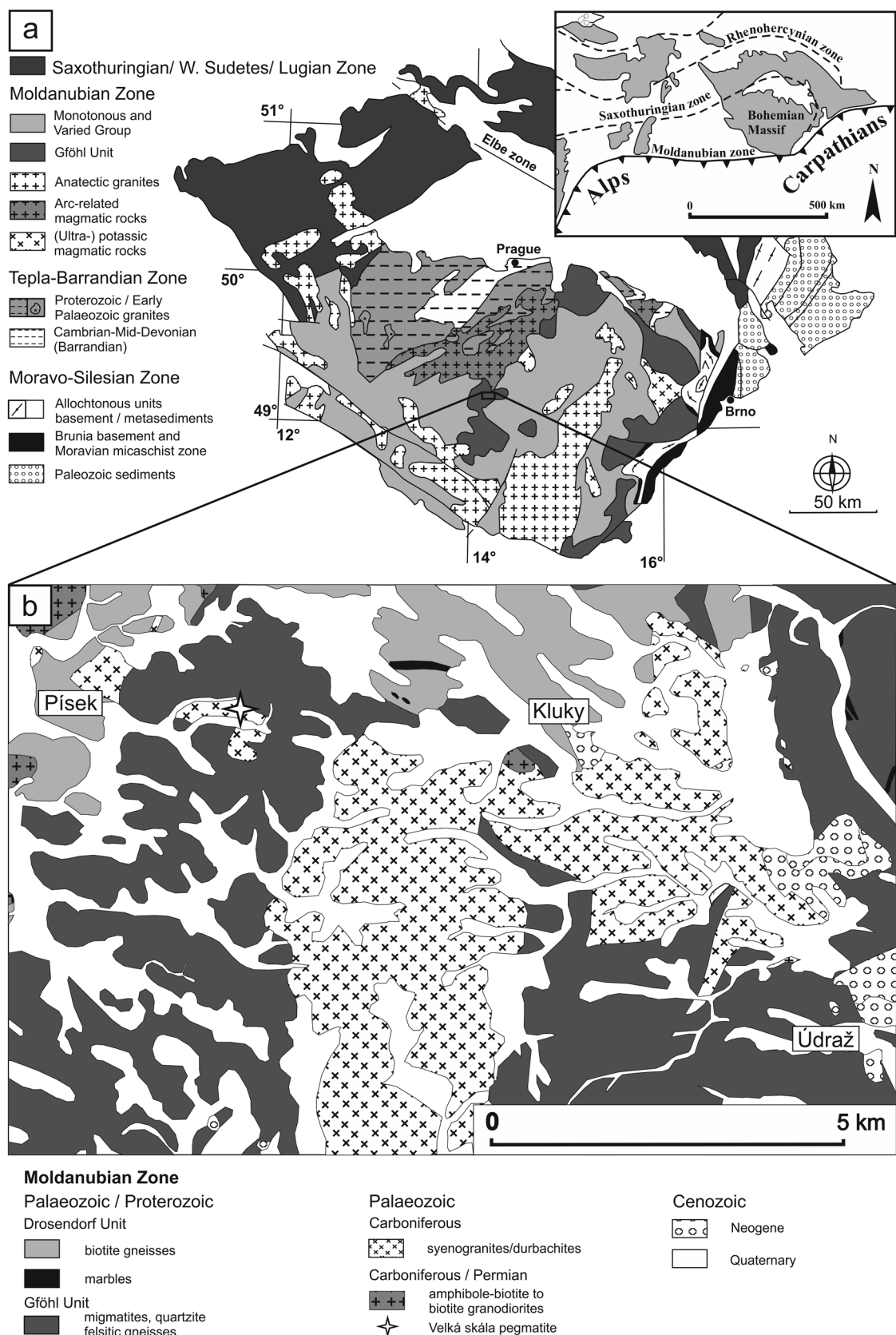


Fig. 1. Geological settings; (a) schematic geological map of the Bohemian Massif and its position within the European Variscides (modified after Franke, 2000; Schulmann *et al.*, 2009); (b) Schematic geological map of the Písek region with position of pegmatite locality (modified after Švecová *et al.*, 2016).

detection limits. The following standards were used: Si, Al, K – sanidine; Ca – wollastonite; Fe – almandine; Mn – spessartine; Mg – Mg_2SiO_4 ; Y – YAG; La–Yb – individual $LnPO_4$; U – U; Pb, V, Cl – vanadinite; Ca, Th – CaTh (PO_4)₂; P – fluorapatite/LaPO₄; Nb – columbite; Ta – CrTa₂O₆; Ti – TiO/titanite; Sn – Sn; Zr – zircon; Sc – ScVO₄; W – scheelite; As – lammerite; Cr – chromite; S – BaSO₄; Sr – SrSO₄; and F – topaz. Possible peak overlaps were checked for in detail, and background positions were chosen carefully with wavelength-dispersive angle scans on natural and synthetic REE phases. Raw intensities were reduced using the X-PHI matrix-correction routine (Merlet, 1994). The formulae of milarite-group minerals were calculated on the basis of 12Si. The amount of Be was calculated from charge balance, and H₂O was calculated from ideal stoichiometry. X-ray element maps were acquired with a step size of 2–4 µm using a fully focused electron beam, an accelerating voltage of 15 kV, a probe current of 60 nA, and 150 ms/pixel dwell time. A panchromatic cathodoluminescence detector attached to the CAMECA SX100 was used for EPMA-CL analysis. The photomultiplier is optimized for the 300–900 nm wavelength range. Digital panchromatic images were taken at 15.0 kV acceleration voltage, 20–40 nA beam current, and a frame time of 60 s.

4.2. Laser-ablation inductively coupled plasma mass spectrometry (LA–ICP-MS)

The Be content was determined by means of LA–ICP-MS. A double focusing ICP-MS Element 2 (Thermo Scientific™) was attached to an Analyte G2 laser-ablation system (Teledyne CETAC Technologies). The samples were placed into a 2-volume cell HelEx and ablated using an ArF* excimer laser operating at a wavelength of 193 nm (pulse length <4 ns). The ablated material was transported from the sample chamber using He carrier gas (total He flow rate of 0.65 L min⁻¹) and mixed with Ar (~1 L min⁻¹) prior to the torch. The content of Be was determined after 60 s of laser ablation to an individual spot with a diameter of 50 µm at a laser beam fluence of 4 J cm⁻² and 10 Hz frequency. Standard reference materials (SRM) NIST 610, 612, and 614, and the content of the internal reference element (Si) determined by EPMA were used for elemental quantification. The calculations were performed on baseline-corrected peak-area integrated intensities. The distribution of selected elements (Be, Sc, Si, Al) was investigated with an identical fluence and repetition rate; however, the spot diameter was significantly lower (4 µm) and the dwell time was reduced from 50 s to 6 s. The spatial resolution was 6 µm in both axes. The total number of analyzed spots (2220) was divided into four segments among which SRM 610 and 612 were ablated in order to correct the time-dependent instrumental drift.

The following abbreviations for rock-forming minerals are used in the text and figures: Mil = milarite, Aes = aeschynite-group minerals; the other abbreviations are after Whitney & Evans (2010). With respect to the recommendation of IUPAC, the term *REE* (rare earth

elements) includes *Ln* as well as Sc and Y. Further dividing of *Ln* according to their ionic size keeps the traditionally used abbreviations *LREE* (light *REE*) for larger *Ln* from La to Gd and *HREE* (heavy *REE*) for smaller *Ln* from Tb to Lu.

5. Geological setting and internal structure of the Velká skála pegmatite

Several small pegmatite dikes cutting migmatite and durbachite crop out at the Velká skála locality near Horní Novosedly, situated NE of the Kamenné doly quarry. The examined pegmatite forms a subvertical NW-trending dike, ~60 cm thick and several meters long, enclosed in a small body of durbachite surrounded by migmatites. The contact of the pegmatite with the host rock is rather sharp in hand specimens, but in thin sections the contact is transitional, with locally abundant apatite in durbachite directly adjacent to the pegmatite. Small enclaves of host durbachite, up to 5 cm in diameter, have transitional contacts. From the contact toward center, the simply zoned internal structure consists of: (i) a border medium-grained granitic unit (Kfs + Qtz + Pl + Bt) ~1 cm thick, (ii) a volumetrically dominant wall aplite unit (Kfs + Ab + Qtz ± Bt), locally with local coarse-grained portions (Kfs + Qtz + Ab), up to 10 cm in diameter, and rare pockets, (iii) a minor graphic unit (Kfs + Qz), and (iv) a heterogeneous coarse-grained unit (Kfs + Qtz + Ab) in the center. Coarse-grained portions are composed of subhedral grains of K-feldspar, massive gray quartz, and subhedral platy grains of yellowish albite. Small pockets lined with crystals of quartz, albite and/or K-feldspar are sporadically present in the coarse-grained portions. In addition to the major minerals and minor biotite that are present in all units, accessory milarite-group minerals, fluorapatite, tourmaline, pyrite altered to Fe-hydroxides oxides, allanite-(Ce), titanite, ilmenite, aeschynite-(Ce), nioboaeschynite-(Ce), monazite-(Ce), xenotime-(Y), zircon, and thorite were identified in the pegmatite. No beryl or pseudomorphs after it and no primary muscovite have been found.

6. Milarite and its mineral assemblages

6.1. Paragenetic and morphological types of milarite and their mineral assemblages

Four distinct types of milarite-group minerals were distinguished in the Velká skála pegmatite. *Milarite I* forms yellowish, subhedral, elongated grains, up to 2.5 cm long, in coarse-grained parts of the aplite unit, and some crystal faces of milarite I are developed in small pockets (Figs. 2a, 3a). Short prismatic crystals with the hexagonal shape of milarite I, up to 1 cm long, are scarcely present in small pockets as well (Fig. 2b). Prismatic subparallel aggregates of white to grayish *milarite II*, up to 1 cm long (Figs. 2c, d, 3b), typically occur in small pockets lined with crystals of albite, quartz, K-feldspar; however,

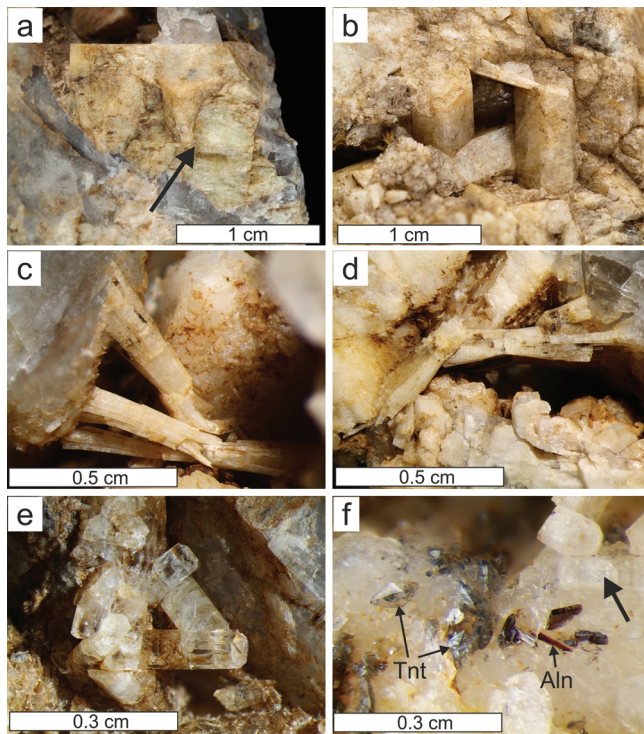


Fig. 2. Photos of milarite-subgroup minerals; (a) subhedral grains of milarite I in coarse-grained parts of the aplite unit; (b) shortly prismatic hexagonal crystals of milarite I in small pocket; (c, d) prismatic subparallel aggregates of milarite II in small pockets; (e) colorless hexagonal prismatic crystals of milarite III lining open fractures in K-feldspar; (f) colorless hexagonal prismatic crystals of milarite III associated with euhedral titanite and allanite-(Ce) crystals lining open fractures in K-feldspar.

crystals and aggregates of morphologically distinct milarite I and milarite II were never found within the same pocket. Milarite III forms colorless hexagonal prismatic crystals, up to 3 mm long, lining open fractures (Figs. 2e, f, 3c) and microscopic fillings in K-feldspar grains (Fig. 3d, e). They occur exclusively in the hydrothermally recrystallized zone of the aplite unit, up to 5 mm thick, adjacent to fractures. This zone consists of recrystallized K-feldspar, albite, quartz, and several newly-formed accessory REE minerals, which are coeval with milarite III, such as subhedral to euhedral allanite-(Ce), ≤ 1 mm long, and titanite ($\leq 250 \mu\text{m}$) with complex zonation in BSE and are commonly intergrown with milarite and K-feldspar (Fig. 3d, e), as well as rare prismatic crystals of aeschynite-(Ce) to nioboaeschynite-(Ce) (Fig. 3d). Allanite-(Ce) and titanite locally enclose tiny relics of monazite and rutile, respectively. Chlorite (commonly altered to vermiculite and Fe oxides) forms vermiciform aggregates enclosed in fracture-filling quartz, K-feldspar, titanite and milarite III. Fracture-filling quartz hosts oval voids filled by calcite and obviously later, tiny, needle-like rhabdophane-(Nd). Very rare milarite IV forms short prismatic crystals with complex oscillatory zoning, ≤ 0.2 mm long, growing on milarite II (Fig. 3b) and thin overgrowths, $\leq 20 \mu\text{m}$ thick, on prismatic or terminal crystal faces of milarite II and milarite III (Fig. 3e, f).

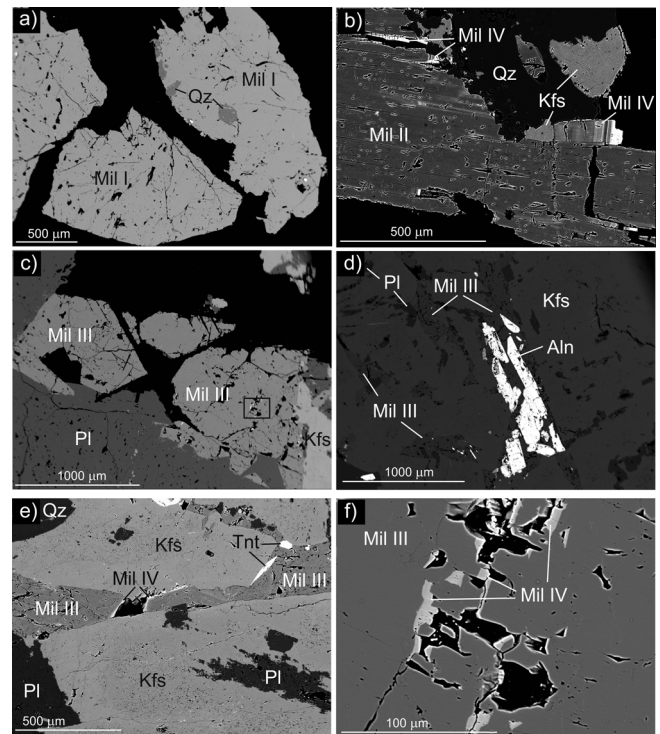


Fig. 3. Backscattered-electron (BSE) images of milarite from the Velká skála pegmatite; (a) subhedral grains of milarite I from coarse-grained parts of the aplite unit; (b) prismatic columnar milarite II composed of subparallel fibers from small pocket, locally with overgrowths of tiny prismatic crystals of milarite IV (brighter in BSE) with oscillatory zoning; (c) euhedral to subhedral crystals of milarite III on the open fracture in the aplite unit associated with albite and K-feldspar; (d) milarite III and allanite crystals filling fractures in K-feldspar; (e) fracture filling milarite III (locally rimmed with milarite IV) and titanite in K-feldspar.

6.2. Chemical composition of milarite-group minerals

All types of milarite are chemically distinct (Table 1). Primary milarite I is homogeneous in the BSE image and X-ray elemental maps (Fig. 4). Its composition is close to the ideal formula ${}^A\text{Ca}_2{}^B\Box{}^C\text{K}^{T2}(\text{Be}_2\text{Al})^{T1}\text{Si}_{12}\text{O}_{30}(\text{H}_2\text{O})$ (Fig. 5a) with an indication of a very minor substitution (1) toward the “alkaline milarite” ${}^A\text{Ca}_2{}^B\text{Na}{}^C\text{K}^{T2}(\text{Be}_3)^{T1}\text{Si}_{12}\text{O}_{30}(\text{H}_2\text{O})$. Only trace amounts of Na_2O (≤ 0.09 wt%) and BaO (≤ 0.11 wt%) were found. Scandium, Y, and Ln are below the EPMA detection limit (b.d.l.; Table 1; Fig. 5a). For milarite II, the distribution maps of Ca, Al, Sc, and Y show zoning that is nearly invisible in BSE images (Fig. 4). The X-ray maps reveal that milarite II is composed of individual parallel needles with variable contents of Sc_2O_3 [0.07–1.26 wt%; 0.01–0.19 atoms per formula unit (apfu) Sc], Ca (1.82–2.02 apfu) and Al (0.78–0.93 apfu). Domains enriched in Sc are depleted in Ca and Al (Fig. 4), thus substitution (2) toward oftedalite ${}^A(\text{ScCa})_2{}^B\Box{}^C\text{K}^{T2}(\text{Be}_3)^{T1}\text{Si}_{12}\text{O}_{30}(\text{H}_2\text{O})$ is apparent (Fig. 5b). Thin zones with slight Y_2O_3 enrichment (≤ 0.28 wt%) locally rim Sc-rich domains (Fig. 4b). Homogeneous milarite III is close to the ideal formula and similar to

Table 1. Representative EPMA analyses of milarite-subgroup minerals from Velká Skála pegmatite. 1–10 correspond to milarite, 11 and 12 to agakhanovite-(Y) and 13 to the Ce-analog of agakhanovite-(Y).

Type	Mil I 1	Mil I 2	Mil I 3	Mil II 4	Mil II 5	Mil II 6	Mil III 7	Mil III 8	Mil III 9	Mil IV 10	Mil IV 11	Mil IV 12	Mil IV 13
SiO ₂	72.60	73.38	72.72	73.14	73.38	72.39	72.51	72.23	71.90	71.77	70.16	69.38	67.99
Al ₂ O ₃	4.94	4.41	4.49	4.50	4.08	4.75	5.28	5.20	4.66	3.95	0.30	0.22	0.79
Sc ₂ O ₃	0.00	0.00	0.00	0.92	1.31	0.16	0.00	0.00	0.06	0.00	0.00	0.11	0.00
Y ₂ O ₃	0.00	0.00	0.00	0.00	0.00	0.27	0.00	0.00	0.15	1.65	5.79	5.09	2.25
La ₂ O ₃	0.00	0.00	0.00	0.00	0.00	0.00	0.00	0.00	0.00	0.00	0.00	0.53	1.78
Ce ₂ O ₃	0.00	0.00	0.00	0.00	0.00	0.16	0.00	0.00	0.00	0.00	0.38	1.51	3.62
Pr ₂ O ₃	0.00	0.00	0.00	0.00	0.00	0.00	0.00	0.00	0.00	0.00	0.00	0.19	0.32
Nd ₂ O ₃	0.00	0.00	0.00	0.00	0.00	0.00	0.00	0.00	0.00	0.00	0.39	0.57	1.18
Sm ₂ O ₃	0.00	0.00	0.00	0.00	0.00	0.00	0.00	0.00	0.00	0.00	0.00	0.13	0.00
Gd ₂ O ₃	0.00	0.00	0.00	0.00	0.00	0.00	0.00	0.00	0.00	0.00	0.27	0.37	0.00
Dy ₂ O ₃	0.00	0.00	0.00	0.00	0.00	0.00	0.00	0.00	0.00	0.09	0.37	0.34	0.18
Ho ₂ O ₃	0.00	0.00	0.00	0.00	0.00	0.00	0.00	0.00	0.00	0.00	0.16	0.19	0.10
Er ₂ O ₃	0.00	0.00	0.00	0.00	0.00	0.00	0.00	0.00	0.00	0.00	0.38	0.30	0.11
Yb ₂ O ₃	0.00	0.00	0.00	0.00	0.00	0.00	0.00	0.00	0.00	0.36	0.85	0.29	0.13
CaO	11.50	11.61	11.33	10.98	10.46	10.91	11.45	11.43	11.21	10.26	7.20	6.48	6.77
BaO	0.00	0.08	0.11	0.00	0.00	0.00	0.00	0.00	0.00	0.00	0.00	0.00	0.00
Na ₂ O	0.00	0.09	0.05	0.06	0.00	0.00	0.05	0.05	0.00	0.00	0.21	0.08	0.05
K ₂ O	4.87	4.98	4.87	4.81	4.65	4.72	4.89	4.83	4.96	4.71	4.40	4.63	4.92
BeO*	5.06	5.48	5.45	5.22	5.66	5.24	4.78	4.81	5.14	5.57	7.42	7.42	6.80
H ₂ O**	1.81	1.83	1.82	1.83	1.83	1.81	1.81	1.80	1.80	1.79	1.75	1.73	1.70
Total	100.78	101.85	100.84	101.45	101.37	100.41	100.77	100.35	99.87	100.15	100.03	99.54	98.69
Si	12	12	12	12	12	12	12	12	12	12	12	12	12
Al	0.962	0.850	0.872	0.870	0.786	0.927	1.030	1.018	0.916	0.779	0.060	0.044	0.165
Be*	2.008	2.152	2.161	2.056	2.224	2.088	1.901	1.918	2.061	2.237	3.050	3.083	2.883
Sc	0.000	0.000	0.000	0.131	0.187	0.023	0.000	0.000	0.008	0.000	0.000	0.016	0.000
Y	0.000	0.000	0.000	0.000	0.000	0.023	0.000	0.000	0.013	0.147	0.527	0.468	0.212
La	0.000	0.000	0.000	0.000	0.000	0.000	0.000	0.000	0.000	0.000	0.000	0.034	0.116
Ce	0.000	0.000	0.000	0.000	0.000	0.009	0.000	0.000	0.000	0.000	0.024	0.095	0.234
Pr	0.000	0.000	0.000	0.000	0.000	0.000	0.000	0.000	0.000	0.000	0.000	0.012	0.021
Nd	0.000	0.000	0.000	0.000	0.000	0.000	0.000	0.000	0.000	0.000	0.024	0.035	0.074
Sm	0.000	0.000	0.000	0.000	0.000	0.000	0.000	0.000	0.000	0.000	0.000	0.008	0.000
Gd	0.000	0.000	0.000	0.000	0.000	0.000	0.000	0.000	0.000	0.000	0.015	0.021	0.000
Dy	0.000	0.000	0.000	0.000	0.000	0.000	0.000	0.000	0.000	0.005	0.020	0.019	0.010
Ho	0.000	0.000	0.000	0.000	0.000	0.000	0.000	0.000	0.000	0.000	0.009	0.011	0.006
Er	0.000	0.000	0.000	0.000	0.000	0.000	0.000	0.000	0.000	0.000	0.021	0.016	0.006
Yb	0.000	0.000	0.000	0.000	0.000	0.000	0.000	0.000	0.000	0.018	0.044	0.015	0.007
Ca	2.036	2.034	2.003	1.930	1.832	1.938	2.031	2.035	2.005	1.838	1.320	1.201	1.280
Ba	0.000	0.005	0.007	0.000	0.000	0.000	0.000	0.000	0.000	0.000	0.000	0.000	0.000
Na	0.000	0.029	0.014	0.020	0.000	0.000	0.015	0.016	0.000	0.000	0.069	0.028	0.018
K	1.027	1.038	1.026	1.006	0.970	0.998	1.033	1.025	1.057	1.004	0.961	1.021	1.108
O	30	30	30	30	30	30	30	30	30	30	30	30	30
H ₂ O**	1	1	1	1	1	1	1	1	1	1	1	1	1
$\sum REE, Y, Sc$	0.000	0.000	0.000	0.131	0.187	0.056	0.000	0.000	0.021	0.170	0.684	0.751	0.685

* BeO was calculated by charge balance; ** H₂O was calculated from ideal stoichiometry. High contents of Sc, Y, and Ce are highlighted in bold.

milarite I except for slightly higher contents of Al (0.94–1.04 apfu) and Y₂O₃ (≤ 0.14 wt%) and lower Ba (b.d.l.). Milarite IV is generally REE-enriched and follows the trend from REE-rich milarite to agakhanovite-(Y) (Fig. 5c). The short prismatic crystals growing on milarite II are highly heterogeneous, with irregular oscillatory zoning (Fig. 3b), where REE contents vary significantly (0.01–0.51 apfu Y; 0.02–0.23 apfu Ln). Yttrium predominates over Ln and the LREE/HREE ratio is 0.5–1.6. Thin overgrowths on milarite II and III (Fig. 4) are REE-rich (≤ 0.46 apfu Y; ≤ 0.49 apfu Ln). They evolve from Y- and

HREE-rich to LREE-rich compositions (LREE/HREE 1.5–12.6), where Ce locally predominates over Y in the most outer parts of overgrowths. Milarite IV is also slightly enriched in Na₂O (≤ 0.24 wt%) and Sc₂O₃ (≤ 0.28 wt%).

High concentrations of BeO, varying in average contents for individual milarite types from 4.94 wt% to 5.33 wt%, were obtained using LA-ICP-MS. However, EPMA and LA-ICP-MS differ significantly in terms of the volume of analyzed material (beam-spot diameter of $\sim 5 \mu\text{m}$ for EPMA and laser-spot diameter of $50 \mu\text{m}$). With respect to the significant heterogeneity of some samples

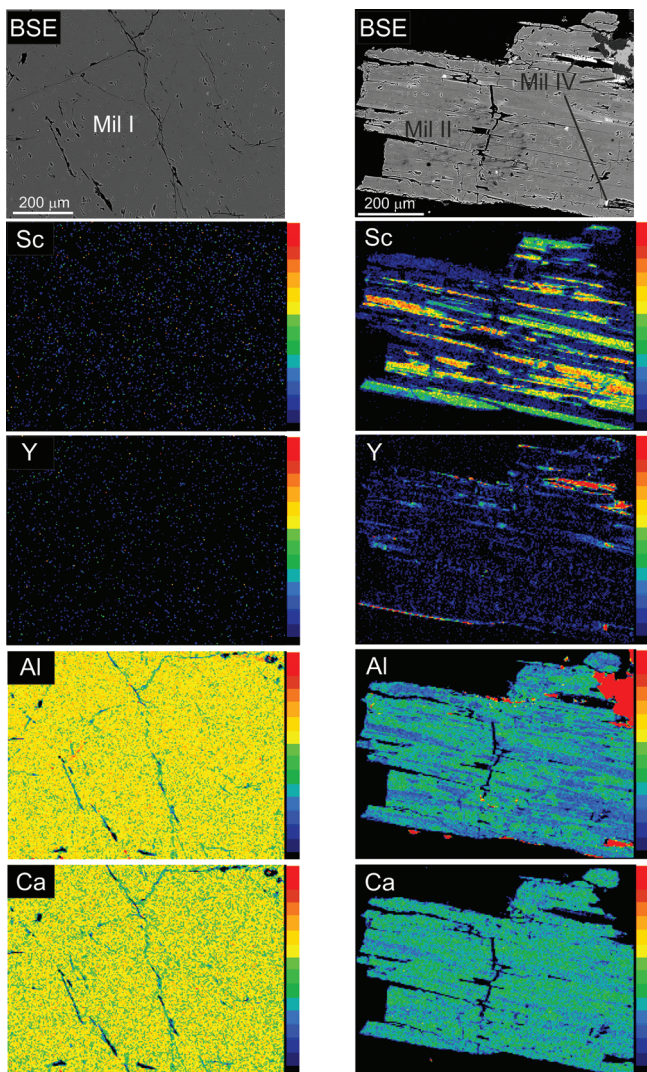


Fig. 4. Wavelength-dispersive X-ray maps of representative elements showing homogeneity of milarite I (on the left) and heterogeneity of milarite II (on the right).

and the small size of some chemically different milarite zones, the given values do not represent a real variability of Be in heterogeneous milarite II and IV. Consequently, Be contents in milarite-group minerals (see Table 1) were calculated from stoichiometry. The analyzed and calculated Be contents are in a good agreement for chemically homogeneous milarite types. The distribution map of Be (Fig. 6) confirms significantly higher Be content in REE-rich milarite IV as well as a less conspicuous variability of Be in milarite II, positively correlating with Sc and corresponding to the substitutions (2) and (3).

6.3. Chemical composition of associated minerals

Magmatic plagioclase ($\text{Ab}_{81-99}\text{An}_{0-16}\text{Or}_{0-5}$) varies from a composition slightly enriched in Ca and K to albite. Such evolution is visible in core-to-rim trends of individual crystals and particularly from the outer to inner pegmatite units. Recrystallized plagioclase associated with milarite III corresponds to almost pure albite, similar to magmatic

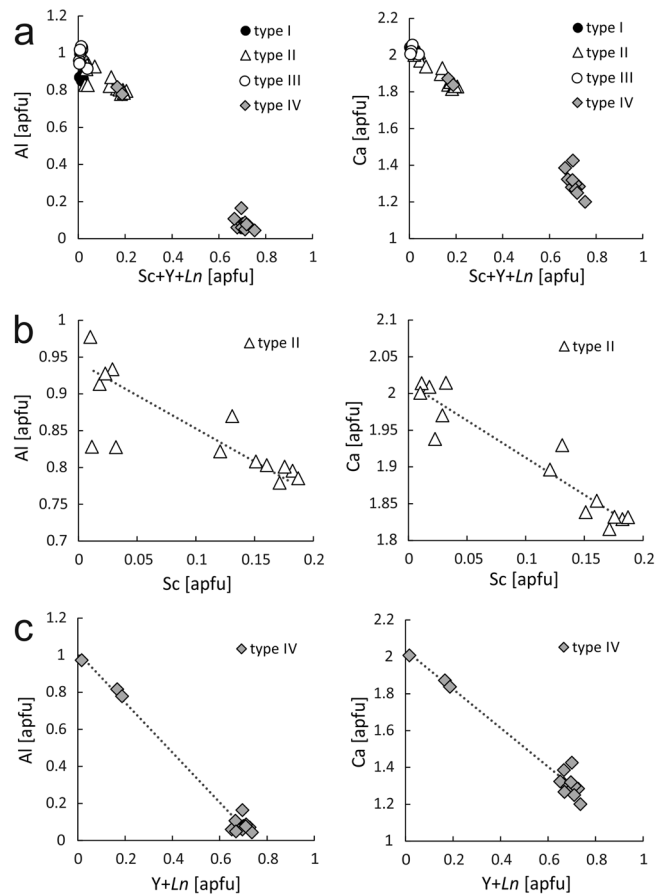


Fig. 5. Substitution trends of major and minor elements in milarite-subgroup minerals.

albite from the coarse-grained unit. Magmatic K-feldspar ($\text{Or}_{92-99}\text{Ab}_{2-9}$) shows slightly higher variability in Na compared to recrystallized K-feldspar that is associated with milarite III ($\text{Or}_{98-99}\text{Ab}_{1-2}$). Feldspars have low P_2O_5 contents (≤ 0.06 wt%) and other trace elements (≤ 0.24 wt% BaO in K-feldspar; ≤ 0.18 wt% Rb_2O in albite). Biotite exhibits rather high Mg ($X_{\text{Mg}} = 0.53$; Si ~ 2.85 ; Al ~ 1.34) and low F (~ 0.2 apfu). Interstitial tourmaline (schorl) exhibits $\text{Fe}/(\text{Fe} + \text{Mg}) = 0.58-0.79$, moderate variations in Al = 5.89–6.40 apfu, high Na = 0.71–0.86 apfu, low Ca = 0.05–0.08 apfu, high Ti (0.05–0.29 apfu), and low to moderate F = 0.19–0.48 apfu.

Minerals associated with milarite III on fractures include allanite-(Ce) with high REE content (0.73–0.92 apfu), Sc (0.58–1.85 wt% Sc_2O_3), Zr (≤ 0.31 wt% ZrO_2), Sn (≤ 0.22 wt% SnO_2) and very low ThO_2 and UO_2 contents (≤ 0.15 wt%; b.d.l. of EPMA). Monazite enclosed in allanite-(Ce) is strongly enriched in LREE and very poor in ThO_2 (≤ 0.20 wt%) and UO_2 wt% (b.d.l.). Titanite shows enrichment in Nb_2O_5 (≤ 5.76 wt%), Ta_2O_5 (≤ 1.74 wt%), SnO_2 (≤ 7.61 wt%), and Sc_2O_3 (≤ 0.62 wt%), whereas the contents of Al_2O_3 (0.58–1.79 wt%), F (0.12–0.36 wt%), and Ln_2O_3 (0.03–0.81 wt%) are rather low. Accessory rutile contains minor Nb_2O_5 (≤ 2.39 wt%), Ta_2O_5 (≤ 0.57 wt%), SnO_2 (≤ 0.41 wt%) and Sc_2O_3 (≤ 0.16 wt%). Aeschynite-(Ce) to nioboaeschynite-(Ce) has a Ti/Nb ratio

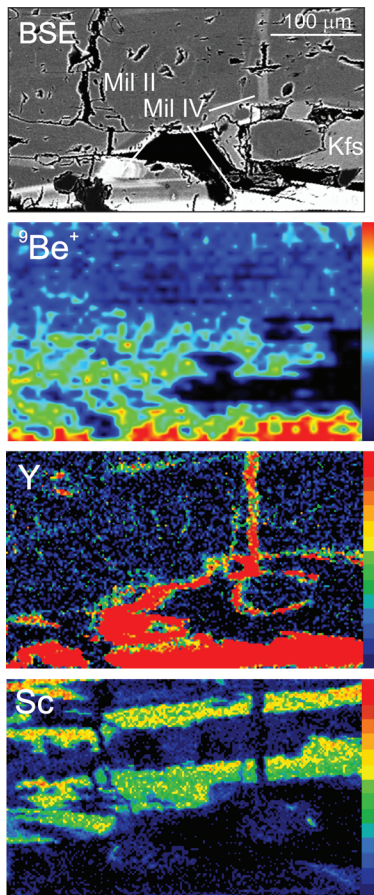


Fig. 6. Distribution maps of Be (LA–ICP–MS), Y (EPMA), and Sc (EPMA) in milarite II and IV.

close to 1 (0.89–1.20 apfu Ti; 0.80–1.02 apfu Nb; 0.03–0.05 apfu Ta), low Ca content (0.25–0.31 apfu), and high $\sum Ln$ (0.70–0.81 apfu) with a strong enrichment in LREE (chiefly Ce and Nd) and low contents of Y (0.02–0.03 apfu) and HREE.

6.4. Cathodoluminescence study

Milarite-group minerals typically exhibit complex optical zoning (*e.g.*, Janeczek, 1986; Černý *et al.*, 1991). Consequently, cathodoluminescence imaging was used as a complementary method to discriminate between different types of milarite. Variation in luminescence within milarite crystals reflects a variety of textural features such as chemical variation, microcracks, healed cracks, recrystallization, inclusions. No cathodoluminescence (black CL with no variation in CL intensity) was observed in the images (Fig. 7). Milarite II and III yielded low to high luminescence with dark gray to light gray CL in panchromatic EPMA-CL images, with rather subparallel zoning in milarite II and complex sector zoning in milarite III (Fig. 7); both types show numerous microcracks and healed cracks. Generally, the lowest CL intensity corresponds to inner (earliest-formed) parts of crystals and its intensity increases toward the outer parts. In case of milarite II, the CL intensity approximately correlates with Sc distribution where Sc-poor domains show the lowest CL intensity. Milarite IV has the

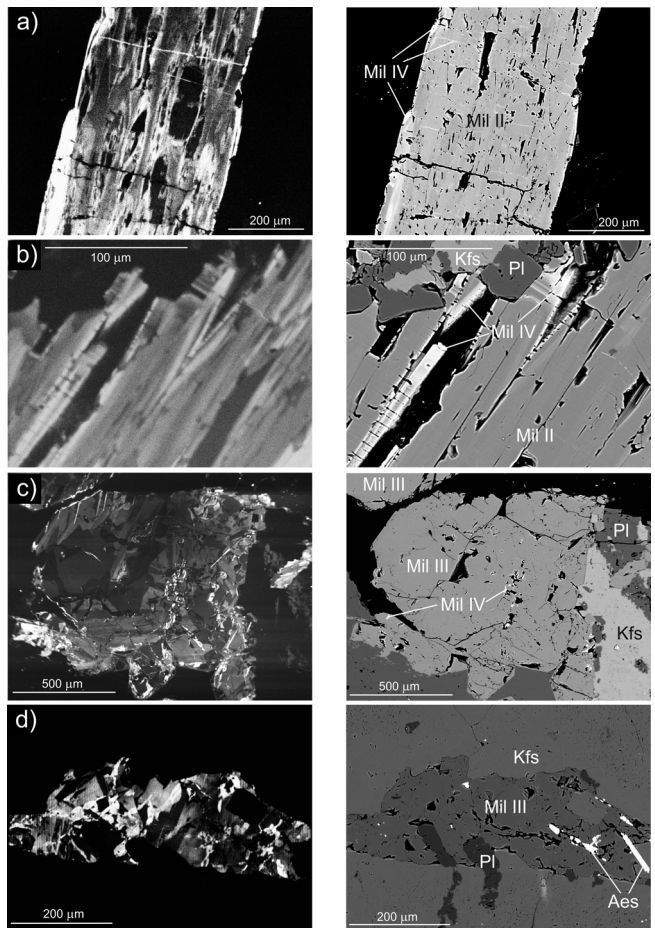


Fig. 7. EPMA-CL images (on the left) and corresponding BSE images (on the right) of milarite; (a) prismatic milarite II composed of subparallel zones with different CL overgrown by milarite IV (bright white CL) and cut by a lot of microcracks (black CL) and cracks healed with milarite IV (bright white CL); (b) detail of subparallel CL zoning of milarite II and oscillatory zoning of milarite IV; (c) complex CL of rather euhedral crystals of milarite III on the open fracture with sector, patchy and oscillatory zoning and common healed cracks; later milarite IV overgrows or infills the cracks in milarite III; (d) complex CL with sector and patchy zoning of milarite III filling fractures in K-feldspar.

strongest luminescence (bright white to light gray in panchromatic EPMA-CL images), locally with oscillatory zoning (Fig. 7b), and its intensity correlates well with elevated contents of REE in BSE images (Fig. 7a–c).

K-feldspar, plagioclase, and quartz associated with milarite III gave homogeneous dark gray to black CL images significantly contrasting with the gray to bright white cathodoluminescence of their primary (magmatic) counterparts (Figs. 7b–d, 8). For example, large magmatic K-feldspar crystals show more complex CL images with light gray to bright white CL of their outer part and darker central part with common tiny bright spots (reflecting micropores and microinclusions of apatite; see Fig. 8). In contrast, the outer recrystallized zones of magmatic feldspars along the fracture and the fracture-filling feldspar show simple homogeneous dark gray to black CL images and only locally with small relics of the original magmatic CL features (Fig. 8).

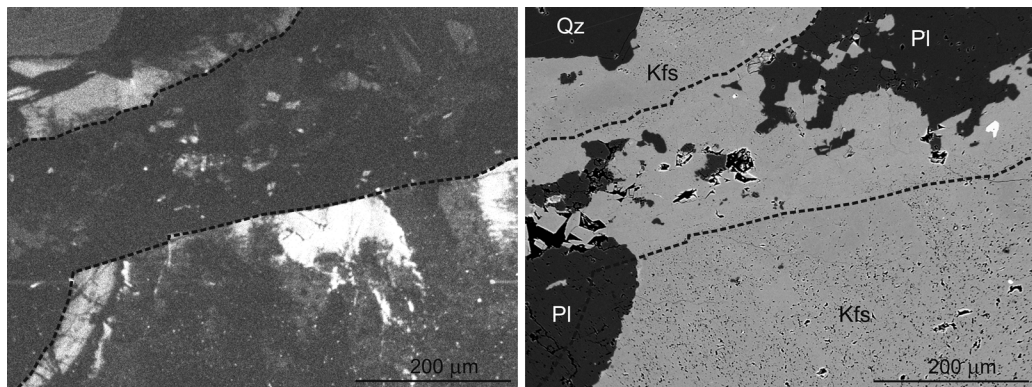


Fig. 8. EPMA-CL image (on the left) and corresponding BSE image (on the right) of minerals along the fracture. Primary magmatic minerals show dark gray to bright white and more complex CL compared with rather homogeneous dark gray CL of fracture filling minerals and recrystallized zones of magmatic minerals close to the fracture (this zone of dark CL is marked with dashed lines in images).

7. Discussion

7.1. Genetic position of the individual types of milarite in the pegmatite

Different chemical compositions (Table 1; Figs. 4, 5), textural features, morphologies (Figs. 2, 3, 7), and associated minerals define the four types of milarite-group minerals and suggest their different genetic position. Milarite I forms (1) rough cm-sized crystals that are intimately intergrown with quartz and feldspars in coarse-grained portions of the aplite unit, or (2) grains that have continually grown from the massive rock into primary pockets (Fig. 2a, b). These crystals are not associated with fractures or with any fluid-penetrating system, and milarite I is chemically homogeneous with homogeneous dark CL image (Fig. 4). Consequently, such paragenetic position (London, 2008) indicates primary late magmatic (igneous) rather than an early subsolidus origin. The occurrence of milarite grains in a massive rock and its mineral assemblage of major minerals (Kfs + Ab + Qz) from the Strange Lake peralkaline granite (Černý *et al.*, 1991) is similar to the Velká skála milarite I.

Aggregates of subparallel needle-like crystals of milarite II are developed in small pockets within the aplite unit. Milarite II always grows on the crystal faces of feldspars and has not been found growing continuously from the aplite matrix. Its chemical composition varies from Sc-poor cores through Sc-rich intermediate zones to Y, Ln-enriched rims of individual needles (Figs. 4, 5a, b). These aggregates show heterogeneous CL images with dark Sc-poor cores and brighter REE-enriched domains (Fig. 7a, b). Milarite II is evidently younger than milarite I and is postmagmatic/hydrothermal. Milarite III lining open fractures or filling space in recrystallized aplite has a similar chemical composition and a similar, very complex CL (Fig. 7c, d). Textural features indicate that crystallization of milarite III is unambiguously related to recrystallization of the narrow zone along open fractures in the aplite unit (Fig. 8). Milarite II and milarite III represent distinct paragenetic and morphological types that are spatially separated in pockets and on fractures (Fig. 2c–f); however, their temporal position in the overall sequence of

crystallization of the pegmatite is not clear. Milarite IV (agakhanovite) represents the latest generation and is found overgrowing or filling cracks of milarite II and III.

7.2. Compositional variations and substitution mechanisms

Four distinct types of milarite-group minerals from the Velká skála pegmatite display varying composition, from rather homogeneous milarite I and milarite III close to the ideal formula through heterogeneous Sc-enriched milarite II to highly heterogeneous Y, Ln-rich milarite IV (milarite to agakhanovite-(Y)) (Figs. 4, 5). Only weak variations in other elements (*e.g.*, Na, Ba) were revealed. The individual types of milarite differ significantly in their substitution mechanisms as well. Milarite I and milarite III that are close to the ideal composition show moderate participation of the substitution (1) toward ${}^A\text{Ca}_2{}^B\text{Na}{}^C\text{K}{}^{T2}(\text{Be}_3){}^{T1}\text{Si}_{12}\text{O}_{30}(\text{H}_2\text{O})$ and only minor toward ${}^A\text{Ca}_2{}^B\Box{}^C\Box{}^{T2}(\text{BeAl}_2){}^{T1}\text{Si}_{12}\text{O}_{30}(\text{H}_2\text{O})$, respectively. Scandium-enriched milarite II undergoes the dominant substitution (2), with up to ~20 mol% of the oftedalite component. In milarite IV, with high contents of Y and Ln (Table 1), the substitution (3) is dominant, reaching up to ~90 mol% of the agakhanovite component. The general trend is illustrated via the simplified evolutions: Al + Ca → Be + Sc → Be + Y, HREE → Be + LREE or without the Sc-rich stage Al + Ca → Be + Y, HREE → Be + LREE.

The compositional variations in milarite s.s. from Velká skála (milarite I and III) are similar to other localities (*e.g.*, Černý *et al.*, 1980, 1991; Hawthorne *et al.*, 1991; Černý, 2002) and the participation of the substitution (1) is minor (0.78–1.06 apfu Al). Ofstedalite from the type locality Heftetjern with ≤0.96 apfu Sc (Cooper *et al.*, 2006), is more enriched in Sc compared to milarite II from Velká skála with ≤0.19 apfu Sc. Milarite II enriched in REE is not associated with any Sc-, Y-, or Ln-rich accessory mineral. This is in contrast to milarite III, which crystallized simultaneously with Sc-rich allanite and titanite, monazite-(Ce) and REE oxides of the aeschynite group. Both milarite II and III might crystallize from the fluids enriched in Sc and Ln, but these

ions entered the structure of other minerals in the mineral assemblage of milarite III. Moreover, milarite III-forming fluids were enriched in Ti, Sn, Nb, and Ta. Milarite IV enriched in Y (≤ 0.51 apfu) is similar to type agakhanovite-(Y) from Heftetjern (Hawthorne *et al.*, 2014) but it exhibits much higher concentrations of *Ln* (≤ 0.67 apfu) and especially Ce (≤ 0.22 apfu); whereas concentrations of Sc are low (≤ 0.04 apfu). Yttrium typically predominates over *Ln*; however, some compositions yielded $\sum Ln$ (Ce dominant) $>$ Y and potentially represent a new phase – a Ce-analog of agakhanovite-(Y) (Fig. 6).

7.3. Assemblages of Be-bearing minerals from pegmatites of the Písek region and Třebíč Pluton, Moldanubian Zone

The Velká skála pegmatite with milarite-group minerals as sole Be minerals is unique not only in the Moldanubian Zone. The spatially associated LCT beryl–columbite pegmatites from the Písek district contain beryl as the dominant primary Be-rich mineral in several distinct paragenetic and compositional types (Sejkora *et al.*, 1998; Novák & Cempírek, 2010). Rare Be-bearing cordierite–sekaninaite was found only at two localities. The hydrothermal Be-rich assemblages, locally developed into open vugs after altered beryl or in primary pockets lined with albite, are rather complex. They include dominant bertrandite (Scharizer, 1888; Vrba, 1895; Novák & Cempírek, 2010) along with minor phenakite and danalite all after beryl, secondary beryl after cordierite–sekaninaite and secondary helvite and phenakite after danalite (Vrba, 1895; Novák & Cempírek, 2010; unpubl. data of the authors). Hydrothermal milarite is known solely from pockets after highly altered beryl. Nevertheless, a detailed study of the individual assemblages of Be minerals in the Písek district is absent.

Elevated alkalinity and low activities of B, P, and F are typical of F-poor NYF pegmatites of both rare-element and miarolitic classes (e.g., Wise, 1999; Ercit, 2005; Černý & Ercit, 2005; Simmons & Webber, 2008; Černý *et al.*, 2012). Affiliation of the Velká skála pegmatite to the NYF family is supported by the occurrence of allanite-(Ce), aeschynite to nioboaeschynite-(Ce), and titanite, the total absence of primary muscovite, and low contents of P in feldspars. These characteristics and primarily the evident spatial relation to the same parental rock (durbachite), similar internal structure, pegmatite textures, mineral assemblages, and chemical composition of minerals (e.g., interstitial tourmaline) are very similar to those of the NYF euxenite-type pegmatites of the Třebíč Pluton (Škoda *et al.*, 2006; Škoda & Novák, 2007; Novák *et al.*, 2011, 2012, Čopjaková *et al.*, 2013). In these pegmatites beryl is a common primary Be mineral, locally enriched in Na, Sc, Mg, Fe, and Cs (Novák & Filip, 2010), and several secondary (hydrothermal) Be-minerals – bavenite, phenakite, milarite, secondary beryl, helvite and bazzite – have also been identified. Hence, the Velká skála pegmatite may represent a specific NYF pegmatite similar to euxenite-type pegmatites of the Třebíč Pluton. However, simili-

ties in chemical composition (Be and REE) of milarite to agakhanovite-(Y) $(YCa_2K(BeAl_2)Si_{12}O_{30}(H_2O))$ from the Velká skála pegmatite and gadolinite $(Y,Ca_2FeBe_2(SiO_4)_2O)$ suggest that the pegmatite may be related to the REL-REE gadolinite-type pegmatites (Černý & Ercit, 2005). Because the pegmatite classifications (e.g., Wise, 1999; Černý & Ercit, 2005; Černý *et al.*, 2012) cannot comprise all variations in mineral assemblages of such extremely variable rocks, the Velká skála pegmatite with milarite as the sole primary mineral of Be does not require a definition of a new specific (sub)type. However, milarite is now established as a further primary (magmatic) Be-rich mineral in NYF pegmatites along with common beryl (e.g., Aurisicchio *et al.*, 1988, 2012; Wise, 1999; Novák & Filip, 2010; Přikryl *et al.*, 2014), gadolinite (Ercit, 2005; Černý & Ercit, 2005), and other rare phases (e.g., Černý, 2002; Cooper *et al.*, 2006). Due to the similar appearance of milarite I with beryl, primary (magmatic–igneous) milarite might have been overlooked at some occurrences of beryl-bearing NYF granitic pegmatites and peralkaline pegmatites/granites (see Černý *et al.*, 1991).

7.4. Primary and secondary mineral assemblages of Be-rich minerals in the NYF pegmatites

Beryllium-rich minerals reflect specific conditions of their origin such as acidity/alkalinity, activity of various elements (Si, Al, Na, Ca, P, S), and *P-T* conditions; hence, they may be used as indicators of the conditions of their origin (see Barton, 1986; Barton & Young, 2002; Černý, 2002; Franz & Morteani, 2002; Markl & Schumacher, 1997). Due to its wide *P-T-X* stability field, beryl is the most widespread Be in granitic pegmatites. From this point of view, the absence of beryl or gadolinite, both typical primary Be-minerals in NYF pegmatites (Černý & Ercit, 2005), as well as the occurrence of several compositional and paragenetic types of primary milarite as the sole Be-bearing mineral at the Velká skála pegmatite are unique. Common primary (magmatic) milarite I (milarite s.s.), hydrothermal milarite II (Sc-rich milarite to milarite) from pockets, hydrothermal milarite III (milarite s.s.) from fractures, and milarite IV [agakhanovite-(Y)] as late hydrothermal overgrowths of milarite II and milarite III imply that alkaline conditions persisted throughout all stages of milarite crystallization starting from late solidus to late subsolidus conditions. This is in contrast with most secondary assemblages of Be-rich minerals in granitic pegmatites, which typically contain several Be species (e.g., Černý, 2002; Cooper *et al.*, 2006). For example, in the Věžná I pegmatite, numerous secondary Be-minerals as alteration products of beryl (bertrandite, bavenite, epididymite; Černý, 1965, 1968; Novák *et al.*, 1991) and Be-bearing cordierite (secondary beryl, bavenite, milarite, epididymite) indicate high variability in composition of hydrothermal fluids in time and space, including acidity/alkalinity and activity of some elements at this locality. At the pegmatite Heftetjern, Norway, a similar compositional evolution of milarite-group minerals including milarite, oftedalite and agakha-

novite-(Y) (Cooper *et al.*, 2006; Hawthorne *et al.*, 2014) was revealed. However, this pegmatite is larger and enclosed in amphibolite. It has a complexly zoned internal structure, an elevated degree of fractionation exhibited by an abundance of Be-minerals, and contains numerous accessory minerals of Sn, Sc, Ta, and Nb (Bergstøl & Juve, 1988; Raade *et al.*, 2004; Cooper *et al.*, 2006; Kolitsch *et al.*, 2010). Several Be-rich minerals were found at the locality: primary – beryl, bazzite, gadolinite, phenakite and helvite, and secondary/hydrothermal – bertrandite, bavenite, bazzite, hingganite-(Ce), and milarite-subgroup minerals. However, the compositional evolution of milarite-subgroup minerals, milarite → oftedalite → milarite → agakhanovite-(Y) is very similar to that of the Velká skála pegmatite.

Dominance of milarite-group minerals in the Velká skála pegmatite implies stable but alkaline conditions throughout both the primary (late magmatic) to hydrothermal stages, which was perhaps enhanced by the small size/volume of the pegmatite relative to host durbachite. It is clear that milarite III and milarite IV crystallized in an open system (addition of Mg) as is evident from the associated chlorite/vermiculite. However, related NYF granitic pegmatites from the Třebíč Pluton have the same host rock (durbachite – K,Mg-rich melasyenite), very similar internal structure and size, but a quite variable suite of secondary/hydrothermal Be-rich minerals including bavenite, secondary beryl, bazzite, milarite, helvite, and phenakite (Novák & Filip, 2010; unpubl. data of the authors). Consequently, why alkaline conditions persist throughout primary and hydrothermal crystallization at the Velká skála pegmatite remains unclear and requires further study.

Acknowledgements: The authors thank Joel Grice and Uwe Kolitsch for constructive criticism that significantly improved the manuscript. We dedicate this paper to Zdeněk Johan, whose contribution to the study of REE-minerals of the Písek district inspired our research. This work was supported by the research project GAČR P210/14/1347S. MVG acknowledges the European Regional Development Fund project “CEITEC” – Central European Institute of Technology (CZ.1.05/1.1.00/02.0068).

References

- Aurisicchio, C., Fooravanti, G., Grubessi, O., Zanazzi, P. (1988): Reappraisal of the crystal chemistry of beryl. *Am. Mineral.*, **73**, 826–837.
- Aurisicchio, C., Conte, A.M., De Vito, C., Ottolini, L. (2012): Beryl from miarolitic pockets of granitic pegmatites, Elba, Italy: characterization of crystal chemistry by means of EMP and SIMS analyses. *Can. Mineral.*, **50**, 1467–1488.
- Barton, M. (1986): Phase equilibria and thermodynamic properties of minerals in the $\text{BeO}-\text{Al}_2\text{O}_3-\text{SiO}_2-\text{H}_2\text{O}$ (BASH) system, with petrologic applications. *Am. Mineral.*, **71**, 277–300.
- Barton, M. & Young, S. (2002): Non-pegmatitic deposits of beryllium: mineralogy, geology, phase equilibria and origin. In “Beryllium – mineralogy, petrology and geochemistry”, E.S. Grew, ed. *Rev. Mineral. Geochem.*, **50**, 591–691.
- Bergstøl, S. & Juve, G. (1988): Scandian ixiolite, pyrochlore and bazzite in granite pegmatite in Tordal, Telemark, Norway. A contribution to the mineralogy and geochemistry of scandium and tin. *Mineral. Petrol.*, **38**, 229–243.
- Bjørlykke, H. (1934): The mineral paragenesis and classification of the granite pegmatites of Iveland, Setesdal, Southern Norway. *Norsk Geol. Tidsskr.*, **14**, 211–311.
- Bouška, V. & Johan, Z. (1972): New data on písekite. *Lithos*, **5**, 93–103.
- Černý, P. (1965): Mineralogy of two pegmatites from the Věžná serpentinite. CSc. Thesis, Geol. Inst. ČSAV, Praha (in Czech).
- (1968): Berylliumwandlungen in Pegmatiten – Verlauf und Produkte. *N. Jb. Mineral. Abh.*, **108**, 166–180.
- (2002): Mineralogy of beryllium in granitic pegmatites. In “Beryllium – mineralogy, petrology and geochemistry”, E.S. Grew, ed. *Rev. Mineral.*, **50**, 405–444.
- Černý, P. & Ercit, T.S. (2005): Classification of granitic pegmatites. *Can. Mineral.*, **43**, 2005–2026.
- Černý, P., Hawthorne, F.C., Jarosewich, E. (1980): Crystal chemistry of milarite. *Can. Mineral.*, **18**, 41–57.
- Černý, P., Hawthorne, F.C., Jambor, J.L., Grice, J.D. (1991): Yttrian milarite. *Can. Mineral.*, **29**, 533–541.
- Černý, P., London, D., Novák, M. (2012): Granitic pegmatites as reflections of their sources. *Elements*, **8**, 289–294.
- Cooper, M.A., Hawthorne, F.C., Ball, N.A., Černý, P. (2006): Ofstedalite, $(\text{Sc}, \text{Ca}, \text{Mn}^{2+})_2\text{K}(\text{Be}, \text{Al})_3\text{Si}_{12}\text{O}_{30}$, a new member of the milarite group from the Heftetjern pegmatite, Tordal, Norway: description and crystal structure. *Can. Mineral.*, **44**, 943–949.
- Copjaková, R., Škoda, R., Vašinová Galiová, M., Novák, M. (2013): Distributions of Y + REE and Sc in tourmaline and their implications for the melt evolution; examples from NYF pegmatites of the Třebíč Pluton, Moldanubian Zone, Czech Republic. *J. Geosci.*, **58**, 113–131.
- Ercit, T.S. (2005): REE-enriched granitic pegmatites. In “Rare-element geochemistry and ore deposits”, R.L. Linnen, I.M. Samson, eds. *Geol. Assoc. Can. Short Course Notes*, **17**, 257–296.
- Franke, W. (2000): The mid-European segment of the Variscides: tectono-stratigraphic units, terrane boundaries and plate tectonic evolution. In “Orogenic processes: quantification and modelling in the Variscan Belt”, W. Franke, V. Haak, O. Oncken, D. Tanner, eds. *Geol. Soc. Lond. Spec. Publ.*, **179**, 35–62.
- Franz, G. & Morteani, G. (2002): Be-minerals: synthesis, stability, and occurrence in metamorphic rocks. In “Beryllium – mineralogy, petrology and geochemistry”, E.S. Grew, ed. *Rev. Mineral.*, **50**, 551–589.
- Grew, E.S. (2002): Mineralogy, petrology and geochemistry of beryllium: an introduction and list of beryllium minerals. *Rev. Mineral.*, **50**, 1–76.
- Grew, E.S. & Hazen, R.M. (2014): Beryllium mineral evolution. *Am. Mineral.*, **99**, 999–1021.
- Hawthorne, F.C., Kimata, M., Černý, P., Ball, N., Rossman, G.R., Grice, J.D. (1991): The crystal chemistry of the milarite-group minerals. *Am. Mineral.*, **76**, 1836–1856.
- Hawthorne, F.C., Abdu, Y.A., Ball, N.A., Černý, P., Kristiansen, R. (2014): Agakhanovite-(Y), ideally $(\text{YCa})_2\text{K}[\square](\text{BeAl}_2)\text{Si}_{12}\text{O}_{30}(\text{H}_2\text{O})$, a new milarite-group mineral from the Heftetjern pegmatite, Tordal, Southern Norway: description and crystal structure. *Am. Mineral.*, **99**, 2084–2088.
- Holland, T.J.B., Babu, E.V.S.S.K., Waters, D.J. (1996): Phase relations of osumilite and dehydration melting in pelitic rocks: a simple thermodynamic model for the KFMASH system. *Contrib. Mineral. Petrol.*, **124**, 383–394.

- Janeczek, J. (1986): Chemistry, optics and crystal growth of milarite from Strzegom, Poland. *Mineral. Mag.*, **50**, 271–277.
- Janoušek, V. & Holub, F.V. (2007): The causal link between HP–HT metamorphism and ultrapotassic magmatism in collisional orogens: case study from the Moldanubian Zone of the Bohemian Massif. *Proc. Geol. Assoc.*, **118**, 75–86.
- Ježek, B. & Krejčí, A. (1920): About minerals from Velká skála near Písek. *Rozpr. Čes. Akad. Věd. Tř. II*, **28**, 1–4 (in Czech).
- Kolitsch, U., Kristiansen, R., Raade, G., Tillmanns, E. (2010): Heftetjernite, a new scandium mineral from the Heftetjern pegmatite, Tørdal, Norway. *Eur. J. Mineral.*, **22**, 309–316.
- Kotková, J., Schaltegger, U., Leichmann, J. (2010): Two types of ultrapotassic plutonic rocks in the Bohemian Massif – coeval intrusions at different crustal levels. *Lithos*, **115**, 163–176.
- London, D. (2008): Pegmatites. The Canadian Mineralogist, Special Publication 10, 347 p.
- London, D. & Evensen, J.M. (2002): Beryllium is silicic magmas and the origin of beryl-bearing pegmatites. In “Beryllium – mineralogy, petrology and geochemistry”, E.S. Grew, ed. *Rev. Mineral.*, **50**, 445–486.
- Markl, G. & Schumacher, J. (1997): Beryl stability in local hydrothermal and chemical environments in a mineralized granite. *Am. Mineral.*, **82**, 195–203.
- Melletton, J., Gloaguen, E., Frei, D., Novák, M., Breiter, K. (2012): How are the emplacement of rare-element pegmatites, regional metamorphism and magmatism interrelated in the Moldanubian domain of the variscan Bohemian massif, Czech Republic? *Can. Mineral.*, **50**, 1751–1773.
- Merlet, C. (1994): An accurate computer correction program for quantitative electron probe microanalysis. *Microchim. Acta*, **114–115**, 363–376.
- Novák, M. & Cempírek, J., eds. (2010): Granitic pegmatites and mineralogical museums in Czech Republic. IMA 2010, Budapest, Hungary. *Acta Mineral. Petrogr. Field Guideb. Ser.*, **6**, 1–56.
- Novák, M. & Filip, J. (2010): Unusual (Na,Mg)-enriched beryl and its breakdown products (beryl II, bazzite, bavenite) from euxenite-type NYF pegmatite related to the orogenic ultrapotassic Třebíč pluton, Czech Republic. *Can. Mineral.*, **48**, 615–628.
- Novák, M., Korbel, P., Odehnal, F. (1991): Pseudomorphs of bertrandite and epididymite after beryl from Vězná, Western Moravia, Czechoslovakia. *Neues Jb. Mineral. Mh.*, **1991**, 473–480.
- Novák, M., Burns, P.C., Morgan VI, G.B. (1998a): Fluorine variation in hambergite from granitic pegmatites. *Can. Mineral.*, **36**, 441–446.
- Novák, M., Černý, P., Kimbrough, D.L., Taylor, M.C., Ercit, T.S. (1998b): U–Pb ages of monazite from granitic pegmatites in the Moldanubian Zone and their geological implications. *Acta Univ. Carol. Geol.*, **42**, 309–310.
- Novák, M., Škoda, R., Filip, J., Macek, I., Vaculovič, T. (2011): Compositional trends in tourmaline from intragranitic NYF pegmatites of the Třebíč pluton, Czech Republic: an electron microprobe, Mössbauer and LA–ICP–MS study. *Can. Mineral.*, **49**, 359–380.
- Novák, M., Škoda, R., Gadas, P., Krmíček, L., Černý, P. (2012): Contrasting origins of the mixed (NYF + LCT) signature in granitic pegmatites, with examples from the Moldanubian Zone, Czech Republic. *Can. Mineral.*, **50**, 1077–1094.
- Novák, M., Kadlec, T., Gadas, P. (2013): Geological position, mineral assemblages and contamination of granitic pegmatites in the Moldanubian Zone, Czech Republic; examples from the Vlastějovice region. *J. Geosci.*, **58**, 21–47.
- Přikryl, J., Novák, M., Filip, J., Gadas, P., Galiová, M.V. (2014): Iron + magnesium-bearing beryl from granitic pegmatites: an EMPA, LA–ICP–MS, Mössbauer spectroscopy, and powder XRD study. *Can. Mineral.*, **52**, 271–284.
- Raade, G., Bernhard, F., Ottolini, L. (2004): Replacement textures involving four scandium silicate minerals in the Heftetjern granitic pegmatite, Norway. *Eur. J. Mineral.*, **16**, 945–950.
- Scharizer, R. (1888): Der Bertrandit von Písek. *Z. Kristallogr. Mineral.*, **14**, 33–43.
- Schulmann, K., Konopásek, J., Janoušek, V., Lexa, O., Lardeaux, J.M., Edel, J.B., Štípká, P., Ulrich, S. (2009): An Andean type Palaeozoic convergence in the Bohemian Massif. *C. R. Geosci.*, **341**, 266–286.
- Sejkora, J., Litočleb, J., Exnar, P., Černý, P., Čech, F. (1998): Some physical–chemical data from pink beryl (morganite) from Písek pegmatites. *Bull. Czech Geol. Surv.*, **73**, 347–350 (in Czech with English summary).
- Simmons, W.B. & Webber, K.L. (2008): Pegmatite genesis: state of the art. *Eur. J. Mineral.*, **20**, 421–438.
- Škoda, R. & Novák, M. (2007): Y,REE,Nb,Ta,Ti-oxide (AB_2O_6) minerals from REL-REE euxenite-subtype pegmatites of the Třebíč Pluton, Czech Republic; substitutions and fractionation trends. *Lithos*, **95**, 43–57.
- Škoda, R., Novák, M., Houzar, S. (2006): Granitic NYF pegmatites of the Třebíč Pluton. *Acta Mus. Morav. Sci. Geol.*, **91**, 129–176 (in Czech with English summary).
- Škoda, R., Novák, M., Cícha, J. (2011): Uranium–niobium-rich alteration products after “písekite”, an intimate mixture of Y, REE, Nb, Ta, Ti-oxide minerals from the Obrázk I pegmatite, Písek, Czech Republic. *J. Geosci.*, **56**, 317–325.
- Švecová, E., Čopjaková, R., Losos, Z., Škoda, R., Nasdala, L., Cícha, J. (2016): Multi-stage evolution of xenotime-(Y) from Písek pegmatites, Czech Republic: an electron probe micro-analysis and Raman spectroscopy study. *Mineral. Petrol.*, **110**, 747–765.
- Vrba, K. (1895): Über Beryllium-Minerale aus der Umgebung von Písek. *Bull. Int. Acad. Sci. Cracovie*, **3**, 1–16.
- Wedepohl, K.H. (1995): The composition of the continental crust. *Geochim. Cosmochim. Acta*, **59**, 1217–1232.
- Whitney, D.L. & Evans, B.W. (2010): Abbreviations for names of rock-forming minerals. *Am. Mineral.*, **95**, 185–187.
- Wise, M.A. (1999): Characterization and classification of NYF-type pegmatites. The Eugene E. Foord Memorial Symposium on NYF-type Pegmatites, Denver, Colorado. *Can. Mineral.*, **37**, 802–803.

Received 28 November 2016

Modified version received 30 March 2017

Accepted 26 April 2017

Sc- and REE-rich tourmaline replaced by Sc-rich REE-bearing epidote-group mineral from the mixed (NYF+LCT) Kracovice pegmatite (Moldanubian Zone, Czech Republic)

RENATA ČOPJAKOVÁ^{1,*}, RADEK ŠKODA¹, MICHAELA VAŠINOVÁ GALIOVÁ^{2,3}, MILAN NOVÁK¹ AND JAN CEMPÍREK^{1,4}

¹Department of Geological Sciences, Faculty of Science, Masaryk University, Kotlářská 2, 611 37 Brno, Czech Republic

²Department of Chemistry, Faculty of Science, Masaryk University, Kotlářská 2, 611 37 Brno, Czech Republic

³Central European Institute of Technology (CEITEC), Masaryk University, Kamenice 5, 625 00 Brno, Czech Republic

⁴Department of Earth, Ocean, and Atmospheric Sciences, University of British Columbia, 2207 Main Mall, Vancouver, British Columbia V6T 1Z4, Canada

ABSTRACT

Primary black thick-prismatic Al-rich schorl to rare fluor-schorl (TurP1), locally overgrown by brownish-green Li-rich fluor-schorl to fluor-elbaite (TurP2) from the Kracovice pegmatite (mixed NYF+LCT signature), was partly replaced by secondary Li-rich fluor-schorl to fluor-elbaite (TurS) plus the assemblage REE-bearing epidote-group mineral + chamosite. Primary Al-rich schorl (TurP1) shows high and variable contents of Sc (33–364 ppm) and Y+REE (40–458 ppm) with steep, LREE-enriched REE pattern. Overgrowing (TurP2) and replacing (TurS) Li-rich fluor-schorl to fluor-elbaite is typically depleted in Sc (21–60 ppm) and Y+REE (3–47 ppm) with well-developed tetrad effect in the first (La-Nd) and the second (Sm-Gd) tetrads. Scandium- and REE-rich black tourmaline (TurP1) crystallized earlier from the melt, whereas crystallization of primary Li-rich fluor-schorl to fluor-elbaite (TurP2) most likely took place during late magmatic to early hydrothermal conditions. Both the secondary Li-rich fluor-schorl to fluor-elbaite (TurS) and the unusual assemblage of REE-bearing epidote-group mineral + chamosite are likely coeval products of subsolidus reactions of the magmatic Al-rich schorl (TurP1) with evolved REE-poor, Li,F-rich, alkaline pegmatite-derived fluids. Well-crystalline REE-bearing epidote-group mineral ($\text{Y}+\text{REE} = 0.42\text{--}0.60 \text{ apfu}$) confirmed by Raman spectroscopy has a steep, LREE-rich chondrite-normalized REE pattern with significant negative Eu anomaly and shows variable and high contents of Sc ($\leq 3.3 \text{ wt\% } \text{Sc}_2\text{O}_3$) and Sn ($\leq 1.0 \text{ wt\% } \text{SnO}_2$). Substitution ScAl_{1-x} and minor vacancy in the octahedral sites are suggested in the REE-bearing epidote-group mineral.

Keywords: Schorl, fluor-elbaite, tourmaline replacement, Sc-rich REE-bearing epidote-group mineral, granitic pegmatite, Bohemian Massif

INTRODUCTION

Tourmaline is a frequent minor to accessory mineral in rocks of widely variable composition formed in various geological settings including magmatic, metamorphic, sedimentary, and hydrothermal environments. Tourmaline is a characteristic mineral of strongly peraluminous granites and pegmatites where it crystallizes either as a primary phase from melt or as a hydrothermal mineral during late-magmatic stage (Wolf and London 1997; London 2014a). Hydrothermal fluids derived from highly fractionated peraluminous granites and pegmatites are commonly enriched in volatiles such as B, Li, and F. Tourmaline has a large stability field in terms of both temperature and pressure (Henry and Dutrow 1996; London 2011) and is quite resistant to weathering (Morton and Hallsworth 2007). Nevertheless, tourmaline namely in granitic pegmatites is locally altered by late hydrothermal fluids to various, mostly aluminous minerals [e.g., muscovite, chlorite, pumpellyite-(Al); e.g., Dietrich 1985; Ahn and Buseck 1998; Novák et al. 2013; Prokop et al. 2013]. The breakdown of tourmaline and its replacement by various Al-

silicates during interaction with hydrothermal and metamorphic fluids also were reported from ore deposits and tourmalinates (Slack and Robinson 1990; Leitch and Turner 1992; Čopjaková et al. 2012).

Rare earth element (REE) rich minerals of the epidote group belong either to the allanite or the dollaseite subgroups. They have a general formula $\text{A}^{1,2}\text{A}_2\text{M}^{1,2,3}(\text{M}_2^{3+}\text{M}^{2+})_3[\text{T}_2\text{O}_7][\text{TO}_4]^{04}(\text{O})^{010}(\text{OH})$ with the site occupancy $\text{A}1 = \text{Ca, Mn}$; $\text{A}2 = \text{REE, Th, U, Ca, Sr}$; $\text{M}1 = \text{Al, Fe}^{3+}, \text{Mn}^{3+}$; $\text{M}2 = \text{Al}$; $\text{M}3 = \text{Fe}^{2+}, \text{Mg}^{2+}, \text{Mn}^{2+}$; $\text{O}4 = \text{O}^{2-}, \text{F}^{-}$; $\text{O}10 = \text{OH}^{-}$ (Gieré and Sorensen 2004; Armbruster et al. 2006). Minerals of the allanite subgroup are derived from clinzozoisite by the substitution $\text{A}^2\text{REE}^{3+}+\text{M}3\text{M}^{2+} \rightarrow \text{A}^2\text{Ca}^{2+}+\text{M}3\text{M}^{3+}$. The most common members of the allanite subgroup, allanite-(Ce) and ferriallanite-(Ce), occur as accessory minerals of metaluminous granitic rocks, carbonatites, metamorphic rocks, and skarns. In granitic pegmatites they crystallize during the primary (magmatic) or secondary (metasomatic) stages (Peterson and MacFarlane 1993; Hoshino et al. 2006; Škoda et al. 2006, 2012). Secondary allanite sometimes occurs as a breakdown product of feldspars, biotite, and eudialyte during interaction of hydrothermal fluids with granitoid rocks (Pantó 1975; Ward et al. 1992; Coulson 1997). Nevertheless, the mineral assemblage

* E-mail: copjak@sci.muni.cz

tourmaline + allanite is very rare in granitic pegmatites and other granitic rocks (Novák et al. 2011a, 2012; Čopjaková et al. 2013a).

In the present study, the assemblage of magmatic Al-rich schorl from the Kracovice pegmatite (Bohemian Massif), which was replaced by the hydrothermal assemblage of REE-bearing epidote-group mineral + chamosite + fluor-elbaite was investigated using EMP, LA-ICP-MS, and Raman spectroscopy. Chemical variations of both major and trace (Y+REE, Sc) elements in tourmaline were used for genetic implications and to decipher the tourmaline evolution and replacement process. Moreover, textural relations, compositional trends and substitutions mechanisms in extraordinarily Sc-rich REE-bearing epidote-group mineral replacing tourmaline are discussed.

GEOLOGICAL SETTING AND HOST PEGMATITE

The Moldanubian Zone, a highly metamorphosed core of the Bohemian Massif, represents a crustal (and upper mantle) tectonic collage assembled during the Variscan orogeny and modified by several events of superimposed deformation and high- to low-grade metamorphic re-equilibration at about ~ 340 – 330 Ma. They are: (1) a HP-HT event in upper amphibolite to granulite facies at $T_{\max} \sim 850$ – 900 °C and $P_{\max} = 1.2$ – 1.8 MPa, more or less overprinted during a rapid decompression by (2) a MP-HT event at $T \sim 700$ °C and $P \sim 0.4$ – 0.6 MPa (e.g., Pertoldová et al. 2009); and (3) LP-HT metamorphic event related to contact envelope of granite plutons.

Extensive Variscan igneous activity shows several distinct stages (see Timmerman 2008 for overview): (1) subduction-related normal and high-K calc-alkaline suites (~ 370 – 345 Ma); (2) (ultra-)potassic, Mg-rich quartz syenitic to melagranitic plutons—durbachites (~ 340 – 335 Ma); (3) moderately to strongly peraluminous anatetic granites formed as a consequence of the LP-HT metamorphic overprint (331–326 Ma); and (4) late small plutons of fine-grained I-type granitoids associated with minor diorites (319–300 Ma).

The Moldanubian Zone is characterized by the presence of numerous granitic pegmatites of different origin and mineralogy (Novák et al. 2013). They frequently belong to the rare-element class and exhibit substantial variability in size, textural differentiation, degree of fractionation, and mineralogy. The pegmatites range from barren to highly fractionated dikes with LCT (enriched in Li, Cs, Ta; dated at 340–325 Ma, Novák et al. 1998a; Melletton et al. 2012), NYF (enriched in Nb, Y, F; dated at ~ 340 – 335 Ma) and mixed NYF+LCT geochemical signatures (Novák et al. 2012, 2013) using the current classification schemes (Černý and Ercit 2005; Černý et al. 2012). The Třebíč syenite (durbachite) Pluton (for more details see, e.g., Janoušek and Holub 2007) hosts a population of intragranitic NYF pegmatites ranging in textural-paragenetic and geochemical features from primitive metaluminous allanite-subtype pegmatites with allanite-(Ce), titanite, ilmenite, and tourmaline (dravite > schorl), to more evolved, metaluminous to slightly peraluminous euxenite-subtype pegmatites containing tourmaline (schorl), ilmenite, titanite, aeschynite-, and euxenite-group minerals, beryl, zircon, tinzenite, and herzenbergite (Škoda and Novák 2007; Novák et al. 2011a, 2012, 2013; Čopjaková et al. 2013a).

The Kracovice pegmatite is a symmetrically zoned dike, ~ 1 m thick and 30 m long, cutting a graphitic gneiss ca. 300 m W of

the edge of the Třebíč Pluton. It represents the most evolved pegmatite body from the population of dominantly NYF pegmatites related to the Třebíč Pluton (Němec 1990; Novák et al. 1999, 2012; Škoda et al. 2006; Čopjaková et al. 2013a). From the contact inward, the pegmatite consists of: a narrow zone of a coarse-grained granitic unit (Kfs+Pl+Qz+Bt+Ms+Ttn), a wide graphic unit (Kfs+Qz+Tu±Bt), which evolves to minor blocky K-feldspar, and an albite unit situated close to a small quartz core in the most differentiated part of the dike. Typical minor-to-accessory minerals include tourmaline, Y,Sc-enriched spessartine, topaz, Li micas (Mn-rich poly lithionite, masutomilite), beryl, cassiterite, zircon, niobian rutile, minerals of the columbite-, fergusonite-, and samarskite-groups, wolframoxyiolite, F-rich hambergite, monazite-(Ce), xenotime-(Y), and an REE-bearing epidote-group mineral (Němec 1990; Novák et al. 1998b, 2012; Čopjaková et al. 2013a). Yttrium- and REE-bearing oxides are almost exclusively associated with garnet in the albite unit. The evident Li enrichment along with the presence of Y,REE-oxides suggests the mixed (NYF+LCT) geochemical signature of the pegmatite (Novák et al. 2012).

Tourmaline is present in several morphological, paragenetic, and compositional types (Novák 2000; Čopjaková et al. 2013a). Black to brown prismatic crystals and their aggregates, up to several centimeters in size, occur in the graphic unit, blocky K-feldspar, albite unit, and massive quartz; their composition correspond to Al-rich schorl ($Al \geq 6.57$ apfu). Brownish-green to yellowish-green prismatic tourmaline crystals and their aggregates up to 1 cm in size as well as narrow rims around grains of the black tourmaline occur especially in the albite unit. Their composition ranges from minor Mn-rich fluor-schorl to common fluor-elbaite (Novák 2000; Čopjaková et al. 2013a).

ANALYTICAL METHODS

Electron microprobe

The tourmaline and associated minerals were studied using the Cameca SX100 electron microprobe (EMP) at Joint Laboratory of Electron Microscopy and Microanalysis, Department of Geological Sciences, Masaryk University, and Czech Geological Survey, Brno. Their chemical composition was analyzed in wavelength-dispersive mode and the accelerating voltage 15 kV. Operating conditions for analyses were as follows: beam currents 10 nA for tourmaline and chlorite and 20 nA for REE-bearing epidote-group mineral, and a spot size ~ 5 μ m. The following standards and X-ray $K\alpha$ lines were used for tourmaline and chlorite analyses: sanidine (Si, Al, K), albite (Na), olivine (Mg), andradite (Ca, Fe), Mn_2SiO_4 (Mn), anatase (Ti), topaz (F), and ZnO (Zn). The following standards and X-ray lines were used for REE-bearing epidote-group mineral analyses: $NaK\alpha$ (albite), $K, Al, Si K\alpha$ (sanidine), $CaK\alpha$ (wollastonite), $FeK\alpha$ (andradite), $ScK\alpha$ ($ScVO_4$), $SnL\alpha$ (Sn), $LaL\alpha$ ($LaPO_4$), $CeL\alpha$ ($CePO_4$), $PrL\beta$ ($PrPO_4$), $NdL\beta$ ($NdPO_4$), $SmL\beta$ ($SmPO_4$), $GdL\beta$ ($GdPO_4$), $HoL\alpha$ ($HoPO_4$), $DyL\alpha$ ($DyPO_4$), $YL\alpha$ (YAG), $UM\beta$ (U), $ThM\alpha$ [$CaTh(PO_4)_2$], $PbM\alpha$ ($PbSe$), $MgK\alpha$ (olivine), $MnK\alpha$ (Mn_2SiO_4), $TiK\alpha$ (anatase), $CrK\alpha$ (chromite), $VK\beta$ (vanadinite), $ZrL\alpha$ (zircon), $SrL\alpha$ ($SrSO_4$), $BaL\alpha$ ($BaSO_4$), $PK\alpha$ (fluorapatite), $FK\alpha$ (topaz), $ClK\alpha$ (vanadinite). The peak counting times were 10 s for major and 20–120 s for minor elements. With regard to the analysis of fluorine, special care was taken to determine the optimal background positions and to minimize the overlap of the $FK\alpha$ peak with the $FeL\alpha$ peak position. The empirically determined correction factor was applied to the coincidence of $FK\alpha$ and $Ce M\beta$. Raw data obtained from the electron microprobe (in the case of tourmaline supplemented by theoretical B and H contents) were reduced using X-Phi matrix correction procedure (Merlet 1994).

Crystal-chemical formulas of Li-rich tourmaline (TurP2, TurS) were calculated on the basis of $Si = 6$ assuming the general formula $XY_2Z_6T_6O_{18}(BO_3)_3V_3W$, where $X = Na, Ca, K, \square$; $Y = Fe, Mg, Mn, Ti, Al, Zn$; $Z = Al, Fe, Mg$; $T = Si, B = B$; $V + W = OH + F + O = 4$ as recommended by Henry et al. (2011) although such approach may overestimate other cations where 7Al is present. Crystal-chemical formulas

of Li-poor tourmaline (TurP1, TurP1c) were calculated on the basis of T+Z+Y site cations = 15, because normalization on the basis of Si = 6 yielded the sum of T+Z+Y cations >15, which indicated a deficiency of Si at the T-site and presence of ¹Al. All Fe is considered as Fe²⁺ although unpublished wet chemical analysis of schorl from Kracovice by P. Povondra yields 2.90 wt% Fe₂O₃ and 11.02 wt% FeO. Crystal-chemical formulas of chamosite were obtained on the basis of 18 anions, all Fe is reported as Fe²⁺ and the water content was calculated assuming OH = 8. Formulas of the REE-bearing epidote-group mineral (EGM) were normalized on the basis of 3 Si cations. The water content was calculated assuming the ideal 1 OH occupancy and the Fe²⁺/Fe³⁺ ratio was calculated to maintain the mineral formula electro-neutral.

Laser ablation-inductively coupled plasma-mass spectrometry

The LA-ICP-MS at the Department of Chemistry, Masaryk University, Brno, consists of a laser ablation system UP 213 (New Wave Research, Inc., Fremont, California, U.S.A.) and an ICP-MS spectrometer Agilent 7500 CE (Agilent Technologies, Santa Clara, California, U.S.A.). The pulsed (4.2 ns) Nd:YAG laser operates at 213 nm and is equipped with an ablation chamber of the type SuperCell. Aerosol generated in the SuperCell was transported by carrier gas (1 L/min He) and mixed with Ar (0.6 L/min) prior to entering the ICP. Helium (2 mL/min) was introduced to the collision cell of the mass spectrometer for minimization of spectral interferences. The tourmaline and allanite-(Ce) surface was ablated in individual spots for 50 and 20 s per spot, respectively, and by laser beam in diameter of 100 and 30

μm, respectively. Laser ablation was carried out using laser pulse fluence of 5 and 3.5 J/cm² and 10 Hz repetition rate. The signals of isotopes of Li, Be, Mg, Sc, Mn, Y, Zr, Nb, Sn, REE, Hf, Ta, and Th for tourmaline and Li, Be, B, Sc, Y, Sn, and La-Dy for allanite-(Ce) were measured. The contents of elements were calculated using NIST SRM 610 and 612 standards, and Si and Al as internal reference elements after baseline correction and integration of the peak area. The areas analyzed by LA-ICP-MS were carefully examined by the EMP prior to the laser ablation.

Raman spectroscopy

Raman spectra of REE-bearing epidote-group mineral were acquired on LabRAM HR Evolution (Horiba, Jobin Yvon) Raman spectrometer system. The Raman spectra were excited by 532 nm Nd:YAG and 633 nm He-Ne lasers and collected in range between 100 and 1500 cm⁻¹ with a resolution of 1 cm⁻¹. Repeated acquisitions were accumulated to improve spectral signal-to-noise ratio. Multiple spot analyses on different areas of REE-bearing epidote-group mineral gave similar spectra and confirmed the spectral reproducibility. The laser spot for the 100× objective used provide approximately <1 μm lateral and 2 μm horizontal resolution. No surface damage was observed after the laser illumination of the measurement. Due to lack of published Raman spectra of allanite, data for well-crystalline allanite-(Nd) from Åskagen, Sweden (Škoda et al. 2012) were collected for a reference. The acquired Raman spectra were processed using Peakfit (Systat) software package. Band fitting was done using Pearson VII function with variable width; the fitting was gradually refined until it produced reproducible results with the square regression coefficient >0.995.

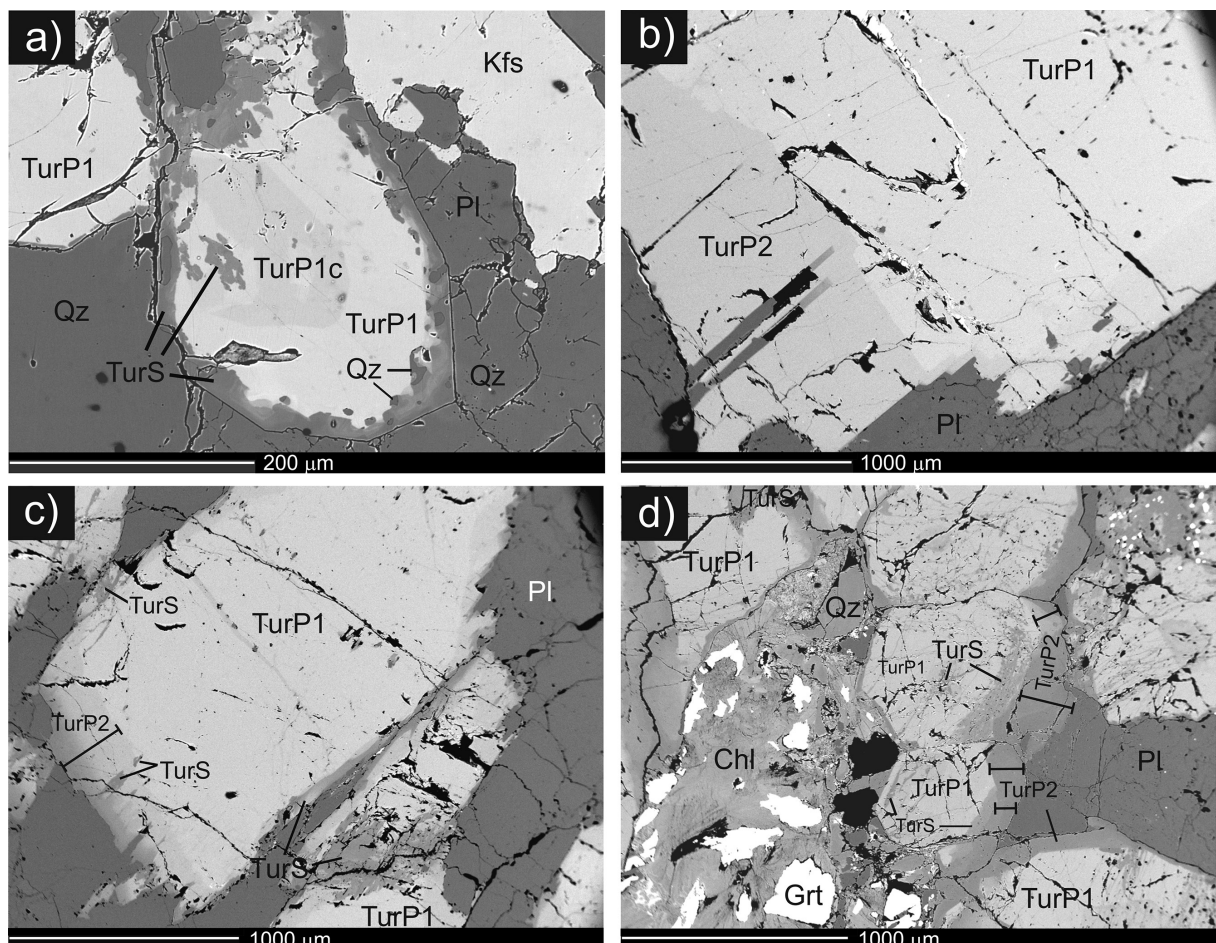


FIGURE 1. BSE images of tourmaline. (a) Al-rich schorl (TurP1) with core (TurP1c) darker in BSE image partly replaced by later fluor-elbaite (TurS) with common quartz inclusions (graphic zone); (b) Al-rich schorl (TurP1) overgrown by fluor-schorl to fluor-elbaite (TurP2) (albite unit); (c–d) Al-rich schorl (TurP1) overgrown and partially replaced by fluor-schorl to fluor-elbaite (TurP2 and TurS) (albite unit and blocky unit, respectively). The abbreviations for rock-forming minerals are after Whitney and Evans (2010).

TABLE 1. Summary of tourmaline-bearing samples including textural-paragenetic units, tourmaline type, replacement products, and average Y+REE and Sc contents in TurP1

	Textural-paragenetic unit	TurP1c abundance	TurP1 abundance	REE (ppm)	Sc (ppm)	TurP2 abundance	TurS abundance	EGM abundance
Sample 1	graphic	++	+++	212	238		+++	+++
Sample 2	graphic	++	+++	151	82	+	+++	+++
Sample 3	graphic/blocky K-feldspar	+	+++	190	113	+++	++	++
Sample 4	graphic/blocky K-feldspar	++	+++	161	87		+	
Sample 5	blocky K-feldspar		+++	104	48	+++	+	+
Sample 6	blocky K-feldspar/albite		+++	95	64	++	+++	++
Sample 7	albite unit	+	+++	87	38	+++	++	+

Notes: Relative abundance of tourmaline types and replacement products are marked: no plus sign = absent; (+) = rare; (++) = common; (+++) = abundant. EGM = REE-bearing epidote-group mineral.

RESULTS

Tourmaline textural and paragenetic types and their chemical composition

Prismatic crystals and grains of tourmaline, 1 mm to 3 cm in diameter, occur in the graphic unit, blocky K-feldspar, and in the albite unit. Based on the textural relations and chemical composition, three major tourmaline types were distinguished in the Kracovice pegmatite (Fig. 1); the types are slightly modified from those given by Čopjaková et al. (2013a). The list of tourmaline samples, their types, Y+REE contents, and their affiliations to the individual pegmatite zones are given in Table 1.

Primary (magmatic) Al-rich schorl (TurP1)

The volumetrically dominant black thick-prismatic tourmaline (TurP1) occurs in all pegmatite units except of the outermost granitic unit. The individual tourmaline grains typically are homogeneous in composition (Fig. 1). Dominant Al-rich schorl to very rare Al-rich fluor-schorl (6.57–7.12 apfu Al; 1.93–2.23 apfu Fe; 0.08–0.15 apfu Mn; $\text{Fe}_{\text{tot}}/(\text{Fe}_{\text{tot}}+\text{Mg}) \sim 0.98$; 0.24–0.68 apfu F) shows moderate to high-X-site vacancy (0.27–0.46 pfu) and Na (0.52–0.70 apfu; Fig. 2; Table 2). Rare, homogeneous cores (TurP1c) darker in BSE with sharp contacts were observed particularly in schorl from the graphic unit (Fig. 1a). The cores (TurP1c) are slightly depleted in Na (0.49–0.58 apfu), Fe (1.88–2.08 apfu), Mn (0.07–0.10 apfu), Ca, Ti, and F (0.18–0.37 apfu) compared to the TurP1 (Fig. 3; Table 2). Lithium contents determined by the LA-ICP-MS are low (80–500 ppm). The tourmaline shows slight deficit in $^{\text{T}}\text{Si}$ (~5.89 apfu Si in TurP1 and ~5.96 apfu Si in TurP1c) using normalization procedure based on 15 cations, which indicates minor incorporation of Al at the T-site. In general, the TurP1 tourmaline typically shows a limited compositional evolution on both the crystal (from core to rim) and the pegmatite (from the graphic unit to the albite unit) scales expressed as a slight enrichment in Na, Fe, Mn, and F, and depletion in Mg (Fig. 3).

Primary (magmatic to hydrothermal) Li-rich fluor-schorl to fluor-elbaite (TurP2)

The tourmaline TurP2 forms overgrowths (up to 2 mm thick) around grains of the Al-rich schorl (TurP1); the TurP2 has sharp and straight contacts without any visible replacement textures (Figs. 1b and 1c). These overgrowths are typical for tourmaline from the blocky K-feldspar and albite units. Rarely, it forms small solitary prismatic crystals. Its chemical composition varies significantly, and corresponds to Li-rich fluor-schorl to fluor-elbaite (LA-ICP-MS data yielded 0.1–1.1 wt% Li). It has high

Al (6.96–7.41 apfu) and Mn (0.18–0.76 apfu), highly variable Fe (0.25–1.82 apfu), and very low Mg (<0.05 apfu). The X-site occupancy is dominated by Na (0.71–0.99 apfu) with very low Ca (≤ 0.03 apfu Ca; Fig. 2; Table 2). The amount of F at the W-site is high (0.67–1.00 apfu). Contents of Fe significantly decrease and Al, Mn, Na, F, and Li increase toward rims of TurP2 crystals (Figs. 1b, 1c, 1d, and 3a; Tables 2 and 3).

Secondary (hydrothermal) Li-rich fluor-schorl to fluor-elbaite (TurS)

Secondary tourmaline (TurS) typically replaces the primary Al-rich schorl (TurP1; Fig. 1) and rarely (in the albite unit) also the inner zones of the TurP2 adjacent to the TurP1 (Fig. 1c). The TurS is highly variable in texture. The replacement typically propagates from the crystal rim inward (Fig. 1a) and along common micro-fractures (Figs. 1c and 1d). In contrast to the overgrowths of the primary Li-rich fluor-schorl to fluor-elbaite (TurP2), the replacement contacts are micro-lobulated, and the secondary tourmaline TurS locally contains numerous oval inclusions of quartz (Fig. 1a). The secondary tourmaline TurS occurs in all pegmatite units, but the most common and intensive replacement was observed in the graphic unit. However, the secondary tourmaline is compositionally almost identical to the texturally distinct primary Li-rich fluor-schorl to fluor-elbaite tourmaline TurP2 (Figs. 2 and 3; Table 2).

Concentrations of Sc and REE in tourmaline

The individual types of tourmaline from the Kracovice pegmatite are generally characterized by variable and relatively high contents of Y+REE (3–458 ppm) and Sc (16–364 ppm; Fig. 4; Table 3). They show enrichment in LREE with nil to weak positive Ce anomalies ($\text{Ce}/\text{Ce}^* = 1.0–1.9$) and deep negative Eu anomalies (Figs. 5a–5c) in chondrite-normalized patterns. The highest Y+REE (40–458 ppm) and Sc (33–364 ppm) contents were found in the primary tourmaline TurP1, whereas the rare cores (TurP1c) contain significantly lower amounts of Y+REE (16–83 ppm) and Sc (50–194 ppm; Figs. 3, 4, 5a, and 5b; Table 3). However, the La_N/Gd_N ratios in both types of the primary tourmaline TurP1c and TurP1 are similar (La_N/Gd_N 11–31 and 10–27, respectively). The contents of REE and Sc in the primary Al-rich schorl generally decrease and the Ce anomalies increase from the graphic unit toward the more evolved blocky K-feldspar and albite units (Table 3).

The primary Li-rich fluor-schorl to fluor-elbaite (TurP2) is significantly depleted in Y+REE (2.6–27 ppm) and has flatter Y+REE patterns ($\text{La}_N/\text{Gd}_N = 2–15$; Figs. 3, 4, and 5; Table 3) compared to the TurP1. Chondrite-normalized REE patterns of TurP2

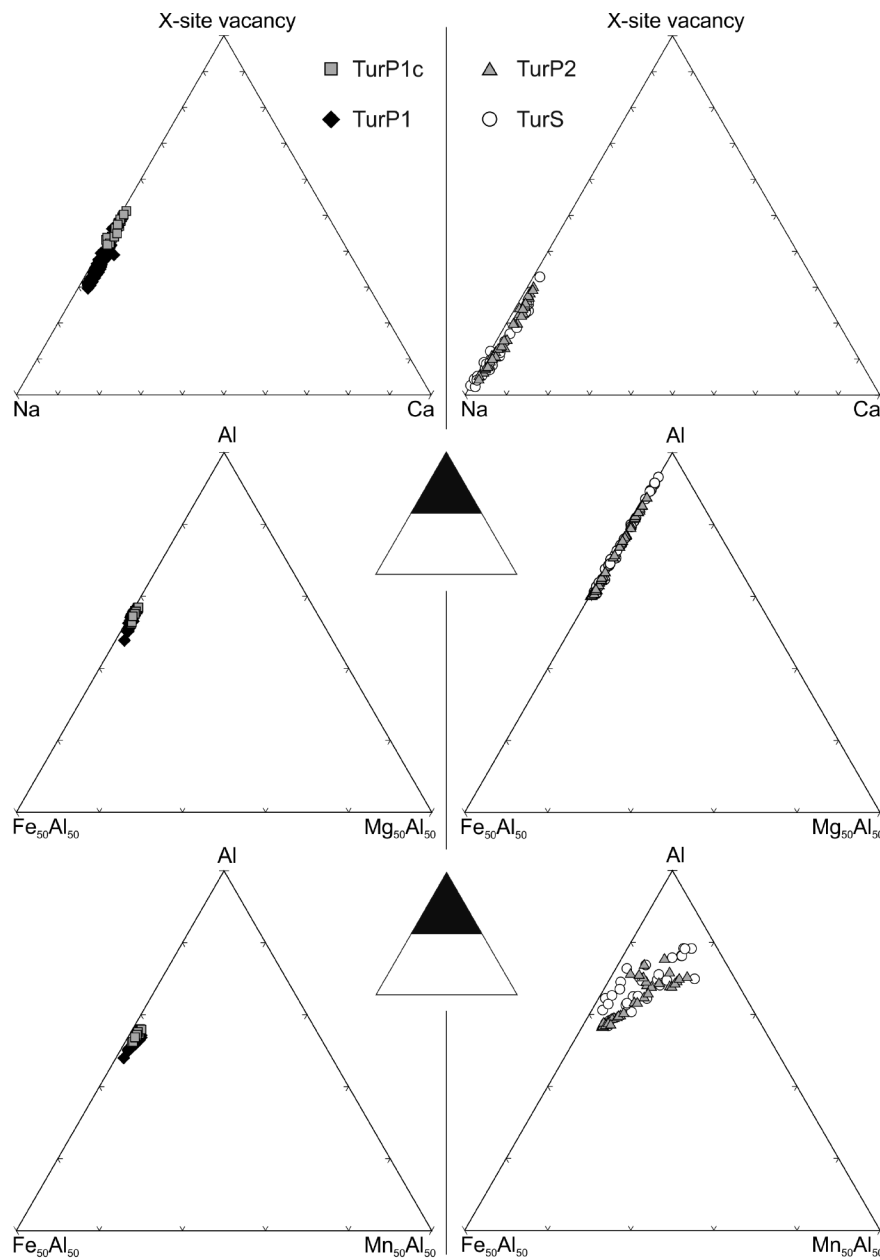


FIGURE 2. Chemical composition of tourmaline; occupancy of the X-site and ratios of cations in the Y+Z sites. (**left**) Al-rich schorl (TurP1 and TurP1c). (**right**) Fluor-schorl to fluor-elbaite (TurP2 and TurS).

show negative Nd anomalies (0.54–0.91) indicating participation of tetrad effect; it is well visible in both the first (La-Nd) and the second (Sm-Gd) tetrads (Fig. 5c). Quantification of the tetrad effect using the parameters given by Irber (1999) or Monecke et al. (2002) was not possible due to the presence of Ce anomaly and too low concentrations of some HREE systematically below the detection limits. Scandium contents are also lower (21–56 ppm) compared to the TurP1 (Fig. 4; Table 3). The REE and Sc contents decrease and the tetrad effect seems to be more pronounced along the crystallization progress toward rims of TurP2 crystals (Fig. 3a).

In contrast to the TurP2, the secondary tourmaline (TurS) shows variable REE contents (5–384 ppm; Fig. 4; Table 3). Its chondrite-normalized patterns significantly vary; they range from those similar to the typical TurP2 to the more Y+HREE-enriched flatter patterns with lower La_N/Gd_N ratio (0.4–12; Fig. 5c). The Y+HREE-enriched patterns are typical for the secondary fluor-elbaite (TurS) replacing TurP1 (primary Al-rich schorl) altered to the secondary assemblage of REE-bearing epidote-group mineral + chamosite.

Replacement products of primary Al-rich schorl

Al-rich schorl (TurP1) is commonly partly replaced by the assemblage REE-bearing epidote-group mineral + chamosite. The replacement products are most common in the graphic unit and rare in more evolved units. The REE-bearing epidote-group mineral forms aggregates of prismatic crystals up 200 µm in size (Fig. 6). They occur exclusively in fractured tourmaline TurP1, which is partly replaced by a F,Na-rich variety of the secondary fluor-elbaite (Figs. 3b and 6). The assemblage of REE-bearing epidote-group mineral + chamosite was not observed in those grains of the primary Al-rich schorl, which: (1) were not altered, or (2) were partly replaced by the secondary tourmaline (TurS) characterized by lower contents of Na, F, and Li

(Fig. 3b). The replacement assemblage is absent exterior of the tourmaline (TurP1); instead, minute crystals (≤ 5 µm) of hydrated arsenate of Y+HREE locally occur around the tourmaline replaced by the REE-bearing epidote-group mineral.

REE-bearing epidote-group mineral

The mineral has Y+REE ranging from 0.42 to 0.60 apfu, with the most frequent value of ~0.57 apfu (Table 4). Majority of 43 EMP analytical points belongs to the allanite subgroup (with Y+REE > 0.5 apfu), only five of them correspond to the clinozoisite subgroup (with Y+REE < 0.5 apfu). In all EMP analyses, Ce (0.19–0.35 apfu) predominates over other REE and Y; the EMP analyses are in a good agreement with the results of LA-ICP-MS. The mineral has steep LREE-rich chondrite-normalized

TABLE 2. Representative EMP analyses of tourmaline

	Graphic unit, EGM+Chl formation during TurP1 replacement								Graphic unit, without EGM+Chl formation							
	1 TurP1c	2 TurP1c	3 TurP1	4 TurP1	5 TurP1	6 TurS	7 TurS	8 TurS	9 TurP1c	10 TurP1c	11 TurP1	12 TurP1	13 TurP1	14 TurS	15 TurS	
SiO ₂	35.67	35.13	34.56	34.71	35.27	36.20	36.70	37.53	34.62	35.29	34.78	34.73	34.85	35.50	35.50	
TiO ₂	0.04	0.07	0.07	0.15	0.17	0.08	0.14	0.09	0.05	0.08	0.19	0.19	0.21	0.17	0.15	
Al ₂ O ₃	35.01	35.33	35.01	33.99	34.15	34.18	36.18	37.33	34.90	34.73	33.75	34.24	34.06	34.65	35.38	
MgO	0.14	0.15	0.15	0.19	0.18	0.13	0.06	bdl	0.17	0.14	0.16	0.16	0.14	0.07	0.08	
CaO	0.04	0.08	0.06	0.15	0.12	bdl	0.15	0.15	0.03	0.05	0.12	0.12	0.09	0.14	0.19	
MnO	0.59	0.66	0.74	0.68	0.68	0.78	3.30	4.06	0.52	0.56	0.66	0.66	0.73	1.96	2.27	
FeO	13.68	13.52	13.87	14.14	14.30	10.82	5.28	2.33	13.67	13.99	14.28	14.69	14.68	10.64	8.98	
ZnO	0.17	0.32	0.26	0.25	0.31	0.20	0.08	bdl	0.28	0.32	0.41	0.39	0.42	0.36	0.39	
Na ₂ O	1.55	1.68	1.92	1.96	1.80	3.02	2.96	3.09	1.53	1.72	1.91	1.94	2.01	2.35	2.42	
K ₂ O	bdl	0.04	0.05	0.04	0.05	0.07	bdl	0.03	0.03	0.04	0.06	0.04	0.04	0.03	bdl	
F	0.38	0.48	0.82	0.76	0.88	1.89	1.76	1.96	0.54	0.64	0.85	0.85	0.86	1.44	1.58	
Sum	87.27	87.46	87.50	87.02	87.92	87.38	86.60	86.55	86.34	87.55	87.16	88.02	88.09	87.30	86.93	
X-site																
Na ⁺	0.505	0.548	0.630	0.650	0.591	0.970	0.938	0.957	0.506	0.562	0.633	0.638	0.661	0.769	0.792	
Ca ²⁺	0.008	0.015	0.012	0.027	0.022	0.000	0.025	0.025	0.006	0.009	0.022	0.022	0.016	0.026	0.034	
K ⁺	0.000	0.009	0.011	0.009	0.012	0.015	0.000	0.006	0.007	0.009	0.013	0.009	0.010	0.006	0.000	
□	0.487	0.427	0.348	0.315	0.376	0.015	0.036	0.012	0.482	0.420	0.332	0.331	0.314	0.199	0.175	
Y,Z-site																
Ti ⁴⁺	0.005	0.009	0.009	0.019	0.021	0.010	0.017	0.010	0.010	0.006	0.011	0.025	0.024	0.027	0.021	0.019
Al ³⁺	6.932	6.917	6.849	6.780	6.774	6.677	6.972	7.034	6.895	6.860	6.746	6.712	6.703	6.903	7.049	
Fe ²⁺	1.923	1.903	1.965	2.021	2.023	1.500	0.722	0.311	1.946	1.974	2.041	2.080	2.079	1.504	1.269	
Mn ²⁺	0.083	0.094	0.107	0.099	0.097	0.110	0.457	0.550	0.076	0.081	0.095	0.095	0.104	0.280	0.325	
Mg ²⁺	0.036	0.038	0.037	0.049	0.046	0.033	0.014	0.000	0.042	0.036	0.041	0.041	0.035	0.017	0.019	
Zn ²⁺	0.021	0.040	0.033	0.032	0.038	0.025	0.010	0.000	0.036	0.039	0.051	0.048	0.052	0.045	0.049	
subtotal	9.000	9.000	9.000	9.000	8.354	8.192	7.905	9.000	9.000	9.000	9.000	9.000	9.000	8.770	8.730	
T-site																
Si ⁴⁺	5.995	5.911	5.857	5.933	5.967	6.000	6.000	6.000	5.893	5.954	5.946	5.880	5.903	6.000	6.000	
Al ³⁺	0.005	0.089	0.143	0.067	0.033	0.000	0.000	0.000	0.107	0.046	0.054	0.120	0.097	0.000	0.000	
F ⁻	0.201	0.254	0.439	0.411	0.472	0.992	0.909	0.991	0.291	0.339	0.457	0.453	0.462	0.770	0.844	
T+Y+Z site	15.000	15.000	15.000	15.000	15.000	14.354	14.192	13.905	15.000	15.000	15.000	15.000	14.770	14.730		
	Blocky K-feldspar, EGM+Chl formation								Albite unit, EGM+Chl formation							
	16 TurP1	17 TurP1	18 TurP1	19 TurP2	20 TurP2	21 TurP2	22 TurS	23 TurS	24 TurP1	25 TurP1	26 TurP1	27 TurP2	28 TurP2	29 TurP2	30 TurS	
SiO ₂	34.87	34.02	34.61	35.19	35.43	36.12	36.27	36.45	34.39	33.81	34.06	34.96	35.19	36.00	36.50	
TiO ₂	0.19	0.23	0.21	0.22	0.19	0.16	0.18	0.06	0.23	0.24	0.22	0.22	0.12	0.10	0.19	
Al ₂ O ₃	34.09	34.33	34.01	35.76	35.82	35.92	35.28	36.21	34.42	34.85	34.48	34.82	35.92	36.30	36.46	
MgO	0.12	0.08	0.07	0.07	0.03	0.03	0.06	bdl	0.07	0.09	0.07	0.08	0.08	0.07	0.07	
CaO	0.08	0.09	0.08	0.16	0.07	0.10	0.05	0.05	0.12	0.15	0.15	0.12	0.10	0.13	0.13	
MnO	0.76	0.80	0.81	2.82	4.62	5.41	3.78	6.06	0.75	0.84	0.86	2.23	3.32	2.36	2.41	
FeO	14.02	13.84	14.03	8.52	5.06	3.37	5.60	2.92	14.11	14.15	13.90	10.25	7.54	6.59	6.88	
ZnO	0.40	0.36	0.41	0.59	0.24	0.11	0.16	0.13	0.40	0.36	0.41	0.59	0.44	0.23	0.29	
Na ₂ O	1.98	2.00	1.99	2.50	2.86	2.95	3.01	2.91	2.00	2.05	2.08	2.35	2.71	2.84	2.74	
K ₂ O	0.06	0.05	0.04	0.03	bdl	0.05	bdl	0.04	0.05	0.05	0.03	0.06	0.05	0.03	0.04	
F	0.82	0.88	0.83	1.63	1.78	1.96	1.87	1.94	0.90	0.89	0.94	1.48	1.69	1.86	1.84	
Sum	87.39	86.68	87.07	87.50	86.09	86.18	86.24	86.76	87.44	87.48	87.20	87.15	87.15	86.52	87.54	
X-site																
Na ⁺	0.653	0.667	0.659	0.827	0.937	0.948	0.966	0.928	0.661	0.676	0.692	0.783	0.896	0.919	0.872	
Ca ²⁺	0.015	0.017	0.015	0.030	0.013	0.017	0.008	0.008	0.023	0.027	0.027	0.021	0.017	0.022	0.022	
K ⁺	0.012	0.011	0.009	0.007	0.000	0.011	0.000	0.008	0.010	0.011	0.007	0.012	0.011	0.007	0.007	
□	0.319	0.305	0.317	0.136	0.050	0.024	0.025	0.056	0.306	0.286	0.274	0.184	0.076	0.052	0.098	
Y,Z-site																
Ti ⁴⁺	0.024	0.029	0.026	0.028	0.024	0.020	0.022	0.007	0.030	0.031	0.028	0.028	0.016	0.012	0.023	
Al ³⁺	6.788	6.800	6.780	7.186	7.149	7.032	6.878	7.024	6.782	6.763	6.789	7.043	7.219	7.130	7.064	
Fe ²⁺	1.998	1.989	2.007	1.215	0.717	0.468	0.774	0.402	2.012	2.016	1.990	1.471	1.075	0.919	0.946	
Mn ²⁺	0.109	0.116	0.117	0.407	0.662	0.762	0.530	0.845	0.108	0.121	0.125	0.324	0.480	0.334	0.336	
Mg ²⁺	0.029	0.020	0.018	0.019	0.006	0.008	0.014	0.000	0.018	0.023	0.017	0.019	0.019	0.017	0.018	
Zn ²⁺	0.051	0.046	0.052	0.074	0.029	0.013	0.019	0.015	0.051	0.045	0.051	0.074	0.055	0.028	0.035	
subtotal	9.000	9.000	9.000	8.930	8.588	8.303	8.237	8.293	9.000	9.000	9.000	8.960	8.864	8.440	8.423	
T-site																
Si ⁴⁺	5.942	5.847	5.922	6.000	6.000	6.000	6.000	6.000	5.864	5.763	5.831	6.000	6.000	6.000	6.000	
Al ³⁺	0.058	0.153	0.078	0.000	0.000	0.000	0.000	0.000	0.136	0.237	0.169	0.000	0.000	0.000	0.000	
F ⁻	0.442	0.476	0.449	0.881	0.953	1.000	0.976	1.000	0.483	0.482	0.510	0.802	0.913	0.981	0.957	
T+Y+Z site	15.000	15.000	15.000	14.930	14.588	14.303	14.237	14.293	15.000	15.000	15.000	14.960	14.864	14.440	14.423	

Notes: Analyses 1–8 are representative analyses from core-to-rim profile across a tourmaline from the graphic unit, where TurP1 replacement is accompanied by the assemblage REE-bearing epidote-group mineral + chlorite. Analyses 9–15 represent analyses from core-to-rim profile across a tourmaline from the graphic unit, where TurP1 replacement is not accompanied by the assemblage of REE-bearing epidote-group mineral + chlorite. Analyses 16–21 represent analyses from core-to-rim profile across tourmaline from blocky K-feldspar unit. Analyses 22–23 are representative analyses of secondary tourmaline replacing magmatic TurP1 from blocky K-feldspar unit. Analyses 24–29 represent analyses from core-to-rim profile across tourmaline from albite unit. Analysis 30 represents analysis of secondary tourmaline replacing magmatic TurP1 from albite unit. TurP1 replacement by TurS in blocky K-feldspar and albite units is accompanied by REE-bearing epidote-group mineral + chlorite formation. Note: The variable content of Li, unknown Fe²⁺/Fe³⁺ ratio and evident substitution of Al or/and B for Si in some tourmalines do not allow reliable calculation of the theoretical H₂O and B₂O₃ contents.

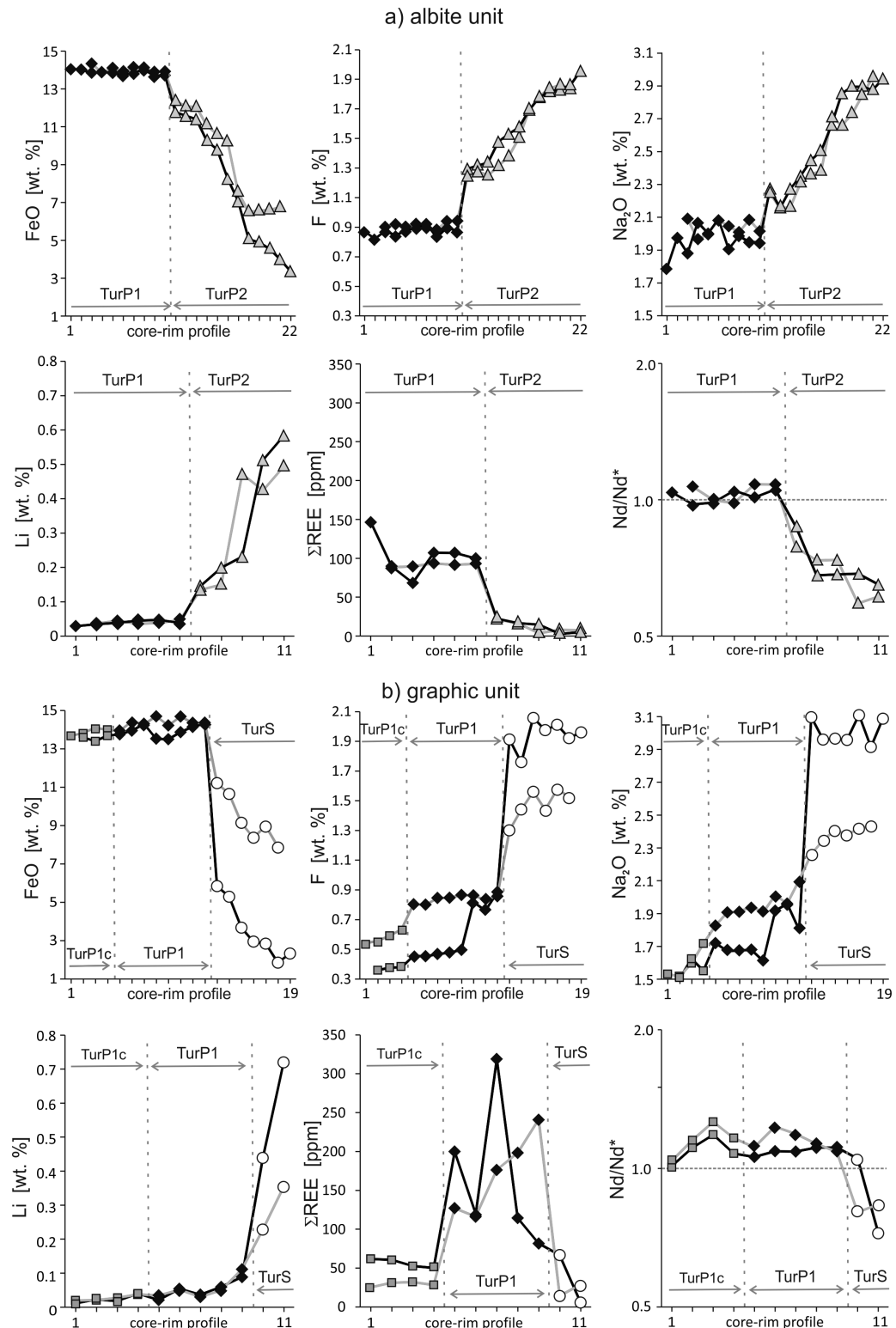


FIGURE 3. Evolution of selected major and trace elements (EMP data: FeO, F, Na₂O and LA-ICP-MS data: Li, Y+REE, Nd/Nd*) during tourmaline growth. **(a)** Albite unit = Al-rich schorl (TurP1) overgrown by later fluor-schorl to fluor-elbaite (TurP2). **(b)** Graphic unit = Al-rich schorl with small core TurP1c replaced on the rim by secondary fluor-schorl to fluor-elbaite (TurS). For the **b** only: gray line = Al-rich schorl replacement is not accompanied by formation of REE-bearing epidote-group mineral + chlorite; black line = common REE-bearing epidote-group mineral + chlorite form during Al-rich schorl replacement.

TABLE 3. Representative LA-ICP-MS analyses of trace elements in tourmaline (in ppm); see Table 2 caption for data description

Peg. unit	Graphic unit, EGM+Chl formation during TurP1 replacement									Graphic unit, without EGM+Chl formation							
	1 TurP1c	2 TurP1c	3 TurP1	4 TurP1	5 TurP1	6 TurP1	7 TurP1	8 TurS	9 TurS	10 TurP1c	11 TurP1c	12 TurP1	13 TurP1	14 TurP1	15 TurS	16 TurS	
Li	115	226	209	368	541	594	541	4389	7193	196	378	297	494	1112	2278	3534	
Sc	103	100	144	255	323	276	59	38	16	69	95	94	115	121	35	35	
Y	0.20	0.25	0.46	3.22	1.49	1.31	0.28	20.30	0.04	0.09	0.12	0.39	0.52	0.60	0.10	3.47	
La	10.4	10.3	32.0	105.6	75.2	76.5	20.5	7.6	0.8	4.8	5.5	33.4	36.3	56.8	2.4	4.1	
Ce	35.3	34.8	114.1	238.1	184.3	182.9	66.3	31.1	2.8	14.0	14.7	95.4	106.6	130.8	8.0	12.8	
Pr	3.69	3.51	12.86	25.41	23.41	19.89	7.42	3.21	0.28	1.42	1.80	11.20	13.25	12.42	0.72	1.39	
Nd	9.87	9.66	33.07	63.81	65.08	53.69	20.86	10.77	1.15	3.89	5.19	30.32	34.80	33.21	1.74	4.05	
Sm	1.69	1.42	4.99	10.78	9.27	9.67	3.25	4.54	0.29	0.65	0.73	3.83	4.71	4.96	0.43	1.11	
Eu	bdl	bdl	bdl	0.02	bdl	bdl	bdl	bdl	bdl	bdl	bdl	bdl	bdl	bdl	0.18	0.03	
Gd	0.65	0.63	2.24	6.73	3.15	2.85	1.20	3.65	0.09	0.14	0.25	1.27	1.56	2.05	0.34	0.69	
Tb	0.05	0.05	0.20	0.66	0.25	0.18	0.07	0.47	0.01	0.03	bdl	0.09	0.11	0.15	0.02	0.11	
Dy	0.05	bdl	0.32	2.28	0.64	0.47	0.16	2.28	0.02	bdl	bdl	0.22	0.16	0.19	0.08	0.51	
Er	bdl	bdl	bdl	0.53	0.15	0.13	bdl	1.18	bdl	bdl	bdl	0.08	bdl	bdl	bdl	0.32	
Yb	0.05	0.10	0.08	0.42	0.25	0.18	0.08	1.50	bdl	bdl	bdl	bdl	bdl	bdl	bdl	0.30	
Lu	0.02	0.04	0.02	0.07	0.06	0.04	bdl	0.23	bdl	bdl	bdl	bdl	bdl	bdl	bdl	0.04	
$\Sigma Y + \text{REE}$	62	61	200	458	363	348	120	87	6	25	28	176	198	241	14	29	
La_N/Gd_N	13.55	13.60	11.96	13.18	20.06	22.59	14.32	1.75	7.52	27.72	18.50	22.03	19.59	23.30	5.87	5.00	
Nd/Nd^*	1.01	1.11	1.06	0.99	1.13	0.99	1.09	1.05	0.72	1.04	1.16	1.19	1.13	1.08	0.80	0.84	
Peg. unit	Blocky K-feldspar, EGM+Chl formation									Albite unit, EGM+Chl formation							Detection limit
Tur type	17 TurP1	18 TurP1	19 TurP1	20 TurP2	21 TurP2	22 TurP2	23 TurS	24 TurP1	25 TurP1	26 TurP2	27 TurP2	28 TurP2	29 TurP2	30 TurS			
Li	288	449	381	1458	2308	5834	4931	362	446	467	1498	4716	4940	4237	Li	6	
Sc	60	47	44	31	26	37	54	34	37	37	23	21	16	21	Sc	0.25	
Y	0.24	0.24	0.18	0.09	0.02	0.03	2.61	0.04	0.15	0.11	0.23	0.02	0.38	5.24	Y	0.02	
La	24.2	16.8	15.9	3.3	2.1	1.0	3.5	13.2	14.0	12.7	1.9	0.7	1.0	1.0	La	0.02	
Ce	87.3	61.9	58.9	12.6	8.1	2.5	13.7	53.4	55.1	55.8	10.6	2.1	4.4	4.0	Ce	0.06	
Pr	7.75	6.16	5.71	1.23	0.83	0.28	1.85	4.88	4.70	5.96	0.88	0.19	0.35	0.32	Pr	0.03	
Nd	21.76	17.75	15.60	3.73	2.27	0.80	6.96	13.56	12.53	15.43	2.05	0.46	0.93	1.04	Nd	0.06	
Sm	3.74	3.07	2.52	0.98	0.88	0.36	2.63	2.17	2.21	2.25	0.58	0.14	0.43	0.64	Sm	0.05	
Eu	bdl	bdl	bdl	bdl	bdl	bdl	bdl	bdl	bdl	bdl	bdl	bdl	bdl	bdl	Eu	0.02	
Gd	1.38	1.09	0.89	0.42	0.26	0.16	2.68	0.87	0.85	0.77	0.22	0.07	0.24	0.53	Gd	0.04	
Tb	0.10	0.08	0.07	0.03	0.03	bdl	0.27	0.06	0.04	0.05	0.03	0.01	0.03	0.04	Tb	0.01	
Dy	0.15	0.13	0.10	0.06	0.06	0.05	1.41	0.19	0.08	0.12	0.05	0.04	0.12	0.26	Dy	0.02	
Er	bdl	bdl	bdl	bdl	bdl	bdl	bdl	bdl	bdl	bdl	bdl	bdl	bdl	bdl	Er	0.04	
Yb	bdl	bdl	bdl	bdl	bdl	bdl	bdl	bdl	bdl	bdl	bdl	bdl	bdl	bdl	Yb	0.04	
Lu	bdl	bdl	bdl	bdl	bdl	bdl	bdl	bdl	bdl	bdl	bdl	bdl	bdl	bdl	Lu	0.02	
$\Sigma Y + \text{REE}$	147	107	100	22	15	5	34	88	90	93	16	4	8	13			
La_N/Gd_N	14.69	12.99	15.01	6.72	6.85	5.02	1.11	12.75	13.91	13.76	7.14	7.93	3.52	1.57			
Nd/Nd^*	1.04	1.05	1.05	0.87	0.68	0.65	0.81	1.07	1.00	1.08	0.73	0.74	0.61	0.59			

REE patterns (avg. $\text{La}_N/\text{Gd}_N \sim 43$) with significantly negative Eu anomalies (Eu contents < 1 ppm; Fig. 5d). The contents of La negatively correlate with Nd (and MREE) and therefore the chondrite-normalized REE patterns vary between steep La-rich domains usually present in central parts of the aggregates and Nd- and MREE-rich ones (Figs. 5d and 7) found in the aggregate rims. Elevated contents of Mn (0.62–1.55 wt% MnO) and Sr (0.22–1.15 wt% SrO) are typical. The M-sites are dominated by Al (2.05–2.50 apfu) and Fe (0.44–0.64 apfu), and contain extraordinarily high contents of Sc (≤ 3.26 wt% Sc_2O_3 ; ≤ 0.25 apfu) and Sn (≤ 1.05 wt% SnO_2). Other analyzed elements (Th, U, Na, K, P, Mg, Pb, Ba, Cr, V, HREE, and Cl) are very close or below the detection limits of EMP except for Ti (≤ 0.43 wt% TiO_2) and F (≤ 0.23 wt%). A significant and variable vacancy occurs in the M-sites (\square cations = 2.76–2.99 apfu; Table 4). A detailed WDX angle scan excluded presence of other elements detectable by EMP that could possibly enter the structure of allanite (Ga, Ge, Zn) in a significant amount. The contents of light elements detected by LA-ICP-MS are low ($B < 320$ ppm; Be 50–175 ppm; Li < 11 ppm). The highest contents of Sc are typical for the central parts of aggregates, whereas the outer parts are Sc-poor (Fig. 7). In general, the contents of Sc and La decrease and MREE and Y increase from the graphic toward the blocky K-feldspar and albite units (Table 4).

Raman spectroscopy

The Raman spectrum of the REE-bearing epidote-group mineral from Kracovice shows several distinct bands. The strongest vibrations occur at 1064, 1048, 971, 927, 875, 687, 569, 458, 427, and 358 cm^{-1} and the spectrum matches well the spectrum of the crystalline allanite-(Nd) from Åskagen (Fig. 8). The narrow vibration bands indicate its good crystallinity. The vibration bands in the regions 1100–830, ~ 570 , and 500–300 cm^{-1} are identical with the spectra of epidote published by Makreski et al. (2007) and Wang et al. (1994). Makreski et al. (2007) interpreted the highest-frequency bands in the region 1100–800 cm^{-1} as a symmetric stretching Si-O_{nb} (O_{nb} -non bridging oxygen) from the $(\text{Si}_2\text{O}_7)^6-$ and $(\text{SiO}_4)^4-$ groups. According to Wang et al. (1994), the symmetric stretching $\text{Si-O}_b-\text{Si}$ bonds (O_b -bridging oxygen) should be expected in the 750–450 cm^{-1} region. Bands in the 550–300 cm^{-1} region should correspond to the vibrations of M-O bonds according to Makreski et al. (2007).

Chamosite

The chamosite has uniform ^{10}Si (2.71–2.85 apfu) and ^{14}Al (1.45–1.56 apfu), and variable, negatively correlated Fe and Mn contents (Fe = 3.18–3.76 apfu, Mn = 0.23–0.75 apfu) indicating homovalent substitution FeMn_{1-x} . Magnesium is present in low amounts ($\text{Mg} \sim 0.37$ apfu) and the contents of Sc, F, and Cl are below the detection limit of EMP.

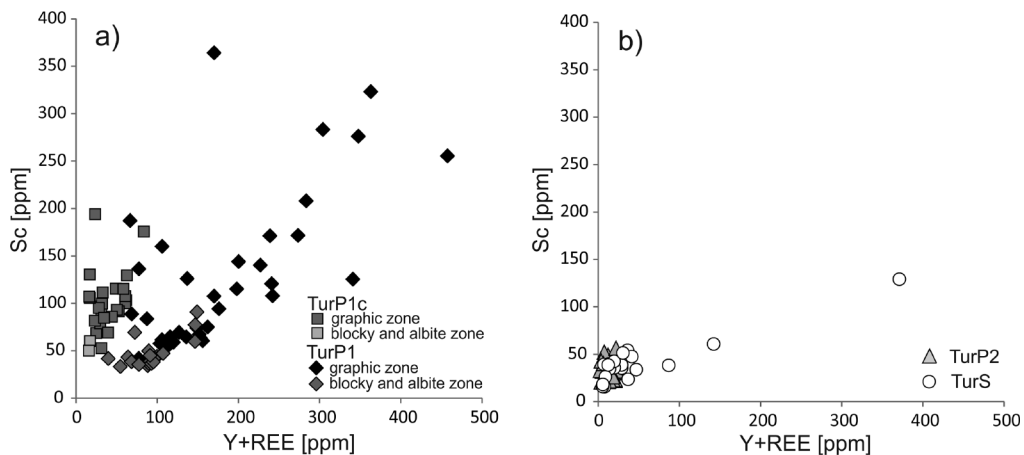


FIGURE 4. Sc vs. REE contents in tourmaline. (a) Al-rich schorl (TurP1c and TurP1); (b) fluor-schorl to fluor-elbaite (TurP2 and TurS).

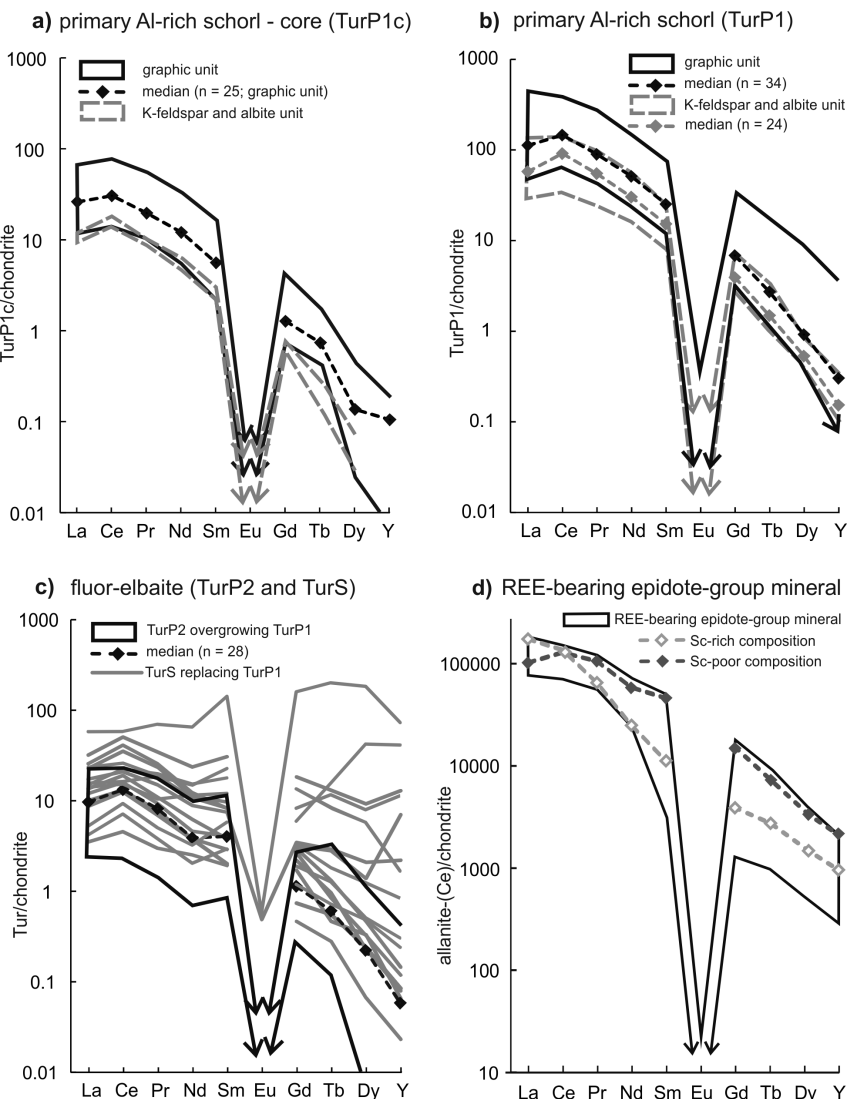


FIGURE 5. Chondrite-normalized Y+REE patterns of (a–c) tourmaline and (d) REE-bearing epidote-group mineral (chondrite values after McDonough and Sun 1995). The patterns of the REE-bearing epidote-group mineral combine the EMP and LA-ICP-MS data.

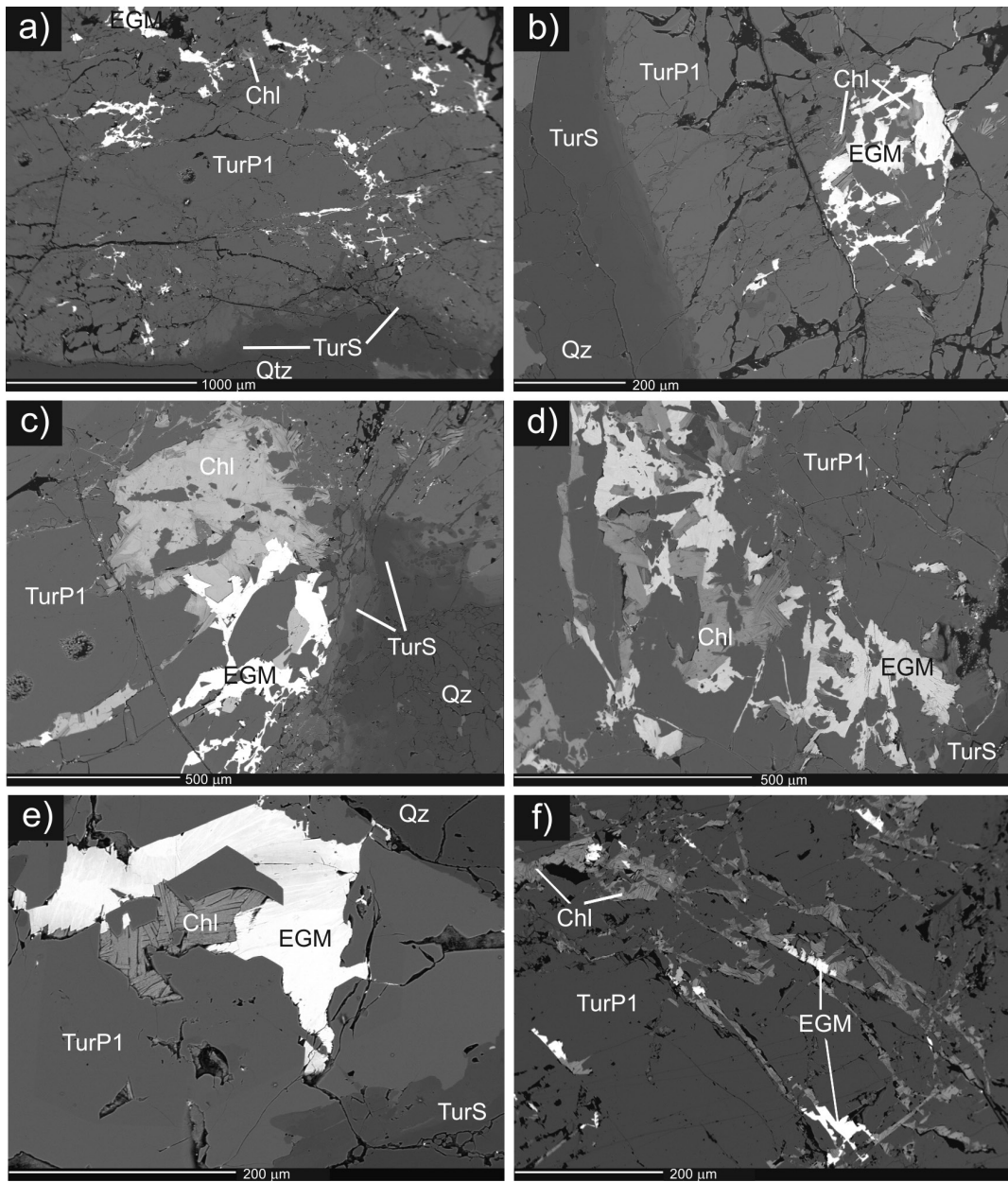


FIGURE 6. BSE images of REE-bearing epidote-group mineral (EGM) and chamosite (Chl) replacing Al-rich schorl (TurP1). (a–e) Graphic unit; (f) albite unit.

DISCUSSION

Compositional evolution of tourmaline, and Y+REE and Sc variations

Concentrations and distributions of Y+REE in tourmaline are controlled mainly by: (1) total contents of REE in granitic melt; (2) crystallization sequence of REE-bearing accessory minerals (Torres-Ruiz et al. 2003; Raith et al. 2004; Čopjaková et al. 2013a); and/or (3) composition of hydrothermal fluids (King et al. 1988; Jiang et al. 2004; Garda et al. 2010; Čopjaková et al. 2013b). The contents of Y+REE in tourmaline from granitic pegmatites are generally low (<30 ppm, Jolliff et

al. 1987; Hellingwerf et al. 1994; Roda et al. 1995; Kontak et al. 2002); hence, the concentrations of Y+REE in tourmaline from the Kracovice pegmatite (up to 458 ppm) are among the highest reported to date. Only the unusual REE-enriched dravite from the granitic pegmatite at Forshammar (Sweden) attains higher contents (Σ REE = 100–1200 ppm; Bačík et al. 2012).

Primary (magmatic) Al-rich schorl (TurP1, TurP1c)

Chemical composition and textural relations of the Al-rich schorl suggest that it crystallized early from melt (Novák et al. 2012; Čopjaková et al. 2013a). The presence of magmatic tourmaline and hambergite indicates high activity of B in the

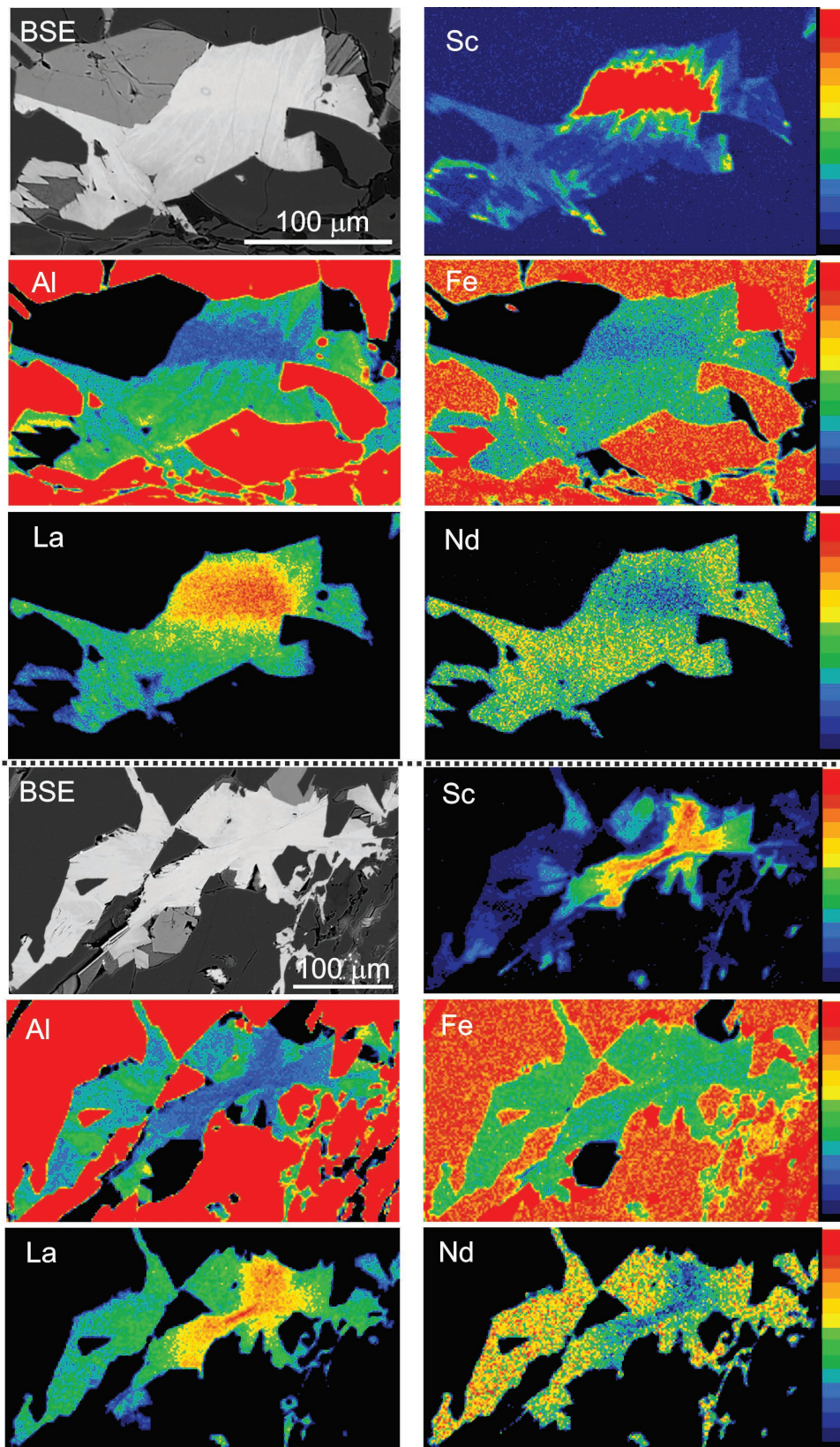


FIGURE 7. Wavelength-dispersive X-ray maps of representative elements for two aggregates of REE-bearing epidote-group mineral.

TABLE 4. Representative EMP analyses of the REE-bearing epidote-group mineral from different textural-paragenetic units

	Textural-paragenetic unit							
	Graphic unit			Blocky K-feldspar unit			Albite unit	
P ₂ O ₅	0.03	0.04	bdl	0.05	0.08	0.13	0.09	bdl
SiO ₂	33.99	33.89	33.89	34.48	33.94	33.59	33.12	34.12
TiO ₂	0.09	0.03	0.20	0.19	0.05	0.03	0.03	0.06
ZrO ₂	0.52	0.47	0.22	0.06	bdl	bdl	0.03	0.04
SnO ₂	0.69	0.53	0.89	1.05	0.20	0.08	0.41	0.52
Al ₂ O ₃	19.84	19.71	20.80	21.86	22.86	23.05	21.45	21.54
Sc ₂ O ₃	3.05	2.82	1.14	0.33	bdl	bdl	0.45	0.25
Fe ₂ O ₃ ^a	5.95	6.74	6.10	6.69	1.37	0.00	1.76	7.35
Y ₂ O ₃	0.14	0.22	0.10	0.11	0.14	0.13	0.43	0.22
La ₂ O ₃	4.57	4.76	3.48	2.66	2.60	2.65	2.83	2.57
Ce ₂ O ₃	10.18	9.75	10.20	8.11	9.29	9.38	9.21	9.07
Pr ₂ O ₃	0.91	0.79	1.20	0.99	1.33	1.17	1.15	1.28
Nd ₂ O ₃	1.54	1.46	2.55	2.52	3.63	3.44	3.11	3.28
Sm ₂ O ₃	0.06	0.12	0.22	0.36	0.53	0.58	0.79	0.87
Gd ₂ O ₃	0.05	0.10	0.04	0.10	0.13	0.16	0.34	0.27
MgO	bdl	bdl	bdl	bdl	bdl	bdl	0.02	bdl
CaO	14.21	13.98	14.68	16.29	14.41	13.94	13.56	14.20
MnO	1.07	1.38	0.80	0.71	1.05	1.26	1.31	1.02
FeO ^a	0.54	0.04	0.77	0.64	5.90	7.11	5.77	0.62
SrO	0.78	1.05	0.31	0.26	0.43	0.69	0.89	0.62
BaO	0.15	bdl	bdl	bdl	bdl	bdl	bdl	bdl
Na ₂ O	bdl	0.02	bdl	0.02	0.05	0.04	bdl	0.02
F	bdl	0.05	0.05	0.04	0.14	0.17	0.10	0.07
Cl	bdl	0.03	bdl	bdl	bdl	bdl	bdl	bdl
F ₂ Cl=O	0.00	-0.03	-0.02	-0.02	-0.06	-0.07	-0.04	-0.03
H ₂ O ^b	1.70	1.70	1.69	1.72	1.70	1.68	1.66	1.71
Total	100.06	99.64	99.29	99.21	99.78	99.20	98.44	99.64
A-sites								
Na ⁺		0.004		0.004	0.009	0.006		0.004
Ca ²⁺	1.343	1.324	1.393	1.517	1.362	1.330	1.313	1.338
Mn ²⁺	0.047	0.059	0.016		0.039	0.060	0.048	0.067
Sr ²⁺	0.040	0.054	0.016	0.013	0.022	0.035	0.046	0.031
Ba ²⁺	0.005							
Y ³⁺	0.006	0.011	0.005	0.005	0.006	0.006	0.021	0.010
La ³⁺	0.149	0.155	0.114	0.085	0.085	0.087	0.094	0.083
Ce ³⁺	0.329	0.316	0.331	0.258	0.300	0.306	0.305	0.292
Pr ³⁺	0.029	0.025	0.039	0.031	0.043	0.038	0.038	0.041
Nd ³⁺	0.049	0.046	0.081	0.078	0.114	0.109	0.100	0.103
Sm ³⁺	0.002	0.004	0.007	0.011	0.016	0.018	0.025	0.026
Gd ³⁺	0.001	0.003	0.001	0.003	0.004	0.005	0.010	0.008
subtotal	2.000	2.000	2.000	2.006	2.000	2.000	2.000	2.000
M-sites								
Mg ²⁺						0.002		
Mn ²⁺	0.033	0.044	0.044	0.052	0.040	0.035	0.051	0.009
Fe ²⁺	0.040	0.003	0.057	0.047	0.435	0.529	0.436	0.419
Al ³⁺	2.062	2.055	2.170	2.239	2.376	2.418	2.285	2.232
Sc ³⁺	0.235	0.217	0.088	0.025			0.035	0.019
Fe ³⁺	0.395	0.449	0.406	0.438	0.091		0.120	0.487
Ti ⁴⁺	0.006	0.002	0.013	0.012	0.004	0.002	0.002	0.004
Zr ⁴⁺	0.022	0.020	0.009	0.002			0.001	0.002
Sn ⁴⁺	0.024	0.019	0.031	0.036	0.007	0.003	0.015	0.018
subtotal	2.818	2.809	2.820	2.851	2.953	2.986	2.947	2.816
T-sites								
Si ⁴⁺	2.998	2.997	3.000	2.997	2.994	2.990	2.993	3.000
P ⁵⁺	0.002	0.003		0.003	0.006	0.010	0.007	
subtotal	3.00	3.00	3.00	3.00	3.00	3.00	3.00	3.00
F ⁻	0.015	0.013	0.011	0.040	0.049	0.030	0.018	0.063
Cl ⁻	0.005							
OH ⁻	1.000	1.000	1.000	1.000	1.000	1.000	1.000	1.000
O ²⁻	24.000	23.980	23.987	23.989	23.960	23.951	23.970	23.982
Czo-Epi	0.44	0.44	0.42	0.53	0.43	0.43	0.41	0.44
All	0.04	0.00	0.06	0.05	0.44	0.53	0.44	0.42
□	0.55	0.56	0.53	0.42	0.11	0.02	0.12	0.53

Notes: Calculated molar amount of the end-members: Czo-Epi = clinozoisite and epidote; All = allanite; □ = theoretical CaREAl₂R_{3/2}_□1/3[Si₂O₇](O)(OH) end-member. ^a Fe²⁺/Fe³⁺ ratio was calculated to maintain the mineral formula electro-neutral. ^b Calculated from ideal stoichiometry.

melt (Wolf and London 1997). Crystallization of the magmatic tourmaline was terminated either by melt depletion in Fe, or due to decrease of B content in the melt as a result of precipitation of B-rich minerals and/or by partitioning of B into exsolved vapor.

Similarities between the REE patterns in magmatic tour-

maline and the whole-rock composition were documented from granites, pegmatites, and orthogneisses worldwide (e.g., Torres-Ruiz et al. 2003; Raith et al. 2004; Pesquera et al. 2005; Čopjaková et al. 2013a). Partition coefficients for REE between tourmaline and silicate melt are invariably close to 1 suggesting

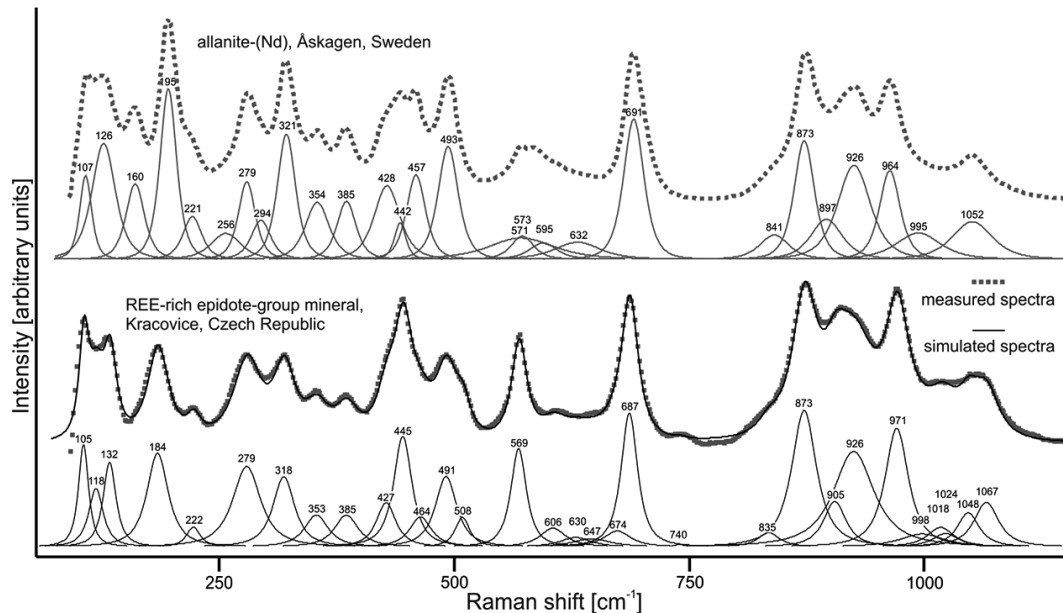


FIGURE 8. Raman spectra of REE-bearing epidote-group mineral compared to the Raman spectra of allanite-(Nd) from Åskagen pegmatite, Sweden.

that magmatic tourmaline does not selectively incorporate any specific REE into its crystal structure (van Hinsberg 2011; Čopjaková et al. 2013a). Increased content of REE+Sc in the magmatic tourmaline TurP1 compared to the early magmatic cores of TurP1c can reflect an enrichment of REE+Sc in the melt during a progressive crystallization of major rock-forming minerals without early precipitation of Y+REE-rich accessory minerals. A similar trend was observed in tourmaline from NYF pegmatites of the Třebíč Pluton (Čopjaková et al. 2013a). The magmatic tourmaline TurP1 shows a decrease in REE contents from the graphic to the blocky K-feldspar and albite units (Figs. 4a, 5a, and 5b; Table 3) reflecting progressive crystallization of the pegmatite melt and fractional crystallization of REE-enriched accessory minerals. This is consistent with the trend reported by Jolliff et al. (1987).

The concentrations of Sc (up to 364 ppm) in the magmatic tourmaline (TurP1) from the Kracovice pegmatite are among the highest published to date. The only higher Sc contents were reported in V-rich oxy-dravite from graphitic quartzites at Bitovánky, and from NYF euxenite-type pegmatites of the Třebíč Pluton [≤ 1290 and 765 ppm, respectively; Cempírek et al. (2013); Čopjaková et al. (2013a)], which are both located nearby the studied locality within the Třebíč region. The evolutionary trends of Sc in tourmaline correlate well with the REE contents (Fig. 4) reflecting their similar geochemical behavior. Tourmaline seems to be an effective sink of Sc from melt under specific circumstances (see Čopjaková et al. 2013a). This does not match with the relatively low experimentally determined distribution coefficients for Sc ($D_{\text{tu}/\text{melt}} \sim 0.71$, van Hinsberg 2011); however, the contrasting Sc behavior in pegmatitic tourmaline can be explained by the difference in melt composition and in the degree of melt undercooling compared to the experimental conditions.

Li-rich fluor-schorl to fluor-elbaite (TurP2 and TurS)

The distinct compositional gap between the magmatic Al-rich schorl (TurP1) and the Li-rich tourmaline (both TurP2 and TurS) indicates a time gap between their crystallization and a significant difference in conditions of their crystallization. The abrupt change from Fe,REE-rich and Na,F,Li-poor magmatic Al-rich schorl to Fe,REE-poor, Li,F,Na-rich fluor-schorl to fluor-elbaite is well documented on Figure 3. London (2014a, 2014b) explains the abrupt transition in pegmatite melt composition by final consumption of the undercooled Fe-bearing bulk melt in the pegmatite core by the boundary layer liquid, and its depletion in Fe by the end of primary crystallization. It is followed by crystallization of the boundary layer liquid in the pegmatite core which has sodic, alkaline composition, and it is enriched in fluxing components (B, P, and F), water (H), and rare alkalis (Li, Rb, Cs). Both textural types of Li-rich tourmaline (overgrowing = TurP2 and replacing = TurS) are characterized by very similar chemical composition and compositional trends (Fig. 3) reflecting their coeval formation.

The textural relations of the primary Al-rich-schorl (TurP1) and the overgrowing primary Li-rich tourmaline (TurP2) from the blocky K-feldspar and the albite unit (Figs. 1b–1d) suggest crystallization of the TurP2 from a highly evolved, F,Li-rich source. Textural evidence indicates that its crystallization proceeded before complete solidification of the host environment, and the sequence of its crystallization may represent the transition from the late magmatic to early hydrothermal conditions, i.e., early crystallization from the fractionated melt (boundary layer liquid; London 2014a, 2014b) in the pegmatite core. Gradual changes of chemical composition of TurP2 reflect evolution of the host environment during its prolonged crystallization. Textural relations and tourmaline composition (Figs. 1c, 1d, and 3) indicate coeval crystallization of the outermost part of TurP2 (the darkest rim on Fig. 1) and the replacing F,Li-rich tourmaline TurS from

the same hydrothermal fluid.

The secondary Li-rich tourmaline (TurS) showing irregular contacts and replacement features (Fig. 1a) is most likely of hydrothermal origin and is interpreted as the product of a subsolidus reaction of fractured Al-rich schorl (TurP1) and rarely TurP2 with evolved pegmatite-derived fluids migrating along grain boundaries and fractures from the central part of the dike. Local differences and evolution in chemical composition of TurS (see Fig. 3) reflect gradually inhomogeneous composition of the reacting hydrothermal fluid (increasing Li, F, Na, decreasing Fe) and the composition of reacting tourmaline. The reason for fracturing of the early solidified units is not clear; it could be triggered by vapor exsolution from the residual melt in the pegmatite core, and loss of aqueous fluid to the host rock (cf. London 2013). Textural differences (overgrowing TurP2 vs. replacing TurS) reflect either the degree of solidification of the melt or differences in local activity of B in fluids.

Generally, low REE contents are expected in tourmaline crystallized from late melt-derived hydrothermal fluids relative to the associated melt-derived tourmalines (Jolliff et al. 1987; Pesquera et al. 2005). It is consistent with the REE evolution in Li-rich tourmaline (TurS and probably TurP2 as well) showing commonly very low Y+HREE contents. Anomalous, significantly HREE, Y-enriched patterns (flatter than those of TurP2; Fig. 5c) were locally observed in the secondary tourmaline (TurS); they reflect local enrichment of these elements in fluids. The HREE+Y were probably released during replacement of the primary tourmaline (TurP1); no other significant local Y+HREE source was observed. Rarely, similar HREE-enrichment was observed in the secondary tourmaline (TurS) replacing garnet (Čopjaková et al. 2014), but only very close to the replaced garnet. This indicates a very limited Y+HREE mobility in the pegmatite-derived fluids where the Y+HREE enter directly to the fluor-elbaite (TurS) structure and yield a tourmaline with flat HREE+Y-enriched patterns. Alternatively, the anomalous patterns could be caused by submicroscopic (below the resolution of EMP) inclusions of a Y+HREE-bearing mineral (hydrated Y+HREE arsenate) enclosed in the fluor-elbaite; small inclusions of hydrated Y+HREE arsenates were sporadically observed around partially replaced magmatic tourmaline or garnet but never in relation to the overgrowing Li-rich tourmaline (TurP2). Intensive replacement of the REE-rich tourmaline (TurP1) could produce a small volume of REE-bearing epidote-group mineral along with a rare submicroscopic Y+HREE phase because the source tourmaline has lower LREE/HREE ratio compared to the secondary REE-bearing epidote-group mineral.

Tetrad effect in tourmaline

The REE patterns of the Li-rich tourmaline (both types TurP2 and TurS; Fig. 5c) as well as the patterns of other REE-bearing minerals in the Kracovice pegmatite (unpublished data of authors) which crystallized either from viscous melt (garnet I, zircon), or from flux-rich liquid (TurP2, garnet II), or from melt-derived hydrothermal fluids (TurS), exhibit M-type tetrad effect. Tetrad effect is typical for highly evolved volatile-rich (e.g., F, H_2O) melts at the final stages of crystallization when F-rich aqueous fluid phase is exsolved from the melt (Irber 1999; Dolejš and Štemprok 2001) or when an F-bearing hydrosaline magmatic li-

uids are separated from granitic magma above its solidus (Veksler et al. 2005; Peretyazhko and Savina 2010; Wu et al. 2011; Cao et al. 2013). A possible factor contributing to the tetrad effect is a fluorine complexation (Irber 1999). M-type tetrads are common in the minerals crystallized from residual silicate melt. In contrast, the exsolved F-rich hydrosaline liquids (according to Veksler et al. 2005; Peretyazhko and Savina 2010; Wu et al. 2011; Cao et al. 2013) or F-rich aqueous fluid (according to Irber 1999; Dolejš and Štemprok 2001) could extract REE and acquire a W-type tetrad effect complementary to the pattern in the silicate melt.

Evolution of REE patterns in tourmaline (from TurP1, through TurP2 and TurS) indicate clearly that tetrad effect is not an original feature of the pegmatitic magma; instead, it gradually evolves during melt crystallization and related processes. Exsolution of fluoride melt with high contents of REE and W-type tetrad effect is one of likely mechanisms yielding the residual melt with M-type tetrad effect. Topaz, a common accessory to minor mineral in the more fractionated units of the Kracovice pegmatite, could hypothetically crystallize from such a fluoride melt. However, topaz is REE-poor (~23 ppm) with a flat REE pattern ($La_N/Yb_N \sim 2.0-3.1$) and it is not associated with any REE-bearing mineral; therefore, the topaz data did not provide any convincing evidence for its crystallization from a REE-rich fluoride melt with W-type tetrad effect.

There is no direct mineralogical evidence that exsolution of F-rich aqueous fluids with complementary W-type tetrad effect (according to Irber 1999; Dolejš and Štemprok 2001) from flux-rich melt is responsible for the development of the M-type tetrad effect in the studied pegmatite body. The secondary tourmaline (TurS) which crystallized from F-rich hydrothermal fluids shows the M-type REE tetrad effect. If it crystallized from such aqueous fluids, then it did not retain their ideal W-type REE pattern and acquired the opposite M-type REE pattern instead. M-type REE tetrad effect in fluorite precipitated from melt-derived hydrothermal fluids was earlier reported by Monecke et al. (2002) and Badanina et al. (2006).

The replacement process of the primary tourmaline

Tourmaline is considered to be a refractory mineral (Henry and Dutrow 1996; London 2011). However, black schorlitic tourmaline in granitic pegmatites is rarely replaced by secondary phases: e.g., muscovite (Dietrich 1985; Ahn and Buseck 1998; Novák et al. 2011b); pumpellyite-(Al) + chlorite, K-feldspar (Prokop et al. 2013) or chlorite + titanite (Novák et al. 2013). In contrast, metasomatic replacement of elbaite by lepidolite or borocookeite is more common (e.g., Beurlen et al. 2011; Novák et al. 2011b). Tourmaline breakdown commonly reflects the input of alkaline, high-pH and B-undersaturated fluids (Morgan and London 1989; Ahn and Buseck 1998; London 2011; Čopjaková et al. 2012).

Mineral textures and chemical composition of tourmaline indicate replacement of the Al-rich schorl (TurP1) during its interaction with highly evolved Li,F-rich, alkaline (high Na) and B-saturated pegmatite-derived fluids. These fluids most likely originated by exsolution from the residual flux-rich silicate melt in the pegmatite center; the process probably caused intensive hydrofracturing (brecciation) of early-crystallized units with Al-rich schorl (TurP1) and formation of the secondary assemblage according to the simplified scheme:

REE-rich Al-rich schorl + Li,F-rich aqueous fluids → fluorite + REE-bearing epidote-group mineral + chamosite.

The paragenetic link between the amount of the REE-bearing epidote-group mineral and concentrations of REE in the magmatic tourmaline TurP1 as well as their spatial relations indicate that REE and Sc necessary for the formation of the Sc-rich REE-bearing epidote-group mineral were released during dissolution of the Al-rich schorl (TurP1). Generally low contents of REE and Sc in Li-rich tourmaline (TurP2 and TurS) suggest depletion of melt-derived hydrothermal fluids in REE and Sc; any external input of Y+REE and Sc is unlikely. Taking into account the average composition of the Al-rich schorl (TurP1) and the REE-bearing epidote-group mineral, and assuming no external input of REE, we calculated the mass-balance between the parental Al-rich schorl and the daughter REE-bearing epidote-group mineral. For precipitation of 1 mol of REE-bearing epidote-group mineral, it is necessary to alter ~460 mol of TurP1. Taking into account different densities of allanite and schorl [3.7 and 3.2 g/cm³, respectively; Anthony et al. (2011)] the mass-balance calculation shows that alteration of a 900 µm side cube of the TurP1 releases enough REE and Sc to form a 100 µm side cube of the REE-bearing epidote-group mineral, which roughly corresponds to the textural relations observed in BSE (Fig. 6).

Crystal chemistry of REE-bearing epidote-group mineral

Natural REE-bearing members of the epidote group of minerals are quite commonly metamict due to their elevated contents

of Th and U; the radiation damage is typically accompanied by hydration and loss of cations (Gieré and Sorensen 2004; Čobić et al. 2010). The high-oxide totals observed in the Sc-rich REE-bearing epidote-group mineral (Table 4) contraindicate significant hydration and its non-metamict nature was also confirmed by the Raman spectroscopy (Fig. 8).

A-site occupancy

The LREE-enriched patterns of the REE-bearing epidote-group mineral are steeper compared to those of the REE-rich magmatic tourmaline; the increased pattern slope manifests strong fractionation of LREE from HREE in allanite (Brooks et al. 1981; Chesner and Ettlinger 1989). Moreover, pronounced negative Eu anomaly is typical for allanite (Gieré and Sorensen 2004). Manganese can occur in both divalent and trivalent states and it can enter three different sites (A1, M1, M3; Bonazzi et al. 1996; Gieré and Sorensen 2004). In our samples, Mn negatively correlates with Ca and most likely enters the A site. Small surplus of cations in the A sites when all Mn is assigned to the A1 site (avg. Σcations in that case = 2.02 apfu) indicates that part of Mn (Mn^{2+} or Mn^{3+}) could be present in the M-sites.

M-site occupancy

Scandium in epidote-group minerals has been reported in dissaksite from the pegmatite at Impilaks, Finland (wet analysis, ~1 wt% Sc_2O_3 ; Meyer 1911) and in allanite-(Ce) from the Crystal Mountains, Montana, U.S.A. (EMP analysis, 0.5 wt% Sc_2O_3 ; Foord et al. 1993). Scandium content in the REE-bearing

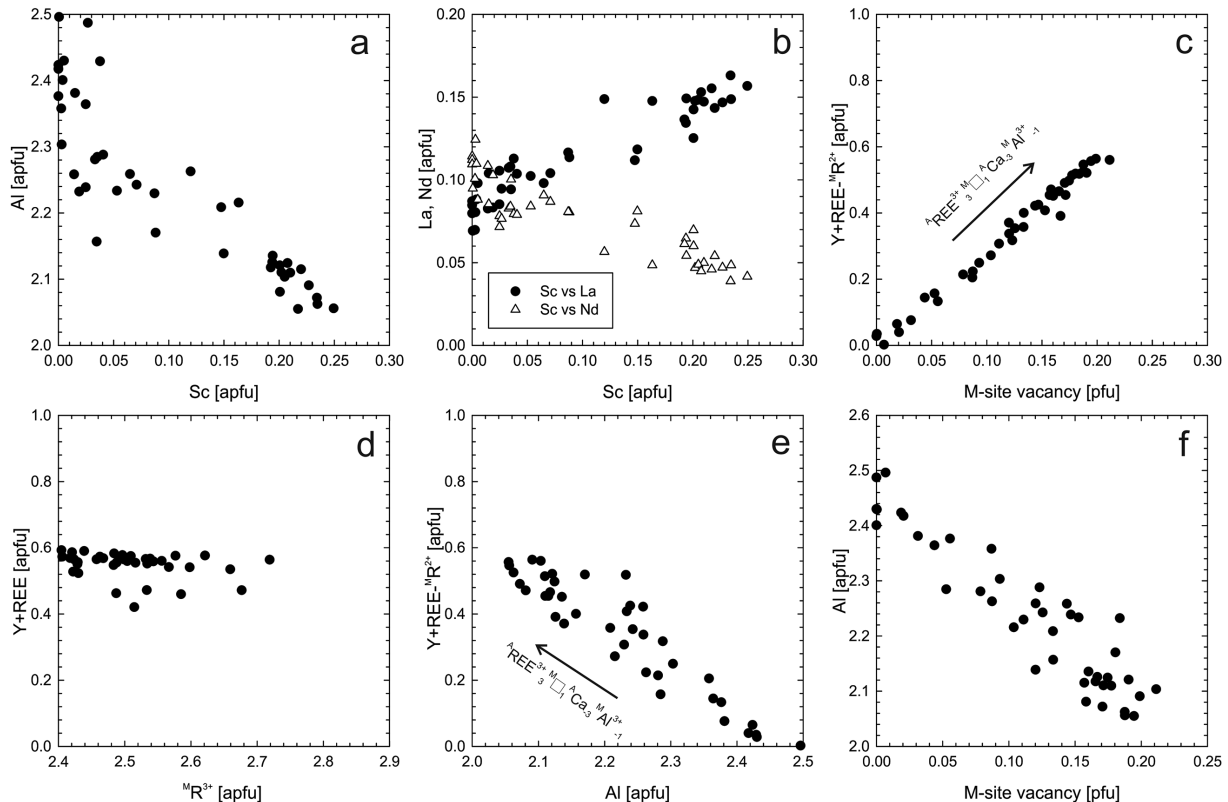


FIGURE 9. Substitution trends of major and minor elements in the REE-bearing epidote-group mineral based on EMP data.

epidote-group mineral from the Kracovice pegmatite (≤ 3.26 wt% Sc_2O_3 ; ≤ 0.25 apfu) is the highest reported to date. The negative correlation Al/Sc (slope of the regression line ~ 1) suggests that Sc enters the octahedral site by the substitution ScAl_{1-i} ; this is also supported by the fully occupied A-sites with Ca, REE, Sr, and Mn. High-Sc contents are typical for domains rich in La, and Sc negatively correlates with Nd (Figs. 9a and 9b).

Tin is a common trace element in allanite (<0.85 wt% SnO_2 ; Gieré and Sorensen 2004); the REE-bearing epidote-group mineral from the Kracovice pegmatite shows the highest Sn contents (up 1.05 wt% SnO_2) found in allanite. The mechanism of Sn incorporation in the M-sites by the substitution $\text{Sn}^{4+}\text{Fe}^{2+}(\text{Fe}^{3+}, \text{Al}^{3+})_2$ has been described for epidote by van Marcke de Lummen (1986) but the chemical complexity of the studied REE-bearing epidote-group mineral does not allow to elucidate the exact Sn substitution scheme.

Allanite can incorporate trace to minor contents of Be (up 2.5 wt% BeO ; Iimori 1939; Quensel 1945; Kimura and Nagashima 1951); however, the presence of Be in detectable amounts has not been confirmed by in situ analytical techniques (Hermann 2002). The LA-ICP-MS data of Sc-rich REE-bearing epidote-group mineral from Kracovice yielded low contents of Be (50–175 ppm), but it is not clear whether Be substitutes for Al in the M-sites or enters the T-site (Iimori 1939; Shannon 1976).

The sum of cations in the M-sites of the REE-bearing epidote-group mineral from the Kracovice pegmatite is often lower than 3 apfu (2.79–3.03 apfu, Table 4); on the other hand, careful control analyses of other minerals of the epidote group [epidote, Vlastějovice, Czech Republic; allanite-(Nd), Åskagen, Sweden; ferriallanite-(Ce), Nya Bastnäs, Sweden] yielded the average sum 3.007 apfu. Detailed WDX angle scan excluded presence of other unanalyzed elements detectable by EMP in significant amount. Moreover, the contents of Li, Be, and B (Li ≤ 11 ppm, Be 50–175 ppm, B ≤ 320 ppm) obtained by LA-ICP-MS cannot significantly affect the sum of cations in the M-sites. Therefore, our observations strongly indicate a vacancy in the M-sites. The

M-site vacancy correlates positively with $(\text{Y}+\text{REE})\text{-Fe}^{2+}$ (Fig. 9c), which represents the surplus of incorporated REE beyond the allanite substitution $\text{REE}^{3+}\text{Fe}^{2+}\text{Ca}_{i-2}^{\square}\text{R}_{i-1}^{3+}$ where $\text{R}^{3+} = \text{Al}, \text{Fe}^{3+}$. Moreover, $\text{Y}+\text{REE}$ does not significantly change with variable R^{3+} in the M-sites (Fig. 9d), whereas $(\text{Y}+\text{REE})\text{-Fe}^{2+}$ and vacancy in the M-sites show a good negative correlation with Al^{3+} (Figs. 9e and 9f). The observed correlations indicate two types of REE substitutions in the structure of the REE-bearing epidote-group mineral: the allanite substitution (1) $\text{REE}^{3+}\text{Fe}^{2+}\text{Ca}_{i-2}^{\square}\text{R}_{i-1}^{3+}$ (where $\text{R}^{3+} = \text{Al}, \text{Fe}^{3+}$) and the substitution (2) ${}^A\text{REE}_{3-}^{3+} {}^M\text{□}_{1-}^A\text{Ca}_{-3}^{\square} {}^M\text{Al}_{1-}^{3+}$ involving vacancy in the M-sites. The electron microprobe data and the observed substitutions trends seem to indicate existence of the theoretical end-member $\text{CaREEAl}_2\text{R}_{2/3}^{3+}\text{□}_{1/3}[\text{Si}_2\text{O}_7][\text{SiO}_4](\text{O})(\text{OH})$ of the allanite subgroup. It is clear (Fig. 10 and Table 4) that the content of the clinozoisite subgroup end-members is constant and the studied REE-bearing epidote-group mineral generally follows the substitution trend $\text{R}_{2-}^{3+}\text{□}_{1-}^A\text{R}_{3-}^{3+}$ from allanite-(Ce) to the $\text{CaREEAl}_2\text{R}_{2/3}^{3+}\text{□}_{1/3}[\text{Si}_2\text{O}_7][\text{SiO}_4](\text{O})(\text{OH})$ end-member. However, an exact determination of the $\text{Fe}^{2+}/\text{Fe}^{3+}$ ratio is necessary to support the conclusions.

IMPLICATIONS OF THE STUDY

This study has been focused on the major- to trace-element compositional changes in tourmaline growth history from magmatic to hydrothermal crystallization stage and tourmaline alteration processes. Compositional trends in tourmaline based on EMP data are widely used as indicators of geological processes (e.g., Henry and Dutrow 1996; van Hinsberg 2011). The results of this work confirm high sensitivity of $\text{Y}+\text{REE}$ contents in tourmaline to the composition of its host rocks, source melt, and hydrothermal fluids. Consequently the $\text{Y}+\text{REE}$ contents in tourmaline seem to be an ideal tool for petrogenetic interpretations as well as for provenance studies of sedimentary rocks. Tourmaline can also serve as an effective sink for Sc from granitic melt and represents another important carrier of Sc along with other Fe-Mg minerals (e.g., amphibole- or pyroxene-group minerals).

This study also revealed the continuous evolution of the M-type tetrad effect from the REE-patterns without tetrad effect to the well evolved M-type tetrad effect in the course of tourmaline crystallization. This clearly indicates the tetrad effect gradually evolves during the progressive solidification of the melt and related processes and the M-type pattern gradates to the metasomatic/hydrothermal stage. The mechanism of formation of the tetrad effect remains still unclear (Irber 1999; Veksler et al. 2005), but it is obviously connected to fluorine complexation in highly evolved volatile-rich (e.g., F, H_2O) melts.

The primary magmatic REE-enriched tourmaline (schorl) was partially replaced by the assemblage of REE-bearing epidote-group mineral + chamosite + fluor-elbaite during its interaction with Li,F-rich fluids. Schorlitic tourmaline generally shows a large stability field and is usually considered to be resistant to hydrothermal alteration and weathering; this study shows that low-temperature hydrothermal alteration and replacement reactions of tourmaline and factors affecting its instability during elevated activity of hydrothermal fluid in early subsolidus stage remain an important direction for future research.

The formation of the REE-rich secondary minerals is commonly coupled to alteration of primary REE-rich minerals (e.g.,

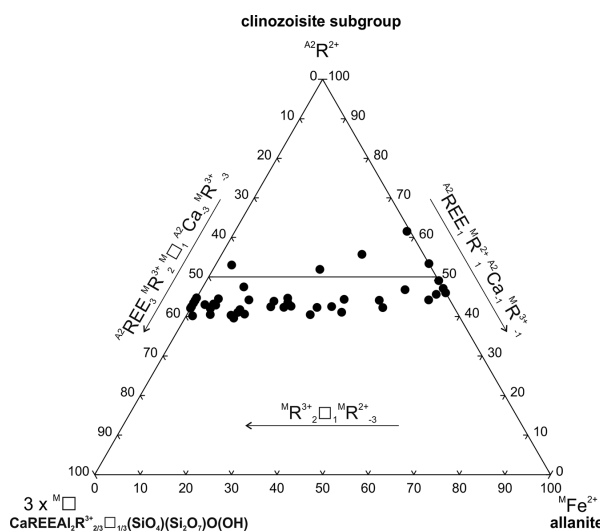


FIGURE 10. Ternary plot of major end-members of the epidote group in the REE-bearing epidote-group mineral from the Kracovice pegmatite.

monazite, xenotime, allanite, titanite, garnet, zircon). However, the source of desirable REE for the formation of REE-minerals could be a nominally REE-free mineral; in this study the source of REE+Sc for Sc- and REE-bearing epidote-group mineral seems to be tourmaline.

The unusual chemical composition of REE-bearing epidote-group mineral replacing magmatic schorl (enrichment in Sc and Sn) indicates that those elements should be sought during developing of the analytical setup routines for measuring of epidote-group minerals. The Sc content can be easily overlooked in the energy-dispersive spectrum because the $\text{ScK}\alpha$ peak coincides with the $\text{CaK}\beta$ line. Possibility of vacancy in the M-sites should be taken into account. Inconsistent stoichiometry of allanite-subgroup minerals can be in some cases caused by vacancy in the M-sites, instead of the more usual explanations such as alteration of metamic allanite or presence of some non-analyzed elements.

ACKNOWLEDGMENTS

The authors are very grateful to Adam Pieczka and to the unknown reviewer for constructive criticism that improved the manuscript. The authors thank Fernando Colombo for editorial handling. All authors thank to the research project GAČR P210/14/13347S, R.Č., R.Š., M.N., and J.C. thank to the research project GAČR P210/10/0743, and M.V.G. acknowledges the European Regional Development Fund project "CEITEC" (CZ.1.05/1.1.00/02.0068).

REFERENCES CITED

- Ahn, J.H., and Buseck, P.R. (1998) Transmission electron microscopy of muscovite alteration of tourmaline. *American Mineralogist*, 83, 535–541.
- Anthony, J.W., Bideaux, R.A., Bladh, K.W., and Nichols, M.C. (2011) *Handbook of Mineralogy*. Mineralogical Society of America, Chantilly, Virginia.
- Armbruster, T., Bonazzi, P., Akasaka, M., Bermanec, V., Chopin, Ch., Gieré, R., Heuss-Assbichler, S., Liebscher, A., Menchetti, S., Pan, Y., and Pasero, M. (2006) Recommended nomenclature of epidote-group minerals. *European Journal of Mineralogy*, 18, 551–567.
- Bačík, P., Uher, P., Ertl, A., Jonsson, E., Nysten, P., Kanický, V., and Vaculovič, T. (2012) Zoned REE-enriched dravite from a granitic pegmatite in Forshamar, Bergslagen Province, Sweden: An EMPA, XRD and LA-ICP-MS study. *Canadian Mineralogist*, 50, 825–841.
- Badanina, E.V., Trumbull, R.B., Dulski, P., Wiedenbeck, M., Veksler, I.V., and Syritso, L.M. (2006) The behavior of rare-earth and lithophile trace elements in rara-metal granites: A study of fluorite, melt inclusions and host rocks from the Khangilay complex, Transbaikalia, Russia. *Canadian Mineralogist*, 44, 667–692.
- Beurlen, H., De Moura, O.J.M., Soares, D.R., Da Silva, M.R.R., and Rhede, D. (2011) Geochemical and Geological controls on the genesis of gem-quality "Paraiba tourmaline" in granitic pegmatites from Northeastern Brazil. *American Mineralogist*, 96, 277–300.
- Bonazzi, P., Menchetti, S., and Reinecke, T. (1996) Solid solution between piemontite and androsite-(La), a new mineral of the epidote group from Andros Island, Greece. *American Mineralogist*, 81, 735–742.
- Brooks, C.K., Henderson, P., and Rřešno, J.G. (1981) Rare-earth partition between allanite and glass in the obsidian of Sandy Braes, Northern Ireland. *Mineralogical Magazine*, 44, 157–160.
- Cao, M.-J., Zhou, Q.-F., Qin, K.-Z., Tang, D.-M., and Evans, N.J. (2013) The tetrad effect and geochemistry of apatite from the Altay Koktokay No. 3 pegmatite, Xinjiang, China: Implications for pegmatite petrogenesis. *Mineralogy and Petrology*, 107, 985–1005.
- Cempírek, J., Houzar, S., Novák, M., Groat, L.A., Selway, J.B., and Šrein, V. (2013) Crystal structure and compositional evolution of vanadium-rich oxydravite from graphite quartzite at Bítovánky, Czech Republic. *Journal of Geosciences*, 58, 149–162.
- Černý, P., and Ercit, T.S. (2005) Classification of granitic pegmatites. *Canadian Mineralogist*, 43, 2005–2026.
- Černý, P., London, D., and Novák, M. (2012) Granitic pegmatites as reflections of their sources. *Elements*, 8, 289–294.
- Chesner, C.A., and Ettlinger, A.D. (1989) Composition of volcanic allanite from the Toba Tuffs, Sumatra, Indonesia. *American Mineralogist*, 74, 750–758.
- Čobić, A., Bermanec, V., Tomašić, N., and Škoda, R. (2010) The hydrothermal recrystallization of metamic allanite-(Ce). *Canadian Mineralogist*, 48, 513–521.
- Čopjáková, R., Škoda, R., and Burianek, D. (2012) Hydrothermal alteration of tourmaline from tourmalinites in the Krkonoše Crystalline Unit, Bohemian Massif, Czech Republic. *Acta Mineralogica-Petrographica*, Abstract Series, Szeged, 7, 30.
- Čopjáková, R., Škoda, R., Vašinová Galiová, M., and Novák, M. (2013a) Distributions of Y+REE and Sc in tourmaline and their implications for the melt evolution; examples from NYF pegmatites of the Třebíč Pluton, Moldanubian Zone, Czech Republic. *Journal of Geosciences*, 58, 113–131.
- Čopjáková, R., Škoda, R., Novák, M., and Vašinová Galiová, M. (2013b) Geochemistry of Y+REE in stratiform tourmalinites and their tourmalines: implications for their genesis. In: Jonsson, Ed., *Mineral Deposit Research for a High-Tech World*, Vols. 1–4. 12th Biennial SGA Meeting on Mineral Deposit Research for a High-Tech World Uppsala, SE, Uppsala University, 1705–1708.
- Čopjáková, R., Škoda, R., Vašinová Galiová, M., and Novák, M. (2014) Behaviour of B and Li during the evolution of the Královce pegmatite related to the formation and stability of tourmaline and garnet. *CEMC 2014 Book of Abstracts*, 21–22.
- Coulson, I.M. (1997) Post-magmatic alteration in eudialyte from the North Qoroq center, South Greenland. *Mineralogical Magazine*, 61, 99–109.
- Dietrich, R.V. (1985) The tourmaline group. *Van Nostrand Reinhold*, New York, p. 300.
- Dolejš, D., and Štemprok, M. (2001) Magmatic and hydrothermal evolution of Li-F granites: Čínovec and Krásno intrusions, Krušné hory batholith, Czech Republic. *Bulletin of the Czech Geological Survey*, 76, 77–99.
- Foord, E.E., Birmingham, S.D., Demartin, F., Pilati, T., Gramaccioni, C.M., and Lichte, F.E. (1993) Thortveitite and associated Sc-bearing minerals from Ravalli County, Montana. *Canadian Mineralogist*, 31, 337–346.
- Garda, G.M., Beljavskis, P., D'Agostino, L.Z., and Wiedenbeck, M. (2010) Tourmaline and rutile as indicators of a magmatic-hydrothermal origin for tourmalinitic layers in the São José do Barreiro Area, NE Ribeira Belt, Southern Brazil. *Geologia USP Série Científica*, São Paulo, 10, 97–117.
- Gieré, R., and Sorensen, S.S. (2004) Allanite and other REE-rich epidote-group minerals. *Reviews in Mineralogy and Geochemistry*, 56, 431–493.
- Hellingwerf, R.H., Gatedal, K., Gallagher, V., and Baker, J.H. (1994) Tourmaline in the central Swedish ore district. *Mineralium Deposita*, 29, 189–205.
- Henry, D.J., and Dutrow, B.L. (1996) Metamorphic tourmaline and its petrologic applications. *Reviews on Mineralogy*, 33, 503–557.
- Henry, D.J., Novák, M., Hawthorne, F.C., Ertl, A., Dutrow, B.L., Uher, P., and Pezzotta, F. (2011) Nomenclature of the tourmaline-group minerals. *American Mineralogist*, 96, 895–913.
- Hermann, J. (2002) Allanite: Thorium and light rare earth element carrier in subducted crust. *Chemical Geology*, 192, 289–306.
- Hoshino, M., Kimata, M., and Shimizu, M. (2006) Allanite-(Ce) in granitic rocks from Japan: Genetic implications of patterns of REE and Mn enrichment. *Canadian Mineralogist*, 44, 45–62.
- Imori, T. (1939) A beryllium-bearing variety of allanite. *Scientific Papers of the Institute of Physical and Chemical Research*, Tokyo, 36, 53–55.
- Irber, W. (1999) The lanthanide tetrad effect and its correlation with K/Rb, Eu/Eu*, Sr/Eu, Y/Ho, and Zr/Hf of evolving peraluminous granite suites. *Geochimica et Cosmochimica Acta*, 63, 489–508.
- Janoušek, V., and Holub, F.V. (2007) The causal link between HP-HT metamorphism and ultrapotassic magmatism in collisional orogens: Case study from the Moldanubian Zone of the Bohemian Massif. *Proceedings of the Geologists Association*, 118, 75–86.
- Jiang, S.-Y., Yu, J.-M., and Lu, J.-J. (2004) Trace and rare-earth element geochemistry in tourmaline and cassiterite from the Yunlong tin deposit, Yunnan, China: Implication for magmatic-hydrothermal fluid evolution and ore genesis. *Chemical Geology*, 209, 193–213.
- Jolliff, B.L., Papike, J.J., and Laul, J.C. (1987) Mineral recorders of pegmatite internal evolution: REE contents of tourmaline from the Bob Ingersoll pegmatite, South Dakota. *Geochimica et Cosmochimica Acta*, 51, 2225–2232.
- Kimura, K., and Nagashima, K. (1951) Chemical investigations of Japanese minerals containing rarer elements. XLII *Journal of the Chemical Society of Japan, Pure Chemistry Sections*, 72, 52–54 (in Japanese).
- King, R.W., Kerrich, R.W., and Daddar, R. (1988) REE distributions in tourmaline: An INAA technique involving pretreatment by B volatilization. *American Mineralogist*, 73, 424–431.
- Kontak, D.J., Dostal, J., Kyser, K., and Archibald, D.A. (2002) A petrological, geochemical, isotopic and fluid inclusion study of 370 Ma pegmatite-aplite sheets, Peggy's Cove, Nova Scotia, Canada. *Canadian Mineralogist*, 40, 1249–1286.
- Leitch, C.H.B., and Turner, R.J.W. (1992) Preliminary field and petrographic studies of the sulphide-bearing network underlying the western orebody, Sullivan stratiform sediment-hosted Zn-Pb deposit, British Columbia. *Geological Survey of Canada Current Research Paper*, 92, 1E, 61–70.
- London, D. (2011) Experimental synthesis and stability of tourmaline: A historical overview. *Canadian Mineralogist*, 49, 117–136.
- (2013) Crystal-filled cavities in granitic pegmatites: Bursting the bubble. *Rocks and Minerals*, 88, 527–534.
- (2014a) A petrologic assessment of internal zonation in granitic pegmatites. *Lithos*, 184–187, 74–104.
- (2014b) Subsolidus isothermal fractional crystallization. *American Mineralogist*, 99, 543–546.

- Makreski, P., Jovanovski, G., Kaitner, B., Gajović, A., and Biljan, T. (2007) Minerals from Macedonia: XVIII. Vibrational spectra of some sorosilicates. *Vibrational Spectroscopy*, 44, 162–170.
- McDonough, W.F., and Sun, S.S. (1995) Composition of the Earth. *Chemical Geology*, 120, 223–253.
- Melleton, J., Gloaguen, E., Frei, D., Novák, M., and Breiter, K. (2012) How are the time of emplacement of rare-element pegmatites, regional metamorphism and magmatism interrelated in the Moldanubian Domain of Variscan Bohemian Massif, Czech Republic? *Canadian Mineralogist*, 50, 1751–1773.
- Merlet, C. (1994) An accurate computer correction program for quantitative electron probe microanalysis. *Microchimica Acta*, 114–115, 1, 363–376.
- Meyer, R.J. (1911) Über einen skandiumreichen Orthit aus Finnland und den Vorgang seiner Verwitterung. *Sitzungsberichte der königlichen preussischen Akademie der Wissenschaften*, Berlin 105, 379–384 (in German).
- Monecke, T., Kempe, U., Monecke, J., Sala, M., and Wolf, D. (2002) Tetrad effect in rare earth element distribution patterns: A method of quantification with application to rock and mineral samples from granite-related rare metal deposits. *Geochimica et Cosmochimica Acta*, 66, 1185–1196.
- Morgan, G.B., and London, D. (1989) Experimental reactions of amphibolite with boron-bearing aqueous fluids at 200 MPa: Implications for tourmaline stability and partial melting in mafic rocks. *Contributions to Mineralogy and Petrology*, 102, 281–297.
- Morton, A.C., and Hallsworth, C. (2007) Stability of detrital heavy minerals during burial diagenesis. In M.A. Mange and D.T. Wright, Eds., *Heavy Minerals In Use. Developments in Sedimentology*, 215–245.
- Němc, D. (1990) Neues zur Mineralogie eines Hambergit-führenden Pegmatitgangs von Královské Poříčí (bei Třebíč, Westmorava, ČSFR). *Zeitschrift für Geologische Wissenschaften*, 18, 1105–1115.
- Novák, M. (2000) Compositional pathways of tourmaline evolution during primary (magmatic) crystallization in complex (Li) pegmatites of the Moldanubium, Czech Republic. *Memorie della Società Italiana di Scienze Naturali a del Museo Civico di Storia Naturale di Milano*, 30, 45–56.
- Novák, M., Černý, P., Kimbrough, D.L., Taylor, M.C., and Ercit, T.S. (1998a) U-Pb ages of monazite from granitic pegmatites in the Moldanubian Zone and their geological implications. *Acta Universitatis Carolinae, Geologica*, 42, 309–310.
- Novák, M., Burns, P.C., and Morgan, G.B. VI (1998b) Fluorine variation in hambergite from granitic pegmatites. *Canadian Mineralogist*, 36, 441–446.
- Novák, M., Černý, P., and Selway, J.B. (1999) The zinnwaldite-masutomilite-elsbauerite pegmatite at Královské Poříčí from the Třebíč durbachite massif—A complex pegmatite related to the NYF family. The Eugene E. Foord Memorial Symposium on NYF-type Pegmatites, Denver, Colorado. *Canadian Mineralogist*, 37, 815–816.
- Novák, M., Škoda, R., Filip, J., Macek, I., and Vaculovič, T. (2011a) Compositional trends in tourmaline from intragranitic NYF pegmatites of the Třebíč Pluton, Czech Republic: An electron microprobe, Mössbauer and LA-ICP-MS study. *Canadian Mineralogist*, 49, 359–380.
- Novák, M., Gadas, P., Škoda, R., Beurlen, H., and Moura, O.J.M. (2011b) Compositional variations in primary and secondary tourmaline from the Quintos pegmatite, Borborema pegmatite province, Brazil; redistribution of Cu, Mn, Fe and Zn in secondary tourmaline. Asociación Geológica Argentina, Serie D, Publicación Especial, 14, 149–151.
- Novák, M., Škoda, R., Gadas, P., Krmíček, L., and Černý, P. (2012) Contrasting origins of the mixed (NYF+LCT) signature in granitic pegmatites, with examples from the Moldanubian Zone, Czech Republic. *Canadian Mineralogist*, 50, 1077–1094.
- Novák, M., Kadlec, T., and Gadas, P. (2013) Geological position, mineral assemblages and contamination of granitic pegmatites in the Moldanubian Zone, Czech Republic; examples from the Vlastějovice region. *Journal of Geosciences*, 58, 21–47.
- Pantó, G. (1975) Trace minerals of the granitic rocks of the Valence and Mecsek Mountains. *Acta Geologica Academiae Scientiarum Hungaricae*, 19, 59–93.
- Peretyazhko, I.S., and Savina, E.A. (2010) Tetrad effects in the rare earth element patterns of granitoid rocks as an indicator of fluoride-silicate liquid immiscibility in magmatic systems. *Journal of Petrology*, 18, 514–543.
- Pertoldová, J., Týcová, P., Verner, K., Košuličová, M., Pertold, Z., Košler, J., Konopásek, J., and Pudilová, M. (2009) Metamorphic history of skarns, origin of their protolith and implications for genetic interpretation; an example from three units of the Bohemian Massif. *Journal of Geosciences*, 54, 101–134.
- Pesquera, A., Torres-Ruiz, J., Gil-Crespo, P.P., and Jiang, S.-Y. (2005) Petrographic, chemical and B-isotopic insights into the origin of tourmaline-rich rocks and boron recycling in the Martinamor Antiform (Central Iberian Zone, Salamanca, Spain). *Journal of Petrology*, 46, 1013–1044.
- Peterson, R.C., and MacFarlane, D.B. (1993) The rare-earth-element chemistry of allanite from the Grenville province. *Canadian Mineralogist*, 31, 159–166.
- Prokop, J., Losos, Z., Čopjaková, R., and Karásek, J. (2013) Mineralogy and genesis of rock fragments with pegmatitic texture from serpentinite eluvium at Nová Ves near Oslavany. *Bulletin mineralogicko-petrologického oddělení Národního muzea v Praze*, 21, 2, 210–222 (in Czech with English summary).
- Quensel, P. (1945) Berylliumorthit (muromontite) från Skuleboda fältspatbrott. *Arkiv för Kemi, Mineralogi och Geologi* 18A (22), 1–17 (in Swedish).
- Raith, J.G., Riemer, N., Schön, N., and Meisel, T. (2004) Boron metasomatism and behavior of rare earth elements during formation of tourmaline rocks in the eastern Arunta Inlier, central Australia. *Contributions to Mineralogy and Petrology*, 147, 91–109.
- Roda, E., Pesquera, A., and Velasco, F. (1995) Tourmaline in granitic pegmatites and their country rocks, Fregeneda area, Salamanca, Spain. *Canadian Mineralogist*, 33, 835–848.
- Shannon, R.D. (1976) Revised effective ionic radii and systematic studies of interatomic distances in halides and chalcogenides. *Acta Crystallographica*, A32, 751–767.
- Škoda, R., and Novák, M. (2007) Y,REE,Nb,Ta,Ti-oxide (AB_2O_6) minerals from REL-REE euxenite-subtype pegmatites of the Třebíč Pluton, Czech Republic; substitutions and fractionation trends. *Lithos*, 95, 43–57.
- Škoda, R., Novák, M., and Houzar, S. (2006) Granitic NYF pegmatites of the Třebíč Pluton. *Acta Musei Moraviae Scientiae geologicae*, 91, 129–176 (in Czech with English summary).
- Škoda, R., Cempírek, J., Filip, J., Novák, M., Veselovský, F., and Čtvrtlik, R. (2012) Allanite-(Nd), $CaNdAl_2Fe_{2-x}(SiO_4)(Si_2O_7)O(OH)$, a new mineral from Åskagen, Sweden. *American Mineralogist*, 97, 983–988.
- Slack, J.F., and Robinson, G.R. Jr. (1990) Retrograde metamorphic breakdown of tourmaline at Broken Hill, Australia. *Geological Society of America Abstracts with Programs*, 22, A126.
- Timmerman, M.J. (2008) Palaeozoic Magmatism. In T. McCann, Ed., *The Geology of Central Europe, Precambrian and Palaeozoic*, 1. Geological Society, London, 665–748.
- Torres-Ruiz, J., Pesquera, A., Gil-Crespo, P.P., and Velilla, N. (2003) Origin and petrogenetic implications of tourmaline-rich rocks in the Sierra Nevada (Betic Cordillera, southeastern Spain). *Chemical Geology*, 197, 55–86.
- van Hinsberg, V.J. (2011) Preliminary experimental data on trace-element partitioning between tourmaline and silicate melt. *Canadian Mineralogist*, 49, 153–163.
- van Marcke de Lummen, G. (1986) Tin-bearing epidote from skarn in the Land's End aureole, Cornwall, England. *Canadian Mineralogist*, 24, 411–415.
- Veksler, I.V., Dorfman, A.M., Kamenetsky, M., Dulski, P., and Dingwell, D.B. (2005) Partitioning of lanthanides and Y between immiscible silicate and fluoride melts, fluorite and cryolite and the origin of the lanthanide tetrad effect in igneous rocks. *Geochimica et Cosmochimica Acta*, 69, 2847–2868.
- Wang, A., Han, J., Guo, L., Yu, J., and Zeng, P. (1994) Database of standard Raman spectra of minerals and related inorganic crystals. *Applied Spectroscopy*, 48, 959–968.
- Ward, C.D., McArthur, J.M., and Walsh, J.N. (1992) Rare earth element behaviour during evolution and alteration of the Dartmoor granite, SW England. *Journal of Petrology*, 33, 785–815.
- Whitney, D.L., and Evans, B.W. (2010) Abbreviations for names of rock-forming minerals. *American Mineralogist*, 95, 185–187.
- Wolf, M., and London, D. (1997) Boron in granitic magmas: stability of tourmaline in equilibrium with biotite and cordierite. *Contribution to Mineralogy and Petrology*, 130, 12–30.
- Wu, Ch.-Z., Liu, S.-H., Gu, L.-X., Zhang, Z.-Z., and Lei, R.-X. (2011) Formation mechanism of the lanthanide tetrad effect for a topaz- and amazonite-bearing leucogranite pluton in eastern Xinjiang, NW China. *Journal of Asian Earth Sciences*, 42, 903–916.

MANUSCRIPT RECEIVED JANUARY 4, 2014

MANUSCRIPT ACCEPTED DECEMBER 26, 2014

MANUSCRIPT HANDLED BY FERNANDO COLOMBO

Vránaite, ideally $\text{Al}_{16}\text{B}_4\text{Si}_4\text{O}_{38}$, a new mineral related to boralsilite, $\text{Al}_{16}\text{B}_6\text{Si}_2\text{O}_{37}$, from the Manjaka pegmatite, Sahatany Valley, Madagascar

JAN CEMPÍREK¹, EDWARD S. GREW^{2,*}, ANTHONY R. KAMPF³, CHI MA⁴, MILAN NOVÁK¹, PETR GADAS¹, RADEK ŠKODA¹, MICHAELA VAŠINOVÁ-GALIOVÁ⁵, FEDERICO PEZZOTTA⁶, LEE A. GROAT⁷, AND SERGEY V. KRIVOVICHEV⁸

¹Department of Geological Sciences, Masaryk University, Brno, 611 37, Czech Republic

²School of Earth and Climate Sciences, University of Maine, 5790 Bryand Center, Orono, Maine 04469 U.S.A.

³Mineral Sciences Department, Natural History Museum of Los Angeles County, 900 Exposition Boulevard, Los Angeles, California 90007 U.S.A.

⁴Division of Geological and Planetary Sciences, California Institute of Technology, Pasadena, California 91125, U.S.A.

⁵Department of Chemistry, Masaryk University, Brno, 611 37, Czech Republic

⁶Mineralogy Department, Museo di Storia Naturale, Corso Venezia 55, Milan, I-20121, Italy

⁷Earth, Ocean and Atmospheric Sciences, University of British Columbia, Vancouver, British Columbia V6T 1Z4, Canada

⁸Department of Crystallography, St. Petersburg State University, University Embankment 7/9, 199034 St. Petersburg, Russia

ABSTRACT

The system $\text{B}_2\text{O}_3\text{-Al}_2\text{O}_3\text{-SiO}_2$ (BAS) includes two ternary phases occurring naturally, boromullite, $\text{Al}_9\text{BSi}_1\text{O}_{19}$, and boralsilite, $\text{Al}_{16}\text{B}_6\text{Si}_2\text{O}_{37}$, as well as synthetic compounds structurally related to mullite. The new mineral vránaite, a third naturally occurring anhydrous ternary BAS phase, is found with albite and K-feldspar as a breakdown product of spodumene in the elbaite-subtype Manjaka granitic pegmatite, Sahatany Valley, Madagascar. Boralsilite also occurs in this association, although separately from vránaite; both minerals form rare aggregates of subparallel prisms up to 100 μm long. Optically, vránaite is biaxial ($-$), $n_\alpha = 1.607(1)$, $n_\beta = 1.634(1)$, $n_\gamma = 1.637(1)$ (white light), $2V_x(\text{calc}) = 36.4^\circ$, $X \approx \mathbf{c}$; $Y \approx \mathbf{a}$; $Z = \mathbf{b}$. An averaged analysis by EMP and LA-ICP-MS (Li, Be) gives (wt%) SiO_2 20.24, B_2O_3 11.73, Al_2O_3 64.77, BeO 1.03, MnO 0.01, FeO 0.13, Li_2O 1.40, Sum 99.31. Raman spectroscopy in the 3000–4000 cm^{-1} region rules out the presence of significant OH or H_2O . Vránaite is monoclinic, space group $I2/m$, $a = 10.3832(12)$, $b = 5.6682(7)$, $c = 10.8228(12)$ Å, $\beta = 90.106(11)^\circ$; $V = 636.97(13)$ Å³, $Z = 1$. In the structure [$R_1 = 0.0416$ for $550 F_o > 4\sigma F_o$], chains of AlO_6 octahedra run parallel to [010] and are cross-linked by Si_2O_7 disilicate groups, BO_3 triangles, and clusters of AlO_4 and two AlO_5 polyhedra. Two Al positions with fivefold coordination, Al4 and Al5, are too close to one another to be occupied simultaneously; their refined site-occupancy factors are 54% and 20% occupancy, respectively. Al5 is fivefold-coordinated Al when the Al9 site and both O9 sites are occupied, a situation giving a reasonable structure model as it explains why occupancies of the Al5 and O9 sites are almost equal. Bond valence calculations for the Al4 site suggest Li is likely to be sited here, whereas Be is most probably at the Al5 site. One of the nine O sites is only 20% occupied; this O9 site completes the coordination of the Al5 site and is located at the fourth corner of what could be a partially occupied BO_4 tetrahedron, in which case the B site is shifted out of the plane of the BO_3 triangle. However, this shift remains an inference as we have no evidence for a split position of the B atom. If all sites were filled (Al4 and Al5 to 50%), the formula becomes $\text{Al}_{16}\text{B}_4\text{Si}_4\text{O}_{38}$, close to $\text{Li}_{1.08}\text{Be}_{0.47}\text{Fe}_{0.02}\text{Al}_{14.65}\text{B}_{3.89}\text{Si}_{3.88}\text{O}_{36.62}$ calculated from the analyses assuming cations sum to 24. The compatibility index based on the Gladstone-Dale relationship is 0.001 (“superior”). Assemblages with vránaite and boralsilite are inferred to represent initial reaction products of a residual liquid rich in Li, Be, Na, K, and B during a pressure and chemical quench, but at low H_2O activities due to early melt contamination by carbonate in the host rocks. The two BAS phases are interpreted to have crystallized metastably in lieu of dumortierite in accordance with Ostwald Step Rule, possibly first as “boron mullite,” then as monoclinic phases. The presence of such metastable phases is suggestive that pegmatites crystallize, at least partially, by disequilibrium processes, with significant undercooling, and at high viscosities, which limit diffusion rates.

Keywords: Vránaite, boralsilite, Madagascar, pegmatite, new mineral, structural complexity, Ostwald step rule, borosilicate minerals

INTRODUCTION

The system $\text{B}_2\text{O}_3\text{-Al}_2\text{O}_3\text{-SiO}_2$ (BAS, Fig. 1) includes two ternary phases occurring naturally, boromullite, $\text{Al}_9\text{BSi}_1\text{O}_{19}$, and boralsilite, $\text{Al}_{16}\text{B}_6\text{Si}_2\text{O}_{37}$, as well as numerous binary and ternary synthetic compounds structurally related to mullite, some of which

are suitable for a wide range of applications as refractory materials because of their high-temperature stability, low-thermal expansion, high-chemical stability, high-creep resistance, and other desirable properties (e.g., Fischer and Schneider 2008; Schneider et al. 2008; Gatta et al. 2010, 2013). One such phase, $\text{Al}_{16}\text{B}_4\text{Si}_4\text{O}_{38}$, was synthesized by Werding and Schreyer (1992), who characterized it as an orthorhombic “B-bearing derivative of sillimanite,” and predicted

* E-mail: esgrew@maine.edu

that it could be found in nature. However, in re-indexing its powder XRD pattern with a mullite cell, Grew et al. (2008) obtained cell parameters very similar to those for “boron-mullite.” Lührs et al. (2014) synthesized an orthorhombic phase $\text{Al}_{16.8}\text{B}_{3.6}\text{Si}_{3.7}\text{O}_{38}$ and successfully refined its structure using the Rietveld method to show it to be closely related to mullite. Novák et al. (2015) reported a naturally occurring phase with the approximate composition $\text{Al}_{16}\text{B}_5\text{Si}_4\text{O}_{38}$, which occurs with boralsilite in the Manjaka pegmatite, Sahatany Valley, Madagascar. Crystallographic study showed that the Manjaka mineral has a structure more closely related to that of boralsilite than to mullite. The mineral is sufficiently distinct chemically from boralsilite to qualify as new. We have named the new borosilicate vránaite for Stanislav Vrána (born 1936), a scientist with the Czech Geological Survey, and an excellent petrologist who, besides numerous other works, has studied petrology and mineralogy of borosilicate minerals. The mineral and its name have been approved by the International Mineralogical Association Commission on New Minerals, Nomenclature and Classification (IMA 2015-84, Cempírek et al. 2016).

The holotype crystal (grain 1) used for single-crystal diffraction and optical measurements is deposited in the Natural History Museum of Los Angeles County under number 65609. Other parts of the holotype are deposited in the collection of the Department of Mineralogy and Petrography, Moravian Museum, Brno, Czech Republic under numbers B11277 (thin sections from which the holotype crystal was extracted) and B11278 (rock sample from which the thin section was prepared).

METHOD

X-ray powder diffraction data were recorded using a Rigaku R-Axis Rapid II curved imaging plate microdiffractometer with monochromatized $\text{MoK}\alpha$ radiation at the Natural History Museum of Los Angeles County. A Gandolfi-like motion on the φ and ω axes was used to randomize the sample. Observed d -spacings and intensities were derived by profile fitting using JADE 2010 software (Materials

Data, Inc.). Data (in Å for $\text{MoK}\alpha$) are given in Table 1¹. Unit-cell parameters were refined from the powder data using JADE 2010 with whole pattern fitting (Table 1¹).

Single-crystal X-ray studies were carried out using the same diffractometer and radiation noted above (Table 2). The Rigaku CrystalClear software package was used for processing of structure data, including the application of an empirical multi-scan absorption correction using ABCOR (Higashi 2001). The structure was solved using SIR2011 (Burla et al. 2012). SHELXL-97 software (Sheldrick 2008) was used for the refinement of the structure.

Single-crystal electron backscatter diffraction (EBSD) analyses at a sub-micrometer scale were performed using an HKL EBSD system on the ZEISS 1550VP scanning electron microscope operated at 20 kV and 4 nA in a focused beam with a 70° tilted stage in variable pressure mode (20 Pa) at Caltech, following the method described in Ma and Rossman (2008, 2009). The EBSD system was calibrated using a single-crystal silicon standard.

Raman spectra of vránaite and reference minerals (boralsilite, muscovite) were acquired on LabRAM HR Evolution (Horiba, Jobin Yvon) Raman spectrometer system, at the Department of Geological Sciences, Masaryk University, Brno. The Raman spectra were excited by 532 nm Nd:YAG and 633 nm He-Ne lasers and collected in a range between 3000 and 4000 cm^{-1} with a resolution of 1 cm^{-1} . The laser spot for the 100× objective used provides approximately <1 μm lateral and 2 μm horizontal resolution. Repeated acquisitions were accumulated to improve spectral signal-to-noise ratio. No surface damage was observed after the laser illumination during the measurement.

Chemical data for boralsilite and vránaite obtained by electron microprobe analysis (EMPA) and by laser ablation-inductively coupled plasma-mass spectroscopy (LA-ICP-MS) are taken from Novák et al. (2015), and thus only selected features of the analytical method are repeated here. The two minerals were analyzed with a Cameca SX100 electron microprobe at the Joint Laboratory of Electron Microscopy and Microanalysis, Department of Geological Sciences, Masaryk University, Brno, and Czech Geological Survey, Brno, in wavelength-dispersive mode, with accelerating voltage 15 kV, beam current 10–20 nA, and spot size ~2–5 μm . The following standards and X-ray $K\alpha$ lines were used: danburite (B), sanidine (Si, Al), albite (Na), almandine (Fe), spessartine (Mn), and topaz (F). The peak counting time was 10 s for major elements and 20–40 s for minor elements. The background counting time was

¹Deposit item AM-16-95686, Supplemental Material, Table 1, and CIF. Deposit items are free to all readers and found on the MSA web site, via the specific issue's Table of Contents (go to <http://www.minsocam.org/MSA/AmMin/TOC/>).

TABLE 2. Data collection and structure refinement details for vránaite^a

Diffractometer	Rigaku R-Axis Rapid II	
X-ray radiation/power	$\text{MoK}\alpha (\lambda = 0.71075 \text{ \AA})/50 \text{ kV}, 40 \text{ mA}$	
Temperature	293(2) K	
Formula from refined occupancies	$\text{Al}_{14.96}\text{B}_5\text{Si}_4\text{O}_{36.83}$	
Space group	$I2/m$	
Unit-cell dimensions	$a = 10.3832(12) \text{ \AA}$ $b = 5.6682(7) \text{ \AA}$ $c = 10.8228(12) \text{ \AA}$ $\beta = 90.106(11)^\circ$ $636.97(13) \text{ \AA}^3$ 1	
V	2.986 g/cm^3	
Z	0.925 mm^{-1}	
Density for $\text{Li}_{1.08}\text{Be}_{0.47}\text{Fe}_{0.02}\text{Al}_{14.65}\text{B}_{3.89}\text{Si}_{3.88}\text{O}_{36.62}$	565.1	
Absorption coefficient	$F(000)$ 35 × 30 × 20 μm θ range Index ranges Reflections collected/unique Reflections with $F_o > 4\sigma(F_o)$ Completeness to $\theta = 24.95^\circ$ Refinement method Parameter/restraints GoF Final R indices [$F_o > 4\sigma(F_o)$] R indices (all data) Largest diff. peak/hole	3.93 to 24.95° $-12 \leq h \leq 12, -6 \leq k \leq 6, -12 \leq l \leq 10$ $2308/620; R_{\text{int}} = 0.048$ 550 98.9% Full-matrix least-squares on F^2 102/0 1.094 $R_1 = 0.0416, wR_2 = 0.0986$ $R_1 = 0.0478, wR_2 = 0.1024$ $+0.69/-0.51 \text{ e A}^{-3}$

Notes: The structural formula is calculated as a sum of refined site occupancies (i.e., numbers of electrons), with no attempt to balance charge. The large negative charge sum (~0.773) is related to the presence of Li and Be in part of Al sites.

^a $R_{\text{int}} = \sum |F_o^2 - F_c^2(\text{mean})| / \sum |F_o^2|$; GoF = $S = [\sum (w(F_o^2 - F_c^2)^2)] / (n - p)]^{1/2}$; $R_1 = \sum |F_o| - |F_c| / \sum |F_o|$; $wR_2 = \{\sum [w(F_o^2 - F_c^2)^2] / \sum [w(F_o^2)^2]\}]^{1/2}$; $w = 1 / [(o^2(F_o^2)) + (aP)^2 + bP]$, where a is 0.0229, b is 3.6767, and P is $[2F_c^2 + \text{Max}(F_o^2, 0)] / 3$.

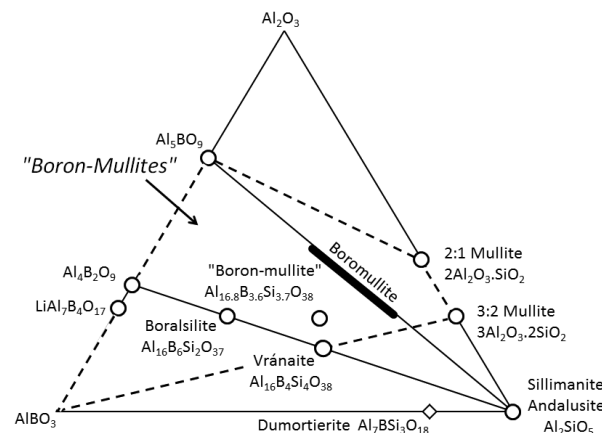


FIGURE 1. Phases related to mullite (circles), including boromullite (bar), together with dumortierite (diamond), plotted in the Al_2O_3 -dominant third, $\text{Al}_2\text{O}_3\text{-AlBO}_3\text{-Al}_2\text{SiO}_5$, of the $\text{Al}_2\text{O}_3\text{-B}_2\text{O}_3\text{-SiO}_2$ (BAS) system. Sources of data: field of “boron-mullites” (dashed lines, Werding and Schreyer 1996); boromullite polysomatic series (Buick et al. 2008); “boron-mullite,” $\text{Al}_{16.8}\text{B}_{3.6}\text{Si}_{3.7}\text{O}_{38}$ (Lührs et al. 2014), $\text{LiAl}_7\text{B}_4\text{O}_{17}$ (Åhman et al. 1997), dumortierite end-member (Pieczka et al. 2013); vránaite (this study); other mullite-related phases (Fischer and Schneider 2008; Grew et al. 2008).

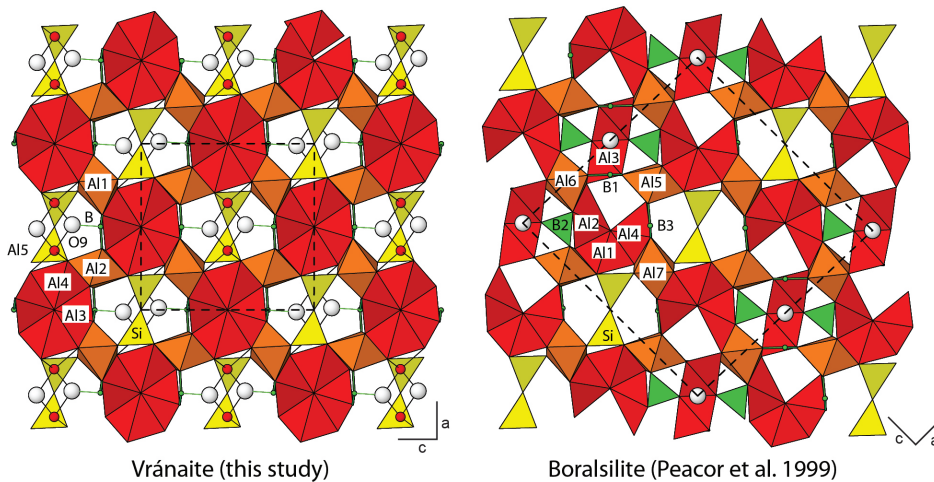


FIGURE 2. Crystal structure of vránaite and comparison with boralsilite. The two structures are oriented such that the Si_2O_7 units (shown in yellow) are parallel. The Al5 (red spheres) and O9 (white spheres) sites are only 20% occupied in vránaite. The B2 site (green triangles) is in tetrahedral coordination in boralsilite; cf. B-O9 in vránaite.

one-half of the peak counting time on the high- and low-energy background positions. Boron was analyzed in peak-area mode on a $\text{BK}\alpha$ line using accelerating voltage 5 kV, beam current 100 nA, and beam diameter 10 μm , and a Ni/C multilayered monochromator with $2d = 95 \text{ \AA}$ (PC2 in terms of CAMECA). Peak-area integration was carried out in the range 62–73 \AA for 240 s over 1000 steps. The first and the last 75 steps were used for background determination. Data were processed using the X-Phi matrix correction of Merlet (1994). The detection limit for B is $\sim 2500 \text{ ppm}$ and the relative error expressed as 3σ is $\sim 10 \text{ rel\%}$ for 15 wt% B_2O_3 content. We chose to operate in peak area mode because of the effect on the shape and position of the $\text{BK}\alpha$ peak due to differences in composition and structure between standard and unknown, the most important being coordination of B (tetrahedral in danburite, but largely trigonal in the unknowns). McGee and Anovitz (1996) showed that the effect of such differences on the $\text{BK}\alpha$ peak is reduced when peak area is measured. We did not attempt to control for crystallographic orientation of standard and unknown given that vránaite and boralsilite are finely fibrous.

LA-ICP-MS equipment at the Department of Chemistry, Masaryk University, Brno, used to determine Li, Be, and B contents in boralsilite and vránaite consists of a UP 213 (New Wave Research, Inc., Fremont, California, U.S.A.) laser-ablation system and an Agilent 7500 CE (Agilent Technologies, Santa Clara, California, U.S.A.) ICPMS spectrometer. A commercial Q-switched Nd:YAG laser ablation device works at the fifth harmonic frequency, which corresponds to the wavelength of 213 nm. Laser ablation was performed with a laser spot of diameter 55 μm , laser fluence 9 J/cm², and repetition rate 10 Hz. Li, Be, and B contents of elements were calculated using NIST SRM 610 and 612 standards and Al was used as an internal reference element after baseline correction and integration of the peak area.

H_2O and CO_2 were not determined directly as the recorded Raman spectra showed no indications of OH^- , H_2O , CO_2 , or CO_3^{2-} .

CRYSTAL STRUCTURE

The crystal structure of vránaite is based upon chains of edge-sharing AlO_6 octahedra that run parallel to [010] and are cross-linked by Si_2O_7 disilicate groups, BO_3 triangles, and clusters of AlO_4 and AlO_5 polyhedra (Fig. 2). Two fivefold-coordinated Al sites, Al4 and Al5, cannot be occupied simultaneously; the refinement gives site-occupancy factors of 54 and 20% occupancy, respectively. Moreover, occupancies of Al5 and O9 sites are approximately equal to 0.20; this could give the following combinations:

- (1) Threecold-coordinated Al when the Al9 site is occupied and the O9 sites are empty;
- (2) Fourfold-coordinated Al when the Al9 site is occupied and only one of two O9 sites is occupied;
- (3) Fivefold-coordinated Al when the Al9 site and both O9 sites are occupied.

There is no problem if two O9 sites are occupied simultaneously; the O9-O9 distance is ca. 2.25 \AA , which is permissible for the shared edge between two adjacent AlO_5 polyhedra. Therefore, the option (3) is plausible and the structure model is very reasonable, indeed, this explains exactly why occupancies of the Al5 and O9 sites are almost equal.

Bond valence calculations for the Al4 site suggest that Li is likely to be sited here, whereas Be is most probably present at the Al5 site. Both Al4 and Al5 sites are dominated by Al, i.e., occupancies of Li and Be are subordinate at their respective sites. Eight of the O sites are fully occupied, whereas the O9 site is only 20% occupied and completes the coordination of the Al5 site. This site is located at the fourth corner of what could be a partially occupied BO_4 tetrahedron, that is, the B site would be shifted out of the plane of the BO_3 triangle. However, our refinement did not give any evidence for a split position of the B atom, so this shift remains an inference.

The refined sum of cation electron densities (270.48 e⁻) obtained from the structural formulas in Table 2 and the measured occupancies listed in Table 3 shows an excellent agreement with the 269.85 e⁻ for the empirical formula $\text{Li}_{1.08}\text{Be}_{0.47}\text{Fe}_{0.02}\text{Al}_{14.65}\text{B}_{3.89}\text{Si}_{3.88}\text{O}_{36.62}$ calculated from the analyses assuming cations sum to 24, an assumption justified by the total obtained if B, Si, Al1, Al2, and Al3 were fully occupied and Al4 and Al5 were 50% occupied, as well as by analogy with boralsilite. Similarly, the refined number of anions matches well with that of the empirical formula (36.83 and 36.62 atoms, respectively).

In discussing the crystallographic relationships between werdingite and other phases with mullite-type structures, Niven et al. (1991) noted that one of two slabs constituting the structure of werdingite, $(\text{Mg},\text{Fe})_2\text{Al}_2(\text{Al},\text{Fe})_2\text{Si}_4(\text{B},\text{Al})_4\text{O}_{37}$, has the ideal composition $[{}^6\text{Al}_8[{}^5\text{Al}_4[{}^4\text{Al}_2\text{B}_4\text{Si}_4]\text{O}_{38}]$, with monoclinic symmetry ($C2/m$). It appears that, both topologically and geometrically, the linkages of $[{}^6\text{Al}_8[{}^5\text{Al}_4[{}^4\text{Al}_2\text{B}_4\text{Si}_4]\text{O}_{38}]$ and vránaite are essentially identical.

Electron backscattered diffraction patterns of grains 1 (Appendix¹ 1) and 3 can be indexed nicely using the vránaite structure in $C2/m$ (converted from $I2/m$), with a mean angular deviation of 0.38 to 0.41°.

TABLE 3. Atomic coordinates, site-occupancy factors (sof), and isotropic displacement parameters (\AA^2), with standard deviation in parentheses

Atom	x	y	z	Occupancy	U_{eq}
B	0.5014(6)	$\frac{1}{2}$	0.2334(8)	1	0.0248(17)
Si	0.34575(15)	0	0.49547(15)	1	0.0166(5)
Al1	$\frac{1}{4}$	$\frac{1}{4}$	$\frac{3}{4}$	1	0.0137(4)
Al2	$\frac{1}{4}$	$\frac{3}{4}$	$\frac{1}{4}$	1	0.0155(5)
Al3	-0.02458(17)	$\frac{1}{2}$	0.33947(16)	1	0.0176(5)
Al4	0.2049(3)	$\frac{1}{2}$	0.4732(3)	0.541(9)	0.0179(13)
Al5	0.3564(10)	$\frac{1}{2}$	0.4997(9)	0.199(10)	0.026(4)
O1	0.3687(4)	$\frac{1}{2}$	0.2260(3)	1	0.0141(9)
O2	0.0690(2)	0.2107(5)	0.7241(3)	1	0.0168(7)
O3	$\frac{1}{2}$	0	$\frac{1}{2}$	1	0.052(2)
O4	0.2957(3)	-0.2326(5)	0.4236(3)	1	0.0222(7)
O5	0.2855(4)	0	0.6342(4)	1	0.0165(9)
O6	0.2283(4)	$\frac{1}{2}$	0.6390(4)	1	0.0187(9)
O7	0.1434(4)	$\frac{1}{2}$	0.2953(4)	1	0.0151(9)
O8	0	$\frac{1}{2}$	$\frac{1}{2}$	1	0.055(3)
O9	0.488(2)	$\frac{1}{2}$	0.6021(18)	0.207(18)	0.026(8)

PHYSICAL AND OPTICAL PROPERTIES

Vránaite forms intergrowths of subparallel prisms up to 100 μm long (Fig. 3a), which are indistinguishable visually and in backscattered electron images (Fig. 3c) from boralsilite. An indistinct lamellar twinning parallel to $\{001\}$ was observed optically. Vránaite is brittle and its hardness (Mohs) is 4½. Cleavage and parting were not observed; its fracture is irregular. Density could not be measured because of the paucity of material and because of the intimate intergrowths with associated phases. The calculated density is 2.99 g/cm³ based on the empirical formula.

Fluorescence bands were observed between 50 and 2500 cm⁻¹ under excitation by 532 nm Nd:YAG and 633 nm He-Ne lasers during Raman spectroscopy measurements.

Vránaite is transparent, colorless, and non-pleochroic with a white streak; its luster is vitreous. It is optically biaxial (-), $n_a = 1.607$ (1), $n_b = 1.634$ (1), $n_g = 1.637$ (1) (white light using a spindle stage). The $2V_x$ was observed to be small, but it could not be measured because of indistinct interference figures and indistinct extinctions in some orientations. The calculated $2V$ angle is 36.4°. Dispersion could not be observed. The orientation is $X \approx \mathbf{c}$; $Y \approx \mathbf{a}$; $Z = \mathbf{b}$.

CHEMICAL COMPOSITION AND COMPATIBILITY INDEX

To select a composition to represent vránaite, we have used the data in Tables 1 and 2 of Novák et al. (2015), as these analyses were obtained on the section from which the crystals used to obtain the X-ray diffraction and optical data were extracted. However, the LA-ICP-MS B₂O₃ contents of vránaite in their Table 2 are higher than the ideal B₂O₃ content inferred for vránaite, whereas the EMPA B₂O₃ contents in their Table 1 cluster around the ideal vránaite B₂O₃ content (Figs. 4 and 5). Consequently, we have used only the EMPA B₂O₃ contents to represent vránaite (Table 4). The resulting composition agrees with the composition determined in the crystal structure refinement if Li and Be are assumed to replace Al as the refinement suggests. The analytical total is 99.31 wt%, a more reasonable value than the totals obtained if ICP-MS B₂O₃ values are assumed, 100.75–103.45 wt%, or on average 101.96 wt% (Novák et al. 2015).

The empirical formula, calculated on the basis of 24 cations per formula unit is $(\text{Al}_{14.65}\text{Li}_{1.08}\text{Be}_{0.47}\text{Fe}_{0.02})_{\Sigma 16.22}\text{B}_{3.89}\text{Si}_{3.88}\text{O}_{36.62}$. The simplified formula, assuming fully occupied B, Si, Al1, Al2,

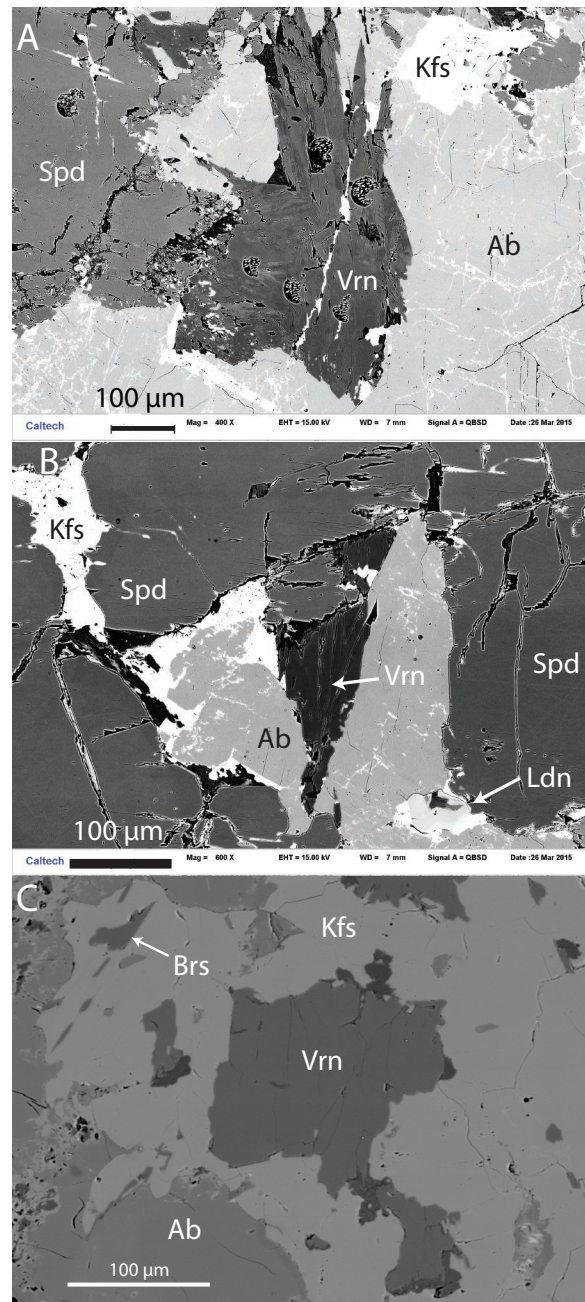


FIGURE 3. Backscattered electron images of vránaite (Vrn) in albite (Ab) or K-feldspar (Kfs) and contiguous with spodumene (Spd). (a) Grain 1 showing fibrous appearance revealed by compositional heterogeneity. This grain was used for the X-ray diffraction and optical work. Image taken at Caltech. (b) Grain 2. Bright grain (Ldn) is londonite. Image taken at Caltech. (c) Grain 3 is a bit farther from spodumene. Note that boralsilite (Brs) is separate from vránaite. Image taken at Masaryk University.

and Al3 sites and half-occupied Al4 and Al5 sites (see above), is $\text{Al}_{16}\text{B}_4\text{Si}_4\text{O}_{38}$, which corresponds to (in wt%): 68.2 Al₂O₃, 11.6 B₂O₃, and 20.1 SiO₂. The Raman spectrum shows no peaks in the range between 3000 and 4000 cm⁻¹ typically attributed to OH

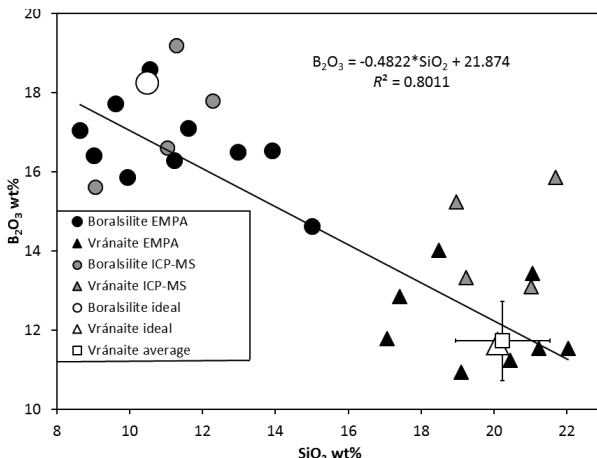


FIGURE 4. Plot of B₂O₃ (EMPA and LA-ICP-MS) and SiO₂ (EMPA only) contents (wt%) of boralsilite and vránaite from Novák et al. (2015), Tables 1 and 2 therein. The average composition of vránaite is from Table 4. Trend line is a least-squares fit to the EMPA data.

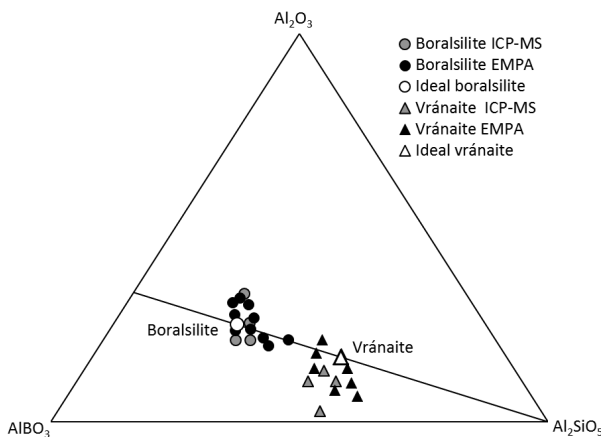


FIGURE 5. Compositions of boralsilite and vránaite (Novák et al. 2015) projected from Li₂O and BeO onto the Al₂O₃-AlBO₃-Al₂SiO₅ part of the Al₂O₃-B₂O₃-SiO₂ (BAS) system. The symbols distinguish between B₂O₃ contents measured with the electron microprobe (black filled) and with the laser ablation ICP-MS (gray filled).

(Fig. 6), and thus vránaite is formulated as an anhydrous mineral.

The Gladstone-Dale relation (Mandarino 1981) gives a compatibility index 1 - (K_P/K_C) = 0.001 (superior).

Novák et al. (2015) showed that both boralsilite and vránaite ("boron mullite") were compositionally heterogeneous with a minimal gap in miscibility between the two minerals. This compositional variation and gap are evident in Figures 4 and 5.

Vránaite Li contents average six times those of associated boralsilite, which contains the most Li reported in boralsilite to date (Fig. 7). Vránaite is also richer in Be than associated boralsilite.

RELATIONS TO OTHER COMPOUNDS: NATURAL AND SYNTHETIC

Vránaite is the third anhydrous ternary SiO₂-B₂O₃-Al₂O₃ mineral, and like the other two, boralsilite and boromullite, it

TABLE 4. Analytical data (in wt%) for vránaite

Constituent	Mean	Used	no.	Range	St.dev.	EMPA Std./method
SiO ₂	20.24	20.24	4	18.98-21.70	1.3	sanidine
B ₂ O ₃ ^a	14.37	—	4	13.09-15.85	1.4	LA-ICP-MS
B ₂ O ₃ ^a	11.73	11.73	5	10.92-13.43	1.0	danburite
Al ₂ O ₃	64.77	64.77	4	62.77-65.51	1.3	sanidine
BeO	1.03	1.03	4	0.47-1.40	0.40	LA-ICP-MS
FeO	0.13	0.13	4	0.08-0.18	0.05	almandine
MnO	0.01	0.01	4	bdl-0.03	0.02	spessartine
Li ₂ O	1.40	1.40	4	1.19-1.54	0.15	LA-ICP-MS
Na ₂ O	0.01	—	4	0.01-0.02	0.01	albite
Na ₂ O	—	—	4	bdl-bdl	—	LA-ICP-MS
F	0.03	0	4	bdl-0.06	0.03	topaz
Total	—	99.31	—	—	—	—

Note: no. = number of analyses. ^aB₂O₃ measured on the same grains. bdl = below detection level. Total includes EMPA B₂O₃ and LA-ICP-MS Na₂O, but not F, which is assumed to be below detection level. Source: Novák et al. (2015), Tables 1-3.

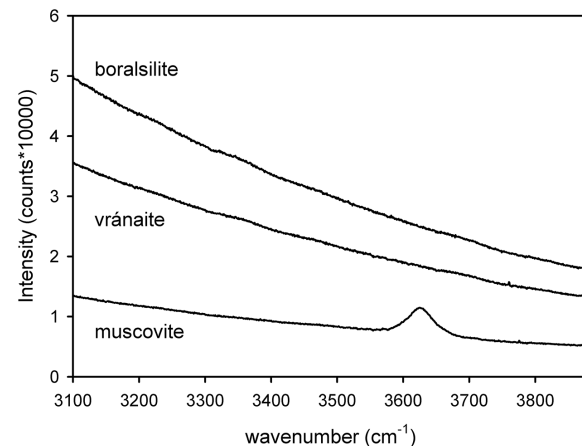


FIGURE 6. Raman spectrum of vránaite compared to spectra of boralsilite and muscovite.

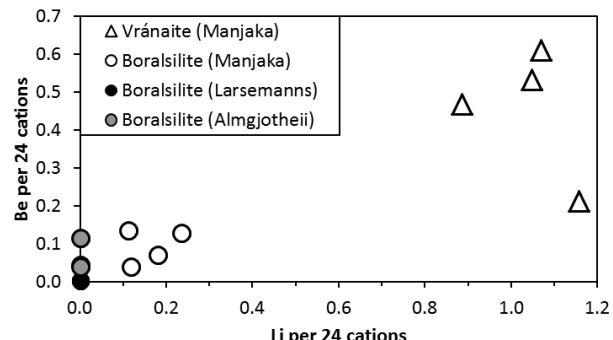


FIGURE 7. Plot of Li contents of boralsilite from the Larsemann Hills, Antarctica, and Almgjotheii, Rogaland, Norway (ion microprobe data, Grew et al. 1998), for comparison with data on boralsilite and vránaite from Manjaka (Novák et al. 2015, Table 2; vránaite formulas calculated using ICP-MS B₂O₃ contents). Vránaite contains 1.19–1.54 wt% Li₂O and 0.47–1.40 wt% BeO, several times their contents in boralsilite at Manjaka.

belongs to the family of mullite-type boron compounds in the classification of Fischer and Schneider (2008), that is, chains of edge-sharing Al octahedra cross-linked by various polyhedra containing Al, B, and Si. The symmetry of vránaite and boralsilite

can be derived from the orthorhombic supergroup *Pbam* represented by B-doped mullite using a Bärnighausen tree (Fischer and Schneider 2008). Vránaite has an index of 4 lower than mullite ($Pbam \rightarrow t2 P2/m \rightarrow k2 I2/m$, where t = translationengleich and k = klassengleich), whereas boralsilite has an index of 8 lower; i.e., the symmetry of vránaite is higher than that of boralsilite (Reinhard Fischer, personal communication, 2016).

Table 5 shows how similar vránaite, boralsilite, and boromullite are to one another. A partial chemical analysis such as EMPA without B_2O_3 would be needed to unambiguously distinguish them, although $2V$ could give a preliminary indication. X-ray powder diffraction patterns of vránaite (this paper) and boralsilite (Grew et al. 2008) are very similar; positions of the most intense peaks differ only slightly, and intensities are similar. Moreover, both minerals have prismatic crystal habit and therefore preferred crystal orientation in a measured sample may affect measured intensities. Consequently, distinguishing vránaite from boralsilite using only powder X-ray diffraction without EMPA may not be possible.

Boromullite differs from boralsilite and vránaite in that it corresponds to a 1:1 polysome composed of an Al_2SiO_5 module having the topology and stoichiometry of sillimanite and of an Al_5BO_9 module that is a type of mullite defect structure (Buick et al. 2008). Vránaite and boralsilite are very similar in structure (Fig. 2). Overall, boralsilite can be considered as a structure in which half of the Si_2O_7 dimers in vránaite are replaced by two B tetrahedra accompanied by some rearrangement of Al polyhedra. Specifically, the BO_3 triangle in vránaite corresponds to the B_3O_3 triangle in boralsilite and the partially occupied tetrahedral B site formed when O9 is occupied in vránaite corresponds to the B_2O_4 tetrahedron in boralsilite. Also, the Al5 site in vránaite corresponds nicely to the Al3 site in boralsilite. A nearly continuous compositional series between vránaite and boralsilite is not surprising given the similarity in the structures, including their geometrical parameters.

A large number of anhydrous, ternary compounds related to

mullite and having orthorhombic symmetry have been synthesized; these have been referred to collectively as “boron mullite” and were thought to occupy a wide field in SiO_2 - B_2O_3 - Al_2O_3 space (Fig. 1, e.g., Werding and Schreyer 1992, 1996; Fischer and Schneider 2008; Lührs et al. 2012, 2013, 2014). One such compound was synthesized by Werding and Schreyer (1992), who reported it to have orthorhombic symmetry and the composition $Al_{16}B_4Si_4O_{38}$ based on the Al:Si ratio in the starting gel and a boron analysis. Similarities in the powder X-ray diffraction patterns between this phase, several aluminoborates and sillimanite led Werding and Schreyer (1992) to suggest that all these phases are boron-bearing derivatives of sillimanite. The reported pattern for $Al_{16}B_4Si_4O_{38}$ included a reflection at $20.301^\circ 2\theta$ that required indexing its powder XRD pattern with a supercell having two doubled cell parameters characteristic of sillimanite (Grew et al. 2008). These authors attributed the reflection at $20.301^\circ 2\theta$ to the incipient development of a boralsilite-like structure; and re-indexed its powder XRD pattern with a mullite cell to give cell parameters very similar to those for other “boron-mullites.” This re-interpretation is consistent with the crystal structure refinement by the Rietveld method (Lührs et al. 2014) of a synthetic compound with the composition determined by prompt γ activation analysis, $Al_{4.19(7)}Si_{0.91(6)}B_{0.90(2)}O_{9.45}$, i.e., very close to $Al_{16}B_4Si_4O_{38}$. The compound has orthorhombic symmetry, space group, *Pbam*: $a = 7.508466(1)$, $b = 7.651508(1)$, $c = 2.832082(7)$ Å, that is, mullite-like (Lührs et al. 2014), and distinct from vránaite.

Analyses of “boron-mullites” give linear arrays radiating from Al_5BO_9 (Figs. 1 and 8) in lieu of a broad area of compositions in the SiO_2 - B_2O_3 - Al_2O_3 system, that is, “boron-mullites” between 3:2 mullite and Al_5BO_9 (Lührs et al. 2014); boromullite and several synthetic compounds between sillimanite and Al_5BO_5 (Buick et al. 2008), and “boron-mullites” between $Al_{16}B_4Si_4O_{38}$ and Al_5BO_9 (Grew et al. 2008).

Not all synthetic anhydrous ternary phases in the “boron-mullite” field of the SiO_2 - B_2O_3 - Al_2O_3 system are “boron-mullite.” Grew et al. (2008) distinguished synthetic disordered boralsilite from “boron-mullite” since its X-ray diffraction pattern resembled that of boralsilite, but differed from that of ordered boralsilite in that reflections were broadened and their intensities modified. These differences could result from either a very small size of coherently scattering domains or strain associated with lattice imperfections (Grew et al. 2008). These authors interpreted the presence of a low “hump” between 20.0 and $20.4^\circ 2\theta$, like the weak reflection at $20.301^\circ 2\theta$ in orthorhombic $Al_{16}B_4Si_4O_{38}$, to represent the incipient conversion of “boron-mullite” to a “boralsilite-like” structure, i.e., a structure like either boralsilite or vránaite. In marked contrast to “boron-mullite,” compositional variation in disordered boralsilite followed a linear trend at high angles to the linear arrays for “boron mullite” and come close to intersecting the boralsilite-vránaite join (Fig. 8), i.e., the disordered phase could be just as well be called “disordered” vránaite.

OCCURRENCE AND ORIGIN

Vránaite occurs in the Manjaka pegmatite, one of the granitic pegmatites in the Sahatany Valley pegmatite field, located about 25 km SW of the town Antsirabe in the northeast part of the Itremo Region, Central Madagascar (Novák et al. 2015).

TABLE 5. Comparison of vránaite to related minerals

Mineral	Vránaite	Boralsilite	Boromullite	Sillimanite	
Formula	$Al_{16}B_4Si_4O_{38}$	$Al_{16}B_6Si_2O_{37}$	$Al_9BSi_2O_{19}$	Al_2SiO_5	
Crystal system	monoclinic	monoclinic	orthorhombic	orthorhombic	
Space group	$I2/m$	$C2/m$	$Cmc2_1$	$Pbnm$	
Z	1	2	2	4	
a (Å)	10.383(1)	14.767(1)	5.717(2)	7.4841(1)	
b (Å)	5.6682(7)	5.574(1)	15.023(5)	7.6720(3)	
c (Å)	10.823(1)	15.079(1)	7.675(3)	5.7707(2)	
β (°)	90.11(1)	91.96(1)	90.00	90.00	
V (Å 3)	636.97(13)	1240.4(2)	659.2(7)	331.34(1)	
n_a	1.607(1)	1.629(1)	1.627(1)	1.653–1.661	
n_β	1.634(1)	1.640(1)	1.634(1)	1.657–1.662	
n_γ	1.637(1)	1.654(1)	1.649(1)	1.672–1.683	
$2V_x$ (°)	36.4	98.2(6)	123(2)	150–159	
Orientation	$Z=b$	$Z=b$	–	$Z=c$	
Cleavage	none	fair	none	perfect	
Powder XRD, d_{obs} (Å), I	5.40, 96 5.19, 99 4.97, 74 3.658, 75 3.403, 100 2.496, 61 2.171, 75 1.5183, 61	5.36, 70 5.19, 100 4.95, 60 4.31, 70 3.378, 60 2.162, 40	5.37, 50 3.38, 100 2.67, 60 2.51, 60 2.19, 80 1.512, 80	5.36, 16 3.42, 100 3.37, 65 2.204, 60 2.541, 40 2.679, 30 2.111, 20	
Reference	1	2, 3	4	5, 6	

Notes: 1 = this study; 2 = Grew et al. (1998); 3 = Peacor et al. (1999); 4 = Buick et al. (2008); 5 = Anthony et al. (2003); 6 = Bish and Burnham (1992).

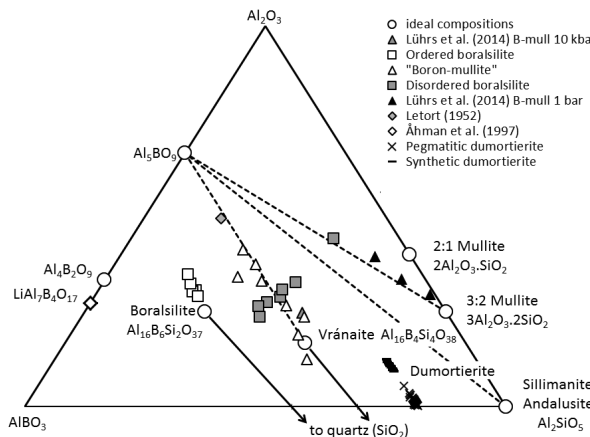


FIGURE 8. Phases related to mullite, together with dumortierite, plotted in the Al_2O_3 - AlBO_3 - Al_2SiO_5 part of the Al_2O_3 - B_2O_3 - SiO_2 (BAS) system, with $\text{LiAl}_1.7\text{B}_4\text{O}_{17}$ projected from Li_2O . Dashed lines mark the linear areas of compositions radiating from Al_5BO_6 . The arrows are tie lines from boralsilite and vránaite to quartz, which plots off the diagram. Sources of data in addition to references cited in the legend: pegmatic dumortierite containing more Al_2O_3 than the AlBO_3 - Al_2SiO_5 join (Cempírek 2003; Cempírek and Novák 2005; Cempírek et al. 2010; Wadoski et al. 2011); dumortierite synthesized at 650–700 °C, 3–5 kbar (Werding and Schreyer 1990); and “boron-mullite,” ordered boralsilite and disordered boralsilite (Grew et al. 2008).

Coordinates in WGS84 (latitude, longitude): 20°04'35"S, 46°57'09"E. Vránaite is in contact with spodumene (Figs. 3a and 3b), K-feldspar (Fig. 3b and 3c), albite, and a secondary Al-rich clay mineral. Boralsilite also occurs in this association, although separately from vránaite, the closest approach being 100 µm (Fig. 3c). Zoned tourmaline 1 (elbaite to fluor-elbaite), zoned londonite-rhodizite, quartz, and beryl are also associated with spodumene, but none of these minerals contacts vránaite. Although the primary assemblage of spodumene + K-feldspar + albite contains minor quartz, vránaite, and boralsilite are part of a later assemblage with albite that is quartz-undersaturated.

Boralsilite and vránaite are inferred to have grown under conditions far from equilibrium resulting from a combined pressure + chemical quenching in the Manjaka pegmatite. We attribute origin of boralsilite and vránaite to a liquid rich in alkalis, Be, and B, and to having high $a(\text{CO}_2)$ together with low $a(\text{H}_2\text{O})$ due to early melt contamination by carbonate in the host rocks. The unusual fluid composition is indicated by the low abundance of hydrous phases, presence of secondary rhodochrosite and minor extent of exocontact reactions adjacent to the pegmatite. Novák et al. (2015) estimated the temperature-pressure conditions for crystallization of boralsilite and vránaite to be ~350–450 °C and ~2–3 kbar (Fig. 9), i.e., very late solidus or early subsolidus conditions that later graded into crystallization of rhodizite-londonite.

DISCUSSION

Ternary phases (either anhydrous or hydrous) in the SiO_2 - B_2O_3 - Al_2O_3 (BAS) system (Fig. 1) are relatively rare in pegmatites; instead, boron is largely tied up in species of the tourmaline supergroup, and the Manjaka pegmatite is no exception.

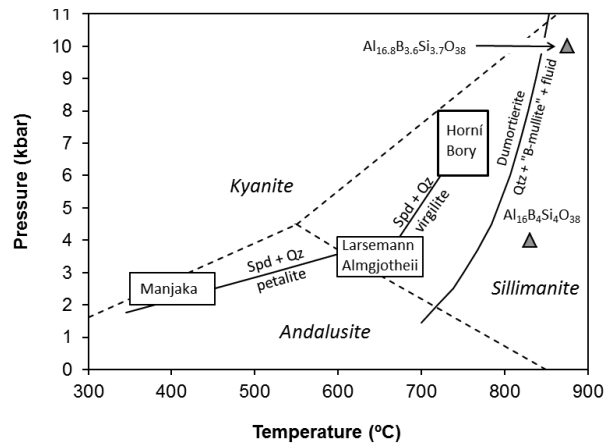


FIGURE 9. Pressure-temperature diagram for boralsilite crystallization (rectangles) in the Larsemann Hills, Antarctica, and Almgjotheii, Norway (Grew et al. 2008), Horní Bory, Czech Republic (Cempírek et al. 2010), and Manjaka, Madagascar (Novák et al. 2015; this paper), and for “boron-mullite” ($\text{Al}_{16}\text{B}_4\text{Si}_4\text{O}_{38}$; Werding and Schreyer 1992; $\text{Al}_{16.8}\text{B}_{3.6}\text{Si}_{3.7}\text{O}_{38}$, Lührs et al. 2014). Source for experimental data: Al_2SiO_5 polymorphs (italics and dashed lines, Pattison 1992), dumortierite breakdown (Werding and Schreyer 1996), breakdown of spodumene + quartz (Spd + Qz, London 1984).

tion. The dumortierite supergroup (Pieczka et al. 2013) is found in a fair number of pegmatites, although much less abundantly than tourmaline. In contrast, boralsilite is known only from four localities worldwide (Grew et al. 1998, 2008; Cempírek et al. 2010; Novák et al. 2015), and vránaite so far from only one locality. Compositions of boralsilite, vránaite, and Al-rich dumortierite (higher Al/Si ratio than the end-member $\text{Al}_1\text{BSi}_1\text{O}_{18}$) containing little Ti, Fe, Mg, As, and Sb projected from H_2O and other non-BAS constituents plot in the Al_2O_3 -dominant third of the SiO_2 - B_2O_3 - Al_2O_3 plane (Al_2SiO_5 - AlBO_3 - Al_2O_3 , Fig. 8). Compositions of dumortierite from pegmatites in the Czech Republic (Cempírek 2003), as well as dumortierite associated with boralsilite, approach that of the ideal anhydrous end-member when projected onto the Al_2SiO_5 - AlBO_3 - Al_2O_3 plane.

In a review of the two original localities of boralsilite (Larsemann Hills, Antarctica; Almgjotheii, Norway), Grew et al. (2008) concluded that a combination of a B-rich source and relatively low water content, together with limited fractionation, resulted in an unusual buildup of B, but not of Li, Be, and other elements normally concentrated in pegmatites. The resulting conditions are favorable for precipitation of boralsilite instead of elbaite, which is often formed in more fractionated pegmatites. An important consideration is the amount of water in the melt: if the residual fluids were drier, there would have been less opportunity for metasomatic loss of B from the pegmatite to the host rock, a process that often depletes pegmatites in B (London et al. 1996). Grew et al. (2008) also noted the common association of boralsilite with graphic tourmaline-quartz intergrowths in the Larsemann Hills; these intergrowths could be the products of rapid crystallization due to oversaturation in tourmaline. London et al. (1996) attributed similar graphic intergrowths of tourmaline and quartz from the Belo Horizonte 1 pegmatite, California, to oversaturation. Rapid growth of

tourmaline and quartz could have left a residual melt or fluid thoroughly depleted in Fe and Mg; less so in B. However, such graphic intergrowths have not been found at Almgjotheii or at the other two world localities for boralsilite, Horní Bory, Czech Republic, and Manjaka. A boron-rich source rock was not found in the immediate vicinity of the boralsilite-bearing veinlets at Almgjotheii or Horní Bory, but more distant rocks of the Gföhrl Unit could have been the source of B for the Horní Bory veinlet (Cempírek et al. 2010). These authors reported that intrusion of the boralsilite-bearing veinlet at Horní Bory post-dated foliation in the host granulite and suggested the veinlet is a product of decompressional melting processes. Boralsilite most likely crystallized in a H_2O -poor system. In contrast to the Larsemann Hills and Almgjotheii, there is evidence for some concentration of Li in the Horní Bory veinlet (Cempírek et al. 2010). Despite the striking differences with the other three localities, notably the much lower temperature of crystallization and Li enrichment indicated by the association with spodumene, the Manjaka pegmatite shares several features with them: little loss of boron to the host rock and possible decompression suggested by the presence of spodumene + quartz intergrowths. Such intergrowths (SQI) are attributed in other pegmatites to petalite breakdown (e.g., Tanco in Manitoba, Canada, London 2008), which implies for Manjaka decompression to form petalite from primary spodumene + quartz, followed by isobaric cooling during which petalite broke down entirely to a second generation of spodumene + quartz. There is an alternative scenario consistent with observed textures and mineral assemblages and not involving an incursion into the petalite stability field, namely, a chemical quench during cooling or decompression within the spodumene + quartz stability field and resulting in sudden saturation in quartz, possibly from loss of alkalis to the fluid phase, and rapid precipitation of spodumene as SQI.

Although the breakdown curve for dumortierite shown in Figure 9 does not represent a univariant reaction in the $SiO_2-B_2O_3-Al_2O_3-H_2O$ system, it is strongly suggestive that dumortierite is a stable ternary $SiO_2-B_2O_3-Al_2O_3$ phase with quartz present up to 700–830 °C at $P < 8$ (Werding and Schreyer 1992, 1996), which is consistent with its widespread occurrence in metamorphic rocks (Grew 1996). Less evident is whether a second BAS phase such as “boron-mullite,” boralsilite, or vránaite, could be stable in addition to or instead of dumortierite, particularly in compositions richer in Al_2O_3 or B_2O_3 as only synthesis data are available on these minerals. Synthesis of a “boron mullite” has been reported at $P-T$ conditions within the dumortierite stability field (500–800 °C, 2–10 kbar, Werding and Schreyer 1984, 1996; Wodara and Schreyer 2001), but this material was not well characterized. Only “boron mullite” synthesized at temperatures above dumortierite breakdown (Fig. 9) has been shown to have a mullite structure by detailed X-ray diffraction study, e.g., 750–800 °C, 1–2 kbar, Grew et al. 2008; 875 °C, 10 kbar, Lührs et al. 2014). In contrast, X-ray diffraction has confirmed the synthesis of disordered and ordered boralsilite at temperatures both within the dumortierite stability field and above the curve for dumortierite breakdown (Pöter et al. 1998; Grew et al. 2008). It is thus possible that Werding and Schreyer (1984, 1996) and Wodara and Schreyer (2001) mistook disordered and ordered boralsilite for “boron

mullite,” and, as a result, there is reason to believe “boron-mullite” is stable only at temperatures above the breakdown of dumortierite at pressures up to at least 10 kbar (Grew et al. 2008; Lührs et al. 2014).

Grew et al. (2008) were not successful in identifying what physical-chemical conditions favor transformation of disordered to ordered boralsilite. No evidence was found that duration, gel composition, proportion of H_3BO_3 or seeding with ordered boralsilite played a critical role. That some experimental runs containing an apparently amorphous phase yielded ordered boralsilite suggests that chance seeding by an unknown impurity could play a role.

Natural boralsilite at all four localities crystallized in the stability field of dumortierite + quartz (Fig. 9). Boralsilite at Manjaka crystallized in the absence of quartz, but at temperatures so much below the temperature of dumortierite breakdown that silica undersaturation is not a plausible explanation for the presence of boralsilite and vránaite and absence of dumortierite in the Manjaka pegmatite. More plausible is the stabilization of vránaite in addition to boralsilite by the presence of significant Li in vránaite (Fig. 7), whereas boralsilite Li contents seem too low to explain its appearance in the Manjaka pegmatite.

Crystallization of boralsilite and vránaite has analogies with that reported for metastable crystallization of cristobalite in crystal-rich fluid inclusions hosted in spodumene in Jiajika pegmatite deposit, China (Li and Chou 2015). These authors attributed the formation of cristobalite to a 1.5–2.4 kbar decrease in pressure inside the inclusions and extension of the cristobalite stability field to lower temperatures by Li and H_2O .

There are two possible scenarios for the crystallization of boralsilite and vránaite.

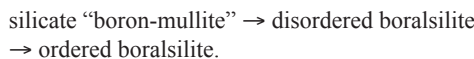
(1) A B- and Al-rich bulk composition favored stable crystallization of boralsilite over dumortierite, even in the presence of quartz at sufficiently high temperatures; additionally isolation from quartz by albite and an assist from Li could have stabilized boralsilite and vránaite at much lower temperatures in the Manjaka pegmatite. Dumortierite is present in pegmatites at three of the four localities for boralsilite (Manjaka is the exception), but interpretation of its relationship with boralsilite is complicated by microstructural evidence for two generations (e.g., Larsemann Hills, Wadoski et al. 2011) and by the variable presence of Ti, Fe, Mg, As, or Sb (Grew et al. 1998; Wadoski et al. 2011; Cempírek et al. 2010), i.e., these impurities, where present in significant amounts, could have stabilized dumortierite in addition to boralsilite. Nonetheless, even dumortierite containing relatively low concentrations of these impurities does not block tie lines from quartz to either vránaite or boralsilite (arrows) in the $Al_2SiO_5-AlBO_3-Al_2O_3$ plane (Fig. 8), which is consistent with higher boron concentrations stabilizing boralsilite or vránaite instead of dumortierite.

(2) Boralsilite and vránaite crystallized metastably instead of dumortierite due to their relative structural simplicity, that is, the system follows the path of metastable crystallization described by the Ostwald principle and the Goldsmith's (1953) “simplicity” rule, which states that, in the Ostwald cascade of phase transformations, phases with higher “simplicity” (lower complexity) crystallize first even if they are unstable from the energetic point of view. Numerical estimates of structural

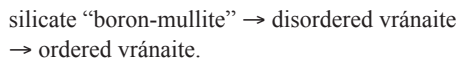
TABLE 6. Structural complexity of selected alumino-borosilicates

Mineral	Chemical formula (average)	v , atoms	I_G (bits/atom)	$I_{G,\text{total}}$ (bits/cell)	References
"boron-mullite"	$\text{Al}_{16.8}\text{B}_{3.6}\text{Si}_{3.7}\text{O}_{38}$	16	2.250	36.000	Lührs et al. (2014)
"boron-mullite"	$\text{LiAl}_7\text{B}_4\text{O}_{17}$	29	2.651	76.881	Åhman et al. (1997)
vránaite	$\text{Al}_8\text{Si}_3\text{B}_2\text{O}_{19}$	34	3.911	132.974	this work
boralsilite	$\text{Al}_{16}\text{Si}_2\text{B}_2\text{O}_{37}$	61	4.619	281.775	Peacor et al. (1999)
dumortierite	$\text{Al}_7\text{Si}_3\text{BO}_{18}$	116	4.099	475.526	Fuchs et al. (2005)

complexity, which were derived by applying Shannon information theory, provided quantitative support to Goldsmith's rule (Krivovichev 2012, 2013). Since structural complexity represents a negative contribution to the total entropy of a crystalline solid (through its configurational part, Krivovichev 2016), crystallization of a metastable phase is entropy driven and governed by kinetics of the process, which favor crystallization of phases with higher configurational entropy first. In the case of the system under consideration, a possible sequence of phase transformations is:



There could be an analogous sequence:



In both cases, crystallization starts with a low-complexity phase and ends with a higher-complexity phase, but not with the most complex phase in the system, which is the stable phase dumortierite (Table 6). Therefore, the occurrence of vránaite at Manjaka pegmatite may be explained by its crystallization under conditions far from equilibrium and the very specific kinetic regime of quenching. This hypothesis also explains the relative rarity of vránaite, as crystallization proceeds to the most stable phase, i.e., dumortierite, at most other localities. Given the inverse relationship between structural complexity and configurational entropy (Krivovichev 2016), it seems plausible that disordered boralsilite and vránaite are less complex than the corresponding ordered phases, but still more complex than silicate "boron-mullite." Compositions plotted in Figure 8 suggest that the succession to form ordered vránaite would be not overly far from isochemical, whereas additional AlBO_3 and Al_2O_3 are needed to form ordered boralsilite from "boron-mullite." However, the latter sequence cannot be ruled out for this reason alone, because it is likely that "boron-mullite" and disordered boralsilite have a wider range of composition than that reported by Grew et al. (2008) and shown in Figure 8. We have included the boron mullite $\text{LiAl}_7\text{B}_4\text{O}_{17}$ in Figure 8 to show that Li, an element not generally encountered in mullite, could be present as a subordinate constituent in the "boron-mullite" precursor, and thus scenario (2) is relevant for the Li-bearing system at Manjaka.

Černý (2000) and London (2008) suggested that both pressure and chemical quenches play important roles in the formation of miarolitic cavities, and similar quenches, for example, abrupt change in chemical composition by crystallization of tourmaline + quartz in the Larsemann Hills (or grandidierite at Horní Bory, Cempírek et al. 2010), could have favored metastable crystal-

lization of the mullite precursors to boralsilite and vránaite. On the other hand, the Manjaka pegmatite containing boralsilite and vránaite was subject to system opening (Novák et al. 2015), and thus metastable crystallization due to rapid pressure decrease is very likely. Given all these opportunities for metastable crystallization, we tend to favor the second scenario, in which some mix of a pressure and chemical quench resulted in conditions favorable to metastable crystallization of disordered "boron-mullite" that subsequently recrystallized into ordered boralsilite and vránaite.

IMPLICATIONS

Vránaite is the third nominally ternary $\text{B}_2\text{O}_3\text{-Al}_2\text{O}_3\text{-SiO}_2$ phase in the mullite-type family of structures to be discovered in nature, the others being boralsilite and boromullite. A greater variety of these mullite-like $\text{B}_2\text{O}_3\text{-Al}_2\text{O}_3\text{-SiO}_2$ phases have been synthesized and studied in detail because of their many potential applications, notably Al borates such as Al_5BO_9 , in optical electronics, structure applications, and tribology—e.g., refractory linings because of their high resistance to corrosion, optically translucent ceramics for high-temperature furnace windows, and linings in nuclear plants because of their capability of absorbing neutrons (Fischer and Schneider 2008; Gatta et al. 2010, 2013 and references cited therein). Most synthetics appear to be B-bearing mullite, and it remains an open question whether any correspond to boromullite, a polysome composed of Al_5BO_9 and sillimanite modules (Buick et al. 2008). Analogs of boralsilite are relatively difficult to synthesize (Pöter et al. 1998; Grew et al. 2008); "boron-mullite" and disordered boralsilite crystallize more readily. The syntheses and the natural occurrences suggest that crystallization of boralsilite and vránaite is a disequilibrium process, beginning with the metastable crystallization of B-bearing mullite and succession by Ostwald step rule to ordered boralsilite and vránaite, but not always reaching dumortierite, the stable phase under the conditions at which pegmatites crystallized. The presence of metastable phases is consistent with increasing evidence for disequilibrium processes in pegmatites, in which high viscosity that slows the movement of constituents, supercooling, and quenches associated with rapid changes in composition or pressure play important roles (Černý 2000; London 2008, 2014).

Disequilibrium conditions in Li, Be, B-rich systems could be also achieved by metamorphic overprint of fractionated systems. For example, metamorphosed pegmatite veins at Vitorco, Argentina (Galliski et al. 2012) evidence remobilization of Li, Be, and B, resulting in secondary tourmaline, chrysoberyl, dumortierite, and holtite. In a situation where the H_2O -depletion at the end of secondary crystallization was accompanied by B_2O_3 activities approaching saturation, anhydrous borosilicates might form instead of dumortierite.

ACKNOWLEDGMENTS

We thank Reinhard Fischer, Alessandro Guastoni, and the Technical Editor for their thoughtful reviews of the manuscript, and we thank members of the IMA CNMNC for constructive comments on the proposal submitted to the Commission for approval. This work was supported by the research project GAČR P210/14/13347S (J.C., M.N., P.G., R.Š., M.V.G.). SEM and EBSD analyses were carried out at the Caltech GPS Division Analytical Facility, which is supported, in part, by NSF Grants EAR-0318518 and DMR-0080065. A portion of this study was funded by the John Jago Trelawney Endowment to the Mineral Sciences Department of the Natural History Museum of Los Angeles County. L.A.G. acknowledges the support of a Discovery Grant from the Natural Sciences and Engineering Research Council of Canada. S.V.K. was supported in this work by the Russian Foundation for Basic Research (grant 16-05-00293).

REFERENCES CITED

- Åhman, J., Svensson, G., and Grins, J. (1997) Lithium aluminium borate, $\text{LiAl}_2\text{B}_4\text{O}_7$. *Acta Chemica Scandinavica*, 51, 1045–1050.
- Anthony, J.W., Bideaux, R.A., Bladh, K.W., and Nichols, M.C., Eds. (2003) *Handbook of Mineralogy*, vol. II. Mineralogical Society of America, Chantilly, Virginia.
- Bish, D.L., and Burnham, C.W. (1992) Rietveld refinement of the crystal structure of fibrolitic sillimanite using neutron powder diffraction data. *American Mineralogist*, 77, 374–379.
- Buick, I., Grew, E.S., Armbuster, T., Medenbach, O., Yates, M.G., Bebout, G.E., and Clarke, G.L. (2008) Boromullite, $\text{Al}_8\text{B}_2\text{Si}_2\text{O}_{19}$, a new mineral from granulite-facies metapelites, Mount Stafford, central Australia and a natural analogue of a “boron-mullite.” *European Journal of Mineralogy*, 20, 935–950.
- Burla, M.C., Caliandro, R., Camalli, M., Carrozzini, B., Cascarano, G.L., Giacovazzo, C., Mallamo, M., Mazzone, A., Polidori, G., and Spagna, R. (2012) SIR2011: a new package for crystal structure determination and refinement. *Journal of Applied Crystallography*, 45, 357–361.
- Cempírek, J. (2003) Mineral associations and chemical composition of dumortierite in granitic pegmatites. M.S. Diplomová práce, Masaryk University, Brno (in Czech).
- Cempírek, J., and Novák, M. (2005) A green dumortierite from Kutná Hora, Moldanubium, Czech Republic: spectroscopic and structural study. *Crystallization Processes in Granitic Pegmatites*, Elba, Italy, 4–5.
- Cempírek, J., Novák, M., Dolníček, Z., Kotková, J., and Škoda, R. (2010) Crystal chemistry and origin of grandidierite, ominelite, boralsilite, and werdingite from the Bory Granulite Massif, Czech Republic. *American Mineralogist*, 95, 1533–1547.
- Cempírek, J., Grew, E.S., Kampf, A.R., Ma, C., Novák, M., Gadas, P., Škoda, R., Vášinová-Galiová, M., Pezzotta, F., and Groat, L.A. (2016) Vránaite, IMA 2015-084. CNMNC Newsletter No. 29, February 2016, page 200; *Mineralogical Magazine*, 80, 199–205.
- Cerný, P. (2000) Constitution, petrology, affiliations and categories of miarolitic pegmatites. *Memoire della Società Italiana di Scienze Naturali e dei Museo Civica di Storia Naturale di Milano*, 30, 5–12.
- Fischer, R.X., and Schneider, H. (2008) Crystal chemistry of borates and borosilicates with mullite-type structures: a review. *European Journal of Mineralogy*, 20, 917–933.
- Fuchs, Y., Ertl, A., Hughes, J.M., Prowatke, S., Brandstaetter, F., and Schuster, R. (2005) Dumortierite from the Gfoehl unit, lower Austria: chemistry, structure and infra-red spectroscopy. *European Journal of Mineralogy*, 17, 173–183.
- Gallissi, M.A., Márquez-Zavalía, M.F., Lira, R., Cempírek, J., and Škoda, R. (2012) Mineralogy and origin of the dumortierite-bearing pegmatites of Virocoro, San Luis, Argentina. *Canadian Mineralogist*, 50, 873–894.
- Gatta, G.D., Rotiroli, N., Fisch, M., and Armbuster, T. (2010) Stability at high pressure, elastic behavior and pressure-induced structural evolution of Al_2BO_5 , a mullite-type ceramic material. *Physics and Chemistry of Minerals*, 37, 227–236.
- Gatta, G.D., Lotti, P., Merlini, M., Liermann, H.-P., and Fisch, M. (2013) High-pressure behavior and phase stability of Al_2BO_5 , a mullite-type ceramic material. *Journal of the American Ceramic Society*, 96, 2583–2592.
- Goldsmith, J.R. (1953) A “simplicity principle” and its relation to “ease” of crystallization. *Journal of Geology*, 61, 439–451.
- Grew, E.S. (1996) Borosilicates (exclusive of tourmaline) and boron in rock-forming minerals in metamorphic environments. In E.S. Grew and L.M. Anovitz, Eds., *Boron: Mineralogy, Petrology and Geochemistry*, 33, p. 387–502. Reviews in Mineralogy, Mineralogical Society of America, Chantilly, Virginia.
- Grew, E.S., McGee, J.J., Yates, M.G., Peacock, D.R., Rouse, R.C., Huijssmans, J.P.P., Shearer, C.K., Wiedenbeck, M., Thost, D.E., and Su, S.-C. (1998) Boralsilite ($\text{Al}_{16}\text{B}_2\text{Si}_2\text{O}_{37}$): A new mineral related to sillimanite from pegmatites in granulite-facies rocks. *American Mineralogist*, 83, 638–651.
- Grew, E.S., Graetsch, H., Pöter, B., Yates, M.G., Buick, I., Bernhardt, H.-J., Schreyer, W., Werding, G., Carson, C.J., and Clarke, G.L. (2008) Boralsilite, $\text{Al}_{16}\text{B}_2\text{Si}_2\text{O}_{37}$, and “boron-mullite”: Compositional variations and associated phases in experiment and nature. *American Mineralogist*, 93, 283–299.
- Higashi, T. (2001) ABCSOR. Rigaku Corporation, Tokyo.
- Krivochev, S.V. (2012) Topological complexity of crystal structures: quantitative approach. *Acta Crystallographica*, A68, 393–398.
- (2013) Structural complexity of minerals: information storage and processing in the mineral world. *Mineralogical Magazine*, 77, 275–326.
- (2016) Structural complexity and configurational entropy of crystals. *Acta Crystallographica*, B72, 274–276.
- Letort, Y. (1952) Contribution à l'étude de la synthèse de la mullite. *Transactions of the International Ceramic Congress*, 19–32.
- Li, J., and Chou, I-M. (2015) An occurrence of metastable cristobalite in spodumene-hosted crystal-rich inclusions from Jiajika pegmatite deposit, China. *Journal of Geochemical Exploration*, <http://dx.doi.org/10.1016/j.gexplo.2015.10.012>.
- London, D. (1984) Experimental phase equilibria in the system $\text{LiAlSiO}_4\text{-SiO}_2\text{-H}_2\text{O}$: A petrogenetic grid for lithium-rich pegmatites. *American Mineralogist*, 69, 995–1004.
- (2008) Pegmatites. Special Publications. *Canadian Mineralogist*, 10, 1–347.
- (2014) A petrologic assessment of internal zonation in granitic pegmatites. *Lithos*, 184–187, 74–104.
- London, D., Morgan, G.B. IV, and Wolf, M.B. (1996) Boron in granitic rocks and their contact aureoles. In E.S. Grew and L.M. Anovitz, Eds., *Boron: Mineralogy, Petrology and Geochemistry*, 33, p. 299–330. Reviews in Mineralogy, Mineralogical Society of America, Chantilly, Virginia.
- Lührs, H., Fischer, R.X., and Schneider, H. (2012) Boron mullite: Formation and basic characterization. *Materials Research Bulletin*, 47, 4031–4042.
- Lührs, H., Senyshyn, A., King, S.P., Hanna, J.V., Schneider, H., and Fischer, R.X. (2013) Neutron diffraction and ^{11}B solid state NMR studies of the crystal structure of B-doped mullite. *Zeitschrift für Kristallographie*, 228, 457–466.
- Lührs, H., Soellradl, S., King, S.P., Hanna, J.V., Konzett, J., Fischer, R.X., and Schneider, H. (2014) Ambient and high-pressure synthesis, composition, and crystal structure of B-mullites. *Crystal Research and Technology*, 49, 21–31.
- Ma, C., and Rossman, G.R. (2008) Barioperovskite, BaTiO_3 , a new mineral from the Benitoite Mine, California. *American Mineralogist*, 93, 154–157.
- (2009) Tistarite, Ti_2O_5 , a new refractory mineral from the Allende meteorite. *American Mineralogist*, 94, 841–844.
- Mandarino, J.A. (1981) The Gladstone-Dale relationship: Part IV. The compatibility concept and its application. *American Mineralogist*, 19, 441–450.
- McGee, J.J., and Anovitz, L.M. (1996) Electron probe microanalysis of geologic materials for boron. In E.S. Grew and L.M. Anovitz, Eds., *Boron: Mineralogy, Petrology, and Geochemistry*, 33, p. 771–788 (second printing 2002). Reviews in Mineralogy, Mineralogical Society of America, Chantilly, Virginia.
- Merlet, C. (1994) An accurate computer correction program for quantitative electron-probe microanalysis. *Mikrochimica Acta*, 114, 363–376.
- Niven, M.L., Waters, D.J., and Moore, J.M. (1991) The crystal structure of werdingite, $(\text{Mg/Fe})\text{Al}_2(\text{Al/Fe})\text{Si}_4(\text{B/Al})\text{O}_{37}$, and its relationship to sillimanite, mullite, and grandidierite. *American Mineralogist*, 76, 246–256.
- Novák, M., Cempírek, J., Gadas, P., Škoda, R., Vášinová-Galiová, M., Pezzotta, F., and Groat, L.A. (2015) Boralsilite and Li_xBe-bearing “boron mullite” $\text{Al}_8\text{B}_2\text{Si}_2\text{O}_{19}$, breakdown products of spodumene from the Manjaka pegmatite, Sahatany Valley, Madagascar. *Canadian Mineralogist*, 53, 357–374.
- Pattison, D.R.M. (1992) Stability of andalusite and sillimanite and the Al_2SiO_5 triple point: Constraints from the Ballachulish aureole, Scotland. *Journal of Geology*, 100, 423–446.
- Peacor, D.R., Rouse, R.C., and Grew, E.S. (1999) Crystal structure of boralsilite and its relation to a family of boroaluminosilicates, sillimanite and andalusite. *American Mineralogist*, 84, 1152–1161.
- Pieczka, A., Evans, R.J., Grew, E.S., Groat, L.A., Ma, C., and Rossman, G.R. (2013) The dumortierite supergroup. I. A new nomenclature for the dumortierite and holomite groups. *Mineralogical Magazine*, 77, 2825–2839.
- Pöter, B., Werding, G., Schreyer, W., and Bernhardt, H.J. (1998) Synthesis and properties of the new borosilicate mineral boralsilite. *Berichte der Deutschen Mineralogischen Gesellschaft*, 1, 220.
- Schneider, H., Schreuer, J., and Hildmann, B. (2008) Structure and properties of mullite—A review. *Journal of the European Ceramic Society*, 28, 329–344.
- Sheldrick, G.M. (2008) A short history of SHELX. *Acta Crystallographica*, A64, 112–122.
- Wadoski, E.R., Grew, E.S., and Yates, M.G. (2011) Compositional evolution of tourmaline-supergroup minerals from granitic pegmatites in the Larsemann Hills, East Antarctica. *Canadian Mineralogist*, 49, 381–405.
- Werding, G., and Schreyer, W. (1984) Alkali-free tourmaline in the system $\text{MgO}\text{-Al}_2\text{O}_3\text{-B}_2\text{O}_3\text{-SiO}_2\text{-H}_2\text{O}$. *Geochimica et Cosmochimica Acta*, 48, 1331–1344.
- (1990) Synthetic dumortierite: its PTX-dependent compositional variations in the system $\text{Al}_2\text{O}_3\text{-B}_2\text{O}_3\text{-SiO}_2\text{-H}_2\text{O}$. *Contributions to Mineralogy and Petrology*, 105, 11–24.
- (1992) Synthesis and stability of werdingite, a new phase in the system $\text{MgO}\text{-Al}_2\text{O}_3\text{-B}_2\text{O}_3\text{-SiO}_2$ (MABS), and another new phase in the ABS-system. *European Journal of Mineralogy*, 4, 193–207.
- (1996) Experimental studies on borosilicates and selected borates. In E.S. Grew and L.M. Anovitz, Eds., *Boron: Mineralogy, Petrology, and Geochemistry*, 33, p. 117–163 (second printing 2002). Reviews in Mineralogy, Mineralogical Society of America, Chantilly, Virginia.
- Wodara, U., and Schreyer, W. (2001) X-site vacant Al-tourmaline: a new synthetic end-member. *European Journal of Mineralogy*, 13, 521–532.

MANUSCRIPT RECEIVED JANUARY 19, 2016

MANUSCRIPT ACCEPTED APRIL 21, 2016

MANUSCRIPT HANDLED BY G. DIEGO GATTA

Reproduced with permission of the copyright owner. Further reproduction prohibited without permission.

Gadolinite-(Nd), a new member of the gadolinite supergroup from Fe-REE deposits of Bastnäs-type, Sweden

RADEK ŠKODA^{1,*}, JAKUB PLÁŠIL², RENATA ČOPJAKOVÁ¹, MILAN NOVÁK¹, ERIK JONSSON^{3,4}, MICHAELA VAŠINOVÁ GALIOVÁ^{1,5,6} AND DAN HOLTSTAM⁷

¹ Department of Geological Sciences, Faculty of Science, Masaryk University, Kotlářská 2, CZ-611 37 Brno, Czech Republic

² Institute of Physics ASCR, v.v.i., Na Slovance 2, Praha 8, CZ-182 21, Czech Republic

³ Department of Mineral Resources, Geological Survey of Sweden, Box 670, SE-751 28 Uppsala, Sweden

⁴ Department of Earth Sciences, Uppsala University, SE-752 36 Uppsala, Sweden

⁵ Department of Chemistry, Faculty of Science, Masaryk University, Kotlářská 2, CZ-611 37 Brno, Czech Republic

⁶ Central European Institute of Technology (CEITEC), Masaryk University, Kamenice 5, CZ-625 00 Brno, Czech Republic

⁷ Swedish Research Council, Box 1035, SE-101 38 Stockholm, Sweden

[Received 26 January 2017; Accepted 7 June 2017; Associate Editor: John Bowles]

ABSTRACT

A new member of the gadolinite supergroup, gadolinite-(Nd), IMA2016-013, ideally $\text{Nd}_2\text{FeBe}_2\text{Si}_2\text{O}_{10}$, was found in the Malmkärra mine, ~3.5 km WSW of Norberg, south-central Sweden, where it occurs in association with fluorbritholite-(Ce), västmanlandite-(Ce), dollaseite-(Ce), bastnäsite-(Ce) and tremolite. Gadolinite-(Nd) forms anhedral grains up to 150 µm in size, commonly occurring as aggregates of olive green colour. The crystals are transparent with vitreous to adamantine lustre. Gadolinite-(Nd) is brittle with conchoidal fracture, no cleavage or parting was observed. It has a white streak, the Mohs hardness is 6.5–7 and the calculated density is 4.86 g cm⁻³. Optically, the mineral is weakly pleochroic in shades of olive green, biaxial (−), $n_\alpha = 1.78(1)$, $n_\beta(\text{calc.}) = 1.80$, $n_\gamma = 1.81(1)$ measured in white light, $2V_{(\text{meas.})} = 62(3)^\circ$. Electron-microprobe and laser ablation inductively coupled plasma mass spectrometry analysis [in wt.%] provided SiO_2 21.77, Y_2O_3 5.49, La_2O_3 2.78, Ce_2O_3 14.04, Pr_2O_3 3.28, Nd_2O_3 19.27, Sm_2O_3 5.30, Eu_2O_3 0.24, Gd_2O_3 4.10, Tb_2O_3 0.36, Dy_2O_3 1.32, Ho_2O_3 0.18, Er_2O_3 0.38, MgO 0.51, CaO 0.14, MnO 0.10, FeO 10.62, B_2O_3 0.10, $\text{BeO}_{\text{calc.}}$ 8.99, $\text{H}_2\text{O}_{\text{calc.}}$ 0.55 and total 99.52 giving the following empirical formula (based on 2 Si): $(\text{Nd}_{0.632}\text{Ce}_{0.472}\text{Y}_{0.268}\text{Sm}_{0.168}\text{Gd}_{0.125}\text{Pr}_{0.110}\text{La}_{0.094}\text{Dy}_{0.039}\text{Ca}_{0.014}\text{Er}_{0.011}\text{Tb}_{0.011}\text{Eu}_{0.008}\text{Ho}_{0.008})_{\sum 1.957}(\text{Fe}_{0.816}\text{Mg}_{0.070}\text{Mn}_{0.008})_{\sum 0.894}(\text{Be}_{1.984}\text{B}_{0.016})_{\sum 2.000}\text{Si}_2\text{O}_{9.660}\text{OH}_{0.337}$. A weak Raman vibration band at ~3525 cm⁻¹ confirms the presence of water in the structure. Gadolinite-(Nd) is monoclinic, $P2_1/c$, with $a = 4.8216(3)$ Å, $b = 7.6985(4)$ Å, $c = 10.1362(6)$ Å, $\beta = 90.234(4)^\circ$, $V = 376.24(6)$ Å³ and $Z = 2$. The strongest X-ray diffraction lines are [d_{obs} in Å (hkl) I_{rel}]: 4.830 (100) 72, 3.603 (021) 37, 3.191 (112) 52, 3.097 (013) 35, 2.888 (121) 100, 2.607 (113) 49, 2.412 (200) 24. Along with the Malmkärra mine, gadolinite-(Nd) was also recorded also at Johannagruvan and Nya Bastnäs. The minerals of the gadolinite subgroup together with fluorbritholite-(Ce) incorporate the highest fraction of medium-to-heavy rare-earth elements among associated rare-earth element minerals in the Malmkärra mine and possibly in all Bastnäs-type deposits.

KEYWORDS: gadolinite-(Nd), rare-earth elements, new mineral, crystal structure, Malmkärra, Bastnäs-type deposits.

*E-mail:rskoda@sci.muni.cz

<https://doi.org/10.1180/minmag.2017.081.047>

This paper is part of a special issue entitled 'Critical-metal mineralogy and ore genesis'. The Geological Survey of Sweden (SGU) has contributed to the costs of Open Access publication for this paper.

© The Mineralogical Society 2018. This is an Open Access article, distributed under the terms of the Creative Commons Attribution licence (<http://creativecommons.org/licenses/by/4.0/>), which permits unrestricted re-use, distribution, and reproduction in any medium, provided the original work is properly cited.

Introduction

THE mineral gadolinite has a special place in the history of science, and specifically so in chemistry and mineralogy. It was the study of what was then called “ytterbite” from the Ytterby pegmatite north of Stockholm, Sweden, by the Finnish-Swedish chemist Johan Gadolin (1760–1852), that led to the first discovery of a rare-earth element (*REE*) in the form of “yttria” (Gadolin, 1794). Gadolin’s yttria was later proven to be a mixture of *REEs*, dominated by yttrium, while the “ytterbite” was finally named gadolinite (Ekeberg, 1802), now gadolinite-(Y). Presently, the *REEs* are very high on the European Union’s lists of critical metals (http://europa.eu/rapid/press-release_IP-14-599_en.htm) and neodymium is the most in demand. Systematic research towards the understanding of *REE* ore-forming processes, a better knowledge of the distribution of these metals among the individual ore minerals, and the origin of these metals is of increasing interest.

The newly-defined gadolinite supergroup (Bačík *et al.*, 2017) includes silicates, phosphates and arsenates with the general formula $A_2MQT_2O_8\varphi_2$, where the individual structural sites are occupied as follows *A*: Ca, *REE* (Y + lanthanoids) > U, Th, Pb, Mn²⁺ and Bi; *M*: Fe²⁺, □ (vacancy) > Mg, Mn²⁺, Zn, Cu, Al; *Q*: Be, B > Li; *T*: Si > P, As, B, Be, S; φ : O, OH > F (Bačík *et al.*, 2017). Based on the *T*-site occupancy, the gadolinite supergroup is divided into the gadolinite [Si⁴⁺ > (P⁵⁺ + As⁵⁺)] and herderite [(P⁵⁺ + As⁵⁺) > Si⁴⁺] groups. Moreover, there are two subgroups within the gadolinite group, of which the gadolinite subgroup is dominated by *REE*³⁺ cations, and the datolite subgroup is dominated by divalent cations, in the *A* site. Accordingly, the *Q*-site is occupied predominantly by Be²⁺ in the gadolinite subgroup and by B³⁺ in the datolite subgroup. The herderite group is also subdivided into the herderite and drugmanite subgroups (cf. Table 1).

Gadolinite-subgroup minerals (particularly gadolinite and hingganite) typically occur in rather metaluminous, fractionated granitic pegmatites with a NYF (Niobium-Yttrium-Fluorine; in the sense of Černý, 1991) signature (e.g. Bjørlykke, 1935; Brotzen, 1959; Haynes, 1965; Vorma *et al.*, 1966; Nilssen, 1973; Bergstøl and Juve, 1988; Smeds, 1990; Kjellman *et al.*, 1999; Pezzotta *et al.*, 1999; Miyawaki *et al.*, 2007; Škoda *et al.*, 2012, 2015; Pieczka *et al.*, 2015), alkaline rocks (e.g. Segalstad and Larsen, 1978; Cámara *et al.*, 2008; Pekov *et al.*, 2007; Lyalina *et al.*, 2014), *REE*-rich

TABLE 1. Minerals of the gadolinite supergroup and their structural formulae (Bačík *et al.*, 2017).

Gadolinite group	
Datolite subgroup	
Datolite	$Ca_2\Box B_2Si_2O_8(OH)_2$
Homilite	$Ca_2Fe^{2+}B_2Si_2O_{10}$
Gadolinite subgroup	
Gadolinite-(Ce)	$Ce_2Fe^{2+}Be_2Si_2O_{10}$
Gadolinite-(Nd)	$Nd_2Fe^{2+}Be_2Si_2O_{10}$
Gadolinite-(Y)	$Y_2Fe^{2+}Be_2Si_2O_{10}$
Hingganite-(Ce)	$Ce_2\Box Be_2Si_2O_8(OH)_2$
Hingganite-(Y)	$Y_2\Box Be_2Si_2O_8(OH)_2$
Hingganite-(Yb)	$Yb_2\Box Be_2Si_2O_8(OH)_2$
Minasgeraisite-(Y)	$Y_2CaBe_2Si_2O_{10}$
Herderite group	
Drugmanite subgroup	
Drugmanite	$Pb_2Fe^{3+}\Box P_2[O_7(OH)](OH)_2$
Herderite subgroup	
Bergslagite	$Ca_2\Box Be_2As_2O_8(OH)_2$
Herderite	$Ca_2\Box Be_2P_2O_8F_2$
Hydroxylherderite	$Ca_2\Box Be_2P_2O_8(OH)_2$

Alpine-type hydrothermal mineralizations (e.g. Demartin *et al.*, 1993; Bonazzi *et al.*, 2003; Pršek *et al.*, 2010), and some iron-oxide skarn deposits (e.g. Geijer, 1961; Holtstam and Andersson, 2007).

The members of the gadolinite subgroup with a magmatic origin are commonly metamict due to significant amounts of actinides substituting for *REE*, which complicates their structural investigation. Well-crystalline samples are scarce and usually of a hydrothermal origin (Demartin *et al.*, 1993).

A neodymium-dominant analogue of gadolinite-(Y) or gadolinite-(Ce) was suggested by Holtstam and Andersson (2007) from Bastnäs-type skarn deposits (Bergslagen ore province, south-central Sweden), but due to the lack of a sufficient amount of material, they did not provide any data apart from the chemical microanalyses. This paper provides a full characterization, including chemical composition, structural, physical and optical properties of the new mineral gadolinite-(Nd), which was approved recently by the Commission on New Minerals, Nomenclature and Classification (CNMNC) of the International Mineralogical Association (IMA), under the number 2016-013. The name is given in analogy with the other members of the gadolinite subgroup (Bačík *et al.*, 2017), as the neodymium-dominant species. Type material is deposited under catalogue number B 11298 at the Moravian Museum, Brno, Czech Republic.

Geological setting and the type locality

Gadolinite-(Nd) was found in samples from the Malmkärra, Johanna and Nya Bastnäs mines, all belonging to the Fe-REE ‘Bastnäs-type’ skarn deposits in the Bergslagen ore province (Geijer, 1961; Holtstam and Andersson, 2007; Jonsson *et al.*, 2014; Holtstam *et al.*, 2014). The present mineral characterization was only undertaken on material from the Malmkärra mine ($60^{\circ}4'N$, $15^{\circ}51'E$), ~ 3.5 km WSW of Norberg due to the very small size of gadolinite-(Nd) crystals ($<30\ \mu m$) at the other localities.

The Bastnäs-type deposits occur in the north-western part of the Bergslagen ore province, south central Sweden, in the so-called ‘REE-line’ (Jonsson and Högdahl, 2013; Goodenough *et al.*, 2016). This is an over 100 km long, north-east-trending, narrow belt within Svecocambrian (1.91–1.88 Ga), mainly felsic metavolcanic rocks with discontinuous, interlayered carbonate (marble) horizons. The volcanic sequences were intensively metasomatized at the synvolcanic stage, and much of the carbonates have been replaced by skarn, hosting the localized Fe-REE mineralizations. The skarn-hosted Fe-oxide-REE-polymetallic mineralization at Bastnäs, in the central part of the REE-line, has been dated from the Re-Os contents of molybdenite to give ages between 1.90 and 1.84 Ga. The mineralization is suggested to be the products of reactions between carbonate interlayers with Si, F, Cl, S, CO₂ and REE-bearing, high-temperature fluids of a magmatic origin (Holtstam *et al.*, 2014; Sahlström *et al.*, 2015). The term

‘Bastnäs-type deposits’ was introduced by Geijer (1961) to characterize a group of similar, Fe + REE ± Cu ± Mo ± Bi ± Au mineralized skarns that supposedly have a common origin to the Nya Bastnäs deposit. Based mainly on differences in mineral assemblages, Holtstam and Andersson (2007) divided them into two subtypes: deposits of subtype 1 are essentially only enriched in light-rare-earth elements (LREE), whereas those of subtype 2 are enriched in both light and heavy-rare-earth elements (LREE and HREE, respectively).

The Malmkärra deposit (subtype 2) is hosted by a partly dolomitic marble that forms a conformable interlayer within the surrounding, typically extensively altered metavolcanic rocks. The skarn ore body, formed through reactions and replacement of parts of the carbonate interlayer, occurs along the contact with the more extensively altered metavolcanic rocks. Magnetite is the sole ore mineral that was mined, and tremolitic amphibole, humite-group minerals, commonly serpentine-altered, biotite and phlogopite make up the main skarn silicates; sulfide minerals (pyrite, chalcopyrite and molybdenite) are locally present as well (Geijer, 1936). Allanites *sensu lato* represent the most widespread REE minerals scattered in the skarn, as well as in the iron ore. During mining, a ~ 0.5 m thick zone of massive REE silicates [dominated by fluorbritholite-(Ce), västmanlandite-(Ce) and dollaseite-(Ce)] was encountered in the deeper levels of the mine, along the contact between the marble and the skarn iron ore (Geijer, 1936; Andersson, 2004). The REE minerals reported from the Malmkärra mine are summarized in Table 2.

TABLE 2. List of REE-minerals from the Malmkärra mine, after Holtstam and Andersson (2007), Holtstam *et al.* (2005).

Mineral	Formula
Allanite-(Ce)	(Ce,La)CaFe ²⁺ Al ₂ [Si ₂ O ₇][SiO ₄]O(OH)
Bastnäsite-(Ce)	(Ce,La)CO ₃ F
Cerite-(Ce)	(Ce,La,Nd) ₉ (Mg,Fe)Si ₇ O ₂₄ (O,OH,F) ₇
Dissakisite-(Ce)	Ca(Ce,La)MgAl ₂ [Si ₂ O ₇][SiO ₄]O(OH)
Dollaseite-(Ce)	Ca(Ce,La)Mg ₂ Al[Si ₂ O ₇][SiO ₄]F(OH)
Fluorbritholite-(Ce)	(Ce,Ca) ₅ [SiO ₄] ₃ F
Gadolinite-(Ce)	Ce ₂ Fe ²⁺ Be ₂ Si ₂ O ₁₀
Gadolinite-(Nd)	Nd ₂ Fe ²⁺ Be ₂ Si ₂ O ₁₀
Gadolinite-(Y)	Y ₂ Fe ²⁺ Be ₂ Si ₂ O ₁₀
Magnesiorowlandite-(Y)	(Y,REE) ₄ MgSi ₄ O ₁₄ F ₂
Västmanlandite-(Ce)	Ca(Ce,La) ₃ Al ₂ Mg ₂ [Si ₂ O ₇][SiO ₄] ₃ F(OH) ₂

The Malmkärra iron mine has a long history. The oldest preserved record is from 1664, with major mining operations taking place from 1885 up to its final closure in 1936 (Geijer and Magnusson, 1944; Andersson, 2004). Malmkärra is also the type locality of västmanlandite-(Ce), see Holtstam *et al.* (2005).

Results

Mineral association, appearance and physical properties

The skarn rock sample ($\sim 10 \text{ cm} \times 10 \text{ cm} \times 5 \text{ cm}$) containing gadolinite-(Nd) was found on the dumps of the Malmkärra mine. Gadolinite-(Nd) forms anhedral grains up to $150 \mu\text{m}$ in size, occurring as aggregates associated with tremolite, dollaseite-(Ce), västmanlandite-(Ce), fluorbritholite-(Ce) and bastnäsite-(Ce) (Fig. 1). Gadolinite-(Nd) is

transparent and, under the optical microscope in thin section, it is pale olive green, while larger fragments are olive green. It has a white streak and a vitreous to adamantine lustre. No visible fluorescence under shortwave or longwave ultraviolet light was observed. The Mohs hardness is between 6.5 and 7. Gadolinite-(Nd) is brittle with a conchoidal fracture; no cleavage or parting was observed. The density (D_{calc}) is 4.86 g cm^{-3} , and was calculated using the empirical formula and unit-cell parameters obtained from the single-crystal X-ray diffraction (XRD) data. A density measurement could not be performed directly due to the lack of suitable material. Optically, gadolinite-(Nd) is weakly pleochroic in shades of olive green, biaxial (-), $n_{\alpha} = 1.78(1)$, $n_{\beta(\text{calc.})} = 1.80$, $n_{\gamma} = 1.81(1)$ measured in white light. The poor optical quality of the measured fragments did not allow more precise determination of the refractive indices. The angle of the optical axes, $2V_{(\text{meas.})}$: $62(3)^\circ$ was

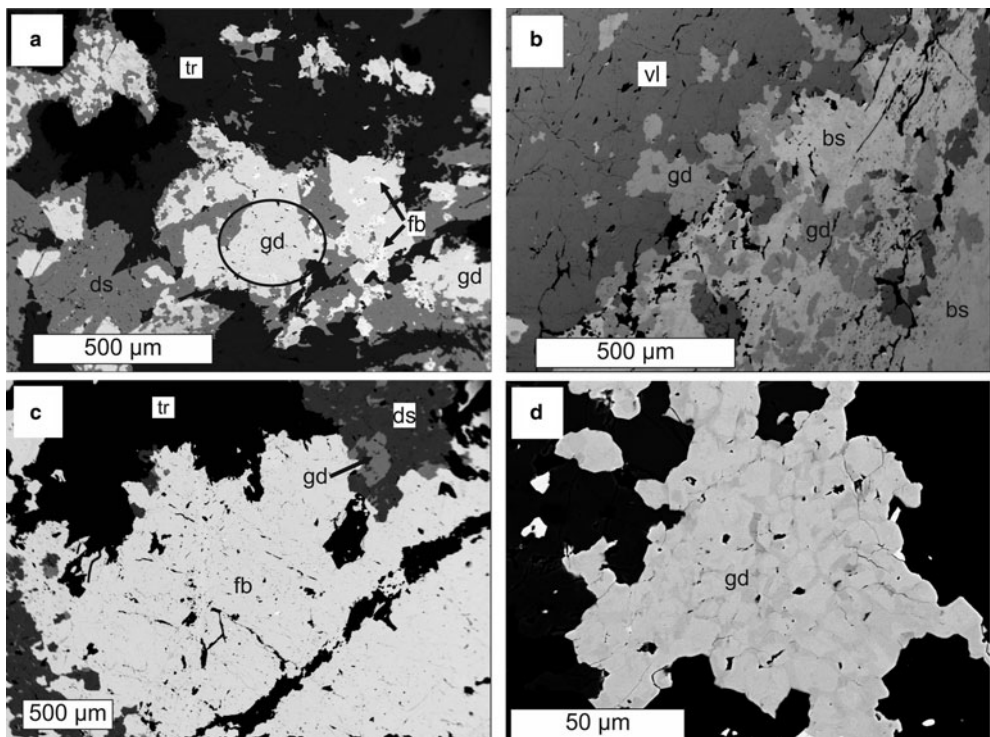


FIG. 1. Back-scattered electron images of gadolinite-(Nd) and associated REE minerals from (a–c) Malmkärra and (d) Johannagruvan. gd-gadolinite-(Nd), ds-dollaseite-(Ce), fb-fluorbritholite-(Ce), tr-tremolite, vl-västmanlandite-(Ce), bs-bastnäsite-(Ce). The aggregate from which the crystals for single-crystal X-ray diffraction and optical study were extracted is indicated by an ellipse. The zoning of the gadolinite-(Nd) from Johannagruvan (d) reflects Y-lanthanoids variability; the Y-rich zones are darker.

GADOLINITE-(Nd) FROM MALMKÄRRA, SWEDEN

TABLE 3. Chemical composition of the gadolinite-(Nd) based on the EMP and LA-ICP-MS data.

Constituent	Mean ⁺	Range [§]	Det. limit. [◊]	Constituent	apfu ⁺	Probe standard; X-ray line
SiO ₂	21.77	21.59–22.27	0.04	Si	2.000	sanidine, K α
Y ₂ O ₃	5.49	3.60–5.83	0.05	Y	0.268	YAG, L α
La ₂ O ₃	2.78	2.04–3.08	0.12	La	0.094	LaPO ₄ , L α
Ce ₂ O ₃	14.04	11.77–14.3	0.13	Ce	0.472	CePO ₄ , L α
Pr ₂ O ₃	3.28	3.12–3.79	0.16	Pr	0.110	PrPO ₄ , L β
Nd ₂ O ₃	19.27	18.88–22.04	0.17	Nd	0.632	NdPO ₄ , L β
Sm ₂ O ₃	5.30	5.04–6.08	0.17	Sm	0.168	SmPO ₄ , L β
Eu ₂ O ₃	0.24	0.16–0.28	0.12	Eu	0.008	EuPO ₄ , L β
Gd ₂ O ₃	4.10	3.60–4.43	0.18	Gd	0.125	GdPO ₄ , L β
Tb ₂ O ₃	0.36	0.31–0.43	0.11	Tb	0.011	TbPO ₄ , L α
Dy ₂ O ₃	1.32	1.05–1.52	0.12	Dy	0.039	DyPO ₄ , L β
Ho ₂ O ₃	0.18	0.11–0.21	0.11	Ho	0.005	HoPO ₄ , L β
Er ₂ O ₃	0.38	0.18–0.38	0.12	Er	0.011	ErPO ₄ , L α
MgO	0.51	0.40–0.92	0.04	Mg	0.070	pyrope, K α
CaO	0.14	0.14–0.24	0.03	Ca	0.014	wollastonite, K α
MnO	0.10	0.10–0.20	0.06	Mn	0.008	spessartine, K α
FeO	10.62	10.09–10.93	0.07	Fe	0.816	almandine, K α
BeO*	8.99			Be	1.984	
B ₂ O ₃ **	0.10	0.06–0.13	0.02	B	0.016	NIST 610
H ₂ O [§]	0.55			OH	0.337	
Total	99.52			O	9.660	
				ΣREE	1.957	
				M-site vac.	0.106	

⁺Mean of three analyses of the crystal used for structural determination; apfu = atoms per formula unit; *determined from stoichiometry; [§]range of all (11) analyses; **measured by LA-ICP-MS; [◊]detection limit in oxides; [§]calculated from charge balance.

measured using extinction by means of a spindle stage and computed by the *EXCALIBR II* software. Dispersion is strong ($r < v$).

Composition

The compositions of gadolinite-(Nd) and associated minerals were determined by means of electron-probe microanalysis (EPMA) with a CAMECA SX100 in wavelength-dispersive mode at an accelerating voltage of 15 kV, a beam current 20 nA and a beam diameter of 5 μm . The standards, X-ray lines and monochromators used for analysis are listed in Table 2. Aluminium, Pb, Tm, Yb and Lu were also analysed for, but their contents were below the detection limit. The peak counting times varied from 10 s for the main elements to 60 s for the minor elements and high and low energy background was counted for $\frac{1}{2}$ of the peak counting time of the relevant analytical line. The raw data were processed using the X-phi matrix correction routine (Merlet, 1994). Based on the counting

statistics, the measurement error expressed as 2σ is approximately <1 rel.% for concentrations of ~20 wt.% and ~8 rel.% for concentrations of ~1=wt.%.

The contents of Be, B and other trace elements below the detection limit of the EPMA were sought for by means of an Agilent 7500ce quadrupole Inductively Coupled Plasma Mass Spectrometer (ICP-MS; Agilent 7500ce, Santa Clara, CA, USA) with an attached UP 213 laser ablation (LA) system (New Wave Research, Inc., Fremont, CA, USA). The LA-ICP-MS system consists of a nanosecond laser Nd:YAG operating at 213 nm (pulse duration of 4.2 ns) and a SuperCell ablation chamber. Ablated material was transported from the sample chamber using helium carrier gas (1 L min⁻¹) and mixed with argon (0.6 L min⁻¹) prior to the torch. Potential polyatomic interferences were minimized by a collision reaction cell in He mode (1 mL min⁻¹). The contents of major to trace elements were determined after laser ablation of individual spots at the following conditions: diameter 55 μm , strength of laser beam 4 J cm⁻², frequency 10 Hz and spot

TABLE 4. LA-ICP-MS data for gadolinite-(Nd) from Malmkärra (in ppm).

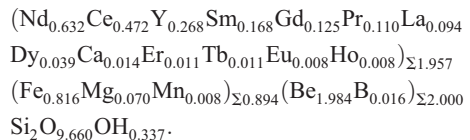
	Mean, $n=9$	Range	Stand. Dev.
Be	36,400	31,300–39,700	2530
B	301	174–393	61
Y	28,200	21,000–35,900	5500
La	35,000	24,800–43,100	7520
Ce	142,200	123,900–167,600	13,540
Pr	32,500	27,900–39,600	3670
Nd	208,200	176,100–255,700	27,890
Sm	40,200	31,500–54,400	7360
Eu	2050	1560–2770	342
Gd	26,700	21,400–31,900	3410
Tb	2560	1690–3330	508
Dy	8920	5730–13,400	2190
Ho	901	629–1310	204
Er	1730	1180–2340	359
Tm	102	66–162	26
Yb	619	351–10,600	195
Lu	58	32–97	17
Th	3.7	1.8–5.6	1
U	83	45–152	32

ablation time 30 s. The contents of elements of interest were determined using SRM NIST 610 and ^{28}Si for internal calibration and the calculations were performed via peak area of isotopes.

The empirical formula has been calculated on the basis of 2 atoms per formula unit of Si and the amount of OH has been charge balanced to keep the empirical formula electroneutral.

The composition of gadolinite-(Nd) was examined from three thin sections prepared from a single piece of the massive REE-silicate-rich sample. The gadolinite shows quite variable chemical composition, particularly in the REE pattern and the Y/(REE) ratio, but all analyses ($n=11$) are Nd-dominant and correspond to gadolinite-(Nd), see Table 3. The calcium content is low (0.14–0.24 wt.% CaO). Holtstam and Andersson (2007) performed Mössbauer spectroscopy on the gadolinite-(Ce/Y) from Malmkärra, which revealed the presence of exclusively divalent Fe. Therefore, all Fe is assumed as divalent in gadolinite-(Nd). Apart from Fe, the M site is occupied by Mg (0.51–0.66 wt.% MgO) and Mn (0.10–0.14 wt.% MnO). All these cations do not fill the M site completely, thus a minor vacancy (0.093–0.143 \square pfu) is present. Seven grains, previously analysed by EPMA, were subsequently analysed by LA-ICP-MS to determine the Be and

B content as well as the whole suite of the REEs and some trace elements (Table 4). A chondrite-normalized REE pattern (using a combination of EPMA and LA-ICP-MS data) shows the maxima at Nd and depletion of the lightest and heavy REE as well as a moderate Eu anomaly ($\text{Eu}_{\text{N}}^*/\text{Eu}_{\text{N}} = 0.16$), see Fig. 2. The content of BeO obtained from the LA-ICP-MS analysis ranges from 8.69 to 11.02 wt.% with a mean of 10.11 wt.%. The theoretical BeO content, calculated from stoichiometry, is ~9.0 wt.%. This discrepancy, ~10 rel.%, is still within the analytical error of LA-ICP-MS for Be (~10 rel.%). The average content of B_2O_3 is 0.10 wt.%. Laser ablation ICP-MS also revealed very low U and Th contents in the gadolinite (~80 and ~5 ppm, respectively). Such a low radioactive element content does not affect the crystallinity of the mineral. A small amount of OH (0.34 pfu) resulted from the calculation of an empirical formula. The empirical formula obtained from the mean of three analyses of the crystal used for structural determination is:



The ideal formula is $\text{Nd}_2\text{FeBe}_2\text{Si}_2\text{O}_{10}$, which requires 58.16 wt.% Nd_2O_3 , 12.42 wt.% FeO, 8.65 wt.% BeO and 20.77 wt.% SiO_2 .

A part of the largest grain (150 $\mu\text{m} \times 100 \mu\text{m}$) of gadolinite-(Nd), carefully measured by EPMA, was extracted subsequently from the thin section for the single-crystal X-ray diffraction study. The other parts of this grain were used for determination of the optical properties.

Raman spectroscopy

Raman analysis of gadolinite-(Nd), performed on uncoated polished sections, was undertaken by means of a Horiba LabRAM HR Evolution spectrometer. This dispersive, edge-filter-based system was equipped with an Olympus BX 41 optical microscope, a diffraction grating with 600 grooves per millimetre, and a Peltier-cooled, Si-based charge-coupled device (CCD) detector. Raman spectra of REE-bearing minerals are commonly obscured by laser-induced emissions of the REE (e.g. Nasdala *et al.*, 2012; Lenz *et al.*, 2015). After careful tests with different lasers (473, 523 and 633 nm), the 633 nm He-Ne laser (10 mW

GADOLINITE-(Nd) FROM MALMKÄRRA, SWEDEN

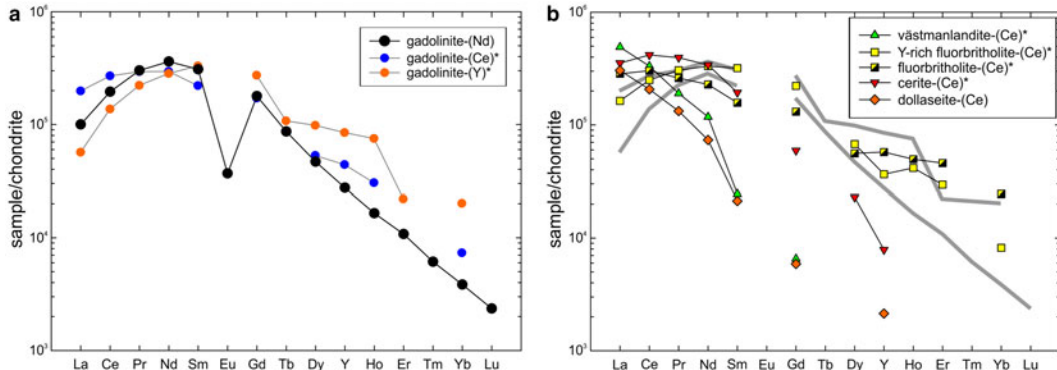


FIG. 2. (a) Chondrite-normalized REE pattern of gadolinite-(Nd) obtained as a combination of EPMA and LA-ICP-MS data. Patterns of gadolinite-(Ce) and gadolinite-(Y) from Holtstam and Andersson (2007) are plotted for comparison. (b) Patterns of other REE-silicates from Malmkärra are plotted for visualization of distribution of REE among individual structural types. Grey, thick, lines indicate the compositional field of gadolinite-subgroup minerals. Chondrite values of McDonough and Sun (1995) were used for normalization. Data for minerals indicated by an asterisk are taken from Holtstam and Andersson (2007).

at the sample surface) was selected for spectral acquisition to minimize analytical artefacts. With the Olympus 100× objective (numerical aperture 0.9) and the system being operated in the confocal mode, the lateral resolution was $\sim 1 \mu\text{m}$. Wavenumber calibration was done using the Rayleigh line and Ne-lamp emissions. The

wavenumber accuracy was $>0.5 \text{ cm}^{-1}$ and the spectral resolution was $\sim 2 \text{ cm}^{-1}$. Band fitting was done after appropriate background correction, assuming combined Lorentzian-Gaussian band shapes using PeakFit (Jandel Scientific Software).

The Raman spectrum of gadolinite-(Nd) is shown in Fig. 3. Following the spectroscopic

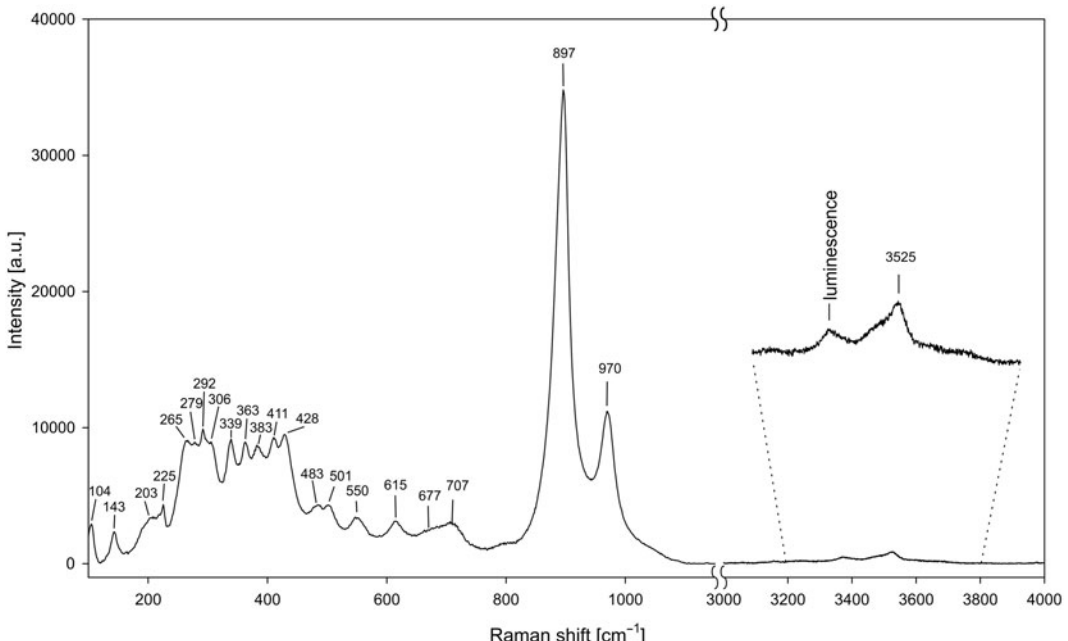


FIG. 3. Raman spectrum of gadolinite-(Nd) excited by a 633 nm laser.

TABLE 5. Powder XRD data of gadolinite-(Nd) from Malmkärra.

$I_{\text{obs.}}$	$d_{\text{obs.}}$	$d_{\text{calc.}}$	$I_{\text{calc.}}$	$h \ k \ l$	$I_{\text{obs.}}$	$d_{\text{obs.}}$	$d_{\text{calc.}}$	$I_{\text{calc.}}$	$h \ k \ l$
8	6.147	6.142	32	0 1 1	8	1.805	1.806	13	0 3 4
13	5.085	5.073	20	0 0 2	<5	1.796	1.803	12	0 4 2
72	4.830	4.826	100	1 0 0	6	1.793	1.796	14	0 2 5
18	4.239	4.239	29	0 1 2	<5	1.789	1.791	19	1 4 0
<5	3.843	3.859	2	0 2 0	<5	1.761	{ 1.764	1	1 4 1
10	3.798	3.798	11	1 1 1	<5	1.761	{ 1.764	2	1 4 1
7	3.776	3.792	13	1 1 1	<5	1.756	1.760	<1	2 3 0
37	3.603	3.607	79	0 2 1	<5	1.734	1.735	4	2 3 1
13	3.491	{ 3.502	16	1 0 2	<5	1.730	1.733	2	2 3 1
		3.492	26	1 0 2			{ 1.707	10	2 1 4
52	3.191	3.189	55	1 1 2	6	1.704	{ 1.703	13	2 1 4
32	3.179	3.181	48	1 1 2	13	1.690	1.691	16	1 3 4
35	3.097	3.098	55	0 1 3	<5	1.682	{ 1.685	9	1 2 5
25	3.014	3.014	25	1 2 0	<5	1.682	{ 1.682	8	1 2 5
100	2.888	{ 2.890	73	1 2 1	8	1.662	{ 1.664	15	2 3 2
		2.888	71	1 2 1			{ 1.662	15	2 3 2
49	2.607	{ 2.610	50	1 1 3	5	1.650	1.652	0	0 1 6
		2.604	55	1 1 3	<5	1.604	1.609	7	3 0 0
8	2.534	2.537	4	0 0 4	6	1.596	1.597	11	1 0 6
6	2.492	2.493	8	0 3 1	<5	1.593	1.595	11	1 0 6
24	2.412	{ 2.413	31	2 0 0	<5	1.586	1.594	1	2 2 4
		2.410	26	0 1 4	<5	1.567	1.564	0	1 1 6
16	2.294	2.294	34	0 3 2	<5	1.554	{ 1.557	1	3 1 1
<5	2.268	2.270	1	1 3 0	<5	1.554	{ 1.556	1	3 1 1
		2.248	3	1 2 3	<5	1.548	1.549	4	0 2 6
11	2.248	{ 2.248	<1	1 0 4	<5	1.533	1.535	1	3 0 2
		2.247	6	2 1 1	<5	1.531	1.532	3	3 0 2
		2.245	1	2 1 1	<5	1.519	1.521	2	2 1 5
6	2.212	2.216	2	1 3 1	<5	1.511	{ 1.514	2	1 3 5
<5	2.204	2.215	4	1 3 1			{ 1.512	3	1 3 5
10	2.185	{ 2.181	5	2 0 2	<5	1.505	1.505	5	3 1 2
		2.177	2	2 0 2	<5	1.503	1.503	4	3 1 2
11	2.156	{ 2.158	10	1 1 4	5	1.467	{ 1.470	9	3 2 1
		2.154	6	1 1 4			{ 1.469	10	3 2 1
6	2.099	{ 2.099	5	2 1 2	<5	1.463	1.464	2	1 4 4
		2.095	6	2 1 2	<5	1.458	1.463	3	1 4 4
12	2.072	{ 2.073	15	1 3 2	5	1.443	1.447	4	2 3 4
		2.071	10	1 3 2	10	1.438	1.439	5	2 2 5
6	2.044	{ 2.047	5	0 3 3	<5	1.429	1.429	9	3 1 3
		2.046	1	2 2 0	<5	1.365	1.365	0	2 1 6
21	2.006	{ 2.006	21	2 2 1	<5	1.355	1.357	6	0 2 7
		2.005	24	2 2 1			{ 1.349	7	1 5 3
<5	1.963	1.963	5	0 1 5	<5	1.347	{ 1.348	7	1 5 3
<5	1.929	1.929	9	0 4 0	<5	1.341	{ 1.344	1	1 4 5
11	1.908	1.906	22	2 1 3	<5	1.341	{ 1.342	2	1 4 5
18	1.901	1.901	22	2 1 3	<5	1.306	{ 1.307	6	1 2 7
		1.896	1	2 2 2	<5	1.306	{ 1.305	7	1 2 7
16	1.892	{ 1.895	4	0 4 1			{ 1.236	6	3 4 0
		1.886	3	1 3 3	<5	1.233	{ 1.234	2	1 6 1
6	1.815	{ 1.820	4	1 1 5	<5	1.227	1.233	3	1 6 1
		1.816	3	1 1 5	<5	1.227	1.228	4	0 5 5

study of isostructural datolite and herderite (Frost *et al.*, 2013, 2014; Goryainov *et al.*, 2015) the most intense Raman bands at 897 and 970 cm⁻¹ are assigned to stretching vibrations of Be–O and Si–O in tetrahedral coordination. The bands in the region 200–750 cm⁻¹ are assigned to banding modes of Si–O and Be–O, stretching vibrations of REE–O and Fe–O and to lattice vibrations. The weak band at 3525 cm⁻¹ is attributed to stretching vibrations of OH units in the gadolinite structure. The local maximum at 3370 cm⁻¹ is caused by luminescence as proven by excitation using a 532 nm laser.

X-ray crystallography and structure determination

Powder X-ray diffraction data for gadolinite-(Nd), carefully extracted from the polished section by a diamond microgrinder and powdered under isopropyl alcohol in an agate mortar, were obtained using an

Empyrean (PANalytical) powder diffractometer with the solid-state PIXcel^{3D} detector operating in Bragg–Brentano geometry. Data were collected over the range of 5–80° θ with a step size of 0.013° and counting time of 2 s per step. Positions and intensities of diffraction maxima were obtained from a profile fitting performed with *High-Score3* software (PANalytical). Unit-cell parameters were refined using least-squares based on the positions of 40 reflections utilizing *Celref* software (Laugier and Bochu, 2004). The experimental powder pattern was indexed in accordance with the calculated values of intensities obtained from the single-crystal structure refinement. Powder X-ray diffraction data are given in Table 5. Unit-cell parameters refined from the powder data are $a = 4.826(1)$, $b = 7.717(2)$, $c = 10.147(2)$ Å, $\beta = 90.16^\circ$ and $V = 377.9(2)$ Å³.

A platy crystal fragment (0.07 mm × 0.06 mm × 0.01 mm) was examined on an Oxford Diffraction Gemini single-crystal diffractometer with Atlas S2 CCD detector, using monochromatized MoK α

TABLE 6. Summary of data collection conditions and refinement parameters for gadolinite-(Nd).

Structural formula	Nd _{1.942} FeBe _{1.931} Si _{2.069} O ₁₀
Unit-cell parameters	
a, b, c [Å]	4.8216(3), 7.6985(4), 10.1362(6)
β	90.234(4)
V [Å ³]	376.24(6)
Z	2
Space group	$P2_1/c$
D_{calc} (g cm ⁻³)	5.044
Temperature	301 K
Wavelength	MoK α , 0.7107 Å
Crystal dimensions (mm)	0.069 × 0.059 × 0.019
Collection mode	ω scans to fill an Ewald sphere
Frame width (°), counting time	1.0, 170 s
Limiting θ angles	3.32–28.16°
Limiting Miller indices	$-6 < h < 6, -10 < k < 9, -13 < l < 12$
No. of reflections	2955
No. of unique reflections	875
No. of observed reflections (criterion)	607 [$I > 3\sigma(I)$]
Absorption correction (mm ⁻¹), method	15.483, Gaussian
T_{\min}/T_{\max}	0.6512/0.8619
R_{int}	0.106
F_{000}	518
Refinement by <i>Jana2006</i> on F^2	
Parameters, constraints, restraints	57, 18, 0
R_1 , wR_2 (obs)	0.0371, 0.0780
R_1 , wR_2 (all)	0.0581, 0.0877
Goof (obs, all)	1.14, 1.05
Weighting scheme, weights	$\sigma, 1/(\sigma^2(F) + 0.0004F^2)$
$\Delta\rho_{\min}, \Delta\rho_{\max}$ (e Å ⁻³)	-1.21, 1.56

radiation ($\lambda = 0.71073 \text{ \AA}$) from a conventional sealed X-ray tube and collimated with fibre optics and Mo-Enhance collimator. The unit cell was refined from 1323 reflections using least-squares with the *Crysalis* software (2014, Agilent Technologies, Oxford, UK); ω rotational scans (frame width 1° , counting time 170 s per frame) were adopted to collect a set of three-dimensional intensity data. From a total of 2955 reflections, 875 were independent and 607 classified as observed, with [$I_{\text{obs}} > 3\sigma(I)$]. Corrections for background, Lorentz effects and polarization were applied; Gaussian correction for absorption (shape + empirical scaling) was done in *JANA2006* (Petříček *et al.*, 2014) giving a data set with R_{int} of $\sim 10\%$. Reduction of the data was performed using the *Crysalis* package. The crystal structure of gadolinite-(Nd) was refined from single-crystal data using the structure model for gadolinite-(Y) published in Demartin *et al.* (1993) by full-matrix least-squares using *JANA2006* (Petříček *et al.*, 2014) based on F^2 . All non-oxygen atoms were refined with anisotropic displacement parameters. Refinement for 57 parameters and 18 constraints converged to $R = 0.0371$, $wR = 0.0780$ for 607 observed reflections ($\text{Goof} = 1.14$). Details of data collection, crystallographic data and refinement details are given in Table 6. Atom coordinates and displacement parameters are listed in Table 7; selected interatomic distances are provided in Table 8.

The structure refinement of gadolinite-(Nd) provides no significant departure from the published structure results of the isostructural gadolinite-(Y) (Miyawaki *et al.*, 1984; Demartin *et al.*, 1993; Cámará *et al.*, 2008). Minerals of the gadolinite group possess a layer structure composed of two distinct sheets, which are alternating in the c direction (Bačík *et al.*, 2014). One sheet is represented by $T\text{O}_4$ and $Q\text{O}_4$ tetrahedra and it alternates with a second sheet of $A\text{O}_8$ polyhedra and $M\text{O}_6$ octahedra. In the structure of gadolinite-(Nd), the T -site is occupied dominantly by Si^{4+} , the Q -site by Be, the A -site by Nd^{3+} (and other REE) and the M -site by Fe^{2+} . During the refinement we treated A -sites as only occupied by Nd. We did not model substitutions of a large number of REE that have very similar scattering curves for X-rays as we are convinced that such a fit would not make much sense. The refined site occupancies for Nd and Be turned out they be slightly lower than unity (due to the effects of mixing with lighter elements at particular sites). The Mg substitution for Fe, as documented from the wavelength-dispersive spectroscopy analyses, was not successfully confirmed by the structure refinement. The structural formula for gadolinite-

TABLE 7. Atom positions, displacement parameters (equivalent and anisotropic, in \AA^2) and bond valences (in valence-units) for gadolinite-(Nd).

Atom	x/a	y/b	z/c	$U_{\text{eq}}/U_{\text{iso}}$	U^{11}	U^{22}	U^{33}	U^{12}	U^{13}	U^{23}	Bond valence
Nd	1.00234(13)	0.10860(8)	0.67237(6)	0.0134(2)	0.0158(4)	0.0122(3)	0.0124(4)	-0.0003(3)	0.0054(3)	0.0006(3)	2.88(2)
Fe	1	0.5	0.5	0.0245(9)	0.0224(15)	0.0322(17)	0.0191(15)	0.0012(13)	0.0066(11)	0.0069(12)	1.83(2)
Si1/Be1 [#]	0.5207(6)	0.2252(4)	0.4201(3)	0.0091(10)	0.0113(17)	0.0102(17)	0.0059(16)	-0.0004(13)	0.0035(12)	-0.0012(12)	3.88(4)/2.01(2)
Be2/Si2 [#]	0.467(2)	0.4134(15)	0.6613(12)	0.010(4)*	0.015(7)	0.003(6)	0.013(7)	0.003(5)	0.003(5)	-0.001(5)	1.96(4)/3.79(7)
O1	0.6835(14)	0.3964(9)	0.3597(7)	0.0092(17)*							2.07(3)
O2	0.7962(15)	0.4120(9)	0.6625(7)	0.0106(17)*							1.72(2)
O3	0.3189(14)	0.1565(9)	0.3014(7)	0.0104(17)*							1.90(3)
O4	0.3272(14)	0.2891(9)	0.5435(7)	0.0079(16)*							2.01(3)
O5	0.7590(14)	0.0913(9)	0.4678(7)	0.0090(16)*							1.92(2)

[#] refined occupancies for Si1/Be1 are 0.982(17)/0.018(17) and for Be2/Si2 0.947(16)/0.053(16).

* refined with isotropic displacement parameter.

GADOLINITE-(Nd) FROM MALMKÄRRA, SWEDEN

TABLE 8. Selected interatomic distances (in Å) in the structure of gadolinite-(Nd).

Nd–O1 ⁱ	2.448(7)	Fe–O1	2.229(7)
Nd–O2	2.540(7)	Fe–O1 ^{vii}	2.229(7)
Nd–O2 ⁱⁱ	2.455(7)	Fe–O2	2.037(7)
Nd–O3 ⁱⁱⁱ	2.576(7)	Fe–O2 ^{vii}	2.037(7)
Nd–O3 ^{iv}	2.701(7)	Fe–O4 ^v	2.305(7)
Nd–O4 ^v	2.471(7)	Fe–O4 ^{viii}	2.305(7)
Nd–O5	2.382(7)	<Fe–O>	2.190
Nd–O5 ^{vi}	2.392(7)		
<Nd–O>	2.496		
Si1/Be1–O1	1.653(7)	Be2/Si2–O1 ^{viii}	1.646(13)
Si1/Be1–O3	1.633(8)	Be2/Si2–O2	1.589(14)
Si1/Be1–O4	1.639(7)	Be2/Si2–O3 ^{ix}	1.680(14)
Si1/Be1–O5	1.616(7)	Be2/Si2–O4	1.669(13)
<Si1/Be1–O>	1.635	<Be2/Si2–O>	1.646
Si1/Be1–Be2/Si2	2.855(12)		
Si1/Be1–Be2/Si2 ^{viii}	2.903(11)		
Si1/Be1–Be2/Si2 ^{ix}	2.843(12)		

Symmetry codes: (i) $x, -y + 1/2, z + 1/2$; (ii) $-x + 2, y - 1/2, -z + 3/2$; (iii) $-x + 1, -y, -z + 1$; (iv) $x + 1, -y + 1/2, z + 1/2$; (v) $x + 1, y, z$; (vi) $-x + 2, -y, -z + 1$; (vii) $-x + 2, -y + 1, -z + 1$; (viii) $-x + 1, -y + 1, -z + 1$; (ix) $x, -y + 1/2, z - 1/2$; (x) $-x + 1, y + 1/2, -z + 1/2$.

(Nd) is therefore $\text{Nd}_{1.942}\text{FeBe}_{1.931}\text{Si}_{2.069}\text{O}_{10}$, $Z=2$. This formula is not electro-neutral due to the fact that the refined occupancies are only a proxy to the real situation, the refinement of all (excluding REE) substituting components is beyond the quality of current dataset. However, the refinement of the data suggested that a small amount of Si can enter the Q -sites and vice-versa.

Concluding remarks

Rare-earth element ores from the Bastnäs-type deposits are in general characterized by LREE enriched and HREE depleted patterns (e.g. Holtstam *et al.*, 2014). Taking into consideration the low activity of P and elevated activity of CO₂, the primary REE minerals are represented as silicates and carbonates. Among the REE phases of the Bastnäs-type mineralization at the Malmkärra mine, the gadolinite-group minerals together with fluorbritholite represent the phases which accommodate the highest amount of middle-rare-earth elements (MREE) and HREE into their structure. On the other hand, epidote-supergroup minerals, including västmanlandite, are strongly depleted in MREE and HREE (Fig. 2).

Notably, the new mineral may represent a locally important sink for the critical metal neodymium in deposits of the Bastnäs-type. Geijer (1936) reported törnebohmite as occurring locally in “not insignificant amounts” at Malmkärra, while Holtstam and Andersson (2007) make no mention of having observed this mineral. Considering their, in part similar, optical properties, it seems possible that Geijer’s törnebohmite could represent (a misidentified) gadolinite. Additionally, new observations also suggest that it may be more abundant than hitherto known in other Bastnäs-type mineralizations, specifically in the Johanna and Nya Bastnäs mines.

Acknowledgements

The authors are grateful to Peter Bačík, Daniel Atencio, an anonymous reviewer and the Structures Editor Peter Leverett for constructive criticism that significantly improved the manuscript, as well as to Editor John Bowles for careful handling of the manuscript. Voting members of the IMA-CNMNC are acknowledged for the constructive remarks to the proposal. This study was supported by the research projects GAČR P210/14/1347S and MUNI/A/1005/2013 for RŠ and RC and MN. Single-crystal X-ray diffraction experiments were done using instruments

of the ASTRA lab established within the Operation program Prague Competitiveness – project CZ.2.16/3.1.00/24510. EJ acknowledges support from the Swedish Research Council (VR) and the Geological Survey of Sweden (SGU) to projects on rare and critical metals in central Sweden at Uppsala University. MVG acknowledges CEITEC 2020 (LQ1601) project with financial contribution made by the Ministry of Education, Youth and Sports of the Czech Republic within special support paid from the National Program for Sustainability II Funds.

References

- Andersson, U.B. (2004) The Bastnäs-type REE-mineralisations in north-western Bergslagen, Sweden. *Sveriges Geologiska Undersökning Rapporter och Meddelanden*, **119**, 34.
- Bačík, P., Fridrichová, J., Uher, P., Pršek, J. and Ondrejka, M. (2014) The crystal chemistry of gadolinite-datolite group silicates. *The Canadian Mineralogist*, **52**, 625–642.
- Bačík, P., Miyawaki, R., Atencio, D., Cámarra, F. and Fridrichová, J. (2017) Nomenclature of the Gadolinite Supergroup. *European Journal of Mineralogy*, **29**, 1–16.
- Bergstøl, S. and Juve, G. (1988) Scandian ixiolite, pyrochlore and bazzite in granite pegmatite in Tørdal, Telemark, Norway. A contribution to the mineralogy and geochemistry of scandium and tin. *Mineralogy and Petrology*, **38**(4), 229–243.
- Bjørlykke, H. (1935) The mineral paragenesis and classification of the granite pegmatites of Iveland, Setesdal, South Norway. *Norsk Geologisk Tidsskrift* **14**, 211–311.
- Bonazzi, P., Bindì, L. and Parodi, G. (2003) Gatelite-(Ce), a new REE-bearing mineral from Trimouns, French Pyrenees: Crystal structure and polysomatic relationships with epidote and törnebohmite-(Ce). *American Mineralogist*, **88**, 223–228.
- Brotzen, O. (1959). Mineral-Association in Granitic Pegmatites: A Statistical Study. *Geologiska Föreningen i Stockholm Förhandlingar*, **81**, 231–296.
- Cámarra, F., Oberti, R., Ottolini, L., Della Ventura, G. and Bellatreccia, F. (2008) The crystal chemistry of Li in gadolinite. *American Mineralogist*, **93**, 996–1004.
- Černý, P. (1991) Rare-element granitic pegmatites, Part 1: anatomy and internal evolution of pegmatite deposits. *Geoscience Canada*, **18**, 49–67.
- Demartin, F., Pilati, T., Diella, V., Gentile, P. and Gramaccioli, C.M. (1993) A crystal-chemical investigation of alpine gadolinite. *The Canadian Mineralogist*, **30**, 127–136.
- Ekeberg, A.G. (1802) Upplysning om ytterjordens egenskaper, i synnerhet i jämförelse med Berylljorden: om de fossilier, hvare förstnämnde jord innehålls, samt om en ny upptäckt kropp af metallisk natur. *Kongliga Vetenskaps Akademiens Nya Handlingar*, **23**, 68–83.
- Frost, R.L., Xi, Y., Scholz, R., Lima, R.M.F., Horta, L.F.C. and Lopez, A. (2013) Thermal analysis and vibrational spectroscopic characterization of the boro silicate mineral datolite-CaBSiO₄(OH). *Spectrochimica Acta Part A: Molecular and Biomolecular Spectroscopy*, **115**, 376–381.
- Frost, R.L., Scholz, R., López, A., Xi, Y., de Siqueira Queiroz, C., Belotti, F.M. and Cândido Filho, M. (2014) Raman, infrared and near-infrared spectroscopic characterization of the herderite–hydroxylherderite mineral series. *Spectrochimica Acta Part A: Molecular and Biomolecular Spectroscopy*, **118**, 430–437.
- Gadolin, J. (1794) Undersökning af en svart tung stenart ifrån Ytterby stenbrott i Roslagen. *Kongliga Vetenskaps Akademiens Nya Handlingar*, **15**, 137–155.
- Geijer, P. (1936) Norbergs berggrund och malmfyndigheter. *Sveriges Geologiska Undersökning*, **Ca 24**, 162 pp.
- Geijer, P. (1961) The geological significance of the cerium mineral occurrences of the Bastnäs type in central Sweden. *Arkiv för mineralogi och geologi*, **3**, 99–105.
- Geijer, P. and Magnusson, N. H. (1944) De mellansvenska järnmalmernas geologi. *Sveriges Geologiska Undersökning*, **Ca 35**, 654 pp.
- Goodenough, K.M., Schilling, J., Jonsson, E., Kalvig, P., Charles, N., Tuduri, J., Deady, E.A., Sadeghi, M., Schiellerup, H., Müller, A., Bertrand, G., Arvanitidis, N., Eliopolous, D.G., Shaw, R.A., Thrane, K. and Keulen, N. (2016) Europe's rare earth element resource potential: an overview of metallogenetic provinces and their geodynamic setting. *Ore Geology Reviews*, **72**, 838–856.
- Goryainov, S.V., Krylov, A.S., Vtyurin, A.N. and Pan, Y. (2015) Raman study of datolite CaBSiO₄(OH) at simultaneously high pressure and high temperature. *Journal of Raman Spectroscopy*, **46**, 177–181.
- Haynes, C.V. (1965) Genesis of the White Cloud and related pegmatites, South Platte Area, Jefferson County, Colorado. *Geological Society of America Bulletin*, **76**, 441–462.
- Holtstam, D. and Andersson U. (2007) The REE minerals of the Bastnäs-type deposits, south-central Sweden. *The Canadian Mineralogist*, **45**, 1073–1114.
- Holtstam, D., Kolitsch, U. and Andersson, U.B. (2005) Västmanlandite-(Ce)-a new lanthanide-and F-bearing sorosilicate mineral from Västmanland, Sweden. *European Journal of Mineralogy*, **17**, 129–141.
- Holtstam, D., Andersson, U.B., Broman C. and Mansfeld, J. (2014) Origin of REE mineralization in the Bastnäs-type Fe-REE-(Cu-Mo-Bi-Au) deposits, Bergslagen, Sweden. *Mineralium Deposita*, **49**, 933–966.

GADOLINITE-(Nd) FROM MALMKÄRRA, SWEDEN

- Jonsson, E. and Högdahl, K. (2013) New evidence for the timing of formation of Bastnäs-type REE mineralisation in Bergslagen, Sweden. *Mineral Deposit Research for a High-Tech World – Proceedings of the 12th Biennial SGA Meeting*, Uppsala, Sweden, 1724–1727.
- Jonsson, E., Högdahl, K., Sahlström, F., Nysten, P. and Sadeghi, M. (2014) The Palaeoproterozoic skarn-hosted REE mineralisations of Bastnäs-type: overview and mineralogical-geological character. *ERES2014: 1st European Rare Earth Resources Conference, Milos – Book of abstracts*, 382–390.
- Kjellman, J., Černý, P. and Smeds, S.A. (1999) Diversified NYF pegmatite populations of the Swedish Proterozoic: Outline of a comparative study. *The Canadian Mineralogist*, **37**, 832–833.
- Laugier, J. and Bochu, B. (2004) *LMPG Suite of Programs for the Interpretation of X-ray Experiments*. ENSP/Laboratoire des Matériaux et du Génie Physique, BP 46. 38042 Saint Martin d'Hères, France. URL: <http://www.ccp14.ac.uk/tutorial/lmpg/> (Accessed: 05 January 2017).
- Lenz, C., Nasdala, L., Talla, D., Hauzenberger, C., Seitz, R. and Kolitsch, U. (2015) Laser-induced REE³⁺ photoluminescence of selected accessory minerals – An “advantageous artefact” in Raman spectroscopy. *Chemical Geology*, **415**, 1–16.
- Lyalina, L.M., Selivanova, E.A., Savchenko, Y.E., Zozulya, D.R. and Kadyrova, G.I. (2014) Minerals of the gadolinite-(Y)-hingganite-(Y) series in the alkali granite pegmatites of the Kola Peninsula. *Geology of Ore Deposits*, **56**, 675–684.
- McDonough, W.F. and Sun, S.S. (1995) The composition of the Earth. *Chemical Geology*, **120**, 223–253.
- Merlet, C. (1994) An accurate computer correction program for quantitative electron probe microanalysis. *Microchimica Acta*, **114/115**, 363–376.
- Miyawaki, R., Nakai, I. and Nagashima, K. (1984) A refinement of the crystal structure of gadolinite. *American Mineralogist*, **69**, 948–953.
- Miyawaki, R., Matsubara, S., Yokoyama, K. and Okamoto, A. (2007) Hingganite-(Ce) and hingganite-(Y) from Tahara, Hirukawa-mura, Gifu Prefecture, Japan: The description on a new mineral species of the Ce-analogue of hingganite-(Y) with a refinement of the crystal structure of hingganite-(Y). *Journal of Mineralogical and Petrological Sciences*, **102**, 1–7.
- Nasdala, L., Beyssac, O., Schopf, J.W. and Bleisteiner B. (2012) Application of Raman-based images in the Earth sciences. Pp. 145–187 in: *Raman Imaging – Techniques and Applications* (A. Zoubir, editor). Springer Series Opti, **168**. Springer, Berlin -Heidelberg.
- Nilssen, B. (1973) Gadolinite from Hundholmen, Tysfjord, North Norway. *Norsk Geologisk-Tidsskrift*, **53**, 343–348.
- Pekov, I.V., Pasero, M., Yaskovskaya, A.N., Chukanov, N. V., Pushcharovsky, D.Y., Merlino, S., Zubkova, N.V., Kononkova, N.N., Menshikov, Y.P. and Zadov, A.E. (2007) Fluorcalcioortholite, $(\text{Ca},\text{REE})_5[\text{Si}_4\text{O}_4]_3\text{F}$, a new mineral: description and crystal chemistry. *European Journal of Mineralogy*, **19**, 95–103.
- Petříček, V., Dušek, M. and Palatinus, L. (2014) Crystallographic computing system JANA2006: general features. *Zeitschrift für Kristallographie*, **229**, 345–352.
- Pezzotta, F., Diella, V. and Guastoni, A. (1999) Chemical and paragenetic data on gadolinite-group minerals from Baveno and Cuasso al Monte, southern Alps, Italy. *American Mineralogist*, **84**, 782–789.
- Pieczka, A., Hawthorne, F.C., Cooper, M.A., Szeleg, E., Szuszkiwicz, A., Turniak, K., Nejbert, K. and Ilnicki, S. (2015) Pilawite-(Y), $\text{Ca}_2(\text{Y}, \text{Yb})_2[\text{Al}_4(\text{SiO}_4)_4\text{O}_2(\text{OH})_2]$, a new mineral from the Pilawa Góra granitic pegmatite, southwestern Poland: mineralogical data, crystal structure and association. *Mineralogical Magazine*, **79**, 1143–1157.
- Pršek, J., Ondrejka, M., Bačík, P., Budzýn, B. and Uher, P. (2010) Metamorphic-hydrothermal REE minerals in the Bacúch magnetite deposit, Western Carpathians, Slovakia: (Sr, S)-rich monazite-(Ce) and Nd-dominant hingganite. *The Canadian Mineralogist*, **48**, 81–94.
- Sahlström, F., Jonsson, E., Högdahl, K., Harris, C., Troll, V.R. and Jolis, E.M. (2015) O and C isotope study of Bastnäs-type rare earth element mineralisation, Bergslagen, Sweden. *PacRim 2015 conference – Book of abstracts*, 439–443.
- Segalstad, T.V. and Larsen, A.O. (1978) Gadolinite-(Ce) from Skien, southern Oslo region, Norway. *American Mineralogist*, **63**, 188–195.
- Škoda, R., Cempírek, J., Filip, J., Novák, M., Veselovský, F. and Čtvrtlik, R. (2012) Allanite-(Nd), $\text{CaNdAl}_2\text{Fe}^{2+}(\text{SiO}_4)(\text{Si}_2\text{O}_7)\text{O}(\text{OH})$, a new mineral from Åskagen, Sweden. *American Mineralogist*, **97**, 983–988.
- Škoda, R., Plášil, J., Jonsson, E., Čopjaková, R., Langhof, J. and Vašinová Galiová, M. (2015) Redefinition of thalénite-(Y) and discreditation of fluorthalénite-(Y): A re-investigation of type material from the Österby pegmatite, Dalarna, Sweden, and from additional localities. *Mineralogical Magazine*, **79**, 965–984.
- Smeds, S.A. (1990) Regional trends in mineral assemblages of Swedish Proterozoic granitic pegmatites and their geological significance. *Geologiska Föreningens i Stockholm Förhandlingar*, **112**, 227–242.
- Vorma, A., Ojanperä, P., Hoffren, V., Siivola, J. and Löfgren, A. (1966) On the rare earth minerals from the Pyörönmaa pegmatite in Kangasala. *Comptes Rendu de la Société Géologique de Finlande*, **38**, 241–274.

GEOCHEMISTRY AND SECONDARY ALTERATIONS OF MICROLITE FROM ELUVIAL DEPOSITS IN THE NUMBI MINING AREA, SOUTH KIVU, DEMOCRATIC REPUBLIC OF THE CONGO

JAN LOUN[§], MILAN NOVÁK, JAN CEMPÍREK, AND RADEK ŠKODA

Department of Geological Sciences, Masaryk University, Kotlářská 2, 611 37 Brno, Czech Republic

MICHAELA VAŠINOVÁ GALIOVÁ AND LUBOMÍR PROKEŠ

Department of Chemistry Masaryk University, Kotlářská 2, 611 37 Brno, Czech Republic

MAREK DOSBABA

TESCAN ORSAY HOLDING, a.s., Libušina tř. 21, 623 00 Brno, Czech Republic

RENATA ČOPJAKOVÁ

Department of Geological Sciences, Masaryk University, Kotlářská 2, 611 37 Brno, Czech Republic

ABSTRACT

Microlite and U-enriched microlite were found in eluvium close to highly weathered granitic pegmatites actively mined as a source of tantalum ore and situated within the ~1000–900 Ma old Kibara belt unit, Numbi mining area, South Kivu province of the Democratic Republic of the Congo. Two examined pegmatites differ in their mineral assemblages and in the degree of fractionation: in the Mungwe pegmatite (lepidolite subtype) cassiterite > microlite-group minerals (microlite + U-enriched microlite) > columbite-group minerals (columbite-tantalite), wodginite + ferrotapiolite; at the Misumari II pegmatite (beryl-columbite subtype) microlite > cassiterite, columbite-tantalite + wodginite–ferrowodginite. Both pegmatites underwent deep tropical weathering; however, the degree of hydrothermal alteration of the (Nb,Ta)-oxide minerals is rather low. Fragments of primary microlite and U-enriched microlite (the latter present only at the Mungwe pegmatite) are mostly homogeneous and compositionally uniform; locally U-enriched microlite forms outer zones of the grains. Primary microlite from the less-fractionated Misumari II pegmatite is rather homogeneous and has $Ta/(Ta + Nb) = 0.74\text{--}0.94$ and higher $Ti = 0.07\text{--}0.23 \text{ apfu}$ at the B-site compared to the Mungwe pegmatite with similar $Ta/(Ta + Nb) = 0.82\text{--}0.88$ and low Ti. Microlite from Misumari II has higher contents of almost all trace elements (including REE) except for Li, Sb, and Pb. Primary microlite from both sites has Ca/Na close to 1, low A-site vacancy, and high F. Uranium-enriched microlite shows $\leq 0.29 \text{ apfu}$ U, moderate A-site vacancy, and lower concentrations of F. Alteration of the U-poor microlite is very limited compared to the U-enriched microlite where radiation damage disrupted the mineral structure prior to the alteration. The altered microlite is depleted in Na and F and has high vacancy at the A-site, but the B-site population is almost identical to that of the primary microlite, as are the U concentrations. Such a composition is typical for secondary low- T alterations related to weathering. We demonstrate that the combined results from Automated Mineralogy, Electron Microprobe Analysis, and LA-ICP-MS techniques (along with the specific alteration features) can be successfully used to prove the provenance of tantalum ore by comparison with other localities where microlite is a major Ta-bearing mineral.

Keywords: microlite, uranium, secondary alteration, granitic pegmatites, Numbi, Democratic Republic of the Congo.

[§] Corresponding author e-mail address: loun.jan@seznam.cz

INTRODUCTION

Tantalum is one of the strategic commodities and an important metal for high-technology applications (e.g., Linnen *et al.* 2012, Melcher *et al.* 2015); hence, columbite-group minerals (henceforth columbite–tantalite), microlite-group minerals (henceforth microlite), and wodginite-group minerals are becoming increasingly important raw materials. Along with knowledge of mineralogical and technological properties, which are necessary for ore processing, ore-origin tracing and responsible sourcing (e.g., Melcher *et al.* 2015) have also become an indispensable part of tantalum production. Thus, any specific mineralogical and geochemical features can be useful in determining the origin of raw ores.

According to the current nomenclature (Atencio *et al.* 2010), microlite belongs to the pyrochlore-supergroup minerals, which are divided into five groups based on the atomic proportions of the B-site atoms Nb, Ta, Sb, Ti, and W (pyrochlore, microlite, roméite, betafite, and elsmoreite groups). The groups are further subdivided based on the occupancies of the A, X, and Y sites. However, detailed nomenclature of microlite-group minerals is beyond the scope of this paper, which is focused on alteration processes and microlite source tracing.

In granitic pegmatites, the microlite-group minerals are most abundant in the LCT family (e.g., Novák & Černý 1998), whereas minerals of the pyrochlore and betafite groups are generally more frequent in NYF pegmatites (e.g., Ercit 2005, Škoda & Novák 2007); both microlite and pyrochlore occur in pegmatites with mixed LCT-NYF signatures (Novák *et al.* 2012, Pieczka *et al.* 2013, 2014). Microlite-group minerals occur in granitic pegmatites either as a primary mineral crystallized from highly evolved pegmatitic melt or as a replacement product of columbite–tantalite, ferrotapiolite, stibiotantalite, simpsonite, and other primary (Nb,Ta)-oxide minerals that formed at various stages of subsolidus hydrothermal alteration (see e.g., Voloshin *et al.* 1989, Wise & Černý 1990, Novák & Černý 1998, Tindle & Breaks 1998, Uher *et al.* 1998, Baldwin *et al.* 2005, van Lichtervelde *et al.* 2007). Microlite with cubic structure has the general formula $A_{2-m}B_2X_{6-w}Y_{1-n}$, where the A site is typically occupied by, e.g., Na, Ca, U, or is vacant, the B site contains mainly Ta, Nb, and Ti, and the Y site may contain O, OH, F, or vacancies (Atencio *et al.* 2010). The X site is usually fully occupied by O and in highly altered specimens by OH as well; however, small amounts of F and vacancies may occur (Lumpkin & Ewing 1992, Atencio *et al.* 2010). The structure can accommodate a wide variety of minor and trace elements (e.g., Cs, Sr, Ba, Bi, Sb, Sn, Pb, Zr, W)

including rare earth elements (mainly Ce, Y) via a number of simple and coupled substitutions.

Primary pyrochlore-supergroup minerals in granitic pegmatites, commonly represented by Na, Ca, and/or U-enriched microlite-group minerals (e.g., Lumpkin *et al.* 1986, Gieré *et al.* 2001, Llorens & Moro 2010), frequently undergo a variety of hydrothermal alterations, resulting in formation of a wide spectrum of secondary pyrochlore-supergroup minerals (see, e.g., Černý *et al.* 1979, von Knorring & Fadipe 1981, Voloshin *et al.* 1989, Černý *et al.* 2004). Lumpkin & Ewing (1992) recognized two principal stages of alteration of primary microlite from granitic pegmatites: the first stage proceeds at relatively high temperature (primary hydrothermal alteration) and is best described by the substitutions $^A\text{Na } ^Y\text{F} \rightarrow ^A\text{Ca } ^Y\text{O}$ and $^A\Box ^Y\Box \rightarrow ^A\text{Ca } ^Y\text{O}$; the second stage takes place at relatively low temperature ('weathering') and the substitutions include $^A\text{Na } ^Y\text{F} \rightarrow ^A\Box ^Y\Box$, $^A\text{Ca } ^Y\text{O} \rightarrow ^A\Box ^Y\Box$, and $^A\text{Ca } ^X\text{O} \rightarrow ^A\Box ^X\Box$. Secondary alteration generates significant losses of A-site elements (Na, Ca, etc.) and increases A-site vacancies and hydration (Ewing 1975). Secondary alteration is typically a near-surface, low-temperature phenomenon often associated with weathering and commonly takes place after the crystal structure has become amorphous (metamict) due to radiation damage. Consequently, pyrochlore-supergroup minerals may serve as a mineral indicator of various processes proceeding during different stages of the geological evolution of granitic systems.

The highly weathered Mungwe and Misumari II granitic pegmatites, located close to the village of Numbi in South Kivu, Democratic Republic of Congo (DRC), are currently actively mined as a source of Ta, with microlite to U-enriched microlite along with minor columbite–tantalite and wodginite *s.l.* as the main economic minerals. These localities are spatially adjacent and seem to be geologically related as well. Typical features at both mines are a rather low degree of hydrothermal alteration of the (Nb,Ta)-oxide minerals and variable low-temperature alteration, even though their parental pegmatites underwent strong weathering in a tropical climate. The weathering caused almost total disintegration of the host pegmatite and the (Nb,Ta)-oxide minerals are therefore mined from eluvial material. Because they were not found in their original rock environment during field work, only a detailed study of eluvial fragments was possible.

Such circumstances complicate the geological and mineralogical study, including paragenetic position and textural relations of the individual minerals. Eluvial occurrences are also challenging in determining the appropriate approach for studying the associated microlite-group minerals. Consequently, we examined eluvial concentrates containing minerals of

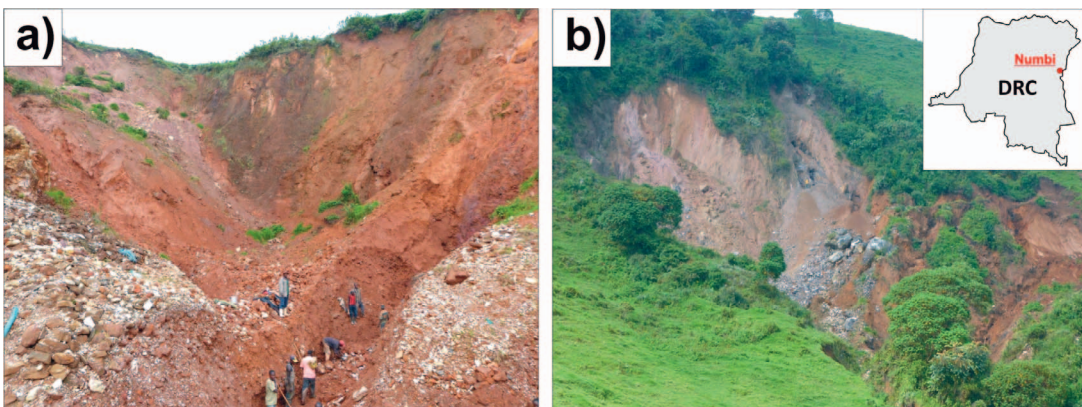


FIG. 1. Field photos of the studied localities. (a) Mungwe mine. (b) Misumari II mine.

the microlite group and other heavy minerals using automated mineralogy (AM), electron microprobe analysis (EMPA), laser-ablation inductively coupled plasma-mass spectroscopy (LA-ICP-MS), and statistical data analysis in order to characterize the mineral assemblage and the alteration processes that play variable roles in the evolution of ore textures and compositional patterns in the two spatially adjacent mineral deposits.

GEOLOGICAL SETTING

The studied area is situated within the Kibara Belt (Great Lakes Region, Central Africa), which is a large geological unit trending in the NNE–SSW direction and extending discontinuously over a distance of *ca.* 1300 km from SW Uganda *via* Rwanda and Burundi into the Katanga region of the DRC (Pohl 1987, Tack *et al.* 2010). The Kibara Belt is of Neoproterozoic age (1000–900 Ma) and consists mainly of Paleo- to Mesoproterozoic clastic metasediments intruded by several generations of granite. The Kibara G4 granites and associated pegmatites, which have been mined in the DRC for the past 100 years, represent one of the world's largest Ta-Nb-Sn-W provinces (Melcher *et al.* 2015). The Ta-Nb mineralization is hosted in pegmatites of variable size and texture, whereas Sn mineralization is more common in greisenized zones and hydrothermal quartz veins; wolframite is restricted solely to hydrothermal quartz veins (Dewaele *et al.* 2010, 2011).

The formation of the rare element-bearing pegmatites is related to post-orogenic tectonic and magmatic episodes (Melcher *et al.* 2015). The comprehensive study of Melcher *et al.* (2015) illustrates an enormous mineralogical diversity of pegmatite-hosted Ta mineralization within the Kibara Belt. U-Pb columbite-

tantalite ages for the Kibara Belt have been obtained by various authors (Romer & Lehmann 1995, Dewaele *et al.* 2011, Melcher *et al.* 2008, 2015) and range from *ca.* 920 to 1030 Ma.

Numbi mining area

Numbi (located 40 km W of Goma) is a village in the mountains of South Kivu, west of Lake Kivu, founded as a mining center near the Sn and Ta deposits, which have been mined for \sim 100 years. The mining area around Numbi consists of *ca.* 25 mine sites, where microlite, columbite–tantalite, cassiterite, gem tourmaline, and gold are being mined. Twelve of the sites are actively mined for columbite–tantalite and cassiterite (Fig. 1a, b). The pegmatites in the Numbi area have LCT geochemical affinities (classification of Černý & Ercit 2005), and they typically intrude mica schists and quartzites associated with less-common metabasites. Given the character of the pegmatites and remoteness of the mine sites, the minerals are extracted exclusively by artisanal mining methods in open pit mines from eluvial deposits near deeply weathered pegmatites.

The Mungwe mine (sample 035) is a relatively large pegmatite body (of \sim 10 m thickness and unverified length) of the lepidolite subtype with a well-preserved lepidolite zone up to 5 m thick. The non-weathered relics of the pegmatite are represented mainly by quartz (quartz core) with less common muscovite, blue and green tourmaline, and rare beryl. Fine-grained, irregularly disseminated Ta-Nb-Sn ore is extracted from deeply weathered pegmatite material belonging to a less-resistant albite unit situated in central parts of the mine; no (Nb,Ta)-oxide minerals have been found in the lepidolite unit.

The Misumari II mine (sample 036) is located approximately 2 km SE of the Mungwe mine. Mining

uncovered a deeply weathered pegmatite dike (of $\sim 1\text{--}2$ m thickness and unverified length) with massive layers of black tourmaline surrounding the pegmatite body along the exocontact. Again, the overall mineralogy can only be determined based on the non-weathered relics of the pegmatite. Quartz (quartz core) is dominant; muscovite is less common, but more abundant than in the Mungwe mine. No Li mineralization was observed. The Ta-Nb-Sn mineralization is extracted from the bright white weathered albite unit, partially *in situ* and partially as an eluvial material, which was transported over a short distance to the foot of the hill. The pegmatite can be classified as beryl-columbite subtype with LCT geochemical signature based on the high Ta contents in primary columbite-tantalite, the presence of abundant Sn minerals, the high bulk B content evidenced as extensive tourmalinization of the pegmatite exocontact (all typical features of the LCT family), and absence of REE mineralization.

SAMPLES AND ANALYTICAL METHODS

Sample collection and preparation

Due to very strong weathering of the pegmatites, the samples were acquired as heavy concentrates panned from several parts of both deposits, with emphasis on thorough coverage of the mineralization. No samples of (Nb,Ta)-oxide minerals from non-weathered parts of the pegmatites were obtained. The sample bulk composition was verified by portable XRF equipment (Innov-X DELTA) and by wet-chemical analysis (ICP-OES and ICP-MS). Representative samples were then formed by quartering and processing to polished mounts (epoxy resin, diameter 25 mm). The surfaces of the polished mounts were coated with a 10 nm-thick carbon layer prior to analysis.

Automated Mineralogy (AM)

Samples were analyzed using TIMA-X (Tescan Integrated Mineral Analyser) based on a field-emission MIRA3 scanning electron microscope. The system is equipped with three EDS detectors with *ca.* 15 mm working distance. An accelerating voltage of 25 kV was applied in order to enable excitation of Ta-*L* lines and avoid the issue of Ta-*M* and Si-*K* line overlap. A beam current of 5.49 nA was used. Spectra were collected with a required intensity of 1000 X-ray counts per pixel. The inner part of the sample, with a diameter of 21 mm, was covered by the automated mineralogical analysis. The size of individual fields was set to 1500 μm , resulting in 129 fields per sample. Pixel spacing was set to 10 μm . High-resolution TIMA analytical mode was applied

and so the pixel spacing refers the distance of both the BSE imaging spots and the EDS analytical spots. Subsequent segmentation applied a phase separation value of 16 (arbitrary unit) enabling sufficient sensitivity in order to discriminate different Nb-Ta solid solution minerals. The classification scheme, enabling the phase identification, was optimized based on EMPA results.

Electron microprobe

Mineral grains for further analyses were selected based on the AM image. Electron microprobe (EMP) analyses were carried out with a Cameca SX 100 instrument using the wavelength-dispersive mode. The following analytical conditions were applied: accelerating voltage of 15 kV, beam diameter of 5 μm , beam current of 20 nA, and counting times of 20 s for Nb, Ta, Ti, Ca, and Y and 30–60 s for the other elements. The following X-ray lines, standards, diffracting crystals, and counting times were used: $K\alpha$ lines – Na (albite; TAP; 10), Al (gahnite; TAP; 20), Mg (pyrope; TAP; 20), F (topaz; PC1; 60), Ti (anatase; PET; 20), Fe (columbite; LIF; 20) Mn (Mn_2SiO_4 ; LIF; 20), Zn (gahnite; LIF; 20), Sc (ScVO_4 ; LIF; 40); $K\beta$ line – Ca (titanite; PET; 20); $L\alpha$ lines – Nb (columbite; PET; 20), Sn (SnO_2 ; PET; 20), Y (YAG; TAP; 20), Zr (zircon; TAP; 20); $L\beta$ line – Sb (Sb; PET; 40); $M\alpha$ lines – Ta (CrTa_2O_6 ; TAP; 20), Th ($\text{CaTh}(\text{PO}_4)_2$; PET; 20); $M\beta$ lines – Pb (vanadinite; PET; 20), U (U; PET; 20), Bi (Bi; PET; 20). Raw data were reduced using the X-PHI matrix correction routine (Merlet 1994). Relative errors are estimated to be $\sim 1\%$ at the ~ 10 wt.% level, 10–20% at the ~ 1 wt.% level, and $\sim 20\%$ at the ~ 0.5 wt.% level. The chemical formula of microlite was calculated following the normalization constraints: $\text{Nb} + \text{Ta} + \text{Ti} + \text{W} + \text{Sn} = 2$ atoms per formula unit (*apfu*); $\text{U}_{\text{tot}} = \text{U}^{4+}$, $\text{Sn}_{\text{tot}} = \text{Sn}^{4+}$, $\text{Fe}_{\text{tot}} = \text{Fe}^{2+}$, and $\text{Mn}_{\text{tot}} = \text{Mn}^{2+}$. SiO_2 contents in microlite were excluded from the formula calculation and in the Tables they are reported as contamination (“silicification” by Si-diffusion; Dumańska-Słowik *et al.* 2014). Formula calculation procedures for other minerals are listed in their respective Tables.

Classification of the microlite-group minerals at the two localities is dubious, as occupancy of the *X* and *Y* sites cannot be estimated reliably. For the primary microlite at both localities, the stoichiometry is close to the ideal fluornatromicrolite (Witzke *et al.* 2011), except for low (F,OH) contents ($\text{F} < 1$ *apfu* and $\text{OH}_{\text{calc}} = 0$); *i.e.*, it should be classified as “F-rich, zero-valence-dominant natromicrolite”. The same rootname can be used for the U-enriched microlite (“U-rich zero-valence-dominant natromicrolite”). Since we cannot estimate the vacancies or H_2O at both A- and

TABLE 1. AMOUNTS (wt.%) OF MINERAL PHASES IN STUDIED SAMPLES FROM THE AUTOMATED MINERALOGY STUDY

wt.%	Mungwe	Misumari II
Cassiterite	47.33	7.09
Albite	0.05	27.79
Quartz	0.15	9.48
Schorl	0.39	7.59
Muscovite	1.65	1.27
Zircon	8.26	0.42
Ilmenite	7.86	1.58
Microlite	14.30	15.74
U-enriched microlite	14.08	0.20
Tantalite-(Fe)	0.03	4.88
Tantalite-(Mn)	2.00	0.69
Columbite-(Fe)	0.00	0.46
Columbite-(Mn)	0.06	0.65
Ferrotapiolite	0.06	2.34
Wodginite <i>s.l.</i>	0.01	5.05
Others	3.77	14.77
Total	100.00	100.00

Y-sites, the secondary microlite should be classified as “(Y-site) zero-valence-dominant (A-site) zero-valence-dominant microlite/calciomicrolite”. We find the naming of the microlite generations useless for the purpose of this study and therefore we use the group name (microlite) with genetic or compositional adjectives only.

Laser ablation-inductively coupled plasma-mass spectrometry

Analyses of the minor and trace elements were obtained using LA-ICP-MS equipment. Analyses were

conducted using a high-resolution double-focusing ICP-MS Element 2 (Thermo Scientific™) instrument with an attached Analyte G2 laser ablation system (Teledyne CETAC Technologies). The samples were placed into a 2-volume HelEx cell and ablated using an ArF* excimer laser operated at a wavelength of 193 nm (pulse length <5 ns). Ablated material was transported from the sample chamber using helium carrier gas (0.65 L/min) mixed with argon (~1 L/min) prior to the torch. Optimization of LA-ICP-MS parameters was performed using the glass reference material NIST SRM 612. The elemental content in the investigated samples was determined after 60 s laser ablation of individual spots with diameter of 110 µm at laser beam fluence of 2 J/cm² and 10 Hz frequency, and quantified using SRM NIST 610, 612, 614, and BCR-2G, and internal reference elements Ta, Nb, Mn, and Fe.

Statistical evaluation of the data

Chondrite-normalized REE + Y spider plots (see Graupner *et al.* 2010, Melcher *et al.* 2015) are based on chondrite composition values after Anders & Grevesse (1989). For trace elements, the spider plots were normalized to the ‘global CGM median’ values (Melcher *et al.* 2015) and chondrite (Anders & Grevesse 1989), respectively. For selection of elements for scatter plots, Classification And Regression Trees (CART; De’ath & Fabricius 2000) and random forests (Cutler *et al.* 2007) were employed. Data analysis was done using the freely available statistical software R (Janoušek *et al.* 2015, Reimann *et al.* 2008) and its external libraries *rpart* (for CART) and *randomForest*.

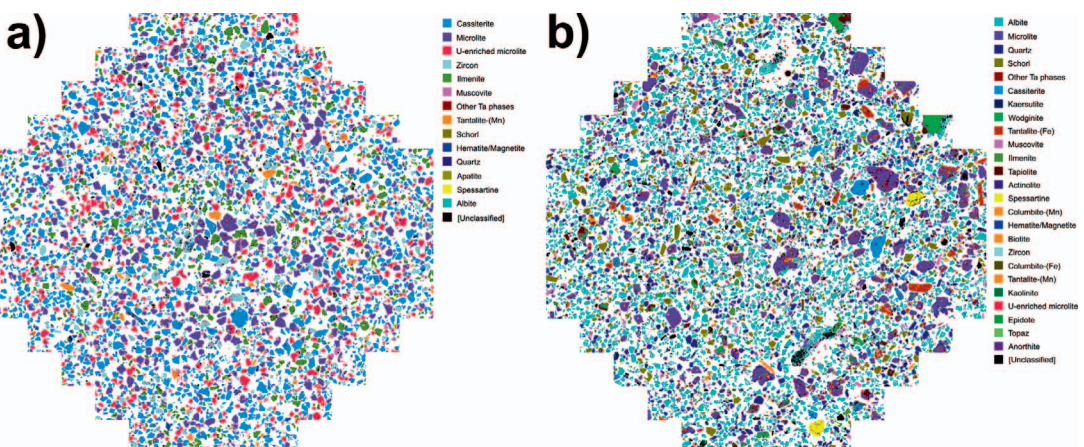


FIG. 2. Automated Mineralogy images of the studied samples. (a) Mungwe mine. (b) Misumari II mine.

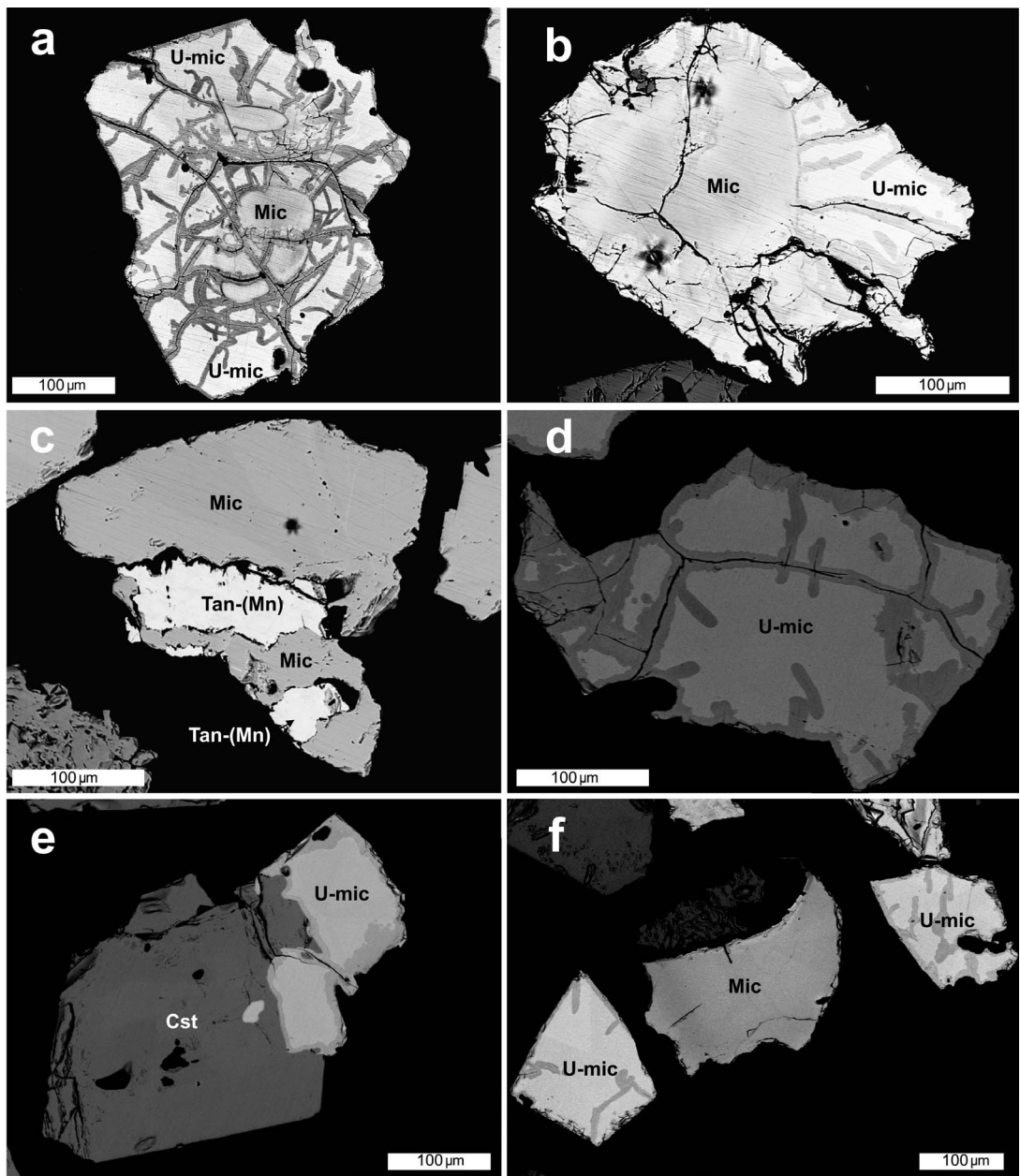


FIG. 3. BSE images of microlite-group minerals from Mungwe. (a) U-enriched microlite (U-mic) with abundant fractures around homogeneous primary microlite (Mic) core. (b) Diffused zoning between U-enriched microlite (U-mic) and microlite core (Mic). (c) Microlite (Mic) + manganontantalite [Tan-(Mn)] aggregates. (d) U-enriched microlite (U-mic) with alteration along the fractures and the rim of the grain. (e) Cassiterite (Cst) intergrown with U-enriched microlite (U-mic) which shows intergranular alteration. (f) Alteration patterns in microlite (Mic) and U-enriched microlite grains (U-mic). In all images, the scale bar is 100 μm long.

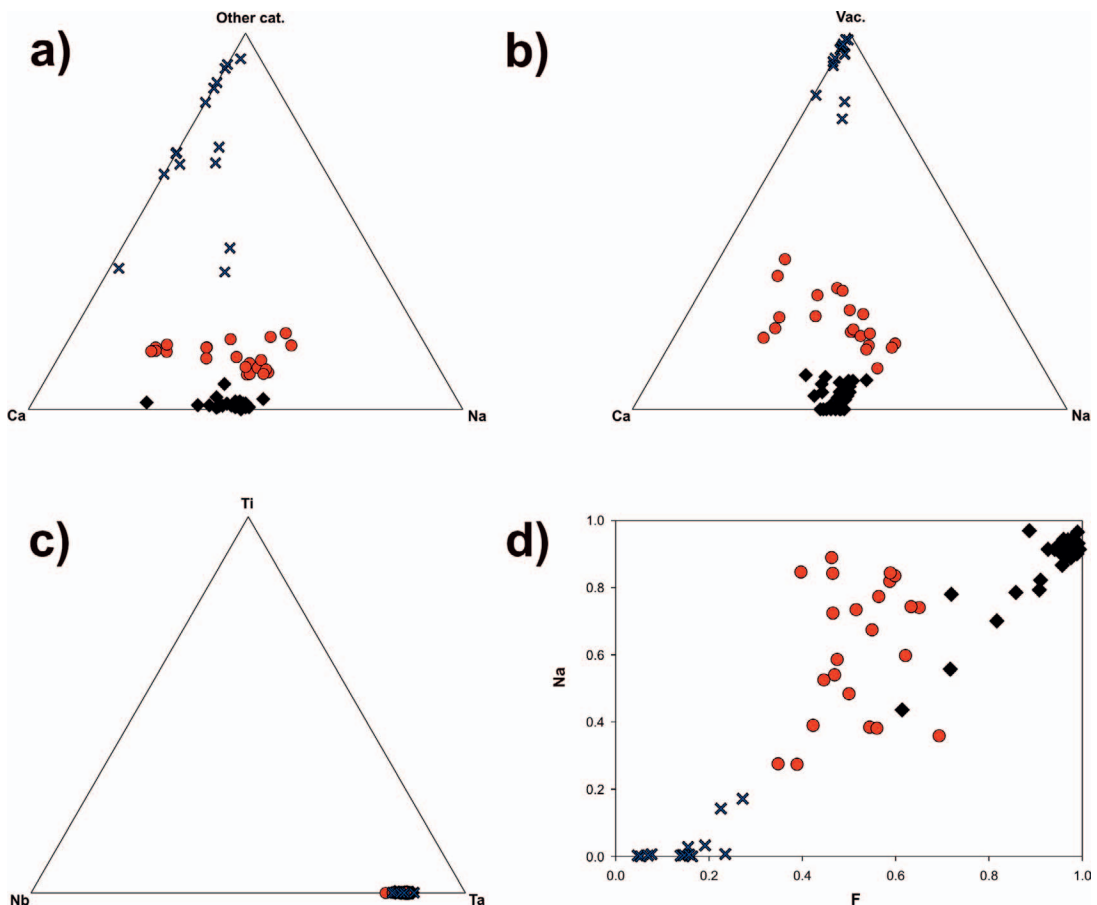


Fig. 4. Composition of microlite-group minerals from Mungwe. (a) A-site population. (b) A-site cations (Ca, Na) and A-site vacancies. (c) B-site population. (d) Na versus F, Microlite = diamonds, U-enriched microlite = circles, secondary altered parts = crosses.

RESULTS

AM

Ore minerals associations in both samples are quite complex [Table 1, Fig. 2 (available from the Depository of Unpublished Data on the MAC website, document CM56-2_10.3749/canmin.1700091)]. The samples are represented by small ($\leq \sim 2$ mm), irregular, and sharp-edged grains.

Mungwe mine (sample 035). Cassiterite is the most common mineral (~50 wt.%), followed by microlite and U-enriched microlite (both ~14 wt.%). Columbite-group minerals are negligible (~2 wt.%), as is wodginitite s.l. (<0.01 wt.%). Quite significant contents of ilmenite and zircon (both ~8 wt.%) are characteristic. The remaining mineral fractions represent minor pegmatite or host-rock minerals (muscovite, magnetite,

schorl, fluorapatite, etc.; Table 1). Microlite and U-enriched microlite are rarely intergrown with muscovite, cassiterite, columbite-tantalite, or wodginitite.

Misumari II mine (sample 036). Albite is the most common mineral, due to imperfect panning. Microlite is the most abundant heavy mineral (~16 wt.%), followed by cassiterite (~7 wt.%), wodginitite s.l. (~5 wt. %), and columbite-tantalite (6.7 wt.%), and all are more abundant relative to sample 035. Tourmaline (uvite-dravite) is quite common (7.6 wt.%), whereas garnet (spessartine) is rather rare (<1 wt.%). The rest of the phases represent minor pegmatite or host-rock minerals (muscovite, ilmenite, schorl etc., Table 1).

EMP

Mungwe mine (sample 035). Primary microlite and U-enriched microlite are mostly homogeneous. Lo-

TABLE 2. REPRESENTATIVE EMP COMPOSITIONS OF MICROLITE (Mic), U-ENRICHED MICROLITE (U-mic), AND SECONDARY ALTERED U-ENRICHED MICROLITE ALONG FRACTURES (Alt.fr.) AND ALONG THE GRAIN BOUNDARIES (Alt.b.) FROM MUNGWE

	Mic	Mic	U-mic	U-mic	Alt.fr.	Alt.fr.	Alt.fr.	Alt.b.	Alt.b.	Alt.b.
	wt. %									
Nb ₂ O ₅	6.81	6.62	7.67	6.71	6.31	7.66	8.03	7.03	7.40	5.46
Ta ₂ O ₅	70.21	71.71	66.03	67.80	68.04	67.30	66.80	65.35	63.21	67.87
SiO ₂	0.00	0.00	0.09	0.00	0.13	0.15	0.00	0.10	0.00	0.00
SnO ₂	0.45	0.36	0.49	0.43	0.84	0.56	0.74	0.62	0.60	0.49
UO ₂	0.00	0.00	5.99	4.67	4.98	5.32	5.44	5.63	6.31	7.54
Sc ₂ O ₃	0.00	0.00	0.07	0.00	0.00	0.00	0.09	0.00	0.00	0.00
FeO	0.00	0.00	0.00	0.43	1.37	0.00	0.10	1.48	1.80	1.68
PbO	0.26	0.35	0.72	1.44	1.50	1.15	1.67	0.80	0.66	0.64
CaO	10.60	10.27	6.78	6.49	1.34	0.85	1.27	0.00	0.00	0.00
Na ₂ O	5.42	5.36	3.76	3.26	0.00	0.00	0.00	0.00	0.00	0.00
F	3.44	3.47	1.88	1.62	0.56	0.51	0.54	0.26	0.15	0.23
O = F	-1.45	-1.46	-0.79	-0.68	-0.24	-0.21	-0.23	-0.11	-0.06	-0.10
Total	95.74	96.68	92.69	92.17	84.83	83.29	84.45	81.16	80.07	83.81
<i>apfu</i>										
A-site	Na ⁺	0.940	0.918	0.674	0.584	0	0	0	0	0
	Ca ²⁺	1.016	0.972	0.672	0.643	0.132	0.083	0.123	0	0
	Fe ²⁺	0	0	0	0.033	0.106	0	0.008	0.117	0.145
	Pb ²⁺	0.006	0.008	0.018	0.036	0.037	0.028	0.041	0.020	0.017
	Sc ³⁺	0	0	0.006	0	0	0	0.007	0	0
	U ⁴⁺	0	0	0.123	0.096	0.102	0.108	0.110	0.118	0.135
	sum	1.962	1.898	1.493	1.392	0.377	0.219	0.289	0.255	0.297
B-site	Nb ⁵⁺	0.275	0.264	0.321	0.280	0.263	0.315	0.329	0.300	0.322
	Ta ⁵⁺	1.708	1.723	1.661	1.704	1.706	1.665	1.645	1.677	1.655
	Sn ⁴⁺	0.016	0.013	0.018	0.016	0.031	0.020	0.027	0.023	0.023
contam.	Si ⁴⁺	0	0	0.008	0	0.012	0.014	0	0.009	0
X-site	O	5.996	5.897	5.996	5.902	4.765	4.486	4.621	4.646	4.796
	OH	0.004	0.103	0.004	0.098	1.235	1.514	1.379	1.354	1.204
Y-site	F	0.973	0.970	0.550	0.473	0.163	0.147	0.155	0.078	0.046

Note: Crystalllochemical formula calculated on the basis of (Nb + Ta + Sn) = 2 *apfu*. SiO₂ contents are regarded as contamination and were not used for formula calculation. Elements sought but below detection limit: W, Ti, Zr, Th, Al, Sb, Mg, Mn.

cally, a microlite core is overgrown by U-enriched microlite (Fig. 3a, b) with a sharp contact. Microlite rarely forms aggregates with manganotantalite (Fig. 3c), muscovite, wodginite *s.l.*, or cassiterite. The chemical compositions of primary microlite and U-enriched microlite are quite uniform (see Fig. 4a–d); the U-enriched microlite is altered along fractures, at the rim of the grains (Fig. 3a, b, d, f), and along intergranular boundaries (Fig. 3e), in contrast to microlite which is typically stable (Fig. 3c, f). The fractures in the U-enriched microlite are either randomly distributed or concentrically oriented around a more or less homogeneous core (see Fig. 3a, b).

Primary microlite and U-enriched microlite have almost identical Ta/(Ta + Nb) values and very low Ti contents (Fig. 4c, Table 2). They differ in concentrations of U, Sn, and A-site vacancies, which are higher in U-enriched microlite (up to 0.16 *apfu* U and 0.03 *apfu* Sn; Fig. 4a, b). High concentrations of F (0.61–1 *apfu*) and very low Sn contents (≤ 0.02 *apfu*) are typical for primary microlite; the U-enriched microlite is F-depleted (0.37–0.69 *apfu*; Fig. 4d). Other elements typically present in primary microlites (*e.g.*, U, Th, Ti, W, Pb, Mn, Fe, and Bi) are below the detection limits of the EMP. Secondary microlite after the primary microlite and U-enriched microlite is typically A-site vacant, strongly depleted in Ca and Na (Fig. 4a, b), and

TABLE 3. REPRESENTATIVE EMP COMPOSITIONS OF Nb-RICH MANGANOTANTALITE (ColTan), MANGANOTANTALITE DIRECTLY ASSOCIATED WITH MICROLITE (Tan), AND FERROTAPIOLITE (Tap) FROM MUNGWE

	ColTan	ColTan	Tan	Tan	Tap	Tap
Nb ₂ O ₅ (wt.%)	36.83	32.59	6.33	7.38	4.97	4.93
Ta ₂ O ₅	44.40	47.57	75.65	75.60	78.74	79.56
TiO ₂	0.00	0.59	0.00	0.00	0.55	0.51
SnO ₂	0.00	0.71	2.92	1.76	0.39	0.00
MnO	17.06	16.59	13.42	13.78	1.03	0.97
FeO	0.00	0.26	1.46	1.33	14.39	14.43
Total	98.29	98.31	99.78	99.85	100.07	100.40
Nb ⁵⁺ (<i>apfu</i>)	1.157	1.036	0.231	0.268	0.182	0.180
Ta ⁵⁺	0.839	0.910	1.660	1.650	1.730	1.748
Ti ⁴⁺	0.000	0.031	0.000	0.000	0.033	0.031
Sn ⁴⁺	0.000	0.020	0.094	0.056	0.013	0.000
Mn ²⁺	1.004	0.988	0.917	0.937	0.070	0.066
Fe ²⁺	0.000	0.015	0.099	0.089	0.972	0.975
O	5.994	5.969	5.930	5.933	5.913	5.923

Note: Crystallochemical formula calculated on the basis of cation sum = 3 *apfu*.

Elements sought but below detection limit: W, Si, Zr, Th, U, Al, Sc, Sb, Mg, Pb, Ca, Na, F.

slightly enriched in other cations (Pb, Sn, Fe). Elevated contents of Si due to contamination by Si-diffusion (Dumańska-Słowik *et al.* 2014) and very low F contents are also typical (Fig. 4d). The alteration pattern in the (U-poor) primary microlite is less intense compared to the U-rich microlite, where radiation damage disrupted the mineral structure prior to alteration.

Representative compositions of columbite–tantalite are given in Table 3 and Figure 7a; manganotantalite associated with microlite shows high Ta contents, similar to the associated ferrotapiolite. Cassiterite is present as loose grains or aggregates with microlite and contains ≤ 6 wt.% Ta₂O₅ and ≤ 0.44 wt.% Nb₂O₅.

Misumari II mine (sample 036). Microlite is present as loose, rather homogeneous grains, and often forms aggregates with wodginite–ferrowodginite and other (Nb,Ta,Sn)-oxide minerals (Fig. 5); it typically replaces primary tantalite and wodginite–ferrowodginite, with secondary columbite and ixiolite as typical reaction products (Fig. 5a, c). Some microlite grains show patchy and/or oscillatory zoning (Fig. 5b); fractures are common in some microlite zones (Fig. 5a, b). Locally, strong alteration along microlite fractures and in replacement zones at grain rims produced dark, hydrated patches of secondary microlite (Fig. 5b, d).

Almost all analyzed microlite grains contain low concentrations of U, generally lower compared to the U-enriched microlite from the Mungwe site (sample 035). The Ta/(Ta + Nb) ratio is similar to that in the

035 sample; however, Ti is apparently higher (Fig. 6c, Table 4). Secondary microlite related to microlite alteration has high A-site vacancies as Na was more or less completely leached out, whereas Ca contents remained almost the same (Fig. 6b). In fresh parts of the microlite grains, F is typically high (≤ 0.97 *apfu*); however, the altered areas with secondary microlite show significant F depletion (Fig. 6d). Occasionally, microlite also forms a small veinlet (secondary filling of a fracture) within a wodginite crystal (Fig. 5d) and shows elevated contents of Sn (0.25 *apfu*), Fe (0.22 *apfu*), Mn (0.15 *apfu*), Zr (0.03 *apfu*), and W (0.02 *apfu*), which were very likely sourced from host/ replaced wodginite.

Minor columbite–tantalite with moderate degree of Mn/(Fe + Mn) and Ta/(Nb + Ta) fractionation (Fig. 7b) is present mostly as loose grains or aggregates with microlite (Fig. 5a). Wodginite–ferrowodginite forms aggregates with cassiterite and columbite–tantalite in close association with microlite, or is present as loose grains. Compositional data for wodginite-group minerals (Fig. 7b and Table 5) yielded relatively stable Ta/(Ta + Nb) and variable Mn/(Fe²⁺ + Mn) ratios ranging from ferrowodginite to wodginite, with representative crystallochemical formulae between $(\text{Mn}_{1.82}\text{Fe}^{2+}_{2.18})_4(\text{Sn}_{2.02}\text{Ta}_{0.52}\text{Fe}^{3+}_{0.64}\text{Ti}_{0.65}\text{Zr}_{0.14}\text{Al}_{0.03})_4(\text{Ta}_{5.79}\text{Nb}_{2.03}\text{W}_{0.18})_8\text{O}_{32.01}$ and $(\text{Mn}_{2.33}\text{Fe}^{2+}_{1.67})_4(\text{Sn}_{2.41}\text{Ta}_{0.64}\text{Fe}^{3+}_{0.51}\text{Ti}_{0.16}\text{Zr}_{0.23}\text{Al}_{0.05})_4\text{Ta}_{6.48}\text{Nb}_{1.44}\text{W}_{0.08})_8\text{O}_{32.07}$. The analyzed wodginites have high Fe³⁺ and Ta contents at the B-site, most likely caused by the substitution Fe³⁺ +

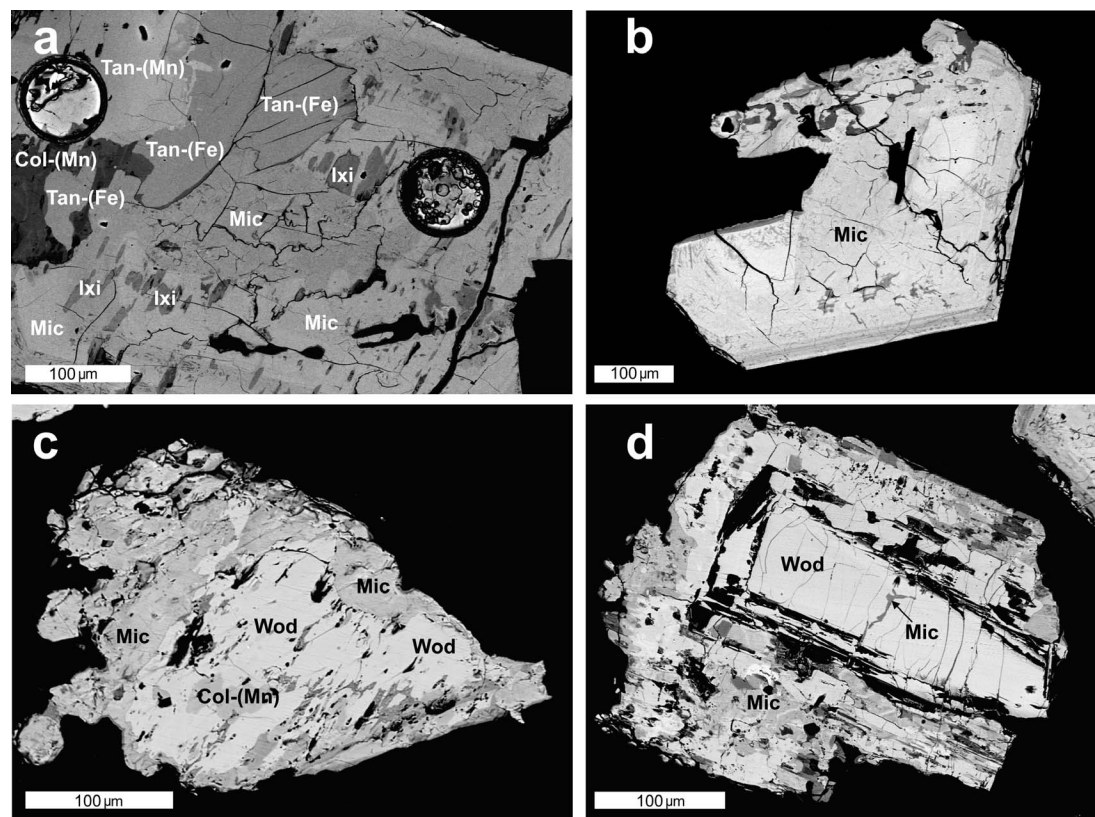


FIG. 5. BSE images of microlite-group minerals from Misumari II (sample 036). (a) Manganocolumbite [Col-(Mn)], ferrotantalite [Tan-(Fe)], and mangantantalite [Tan-(Mn)] replaced by microlite (Mic) and secondary ixiolite (Ixi). (b) Microlite (Mic) grain with oscillatory zoning. (c) Wodginite *s.l.* (Wod) overgrowing relics of manganocolumbite [Col-(Mn)] hosted by microlite (Mic). (d) Microlite (Mic) overgrowing crystal of wodginite *s.l.* (Wod) and penetrated by a small microlite veinlet. In all images, the scale bar is 100 μm long.

Ta = 2Sn, and Mn/(Fe²⁺ + Mn) ratios on both sides of the wodginite–ferrowodginite border (Fig. 7b). Cassiterite contains ≤ 7 wt.% Ta₂O₅ and ≤ 0.48 wt.% Nb₂O₅. Spessartine with the formula (Mn_{1.82}Fe²⁺_{1.15}Ca_{0.02}Mg_{0.01})_{3.00}(Al_{1.97}Fe³⁺_{0.03})_{2.00}Si_{3.00}O₁₂ is clearly of pegmatitic origin, whereas uvitic tourmaline with ~ 2.6 wt.% CaO and ~ 10 wt.% MgO is most likely from the pegmatite exocontact.

LA-ICP-MS

A larger number of microlite grains (40 and 31 from the 035 and 036 samples, respectively) was analyzed for trace elements in both samples; this was chosen to ensure a statistically representative data set. Only primary microlites were involved, whereas areas with secondary alteration processes (especially in the

035 sample) were omitted. Medians of the trace element compositions are given in Table 6. Microlite in sample 035 contains very low concentrations of both LREE and HREE (below 1 ppm each) compared to sample 036 which has high contents of LREE (mainly Ce, Nd, La, Pr), HREE ≤ 12 ppm, and a relatively insignificant Eu anomaly (Fig. 8a). Along with REE, the microlite in sample 036 is enriched in other minor and trace elements compared to sample 035 (Fig. 8b), with the exception of Li, Sb, and Pb. The Ti difference is especially noteworthy.

DISCUSSION

Mineral assemblages of Ta,Nb,Sn,Ti-oxide minerals

The two examined localities differ in their mineral assemblages. They both belong to the rare-element class and REL-Li subclass of pegmatites (according to

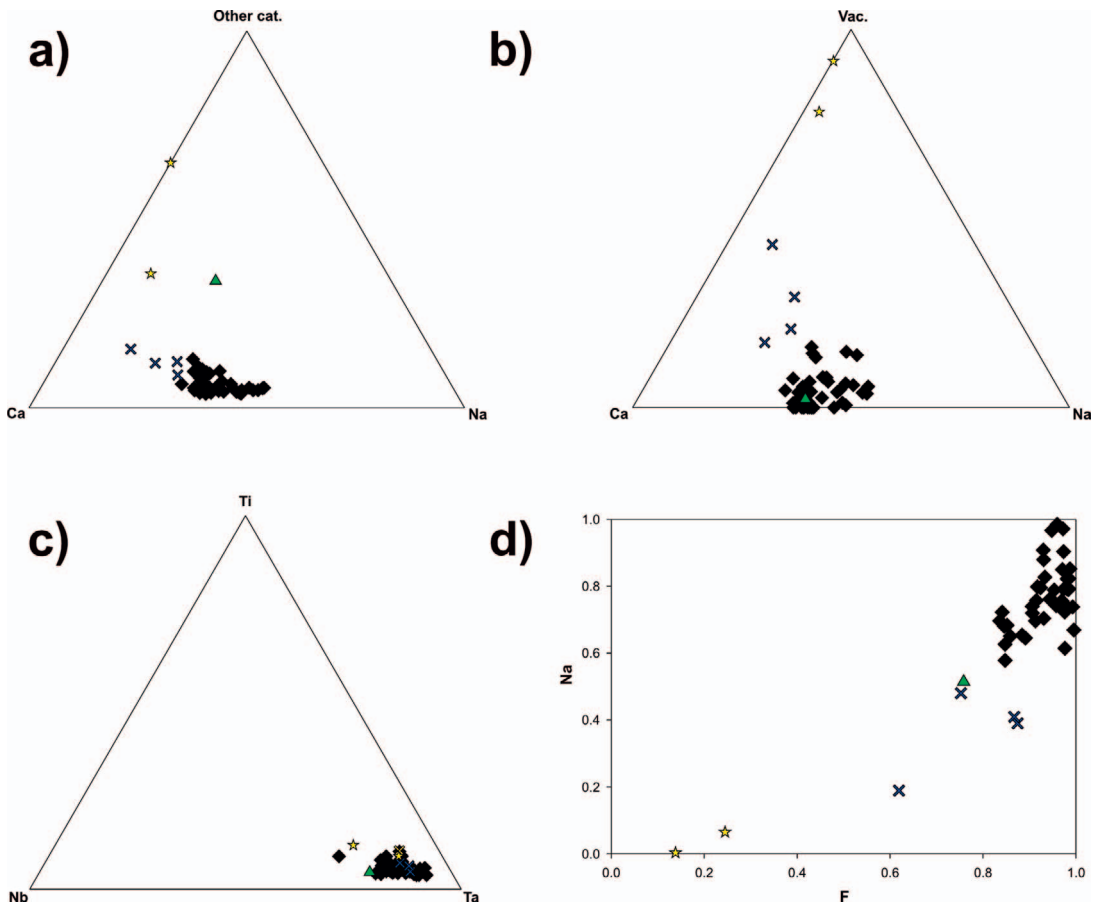


FIG. 6. Composition of microlite-group minerals from Misumari II. (a) A-site population. (b) A-site cations (Ca, Na) and A-site vacancies. (c) B-site population. (d) Na *versus* F, Microlite = diamonds, secondary alteration along fractures = crosses, secondary altered zones = stars, microlite veinlet in wodginite = triangle (see Fig. 6d).

Černý & Ercit 2005). In the pegmatite at Mungwe (sample 035), which belongs to the complex type and lepidolite subtype of pegmatites, the ore minerals are dominated by cassiterite, along with less-common microlite (primary microlite and U-enriched microlite). Other (Ta,Nb,Sn,Ti)-oxide minerals – columbite-tantalite, wodginite *s.l.*, and ferrotapiolite – occur in minor to negligible amounts (Table 1). In contrast, the Misumari II (sample 036) pegmatite, which most likely belongs to the beryl type and beryl-columbite subtype of pegmatites (according to Černý & Ercit 2005), contains abundant microlite and less-common cassiterite, wodginite–ferrowodginite, and columbite-tantalite (Table 1). Chemical compositions show generally higher ratios of Mn/(Mn + Fe) in columbite-tantalite from Mungwe (Fig. 7a), whereas Ta/(Ta + Nb) in both columbite-tantalite and primary micro-

lite are similar at both localities. The Mungwe locality features higher contents of F and lower Ti in microlites (Fig. 4c, d). Along with the heavy mineral assemblage, the mineral composition confirms the higher degree of fractionation and fluorine content, in the field manifested by the presence of the lepidolite core at Mungwe. The behavior of Sn is also distinct at both localities; it is mostly contained in cassiterite at Mungwe, but cassiterite and wodginite–ferrowodginite are present in almost equal amounts at the Misumari II locality. We suggest that the (Nb,Ta,Sn,Ti)-oxide diversity and Mn/(Fe + Mn) fractionation is related to a higher fluorine content in the primary melt at Mungwe, as evidenced by the lepidolite core; Černý (1989) demonstrated very distinct fractionation patterns in F-poor and F-rich pegmatites, with very high

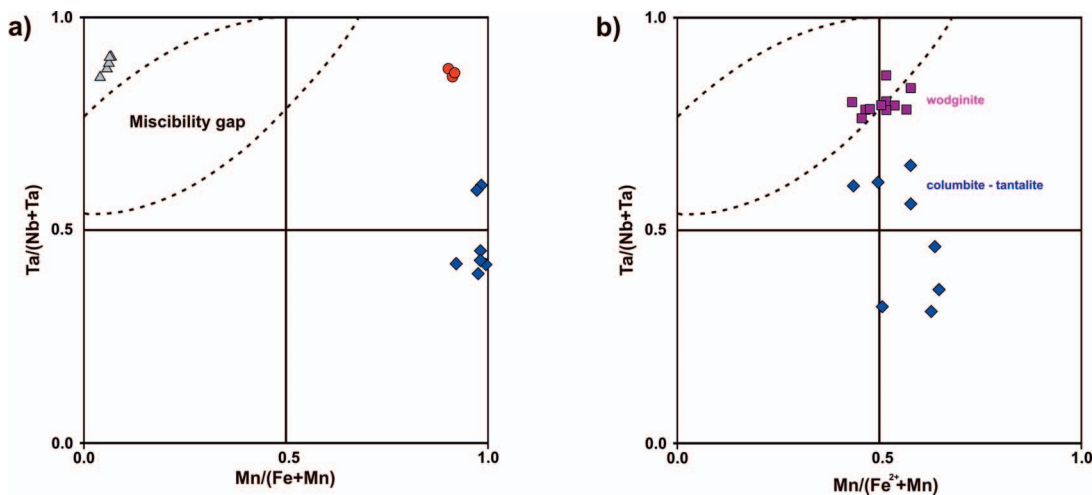


FIG. 7. Columbite–tantalite quadrilateral for (Nb,Ta)-oxides from both localities. (a) Mungwe (columbite–tantalite = diamonds, manganotantalite intergrown with microlite = circles, ferrotapiolite = triangles). (b) Misumari II (columbite–tantalite = diamonds, wodginite–ferrowodginite = squares).

$Mn/(Mn + Fe)$ and less-diverse mineralogy in the latter.

Data for granitic pegmatites where microlite-group minerals may volumetrically predominate or are present in nearly equal amounts with other (Nb,Ta)-oxide minerals (columbite–tantalite, wodginite, ixiolite) are not common (*e.g.*, see Table 1 in Melcher *et al.* 2015), and quantitative data for the individual localities are usually missing. Only some highly evolved Li-rich pegmatites may contain abundant microlite relative to other (Nb,Ta,Ti)-oxide minerals, *e.g.*, Kibara Belt, DRC, and Alto Ligonha province, Mozambique (Melcher *et al.* 2015); Harding, Taos County, New Mexico (Lumpkin & Ewing 1992); Brown Derby, Gunnison County, Colorado (Heinrich 1967); and Tin Mountain, Custer, South Dakota (Spilde & Shearer 1992). In general, high microlite content reflects high alkalinity (Ca,Na) and high F content, either of the primary melt (*typical*, *e.g.*, in carbonatites or other alkaline igneous rocks) or the late magmatic-hydrothermal fluid that reacts with primary (Nb,Ta,Ti)-oxides, typically with strong Ta-enrichment in secondary microlite (*e.g.*, Černý 1989, Novák & Černý 1998). The presence of dominant microlite together with the absence of significant amounts of Nb-rich secondary columbite in both the lepidolite-subtype pegmatite at Mungwe mine and the beryl-columbite subtype pegmatite at Misumari II mine is therefore surprising; the most likely explanation is a high fractionation of the parent granite that produced F-rich pegmatite melts with high Ta/Nb ratios and primary tantalite. An initially high F content in the

Misumari II pegmatite was most likely dramatically reduced by massive fluid loss, as documented by the extensive tourmalinization of the pegmatite exocontact.

Chemical compositions of microlite

Three compositional types of microlite were defined at Mungwe (primary, U-enriched, and secondary alteration) and two types at the Misumari II locality (primary microlite and secondary alterations; Tables 2 and 4, Figs. 4 and 6). Primary and U-enriched microlites from Mungwe are rather homogeneous with Ca/Na close to 1:1 and with the same very narrow $Ta/(Ta + Nb)$ ratio. The primary microlite from Mungwe also has high F contents and very low A-site vacancies, whereas the U-enriched microlite contains up to 0.29 *apfu* U, moderate A-site vacancies, and rather lower concentrations of F (Fig. 4d). The identical B-site occupancy but sharp increase of U-content (Fig. 4a) and moderate decrease in F (Fig. 4d) have no straightforward explanation; microlite cores with U-enriched microlite overgrowths can be related to leaching of some early U-bearing minerals (*e.g.*, zircon). Nevertheless, such compositional zoning with U-enriched rims has been found at other localities, *e.g.*, Harding, New Mexico (Lumpkin *et al.* 1986).

The primary microlite from the Misumari II site is similar with Ca/Na close to 1, low A-site vacancy, high F (Fig. 6d), and variable $Ta/(Ta + Nb)$; typically, it has higher Ti contents at the B-site (Fig. 6c). The

TABLE 4. REPRESENTATIVE EMP COMPOSITIONS OF MICROLITE (Mic), SECONDARY ALTERATIONS ALONG FRACTURES (Alt.fr.), AND SECONDARY ALTERED ZONES (Alt. zone) FROM MISUMARI II

	Mic	Mic	Alt.fr.	Alt.fr. wt.%	Alt. zone	Alt. zone
WO ₃	0.00	0.00	1.48	0.00	0.51	0.00
Nb ₂ O ₅	3.31	2.98	4.21	4.38	5.10	10.39
Ta ₂ O ₅	70.74	72.34	63.57	63.77	68.37	62.39
SiO ₂	0.00	0.00	4.34	0.49	1.06	0.51
TiO ₂	1.61	1.10	1.26	2.94	2.70	3.85
SnO ₂	1.37	1.72	0.99	2.21	1.84	1.89
ThO ₂	0.30	0.13	0.00	0.17	0.19	0.28
UO ₂	1.28	0.85	0.54	2.98	2.24	2.74
Al ₂ O ₃	0.00	0.00	0.53	0.07	0.15	0.06
MgO	0.00	0.00	0.08	0.00	0.00	0.00
FeO	0.00	0.00	1.08	0.18	1.07	1.79
CaO	8.70	9.04	9.74	9.11	3.66	1.68
Na ₂ O	5.59	5.11	1.21	2.34	0.40	0.00
F	3.34	3.37	2.43	3.04	0.93	0.55
O = F	-1.41	-1.42	-1.02	-1.28	-0.39	-0.23
Total	94.83	95.22	90.44	90.40	87.83	85.90
<i>apfu</i>						
A-site	Na ⁺	0.964	0.879	0.224	0.405	0.065
	Ca ²⁺	0.829	0.860	0.998	0.871	0.330
	Mg ²⁺	0.000	0.000	0.011	0.000	0.000
	Fe ²⁺	0.000	0.000	0.086	0.013	0.075
	Al ³⁺	0.000	0.000	0.060	0.007	0.015
	Th ⁴⁺	0.006	0.003	0.000	0.003	0.004
	U ⁴⁺	0.025	0.017	0.011	0.059	0.042
	sum	1.824	1.759	1.390	1.358	0.531
B-site	W ⁶⁺	0.000	0.000	0.037	0.000	0.011
	Nb ⁵⁺	0.133	0.120	0.182	0.177	0.194
	Ta ⁵⁺	1.711	1.746	1.653	1.547	1.563
	Ti ⁴⁺	0.108	0.073	0.091	0.197	0.171
	Sn ⁴⁺	0.049	0.061	0.038	0.079	0.062
contam.	Si ⁴⁺	0.000	0.000	0.415	0.044	0.089
X-site	O	5.652	5.596	5.814	5.312	4.633
	OH	0.348	0.404	0.186	0.688	1.367
Y-site	F	0.939	0.946	0.735	0.858	0.247

Note: Crystalliochemical formula calculated on the basis of (W + Nb + Ta + Ti + Sn) = 2 apfu. SiO₂ contents are regarded as contamination and were not used for formula calculation. Elements sought but below detection limit: Zr, Sb, Sc, Pb, Mn.

concentrations of U and other cations except for Ca and Na are low to moderate (Fig. 6a). The Misumari II primary microlite is enriched in almost all trace elements (including REE) with the exception of Li, Sb, and Pb compared to microlite from Mungwe. The compositions of microlites from both samples have typical features of a primary microlite from granitic pegmatites (Lumpkin & Ewing 1992). Microlites at both localities seem to replace earlier (Nb,Ta,Ti,Sn)-oxide minerals; however, their paragenetic relations

are commonly unclear due to complex textural relations, and we cannot exclude simultaneous crystallization (or overgrowths without alteration) of primary microlite with wodginite or tantalite (e.g., Figs. 3c and 5d).

Secondary microlite was found mainly at Mungwe site as a replacement product of U-enriched microlite (Fig. 3a, b, d, e, f), whereas the primary microlite in the same sample is stable. Secondary microlite is less common at Misumari II (Fig. 6). Compositional trends

TABLE 5. REPRESENTATIVE EMP COMPOSITIONS OF MANGANOCOLUMBITE (Col), FERROTANTALITE (Tan), AND WODGINITE–FERROWODGINITE (Wod, Fe-Wod) FROM MISUMARI II

	Tan	Col	Site	Fe-Wod	Wod
WO ₃ (wt.%)	0.54	1.33		WO ₃ (wt.%)	1.69
Nb ₂ O ₅	22.56	44.97		Nb ₂ O ₅	10.91
Ta ₂ O ₅	57.69	33.49		Ta ₂ O ₅	56.37
TiO ₂	0.85	0.72		TiO ₂	2.10
SnO ₂	0.46	0.24		ZrO ₂	0.69
MnO	8.00	11.45		SnO ₂	12.33
FeO	8.25	6.70		Al ₂ O ₃	0.07
Total	98.35	98.90		MnO	5.23
W ⁶⁺ (<i>apfu</i>)	0.010	0.023		FeO _{calc}	6.33
Nb ⁵⁺	0.755	1.334		Fe ₂ O ₃ calc	2.06
Ta ⁵⁺	1.161	0.598		Total	97.78
Ti ⁴⁺	0.047	0.036	C-site	W ⁶⁺ (<i>apfu</i>)	0.180
Sn ⁴⁺	0.014	0.006		Nb ⁵⁺	2.029
Mn ²⁺	0.502	0.636		Ta ⁵⁺	5.790
Fe ²⁺	0.511	0.368	B-site	Ta ⁵⁺	0.517
O	5.956	5.984		Ti ⁴⁺	0.650
				Zr ⁴⁺	0.138
				Sn ⁴⁺	2.023
				Al ³⁺	0.034
				Fe ³⁺	0.638
			A-site	Fe ²⁺	2.177
				Mn ²⁺	1.823
				O	32.013
					32.075

Note: Crystallochemical formula calculated on the basis of cation sum = 3 (for columbite–tantalite) and = 16 *apfu* (for wodginite–ferrowodginite). Elements sought but below detection limit: Zr and Al (columbite–tantalite only), Si, Th, U, Sc, Sb, Mg, Pb, Ca, Na, F.

in secondary microlite may be expressed by the exchange vectors: ^ANa YF → ^A□Y□, ^ACa YO → ^A□Y□, and ^ACa XO → ^A□X□ (Lumpkin & Ewing 1992).

In general, the secondary microlites are apparently depleted in Na and F and have high A-site vacancies, but the B-site composition is almost identical to the primary microlite, as well as the concentrations of U. Such a composition is typical for secondary low-*T* alterations related to weathering (Lumpkin & Ewing 1992, Gieré *et al.* 2000, Geisler *et al.* 2004).

Microlite as an indicator of geochemical processes in pegmatite evolution and implications for nuclear waste disposal

Textural relations and chemical composition of secondary microlite from Mungwe suggest that secondary low-*T* alteration is a dominant process that affected the primary microlite. The U-enriched microlite is obviously altered along fractures and at the rim of the grains; this phenomenon is considered to be secondary alteration at the relatively low *T* involved

(Lumpkin & Ewing 1992). Such microlite was produced in the experiments of Geisler *et al.* (2004) conducted at *T* = 175 °C and neutral to acidic conditions. However, the starting microlite was U-poor and compositionally similar to the microlite from Misumari II. The dominant alteration mechanism was apparently fluid transport through preexisting fractures and vugs (with limited intracrystalline diffusion), which resulted in a large number of vacancies due to leaching of A-site cations and Y-site anions. The B-site cation contents remained unchanged due to very low mobility of these elements caused by their strong bonds with the coordinated oxygen atoms. Surprisingly, no features of primary high-*T* alteration (Lumpkin & Ewing 1992) were observed; consequently, this stage was likely significantly depressed in the examined pegmatites.

Differences in the degree of alteration between primary microlite and U-enriched microlite are apparent and suggest that even moderate concentrations of U in microlite significantly change its sensitivity for alteration in low-*T* hydrothermal conditions. However, these alterations did not change compositions at the B-site

TABLE 6. MEDIAN OF TRACE-ELEMENT CONTENTS (PPM) IN MICROLITE FROM MUNGWE (SAMPLE 035) AND MISUMARI II (SAMPLE 036)

Sample	035 <i>n</i> = 40	036 <i>n</i> = 31		035	036
Li	96.0	5.0	La	0.6	66.7
Mg	13.6	45.4	Ce	0.9	198.5
Sc	0.0	1.4	Pr	0.1	21.5
Ti	6.9	7401.2	Nd	0.3	83.5
Y	0.5	24.6	Sm	0.1	16.6
Zr	4.7	169.9	Eu	0.1	8.9
Sn	1839.4	9147.1	Gd	0.2	11.9
Sb	228.6	16.2	Tb	0.0	1.7
Hf	15.8	137.4	Dy	0.1	9.5
W	663.6	2635.5	Ho	0.0	1.6
Pb	1681.2	60.8	Er	0.0	3.8
Th	858.7	1009.5	Tm	0.0	0.4
U	281.3	5873.3	Yb	0.0	2.3
			Lu	0.0	0.2

and the concentrations of U are also stable. This is in agreement with the alteration patterns observed for U-rich pyrochlore, which maintains stable U contents after metamictization and secondary recrystallization (Lumpkin & Ewing 1995). The mobility of elements has been tested mainly on titanate and zirconate (betafite and its Zr-analogue) compounds to date (Lumpkin 2006), however, a limited amount of data is available on microlite-group minerals. Hence, natural systems can be valuable sources of information on long-term stability.

Use of microlite-group minerals for determination of Ta-ore provenance

Microlite *s.l.* as a major or significant constituent of tantalum mine production is not very common. Our preliminary data for other studied and not yet published actively mined localities (North Kivu mine, DRC; Muhanga district mine, Rwanda; Ile district mine, Mozambique) show that the microlites from Mungwe and Misumari II can easily be distinguished from microlites from the other sites, which can also be distinguished from each other. Ratios of significant elements selected by statistical tests were used for the comparison: Sb/Ti (Fig. 8c), Ti/W (Fig. 8d), and Sb/W (Fig. 8e). The Mungwe locality is easily distinguishable from Misumari II using all three charts. Each of the plotted localities clusters separately in at least one of these charts, except the Ile district mine; however, this mine differs significantly in its negative Eu anomaly (see Fig. 8f). Similar negative Eu-anomalies were observed in microlite from all the Mozambiquan

localities (and were absent in those from DRC), in agreement with the study of Melcher *et al.* (2015). These results must be combined with the other features, *e.g.*, major element trends, degree and textures of alteration, and associated minerals.

CONCLUSIONS

Fluorine-rich (U-poor) primary microlite and U-enriched microlite are the most abundant Ta-bearing minerals in eluvial deposits derived from two highly weathered pegmatites, Mungwe and Misumari II. The studied mines are relatively close to each other and the geological setting is similar; consequently, both pegmatites underwent deep tropical weathering under very similar conditions, manifested by breakdown of feldspars and micas to clay minerals in those parts of the pegmatites from which microlite is extracted; however, alteration of the primary U-poor microlite is very limited in contrast with the U-enriched microlite where radiation damage disrupted the mineral structure prior to the alteration. The composition of microlite-group minerals indicates secondary low-*T* alteration during weathering of the pegmatite, during which U remained in the microlite structure. As the conditions are similar to those in radioactive waste repositories, microlite-group minerals can be potentially used for U immobilization. Low and high concentrations of trace REE in microlites from the Mungwe and Misumari II sites, respectively, and variable trace element compositions along with the revealed specific alteration features permit determination of the provenance of the tantalum ores for end-users.

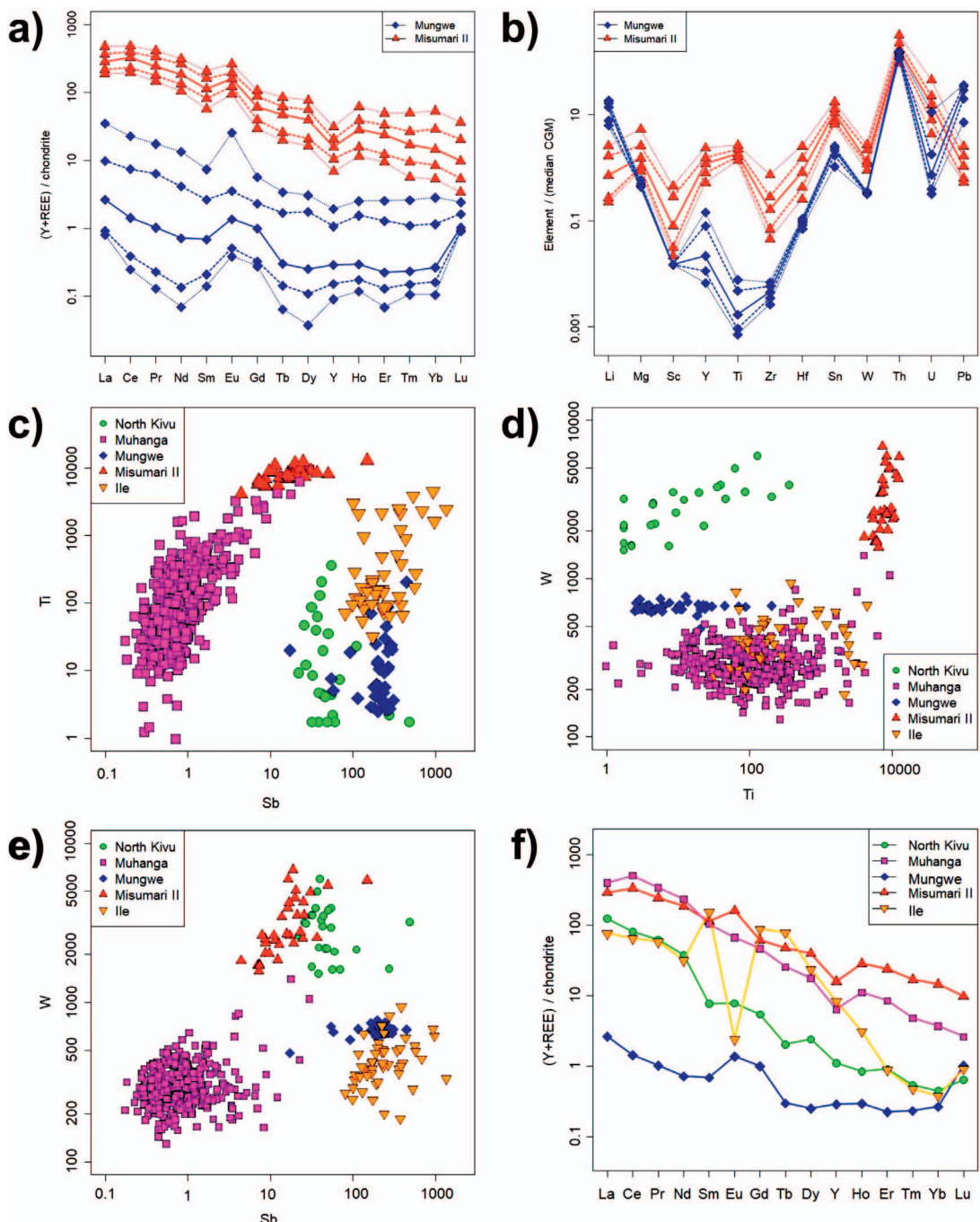


FIG. 8. REE and trace-element contents in microlite-group minerals from Mungwe and Misumari II sites and comparison to other localities. (a) Chondrite-normalized $Y + \text{REE}$ diagram. (b) Trace elements diagram normalized to the 'global CGM median' value (Melcher *et al.* 2015). For (a) and (b), median (middle continuous line) and main percentiles (P25 – lower dashed line, P75 – upper dashed line, P10 – lower stippled line, and P90 – upper stippled line) are presented. (c) Sb/Ti ratio. (d) Ti/W ratio. (e) Sb/W ratio. (f) Chondrite-normalized $Y + \text{REE}$ diagram for all compared localities.

ACKNOWLEDGMENTS

The authors thank both reviewers (A. Pieczka and F. Melcher) for constructive comments that improved the manuscript, and Associate Editor L.J. Millonig for handling the editorial matters. The study was supported by Masaryk University project MUNI/A/1653/2016.

REFERENCES

- ANDERS, E. & GREVESSE, N. (1989) Abundances of the elements: meteoritic and solar. *Geochimica et Cosmochimica Acta* **53**, 197–214.
- ATENCIO, D., ANDRADE, M.B., CHRISTY, A.G., GIERE, R., & KARTASHOV, P.M. (2010) The pyrochlore supergroup of minerals: nomenclature. *Canadian Mineralogist* **48**, 673–698.
- BALDWIN, J.R., HILL, P.G., FINCH, A.A., VON KNORRING, O., & OLIVER, G.J.H. (2005) Microlite–manganotantalite exsolution lamellae: Evidence from rare-metal pegmatite, Karibib, Namibia. *Mineralogical Magazine* **69**, 917–935.
- ČERNÝ, P. (1989) Characteristics of pegmatite deposits of tantalum. In Lanthanides, Tantalum and Niobium (P. Möller, P. Černý, & F. Saupé, eds.). Springer, Berlin, Heidelberg, New York, 195–239.
- ČERNÝ, P. & ERCIT, T.S. (2005) The classification of granitic pegmatites revisited. *Canadian Mineralogist* **43**, 2005–2026.
- ČERNÝ, P., HAWTHORNE, F.C., LAFLAMME, J.H.G., & HINTHORNE, J.R. (1979) Stibiotantite, a new member of the pyrochlore group from Vežná, Czechoslovakia. *Canadian Mineralogist* **17**, 583–588.
- ČERNÝ, P., CHAPMAN, R., FERREIRA, K., & SMEDS, S.-A. (2004) Geochemistry of oxide minerals of Nb, Ta, Sn, and Sb in the Varutrask granitic pegmatite, Sweden: The case of an “anomalous” columbite–tantalite trend. *American Mineralogist* **89**, 505–518.
- CUTLER, D.R., EDWARDS, T.C., BEARD, K.H., CUTLER, A., HESS, K.T., GIBSON, J., & LAWLER, J.J. (2007) Random forests for classification in ecology. *Ecology* **88**, 2783–2792.
- DE'ATH, A.G. & FABRICIUS, K.E. (2000) Classification and regression trees: a powerful yet simple technique for the analysis of complex ecological data. *Ecology* **81**, 3178–3192.
- DEWAELÉ, S., DE CLERQ, F., MUCHEZ, P., SCHNEIDER, J., BURGESS, R., BOYCE, A., & FERNANDEZ-ALONSO, M. (2010) Geology of the cassiterite mineralisation in the Rutongo area, Rwanda (Central Africa): current state of knowledge. *Geologica Belgica* **13** (1–2), 91–112.
- DEWAELÉ, S., HENJES-KUNST, F., MELCHER, F., SITNIKOVA, M., BURGESS, R., GERDES, A., FERNANDEZ-ALONSO, M., DE CLERQ, F., MUCHEZ, P., & LEHMANN, B. (2011) Late Neoproterozoic overprinting of the cassiterite and columbite–tantalite bearing pegmatites of the Gatumba area, Rwanda (Central Africa). *Journal of African Earth Sciences* **61**, 10–26.
- DUMAŃSKA-SŁOWIK, M., PIECZKA, A., TEMPESTA, G., OLEJNICZAK, Z., & HEFLIK, W. (2014) ‘Silicified’ pyrochlore from nepheline syenite (mariupolite) of the Mariupol Massif, SE Ukraine: a new insight into the role of silicon in the pyrochlore structure. *American Mineralogist* **99**, 2008–2017.
- ERCIT, T.S. (2005) REE-enriched granitic pegmatites. In Rare-element geochemistry and mineral deposits (R. Linnen & I. Samson, eds.). GAC Short Course Notes **17**, 175–199.
- EWING, R.C. (1975) Alteration of metamict, rare-earth, AB_2O_6 -type Nb-Ta-Ti oxides. *Geochimica et Cosmochimica Acta* **39**, 521–530.
- GEISLER, T., BERNDT, J., MEYER, H.W., POLLOK, K., & PUTNIS, A. (2004) Low-temperature aqueous alteration of crystalline pyrochlore: correspondence between nature and experiment. *Mineralogical Magazine* **68**, 905–922.
- GIERÉ, R., SWOPE, R.J., BUCK, E.C., GUGGENHEIM, R., MATHYS, D., & REUSSER, E. (2000) Growth and alteration of uranium-rich microlite. Materials Research Society, Symposium Proceedings **608**, 519–524.
- GIERÉ, R., BUCK, E.C., GUGGENHEIM, R., MATHYS, D., REUSSER, E., & MARQUES, J. (2001) Alteration of Uranium-rich Microlite. In Scientific Basis for Nuclear Waste Management XXIV (K.P. Hart & G.R. Lumpkin, eds.). Materials Research Society, Symposium Proceedings **663**, 935–944.
- GRAUPNER, T., MELCHER, F., GÄBLER, H.E., SITNIKOVA, M., BRÄTZ, H., & BAHR, A. (2010) Rare earth element geochemistry of columbite-group minerals: LA-ICP-MS data. *Mineralogical Magazine* **74**, 691–713.
- HEINRICH, E.W. (1967) Micas of the Brown Derby pegmatites, Gunnison County, Colorado. *American Mineralogist* **52**, 1110–1121.
- JANOUŠEK, V., MOYEN, J.F., MARTIN, H., ERBAN, V., & FARROW, C. (2015) *Geochemical modelling of igneous processes – principles and recipes in R language*. Springer-Verlag, Berlin, Heidelberg, 346 pp.
- LINNEN, R.L., VAN LICHTERVELDE, M., & ČERNÝ, P. (2012) Granitic pegmatites as sources of strategic metals. *Elements* **8**, 275–280.
- LLORENS, T. & MORO, M.C. (2010) Microlite and tantalite in the LCT granitic pegmatites of La Canalita, Navasfrías Sn-W District, Salamanca, Spain. *Canadian Mineralogist* **48**, 375–390.
- LUMPKIN, G.R. (2006) Ceramic waste forms for actinides. *Elements* **2**, 365–372.
- LUMPKIN, G.R. & EWING, R.C. (1992) Geochemical alteration of pyrochlore group minerals: microlite subgroup. *American Mineralogist* **77**, 179–188.
- LUMPKIN, G.R. & EWING, R.C. (1995) Geochemical alteration of pyrochlore group minerals: pyrochlore subgroup. *American Mineralogist* **80**, 732–743.
- LUMPKIN, G.R., CHAKOUMAKOS, B.C., & EWING, R.C. (1986) Mineralogy and radiation effects of microlite from the

- Harding pegmatite, Taos County, New Mexico. *American Mineralogist* **71**, 569–588.
- MELCHER, F., SITNIKOVA, M.A., GRAUPNER, T., MARTIN, N., OBERTHÜR, T., HENJES-KUNST, F., GÄBLER, E., GERDES, A., BRÄTZ, H., DAVIS, D.W., & DEWAELE, S. (2008) Fingerprinting of conflict minerals: columbite–tantalite (“coltan”) ores. *SGA News* **23**, 1–14.
- MELCHER, F., GRAUPNER, T., GÄBLER, H.-E., SITNIKOVA, M., HENJES-KUNST, F., OBERTHÜR, T., GERDES, A., & DEWAELE, S. (2015) Tantalum–(niobium–tin) mineralisation in African pegmatites and rare metal granites: Constraints from Ta–Nb oxide mineralogy, geochemistry and U–Pb geochronology. *Ore Geology Reviews* **64**, 667–719.
- MERLET, C. (1994) An Accurate Computer Correction Program for Quantitative Electron Probe Microanalysis. *Microchimica Acta* **114/115**, 363–376.
- NOVÁK, M. & ČERNÝ, P. (1998) Niobium-tantalum oxide minerals from complex granitic pegmatites in the Moldanubium, Czech Republic: Primary versus secondary compositional trends. *Canadian Mineralogist* **36**, 659–672.
- NOVÁK, M., ŠKODA, R., GADAS, P., KRMÍČEK, L., & ČERNÝ, P. (2012) Contrasting origins of the mixed (NYF + LCT) signature in granitic pegmatites, with examples from the Moldanubian Zone, Czech Republic. *Canadian Mineralogist* **50**, 1077–1094.
- PIECZKA, A., SZUSZKIEWICZ, A., SZEŁĘG, E., NEJBERT, K., ŁODZIŃSKI, M., ILNICKI, S., TURNIAK, K., BANACH, M., HOLUB, W., MICHALOWSKI, P., & RÓŻNIAK, R. (2013) (Fe,Mn)-(Ti,Sn)-(Nb,Ta) oxide assemblage in a little fractionated portion of a mixed (NYF + LCT) pegmatite from Piława Góra, the Sowie Mts. block, SW Poland. *Journal of Geosciences* **58**, 91–112.
- PIECZKA, A., SZUSZKIEWICZ, A., SZEŁĘG, E., ILNICKI, S., NEJBERT, K., & TURNIAK, K. (2014) Samarskite-group minerals and alteration products: An example from the Julianna pegmatitic system, Piława Góra, SW Poland. *Canadian Mineralogist* **52**, 303–319.
- POHL, W. (1987) Metallogeny of the northeastern Kibaran belt, Central Africa. *Geological Journal* **22**, 103–119.
- REIMANN, C., FILZMOSER, P., GARRETT, R.G., & DUTTER, R. (2008) *Statistical Data Analysis Explained: Applied Environmental Statistics*. John Wiley & Sons, Chichester, England, 362 pp.
- ROMER, R.L. & LEHMANN, B. (1995) U-Pb columbite age of Neoproterozoic Ta-Nb mineralization in Burundi. *Economic Geology* **90**, 2303–2309.
- ŠKODA, R. & NOVÁK, M. (2007) Y, REE, Nb, Ta, Ti-oxide (AB_2O_6) minerals from REL–REE euxenite-subtype pegmatites of the Třebíč Pluton, Czech Republic; substitutions and fractionation trends. *Lithos* **95**, 43–57.
- SIPILDE, M.N. & SHEARER, C.K. (1992) A comparison of tantalum-niobium oxide assemblages in two mineralogically distinct rare-element granitic pegmatites, Black Hills, South Dakota. *Canadian Mineralogist* **30**, 719–737.
- TACK, L., WINGATE, M.T.D., DE WAELE, B., MEERT, J., BELOUsova, E., GRIFFIN, B., TAHON, A., & FERNANDEZ-ALONSO, M. (2010) The 1375 Ma “Kibaran event” in Central Africa: Prominent emplacement of bimodal magmatism under extensional regime. *Precambrian Research* **180**, 63–84.
- TINDLE, A.G. & BREAKS, F.W. (1998) Oxide minerals of the Separation Rapids rare-element granitic pegmatite group, northwestern Ontario. *Canadian Mineralogist* **36**, 609–635.
- UHER, P., ČERNÝ, P., CHAPMAN, R., HATÁR, J., & MIKO, O. (1998) Evolution of Nb,Ta-oxide minerals in the Prašivá granitic pegmatites, Slovakia. II. External hydrothermal Pb,Sb overprint. *Canadian Mineralogist* **36**, 535–545.
- VAN LICHTERVELDE, M., SALVI, S., BÉZIAT, D., & LINNEN, R.L. (2007) Textural features and chemical evolution in tantalum oxides: magmatic versus hydrothermal origins for Ta mineralization in the Tanco Lower Pegmatite, Manitoba, Canada. *Economic Geology* **102**, 257–276.
- VOLOSHIN, A.V., PAKHOMOVSKIY, YA.A., PUSHCHAROVSKIY, L.YU., NADEZHINA, T.N., BAKHCHISARAYTSEV, A.Y., & KOBASHEV, YU.S. (1989) Strontium pyrochlore: composition and structure. *Novye Dannye o Mineralah SSSR* **36**, 12–24 (in Russian).
- VON KNORRING, O. & FADIPE, A. (1981) On the mineralogy and geochemistry of niobium and tantalum in some granite pegmatites and alkali granites of Africa. *Bulletin de Minéralogie* **104**, 496–507.
- WISE, M.A. & ČERNÝ, P. (1990) Primary compositional range and alteration trends of microlite from the Yellowknife Pegmatite Field, Northwest Territories, Canada. *Mineralogy and Petrology* **43**, 83–98.
- WITZKE, T., STEINS, M., DOERING, T., SCHUCKMANN, W., WEGNER, R., & PÖLLMANN, H. (2011) Fluornatromicrolite, $(\text{Na},\text{Ca},\text{Bi})_2\text{Ta}_2\text{O}_6\text{F}$, a new mineral from Quixaba, Paraíba, Brazil. *Canadian Mineralogist* **49**, 1105–1110.

Received December 8, 2017. Revised manuscript accepted January 17, 2018.

ORIGINAL PAPER

Laser microsampling and multivariate methods in provenance studies of obsidian artefacts

^{a,b,c}**Lubomír Prokeš**, ^{a,d}**Michaela Vašinová Galiová**, ^a**Simona Hušková**,
^{a,d}**Tomáš Vaculovič**, ^d**Aleš Hrdlička**, ^e**Andrew Zed Mason**, ^f**Hector Neff**,
^g**Antonín Přichystal**, ^{a,d}**Viktor Kanický***

^a*Department of Chemistry*, ^b*Department of Physical Electronics*, ^g*Department of Geological Sciences, Faculty of Science, Masaryk University, Kotlářská 2, 611 37 Brno, Czech Republic*

^c*R&D Centre for Low-cost Plasma and Nanotechnology Surface Modifications, Masaryk University, Kotlářská 2, 611 37 Brno, Czech Republic*

^d*Central European Institute of Technology, Kamenice 5, 625 00 Brno, Czech Republic*

^e*Department of Biological Sciences*, ^f*Department of Anthropology and Institute for Integrated Research in Materials Environments, and Society (IIRMES), California State University, Long Beach, 1250 Bellflower Blvd, 90840 Long Beach, CA, USA*

Received 28 April 2014; Revised 7 October 2014; Accepted 15 October 2014

The provenance of obsidian artefacts and raw materials was studied by the multivariate statistical analysis of forty-five samples using elemental composition data obtained by laser ablation-inductively coupled plasma-mass spectrometry (LA-ICP-MS). One ICP-MS instrument equipped with a quadrupole mass filter and the other based on a time-of-flight analyser were coupled to the same type of laser ablation device (Nd:YAG 213 nm), thereby affording a comparison of the different mass spectrometers in terms of precision and verification of the consistency of the results. The influence of surface roughness (polished raw material vs artefact) and microinhomogeneity on the LA-ICP-MS signal was studied under the optimised working conditions of the laser ablation device. Principal component analysis, correspondence analysis, independent component analysis, multi-dimensional scaling, Sammon mapping and fuzzy cluster analysis were applied and compared in order to reveal statistically significant compositional differences between particular geological sites and to disclose the provenance of the raw materials used in manufacture of the artefacts. Twenty-seven artefacts and eighteen raw material samples from natural resources in the Czech Republic, Slovakia, Italy, Greece, Syria, Iraq, Turkey, Mexico and Nicaragua were examined with special attention focused on samples from Moravia (Czech Republic) and some Near East sites (Tell Arbid, Tell Asmar). The Carpathian origin of the obsidian artefacts was investigated in the Moravian samples using the Pb, Rb and U contents. The Near East samples were classified according to their Sr, Ba, Zr and REE contents as per-alkaline obsidians (Bingöl A/Nemrut Dağ) originating from Southeast Anatolia.

© 2014 Institute of Chemistry, Slovak Academy of Sciences

Keywords: ICP-MS, laser beam sampling, principal component analysis, correspondence analysis, archaeological objects, volcanic glasses

*Corresponding author, e-mail: viktork@chemi.muni.cz

Introduction

From the archaeological perspective, obsidian is the most important of the volcanic glasses. It was widely used for tool-making, especially in the European Neolithic period. Obsidian artefacts are often found in archaeological sites located at a great distance from the potential natural sources, hence may indicate cultural interaction between distant geographical areas. The study of ancient inter-regional contacts and exchange systems is one of the fundamental topics of modern archaeological research (Healey, 2007; Golitko et al., 2012; Shackley, 2005). Reconstruction of the trade connections may shed light on the economic aspects of ancient societies and the former social and political climate (Tykot, 2002).

Obsidian exhibits properties that favour its characterisation in terms of chemical composition and, hence, geographical origin. The obsidian raw material suitable for making tools is relatively homogeneous, i.e. uniform as regards craft-processing. Hence, it makes sense to determine its average chemical composition by methods of chemical or physicochemical bulk analysis. Obsidian sources are located in just a few volcanic districts. For instance, the deposits in the Middle East are situated in limited areas of Turkey, Armenia and Yemen.

This study sought to characterise obsidian archaeological finds from South Moravia (Czech Republic) and their provenance. Obsidian artefacts in South Moravia were rarely observed at Upper Palaeolithic sites (e.g. Nová Dědina, Pavlov) (Přichystal, 2013). Obsidian was commonly used in the Neolithic period, especially in the early phase of the Moravian Painted Pottery Culture (Lengyel Cultural Complex). It was present in the form of minor chips, small blades and cores chipped from small nodules. In the later phases of this culture, obsidian was replaced by rock crystal and moldavite; its incidence decreased and in the Eneolithic (Copper Age) almost disappeared. Because there are no sources of obsidian in Moravia and the surrounding countries, the raw material had to be imported from distant areas. The most probable raw obsidian sources for Moravian obsidian artefacts are located on the border between the Western and Eastern Carpathians, about 400 km to the east – in the Zemplínske vrchy (mountains in Southeast Slovakia) or the Tokaj hills (Northeast Hungary) (Přichystal, 2013; Williams Thorpe et al., 1984; Biró, 2004).

The other task was to determine the provenance of five obsidian artefacts from Neolithic tell sites Tell Arbid (Syria) and Tell Asmar (Iraq). Obsidian sources in Anatolia (Chataigner et al., 1998; Gratuze, 1999; Forster & Grave, 2012) can be regarded as potential places of origin for the above five samples.

For the purpose of finding a suitable combination of the elements which can help to reveal the elemental differences between localities investigated,

some multivariate data analytical and visualisation techniques, such as principal component analysis (PCA), correspondence analysis (CA), independent component analysis (ICA), multi-dimensional scaling (MDS), Sammon mapping (SM) and fuzzy non-hierarchical cluster analysis were deployed. Scatter plots were also applied as supplements to the multivariate methods.

For the elemental analysis of obsidian raw materials and related artefacts, laser ablation-inductively coupled plasma-mass spectrometry (LA-ICP-MS) was employed in this work. Although the LA-ICP-MS method is widely used in the analysis of a large variety of solid samples (Novotný et al., 2008; Hare et al., 2011; de Barros et al., 2010; Wu & Becker, 2012; Lu et al., 2009; Gholap et al., 2010; Galiová et al., 2010), its application to objects of cultural heritage is limited by the requirement for any damage to be negligible. Only local damage, if possible invisible to the naked eye, is permitted in the case of such precious exhibits. This requirement is met by keeping the diameter of an ablation crater within tens of micrometers. However, representative sampling by ablation is in conflict with this requirement, as obsidians generally exhibit microinhomogeneity. Moreover, the degree of sample surface roughness affects the amount of ablated material, which provides a different intensity of analytical signals for materials of the same chemical composition. Unlike artefacts, the polishing of obsidian raw material samples is permitted, rendering it possible to achieve an equal surface quality in terms of optical reflectivity, laser energy absorption and, consequently, ablation efficiency for samples originally differing in roughness. By contrast, where artefacts are concerned, we have to accept the variability in both the surface roughness and the angle between the laser beam and the normal to surface following on from the difficulty in positioning an artefact of uneven shape in the ablation chamber. The laser spot diameter should be kept at 100 µm at a minimum for obtaining acceptable limits of detection at the level of units of $\mu\text{g g}^{-1}$ for trace elements and tens of $\mu\text{g g}^{-1}$ for minor elements. A larger ablation spot yields a greater amount of ablated material and at the same time compensates for any local inhomogeneity, thereby improving the limits of detection. Moreover, the accuracy of the results is influenced also by the selection of a suitable analyser. The time-of-flight (TOF) ICP-MS (ICP-TOF-MS) is characterised by faster data acquisition, hence is better suited for the simultaneous measurement of several transient signals than the quadrupole-based ICP-MS (ICP-Q-MS).

In order to verify the reliability of the ICP-MS measurements, a part of the current study was devoted to *i*) the application of optimised experimental parameters in terms of stability of signals of isotopes and microinhomogeneity, *ii*) the verification of Q-MS using faster data acquisition by means of TOF-MS

and *iii)* the influence of the ablation of polished and untreated surface on the analytical results.

Experimental

Samples and methods

The samples of obsidians from various archaeological localities in Moravia (Czech Republic) and from Neolithic tell localities from Syria (Tell Arbid) and Iraq (Tell Asmar) were analysed, together with archaeological and geological samples from Southeast Slovakia, Lipari, Greece, Cappadocia (Turkey) and East Anatolia (Turkey), Mexico and Nicaragua (Table 1).

LA-ICP-MS was commonly used for the trace element analysis of obsidian in the provenance study (e.g. Gratuze, 1999). Laser ablation experiments with LA-ICP-Q-MS were performed at the Laboratory of Atomic Spectrochemistry, Department of Chemistry, Faculty of Science, Masaryk University, Brno, Czech Republic and measurements using LA-ICP-TOF-MS were carried out at the Institute for Integrated Research in Materials Environments, and Society (IIRMES), California State University, Long Beach, CA, USA.

LA-ICP-Q-MS

A pulsed Nd:YAG-based laser ablation system UP 213 (New Wave Research, Fremont, CA, USA) operating at 213 nm with a pulse duration of 4.2 ns, equipped with a SuperCell (working area of 18.5 cm^2) designed for rapid eluting of the ablation-generated aerosol with a carrier gas (1.0 L min^{-1} He) was used. The aerosol was transported through 1 m of polyurethane tubing (i.d. of 4 mm) into the ICP source of the Q-MS Agilent 7500ce (Agilent Technologies, Santa Clara, CA, USA). This model (ce) of Q-MS was equipped with a collision-reaction cell for minimisation of potential polyatomic interferences. Measurements were carried out with He as a collision gas at a flow-rate of 2.5 mL min^{-1} . Laser ablation was accomplished under the optimal conditions: laser spot diameter of $100\text{ }\mu\text{m}$, frequency of 20 Hz and 5.0 J cm^{-2} fluence. The sample surface was ablated for 120 s at ten different positions (see Results and discussion).

The provenance study was based on finding such a group of elements as would be decisive in distinguishing various geological source, hence a large group of elements was investigated. Where possible, several isotopes were measured for each element to detect potential spectral interferences. Signals of ${}^{7}\text{Li}^{+}$, ${}^{9}\text{Be}^{+}$, ${}^{23}\text{Na}^{+}$, ${}^{24,26}\text{Mg}^{+}$, ${}^{27}\text{Al}^{+}$, ${}^{28,29,30}\text{Si}^{+}$, ${}^{31}\text{P}^{+}$, ${}^{39}\text{K}^{+}$, ${}^{43,44}\text{Ca}^{+}$, ${}^{45}\text{Sc}^{+}$, ${}^{47,49}\text{Ti}^{+}$, ${}^{51}\text{V}^{+}$, ${}^{52}\text{Cr}^{+}$, ${}^{55}\text{Mn}^{+}$, ${}^{56,57}\text{Fe}^{+}$, ${}^{60}\text{Ni}^{+}$, ${}^{63}\text{Cu}^{+}$, ${}^{66}\text{Zn}^{+}$, ${}^{75}\text{As}^{+}$, ${}^{85}\text{Rb}^{+}$, ${}^{86,88}\text{Sr}^{+}$, ${}^{89}\text{Y}^{+}$, ${}^{90}\text{Zr}^{+}$, ${}^{93}\text{Nb}^{+}$, ${}^{118,120}\text{Sn}^{+}$, ${}^{121}\text{Sb}^{+}$, ${}^{133}\text{Cs}^{+}$, ${}^{135,137}\text{Ba}^{+}$, ${}^{139}\text{La}^{+}$, ${}^{140}\text{Ce}^{+}$, ${}^{141}\text{Pr}^{+}$, ${}^{142,144,146}\text{Nd}^{+}$, ${}^{147}\text{Sm}^{+}$, ${}^{153}\text{Eu}^{+}$, ${}^{155,157}\text{Gd}^{+}$, ${}^{159}\text{Tb}^{+}$,

Table 1. Obsidian samples of geological (geo) and archaeological (archeo) origin analysed using LA-ICP-MS

Sample	Locality	Country	Region	Origin
1	Březník	Czech	Moravia	archeo
2	Mor. Bránice	Czech	Moravia	archeo
3	Prštice	Czech	Moravia	archeo
4	Žebětín D	Czech	Moravia	archeo
5	Těšetice	Czech	Moravia	archeo
6	Spytlhnev	Czech	Moravia	archeo
7	Rozdrojovice	Czech	Moravia	archeo
8	Jaroměřice	Czech	Moravia	archeo
9	Žebětín KB	Czech	Moravia	archeo
10	Horákov	Czech	Moravia	archeo
11	Těšetice	Czech	Moravia	archeo
12	Nová Dědina	Czech	Moravia	archeo
14	Kašov	Slovakia	SE Slovakia	archeo
15	Kašov	Slovakia	SE Slovakia	archeo
16	Malá Bara	Slovakia	SE Slovakia	geo
17	Barca	Slovakia	SE Slovakia	geo
18	Viničky	Slovakia	SE Slovakia	geo
19	Brehov	Slovakia	SE Slovakia	archeo
20	Slivník	Slovakia	SE Slovakia	archeo
21	Slančík	Slovakia	SE Slovakia	archeo
22	Kašov	Slovakia	SE Slovakia	archeo
23	unknown	Mexico	—	geo
24	Sebaco	Nicaragua	Matagalpa	archeo
25	Somoto 368	Nicaragua	Madriz	archeo
26	Somoto AQ	Nicaragua	Madriz	archeo
27	Tell Arbid	Syria	NE Syria	archeo
28	Tell Arbid	Syria	NE Syria	archeo
29	Tell Arbid	Syria	NE Syria	archeo
30	Tell Asmar	Iraq	Cent. Iraq	archeo
31	Tell Asmar	Iraq	Cent. Iraq	archeo
32	La Castagne	Italy	Lipari	archeo
33	Alatepe I	Turkey	SE Anatolia	geo
34	Alatepe III	Turkey	SE Anatolia	geo
35	Kömürçü I	Turkey	Cappadocia	geo
36	Kömürçü II	Turkey	Cappadocia	geo
37	Bözkoy	Turkey	Cappadocia	geo
38	Çavuşlar III	Turkey	SE Anatolia	geo
39	Pasinler II	Turkey	NE Anatolia	geo
40	Baclama	Turkey	Cappadocia	geo
41	Serinbayrir	Turkey	SE Anatolia	geo
42	Olaszliszka	Hungary	NE Hungary	geo
43	Mád	Hungary	NE Hungary	geo
44	Rokosovo	Ukraine	—	geo
45	Nisyros	Greece	—	geo
46	Milos	Greece	—	geo

SE – South-Eastern; NE – North-Eastern.

${}^{163}\text{Dy}^{+}$, ${}^{165}\text{Ho}^{+}$, ${}^{166}\text{Er}^{+}$, ${}^{169}\text{Tm}^{+}$, ${}^{172}\text{Yb}^{+}$, ${}^{175}\text{Lu}^{+}$, ${}^{178,179}\text{Hf}^{+}$, ${}^{181}\text{Ta}^{+}$, ${}^{197}\text{Au}^{+}$, ${}^{202}\text{Hg}^{+}$, ${}^{205}\text{Tl}^{+}$, ${}^{206,208}\text{Pb}^{+}$, ${}^{232}\text{Th}^{+}$, ${}^{238}\text{U}^{+}$ isotopes were measured. Elemental contents were quantified using calibration with standard reference materials (SRM) NIST 612 and NIST 610.

LA-ICP-TOF-MS

Laser ablation settings for the TOF analyses were similar to those used for the Q-MS analyses, except that the spot size was $75\text{ }\mu\text{m}$. The ICP-MS used was a

GBC Optimass 8000 ICP-TOF-MS. Signal intensities for the selected analytes were collected in five one-second integrations, each of which recorded the results of 30000 push-outs. A sample uptake time of eight seconds preceded collection of the signal intensities. The carrier gas flow-rate ($1.1\text{--}1.3 \text{ L min}^{-1}$ He) and the torch position were optimised at the beginning of each shift using NIST SRM 612. Standards (NIST 612, NIST 610, NIST 614 and NIST GB) were run approximately every half hour over the course of the analysis.

Data analysis

Data analysis was performed using the freely available R statistical software (<http://cran.r-project.org/>; Reimann et al., 2008), commonly used in geochemical data analyses.

Principal component analysis (PCA) is commonly used in archaeometry (Peisach et al., 1982; Baxter, 2006). For calculation, R-library *rrcov* was used. Because logarithmic transformation is not suitable for obtaining multivariate normality (Reimann et al., 2002), multivariate Box–Cox transformation (Velilla, 1993; Venables & Ripley, 2002) was used (R-library MASS). The number of dimensions can be estimated using the scree plot.

A variant of correspondence analysis (CA) for continuous data with column mean normalisation (Underhill & Peisach, 1985) was applied to the data visualisation. For calculation, the R-library *anacor* was used. The number of dimensions can be estimated using the scree plot, as in PCA. This approach was also used in previous provenance studies of archaeological artefacts (e.g. Bollong et al., 1997; Punyadeera et al., 1997).

Independent component analysis (ICA) is a computational method for separating a multivariate signal into additive subcomponents by a linear transformation that minimises their statistical dependence (Baxter, 2006; Venables & Ripley, 2002; Hyvärinen & Oja, 2000). In the context of ICA computation, R-library *fastICA* was used. ICA is a general and robust approach in comparison with PCA, but the interpretation of results is more difficult (Baxter, 2006).

Multi-dimensional scaling (principal coordinate analysis) (MDS) seeks a structure in a set of distance measures between objects or cases. For this purpose, Euclidean distance calculated from autoscaled data is commonly used. The high-dimensional distance matrix is transformed to a space of lower dimensionality while preserving the structure of inter-point distances (Baxter, 2006; Venables & Ripley, 2002; Bollong et al., 1997). An optimal number of dimensions is determined, using the plot of the calculated loss function (stress) versus the number of dimensions. For the calculation, R-library *smacof* was used.

Sammon mapping (SM) (Venables & Ripley, 2002;

Sammon, 1969; Kowalski et al., 1972) is a generalised variant of MDS, which employs non-linear transformation for the dimensions reduction of the distance matrix. The results of MDS are often used as input values for calculating the Sammon projection. For determining the optimal number of dimensions, the plot of the calculated Sammon stress versus the number of dimensions was employed. The calculation in R software was made using the MASS library.

Cluster analysis methods are also frequently used in archaeometry. Hierarchical cluster analysis was employed in this study; the most suitable method of clustering was chosen using cophenetic correlation (Lessig, 1972) between dendograms and the original distance matrix. On the other hand, the hierarchical clustering methods in common use were not suitable because of the assumed spherical shape of clusters (Baxter, 2006). Hence, the fuzzy c-means method, an extension of non-hierarchical k-means cluster analysis (R-library *e1071*; Baxter, 2009), was chosen for cluster evaluation. Unlike in “hard” clustering methods, where each object is assigned to one cluster, in fuzzy clustering the image of each object is, more or less, distributed in the various clusters via the value of the membership function. The optimal number of clusters for all the cluster analysis methods used was calculated using the criteria included in R-libraries *clValid* and *NbClust*.

Results and discussion

Laser beam – volcanic glass interaction

The first step in development of the LA-ICP-MS method consisted of minimising the effect of sample surface roughness on signal intensity and its time-dependence. The roughness of the sample surface makes it difficult to focus the laser beam onto the entire area investigated at the selected diameter, resulting in ablation of a small amount of material and decrease in the isotopic signal. Bulges on the sample surface reduce the distance between the laser-focusing objective and the particular bulge. The laser beam is defocused, the fluence on the bulge spot is decreased and the ablated amount of the sample and, consequently, the MS isotopic signal measured are lower. As a result of this, the underestimated elemental contents are calculated. It is possible that improper selection of laser parameters, such as the diameter of the laser beam, laser beam fluence, laser repetition rate and dwell time of laser ablation may cause an unwanted time-dependent decrease in signal intensity. The above laser parameters were optimised on the untreated (rough) surface of the raw material originating from Slovakia (Viničky) using Q-MS. The laser spot diameter of $100 \mu\text{m}$ and fluence of 5.0 J cm^{-2} were found to be optimal for the analysis of specimens with uneven surfaces, i. e. artefacts, and they were employed throughout this work. The repetition rate

was largely selected in respect of a satisfactory LOD which is generally improved by increasing the ablated mass. The LOD represents one of the most important provenance study parameters as the major and quite often the minor elements do not provide adequate information on variability in the elemental composition of obsidians from various archaeological sites and raw material deposits. On the other hand, a certain signal instability results from the higher repetition rate. Optimisation yielded the laser repetition frequency of 20 Hz as a compromise value ensuring acceptable limits of detection and minimum signal drop at the same time. The magnitude of the signal intensity fluctuation varies from isotope to isotope. Fig. 1a shows that the signal versus time dependence of selected isotopes, which could play an important role in the provenance study ($^{93}\text{Nb}^+$, $^{153}\text{Eu}^+$ and $^{175}\text{Lu}^+$), exhibits only a moderate decrease with acceptable short-term fluctuations. The time-integrated signals of the laser ablation sampling performed at five points randomly distributed over the target area represent the variability in elemental content over the sample surface. Signal fluctuations within an individual sampling experiment at each point indicate the degree of stability afforded by the experimental conditions, the sample surface roughness, and, last but not least, by the microinhomogeneity within the ablated volume. The relative combined standard uncertainty of signal obtained on minor and detectable trace contents ranged from 3 % to 16 % with a median value of 12 %. This uncertainty was measured on the basis of a group of 117 time-averaged values obtained at five different locations on the untreated sample surface. The evidence of the microinhomogeneity contribution to signal fluctuations both within a single spot ablation event and between individual ablation pits derives from Fig. 1b where a volcanic glass raw material from the Viničky region in Slovakia exhibits a distinct microstructure. The light minerals represent feldspar, the brownish phase corresponds to biotite and the capillary crystallites are composed of trichite. Clearly, this inhomogeneity applies to the whole volume of a particular ablation pit. Individual mineral grains/phases exhibit dimensions in the range of 30–100 μm which is comparable with the laser spot diameter of 100 μm and results in short-term fluctuations observed in the signal.

The TOF-MS instrument was used to confirm the applicability of the Q-MS to the provenance study. The reason for this comparison consists in faster data acquisition by TOF-MS, which is better suited to the simultaneous measurement of multiple transient signals.

The comparison of results obtained using TOF and Q mass spectrometers is shown in Fig. 2. The obsidian raw material sample from a geological source in Turkey (Bozköy) was used in this comparative test without any surface treatment. Analyses using TOF-MS were performed under the same laser experimen-

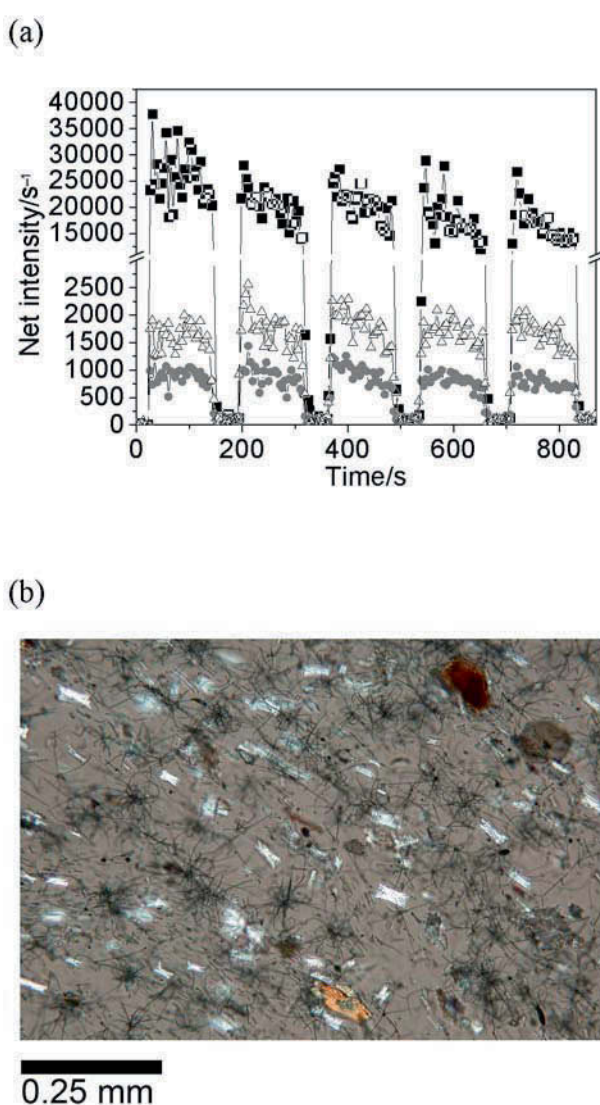


Fig. 1. Stability of selected isotopic signals (^{93}Nb (■), ^{153}Eu (●), ^{175}Lu (Δ)) during ablation of volcanic glass raw material from Viničky region in Slovakia obtained by means of NWR UP213 using laser beam diameter of 100 μm , frequency of 20 Hz and 5.0 J cm^{-2} fluence and detected by Q-MS (a); image of thin section through sample obtained using polarising microscope (b).

tal conditions as for Q-MS with the sole exception of the laser spot diameter, which was reduced from 100 μm to 75 μm due to the greater sensitivity of the TOF mass spectrometer than the Q-MS. Fig. 2 clearly shows that both analysers provided similar elemental contents at trace levels despite the existing obsidian microinhomogeneity which is included into the standard deviation (SD) of laser ablation. Each of the contents determined is well above the LOD of a particular element. The LODs, marked within each column, were estimated on the basis of background fluctuation. The third column represents the bulk elemental content determined in Acme Analytical Laboratories Ltd., Vancouver, Canada (ACME). Consequently, both types

Table 2. Comparison of contents of oxides (C) determined by LA-ICP-TOF-MS on polished and untreated raw obsidian from Bozköy locality with results obtained from ACME.

Oxide	LA-ICP-TOF-MS		C^c /mass %
	C^a /mass %	C^b /mass %	
SiO_2	75.55 ± 0.16	74.3 ± 2.6	76.38
Al_2O_3	14.03 ± 0.33	13.57 ± 0.63	12.86
K_2O	5.13 ± 0.26	5.9 ± 1.4	4.52
Na_2O	4.25 ± 0.39	4.54 ± 0.82	4.08
Fe_2O_3	0.69 ± 0.12	0.80 ± 0.24	0.92
TiO_2	0.0617 ± 0.0028	0.074 ± 0.012	0.07
MgO	0.0366 ± 0.0030	0.043 ± 0.014	0.06
MnO	0.0394 ± 0.0031	0.049 ± 0.013	0.06
Sum	99.80 ± 0.54	99.2 ± 2.8	98.95

a) Polished sample surface; b) untreated sample surface; c) results from ACME.

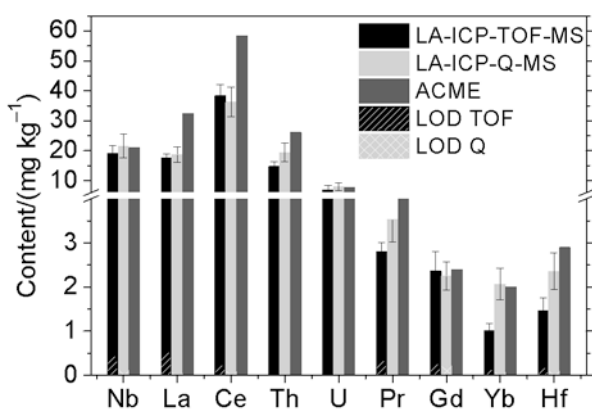


Fig. 2. Comparison of contents of selected trace elements in raw obsidian from Turkey (Bozköy) obtained using TOF-MS and Q-MS equipment and analysed in ACME.

of mass spectrometers are equivalent in terms of their applicability to the analysis of obsidian.

The influence of sample surface roughness on the analytical results was also investigated. The test was performed on the raw material sample from a geological source in Turkey (Bozköy) using the time-of-flight analyser. For this purpose, the sample was cut into two pieces and the surface of one piece was polished. The oxide contents of major and minor constituents and the corresponding standard deviations calculated using data obtained from ablation experiments performed at five points ($n = 5$) uniformly distributed over the polished and untreated surfaces examined are shown in Table 2. The third column displays the bulk elemental contents determined in ACME. The results obtained by ablation of an untreated surface were subjected to accuracy t -test ($t = |(X - \mu)| / (s / \sqrt{n})$) in respect of the ACME results (μ), where X is the sample mean of the data, n is the number of samples (5), and (s / \sqrt{n}) is the sample standard deviation of the sample mean X . The accuracy testing of

the LA-ICP-MS results acquired from the untreated sample surface and the ACME results indicates that the differences between contents values are not statistically significant for all the oxides in Table 2. Although the oxide contents achieved by microsampling polished surfaces appear to be consistent with the results from the untreated sample and ACME, their low sample standard deviations result in significant differences following from the t -test, except for Na_2O . On the other hand, the low SDs confirm the acceptable homogeneity of volcanic glasses and reveal a minimal influence of the inequality of surface on the analytical result. Nevertheless, the statistical test, based on the $t = |(X_A - X_B)| / \sqrt{(s_A^2 + s_B^2) / (n - 1)}$ equation, where X_A and X_B are the mean values of the oxides contents obtained on the polished and untreated surfaces, s_A and s_B are the standard deviations and n is the number of ablated spots, demonstrates the equality of the results for both surfaces. Although the differences between the contents obtained by ablation of the polished and untreated sample surfaces appear to be high, the Student test confirmed the results as statistically non-significant; however, the calculated value of the t -test was very close to the critical value at a confidence level of 95 %.

Both accuracy and identity were also calculated using i) the Lord u -test, which is appropriate for a low number of measurements and ii) the Moore U -test, which endorses the results of the t -test and, moreover, shows the t -test to be stricter to data treatment.

On the basis of the results presented here, it may be concluded that the artefacts can be analysed without any surface treatment, but the spot where the laser microsampling is to be performed has to be carefully selected and analysed under optimised laser operating conditions which make it possible to achieve a stable signal of isotopes. Although higher standard deviations are obtained as the untreated surface is investigated, the artefact's origin can be established because the differences in the elemental and/or oxides contents between localities showed a higher variability.

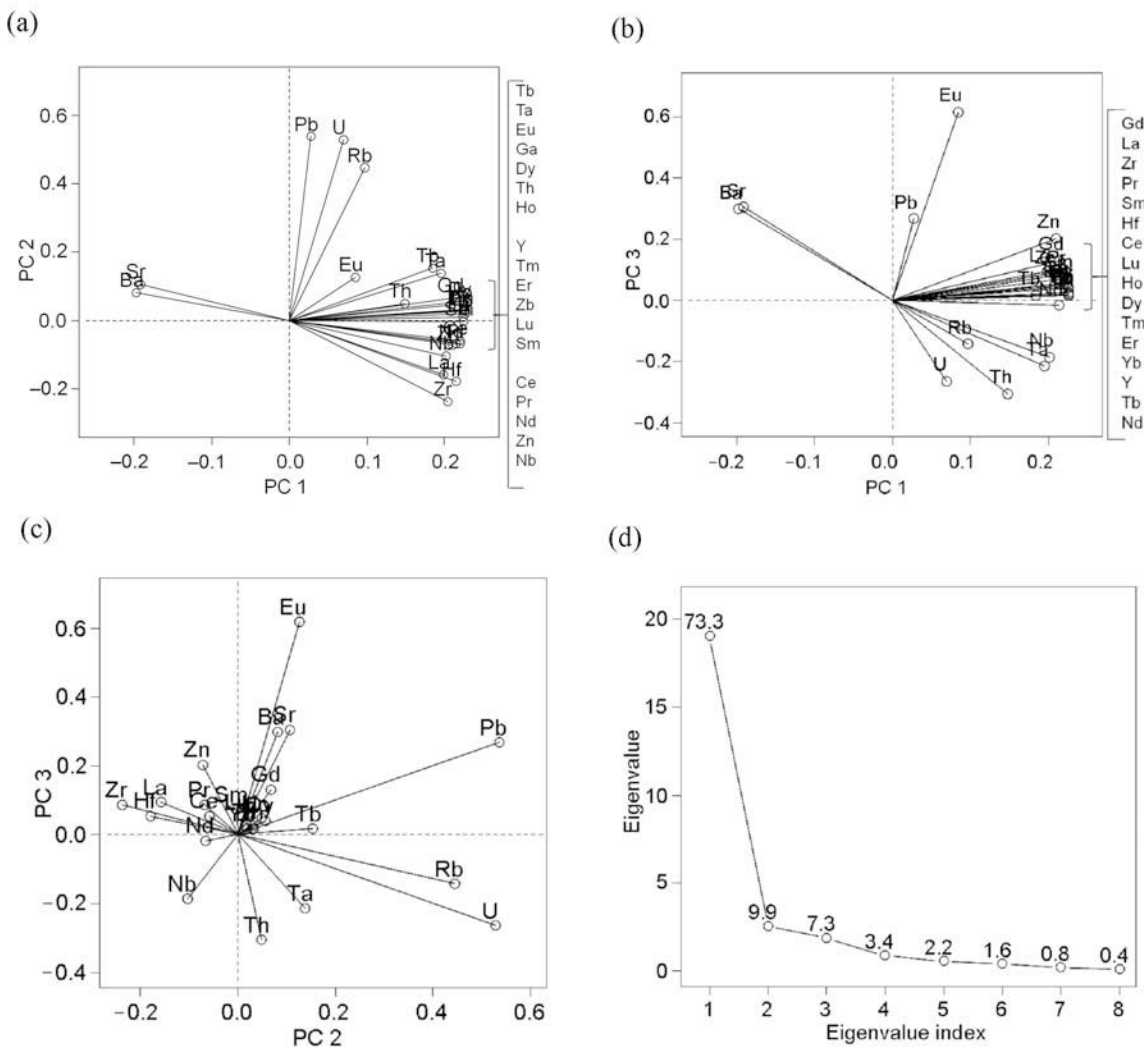


Fig. 3. Loadings plots (a)–(c) and scree plot (d) for three calculated PCs.

Multivariate data analysis and interpretation of results

Principal component analysis (PCA)

The singular value decomposition of the Box-Cox transformed and autoscaled data matrix was used for PCs calculation. Using the scree plot, two PCs (73.3 % and 9.9 % of total variance) were significant (Fig. 3d).

Loading plots between PC 1, PC 2 and PC 3 (Figs. 3a–3c) were used to visualise the dependence between various elements. The strong angles in these plots indicate a close positive correlation between Sr and Ba and between some REE and a negative correlation between Sr and Ba versus Zr and REE. These elements are described with PC 1, in particular. Independence between Sr/Ba or Zr/REE and Pb/Rb/U was also observed (Fig. 3a) due to the correlation of Rb, Pb and U with PC 2. PC 3 relates especially to Pb, Eu and U, Th.

Looking at the score plots of the first three PCAs

(Figs. 4a–4c), some interesting patterns of the sample points are visible. The first principal component (PC1) separates the Mexican, Syrian, Iraqi and some South-Eastern Anatolia samples (Çavuşlar, Serinbayır) from the other samples. Considering the PCA loadings, this is due to the high content of REE and Zr, especially. Accordingly, these Anatolian samples may be preliminarily classified as per-alkaline obsidians (Chataigner et al. 1998; Gratuze, 1999). The similar composition of the Syrian and Iraqi obsidian artefact samples indicates their South-Eastern Anatolia provenance, probably from Bingöl A or Nemrut Dağ provinces. The second principal component (PC 2) separates the Nicaragua and Greece samples; the Carpathian and Cappadocia samples are in a partial superposition. Because PC 1–2 in the score plot (Fig. 4a) was not able to separate the Cappadocia and Central European sample points, PC 3 (7.3 % of total variance) was also included in the data analysis (Figs. 4b, 4c). The third principal component (PC 3) makes it possible to separate the Cappadocia, Lipari

and Pasinler (North-Eastern Anatolia) samples from the Carpathian and the other Anatolian samples (according to their U, Th, Rb and Pb contents). The points of the obsidian samples from Alatepe (South-Eastern Anatolia) are situated close to the Central European samples; this is due to the high Sr and Ba contents and lower REE and Zr contents in comparison with the other South-Eastern Anatolia samples (Cavuslar, Serinbayir). The samples may then be classified as calc-alkaline obsidians of the Bingöl B group (Chataigner et al. 1998; Gratuze, 1999). The samples of obsidian artefacts from Moravia (Czech Republic) are in superposition with the Slovak and Hungarian samples. Hence the Carpathian origin of these obsidians is proved.

Correspondence analysis (CA)

The results of CA (Figs. 5a–5c) have an interpretation similar to the PCA results (Figs. 3a–3c and Figs. 4a–4c). Using the scree plot (Fig. 5d), two dimensions (65.5 % and 14.4 % of total inertia) or three dimensions (65.5 %, 14.4 % and 6.5 % of the total inertia) were found to be sufficient for data representation in the CA. In the interpretation of the sample clusters in the CA plots (Figs. 5a–5c), the positions of the trace element points according to the main dimension axes in the CA plot must be taken into account, as in the PCA loadings plots.

For efficient separation of some sample point clusters, just two main dimensions are sufficient (Fig. 5a): separation of Nicaraguan samples due to their high Sr and Ba contents, the per-alkaline Near East obsidians and the Mexican sample due to their high Zr and REE, separation of Lipari, Cappadocia and Pasinler (North-Eastern Anatolia) samples. The third dimension is not significant for the results interpretation (Figs. 5b, 5c). The Central European (Moravian, Slovak and Hungarian) samples are concentrated in one cluster, due to their close similarity.

Multivariate visualisation techniques

Independent component analysis (ICA)

For the ICA calculation using autoscaled raw data, the number of three ICA was chosen as optimal for the best separation of the sample points clusters. The sample point clusters in the ICA plots (Figs. 6a, 6b) are related to those in the PCA score plots, but better separation was obtained using ICA. The Anatolian samples are separated into three clusters: Cappadocian and North-Eastern Anatolian samples, Alatepe samples (South-Eastern Anatolian calc-alkaline obsidians) and the remaining South-Eastern Anatolian samples (South-Eastern Anatolian per-alkaline obsidians) with the samples from Iraq and Syria.

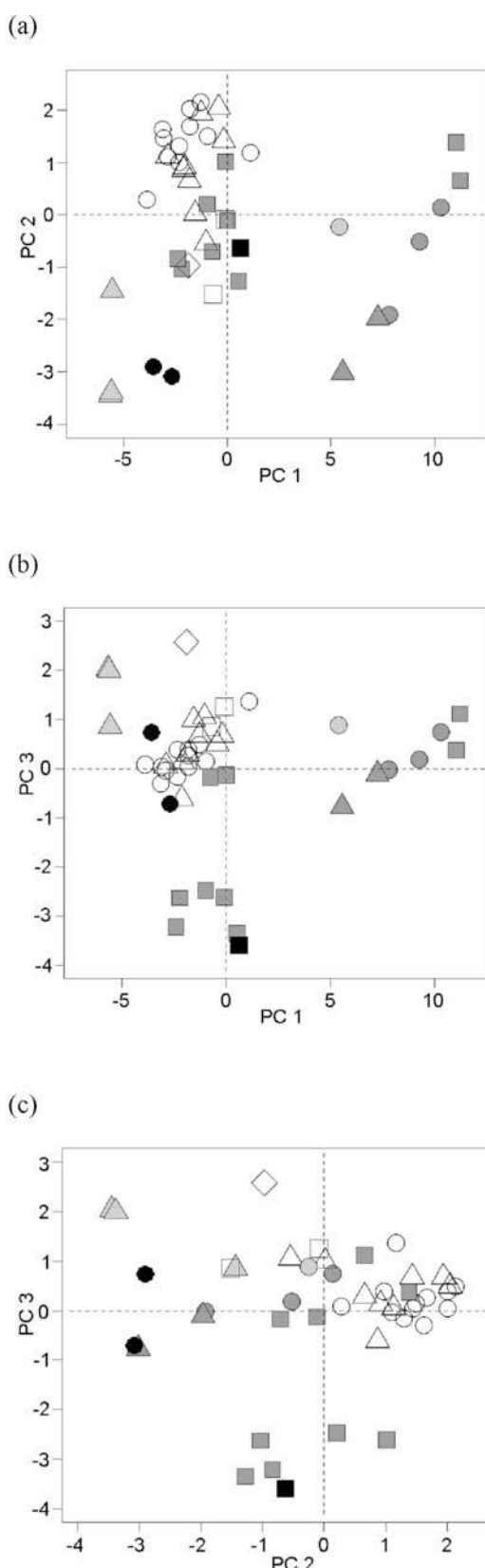


Fig. 4. Score plots (a)–(c) for first three PCAs. Points: Moravia (○), Slovakia (△), Hungary (□), Ukraine (◇), Lipari (●), Greece (■), Syria (●), Iraq (▲), Anatolia (■), Mexico (●), Nicaragua (▲).

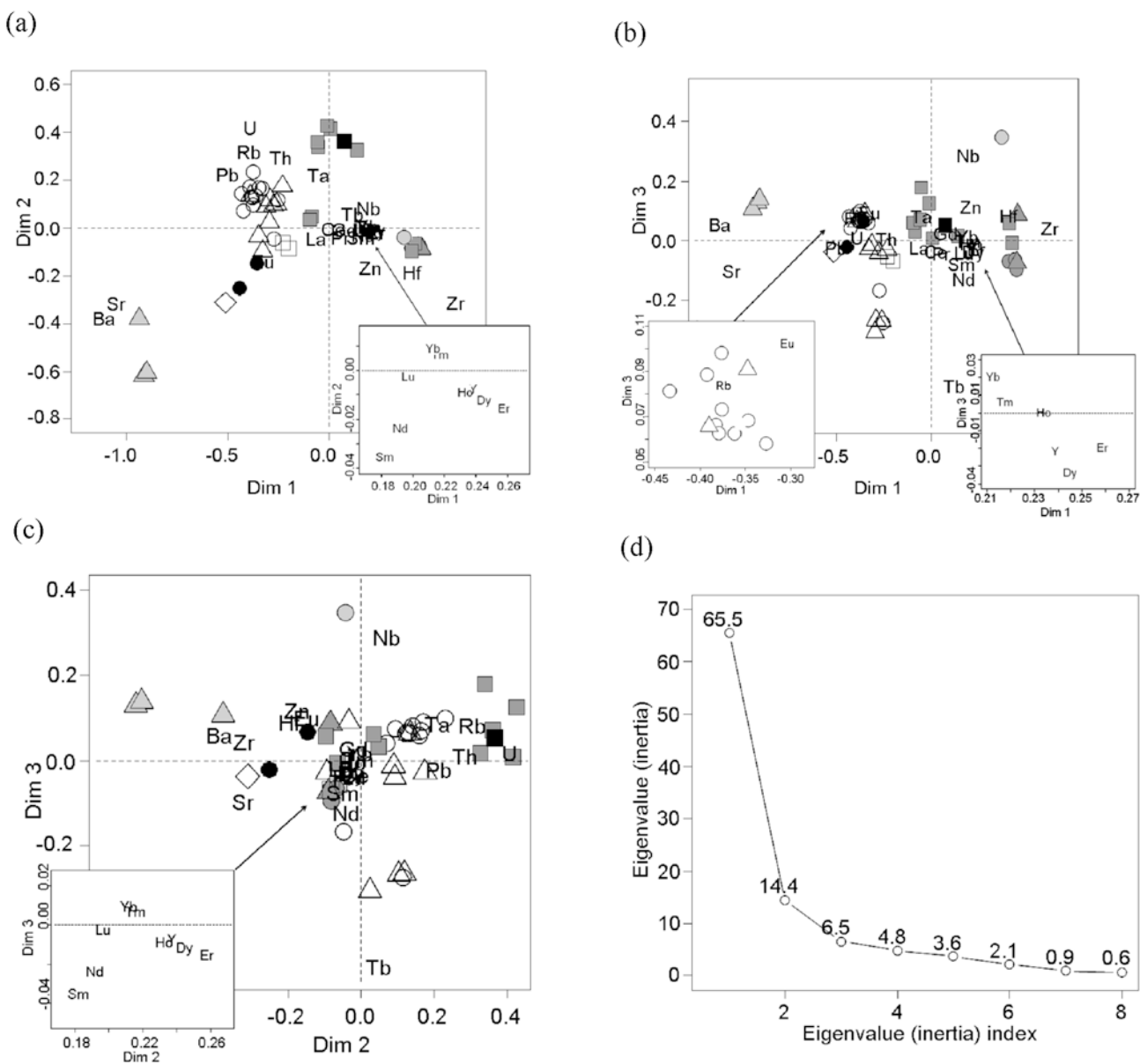


Fig. 5. Results of CA in three main dimensions (a)–(c) and scree plot (d). Points: Moravia (○), Slovakia (△), Hungary (□), Ukraine (◇), Lipari (●), Greece (■), Syria (●), Iraq (▲), Anatolia (■), Mexico (●), Nicaragua (▲).

Multidimensional scaling (MDS)

In MDS, the Euclidean distance of autoscaled data was used for calculating the distance matrix. The plot of stress against the number of dimensions (Fig. 7d) indicates three dimensions as optimal.

Although MDS is based on a different approach to the previous methods, the interpretation of the results is similar. The first two dimensions make it possible to separate the per-alkaline obsidians with the Mexican sample and the Nicaraguan and Greece samples from the other samples (Fig. 8a). The Central European and Cappadocia with Lipari samples are distinguishable according to the third dimension (Figs. 8b, 8c).

Sammon mapping (SM)

In the SM procedure, the Euclidean distance of autoscaled data was used for calculating the distance matrix. The plot of Sammon stress against the number of dimensions (Fig. 8d) indicates three dimensions as optimal.

The plots afforded by the SM procedure (Figs. 8a-8c) are practically identical with the MDS plots (Figs. 7a-7c): the first two dimensions make it possible to separate the per-alkaline obsidians with the Mexican sample and the Nicaraguan and Greece samples from the other samples (Fig. 8a). The Central European and Cappadocia with Lipari samples are distinguishable according to the third

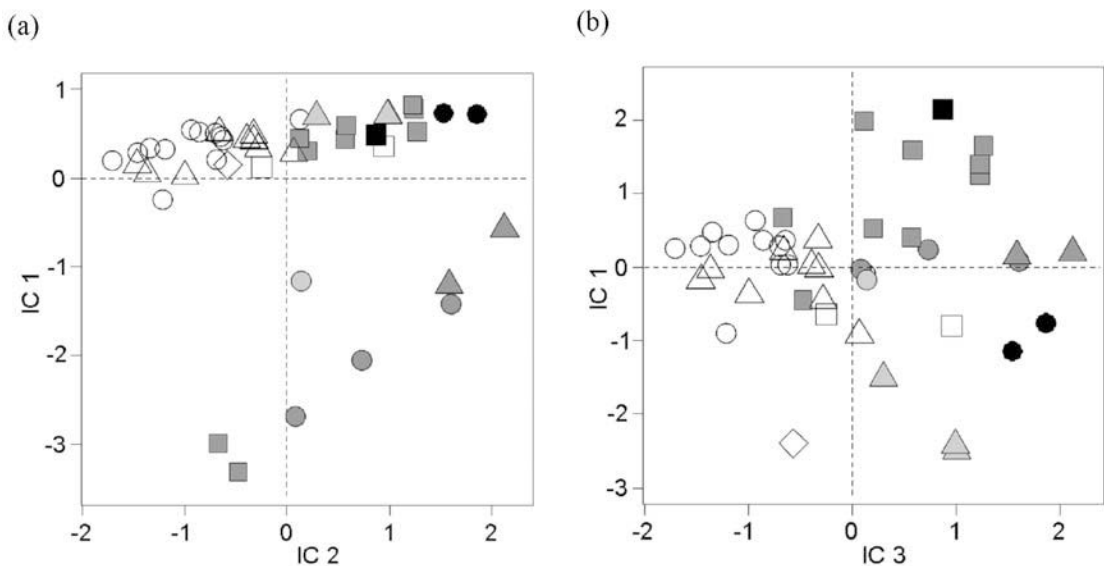


Fig. 6. Plots of IC 1 versus IC 2 (a) and IC 1 versus IC 3 (b) of the data: Points: Moravia (○), Slovakia (△), Hungary (□), Ukraine (◊), Lipari (●), Greece (■), Syria (●), Iraq (▲), Anatolia (■), Mexico (●), Nicaragua (▲).

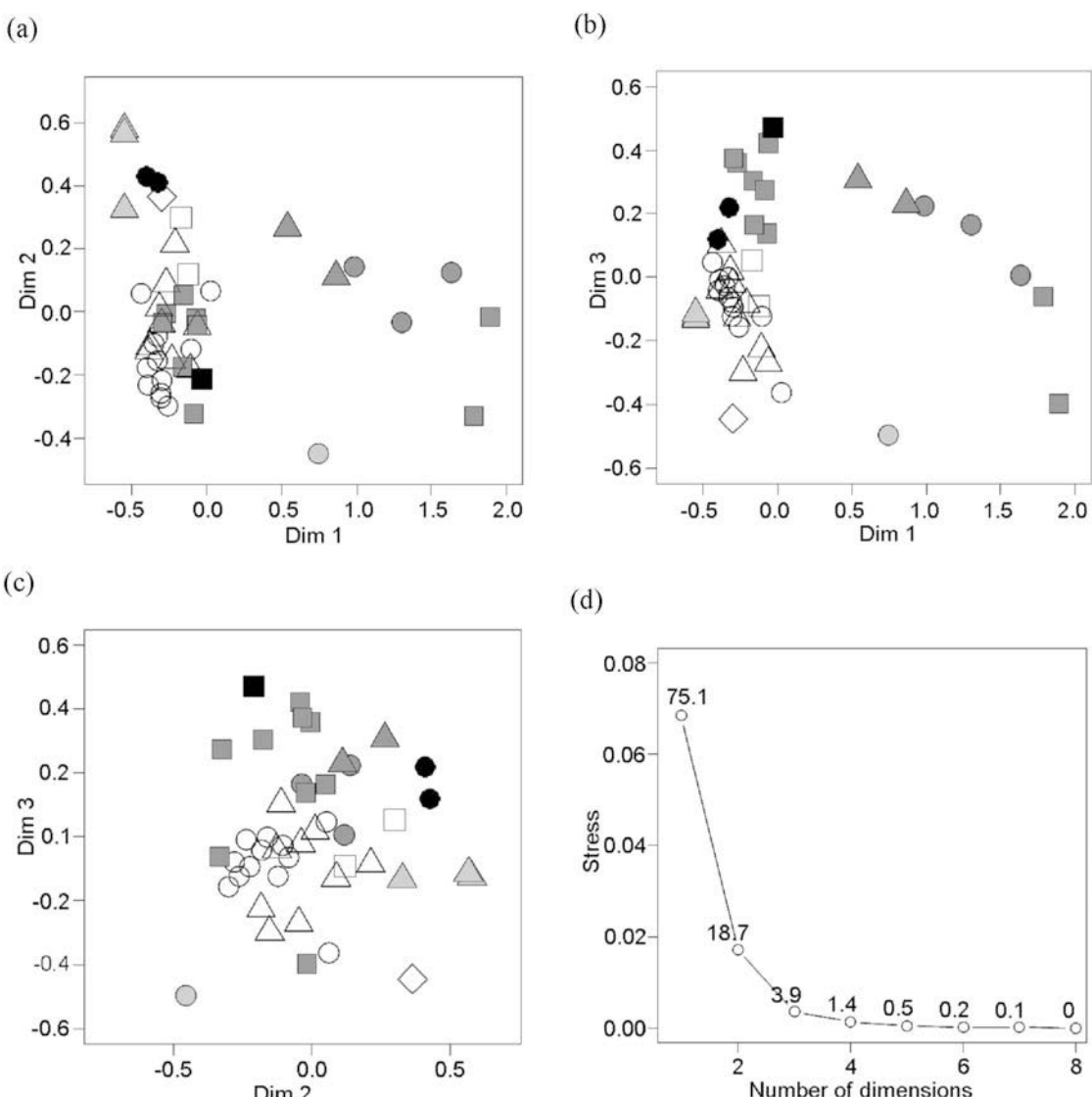


Fig. 7. Plots of dimensions of MDS (a)–(c) and value of stress against number of dimensions (d): Points: Moravia (○), Slovakia (△), Hungary (□), Ukraine (◊), Lipari (●), Greece (■), Syria (●), Iraq (▲), Anatolia (■), Mexico (●), Nicaragua (▲).

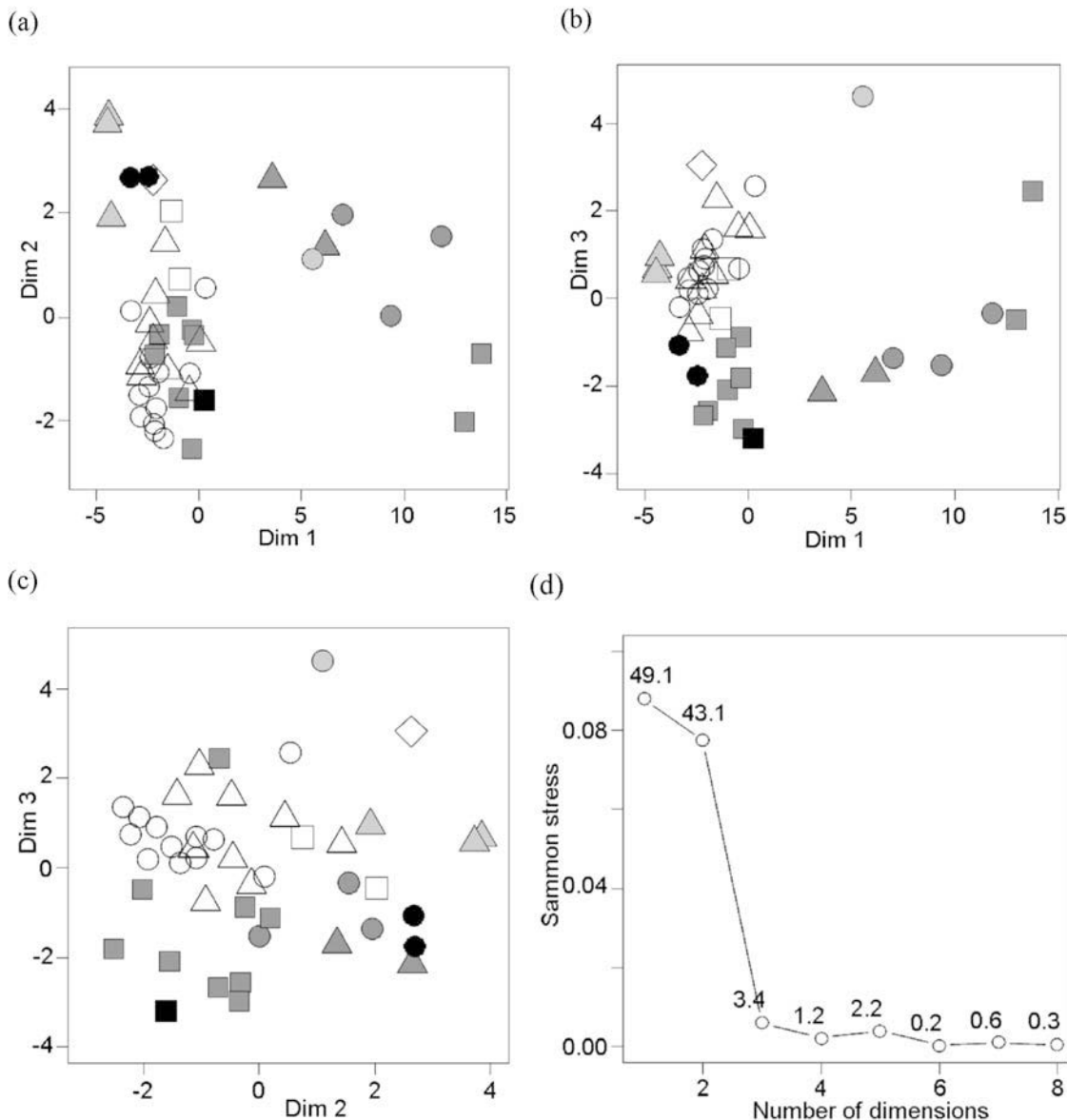


Fig. 8. Plots of dimensions of SM (a)–(c) and Sammon stress against number of dimensions (d). Points: Moravia (○), Slovakia (△), Hungary (□), Ukraine (◇), Lipari (●), Greece (■), Syria (●), Iraq (▲), Anatolia (■), Mexico (●), Nicaragua (▲).

dimension (Figs. 8b, 8c).

Cluster analysis

The hierarchical clustering method was applied to the autoscaled raw data and the scores of PCA and CA. Cluster analysis on the PCA and CA scores is more suitable than clustering on raw data where the correlation structure of the data plays the role. For hierarchical clustering, the Euclidean distance was used and the Ward method was selected as the most suitable according to cophenetic correlation. In all cases, the count of clusters 2, 4 or 6 was estimated according to various criteria. Finally, the count of clusters 4 was defined as optimal.

In the hierarchical clustering of raw data (Fig. 9a),

the Central European samples (Moravia, Slovakia, Hungary, Ukraine) fall into one cluster. In the second cluster, samples from Syria, Iraq and two samples from South-Eastern Anatolia (per-alkaline samples; Çavuşlar and Serinbayırı) are included together with the sample from Mexico. The other two clusters were created from the Nicaragua and Greece samples or the remaining Anatolian samples and the Lipari sample, respectively.

Hierarchical clustering of the PCA scores (Fig. 9b) gives analogical results; only two South-Eastern Anatolian samples (calc-alkaline samples; Alatepe) are included in one cluster with the Central European samples. Moreover, the CA scores classify the samples from Greece into the same cluster (Fig. 9c).

The fuzzy clustering method was applied to the au-

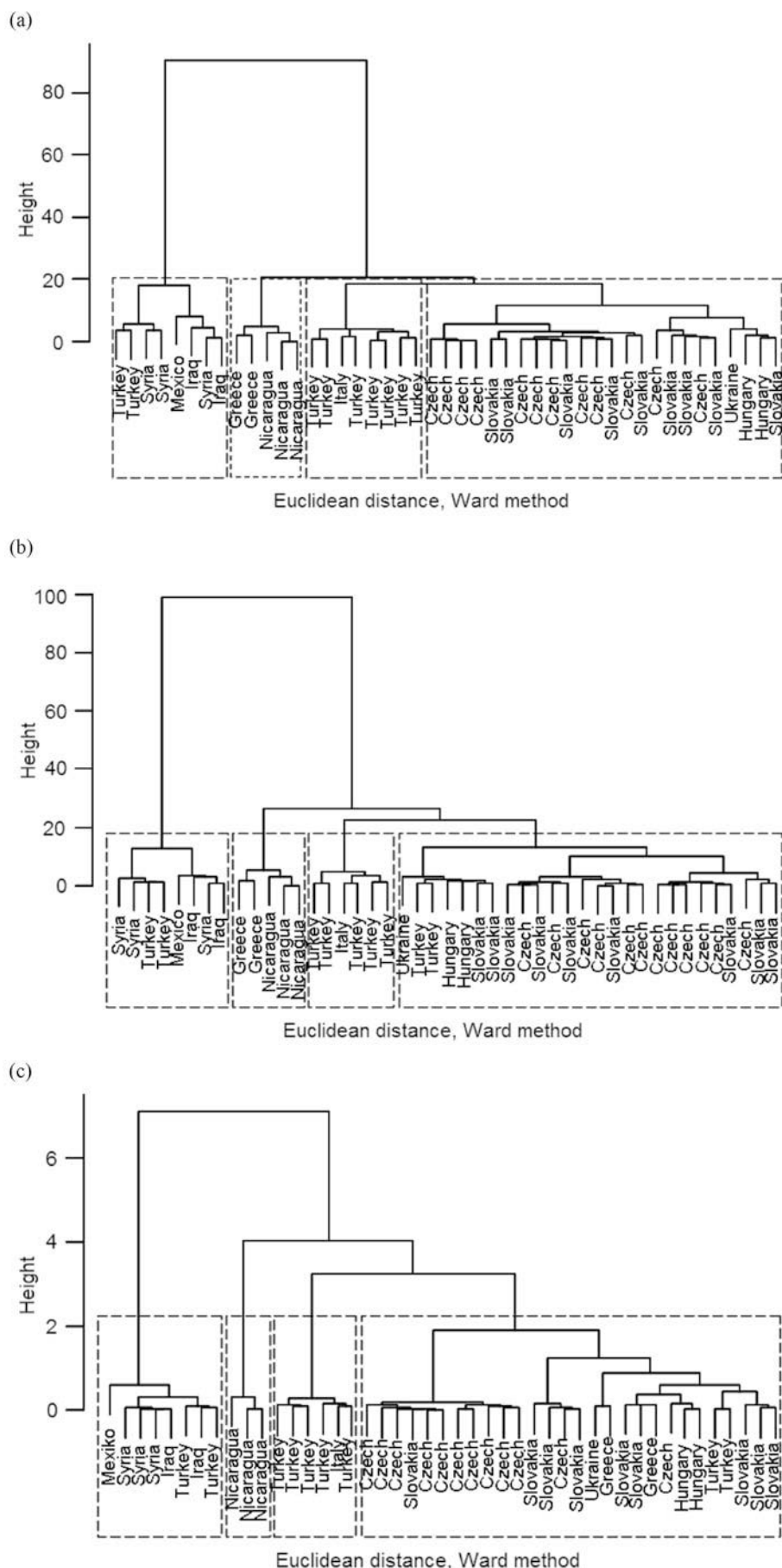


Fig. 9. Results of hierarchical cluster analysis using autoscaled raw data (a), PCA scores (b) and CA scores (c).

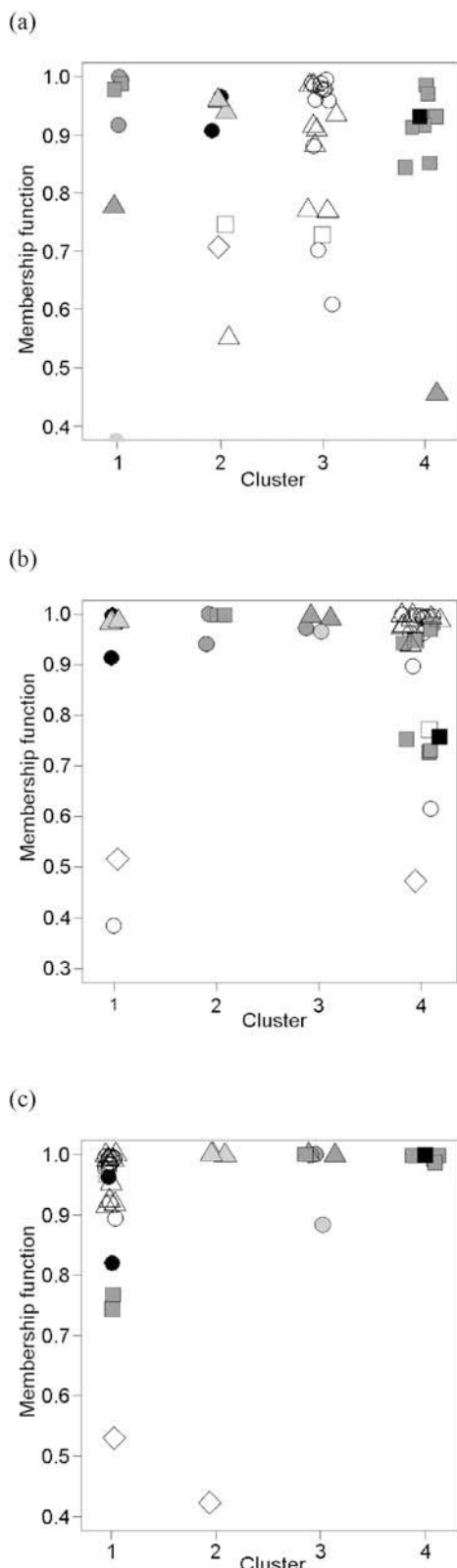


Fig. 10. Results of fuzzy cluster analysis using autoscaled raw data (a), PCA scores (b) and CA scores (c). In all cases, the fuzzification measure $m = 1.5$ was used. Points: Moravia (\circ), Slovakia (Δ), Hungary (\square), Ukraine (\diamond), Lipari (\bullet), Greece (\blacksquare), Syria (\bullet), Iraq (\blacktriangle), Anatolia (\blacksquare), Mexico (\bullet), Nicaragua (\blacktriangle). Sample points are jittered for better resolution.

toscaled raw data and the scores of PCA and CA. As in the SM and hierarchical clustering, the Euclidean distance was used. The coefficient of fuzzification (m) was 1.5 and 2, respectively, in accordance with the recommendation of Baxter (2009). As in the hierarchical clustering, the number of clusters used was 4 and $m = 1.5$ were selected as optimal (Fig. 10).

In the results of the cluster analysis of the autoscaled raw data, the Central European (Hungary, Moravia and Slovakia) samples are distributed in particular in cluster 1, two Carpathian samples (Slivník and Olaszliszka) are in cluster 2, where samples from Ukraine, Greece and Nicaragua are also included. The per-alkaline samples are included in cluster 3, one sample from Tell Asmar (Iraq) belongs in cluster 4 but the membership coefficient is low (under 0.5). The samples from Lipari (in the Mediterranean, near Italy), Cappadocia, Alatepe (SE Anatolia calc-alkaline obsidians) and North-Eastern Anatolia (Pasinler) are related to cluster 4.

Three PCA scores distribute the Moravian, Slovak and Hungarian samples in one cluster (cluster 4) together with samples from Ukraine and Alatepe (SE Anatolia). Cluster 2 includes only the Nicaraguan and Greek samples. The samples from Lipari, Cappadocia and North-Eastern Anatolia (Pasinler) are present in cluster 3. Cluster 1 contains per-alkaline samples and the sample from Mexico.

Three CA scores separate the Central European samples into one cluster (cluster 1) together with samples from Greece, Ukraine and Alatepe. In cluster 3, Lipari, Cappadocia and Pasinler (NE Anatolia) are present. The Nicaraguan samples were included in cluster 4, and per-alkaline samples together with Mexican sample in cluster 2.

The splitting of samples of the same origin into two clusters (Fig. 10 a) is due to the low number of samples and also the elongated shape of the clusters (for example, compare the shape of the cluster of per-alkaline samples in the PCA score plot (Figs. 4a–4c) and in the CA plot (Figs. 5a–5c)). For the elongated clusters, model-based cluster analysis (Baxter, 2009) is suitable, but it is only usable for data matrices with a high number of samples and a low number of dimensions.

Both clustering methods (hierarchical and fuzzy c-means) give identical results for PCA and CA scores. For the autoscaled raw data, the hierarchical cluster analysis gives better results.

Provenance studies using scatter plots

For differentiation of the Anatolian samples, Gratuze (1999) proposed a combination of the Nb/Zr vs Y/Zr plot and the Sr vs Ba plot. The high apparent Sr and Ba contents in a scatter plot were also used successfully in our previous study of volcanic glasses based on laser-induced breakdown spec-

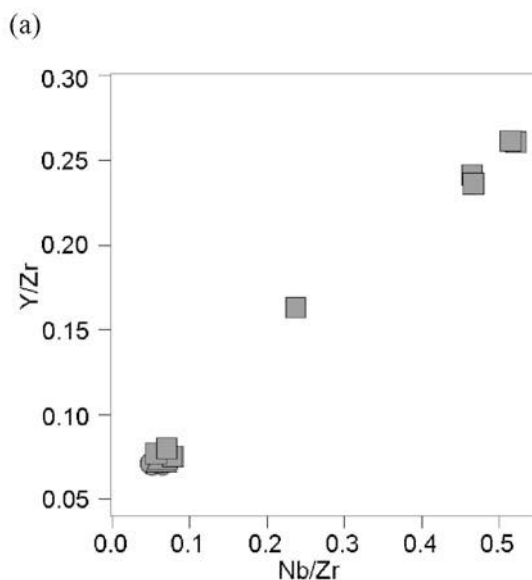


Fig. 11. Y/Zr versus Nb/Zr plot (a) and Ba versus Sr plot (b) of obsidian samples. Only Anatolian and Near East samples are included. Points: Syria (●), Iraq (▲), Anatolia (■).

troscopy (Hrdlička et al., 2013). The Nb/Zr vs the Y/Zr plot is capable of differentiating the main Anatolian obsidian groups according to their geography (Gratuze, 1999; Abbés et al., 2001). The Sr versus Ba plots can distinguish the local obsidian variants (e.g. per- and calc-alkaline SE Anatolian obsidians). The Nb/Zr versus the Y/Zr plot differentiates between three groups of the Anatolian samples: the South-Eastern Anatolian samples in the bottom left corner, the North-Eastern sample (Pasinler) in the central part and the Cappadocia samples in the upper right corner of the plot (Fig. 11a).

Using the Ba versus Sr plot (Fig. 11b), three groups of the Anatolian obsidians were recognised: *i*) ex-

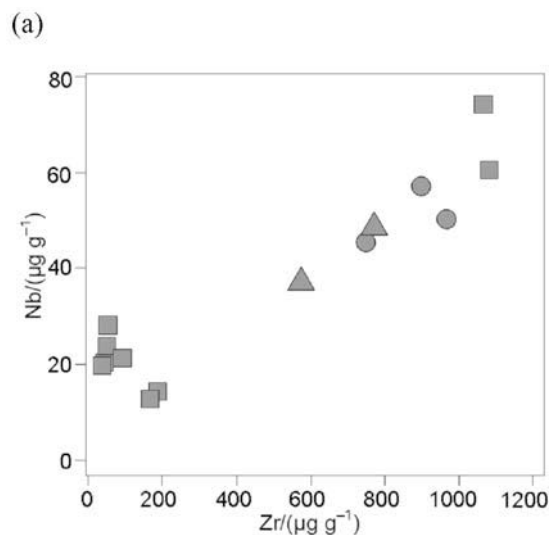


Fig. 12. **Fig. 12.** Zr versus Nb plot (a) and Sr versus Zr (b) of obsidian samples. Only Anatolian and Near East samples are included. Points: Syria (●), Iraq (▲), Anatolia (■).

tremely low Sr and Ba contents were in some South-Eastern Anatolia samples (Çavuşlar, Serinbayır) and North-Eastern Anatolia sample (Pasinler); *ii*) higher Sr and Ba contents were in the Cappadocia samples and *iii*) the richest in Sr and Ba out of the Anatolia samples were the samples from Alatepe (South-Eastern Anatolia).

Instead of scatter plots from the literature, useful combinations of elements for the visualisation of particular obsidian groups may also be found by inspecting the position of the elements in the CA and/or PCA loadings plot with regard to the position of the samples in the particular score plots. For example, the Anatolian obsidians are distributed according to the

PC 1 in PCA or Dim 1 in CA. For effective visualisation of the Anatolian samples, elements from opposite ends of these axes must be used. Besides Zr versus Sr, there can be combinations of Sr or Ba with Zr, Zn, Nb or REE.

Due to the similar behaviour of Zr and Nb, as is also visible in their proximity in the PCA loadings plot (Figs. 3b–3d) and CA plots (Figs. 5a–5c), a correlation pattern is evident in the Zr versus the Nb plot (Fig. 12a). A similar pattern is also present in the Nb/Zr versus Y/Zr plot (Fig. 11a) and the Sr versus Ba plot (Fig. 11b), due to the similar chemical behaviour of Nb and Y versus Sr and Ba, respectively. On the other hand, the absence of any correlation pattern in the Sr versus Zr plot (Fig. 12b) is related to

the antagonistic position of these elements in the PCA loadings plots (Figs. 3b–3d) and CA plots (Figs. 5a–5c).

The samples from Tell Arbid (Syria) and Tell Asmar (Iraq) were identified as per-alkaline obsidians (Bingöl A/Nemrut Dağ). The differentiation of various per-alkaline obsidians (Bingöl A and Nemrut Dağ) is also possible (Frahm, 2012) but was not investigated here due to the small number of available samples. However, among the per-alkaline obsidians imported from Anatolia to the Near East, the Nemrut Dağ obsidians dominate and the Bingöl A obsidians are found only rarely in archaeological obsidian collections, especially as an accessory of Bingöl calc-alkaline obsidians (Chataigner et al., 1998). For accurate con-

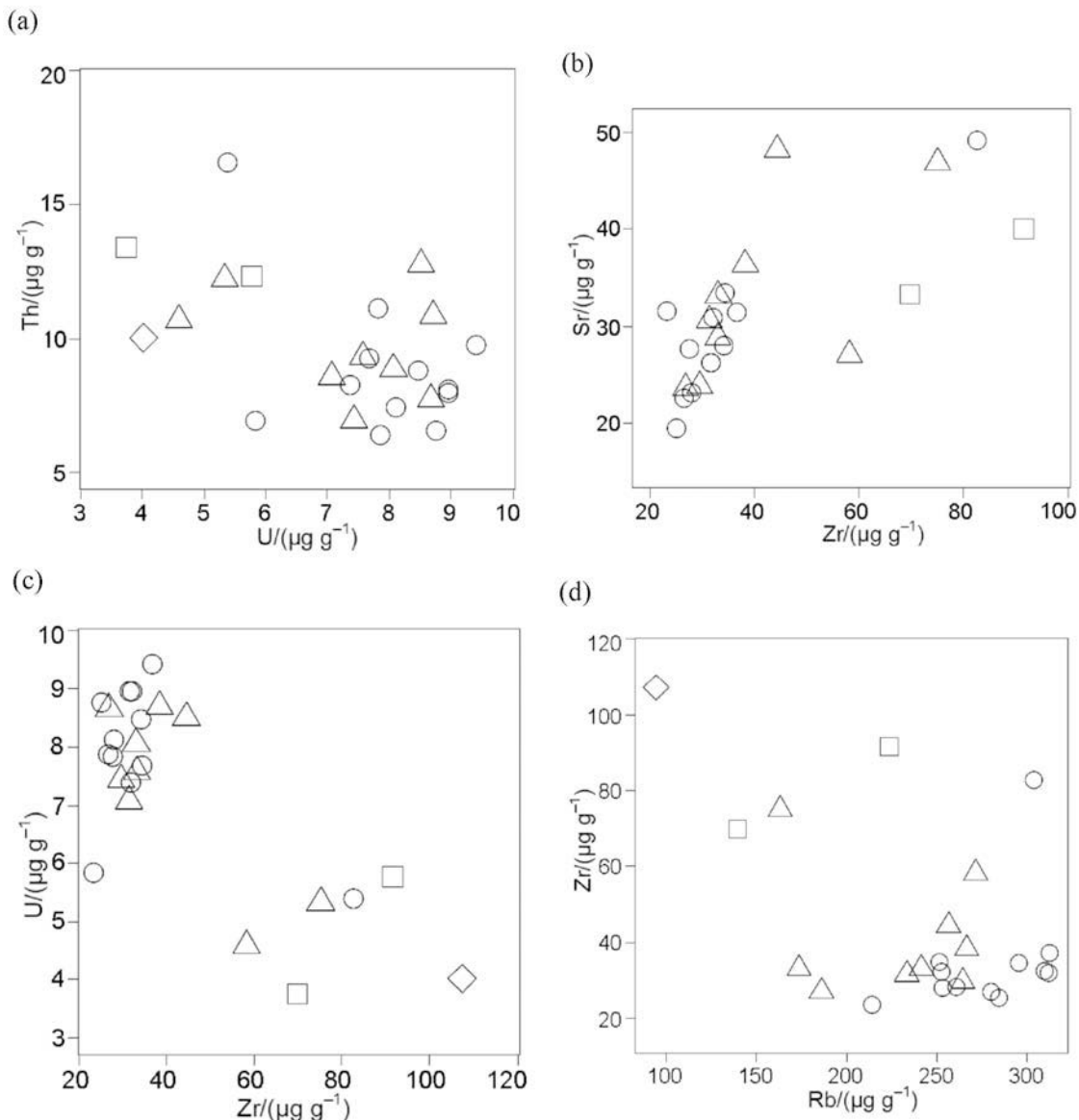


Fig. 13. U versus Th plot (a), Zr versus Sr (b), Zr versus U (c) and Rb versus Zr (d) of obsidian samples. Only Moravian, Slovak and Hungarian samples are included. Points: Moravia (○), Slovakia (△), Hungary (□). Error bars are not visible in plot due to size of symbols.

clusions about obsidian variants' distribution on Tell Arbid and Tell Asmar, many more samples from these localities need to be analysed.

Distinguishing the two main variants of the Carpathian obsidian samples is a topic of interest in archaeological studies; it concerns lithic raw materials exchange and distribution in Central Europe (Williams Thorpe et al., 1984). For this purpose, the U versus Th plot (Fig. 13a) could be useful (Oddone et al., 1999). Other suitable combinations of elements (Figs. 13b–13d) were selected in accordance with the PCA and CA results (Figs. 3 and 5).

According to Figs. 13a–13d, almost all the Moravian (Czech Republic) archaeological samples are included in one cluster with the Slovak samples (both geological and archaeological); these samples fall into the "Carpathian 1" group (South-Eastern Slovakia provenance). The origin of some Moravian Neolithic archaeological obsidian artefacts from sources in South-Eastern Slovakia (Carpathian 1 group) was assigned previously (Williams Thorpe et al., 1984; Zeman & Navrátil, 1987). Only one sample from Moravia (Nová Dědina site, from surface prospection) falls into the second group, which also comprises samples from Hungary, Ukraine and two archaeological samples from Slovakia (Kašov, Slivník). However, the obsidian artefact from the Nová Dědina site related to the Carpathian 2 group (Hungarian origin) is known in the literature (Williams Thorpe et al., 1984).

In Neolithic archaeological finds from Moravia, obsidian of Carpathian 1 type (South-Eastern Slovakia) is dominant, just as in the neighbouring countries. This dominance of obsidian Carpathian 1 type in Moravian archaeological samples is not surprising, in view of the distribution of obsidian types in neighbouring countries. Obsidian of Carpathian 1 dominates in the Neolithic obsidian chipped stone industry in the whole of Central Europe (Biró, 2004), Romania (Transylvania and Banat) (Constantinescu et al. 2002; Biagi et al. 2007; Culicov et al., 2012), Serbia (Tripković & Milić, 2008), Croatia and Bosnia (Kasztovszky et al., 2009). It was found in Macedonia (Mandalo) (Kilikoglou et al., 1996), and probably also in Northern Italy (Sammardechia) (Randle et al., 1993) and East Germany (Zauschwitz and Dresden-Nickern) (Elburg et al., 2002).

Conclusions

The study of obsidians has shown that the quadrupole-based ICP mass spectrometer provides analytical results that are equivalent to those obtained with the ICP-TOF-MS in terms of elemental content and precision. Statistical testing of the elemental contents yielded by ablation of untreated and polished sample surfaces has revealed that the artefacts can be analysed without sample preparation prior to laser ablation. No statistically significant difference has been

demonstrated between LA-ICP-Q-MS and bulk analysis results, which indicates the low impact of the microinhomogeneity presence on the calculated values.

Principal component analysis and correspondence analysis combined with scatter plots and cluster analysis have been proven as efficient tools for the interpretation of multivariate geochemical data on obsidians. Independent component analysis, multi-dimensional scaling and Sammon mapping have been shown to be only supplementary techniques, appropriate for visualisation and classification in this work. Hierarchical and fuzzy c-means cluster analysis can be used for the evaluation of clusters in the data. Using these methods, samples of Tell Arbid and Tell Asmar obsidian artefacts were classified as South-Eastern Anatolian per-alkaline obsidians. In their provenance determination, the content of Sr, Ba, Zr and REE plays a key role. The Moravian artefacts are related to Carpathian obsidian sources (South-Eastern Slovakia, North-Eastern Hungary), from their content of Sr, Ba, Rb, U and Zr.

Acknowledgements. The Czech Ministry of Education, Youth and Sports and the American Science Information Centre, Prague, Czech Republic, are acknowledged for their support of the project of Czech-US Cooperation KONTAKT ME10012. This work was also supported by the European Regional Development Fund project "CEITEC" (CZ.1.05/1.1.00/02.0068). The authors wish to thank M. Kuča for providing some of the obsidian samples.

References

- Abbés, F., Bellot-Gurlet, L., Bressy, C., Cauvin, M. C., Gratuze, B., & Poupeau, G. (2001). Nouvelles recherches sur l'obsidienne de Cheikh Hassan (vallée de l'Euphrate, Syrie) au néolithique: PPNA et PPNB ancien. *Syria*, 78, 5–17. DOI: 10.3406/syria.2001.7727. (in French)
- Baxter, M. J. (2006). A review of supervised and unsupervised pattern recognition in archaeometry. *Archaeometry*, 48, 671–694. DOI: 10.1111/j.1475-4754.2006.00280.x.
- Baxter, M. J. (2009). Archaeological data analysis and fuzzy clustering. *Archaeometry*, 51, 1035–1054. DOI: 10.1111/j.1475-4754.2008.00449.x.
- Biagi, P., de Francesco, A. M., & Bocci, M. (2007). New data on the archaeological obsidian from the Middle-Late Neolithic and Chalcolithic sites of the Banat and Transylvania (Romania). In J. K. Kozłowski, & P. Raczyk (Eds.), *The Lengyel, Polgár and related cultures in the Middle/Late Neolithic in Central Europe* (pp. 309–326). Kraków, Poland: PAAS.
- Biró, K. T. (2004). Carpathian obsidians: Myth and reality. In *Proceedings of the 34th International Symposium on Archaeometry*, May 3–7, 2004 (pp. 267–277). Zaragoza, Spain: C.S.I.C.
- Bollong, C. A., Jacobson, L., Peisach, M., Pineda, C. A., & Sampson, C. G. (1997). Ordination versus clustering of elemental data from PIXE analysis of herder–hunter pottery: a comparison. *Journal of Archaeological Science*, 24, 319–327. DOI: 10.1006/jasc.1996.0116.
- Chataigner, C., Poidevin, J. L., & Arnaud, N. O. (1998). Turkish occurrences of obsidian and use by prehistoric peoples in the Near East from 14,000 to 6000 BP. *Journal of Volcanology and Geothermal Research*, 85, 517–537. DOI: 10.1016/s0377-0273(98)00069-9.

- Constantinescu, B., Bugoi, R., & Sziki, G. (2002). Obsidian provenance studies of Transylvania's Neolithic tools using PIXE, micro-PIXE and XRF. *Nuclear Instruments and Methods in Physics Research B*, 189, 373–377. DOI: 10.1016/s0168-583x(01)01092-8.
- Culicov, O. A., Frontasyeva, M. V., & Daraban, L. (2012). Characterization of obsidian found in Romania by neutron activation method. *Romanian Reports in Physics*, 64, 609–618.
- de Barros, C. E., Nardi, L. V. S., Dillenburg, S. R., Ayup, R., Jarvis, K., & Baitelli, R. (2010). Detrital minerals of modern beach sediments in southern Brazil: A provenance study based on the chemistry of zircon. *Journal of Coastal Research*, 26, 80–93. DOI: 10.2112/06-0817.1.
- Elburg, M., Elburg, R., & Greig, A. (2002). Obsidian in Sachsen und die Verwendung von ICP-MS zur Herkunftsbestimmung von Rohmaterialien. *Arbeits- und Forschungsberichte zur Sächsischen Bodendenkmalpflege*, 44, 391–397. (in German)
- Forster, N., & Grave, P. (2012). Non-destructive PXRF analysis of museum-curated obsidian from the Near East. *Journal of Archaeological Science*, 39, 728–736. DOI: 10.1016/j.jas.2011.11.004.
- Frahm, E. (2012). Distinguishing Nemrut Dağ and Bingöl A obsidians: geochemical and landscape differences and the archaeological implications. *Journal of Archaeological Science*, 39, 1436–1444. DOI: 10.1016/j.jas.2011.12.038.
- Galiová, M., Kaiser, J., Fortes, F. J., Novotný, K., Malina, R., Prokeš, L., Hrdlička, A., Vaculovič, T., Nývltová Fišáková, M., Svoboda, J., Kanický, V., & Laserna, J. J. (2010). Multielemental analysis of prehistoric animal teeth by laser-induced breakdown spectroscopy and laser ablation inductively coupled plasma mass spectrometry. *Applied Optics*, 49, C191–C199. DOI: 10.1364/ao.49.00c191.
- Gholap, D. S., Izmer, A., De Samber, B., van Elteren, J. T., Selih, V. S., Evens, R., De Schamphelaere, K., Janssen, C., Balcaen, L., Lindemann, I., Vincze, L., & Vanhaecke, F. (2010). Comparison of laser ablation-inductively coupled plasma-mass spectrometry and micro-X-ray fluorescence spectrometry for elemental imaging in *Daphnia magna*. *Analytica Chimica Acta*, 664, 19–26. DOI: 10.1016/j.aca.2010.01.052.
- Golitko, M., Meierhoff, J., Feinman, G. M., & Williams, P. R. (2012). Complexities of collapse: the evidence of Maya obsidian as revealed by social network graphical analysis. *Antiquity*, 86, 507–523.
- Gratuze, B. (1999). Obsidian characterization by laser ablation ICP-MS and its application to prehistoric trade in the Mediterranean and the Near East: Sources and distribution of obsidian within the Aegean and Anatolia. *Journal of Archaeological Science*, 26, 869–881. DOI: 10.1006/jasc.1999.0459.
- Hare, D., Austin, C., Doble, P., & Arora, M. (2011). Elemental bio-imaging of trace elements in teeth using laser ablation-inductively coupled plasma-mass spectrometry. *Journal of Dentistry*, 39, 397–403. DOI: 10.1016/j.jdent.2011.03.004.
- Healey, E. (2007). Obsidian as an indicator of inter-regional contacts and exchange: three case-studies from the Halaf period. *Anatolian Studies*, 57, 171–189. DOI: 10.1017/s006615460008590.
- Hrdlička, A., Prokeš, L., Vašinová Galiová, M., Novotný, K., Vitešníková, A., Helešicová, T., & Kanický, V. (2013). Provenance study of volcanic glass with 266–1064 nm orthogonal double pulse laser induced breakdown spectroscopy. *Chemical Papers*, 67, 546–555. DOI: 10.2478/s11696-013-0332-x.
- Hyväriinen, A., & Oja, E. (2000). Independent component analysis: algorithms and applications. *Neural Networks*, 13, 411–430. DOI: 10.1016/s0893-6080(00)00026-5.
- Kasztovszky, Z., Szilágii, V., Biró, K. T., Težak-Gregl, T., Burić, M., Šošić, R., & Szakmány, G. (2009). Horvát és Bosnyák régészeti lelöhelyekről származó obszidián eszközök eredményes PGAA-val. *Archeometriai Műhely*, VI/3, 5–14. (in Hungarian)
- Kilikoglou, V., Bassiakos, Y., Grimanis, A. P., Souvatzis, K., Pilali-Papasteriou, A., & Papanthimou-Papaefthimiou, A. (1996). Carpathian obsidian in Macedonia, Greece. *Journal of Archaeological Science*, 23, 343–349. DOI: 10.1006/jasc.1996.0032.
- Kowalski, B. R., Schatzki, T. F., & Stross, F. H. (1972). Classification of archaeological artifacts by applying pattern recognition to trace element data. *Analytical Chemistry*, 44, 2176–2180. DOI: 10.1021/ac60321a002.
- Lessig, V. P. (1972). Comparing cluster analyses with coprothetic correlation. *Journal of Marketing Research*, 9, 82–84. DOI: 10.2307/3149615.
- Lu, Y., Zhang, Y., Lai, Y., & Wang, Y. (2009). LA-ICPMS zircon U-Pb dating of magmatism and mineralization in the Jinchang gold ore-field, Heilongjiang province. *Acta Petrologica Sinica*, 2009, 2902–2912.
- Novotný, K., Kaiser, J., Galiová, M., Konečná, V., Novotný, J., Malina, R., Liška, M., Kanický, V., & Otruba, V. (2008). Mapping of different structures on large area of granite sample using laser-ablation based analytical techniques, an exploratory study. *Spectrochimica Acta Part B: Atomic Spectroscopy*, 63, 1139–1144. DOI: 10.1016/j.sab.2008.06.011.
- Oddone, M., Márton, P., Bigazzi, G., & Biró, K. T. (1999). Chemical characterisations of Carpathian obsidian sources by instrumental and epithermal neutron activation analysis. *Journal of Radioanalytical and Nuclear Chemistry*, 240, 147–153. DOI: 10.1007/bf02349147.
- Peisach, M., Jacobson, L., Boulle, G. J., Gihwala, D., & Underhill, L. G. (1982). Multivariate analysis of trace elements determined in archaeological materials and its use for characterisation. *Journal of Radioanalytical Chemistry*, 69, 349–364. DOI: 10.1007/bf02515934.
- Přichystal, A. (2013). *Lithic raw materials in prehistoric times of Eastern Central Europe*. Brno, Czech Republic: Masaryk University Press.
- Punyadeera, C., Pillay, A. E., Jacobson, L., & Whitelaw, G. (1997). Application of XRF and correspondence analysis to provenance studies of coastal and inland archaeological pottery from the Mnjeni river area, South Africa. *X-Ray Spectrometry*, 26, 249–256. DOI: 10.1002/(SICI)1097-4539(199709)26:5<249::AID-XRS188>3.0.CO;2-5.
- Randle, K., Barfield, B. H., & Bagolini, B. (1993). Recent Italian obsidian analyses. *Journal of Archaeological Science*, 20, 503–509. DOI: 10.1006/jasc.1993.1031.
- Reimann, C., Filzmoser, P., & Garrett, R. G. (2002). Factor analysis applied to regional geochemical data: problems and possibilities. *Applied Geochemistry*, 17, 185–206. DOI: 10.1016/s0883-2927(01)00066-x.
- Reimann, C., Filzmoser, P., Garrett, R., & Dutter, R. (2008). *Statistical data analysis explained: Applied environmental statistics with R*. Chichester, UK: Wiley.
- Sammon, J. W. (1969). A nonlinear mapping for data structure analysis. *IEEE Transactions on Computers*, C-18, 401–409. DOI: 10.1109/t-c.1969.222678.
- Shackley, M. S. (2005). *Obsidian. Geology and archaeology in the North American Southwest*. Tucson, AZ, USA: University of Arizona Press.
- Tripković, B., & Milić, M. (2008). The origin and exchange of obsidian from Vinča – Belo Brdo. *Starinar*, 58, 71–86. DOI: 10.2298/sta0858071t.
- Tykot, R. H. (2002). Chemical fingerprinting and source tracking of obsidian: The Central Mediterranean trade in black

- gold. *Accounts of Chemical Research*, 35, 618–627. DOI: 10.1021/ar000208p.
- Underhill, L. G., & Peisach, M. (1985). Correspondence analysis and its application in multielemental analysis. *Journal of Trace and Microprobe Techniques*, 3, 41–65.
- Velilla, S. (1993). A note on the multivariate Box–Cox transformation to normality. *Statistica & Probability Letters*, 17, 259–263. DOI: 10.1016/0167-7152(93)90200-3.
- Venables, W. N., & Ripley, B. D. (2002). *Modern applied statistics with S*. New York, NY, USA: Springer.
- Williams Thorpe, O., Warren, S. E., & Nandris, J. G. (1984). The distribution and provenance of archaeological obsidian in central and eastern Europe. *Journal of Archaeological Science*, 11, 183–212. DOI: 10.1016/0305-4403(84)90001-3.
- Wu, B., & Becker, J. S. (2012). Bioimaging of metals in rat brain hippocampus by laser microdissection inductively coupled plasma mass spectrometry (LMD-ICP-MS) using high-efficiency laser ablation chambers. *International Journal of Mass Spectrometry*, 323–324, 34–40. DOI: 10.1016/j.ijms.2012.06.012.
- Zeman, A., & Navrátil, O. (1987). Obsidian artifacts from the Neolithic locality Tešetice in Southern Moravia. In J. Konta (Ed.), *Proceedings of the 2nd International Conference on Natural Glasses* (pp. 177–181). Prague, Czech Republic: Charles University.